

JPRS-EST-92-015

8 MAY 1992



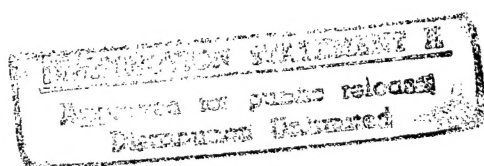
**FOREIGN  
BROADCAST  
INFORMATION  
SERVICE**

# ***JPRS Report***

# **Science & Technology**

***Europe***

EUROPEAN CONGRESS ON OPTICS



**DTIC QUALITY INSPECTED 2**

19980115 017

REPRODUCED BY  
U.S. DEPARTMENT OF COMMERCE  
NATIONAL TECHNICAL INFORMATION SERVICE  
SPRINGFIELD, VA. 22161

JPRS-EST-92-015

8 MAY 1992

## SCIENCE & TECHNOLOGY

### EUROPE

### EUROPEAN CONGRESS ON OPTICS

36980005 The Hague EXCIMER LASERS AND THEIR APPLICATIONS in English 1991 pp 28-52, 62-125, 134-153, 160-184, 197-203, 215-230, 238-268, 280-291, 299-320, 338-390, 430-437, 453-462, 467-478, 492-502, 510-511

[Proceedings of the European Conference on Optics held in The Hague, Netherlands, 13-15 March 1991; sponsored by the Congress of the European Physical Society (EPS), the European Federation for Applied Optics (Europtica) and the International Society for Optical Engineering (SPIE); edited by Tommaso Letardi and Lucien D. Laude; The Hague, SPIE, 1991]

### CONTENTS

Recent Progress Toward Multikilowatt Output (Invited Paper) [E. Muller-Horsche, P. Oesterlin, et al.] .....	1
Kilowatt Range High Repetition Rate Excimer Lasers (Invited Paper) [V.M. Borisov, O.B. Khristoforov, et al.] .....	14
Design Considerations for High-Power Industrial Excimer Lasers [H.L. Jetter] .....	22
Parametric Study of Small-Volume Long-Pulse X-Ray Preionized XeCl Laser With Double Discharge and Fast Magnetic Switch [J.M. Hueber, B.L. Fontaine, et al.] .....	27
Parametric Study of a High Average Power XeCl Laser [B. Godard, E. Estocq, et al.] .....	37



Excimer Laser Development at the ENEA Frascati Centre: Discharge Instabilities Study [S. Bollanti, P. Di Lazzaro, et al.] .....	45
Modeling of a Long-Pulse High-Efficiency XeCl Laser With Double Discharge and Fast Magnetic Switch [M.N. Kobhio, B.L. Fontaine, et al.] .....	53
Theoretical and Experimental Investigations on Pressure Wave Reflections and Attenuation in High-Power Excimer Lasers [A. Holzwarth, J. Griebisch, et al.] .....	64
Super Small Excimer Laser [A.A. Vill, A.A. Salk, et al.] .....	77
Experimental Studies of an XeCl Laser with UV Preionization Perpendicular and Parallel to the Electrode Surfaces [V. Nassisi] .....	83
Excitation of an Excimer Laser with Microwave Resonator [L. Hunermann, R. Meyer, et al.] .....	94
Excimer Laser Performance Under Various Microwave Excitation Conditions [H.H. Klingenberg, F. Gekat] .....	101
Low-Loss Line-Narrowed Excimer Oscillator for Projection Photolithography: Experiments and Simulation [G.S. Volkov, D.Yu. Zaroslov] .....	108
Evolution of an Excimer Laser Gas Mix [A.D. Boardman, E.M. Hodgson, et al.] .....	116
High-Repetition Rate Pseudospark Switches for Pulsed High-Power Lasers [P. Bickel, J. Christiansen, et al.] .....	124
Damage Testing of Optical Components for High Power Excimer Lasers [K.R. Mann, H. Gerhardt] .....	133
Excimer Laser with Sealed X-Ray Preionizer [V.V. Atezhev, S.R. Belov, et al.] .....	143
Part Two: Laser Applications [L.D. Laude] .....	147
Excimer Laser Patterning of Flexible Materials [Z. Kollia, E.I. Hontzopoulos] .....	148

Influencing Adherence Properties of Polymers by Excimer Laser Radiation	
[J. Breuer, S. Metev, et al.] .....	156
Excimer Laser Processing of Ceramics and Fiber Reinforced Polymers Assisted by a Diagnostic System	
[M. Geiger, N. Lutz, et al.] .....	164
Excimer Laser Surface Treatment of Ceramics	
[G. Hourdakis, E. Hontzopoulos, et al.] .....	176
Surface Nitride Synthesis by Multipulse Excimer Laser Irradiation	
[E. D'Anna, G. Leggieri, et al.] .....	184
In Situ Growth of $Y_1Ba_2Cu_3O_{7-x}$ Thin Films Using XeCl Excimer and Nd:YAG Lasers	
[M. Gerri, W.I. Marine, et al.] .....	198
Investigations on Excimer Laser Treated Cu/Cr Contact Materials	
[E. Schubert, S. Rosiwal, et al.] .....	211
Excimer Laser Deposition and Characterization of Tin and Tin-Oxide Films	
[E. Borsella, P. De Padova, et al.] .....	223
Photochemical Changes of Rare-Earth Valent State in $\gamma$ -Irradiated $CaF_2:Pr$ Crystals by the Excimer Laser Radiation: Investigation and Application	
[S.G. Lukishova, A.Z. Obidin, et al.] .....	233
Use of Excimer Lasers in Medicine: Applications, Problems, and Dangers	
[J. Mommsen, M. Sturmer] .....	242
Bundle of Tapered Fibers for the Transmission of High-Power Excimer Laser Pulses	
[H. Hitzler, N. Leclerc, et al.] .....	249
Spectral and Time-Resolved Measurements of Pollutants on Water Surface by an XeCl Laser Fluorosensor	
[R. Barbini, R. Fantoni, et al.] .....	257
Excimer Laser Cutting of Corneal Transplants	
[R. Tamkivi, L.L. Schotter, Jr., et al.] .....	270
Laser Plasma XUV Sources: A Role for Excimer Lasers? (Invited Paper)	
[F. Bijkerk, A.P. Shevelko] .....	274

Efficient Population of Low Vibrational Number Electronic States of Excimer Molecules: The Argon Dimer [T. Efthimiopoulos] .....	286
Excimer Laser Processing of Diamond-Like Films [V.P. Ageev, T.N. Glushko, et al.] .....	294
Excimer-Dye Laser System for Diagnosis and Therapy of Cancer [L. Pokora, Z. Puzewicz] .....	305
Multistage XeCl Excimer System 'Cactus' and Some Investigations of Stimulated Scattering in Liquids [V.B. Karpov, V.V. Korobkin, et al.] .....	318
Author Index .....	330

## Recent Progress Toward Multikilowatt Output (Invited Paper)

36980005 The Hague EXCIMER LASERS AND THEIR APPLICATIONS in English 1991 pp 28-39

[Article by Elmar Muller-Horsche, Peter Oesterlin and Dirk Basting of Lambda Physik Forschungsgesellschaft mbH]

[Text]

### ABSTRACT

Experimental results obtained from a 500 Hz, 750 Watt average output power XeCl laser are presented. The dynamical behaviour of the pulse energy and optical investigations of the discharge volume pointed out the limits of the present design. There are strong indications that acoustic perturbations currently prevent the efficient operation of the module at repetition rates higher than 500 Hz.

To pass the 1 kW-level, further improvements have to be done. Increasing the discharge efficiency from 1.1 % to date will reduce the creation of shock waves. An aerodynamically designed flow loop will help to shift the ratio of fan power to excitation power (currently 40 kW and 66 kW respectively) to more reasonable values. The additional use of pulse compression techniques will simplify the choice of adequate high voltage switching elements.

### 1. INTRODUCTION

Excimer lasers with very high average power are required in the domain of industrial applications. In this field reliability and durability are even more important than pure output power. Therefore, only discharge pumped excimer lasers can be taken into consideration for this purpose. While discharge pumped excimer lasers in the 0.1 kW range are meanwhile state of the art, the step into the 1 kW class necessitates a rather new technology. This holds in particular with respect to the electrical circuit including the high power switch, the preionization assembly and the gas flow system.

## 2. HIGH POWER XeCl-LASER (750 WATT)

Research lasers with power levels of several hundred Watt have been built and operated at different locations around the world<sup>1-4</sup>. The high power XeCl laser at Lambda Physik is an experimental setup especially tailored to get the gas flow speed in the discharge region required for high repetition rate operation (500 Hz).

In its final state the electrodes were 3.7 cm apart resulting in a discharge volume of 0.73 litre, which was exchanged at a flow speed up to 50 m/s. While pulse energies of 2.75 Joules could be obtained in single shot experiments, the output characteristic at

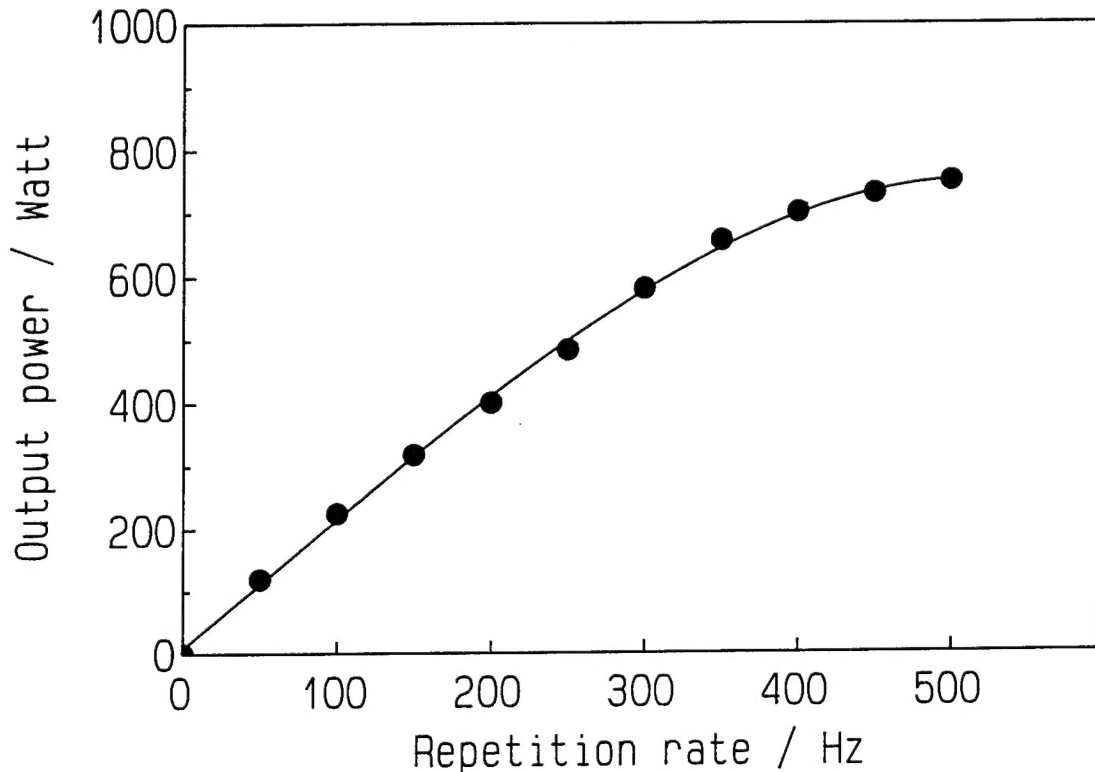


Fig.1. Power against repetition rate of the high power excimer laser at Lambda Physik.

repetitive operation is shown in fig. 1. The discharge was preionized by UV-light. The discharge circuit consisted of two banks of storage capacitors (163 nF and 129 nF). After charging both capacitors up to 32 kV, the polarity of the larger capacitor was reversed with help of four thyratrons (EEV CX 1625) connected

in parallel and fired synchronously by an intense trigger pulse. The thermal current through the high voltage switch determined the number of thyratrons. After inversion, the electrical energy in both capacitors was transferred to the discharge capacitors (120 nF) via a saturable magnetic switch.

Only gas mixtures of quite low HCl content (typically 1 - 1.5 mbar) could be used. Otherwise excessive discharge instabilities built up causing the output energy to drop. Therefore the breakdown voltage had a value of 30 to 33 kV only at a total pressure of the neon based gas mixture of 4.5 - 5 atmospheres. This low value also resulted from the relatively long voltage rise at the electrodes of 200 ns, mainly limited by the high capacitance values in use.

The preionization was fed by a separate discharge loop comprising an auxiliary capacitor of 19 nF, which was charged by one of the main thyratrons. The variation of the preionization parameters showed little effect on the performance of the laser system.

The gas tank made out of aluminium had a volume of more than 1 cbm. Two radial fans of 26 cm diameter were driven by 20 kW motors each. Large sized magnetic couplings guaranteed a hermetic seal between gas tank and ambient air.

The design goal to get a gas flow system as compact as possible had several drawbacks. First of all it is easy to calculate that several times the kinetic energy of the laser gas flowing each second across the discharge volume had to be dumped into the fan driving motors. This indicates poor efficiency of the gas conducting elements and especially large losses in all parts of the flow system where the gas flow gets decelerated (low or absent pressure recovery).

A lamella type heat exchanger has been used in the setup. These components have good thermal transfer properties at low volume but are hard to clean properly. Also a large amount of dust can be trapped and eventually released by these modules.

Nevertheless, the gas flow system accomplished a clearing ratio of 3 at 500 Hz as can be seen in fig. 2, where the discharge induced turbulences in the laser gas flow were investigated by measuring the undistorted transmission of a He-Ne laser beam through a path parallel to the electrodes located midgap and 8 mm downstream the discharge volume.

Therefore the deviation of the power curve in fig. 1 from a straight line must be ascribed to a different mechanism than insufficient gas flow. A closer look to fig. 2 reveals a small

baseline shift in transmission at higher repetition rates, which is amplified by higher pump energy loadings as seen when varying the charging voltage. The settling time constant of this shift agrees with the respective fall in pulse energy after switching on the laser (fig. 3). A smaller relative drop in pulse energy is achieved at lower charging voltage in accordance with the smaller baseline shift in fig. 2. So there is a strong evidence, that acoustic turbulences built up, which do not damp out in high repetition rate operation. The time constant for creation of these stationary shock wave systems agrees with experiments done by other groups <sup>4-6</sup>.

One of the most reasonable methods to suppress detrimental acoustic turbulences is to increase the discharge efficiency thereby lowering the pump energy responsible for the creation of the shock waves. Unfortunately, discharge efficiency in the current setup was quite low. Only 1.1 % of the energy stored in the primary capacitors was converted to optical output. We believe that this is mainly due to the very large head inductance (approximately 25 nH) which resulted from the current return vanes necessary in fast flow systems and conservatively large insulating gaps between conducting elements to prevent breakdown and flashover.

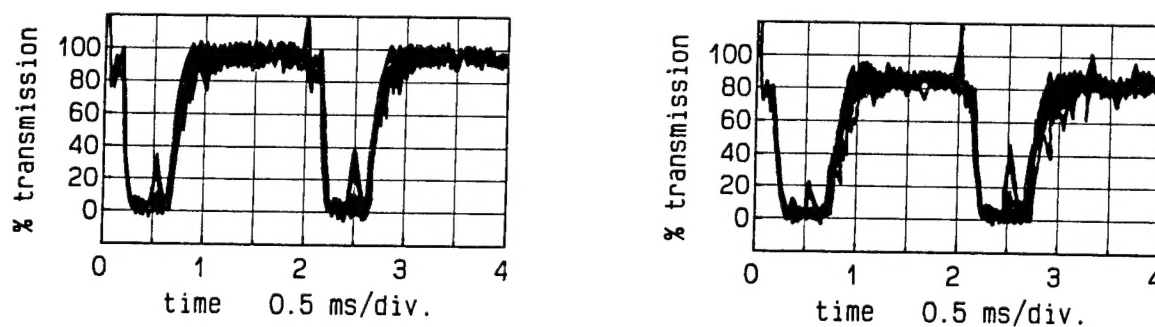


Fig.2. Transmission of a He-Ne probe laser through the gas flow, which becomes periodically disturbed by the laser discharges. Left 23 kV, right 28 kV operating voltage.

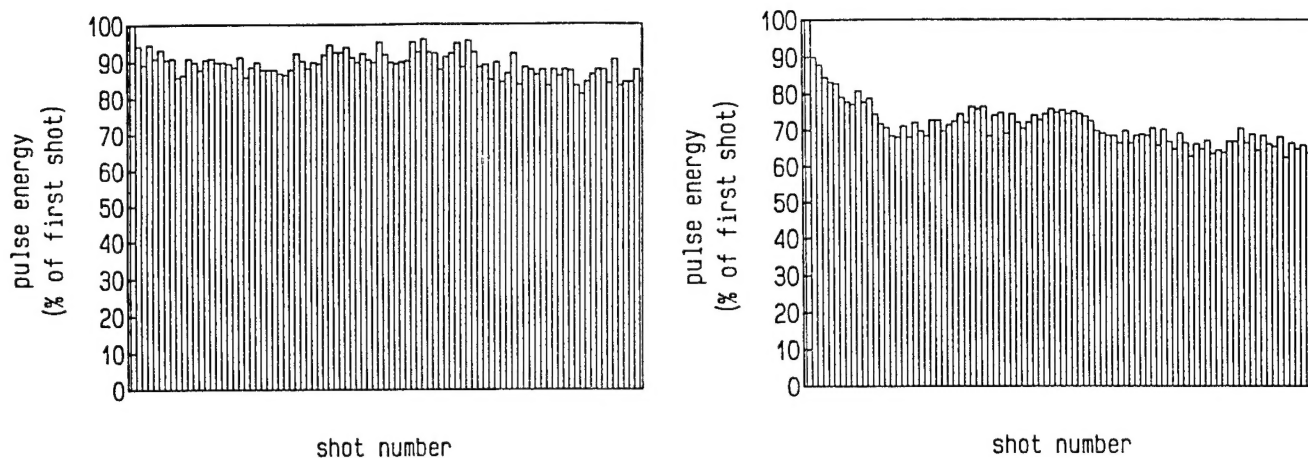


Fig.3. Evolution of the pulse energy after starting the laser at 500 Hz. Left 23 kV , right 28 kV operating voltage.

Meanwhile a number of studies have been pursued at Lambda Physik to improve the overall performance of a high power excimer laser to efficiency values around 2 percent and to extend its output power into the kilo- and multikilowatt regime.

### 3. GAS-FLOW-SYSTEM

The next step in scaling the gas loop was to increase the gas velocity between the electrodes by more than a factor of 3 to 150 m/s. Taking a cross section of  $4 \times 100 \text{ cm}^2$ , the kinetic energy flowing each second across the electrodes is 270 kW. The only way not to waste all this power is to design each component especially in the high speed section of the flow loop according to aerodynamical criteria and to add an efficient diffuser downstream the discharge region, which converts kinetic energy of the gas into static pressure. This diffuser is necessarily a long part because only very small effective apex angles can be tolerated.

One possible geometric contour is outlined in fig. 4. Notice that this machine gets nearly 6 m long! Because of the high aerodynamical quality of the flow loop around 100 kW are sufficient to power the fan, which in this case is a single stage radial fan.

According to the material in use, ribs have to be welded to the walls to get the necessary stiffness and to reduce the material stress. We chose aluminium as base material. But also nickel plated steel can be an attractive alternative with respect to stiffness, weldability and costs.



As mentioned earlier, the heat exchanger should be selected carefully. An ideal choice concerning cleanliness and corrosion resistance would be a shell and tube type made out of steel, nickel and copper-nickel alloy. Unfortunately such a part turns out to be quite heavy (2700 kg, dry) bulky (1 m dia. 1 m long) and expensive (200.000 DM) in our case. But there are fin type heat exchangers with large and smooth lamella surfaces cooled by stainless steel tubes, which can also be taken into account. Table 1 gives a summary of the expected costs of a gas flow loop as presented.

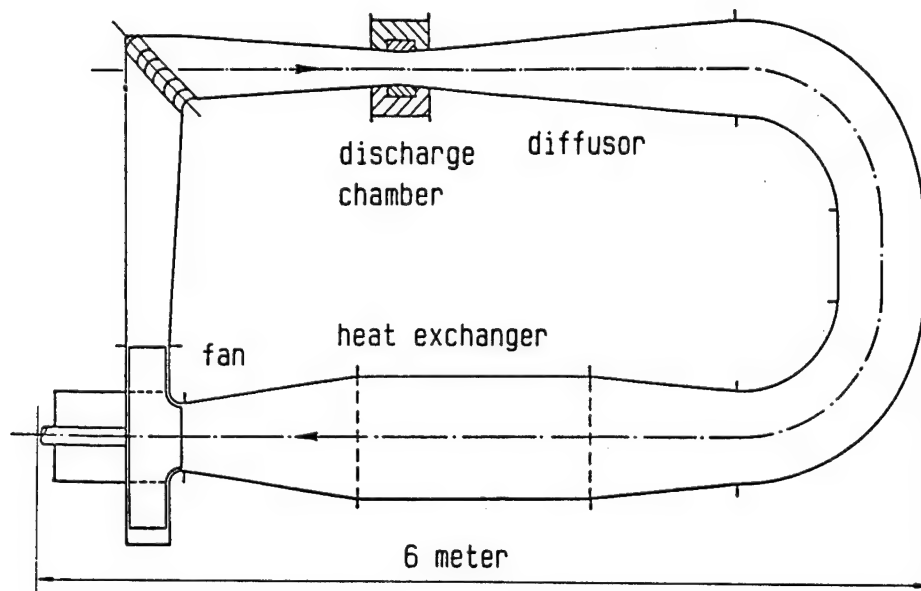


Fig.4. Flow system for gas velocities up to 150 m/s.

radial fan, magnetic coupling, motor, gas in- and outlet duct, motor control unit	300.000 DM
knees, diffuser, nozzle	400.000 DM
heat exchanger	60.000 DM
compensator	40.000 DM

Table 1. expected costs of a 150 m/s gas flow system.

#### 4. LASER HEAD DESIGN

The efficiency of the discharge mainly depends on the design of the discharge head. We think that long lifetime operation of a high repetition rate system can only be achieved with solid electrodes. Mesh electrodes or thin aluminium electrodes as used in "through the electrode" preionized systems suffer from field inhomogenities at the electrode and high erosion rate respectively. As there is no way to locate an X-ray tube in the gas flow, the only possible arrangement for an aerodynamically "invisible" preionizer is as given in fig. 5. If the top electrode is operated as cathode, part of the anode region is not properly preionized as can be seen in the figure. Secondary emission of soft X-rays is used for auxiliary illumination of the discharge volume.

Most of the X-ray guns used for preionization are limited in repetition rate and lifetime, as far as reliable data are published. At Lambda Physik a hard sealed vacuum tube with a powerful cathode has been developed and successfully applied to excimer lasers. In a lifetime test nearly 1 billion shots have been accumulated. But the maximum repetition rate is currently limited to 500 Hz because of anode heating. To increase this figure, further work has to be done.

A second way to incorporate a simple preionizing system with low drag coefficient, which will be investigated at Lambda Physik, is the positioning of corona bars close to one or both electrodes. Particularly XeCl is known not to demand too severe requirements to the preionization density and timing. In the case of moderate pulse energy systems this could be a feasible method to integrate the preionization.

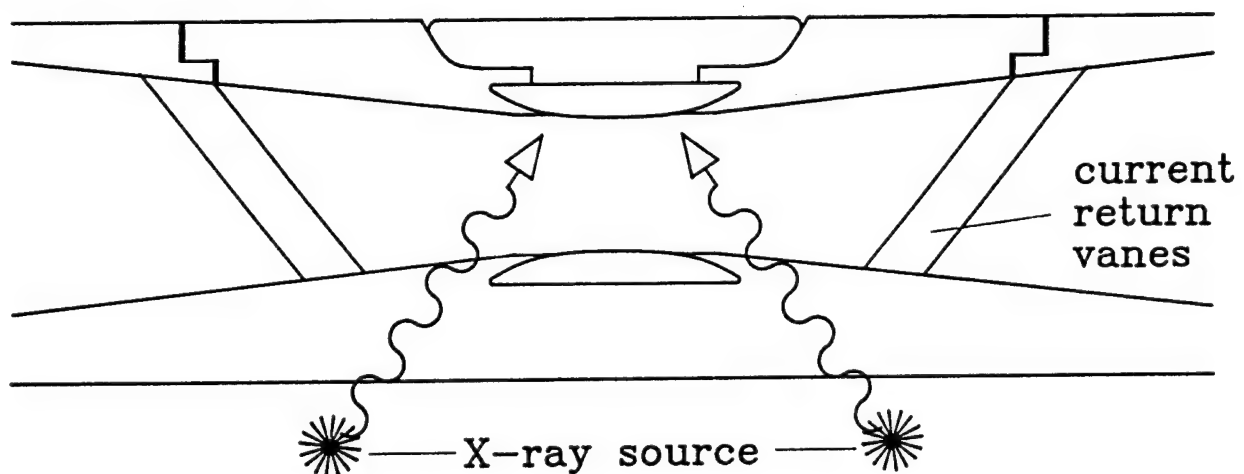


Fig.5. Cross section of a low inductive discharge head with high cross flow velocity.

To avoid losses in the gas flow, the current return vanes in fig. 5 have to be air foil shaped with a length to thickness ratio of at least 3 : 1. Of course the edge radii must be chosen so that especially in upstream direction flashovers cannot occur to the cathode. For similar reasons the field strength and field direction along the insulator surface surrounding the cathode have to be carefully controlled. Field shaping elements outside the gas chamber can help to reduce the electric field to harmless levels<sup>7</sup>. In designing cross sections of the kind given in fig. 5 numerical methods become an inevitable tool. Fig. 6 gives potential and field contours as obtained by a finite element program<sup>8</sup>.

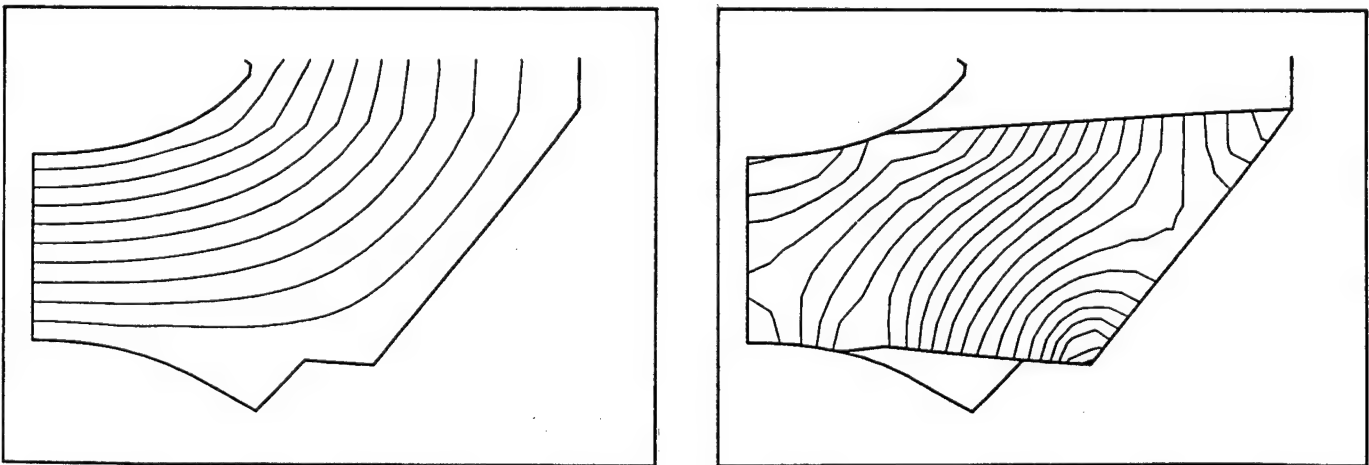


Fig.6. Electric potential and field contours in the discharge geometry of fig.5.

The high pressure inside the gas tank normally will cause a catastrophic deformation of the insulator in which the cathode is embedded. Therefore, additional support structures are necessary. They can be kept at ground potential and are ideally suited for housing the discharge capacitors. Ceramic capacitors have a proven reliability in this application. But one can also think about a water capacitor, if it can be integrated in compact size at the required capacitance (0.3...0.5 nF per cm discharge length).

According to our experience the discharge energy should be offered at the maximum voltage compatible with

- \* reliable operation of the discharge circuit and discharge head
- \* breakdown voltage of the gap (as determined by gas mixture, gap distance and voltage rise).

This recipe keeps the specific capacitance of the discharge head low thereby improving discharge speed and efficiency.

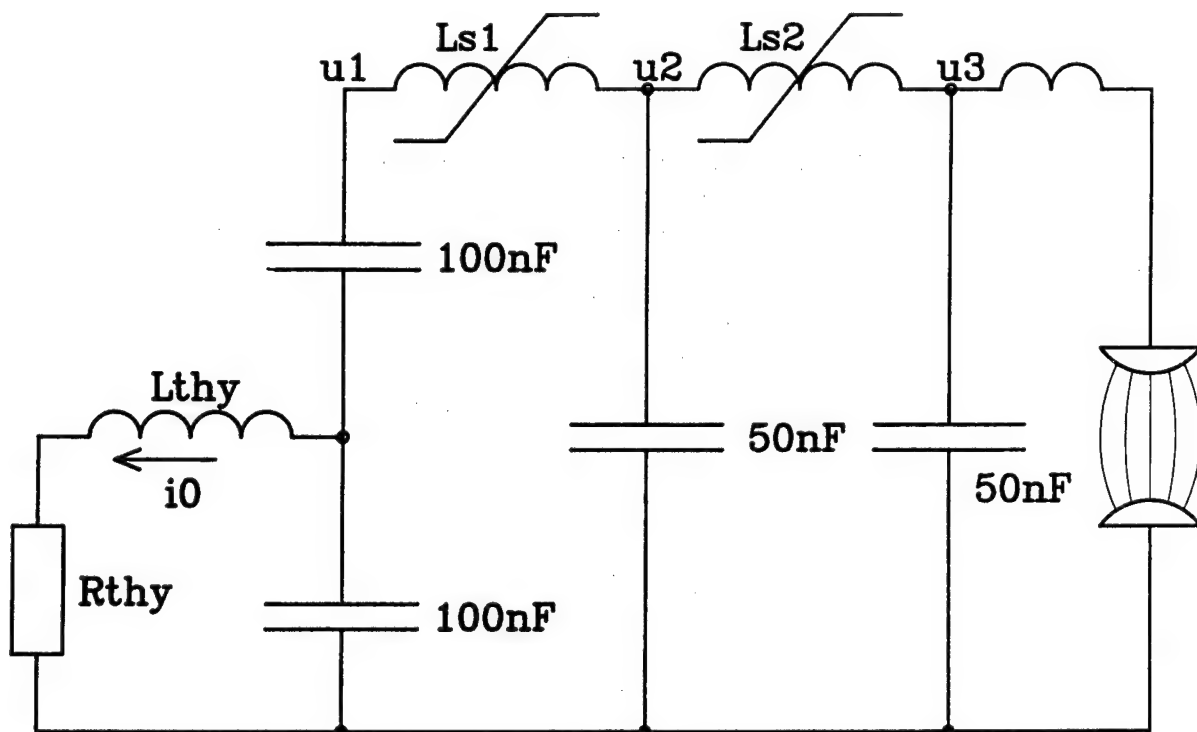


Fig.7. Discharge circuit for multikilowatt output.

### 5.DISCHARGE CIRCUIT

The key element, from which all consideration should proceed when designing the discharge circuit, is the thyristor switching the high voltage. According to experience it is a service part which wears out after about  $10^9$  pulses. That is why simple and versatile tubes should be used. A good candidate is for example a 5 inch, single grid thyristor. At high repetition rate operation the maximum average current limits the ultimate repetition frequency. Assuming a LC inversion circuit with multistage magnetic compression<sup>1</sup>, the proposed values in fig. 7 will result in 5 millicoulomb flowing through the switch each shot at 25 kV charging voltage. With 8 Amp. maximum average current this allows operation up to 1.6 kHz. At an overall efficiency of 2 % more than 2 kW would be emitted! The specified maximum thermal current of the thyristor determines the necessary pulse compression ratio. In the case of the HY 5 for example, the thermal current is 125 A at maximum and can be computed from the square root of average current times peak current. This limits the peak current to 2 kA. Taking a sinusoidal current, the half periode of the current pulse should last for at least 4 microseconds. A double stage

compression circuit as shown in fig. 7 would be sufficient to compress the pulse to a short enough value so that a high overvoltage at the electrodes and a subsequent stable discharge could be achieved.

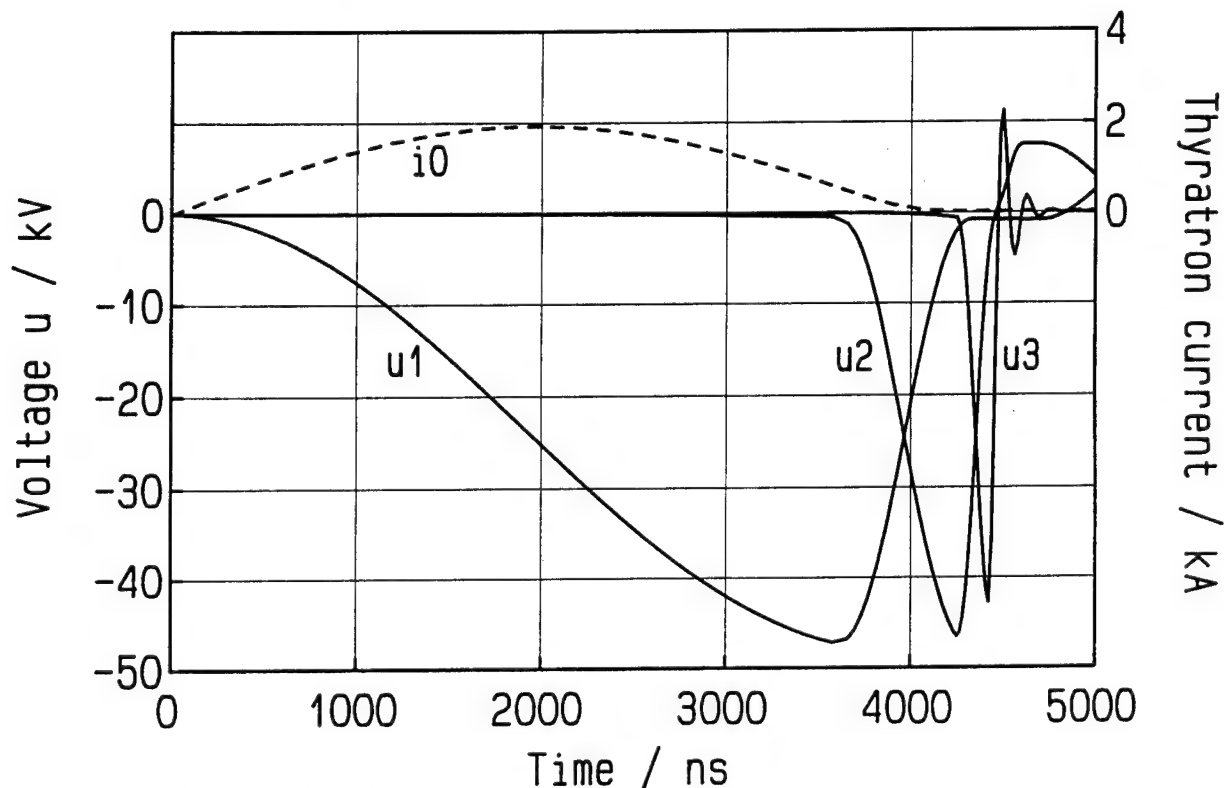


Fig.8. Evolution of thyatron current and voltages in the circuit of fig.7. Charging voltage is 25 kV.

In fig. 8 a computer simulation of the circuit in fig. 7 is presented. Lumped circuit elements are used as far as possible. The discharge has been modelled in the following way:

- \* a power law dependence controls the electron generation rate. Data have been obtained in preionization triggered discharges, where the time lag between preionizing pulse and breakdown was measured as a function of the reduced electric field strength<sup>9</sup>.
- \* data on the mobility of electrons in neon have been taken from literature<sup>10</sup>.

With smaller adjustments, the breakdown voltage and the voltage ringing are reproduced quite well by the computer model, so that it can be favourably used to optimize the circuit. The percentage of energy dumped into the discharge during the first half period of the discharge current can be taken as a figure of merit. In the case of fig. 8 this is more than 75 %, quite a good value having all the electrical components of the circuit and the ill natured characteristic of the discharge in mind.

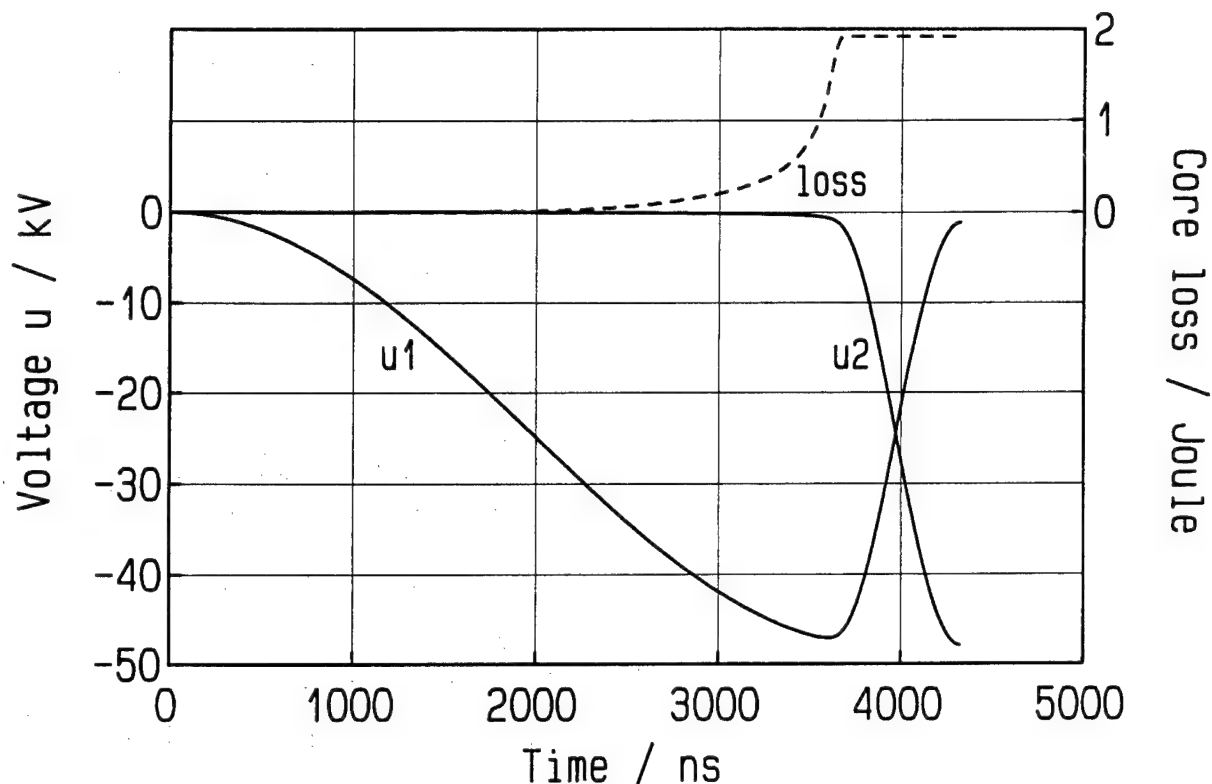


Fig.9. Evolution of the losses in  $Ls_1$  of fig.7, when the magnetic core gets saturated.

Magnetic compressors comprising tape wound cores are known to be very resistant to a computational treatment. The saturation wave theory <sup>11,12</sup> leads to an estimation of the core losses under the assumption of a constant magnetic field path length throughout the core. Recently we developed a continuum model <sup>13</sup> of this theory which accurately describes the current-voltage characteristic and the dynamical saturation behaviour of toroidal cores with arbitrary dimensions. In fig. 9 results of this study are presented which refer to the first compression stage in fig. 7. Outlined are in- and output voltage and losses in the core, which add up to 1.9 Joule in this special case.

## 6. CONCLUSIONS

According to our experience two limitations will strongly affect the development of excimer lasers having kilo- or multikilowatt output power. As fan power scales like the third power of gas speed, there will be a practical limit to the gas velocity and hence to the repetition rate of the system. We think that the system presented in this report is close to this limit with 100 kW fan power and 150 m/s gas velocity. Acoustic turbulences on the other hand can deteriorate the performance of

the laser before the above mentioned limit is reached. Criteria for the occurrence of this phenomenon are partly developed but can hardly be used to make predictions in the design phase. One way to go around the problem is to increase the discharge efficiency to the utmost level. Dampers in the flow loop seem to have adverse effects on the aerodynamical quality or on the long lifetime capability of the system.

Known techniques in high voltage circuitry should be sufficient to extend the output power into the kilowatt region. Thereby, magnetic pulse compression will help to make full use of versatile standard thyratrons. Computer simulations either especially developed or already existing for different applications turn out to be valuable tools in designing discharge circuits and discharge geometries.

## 7. ACKNOWLEDGMENTS

Part of this work has been supported by the Bundesministerium für Forschung und Technologie under contract number 13N5358/4 and under the Eureka project number EU205.

## 8. REFERENCES

1. H.B. von Bergmann and P.H. Swart, "Industrial excimer and CO<sub>2</sub> TEA lasers with kilowatt average output power", paper presented at the 8<sup>th</sup> Intl. Symp. on Gas flow and Chemical lasers, Madrid, Sept.1990.
2. R.R. Butcher and T.S. Fahlen, "Corona preionized 300-W excimer laser", paper presented at the Conference on Lasers and Electrooptics, San Francisco, 1986.
3. D. Jetter, "Components for high power excimer lasers", paper presented at the Intl. Meeting EUREKA EU205, Karlstein FRG, Oct. 1989.
4. V.M. Borisov, A.Yu. Vinokhodov and Yu.B. Kiryukhin, "Output energy evolution in a pulse periodic XeCl excimer laser with an average power of 400 W", Sov. J. Quantum Electron. 17, 595-598, 1987.
5. M.L. Sentis, P. Delaporte, B.M. Forestier and B.L. Fontaine, "Parametric studies of X-ray preionized discharge XeCl laser at single shot and at high pulse rate frequency (1 kHz)", J. Appl. Phys. 66, 1925-1930, 1989.
6. M. Bessafi, D. Zeitoun, B.L. Fontaine and B.M. Forestier, "Two dimensional numerical study of wave damping in high average power excimer laser", paper 1278-18 presented at the Intl. Congress on Optical Science and Engineering, The Hague, Mar. 1990.
7. "Spectra Technology demonstrates 20 J XeCl excimer laser", Laser Focus, p.23, Oct. 1989.
8. ANSYS Revision 4.4A, Swanson Analysis Systems Inc., P.O. Box 65, Johnston Road, Houston, PA 15342-0065.

9. E. Müller-Horsche, D. Basting, U. Brinkmann, P. Klopotek, P. Oesterlin and W. Mückenheim, "Preionisation Switching of Excimer lasers with X-ray pulses", paper FC3 presented at the Conference on Lasers and Electrooptics, Baltimore, Apr. 1987.

10. Y.S. Wang, Ph.D. Thesis, University of Southern California at San Diego, 1982.

11. A.G. Ganz, "Application of thin Permalloy tape in wide-band telephone and pulse transformers", AIEE Trans. 65, 177-183, Apr. 1946.

12. W.C. Nunally, "Magnetic Switches and Circuits", LANL Report No. LA-8862-MS, 1981.

13. E. Müller-Horsche, "A continuum model of the Saturation Wave Theory", to be published.



Kilowatt Range High Repetition Rate Excimer Lasers (Invited Paper)

36980005 The Hague EXCIMER LASERS AND THEIR APPLICATIONS in English 1991 pp 40-47

[Article by V.M. Borisov, O.B. Khristoforov, Yu.B. Kirykhin, S.G. Kuznetsov, Yu.Yu. Stepanov, and A.Yu. Vinokhodov of Kurchatov Research Institute]

[Text]

### ABSTRACT

High power operation of excimer lasers was investigated using UV-preionization schemes based on a dielectric surface creeping discharge. The design and operation of the high average power excimer laser systems are described. A large-aperture ( $10 \times 7 \text{ cm}^2$ ) XeCl laser with UV preionization can produce 10 J per pulse at a repetition rate of up to 100 Hz. When aperture was decreased, the XeCl laser operated at repetition rates of up to 500 Hz and could produce the average output power more than 600 W.

### 1. INTRODUCTION

Excimer lasers are the most intense ultraviolet light sources available today and are used for scientific and industrial applications. Now commercial lasers are capable of delivery of 150 W<sup>1</sup> and a number of research teams study the possibilities to reach the 1 kW level. Average powers of 0,5 kW have been achieved at the pulse repetition rate up to 1600 Hz<sup>2,3</sup>. A maximum of average power 0,75 kW has been reported by the Lambda Physik at 500 Hz<sup>1</sup>.

Within the Eureka cooperation a design of 1 kW XeCl excimer laser system operating at a repetition frequency of 1 kHz was described at the Netherlands Center for Laser Research<sup>4</sup>.

The potential application of high power excimer lasers have stimulated an interest in scaling laser discharge systems to larger apertures and volumes. The research group at Siemens have created the XeCl laser emitting 225 W at 100 Hz<sup>5</sup>. A 10-liter active volume laser device has been realized at the ENEA Frascati Center, as a technical base for the high average power excimer laser<sup>6</sup>. The Spectra Technology, Inc (STI) has designed a 20 J per pulse, 50 Hz, 1 kW average power XeCl excimer laser<sup>7</sup>.

In the following, we describe some results, obtained at the Pulse Laser Systems Laboratory (PLSL) of the Troitsk Kurchatov Research Institute.

### 2. PREIONIZATION OF A DISCHARGE VOLUME

In the most part of our experiments a high (about  $10^9 \text{ cm}^{-3}$ ) initial electron concentration was achieved using a creeping discharge on the dielectric surface (CDDS) as a UV-source. The scheme of the CDDS is

shown in Fig.1. Attractive features of this preionizer used in our lasers are its simplicity, reliability, and ability to provide the high energy output in both HCl and F<sub>2</sub> based gas mixtures.

We found the conditions necessary to cover all the dielectric surface area (up to 100x20 cm<sup>2</sup>) with plasma and demonstrated that the creeping discharge remains uniform at repetition rate as high as 500 Hz. The lifetime evaluation tests proved that the dielectric on a water-cooled substrate had no damage after 10<sup>7</sup> pulses at 100 Hz. Electron production rate at the level of 7x10<sup>17</sup> cm<sup>-3</sup> s<sup>-1</sup> can be achieved in Ne at the distance of 5 cm from the surface and energy input to the CDDS 30 mJ/cm<sup>2</sup> in 100 ns.

Using this electrode system a few years ago we have created a single-pulse XeCl laser with the discharge aperture 12x10 cm<sup>2</sup> and output energy of 20 J<sup>8</sup>. In this laser the CDDS was used as a UV-source and placed behind a grid electrode. The distribution of specific lasing output in the spacing between the electrodes for this laser is plotted in Fig.2. Curve 1 was obtained for the XeCl laser with a very low (10<sup>-3</sup> J/cm<sup>2</sup>) energy being put in the creeping discharge. Curve 1 shows that no lasing occurs near the anode in this system. However, if the energy input to the CDDS is sufficiently high (20 mJ/cm<sup>2</sup>), the XeCl laser output distribution is practically uniform at the distance of 8 cm from the cathode (curve 2 in Fig.2). The lasing distribution is homogeneous for both XeF and KrF lasers with electrodes situated 5 cm apart (curves 3 and 4 in Fig.2). Results presented in Fig 4 demonstrate that "face to face" preionization from both cathode and anode sides would result in a sufficiently uniform lasing at electrode distances in the range from 10 to 15 cm for XeCl, XeF or KrF mixtures.

### 3.LASER DEVICE.

The PLSL have created several models of excimer lasers with different combinations of energy per pulse and repetition rate based on a single type of a gas flow system. The family name of these models is GEFEST.

Figure 3 presents a schematic drawing of the high-repetition rate excimer laser. The flow loop has the volume of 1500 l and pressure up to 4 atm. It contains 3 parallel axial fans providing the gas circulation flow about 3 m<sup>3</sup>/s. The heat exchanger has a capacity of 100 kw and gives a relatively large pressure drop in the flow loop. The flow loop has the window for X-rays. This gives possibility to compare a character of X-ray and UV preionization. Maximum of distance between the electrodes can be ~ 10 cm. In this case the gas reaches the speed up to 30 m/s between the electrodes. Decreasing the distance between the electrodes allows one to considerably increase the speed.

In our experiments we can change the active volume by the decreasing of the distance between the electrodes or by changing electrode systems.

For an average distance between the electrodes 6 cm and active volume 6x3x80 cm<sup>3</sup> we used an excitation circuit based on LC-inversion with single-stage pulse compression (model GEFEST-2). Four commercially available thyatrones which work simultaneously were used as a commutator. The excitation circuit contains capacitors of 4 different types C<sub>1</sub> =100 nF, C<sub>2</sub> =100 nF, C<sub>3</sub> =60 nF, C<sub>4</sub> =18 nF as shown schematically in Fig 3.

Along with the described pulser (for a larger active volume) we have also developed another pulser, based on a double Blumlein line and a low-inductance switch (model "GEFEST-3"). This excitation circuit is shown in Fig.4. The double pulse-forming line (DPFL) can consist of several identical units. Each of them includes several high-voltage low-inductance oil capacitors contained within a single case. Operational ("shock") capacity of the unit is 28 nF, the wave resistance, 2 Ohm. The unit 0,3 m in length provides for

electrical pulse width of 0,1 ms. The waveform of the pulse on the matching load is almost hat top. DPFL for high-repetition-rate lasers with different aperture, includes 4 or 6 units with total resistance 0,5 or 0,33 Ohm, respectively. Nominal charge voltage for the DPFL is 80 kV and the line is designed to operate at repetition rates up to 300 Hz. The pulse charge of the capacitor  $C_4$ , shown in Fig.4, provides the creeping discharge and this results in preionization of the discharge volume by UV radiation. The rail spark gap with 1 m long electrodes and an autonomous gas flow is used as a switch in this pulser.

Unlike the models GEFEST-3 and GEFEST-2, in which we used UV preionization by the CDDS behind the screen type electrode, for a small distance between the electrodes ( $\sim 3$  cm) and small active volume ( $3 \times 1 \times 80$  cm<sup>3</sup>) we used UV preionization by 2 rows of the sparks near the high-voltage solid electrode. The dimensions of the discharge head in fig 3 gave possibility to use a 3-electrodes system in which the ground electrode was one and the same for 2 active volumes ( $3 \times 1 \times 80$  cm<sup>3</sup>). In this case two simple excitation circuits (C-C transfer) were used. (model GEFEST-1)

#### 4. EXPERIMENTAL RESULTS.

A part of the experimental results have been presented in our preceding report<sup>8</sup>.

The measured power versus the repetition rate for various models of excimer lasers is shown in Fig.5.

Slope 1 was obtained with the XeCl laser of the model GEFEST-1 a few years ago<sup>9</sup>. The output power at 500 Hz was 420 w.

Slope 2 was obtained by the XeCl laser of the model GEFEST-2. In single shot operation the laser delivered a pulse energy of 3 J at  $\text{HC1:Xe:He} = 1:5:1000$ , pressure 4 bar, charging voltage 40 kV. As shown in Fig 5 the slope is linear up to repetition rate  $\sim 160$  Hz. The maximum output power at 300 Hz is 650 W, which corresponds to a 30% decrease in the pulse energy.

We have found out that there are two main causes for the discharge contraction in the high-repetition-rate regime: 1. local inhomogeneities of the energy input to a discharge resulting from gas density fluctuations due to acoustic disturbances; 2. local overheating of some spots on the surface of electrodes and as a result metal vaporization in the zones with an increased energy input during previous pulses.

Nevertheless we connect the non-linearity of slope 1 and 2 in Fig 5 after 250 Hz and 160 Hz also with a disadvantage of the electrical power supply, used.

The excitation circuit similar to that presented in Fig.4 was used to pump XeCL lasers with UV preionization by the CDDS with active volumes  $7,8 \times 6,4 \times 75$  cm<sup>3</sup> = 3.5 l,  $10,7 \times 7,0 \times 80$  cm<sup>3</sup> = 5.6 l and

$12 \times 8 \times 68$  cm<sup>3</sup> = 6.5 l. The output energy of these lasers was 7.6; 10.2 and 16 J, respectively. The energy stored in the line is converted into laser output energy with the efficiency 1-1.25%. The same type of the excitation circuit was used for the XeCl laser with active volume  $6 \times 5 \times 80$  cm<sup>3</sup> = 2.4 l, but active volume was preionized by X-rays. The X-ray preionizer had a field emission cathod and operated with high voltage pulse  $\sim 120$  kv. In single shot operation this laser delivered a pulse energy of 5.2 J. This tentative result gives an impression that the using of X-rays preionization as compared with UV preionization by the CDDS lead to no benefits for achieving the highest output energy.

If we used the same active volume ( $\sim 2.4$ l), which was preionized by X-rays, but the excitation circuit based on the L-C inverter with single stage pulse compression, the output energy was only 4.1 J.

The XeCl laser with the active volume 5.6 l and with UV preionization by the CDDS (model GEFEST-3) was tested with repetition rate up to 100 Hz. The rail spark gap, as a switching element operated reliable in the high repetition rate regime if pulse charging of the DPFL was used. The charging voltage ~80kV of the DPFL was reached by a electrical circuit contained a capacity, switched by multiple parallel thyratrons, and a pulse transformer. The duration of the charging pulse ~  $10^{-5}$  s.

The average output power versus the repetition rate is plotted in Fig 5 for the XeCl laser of the model GEFEST-3.

## 5. CONCLUSION.

Several models of high repetition rate high power XeCl excimer lasers with different combinations of energy per pulse and repetition rate have been described.

The models use of a single type compact flow system. The model GEFEST -3 of the XeCl laser with UV preionization by a creeping discharge on the dielectric surface and the excitation circuit based on a double-pulse forming line and a rail gap switch is capable to emit more than 10 J per pulse at the repetition rate up to 100 Hz. Using of the excitation circuit based on the L-C-inventor and commercially available thyratrons (model GEFEST-2) allows to obtain 650 W.

Thus, the possibility of the creation 1 kW excimer laser with energy per pulse up to 10 J was demonstrated.

Further work will be connected with achieving a reliable operation of all laser elements. We are also planning to investigate KrF output parameters for the models GEFEST. We hope that the models GEFEST can be used as a prototype for the development of commercial high power excimer lasers for industrial applications.

## 6. REFERENCES.

1. E.Muller-Horsche, P.Oesterlin, D.Basting "Highest power excimer lasers". SPIE, Vol 1225 High-Power Gas Lasers, p.p.142-148, 1990.
2. J.Fahlen, XMR Inc. Private communication, 1990 (from T.M.Green, M.R.Osborn "Developments in Excimer Lasers for Photochemical Processing" Report AEA Industrial technology-0219, 1991).
3. H.M.von Bergman and P.H.Swart "High repetition rate excimer and CO<sub>2</sub> TEA lasers" Proc.Int.Conf. on Lasers '89, p.p.80-89, STS Press. McLean, 1990.
4. W.J.Witteaman, F.A.van Coor, O.B.Ekelmans, M.Trentelmen, C.J.Ernst "Design studies of a high pulse excimer Eurolaser", SPIE, vol 1225 High-Power Gas Lasers, p.p.132-141, 1990.
5. H-L.Jetter, K-J.Schmatjko, M.Schroeder "Excimer laser with high pulse energy and typical applications" SPIE, vol 1132 High Power Laser Machining Technology, p.p.92-101, 1989.
6. S.Bollanti, P.Dilazzaro, F.Flora, G.Giordano, T.Letardi, T.Hermesen, C.E.Zheng "Performances of a ten-liter volume electron avalanche-discharge XeCl laser device" ENEA.Preprint 1988.
7. C.T.Forest "Demonstrates 20 J XeCL excimer laser", Laser Focus World 25 }1023, 1989.
8. V.Yu.Baranov, V.M.Borisov, D.N.Molchanov, V.P.Novikov and O.B.Khristoforov "Wide-aperture electric-discharge XeCL laser with UV preionization and 20 J output energy, Sov.T.Quantum Electronics, vol 17, p.p.978-983, 1987.
9. V.Yu.Baranov, V.M.Borisov, A.Yu.Vinokhodov, Yu.B.Kiryukhin, Yu.Yu.Stepanov, O.B.Khristoforov "Intense high repetition-rate excimer lasers and applications" SPIE, Vol 1225 High-Power Gas Lasers p.p.164-172, 1990.
10. V.M.Borisov, A.Yu.Vinokhodov, Yu.B.Kiryukhin "Output energy evolution in high-repetition rate XeCl laser with 400 W average output", Sov.J.Quantum Electronics vol 17, p.p.936-942, May 1987.

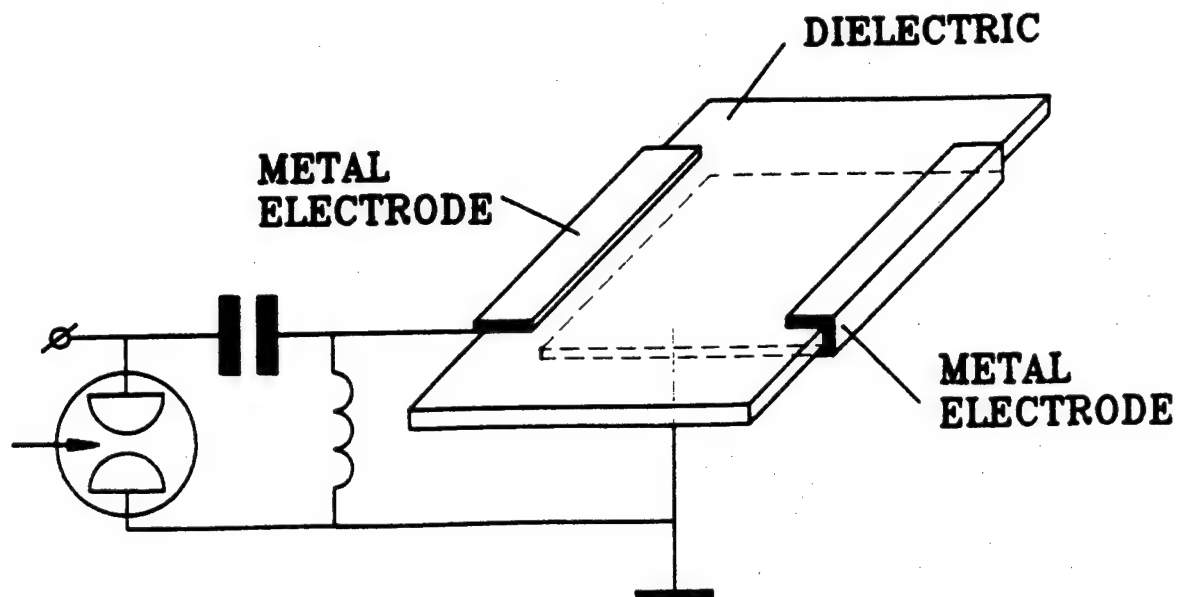


Fig.1. Creeping discharge on dielectric surface (CDDS).

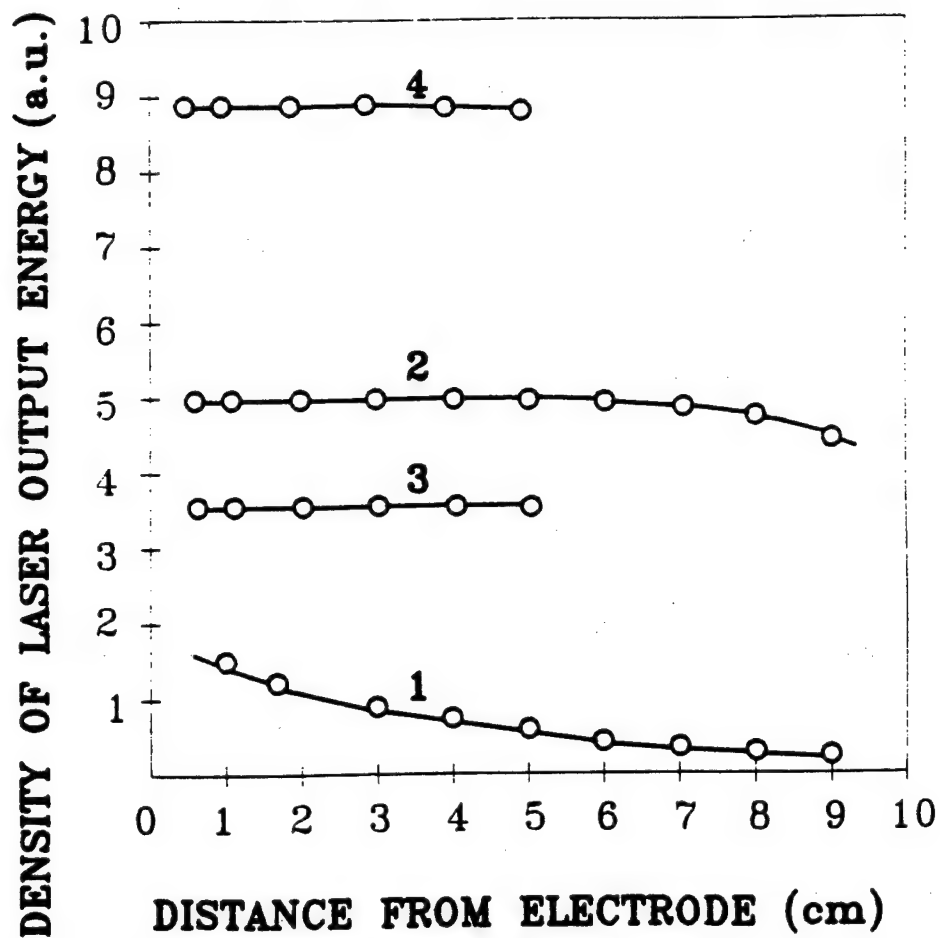


Fig.2. Distribution of specific lasing output in the spacing between the electrodes for various lasers.

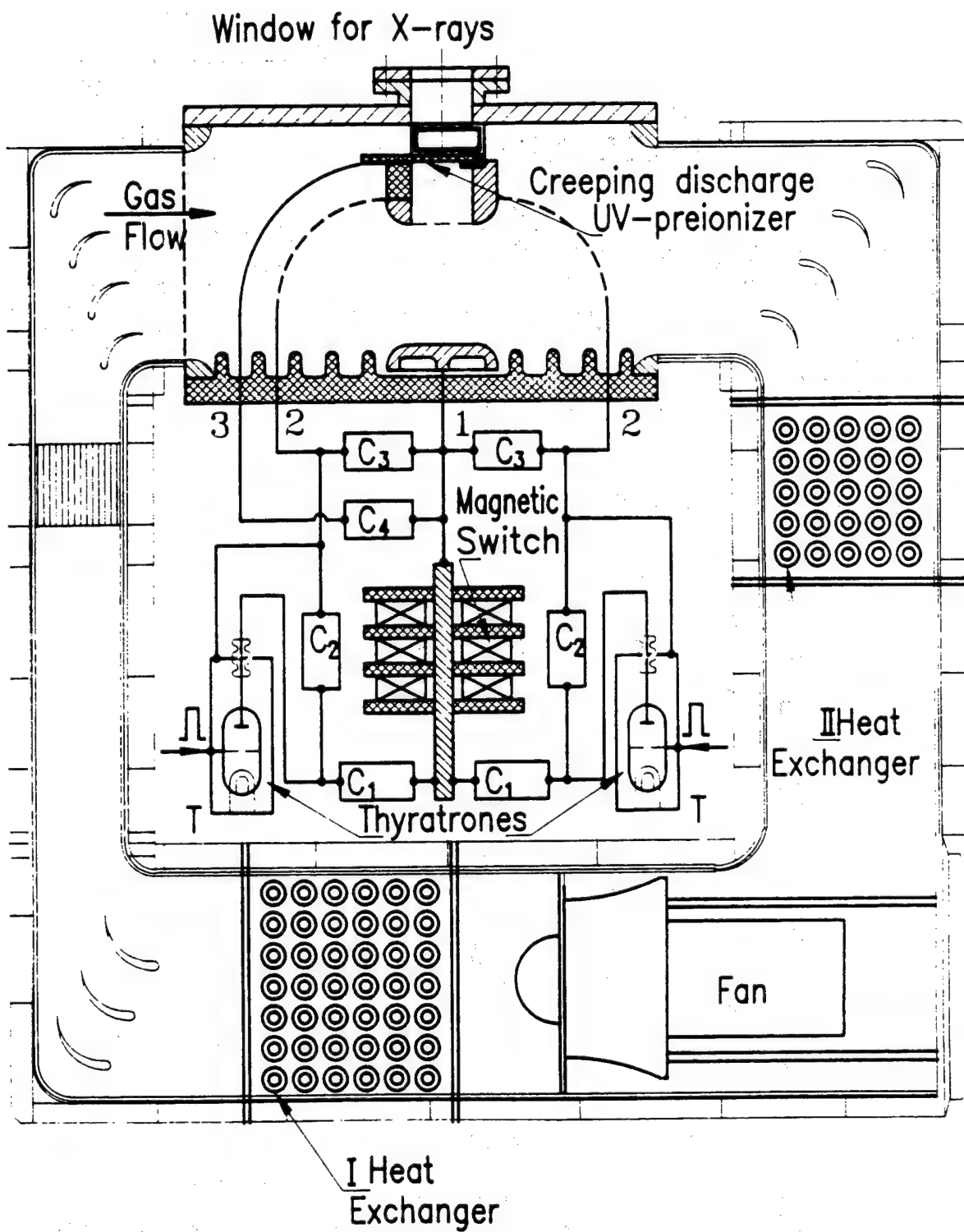


Fig.3. High-repetition rate laser (GEFEST-2).

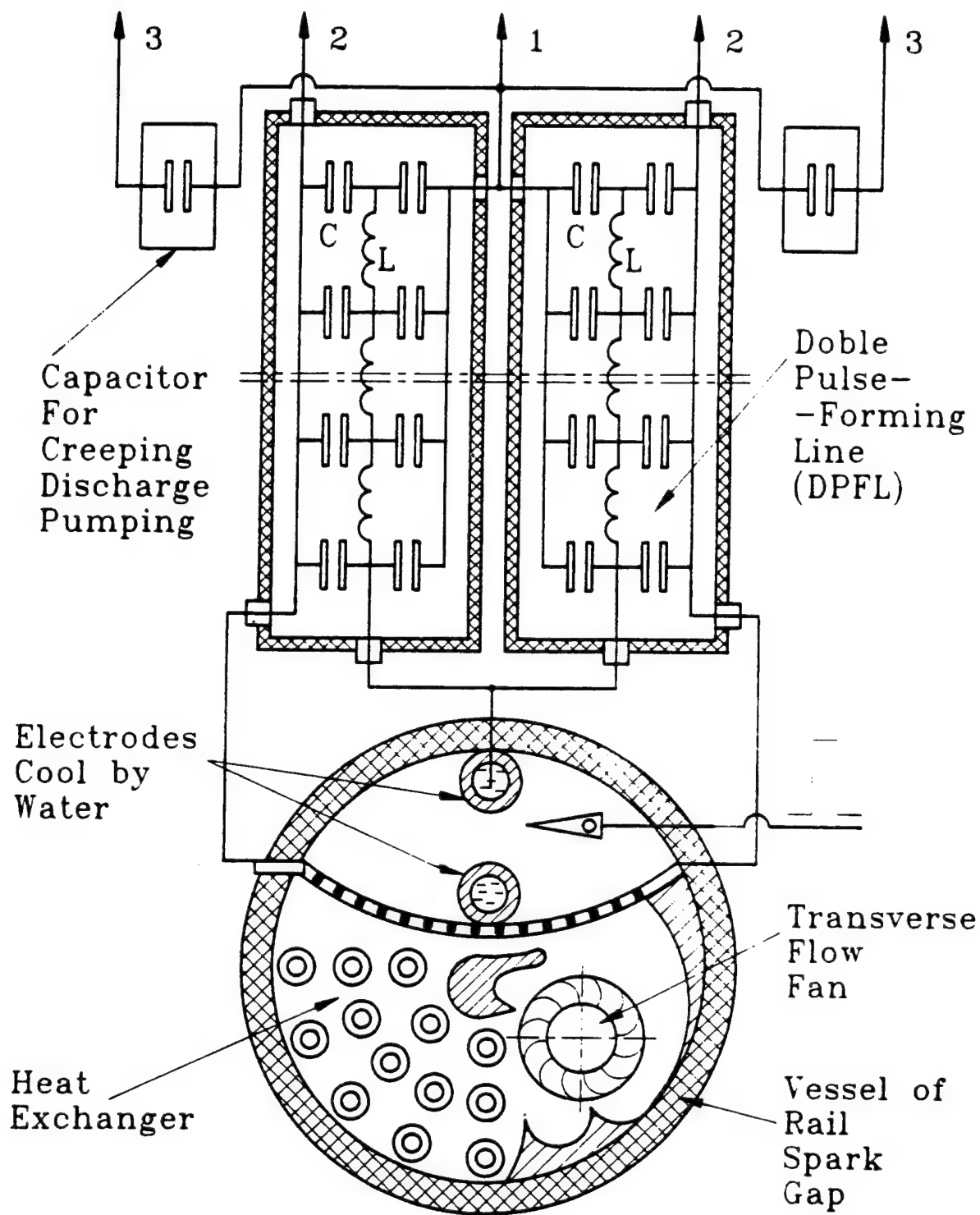


Fig.4. The excitation circuit for large aperture excimer laser (GEFEST-3)

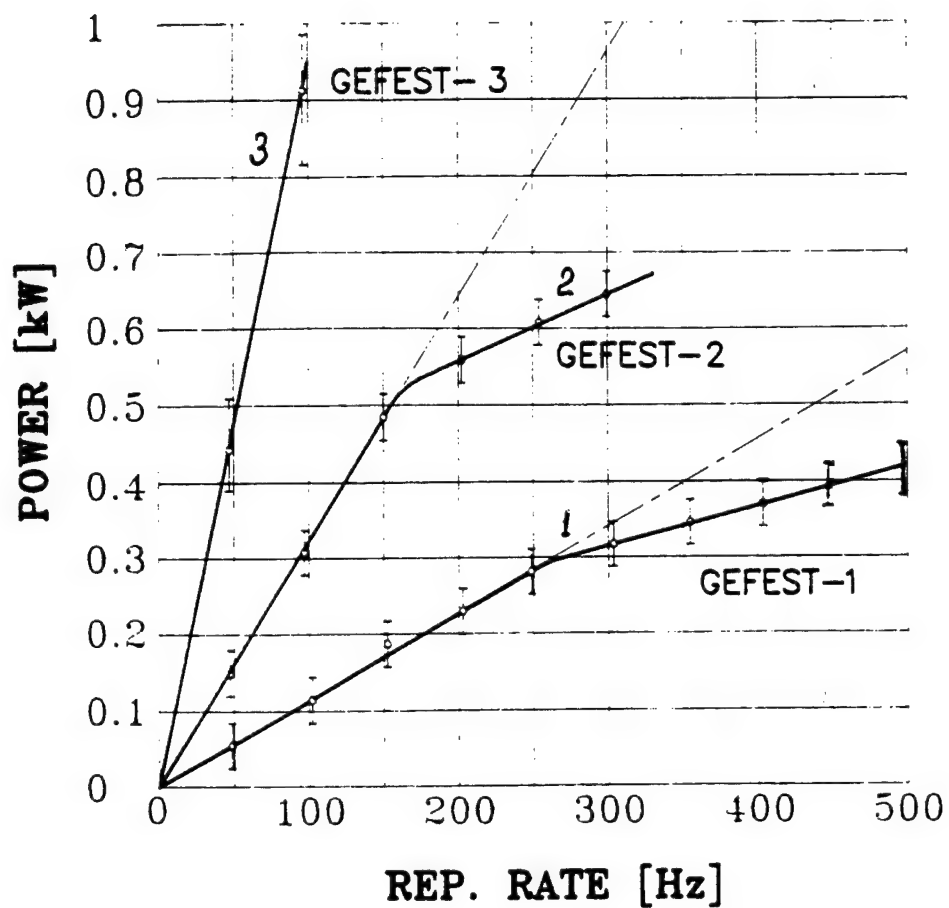


Fig.5. Average output power vs repetition rate of models high power excimer laser GEFEST (PLSL).



## Design Considerations for High-Power Industrial Excimer Lasers

36980005 The Hague EXCIMER LASERS AND THEIR APPLICATIONS in English 1991 pp 48-52

[Article by Dr. H.L. Jetter of Siemens AG]

[Text]

### **Abstract:**

The Siemens excimer laser is designed for industrial scale production processes. Its unique features are liquid dielectric capacitors, side-wise x-ray preionization, efficient cross flow gas circulation and an all metal/ceramic discharge head. All parts are integrated inside a hermetically sealed pressure vessel.

### **Introduction:**

Industrial scale production processes with excimer lasers demand degrees of reliability and reproducibility in performance, which surpass the common demands in R & D labs by several orders of magnitude.

Since investment costs for the laser normally are only a fraction of the total costs of the process, factors like MTBF, operating costs or ease of serviceability play in most cases the dominant role for industrial lasers. Therefore these lasers constitute a great challenge for laser development, which cannot be met by straightforward improvements to established technologies.

At Siemens we are developing industrial excimer lasers with high pulse energy. These lasers are distinguished by unique features, which take into account the mandatory industrial requirements.

### **The Siemens Excimer Laser:**

High pulse energy at good efficiency calls for a very fast, low inductance excitation circuit. This is realized in our laser by a compact

PFN, using capacitors with a liquid dielectric. These capacitors, formed by parallel metal plates, can be tailored to the required capacity, charging voltage and geometrical contours. The liquid dielectric (glycol/water mixture) offers the additional advantage of serving as cooling liquid for removing the loss-related heat. This is of great importance at high average powers. Also the dielectric liquid is selfhealing. As opposed to ceramic capacitors a voltage breakdown in the capacitor does not lead to a catastrophic failure of the laser, with sometimes considerable downtimes.

The fast excitation circuit of an excimer laser demands HV-switching capabilities, which in most laser can only be barely met by the normally used thyratrons. Ware of thyatron is therefore a major cause for excimer laser downtime. It also contributes substantially to its operating costs. This is especially true, for high pulse energy and/or high average power excimer lasers.

We addressed this problem, by using a spiker-sustainer circuit. A thyatron is only required to generate a low energy ignition pulse. The main discharge is switched by a saturable inductance. This magnetic switch is of the race-track type and made of amorphous metal strips. It is integrated in the PFN and together with it immersed into the dielectric liquid to provide efficient cooling. Since the energy of the ignition pulse is only a fraction of the total discharge energy, the thyatron is operated well below its maximum rating. Therefore thyatron lifetime constitutes no problem anymore.

The high pulse-to-pulse stability, which is mandatory for most industrial processes, requires a very homogeneous, reproducible preionization of the entire discharge volume. For large volumes, this cannot be achieved with the standard UV preionization.

We are using high intensity x-ray bursts to preionize the laser gas. The x-ray source is a pulsed low pressure, high current discharge, which produces by ion bombardment a shield of secondary electrons impinging on a thin gold layer there generating the x-rays. So far we have scaled this technique to repetition rates > 250 Hz and electrode length up to 80 cm. The x-ray dose is extremely homogeneous over the entire discharge volume.

With this preionization, a very homogeneous large aperture laser discharge can be operated very reliably. The observed fluctuations of the pulse energy are well below 1 %.

An additional advantage of the homogenous, large aperture discharge is the even distribution of the discharge current across a big surface on the electrodes. Consequently the current density on the electrodes is low, therefore the erosion of the surface small.

Furthermore the x-ray tube is located sidewise to the electrodes. Since the x-radiation does not have to penetrate the electrodes, there is no restriction in shape and material of these electrodes. Solide nickel electrodes are used. In combination with the low current density, these electrodes show an exceptionally long lifetime.

In the design of an industrial laser the gas flow has to be taken into account very carefully. All components such as the laser head, heat exchanger, ducts, bends etc. have to be optimized with regard to flow resistance. This is especially important for high repetition rate operation.

The flow resistance increases proportional to the second power of the gas velocity and the required compressor power in proportion to the third power of the gas velocity. An unfavourable gas flow system will therefore restrict the laser operating to low repetition rates. As the most critical part of the gas flow system, we have developed a laser head which combines low inductance - obligatory for high pulse energy - with low flow resistance - obligatory for high repetition rates.

Beside a flat ceramic plate, which seperates the dielectric filled PFN from the discharge chamber, the laser head is all metal. No plastic material is needed for HV-insulation. The current returns are a multitude of blank wires optimized in respect to minimum inductance and flow resistance as well as to safe operation against creeping discharges.

Gas lifetime and window degradation are strongly susceptible to gaseous impurities generated by chemical reactions of the laser gas with elastomers, bearing lubricant and organic structural materials. Care was taken to minimize these materials as far as possible. By these means, gas costs and maintenance routines could be achieved, which are quite acceptable to industrial production.

Industrial production environments impose stringent safety standards. Therefore the corrosive, toxic laser gas should be contained in a hermetically sealed pressure vessel. Our design takes care of this requirement by integrating laser discharge unit, PFN, x-ray preionizer, blower and heat exchanger inside a stainless steel pressure vessel.

Fig 1 shows a sectional drawing of the laser head.

The down-times for maintenance and repair are governed by the ease of serviceability. Fig 2 shows the modular design of the laser. Broken units can be pulled out of the laser very easily and replaced by new ones. So the laser can be back into operation in a minimum of time.

The total laser system consists of three cabinets (Fig 3), the laser unit itself, the highvoltage supply and the control rack. Command and control of the laser are done by a PC installed in the control rack. The remote control rack is connected to the laser by fiber optic links.

We have operated lasers of the described concept with a variety of emission parameters. With XeCl, average powers up to 300 W were achieved. By varying the capacity of the PFN and adjusting the operating voltage, pulse energies in the range of 1,5 to 3 J were obtained with efficiencies  $> 2,0 \%$ . The optical pulse width is in the range of 80 - 200 ns depending on the characteristic data of the PFN.

**SIEMENS**

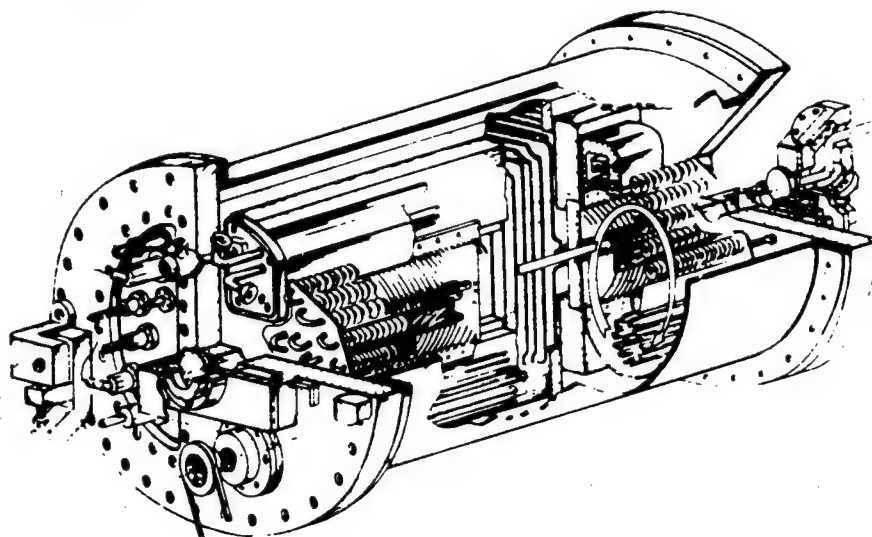


**Fig. 1 Laser head**

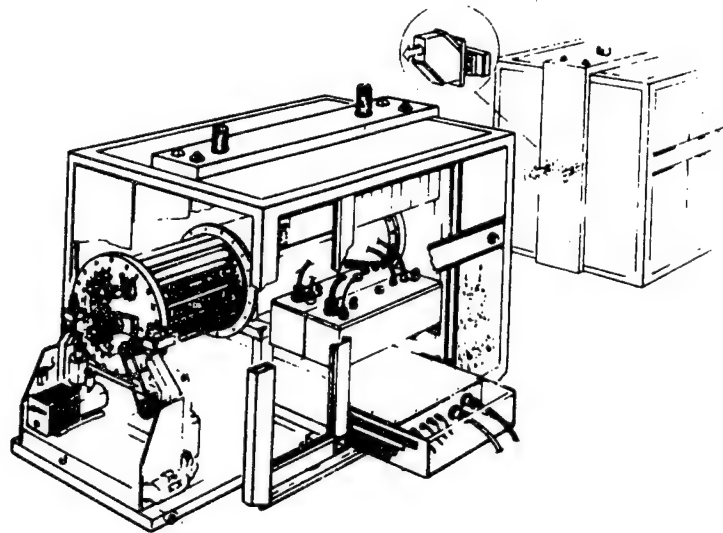


**Fig. 2 High-Power-Excimer-Laser (service concept)**

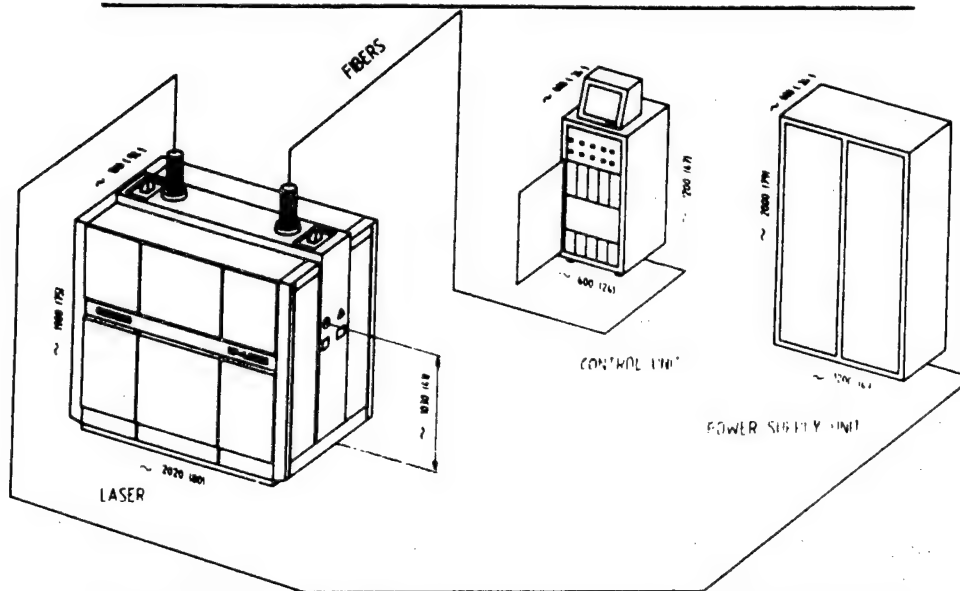


**Fig. 3 Excimerlaser-System**

Parametric Study of Small-Volume Long-Pulse X-Ray Preionized XeCl Laser With Double Discharge and Fast Magnetic Switch

36980005 The Hague EXCIMER LASERS AND THEIR APPLICATIONS in English 1991 pp 62-70

[Article by J.M. Hueber, B.L. Fontaine, M.N. Khobio, P.C. Delaporte, B.M. Forestier, and M.L. Sentis of Aix-Marseille University]

[Text]

ABSTRACT

An experimental parametric study of a small volume X-Ray preionized XeCl laser which uses the double discharge (spiker-sustainer) principle and a new fast ferrite magnetic switch is presented. This High efficiency discharge excitation system has allowed to achieve with a Ne/Xe/HCl mixture at relatively low pressure ( $P=2,5$  atm.), in a  $50\text{ cm}^3$  active volume ( $25 \times 2 \times 1\text{ cm}^3$ ), an efficiency 3,2% in energy and 4% in power at maximum with up to 140 mJ extracted optical energy in a 130 ns (FWHM) laser pulse in switch mode. Focus is made on laser characteristics dependence with magnetic switch and electrical circuit parameters, for switch mode. At the end, planned further studies of the present advanced excitation system for conditions of very high PRF, in the frame of Eureka EU205 Eurolaser program, are presented. The experimental part of these planned studies will be made with LUX very high PRF high average power IMFM test-bed.

1. INTRODUCTION

Potential applications of high power pulsed ultraviolet lasers have recently stimulated considerable interest in the scaling of excimer lasers to higher output energy, pulse length, pulse repetition frequency (PRF), average laser power and efficiency<sup>1</sup>. Discharge pumped excimer lasers are extensively used in various domains of scientific research and industrial processing. However, the classical excitation schemes like C-L-C circuit limit laser emission to short pulses (20-80 ns) and relatively low efficiency ( $< 2\%$ ). Recent developments of long pulse high efficiency self sustained discharge excimer lasers provide a number of opportunities in terms of lower stress on electrical components, lower heat and acoustic load by extracted photon, higher energy transmission

capability through optical fiber, and better control of laser beam divergence, polarization and line-width<sup>2</sup>. These developments have important issues on applications, notably for medical and doppler laser radar. Several means to increase either pulse width or efficiency have been studied recently<sup>3</sup>, namely control of discharge parameters with a classical C-L-C circuit, double discharge ( spiker-sustainer )<sup>4-10</sup> and stabilization by segmented electrodes associated to resistors or inductors<sup>11</sup>. However only very few parametric studies of these systems, particularly for small volume and high PRF capabilities, appear in literature.

A program to extensively investigate the key parameters which may limit scaling of the XeCl laser ( $\lambda = 308 \text{ nm}$ ) to very high average power ( $P_f > 1 \text{ kW}$ ) and pulse rate frequency has been undertaken at IMFM<sup>12-16</sup>. This program includes study of possible advanced excitation schemes in order to increase whole system efficiency and laser pulse length and reduce acoustic load in active volume.

This paper presents results of an experimental parametric study of a small volume X-Ray preionized XeCl laser which uses the double discharge principle (spiker-sustainer)<sup>4</sup> associated with magnetic switching<sup>5-10,15,16</sup> and a new fast ferrite magnetic switch with pulsed reset, allowing both long pulse, high efficiency and high PRF capability. Focus is made, in the present paper, on laser characteristics dependance with magnetic switch and electrical circuit parameters for switch mode.

## 2. EXPERIMENTAL DEVICE

The electrical excitation system includes a preionization X-Ray gun energized by a 120 kV pulse transformer<sup>15</sup> and delivering 10 mRad X ray dose in a 200 ns (FWHM) pulse inside the 2 cm (H)\*1 cm (W)\*25 cm (L) laser head active volume, and an advanced electrical excitation system.

The double discharge excitation system consists in a fast high voltage and low energy spiker and a high energy and low voltage sustainer transiently isolated by a fast ferrite magnetic switch.

The spiker is made of a 2.7 nF ceramic capacitor switched by a triggered spark gap and charging up to 40 kV in 50 ns 4 TDK ceramic transfer capacitors of 2.2 nF total capacitance set in a very low inductance loop between laser electrodes. The spiker is fired within 1  $\mu\text{s}$  after the sustainer pulse forming line (PFL) has reached its maximum voltage. Time delay between spiker triggering and x-ray gun pulsed voltage maximum can be varied from 0 to 1  $\mu\text{s}$  by use of a delay generator.

The sustainer consists in a .6 ohm characteristic impedance double sided solid state PFL line made, for each side, with 8 or 11 rows of 6 \* 1.4 nF TDK ceramic capacitors (150-200 ns electrical time). The PFL is pulse charged up to 10 kV in 4  $\mu\text{s}$  through a thyatron.

The magnetic switching device is made of several coaxial structures in parallel, each of them comprising many low losses high frequency Ni-Zn ferrite tores ( $\mu_r = 20-800$ ) set in serie. Ferrites are pulse reset between shots by a single turn auxiliary capacitor circuit delivering a current of 60 amperes during  $10 \mu s$ , in order to minimize switch inductance for the needed magnetic surface. The losses of this advanced magnetic switch are estimated to be less than 10% which allows a very high pulse rate capability ( $> 1 \text{ kHz}$ ).

The magnetic switch is designed in order to automatically switch very rapidly (20-30 ns) following magnetic material saturation at the time of maximum transfer capacitor voltage. Measured currents through each of the switches set in parallel are equal within 10 %. A reverse polarity is used between spiker and sustainer circuit (switch mode). A schematic diagram of laser electrical circuit is shown on Fig. 1.

Various low losses flat multi-dielectric coated mirrors are used for the output coupler of the stable optical resonator used which is set in direct contact with gas mixture to reduce losses. A 99% Reflectivity rear mirror with 2 m radius centered at  $\lambda=308 \text{ nm}$  also set in direct contact with gas mixture completes the resonator.

Various Ne/Xe/HCl gas mixtures prepared with an home made high purity gas manifold are used. Safe working maximum gas pressure in laser cavity is 4 atmospheres.

Discharge currents are measured with home made calibrated Rogowski coils and Pierson fast current transformers. Pulse voltages are measured with low impedance home made resistive voltage dividers. Laser time variations are determined by use of a ITL TF1850UV vacuum photodiode with sapphire window while a GENTECH ED500 Joulemeter is used for laser energy measurements. Signals are recorded with an HP54112D four channels 400 MSa/s and an HP54502A two channels 400 MSa/s digitizing oscilloscopes set in a screen room which are connected to a microcomputer, and periferics.

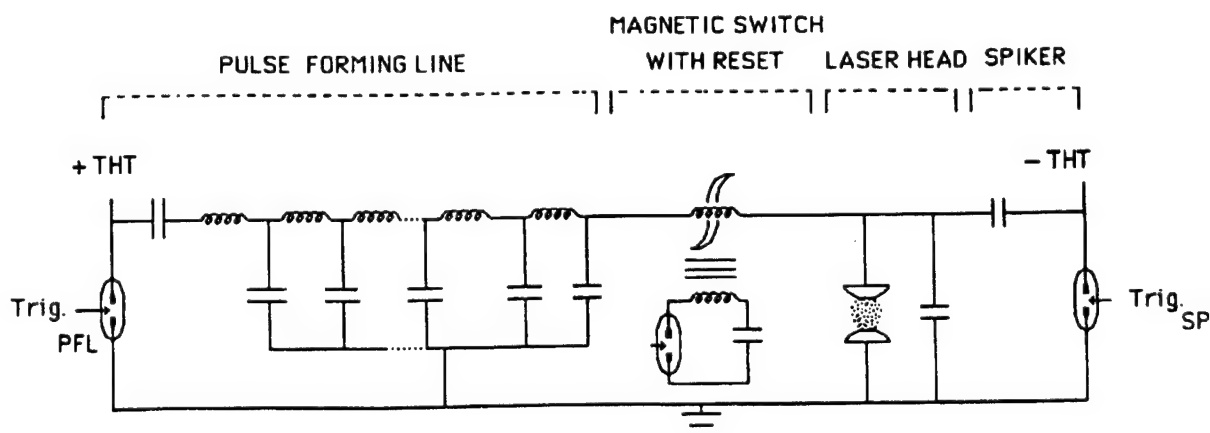


**Fig.1** : Schematic diagram of laser electrical circuit with double discharge and magnetic switching



### 3. EXPERIMENTAL RESULTS

A parametric study of the double discharge XeCl laser has been fulfilled with the above described experimental apparatus. For this study the magnetic switch consists in two rows of  $N$  ferrites ( $\phi_{\text{int}} = 15 \text{ mm}$ ,  $\phi_{\text{ext}} = 25 \text{ mm}$ ,  $h = 10 \text{ mm}$ ), set in parallel ( $20 < N < 30$ ). The total magnetic surface of each row  $S_m$  is varied between 10 and  $15 \text{ cm}^2$ . The pulse reset current is equal to 60 A ( $1000 \text{ A/m}$ ).

The magnetic switch was characterized on laser electrical system, without preionization in order to avoid breakdown in the range of voltages of this study (0-35 kV). The figure 2 shows the voltage time variation measured between switch on electrode side and ground and the current through one magnetic switch path.

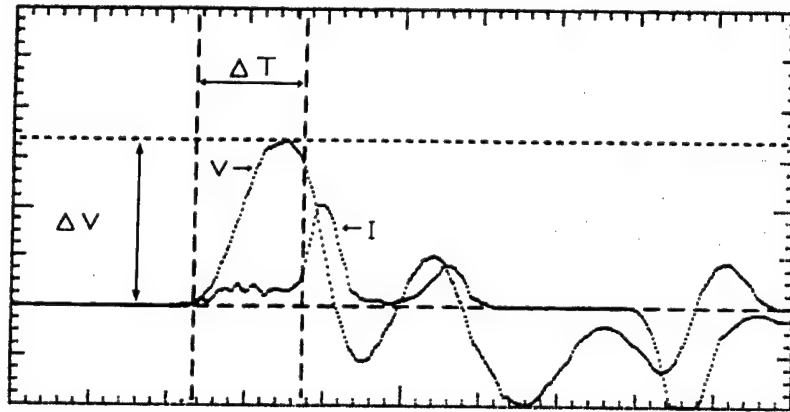


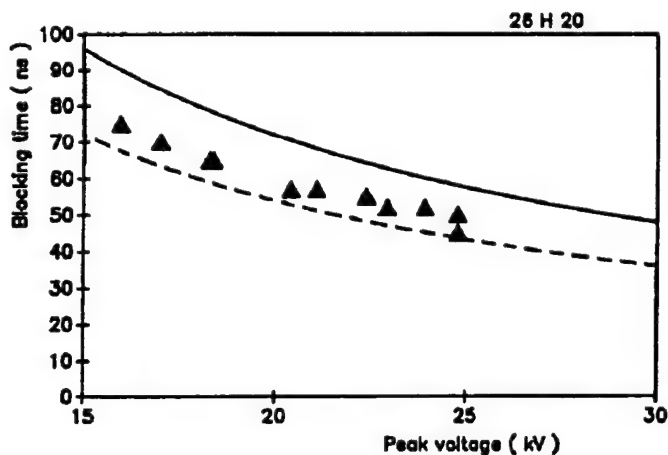
**Fig. 2:** typical waveforms of voltage on spiker transfer capacitors (4,7 kV/div) and current through one magnetic switch (0.4 kA/div) for 26 H 20 ferrite torus. Time base is 50 ns/div. Magnetic switch blocking time and peak voltage are indicated by  $\Delta T$  and  $\Delta V$ .

The electromagnetic field induced by the magnetic material depends on the law of induction  $e = -S \Delta B / dt$  for each path.  $S$  is the cross section area of the magnetic material and  $\Delta B$  is the flux density. A simple integration of this equation, with hypothesis of linear voltage time variation, gives:

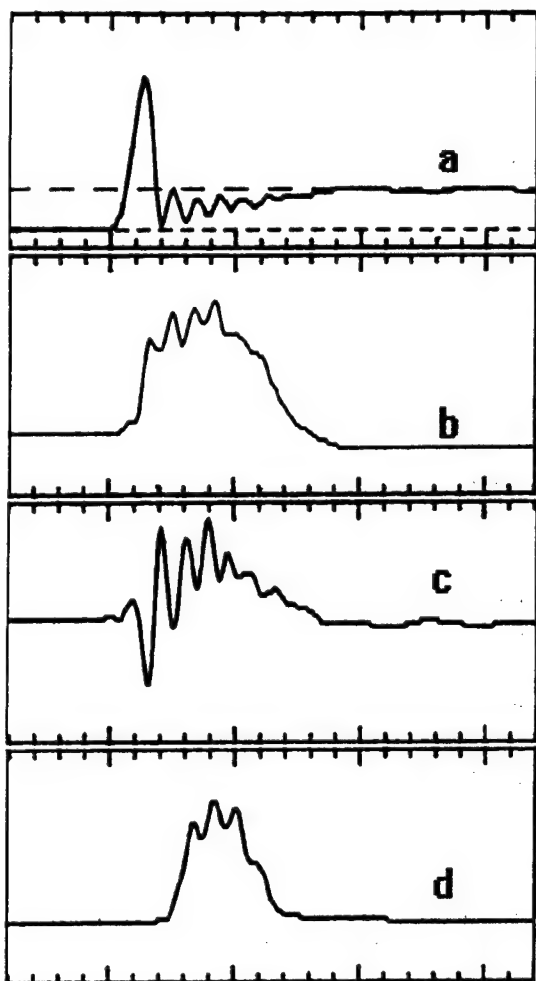
$$\Delta t = 2 S \Delta B / \Delta V$$

On figure 3 are presented calculated and measured values of magnetic switch blocking time  $\Delta T$  for two different flux density swing in the case of 26 H 20 ferrite torus. The solid line corresponds to a maximum amplitude flux density swing ( $\Delta B = 0.6 \text{ T}$ ) and the dashed one corresponds to a swing from remanent field  $B_r$  to saturation ( $\Delta B = 0.45 \text{ T}$ ). Experimental data (filled triangles) are set between these two boundaries. Measured blocking time is slightly lower than expected with pulsed reset.

Schematic experimental waveforms of switch and discharge currents, electrodes voltage and laser output oscilloscope traces are shown in Figure 4, for 35 kV spiker and 7 kV PFL voltages and two magnetic switches in parallel ( $N = 24$ ). PFL electrical time is 150 ns and total capacitance is 134 nF. Gas mixture for this case is Ne/Xe/HCl (7950/75/10) at 2.5 atm. total pressure. A 60% Transmission output mirror is used. Delay time between X-Ray gun and spiker triggering is 340 ns. Measured blocking and switching times of magnetic switch following spiker triggering are 50 ns and 25 ns respectively. After spiker switching, electrodes voltage varies from - 8 kV (PFL charge voltage) to 25 kV when breakdown occurs. Needed time to reach stationary conditions in term of injected electrical energy is about 60 ns showing that the remaining PFL circuit inductance after switching is relatively high. Voltage waveform oscillations are strongly dependant of transfer capacitor value and their amplitude is decreasing when lowering its value. Delay time between active medium breakdown and beginning of laser emission is about 50 ns. Parts of this delay are attributed to current rise time and intra-cavity laser field buildup. However a part of this delay time must be attributed to magnetic switch behavior.

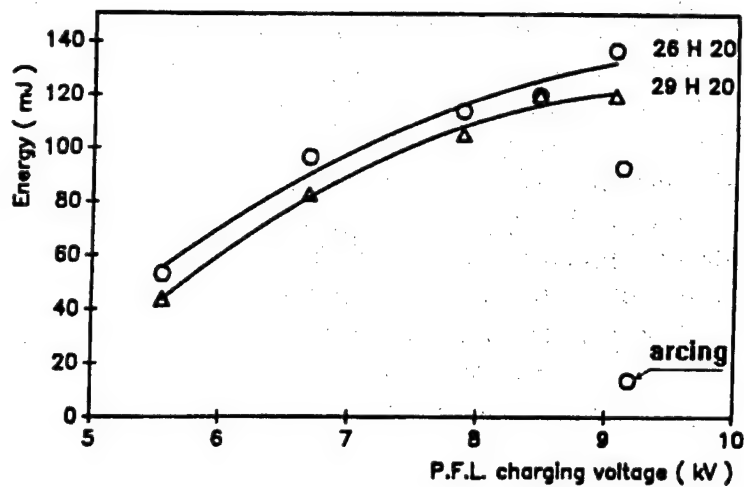


**Fig. 3:** Calculated and experimental magnetic switch blocking time versus peak voltage  $\Delta V$ . lines corresponds to calculated values  
 (---  $\Delta B = 0.45 \text{ T}$ )  
 (—  $\Delta B = 0.6 \text{ T}$ )  
 Triangles correspond to experimental data.



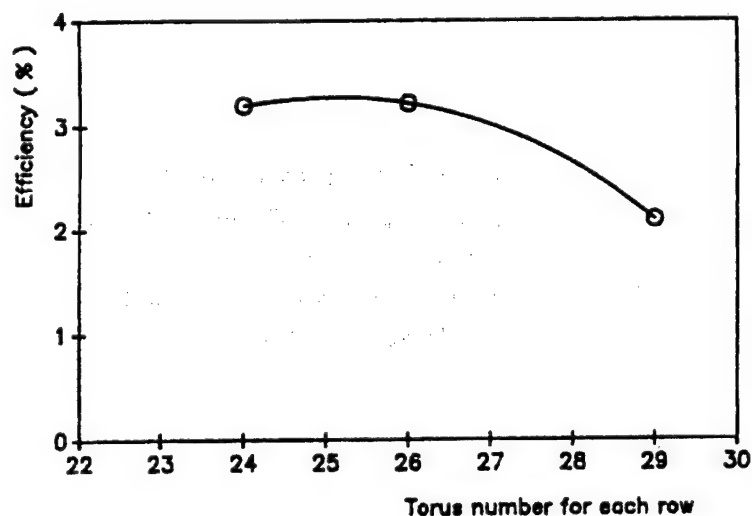
**Fig. 4:** Typical experimental waveforms of (a) electrodes voltage, (b) current through magnetic switch, (c) discharge current and (d) optical output. Time base is 50 ns/div.

Figure 5 shows measured laser energy versus PFL charge voltage for two numbers of torus ( $N=26$  and  $29$ ). One observes that laser energy is always higher for a given charge voltage for  $N=26$  and varies slightly with ferrites number.



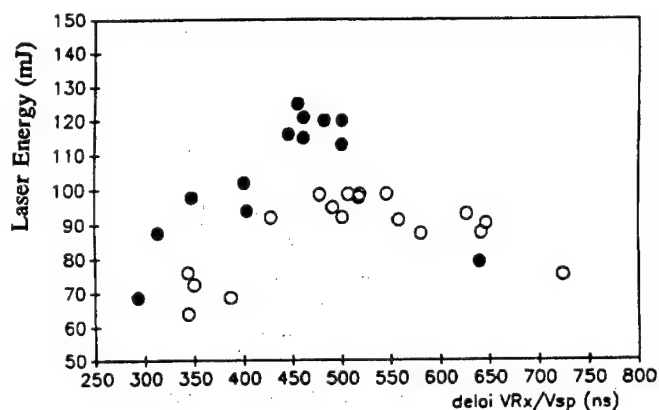
**Fig 5 :** Laser energy vs PFL charging voltage for two numbers of torus.

Figure 6 shows measured maximum laser efficiency ( $W_l/W_{PFL}$ ) versus number of torus for one row. Spiker and P.F.L. voltage are optimized to obtain the maximum efficiency for each number of torus. It is noteworthy that laser efficiency decreases when magnetic material surface increases. This loss in efficiency is attributed to an increase of P.F.L. switching time after spiker triggering. For a relatively small number of torus ( $N < 27$ ), the P.F.L. is rapidly switched and PFL energy is transferred to the discharge before strong plasma recombinaison. When  $N$  is decreased below a threshold, laser discharge instabilities appear. An increase of magnetic material surface leads to a late P.F.L. commutation. Time delay after spiker discharge breakdown is then important as well as plasma recombinaison. In such case streamers are visibles in discharge.



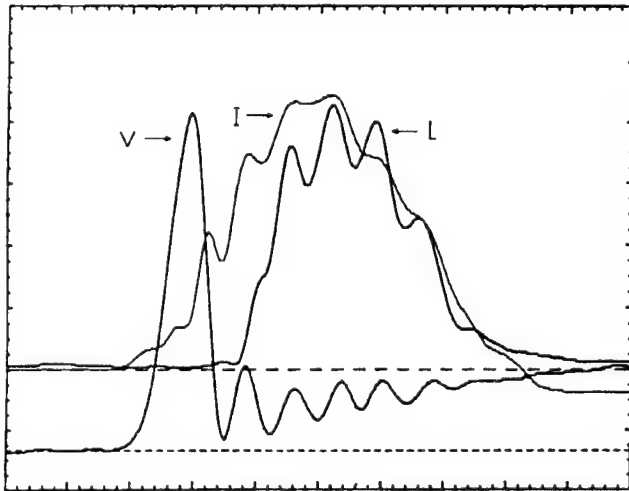
**Fig. 6:** Double discharge XeCl laser maximum efficiency for different quantities of magnetic material.

Laser efficiency is observed to be strongly dependant with delay time between spiker and X ray preionization for a given magnetic material in the switch. On fig 7 is shown laser energy dependance with delay time beetwen X-Ray gun triggering and spiker peak voltage. Gun voltage rise time is 300 ns while spiker transfer capacitor voltage rise time is 50 ns. Preionization density controls breakdown voltage which decreases when delay time is increased for given spiker and sustainer charge voltages. This laser efficiency dependance is attributed to variations of magnetic switch blocking time with peak voltage.

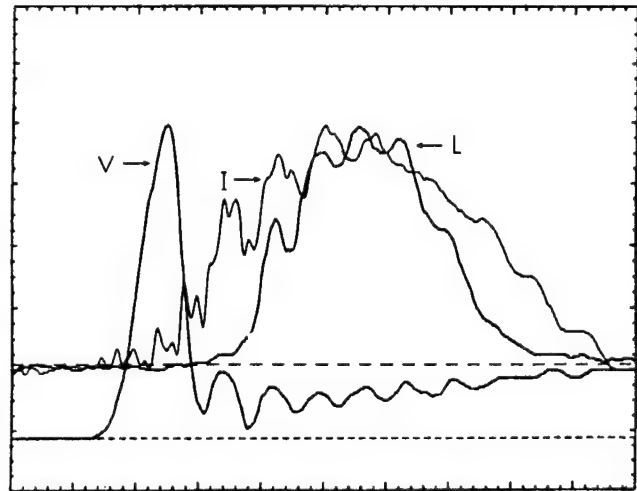


**FIG. 7:** Laser energy vs delay time between Xray gun triggering and spiker peak voltage for typical conditions  
 Ne/Xe/HCl (7950/75/10)  
 $P = 2.3$  atm.,  $T_{\text{mirror}} = .40$   
 ○  $V_{cp} = 6$  kV  
 ●  $V_{cp} = 7$  kV

Figures 8a and 8b represent typical experimental oscilloscope traces of voltage, current and laser output for two different PFL capacitances (134 nF and 184 nF) and electrical time (150 ns and 200 ns). Stored energy (2.7 J) is the same for the two cases.



8a) 134 nF



8b) 184 nF

**Fig.8:** oscilloscope traces of voltage between laser electrodes (4.7 kV/div), current through one switch path (800 A/div) and optical output (a.u.) for two PFL a) 134 nF (150 ns electrical time) and b) 185 nF (200 ns electrical time). Time base is 50 ns/div.

Laser emission time duration is about 130 ns for the 150 ns electrical time PFL and 150 ns for the 200 ns electrical time PFL. The laser pulse follows energy injection for the 150 ns electrical time case, while it terminates before the end of energy injection for 200 ns. This result is attributed to a discharge instability appearing in the 200 ns PFL case. The laser output energy per pulse is higher for the first case ( $W_l = 135$  mJ) than for the second one ( $W_l = 90$  mJ), but it is noteworthy that present conditions are not yet optimized in terms of output coupling, magnetic material and working pressure for both cases and specially for the second one (200 ns PFL electrical time). In ranges of pressure and PFL voltage where laser efficiency is high, discharge, as observed visually through lucite laser head side window, is very homogeneous.

#### 4. CONCLUSION

An experimental parametric study of a small volume XeCl laser excited by a double discharge circuit using an advanced magnetic switch has been made with focus on the effects of magnetic switch characteristics on discharge electrical behavior and laser extracted energy. This laser has a

very high pulse rate frequency capability ( $> 1$  kHz). An efficiency of 3,2 % in energy and 4% in power at the maximum, with up to 140 mJ extracted optical energy in a 140 ns (FWHM) laser pulse length, has been demonstrated with this small volume not optimized device. This study shows that a very fast magnetic switch made of small commercial Ni/Zn ferrite torus associated with a pulsed reset allows very good performance from a double discharge excitation XeCl excimer laser in terms of efficiency and pulse length. It is shown that laser characteristics are relatively insensitive to the quantity of magnetic material used for the switch in a range of more or less 10 % around an optimum value. The study shows also an optimum for delay between spiker and preionization which is more critical than with the C-L-C excitation scheme for the same specific electrical energy<sup>(14)</sup>.

This study will be pursued, including a parametric study of magnetic switch performances with various magnetic materials and an increase of working pressure up to 4 atm. The use of thyatron, associated to a fast inverting high voltage ferrite pulse transformer to charge the spiker transfer capacitors for high PRF working condition in switch mode, is also planned.

At the end, further studies of the present advanced excitation system are planned for conditions of very high PRF, in the frame of EUREKA EU205 Eurolaser program. The experimental part of these planned studies will be made with LUX very high PRF high average power IMFM laser test-bed<sup>12,13,14</sup>.

## 5. ACKNOWLEDGMENTS

This research was supported by french DRET

## 6. REFERENCES

1. See, for example, papers on XeCl lasers in Techn. digests, Conference on Lasers and Electro-Optics, OSA, 1983-1990.
2. T.J. McKee, Appl. Opt., 30, 365, 1991.
3. R.C. Sze, SPIE, Vol 1041, Metal Vapor, Deep Blue, and Ultraviolet Lasers, p. 176, 1989.
4. W.H. Long Jr, M.J. Plummer and E. Stappaerts, Appl. Phys. Lett., 43, p. 735, 1984.
5. C.H. Fisher, M.J. Kushner, T.E. Dehart, J.P. McDaniel, R.A. Petr and J.J. Ewing, Appl. Phys. Lett. 48, p.1574, 9 june 1986.
6. R.S. Taylor and K.E. Leopold, J. Appl. Phys., 65, p. 22, 1 january 1989.
7. T.J. Mc Kee, G. Boyd and T.A. Znotins, Photonics Technology Lett., March 1989.
8. R.J. Winfield, SPIE, Vol 1046, Pulse power for Lasers II, p. 98, 1989.

9. A.J. Brown, E.G. Sergoyan, F.E. White, M. Vondadelszen, C.E. Fisher, Laser 89', New Orleans, Dec. 1989, Proceed., STS Press, D.G. Harris and T.M. Shay Ed. p 134, 1990.
10. J.W. Gerritsen, A.L. Keet, G.J. Ernst, W.J. Witteman, J. Appl. Phys., 67, 3517, 1990.
11. R.C. Sze, J. Appl. Phys., 54, p. 1227, 1983.
12. B.L. Fontaine, B.M. Forestier, M.L. Sentis, R.C. Sze and M.L. Vanini, in Technical Digest, Conference on Lasers and Electro-Optics (OSA, Washington DC, 1987), paper FC1, p.310, 1987.
13. M.L. Sentis, Ph. Delaporte, B.M. Forestier and B.L. Fontaine, J. Appl. Phys. 66, 1925, 1989.
14. M.L. Sentis, Thesis, Aix-Marseille University, France, may 1988.
15. J.M. Hueber, B.L. Fontaine, Ph. Delaporte, B.M. Forestier, M.L. Sentis, Opt. Comm., to be published, 1991.
16. M.N. Khobio, B.L. Fontaine, J.M. Hueber, Ph. Delaporte, B.M. Forestier, M.L. Sentis, International Congress on Optical Science and Engineering (E.C.O)- Excimer Lasers and Applications III, The Hague, Mars1991 , SPIE Proceed. Vol 1503, 1991.

## Parametric Study of a High Average Power XeCl Laser

36980005 The Hague EXCIMER LASERS AND THEIR APPLICATIONS in English 1991 pp 71-77

[Article by Bruno Godard, Emmanuel Estocq, Franck Joulain, Pierre Murer, and Marc Stehle of SOPRA and Jean Bonnet and Daniel Pigache of ONERA]

[Text]

### ABSTRACT

A wide aperture, X-ray preionized discharge pumped XeCl laser, is described. The laser head is included in a gas circulation loop. The X-ray generator is made of a secondary emission electron gun. The X-ray pulse duration is 400 ns (FWHM).

The laser energy ( $E_L$ ) and the average power are given as a function of various parameters: charging voltage ( $V_c$ ), buffer gas pressure ( $P_L$ ), total capacitance ( $C_T$ ), the interelectrode distance ( $d$ ) and the repetition rate.

The laser discharge is driven by a classical LC-inversion circuit. The stored energy ( $E_S$ ) in the capacitor bank is  $C_T \times V_c^2 / 2$  and the efficiency is defined by  $E_L / E_S$ . Up to a repetition rate of 50 Hz, the laser energy per pulse remains almost constant with low fluctuations. The best efficiency, for different pressures, is obtained for the same  $V_c / P_L$  value. The optimal buffer gas pressure decreases with an increase of the total capacitance.

More than 4.5 Joules per pulse, single shot, have been extracted from a  $40 \times 5.8 \times 4 \text{ cm}^3$  discharge (efficiency = 1 %). At a lower laser energy level (2.5 J) the maximum efficiency reaches 2.5 %. An average output power of 175 Watts has been obtained. With this device, good preliminary results on Kr/F<sub>2</sub>/Ne mixture are given.

### 1. INTRODUCTION

Several applications like photolithography, photoablation, photodeposition, contact cleaning, planarisation or surface processing stimulate a great interest in development of excimer lasers. Small systems operating at high pulse repetition rate<sup>1</sup> and wide aperture X-ray preionized lasers of several liters active volume<sup>2</sup> have been realized. We present here an intermediate laser: 1 liter of active volume and a repetition rate of some tens of Hertz.

### 2. EXPERIMENTAL DEVICE

The X-ray generator is made of a secondary emission electron gun as described previously<sup>3,4</sup>. The electron gun is composed of a pulsed ions source and a cathode polarized up to -150 kV. The integrated X-ray dose, measured



with a pen dosimeter, in the laser chamber, reached 20 mrad at -150 kV. An X-ray dose 5 times higher can be obtained simply by removing the extraction grid with deleterious consequence of an increase of the length and intensity of the tail. The second configuration is used for present results. The X-ray pulse duration is about 400 ns (FWHM).

A classical LC-inversion circuit is employed (see figure 1). Electric energy is stored in two banks of ceramic capacitors ( $C_1 = C_2$ ). The total capacitance ( $C_T$ ) is adjusted from 143 nF to 454 nF. The laser discharge is triggered by two parallel thyratrons.  $C_2$  is charged through the inductance  $L_3$ . The discharge voltage rise time is imposed by  $C_1$  voltage inversion time. The charging voltage can be adjusted up to 50 kV. The active medium length is 40 cm and three interelectrode distances are used: 4.2, 5 and 5.8 cm.

The laser chamber, made of Ni-coated aluminum, is included in a gas circulation loop and has been described previously<sup>4,5</sup>. Two loops are tested: one with an important pressure drop due to a heat exchanger, the other one without this pressure drop. The loop volume is 150 liters. The centrifugal fan motor is equipped with a frequency converter providing continuous regulation of the speed from 0 to 4800 rpm.

For XeCl laser, the laser optical cavity is made of a five meters radius multilayer dielectric mirror and an uncoated plane window separated by 70 cm. The mirrors diameter is 7 cm. The optimal partial pressure of gas mixture is, in mbar, Xe/HCl/Ne : 30/4/ $P_L$  ( $1000 \leq P_L \leq 8000$ ).

This setup is fitted by the following diagnostics: each thyatron current, discharge current, charging voltage, gas pressure, transverse luminescence, laser energy and pulse duration, electron gun and ions source current and voltage, X-ray pulseshape. Thyratrons and discharge current probes are homemade.

### 3.RESULTS

A scheme of the LC-inversion circuit is presented in figure 1. The inductance value ( $L_1$ ) of thyatron circuit is obtained from the current oscillation time without laser discharge.  $L_1$  is equal to 175 nH. With a laser discharge,  $L_2$  is approximately obtained from the laser discharge current oscillation time without taking into account the plasma resistance evolution.  $L_2$  increases with the interelectrode distance ( $d$ ). At  $C_T = 286$  nF and  $d = 5$  cm,  $L_2$  is equal to 20 nH. At  $C_T = 454$  nF and  $d = 5$  cm,  $L_2$  is equal to 22 nH and at  $d = 5.8$  cm  $L_2$  increases to 25 nH.  $R_T$  is thyatron resistance and a part of thyatron circuit resistance.  $R_1$  and  $R_2$  are resistance losses of capacitors banks  $C_1$  and  $C_2$ . In parallel of the present experimental results, a self consistent model of the laser including preionization, kinetics and electrical circuit has been developed by J.Bretagne et al.<sup>6</sup> From this model,  $R_1$ ,  $R_2$  and  $R_T$  are estimated to a few hundred m $\Omega$  in order to reproduce experimental values of the thyratrons and discharge currents shown in figure 2.

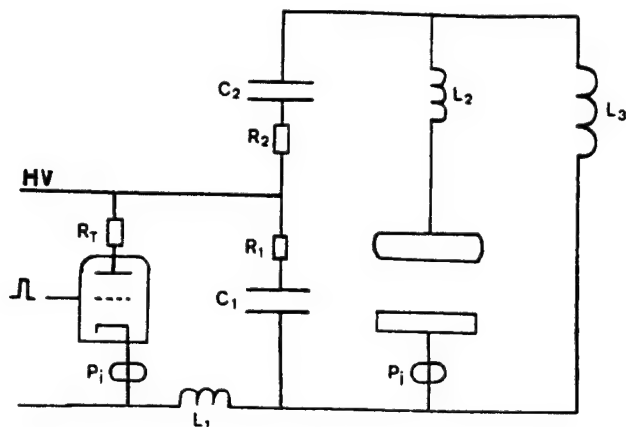


Fig.1: Schematic diagram of the L-C inversion circuit.  $L_1$ : thyatron circuit inductance;  $L_2$ : discharge circuit inductance;  $L_3 = 38 \mu\text{H}$ ;  $R_T$ : thyatron resistance;  $R_1$  and  $R_2$  resistance losses;  $C_1 = C_2$ ;  $P_i$ : current probes.

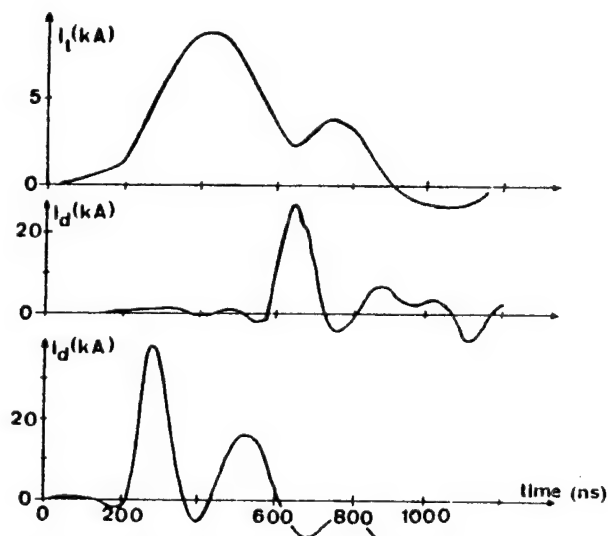


Fig.2: Thyatron (top curve) and discharge current waveforms. Gas mixture:  $\text{Xe/HCl/Ne} = 30/4/4000$  mbar.  $C_T = 454 \text{ nF}$ ,  $d = 5 \text{ cm}$ . Top and middle curves are at 20 kV charging voltage. Bottom curve is at 40 kV charging voltage.

The thyatron current waveform is given at the top of the figure, the charging voltage is 20 kV. The gas mixture is the optimal one at 4 bar,  $C_T = 286 \text{ nF}$  and  $d = 5 \text{ cm}$ . The first hole is due to the laser discharge breakdown. The maximum thyatron current increases linearly with the charging voltage from 8.5 kA at 20 kV to 23 kA at 50 kV. The laser discharge current is given at 20 kV (middle curve) and 40 kV charging voltage (bottom curve). The discharge current rise time is about 80 ns. At 40 kV, breakdown delay time is lower than at 20 kV. The dependence of the breakdown delay time versus the charging voltage is given in figure 3. When the charging voltage increases, the breakdown takes place before the  $C_1$  voltage total inversion.

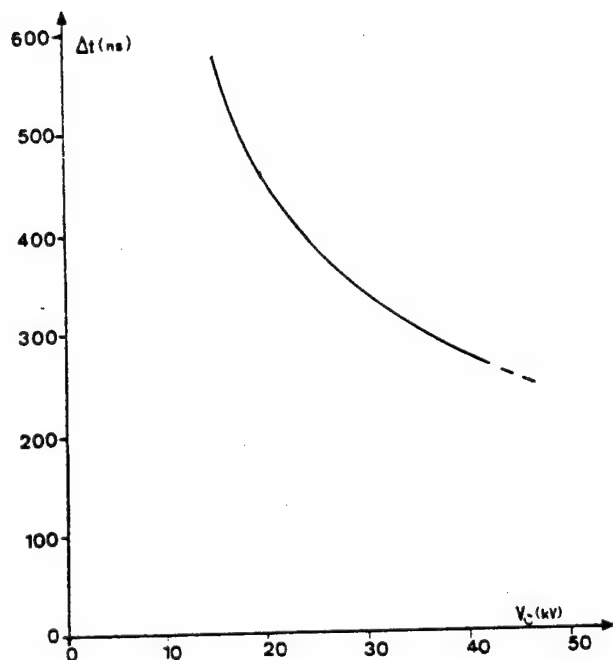


Fig.3: Breakdown delay time versus charging voltage. same gas mixture as in figure 2.

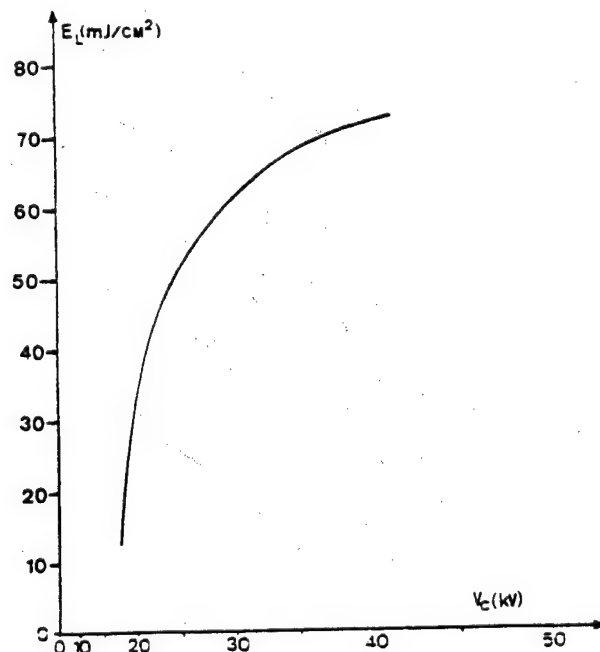


Fig.4: Laser energy per square centimeter versus charging voltage with a square scale. The mixture is in mbar:  $Kr/F_2/Ne = 50/2/4000$ .

For KrF laser study, the same device is used. Only the optical laser cavity is changed. The cavity consists of two multilayer dielectric plane mirrors with 99 % and 30 % reflectivities at 249 nm wavelength laser emission. The mirrors diameter is 3.6 cm. The interelectrode distance is 5 cm and the unoptimized gas mixture is  $Kr/F_2/Ne : 50/2/4000$  mbar. Because of the small mirrors diameter compared to the active medium surface, the laser energy per surface unit is presented in figure 4. These preliminary results, obtained with a long X-ray pulse duration and a slow laser discharge voltage rise time are very promising. With a well passivated discharge chamber, large enough mirrors and optimized gas mixture, better results will be obtained.

Figure 5 presents the laser energy per pulse as a function of the total capacitance for different charging voltage and at the optimal pressure. The interelectrode distance is 5 cm. The optimal pressure is the pressure for which the laser energy, for a given charging voltage, is the best one. From 143 nF to 454 nF, the laser energy increases. The efficiency corresponding to these laser energies is shown in figure 6. The best efficiency is obtained at a charging voltage of 20 kV, the laser energy is 1.6 J. With a total capacitance higher than 300 nF the efficiency decreases in all cases. Meanwhile, to reach high energy per pulse, the efficiency is better working at low charging voltage and high total capacitance.

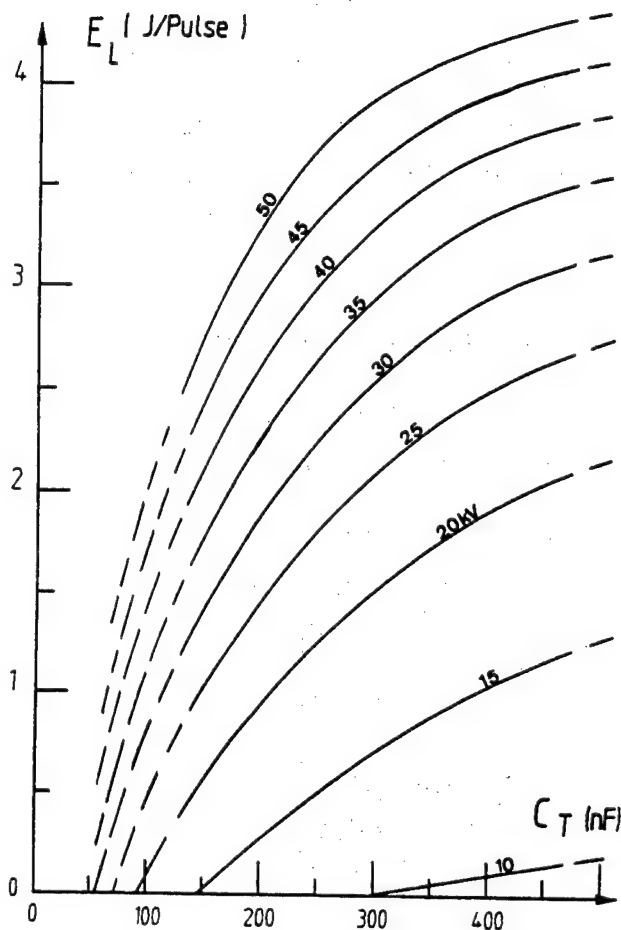


Fig.5: Laser energy versus the total capacitance for different charging voltage and at the optimal pressure. ( $d = 5$  cm).

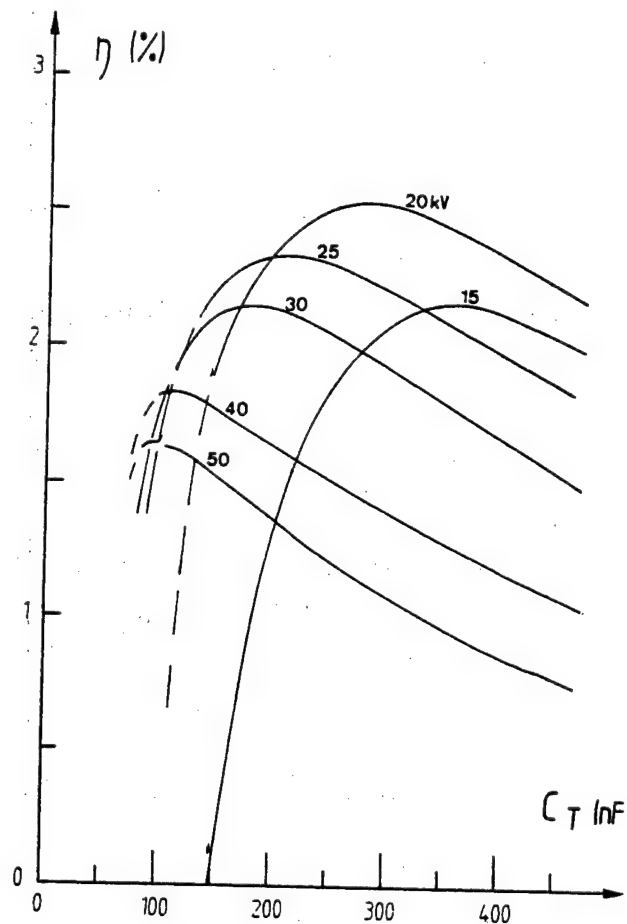


Fig.6: Efficiency corresponding to the laser energy given in figure 5.

Figure 7 presents the laser energy per pulse as a function of the interelectrode distance for different charging voltage and at the optimal pressure. The total capacitance is 454 nF. For large interelectrode distance, when the charging voltage is too small the energy deposition in the gas is not sufficient to permit a high inversion of population. Up to 20 kV charging voltage, a maximum of the laser energy is reached at an interelectrode distance lower than 5.8 cm. The corresponding efficiency is shown in Figure 8. At 20 kV charging voltage, the efficiency reaches 2.5 % at an interelectrode distance of 5.8 cm and with total capacitance of 454 nF. This efficiency can be reached too, at an interelectrode distance of 5 cm and with total capacitance of 286 nF at the same charging voltage (see figure 6).

The optimal pressure is inversely proportional to the total capacitance and the interelectrode distance as shown in figure 9 and figure 10 respectively. And referred to figure 5 and 7 the laser energy increases a lot when the optimal pressure decreases slowly. Figure 11 and figure 12 show that the influence of pressure and the influence of the interelectrode distance are in the same order for the laser energy per unit volume. Therefore, at a larger interelectrode distance, an higher laser energy is reached as already shown in figure 7. Probably, these results can be connected to the reduced electric field ( $E/N$ ) but only the charging voltage is well-known.

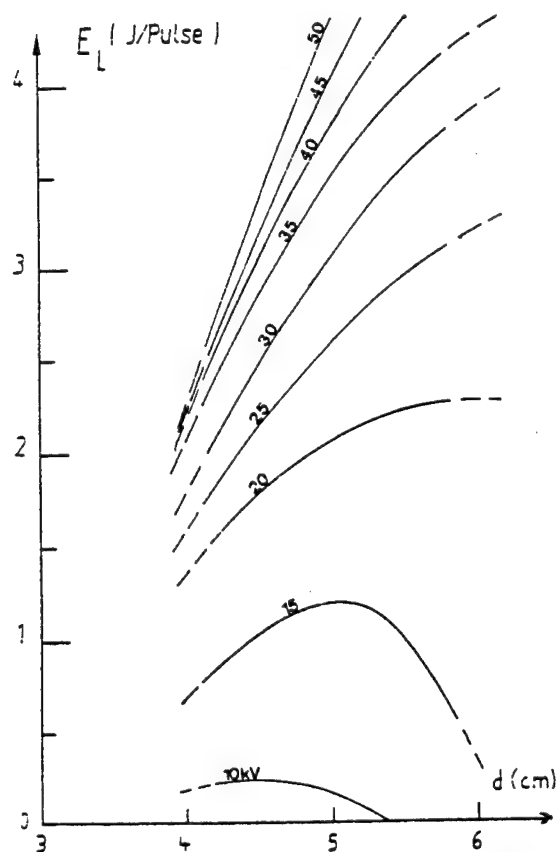


Fig.7: Laser energy versus interelectrode distance for different charging voltage at the optimal pressure.

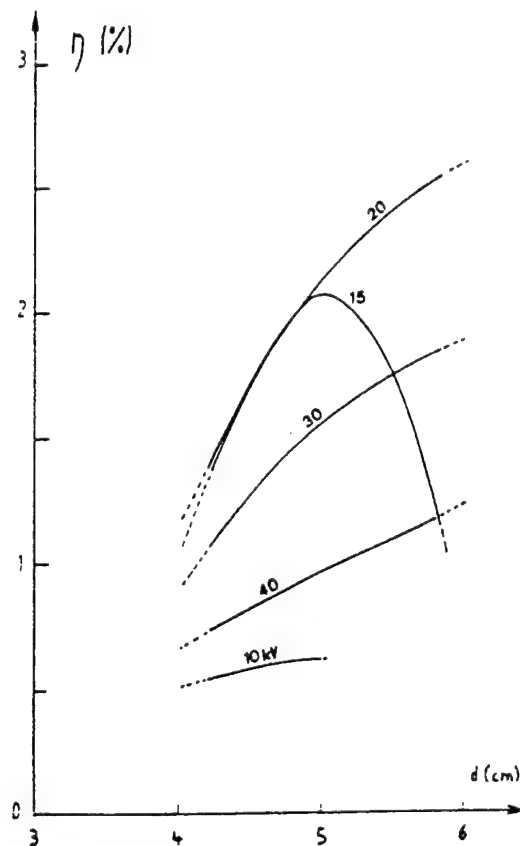


Fig.8: Efficiency corresponding to the laser energy given in figure 7. ( $C_T = 454 \text{ nF}$ ).

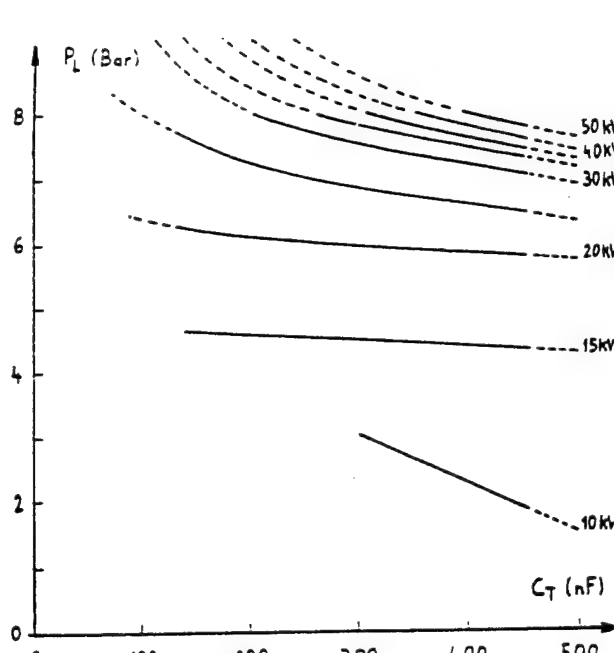


Fig.9: Optimal pressure versus the total capacitance for different charging voltage ( $d = 5 \text{ cm}$ ).

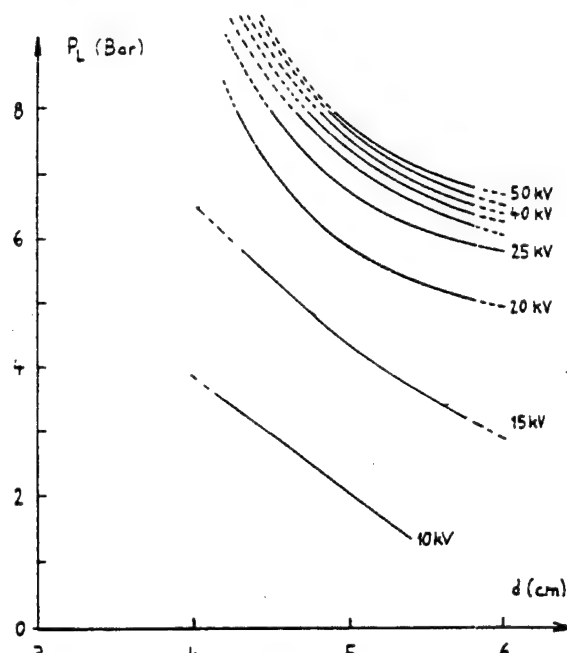


Fig.10: Optimal pressure versus the interelectrode distance for different charging voltage ( $C_T = 454 \text{ nF}$ ).

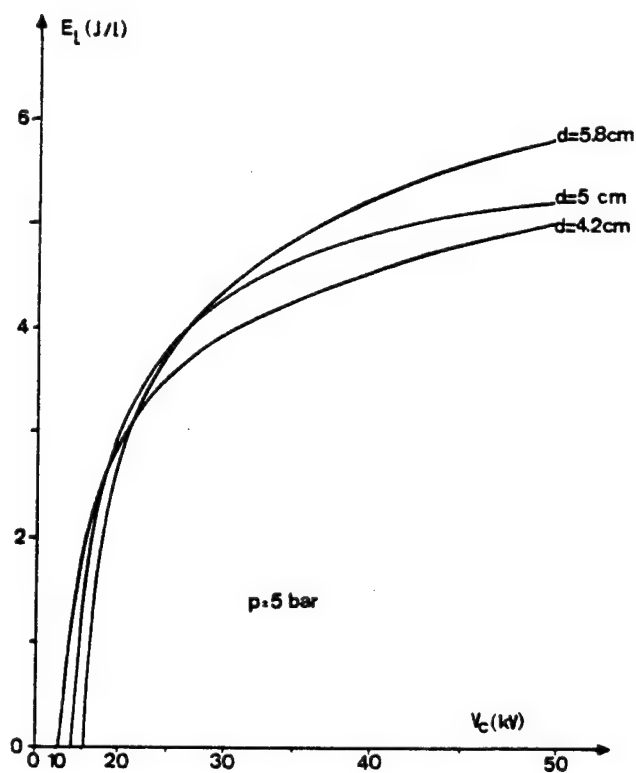


Fig.11: Laser energy per unit volume versus the charging voltage at 5 bar for  $d = 4.2, 5$  and  $5.8$  cm.

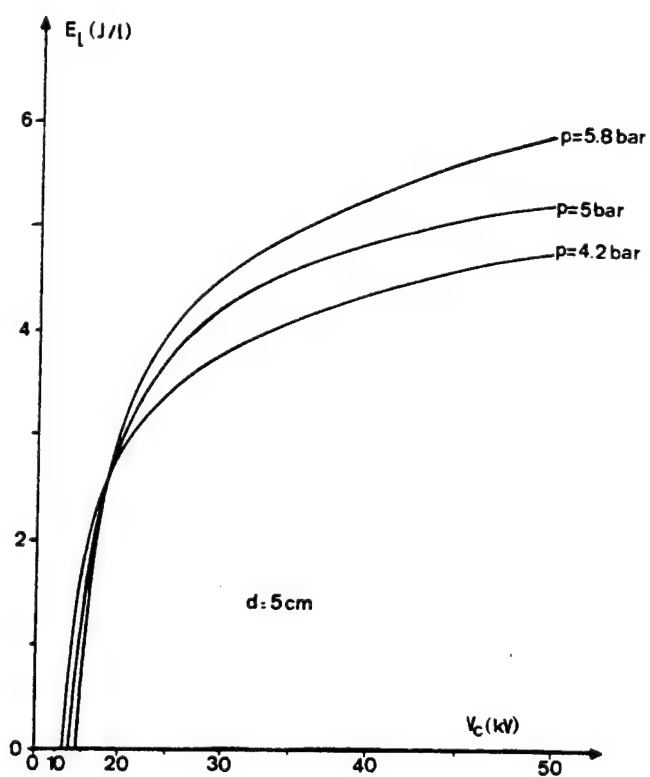


Fig.12: Laser energy per unit volume versus the charging voltage at 5 cm for  $P_L = 4.2, 5$  and  $5.8$  bar.

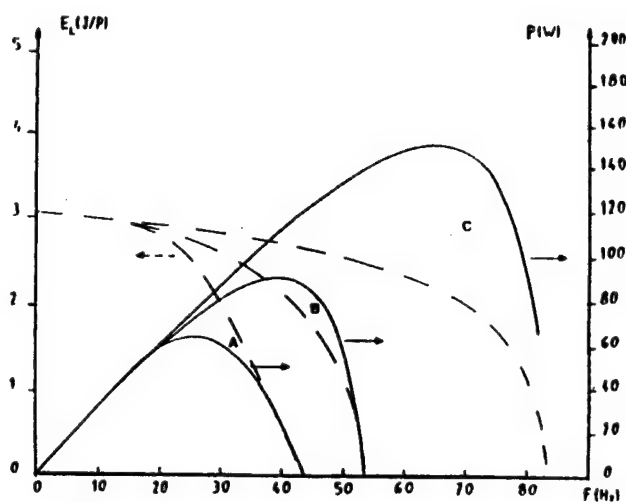


Fig.13: Laser energy per pulse and average power versus the repetition rate. Curves A; motor speed 3000 rpm, loop with important pressure drop; curves B; motor speed 3000 rpm, loop with less pressure drop; curves C; motor speed 4800 rpm, same loop as B.  $V_C = 25$  kV,  $P_L = 6$  bar,  $C_T = 454$  nF,  $d = 5.8$  cm.

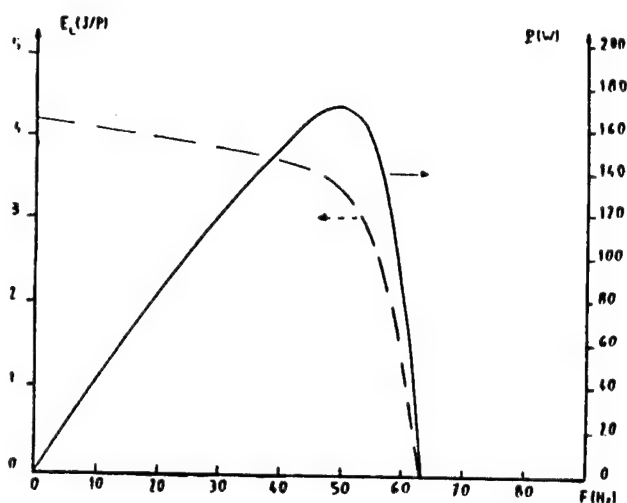


Fig.14: Laser energy per pulse and average power versus the repetition rate. Motor speed 4800 rpm, same loop as in figure 13 B.  $V_C = 35$  kV,  $P_L = 6$  bar,  $C_T = 454$  nF,  $d = 5.8$  cm.

For last figures, the interelectrode is 5.8 cm, the pressure is 6 bar and the total capacitance is 454 nF. The average power and the laser energy per pulse are given in **figure 13**. The charging voltage is 25 kV. Curves A correspond to a loop with an important pressure drop due to a heat exchanger. At 3000 rpm motor speed of the centrifugal fan, the maximum gas flow velocity measured with a wind-gauge in the discharge region is about  $6 \text{ m.s}^{-1}$ . The gas velocity is increased by two means: first reducing pressure drop (curve B) and second increasing the motor speed up to 4800 rpm (curve C). In both cases, the increase of the gas flow velocity permits to reached an higher average power with an higher repetition rate. At a charging voltage of 35 kV and at 4800 rpm motor speed the average power reached 175 Watts at a repetition rate of 50 Hz as shown in **figure 14**. The efficiency is 0.65 %. The maximum repetition rate is lower at 35 kV than at 25 kV.

#### 4.CONCLUSION

In spite of a long X-ray pulse duration and a slow laser discharge voltage rise time, very promising preliminary results on KrF laser study have been obtained. For XeCl laser, maximum energy of 4.5 Joules per pulse single shot with an efficiency of 1 % has been reached. The best efficiency is 2.5 % for 2.3 J laser energy. For a given charging voltage, even if the interelectrode distance is increased, the same efficiency can be reached, increasing the total capacitance too. The best average power is 175 Watts with an efficiency of 0.65 %. At a lower average power (80 Watts at repetition rate of 30 Hz) the efficiency is 1.9 %. It appears possible to achieve a few hundred Watts with good reliability.

#### 5.ACKNOWLEDGEMENTS

The authors gratefully acknowledge funding support from MRES within the framework of the Eurolaser-Eureka project EU.205.

#### 6.REFERENCES

1. M. Sentis et al. Gas flow and chemical laser, Ed. S. Rosenwaks, Springer-Verlag (1986).
2. T. Letardi et al, "Study of a 10-Liters Active Volume, X-Ray preionized XeCl Discharge Laser System", "Excimer Lasers and Applications", SPIE, Vol 1023, pp. 30-37, Hamburg 1988.
3. D. Pigache et al, "A Secondary Emission Electron Gun for X-Ray Preionization of High Repetition Rate XeCl Lasers", XIX ICPIG, Belgrade, 1989.
4. B. Godard et al, "Study of High Average Power Excimer Laser with Circulation Loop", 8<sup>th</sup> international symposium on gas flow and chemical lasers, Madrid, 1990.
5. B. Godard et al, "Parametric Study of a 3 Joules XeCl X-ray Preionized Excimer Laser", SPIE, vol 1278, pp.92-101, The Hague, 1990.
6. E. Estocq and J. Bretagne, "A Self-consistent Model for X-ray Preionized XeCl Laser", Submitted to XX ICPIG, Pise, 1991.

Excimer Laser Development at the ENEA Frascati Centre: Discharge  
Instabilities Study

36980005 The Hague EXCIMER LASERS AND THEIR APPLICATIONS in English 1991 pp  
80-87

[Article by Sarah Bollanti, Paolo Di Lazzaro, Francesco Flora, Shufen Fu,  
Gualtiero Giordano, Tommaso Letardi, Nicola Lisi, Giovanni Schina, and Cheng-  
En Zheng of ENEA]

[Text]

### ABSTRACT

Increasing the interest in high power coherent u.v. light sources, the ENEA Frascati Centre is developing 1 kW average power XeCl laser systems. In order to analyze the physical behaviour of these sources, net gain measurements spatially and temporally resolved have been done on a large volume prototype and compared with the results of a numerical 2-D simulation code.

### 1. GENERAL OVERVIEW

The ENEA Frascati Centre is involved in a European collaboration project (Eureka EU213) for developing 1 kW average power excimer laser. In order to satisfy different applications requirements, two approaches have been followed in this laboratory: 1) high energy per pulse (10 J); 2) high repetition rate (1 kHz).

As an intermediate step we have developed two x-ray preionized, discharge pumped XeCl laser devices: a 10 l active volume, 10 J/shot, 6 Hz and a 0.5 l, 1 J/shot, 100 Hz systems<sup>1-5</sup>. The main parameters of the two laser sources as experimentally measured are reported in Table 1. Several measurements have been devoted to a better understanding of the physical processes governing the laser behaviour. In particular we investigated the growth of discharge instabilities in the large active volume laser, where preionization disuniformity and streamers formation severely compromise the discharge quality.



Laser prototype	High energy per pulse	High repetition rate
Pumping schemes	a) spark-gap switched discharge b) photoswitched discharge	spark-gap switched discharge
Active volume	a) 10x10x100 cm <sup>3</sup> b) 7x10x100 cm <sup>3</sup>	3x3x50 cm <sup>3</sup>
Flow mode	Longitudinal	Transverse
Min. clearing ratio	1.1	1.7
Max. output energy (single shot)	a) 11 J b) 8 J	0.8 J
Max. repetition rate	6 Hz	100 Hz
Max. average output power	a) 30 W (at 5 Hz) b) 40 W (at 6 Hz)	40 W (at 60 Hz)
Laser pulse duration (FWHM)	100-270 ns (HCl and total pressure dependent)	130 ns
Maximum overall efficiency	a) 1.1 % b) 0.8 %	1.2 %

Table 1. Main characteristics of the high energy per pulse and high repetition rate laser prototypes.

To this end, here we present some recent results of time and space resolved net gain measurements performed on our 10 l active volume laser, operated with a phototriggered discharge. The set of measurements has been performed in a wide range of working points, in order to investigate the influence of the gas mixture components on the temporal and spatial stability of the discharge. A simplified 2-D numerical model has been developed and its theoretical predictions are compared with the experimental results.

## 2. GAIN MEASUREMENTS AND NUMERICAL CODE

In the experiment presented here, a 640 nF main capacitor bank is resonantly charged in  $\sim 1 \mu\text{s}$  and is directly connected to the discharge electrode. When the voltage approaches the breakdown value, the x-ray pulse is fired and, through the avalanche multiplication of the generated electrons, the main discharge is switched on. For further specifications refer to Refs.2,3,4. Fig.1 shows the spatial distribution of the x-ray dosage in the laser chamber in the direction perpendicular to both the electric field and the optical axis.

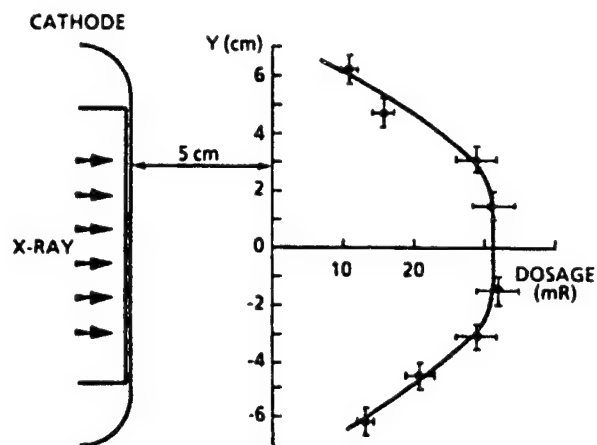
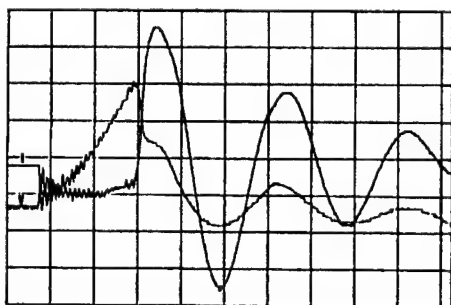
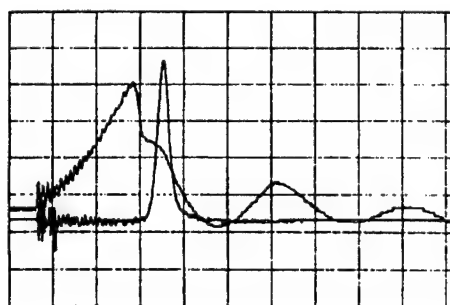


Fig.1. X-ray dosage distribution in the middle of the discharge region, in the direction perpendicular to both the electric field and the optical axis.

Typical discharge voltage and current waveforms are shown in Fig.2a: secondary oscillations of current and voltage are the effect of the mismatch between the very low laser cell impedance ( $< 0.1 \Omega$ ) and the pumping circuit one ( $\sqrt{L/C} \sim 0.3 \Omega$ ). Laser radiation is emitted (see Fig.2b) with a pulse duration of 130 to 210 ns and a maximum output energy of 8 J only during the first half period of the current.



a)



b)

Fig.2. a) Discharge voltage V and current I, b) discharge voltage and laser intensity waveforms for the photo-triggered operation. Hor. 500 ns/div; Ver. V : 10 kV/div, I : 22 kA/div.

Fig.3 shows the experimental value of the laser pulse duration and output energy versus the HCl partial pressure using a plano-plano resonator. The behaviour of both the energy and the duration are well explained and consistent with the following net gain measurements. Unless otherwise specified, the used gas mixture composition was  $\text{HCl/Xe/Ne} = 0.66/4.4/1000$ , with a total absolute pressure of 3 atm.

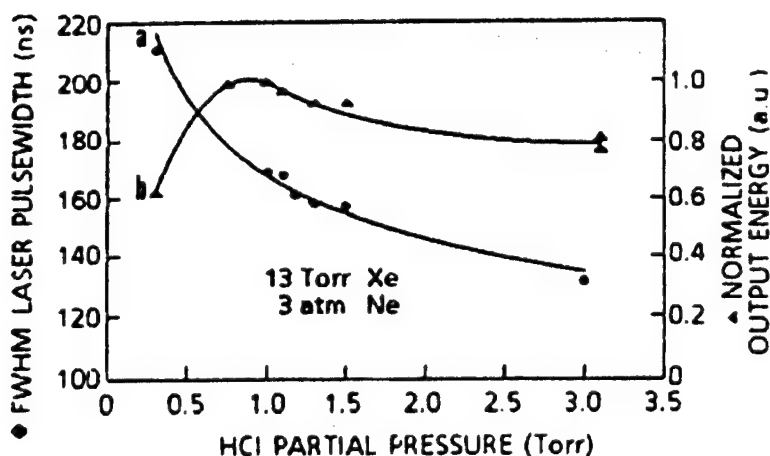


Fig.3. Laser pulse duration (a) and output energy (b) vs HCl partial pressure.

Gain measurements spatially and temporally resolved have been performed using the 5 mm diameter, 14 ns pulse duration (FWHM) mode selected output of an EMG 50 XeCl Lambda Physik probe laser equipped with a positive branch unstable resonator. The measurements, integrated along the optical axis, are resolved in both direction along (x-axis) and perpendicular (y-axis) to the electric field.

The experimental set-up is shown in Fig.4: three vacuum photodiodes, PD1, PD2, PD3, are used to monitor, respectively, the input laser probe pulse, the amplified one and the amplifier fluorescence. The gain, obtained from the ratio between the PD1 and PD2 signals, is then normalized according to the fluorescence intensity in order to remove effects of mixture deterioration during the measurements. The zero of the time scale is referred to the start of the discharge current.

Fig.5a shows the net gain time evolution on the optical axis for different halogen concentrations: as can be seen, the higher the HCl concentration, the shorter the gain risetime and also the gain duration, and this result explains the behaviour of the laser output energy and pulse duration of Fig.3. This effect is attributed to a faster growing of streamers in the electric discharge for high HCl pressures <sup>6,7</sup>. In fact, the experimental time evolution of the gain is shorter than that predicted by a simplified 2-D (x,y) kinetic code, especially for high HCl concentration (see Fig.5b).

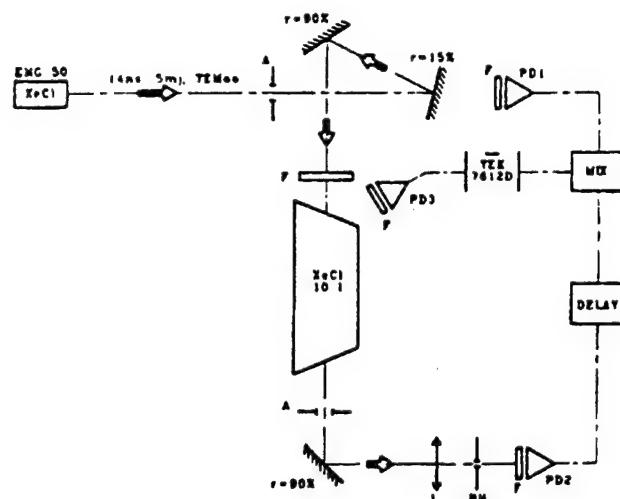
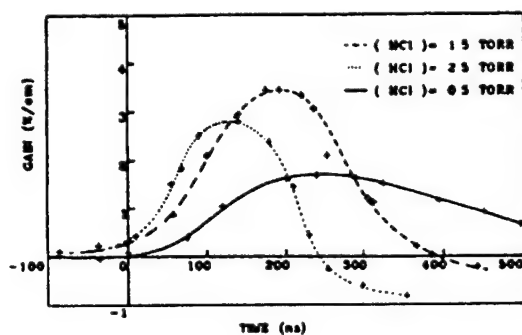
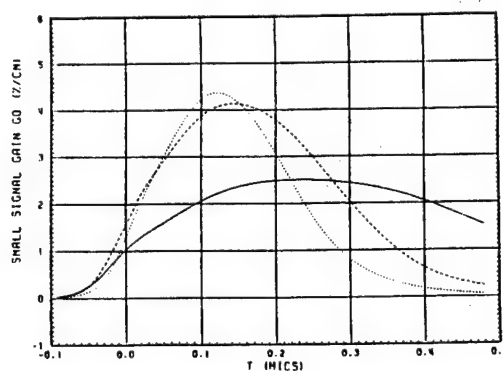


Fig.4. Schematic diagram of the experimental set-up used for the spatially and temporally resolved net small signal gain measurements in the XeCl 101 laser. A = spatial filter, PD = photodiode, L = lens, PH = pinhole, F = filter, r = reflectivity at 308 nm, MIX = electrical signal mixer.



a)



b)

Fig.5. Net small signal gain temporal evolution on the optical axis for different HCl partial pressures ( $p_{Xe} = 10$  Torr,  $p = 3$  atm), a) experimental data; b) numerical results from the simplified theoretical model, solid line:  $p_{HCl} = 0.5$  Torr; dashed line:  $p_{HCl} = 1.5$  Torr; dotted line:  $p_{HCl} = 2.5$  Torr.

The code is based on "a priori" solution of the Boltzmann equation with a reduced number of considered species and in a given range of E/N. The values of the rate constants for the electronic reactions are taken from the resulting look-up table and used to solve the set of equations relative to the chemical reactions summarized in Table 2.

The plane (x,y) perpendicular to the optical axis has been divided into 10x10 sections and the kinetic equations are solved separately in each section. The input difference among the sections consists only on a different value of preionization, according with the experimental distribution shown in Fig.1 along the y-axis and with a measured exponential decay with a characteristic length of 2.5 times the electrodes gap along the x-axis. The integration of the circuital equations is coupled with this kinetic part through the electron number density and the discharge voltage and is the only link among the different sections.

1)	$\text{Xe} + e \rightarrow \text{Xe}^+ + 2e$	7)	$\text{Xe}^+ + \text{Cl}^- \rightarrow \text{XeCl}^*$
2)	$\text{Xe} + e \rightarrow \text{Xe}^* + e$	8)	$\text{XeCl}^* + h\nu \rightarrow \text{XeCl} + 2h\nu$
3)	$\text{Xe}^* + e \rightarrow \text{Xe}^+ + 2e$	9)	$\text{XeCl}^* + \text{Ne} \rightarrow \text{XeCl} + \text{Ne}$
4)	$\text{HCl(O)} + e \rightarrow \text{H} + \text{Cl}^-$	10)	$\text{XeCl}^* + \text{HCl(O)} \rightarrow \text{XeCl} + \text{HCl(O)}$
5)	$\text{HCl(O)} + e \rightarrow \text{HCl(1)} + e$	11)	$\text{XeCl}^* + \text{Xe} \rightarrow \text{XeCl} + \text{Xe}$
6)	$\text{HCl(1)} + e \rightarrow \text{H} + \text{Cl}^-$		

Table 2. Theoretical model: considered chemical reactions.

The negative values of the gain shown in Fig.5a are a spurious effect of the measurement. In fact at a given time the laser probe beam divergence is increased by the streamers growing in the discharge, and, consequently, the spatial filter PH of Fig.4 cuts the deflected beam. Substituting this spatial filter with photosensitive paper, a measurement of the laser spot size, i.e. divergence increase, versus time has been done. It is significant that the divergence increases only in the direction y perpendicular to the electric field, i.e. perpendicular to the streamer direction, as shown in Fig.6.

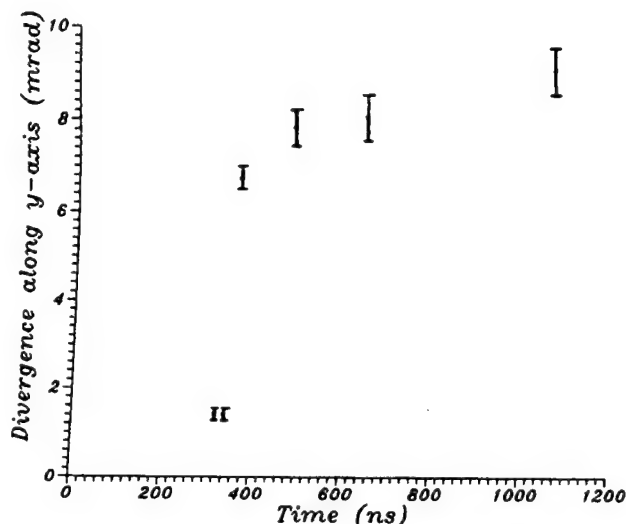


Fig.6. Probe laser measured divergence along y direction vs. time.

Figs. 7a,b show the net small signal gain spatial profile, respectively, parallel and perpendicular to the electric field direction for different time values; Fig. 7a leads to the conclusion that the gain falls down sooner in the cathode sheath, where streamers start to grow; Fig. 7b demonstrates that the high gain region (and the discharge current) rises first in the middle of the discharge (where the preionization is higher) but then propagates toward the edges, leaving a hole in the centre. This phenomenon is also predicted by the numerical code (see Fig. 8) and can be attributed to a faster HCl consumption in the central region.

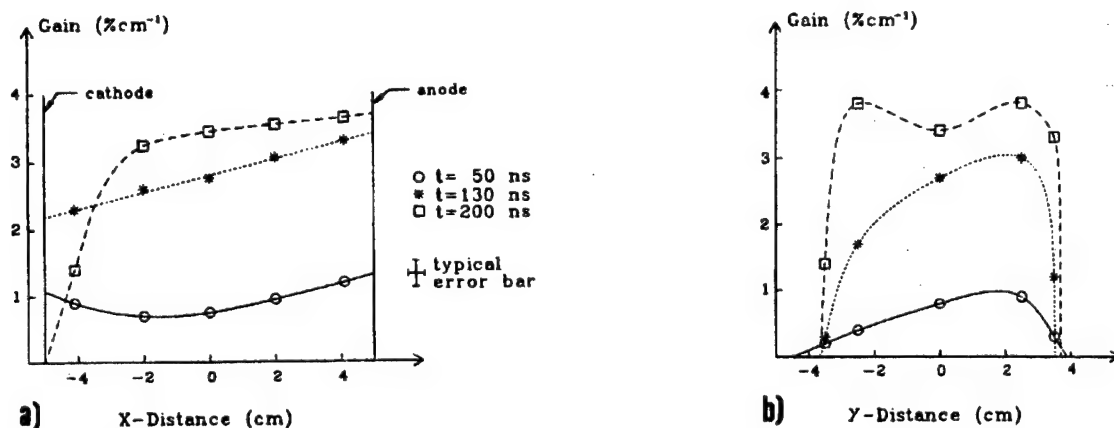


Fig. 7. Measured net small signal gain spatial distribution a) along x-axis ( $y = 0$ ), b) along y-axis ( $x = 0$ ) at different time values.

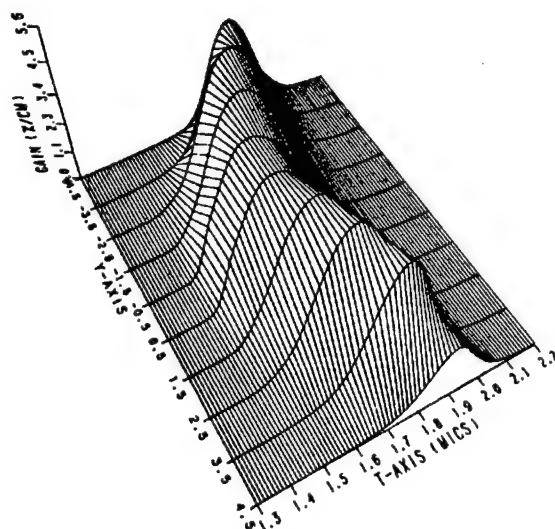


Fig. 8. Computed net small signal gain vs. y-axis and time (temporal scale has a shifted origin).

Finally, Figs.9a,b show the measured and computed time of maximum gain along the direction perpendicular to the electric field; the behaviour of these curves is a direct consequence of the results of Figs. 7b and 8, respectively.

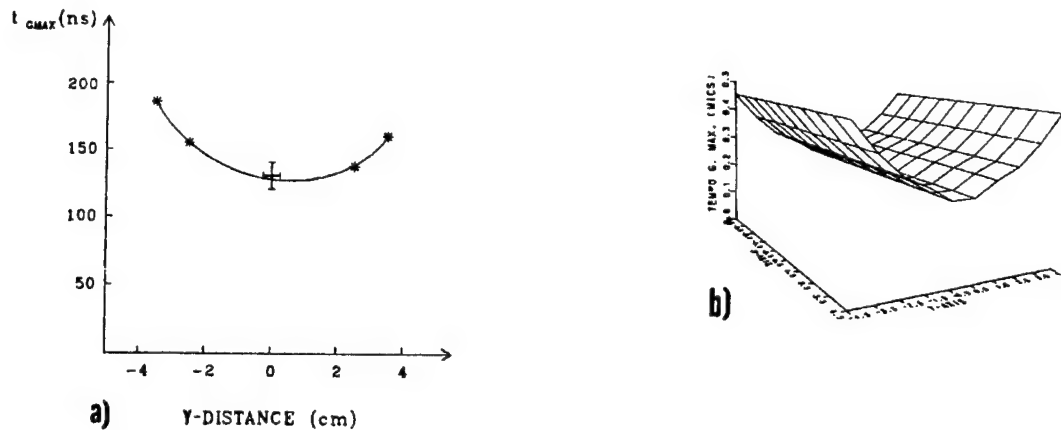


Fig.9. Time of maximum net gain vs. y-axis: a) experimental ( $x = 0$ ), b) computed;  $p_{\text{HCl}} = 2.5$  Torr.

### 3. REFERENCES

1. S. Bollanti, P. Di Lazzaro, F. Flora, G. Giordano, T. Letardi, C.E. Zheng, "High Repetition Rate X-Ray Preionizer for Discharge Pumped Lasers", Proc. of Int. Conf. on Laser 88, R.C. Sze, F.J. Duarte Eds. (STS Press, McLean VA 1989), p.141.
2. T. Letardi, P. Di Lazzaro, G. Giordano, C.E. Zheng, "Large Area X-Ray Preionizer for Electric Discharge Lasers", *Appl. Phys. B* 48, 55-58 (1989).
3. S. Bollanti, P. Di Lazzaro, F. Flora, G. Giordano, T. Hermesen, T. Letardi, C.E. Zheng, "Performance of a Ten-Liter Electron Avalanche Discharge XeCl Laser Device", *Appl. Phys. B* 50, 415-423 (1990).
4. S. Bollanti, P. Di Lazzaro, F. Flora, G. Giordano, T. Letardi, N. Lisi, G. Schina, C.E. Zheng, "X-Ray Triggering of a Ten-Liter Discharge Excimer System", Proc. of Int. Conf. on Laser 89, D.G. Harris, T.M. Shay Eds. (STS Press, McLean VA 1990), p.139. New Orleans, 1989.
5. S. Bollanti, P. Di Lazzaro, A. Dipace, F. Flora, G. Giordano, T. Hermesen, T. Letardi, E. Sabia, C. E. Zheng, "Status of the work at Frascati on large aperture and high repetition rate excimer laser", *High power lasers and laser machining technology*, eds. Gaillard and Quencer, Vol. 1132 p. 73, SPIE, Bellingham, Washington 1989.
6. J. Coutts and C.E. Webb, "Stability of Transverse Self-Sustained Discharge-Excited Long-Pulse XeCl Laser", *J. Appl. Phys.* 59, 704-710 (1985).
7. M.R. Osborne, "Rare-Gas-Halide Discharge Stability", *Appl. Phys. B* 45, 285-291 (1989).

Modeling of a Long-Pulse High-Efficiency XeCl Laser With Double Discharge and Fast Magnetic Switch

36980005 The Hague EXCIMER LASERS AND THEIR APPLICATIONS in English 1991 pp 88-97

[Article by M.N. Kobhio, B.L. Fontaine, J.M. Hueber, P. Delaporte, B.M. Forestier, and M.L. Sentis of Aix-Marseille University]

[Text]

ABSTRACT

A complete model of long pulse X-ray preionised self-sustained discharge XeCl excimer laser has been established for the case of excitation by an advanced electrical circuit associating a double discharge (spiker/sustainer) and a fast low losses ferrite magnetic switch with pulsed reset. This model allows to simulate one of the potential working conditions of the IMFM high average power very high repetition rate LUX test-bed. The model, which considers Ne as buffer gas and HCl as halogen donor, includes rate equation for species with most recent available rate constant values, circuit equations with time dependant ferrite inductance and plasma impedance and rate equation for laser emission taking into account absorbtions. Modeling takes into account time delay beetwen spiker and sustainer, low value of sustainer field and dynamics of magnetic switch. The model has been validated with a long pulse X-ray preionised XeCl laser, with double discharge and magnetic switching, developped at IMFM, which as already allowed to obtain over 3 % efficiency and 140 mJ extracted energy in 150 ns (FWHM) from a 50 cm<sup>3</sup> active volume at 2.5 atm. pressure. Numerical results are in good agreement (within 30 %) with IMFM experimental results. A parametric study of the XeCl laser with double discharge and fast magnetic switch is presented as well as a comparison with both experiments and numerical results of excitation by a C-L-C classical circuit for the same geometric and gas conditions and the same imput energy.

1. INTRODUCTION

Potential applications of high power pulsed ultraviolet lasers have recently stimulated considerable interest in scaling excimer lasers to higher output energy, pulse length, pulse repetition frequency, average laser power and efficiency. A program to extensively investigate key parameters which may limit scaling of the XeCl laser (  $\lambda = 308$  nm) to very high average power ( $P_1 > 1$  kW) and PRF (1-5 kHz) has been undertaken at IMFM<sup>1</sup>. This program includes study of possible advanced excitation schemes, compatibles with high PRF, to increase whole system efficiency and laser pulse length and reduce acoustic load into active volume. It is noteworthy that an increase of laser pulse length provides a number of opportunities in terms of lower stress on electrical components, high energy transmission capability through optical fiber, and better control of laser beam divergence, polarization and linewidth<sup>2</sup>.



A complete model of long pulse X-ray preionised self-sustained discharge XeCl laser has been established for the case of excitation by an advanced electrical circuit associating a double discharge (spiker/sustainer) and a fast, low losses ferrite magnetic switch with pulsed reset. This excitation scheme has already shown high capabilities in terms of laser efficiency and pulse length<sup>3-9</sup>. This model is, to our knowledge, the first to take into account the specificities of such a circuit : very fast high voltage spiker for avalanche discharge, delay time between spiker and sustainer, dynamics of magnetic switch saturated by spiker and low value of sustainer field. The model simulates a long pulse X-ray preionised XeCl laser with double discharge and magnetic switching developed at IMFM, which has already allowed to obtain over 3 % efficiency and 140 mJ extracted optical energy in 150 ns (FWHM) from a 50 cm<sup>3</sup> active volume and an Ne/Xe/HCl working mixture at relatively low pressure (P=2.5 atm.)<sup>7,8,9</sup>. The aim of this paper is to present briefly the IMFM model and to describe results of a parametric study of the XeCl laser with double discharge and magnetic switch made with the model, as well as comparisons with both experiments and results of a numerical modeling of excitation by a C-L-C classical circuit for the the same geometric and gas conditions and the same input energy.

## 2. MODEL STRUCTURE

The model, which considers Ne as the buffer gas and HCl as the halogen donor is based on a model developed at IMFM for the case of classical C-L-C excitation<sup>10,11</sup>. This model has been modified to take into account both specificities of double discharge and fast magnetic switching and most recent rate constants available. The model organization is shown schematically in Fig. 1.

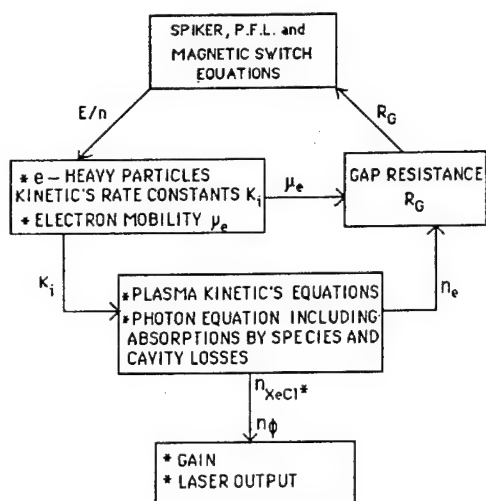
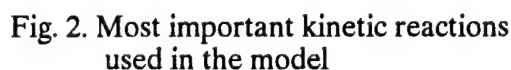


Fig. 1. I.M.F.M. model organization

The IMFM model includes kinetics rate equation, circuit equations, magnetic switch inductance equation, and equation for laser emission<sup>12,13</sup>:

(A) the rate equation for 23 species takes into account 72 reactions, with the most recent values of rate constants<sup>14,15</sup>, including Xe<sub>2</sub>Cl and HCl(v=1 and 2) formation and XeCl (B-X) stimulated emission and absorption cross sections at laser wavelength. XeCl B and C states are considered as instantaneously mixed by collisions and lower laser level is always empty. The most important kinetic reactions used in the model are shown in Fig. 2



The diagram illustrates a laser system divided into four functional sections: Sustainer, Magnetic switch with reset, Laser head, and Spiker. The Sustainer section consists of a series of LC circuits connected between HT (High Voltage) terminals. It includes components  $C_p$ ,  $L_p$ ,  $R_p$ ,  $L_{11}$ ,  $L_{12}$ ,  $L_{1i}$ ,  $L_{1n-1}$ ,  $L_{1n}$ ,  $C_{11}$ ,  $C_{12}$ ,  $C_{1i}$ ,  $C_{1n-1}$ , and  $C_{1n}$ . The Magnetic switch with reset section features a switch with current  $I_s$  and inductance  $L_s$ , and a reset coil connected to a battery. The Laser head section includes a pump source  $U_g$ , resistors  $R_{GP}$ ,  $R_t$ ,  $R_{sp}$ , inductors  $L_{GP}$ ,  $L_t$ , and a target with distance  $d$ . The Spiker section includes a series of LC circuits with components  $R_{sp}$ ,  $L_{sp}$ ,  $C_{sp}$ , and  $U_{sp}$ . The diagram is labeled with HT at both ends and includes various current and voltage labels such as  $U_p$ ,  $I_p$ ,  $U_{Li}$ ,  $I_{Li}$ ,  $I_{sp}$ , and  $U_{sp}$ .

Component values listed below the diagram:

$C_p = 200 \text{ nF}$	$L_{sp} = 700 \text{ nH}$
$L_p = 1.3 \text{ } \mu\text{H}$	$C_t = 2.8 \text{ nF}$
$C_{p1} = 134 \text{ nF}$	$C_{sp} = 2.7 \text{ nF}$
$Z_{p1} = 0.5 \text{ } \Omega$	$R_s = R_t = 0.1 \text{ } \Omega$
$L_{gp} = 1 \text{ nH}$	$R_p = 0.01 \text{ } \Omega$
$R_{gp} = 0.15 \text{ } \Omega$	$R_{sp} = 1 \text{ } \Omega$
$L_t = 12 \text{ nH}$	$d = 2 \text{ cm}$

**Fig. 3. Equivalent circuit of double discharge XeCl apparatus**

The electrical circuit equations introduced in the model, with the various parameters as indicated on fig.3, are detailed as following:

$$\frac{dU_p}{dt} = -\frac{I_p}{c_p}$$

$$\frac{dU_{l_1}}{dt} = \frac{I_{l_1} - I_p}{c_{l_1}}$$

$$\frac{dU_{l_i}}{dt} = -\frac{(I_i - I_{i-1})}{c_{l_i}} \quad \text{for } i = 1 \text{ to } N$$

$$\frac{dI_p}{dt} = \frac{1}{L_p} (U_p - U_{l_1} - R_{lp} I_p)$$

$$\frac{dI_{l_i}}{dt} = \frac{1}{L_{l_i}} (U_{l_i} - U_{l_{i+1}}) \quad \text{for } i = 1 \text{ to } N-1 \quad (R_d = R_G + R_{GP})$$

$$\frac{dI_s}{dt} = \frac{1}{L_s + L_{l_N}} \left\{ \begin{array}{l} U_{l_N} \left( 1 + \frac{L_d}{L_{sp}} + \frac{L_d}{L_T} \right) - U_{sp} \frac{L_d}{L_p} - U_T \frac{L_d}{L_T} \\ - I_s \left[ R_s + R_d + R_s \left( \frac{L_d}{L_p} + \frac{L_d}{L_T} \right) \right] \\ - I_{sp} \left( R_d + R_p \frac{L_d}{L_p} \right) + I_T \left( R_d + R_T \frac{L_d}{L_T} \right) \end{array} \right\}$$

$$\frac{dU_T}{dt} = \frac{I_t}{c_t}$$

$$\frac{dU_{sp}}{dt} = \frac{I_{sp}}{c_{sp}}$$

$$\frac{dI_{sp}}{dt} = \frac{1}{L_{sp}} \left\{ -U_{sp} - U_{l_N} + (L_s + L_T) \frac{dI_s}{dt} + R_s I_s - R_{sp} I_{sp} \right\}$$

(C) the magnetic switch inductance equation includes saturation time behavior (saturation wave) of pulse reset several coaxial structures in parallel, each of them comprising many low losses high frequency Ni/Zn ferrite torus. B-H Hysteresis curve as shown on fig 4 is considered in the model<sup>16</sup>.

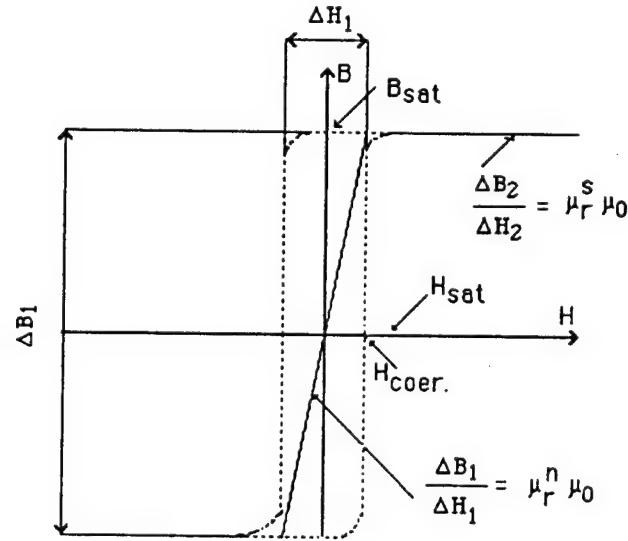


Fig. 4. ferrite hysteresis curve taken into account in model

From electromagnetic conservation flux, time dependant magnetic switch inductance  $L_s(t)$  relationship introduced in model is:

$$L_s(t) = \mu_0 N_t^2 \phi \left( \mu_r^n \cdot \text{Log } R_1 / R_{sat}(t) + \mu_r^s \cdot \text{Log } R_{sat}(t) / R_0 \right) / 2\pi$$

$$\text{where } R_{sat}(t) = I_s(t) / 2\pi H_{sat}$$

Assumption is made of very soft magnetic material ( $H_{coerc.} < 10 \text{ A/cm}$ ). Geometric and magnetic characteristics of ferrites used in this study (H20 ferrite torus from THOMSON-LCC) are presented on Table 1.

$H_{coer} = 0,8 \text{ A/cm}$	$B_{sat} = 0,3 \text{ T}$	$R_0 = 0,75 \text{ cm}$
$H_{sat} = 1,6 \text{ A/cm}$	$N_t = 1 \text{ turn}$	$R_1 = 1,25 \text{ cm}$
$\mu_i = 250$		$\phi = 1 \text{ cm}$

Table 1 characteristics of Ni/Zn magnetic switch ferrite torus

(D) rate equation for laser emission (photon equation) includes absorption by various species created in active medium by the discharge.

Coupling between these equations is made through step by step calculations of electron-heavy particles rate constant time variation following electric field time variation and effects of these variations on electric field value through variation of plasma resistance. Solution of Boltzmann equation as given by recent literature is used for rate constant calculation<sup>17-20</sup>. The coupled non linear differential equations are solved numerically using Runge-kutta method modified by Gill.

### 3. RESULTS OF THE MODEL AND COMPARISON WITH IMFM EXPERIMENTS

A parametric study of XeCl laser behavior was made by use of the IMFM numerical code. This study allowed for effects of key reaction rate constants and optical cavity characteristics on electrical parameters and laser output. In order to validate the model with experiments, conditions corresponding to experiments fulfilled in parallel in the laboratory<sup>8,9</sup> have been chosen. The electrical parameters are given in Fig. 3. Active medium is Ne/Xe/HCL (7950/75/10) at a pressure of 2.3 atm. and the spiker charging voltage is 30 KV. Active volume is  $25 (L) \times 2 (H) \times 1 (W) \text{ cm}^3$ . The optical cavity is considered to connect a fully reflective mirror and a 60 % reflective mirror at  $\lambda = 308 \text{ nm}$

In Fig. 5 are shown calculated and experimental waveforms representing : (a) time variation of magnetic switch voltage, (b) current through the switch and (c) laser emission for a sustainer voltage of 7 KV and a magnetic switch made of two coaxial structures in parallel<sup>7,8,9</sup>. Voltage, current and laser oscillations are attributed to repeated spiker transfer capacitor charges and discharges, while shorter measured laser pulse duration compared to calculated one is attributed to discharge instability. Fig 6 represents calculated and measured laser energy versus PFL voltage for the same conditions. Comparison between numerical modeling and experimental results from IMFM experiments shows a very good quantitative agreement for electrical parameters behavior as well as for XeCl laser power and energy for various conditions. The model simulates very well the delay between spiker and sustainer, (i.e. the dynamics of ferrite magnetic switch saturation by the spiker), as well as the delay to reach threshold for lasing and laser pulse length. Difference between computed and measured values of laser output energy is typically 30 %.

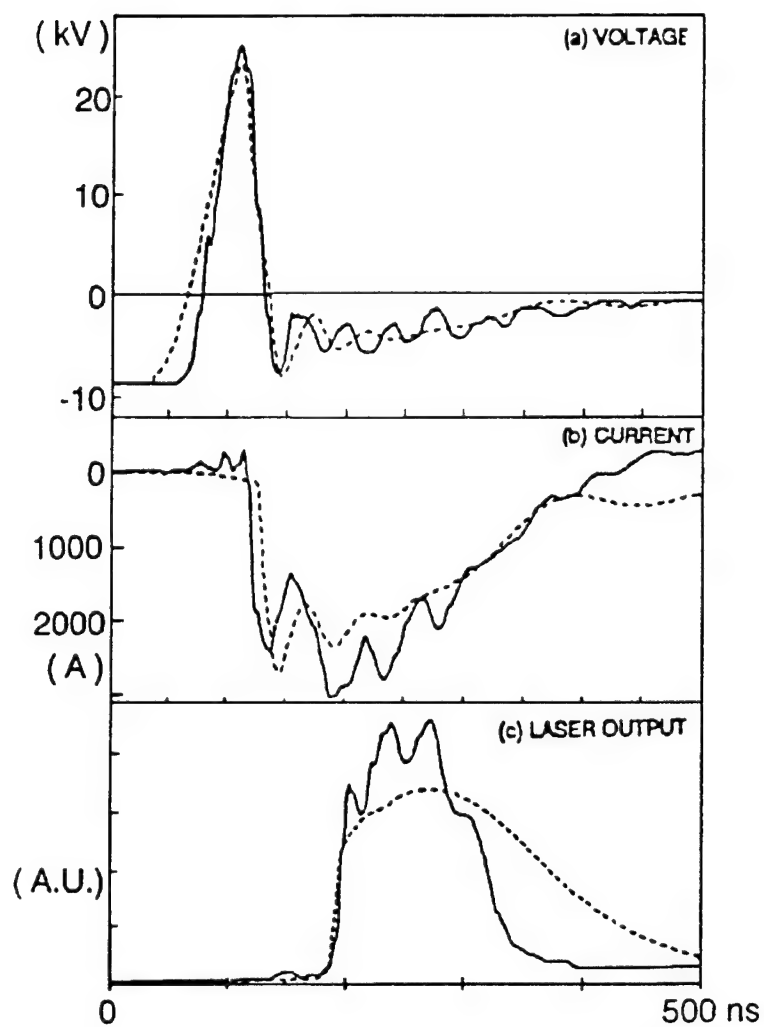


Fig. 5. Calculated and experimental time variation of:  
a) laser electrodes voltage  
b) current (1 switch path)  
c) laser output  
Ne/Xe/HCl (7950/75/10),  $P=2,3\text{atm}$ ,  
 $V_{\text{PFL}}=7\text{KV}$

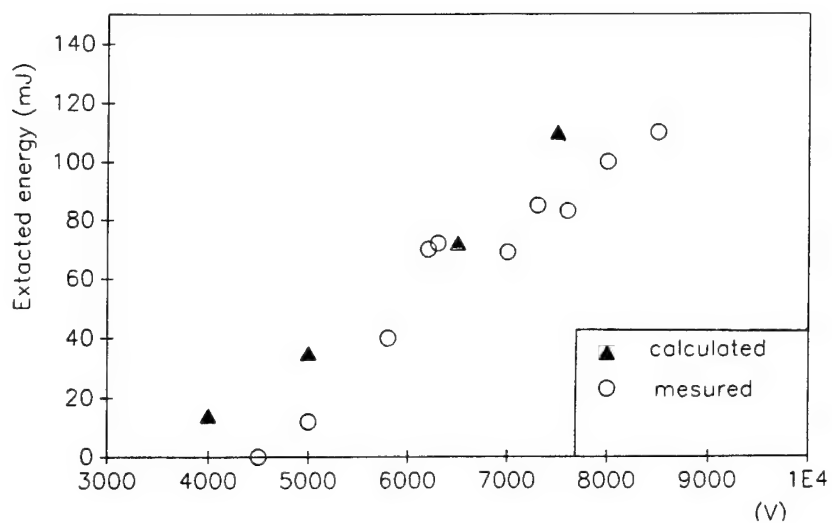


Fig. 6. Calculated and measured XeCl laser energy v.s. sustainer voltage

As an exemple of active medium internal parameters behavior given by the model, Fig. 7 shows calculated electron density versus time for several sets of torus in serie inside each of the two coaxial magnetic switch structures. The sustainer PFL voltage is 7.2 kV and the conditions are otherwise the same as in Fig 5 and 6. One observes a first electron density peak of short duration (20-30 ns FWHM), created by the spiker discharge. This first electron density pulse is followed by a second one of much longer duration ( $N_e = 4 \cdot 10^{14} \text{ cm}^{-3}$ , 200-250 ns FWHM) created by the main discharge from PFL after magnetic switch saturation. It is noteworthy that electron density behavior is strongly dependent of ferrite torus number (i.e. time needed for magnetic switch saturation). For the case of long saturation time (high number of ferrites in serie), the first electron density pulse reaches its maximum value ( $N_e = 4 \cdot 10^{14} \text{ cm}^{-3}$ ), but the main electron density pulse peaks only at a low value due to plasma recombinaison during the relatively long time needed for switch saturation and low value of main discharge electric field. In this case plasma impedance remains relatively high and gain during main discharge excitation is reduced. At the opposite when magnetic switch saturation time is very short an important part of spiker energy flows into the PFL before or during breakdown and the electron density created by the spiker is lower. For this case the discharge initiated by the speaker may be poorly homogeneous and the IMFM model which assumes homogenous excitation is not valid anymore. There exists an optimum for the number of ferrites in order to extract the maximum of energy from active medium.

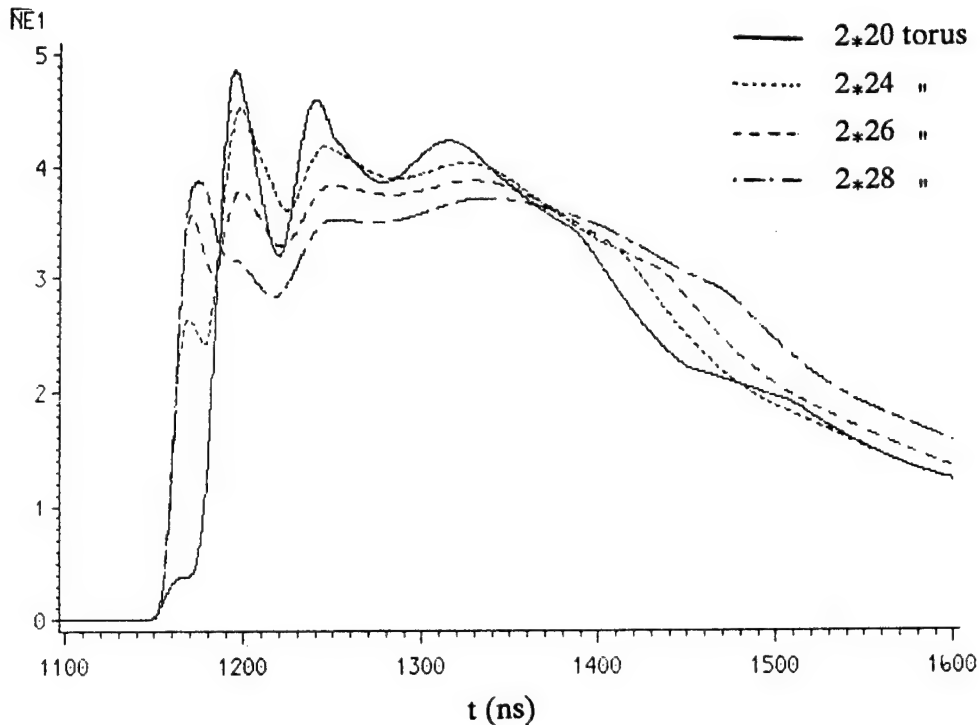


Fig. 7. calculated electron density v.s. time for several numbers  $N$  of ferrite torus in serie  
 $\text{Ne/Xe/HCl}$  (7950/75/10),  $P = 2,3 \text{ atm.}$ ,  $V_{\text{PFL}} = 7,2 \text{ kV}$ ,  $N = 20, 24, 26$  and  $28$  torus for each row

In Fig. 8 is shown the calculated variation of laser energy with number of ferrites in each of the two magnetic switch rows for typical conditions. One observes that the optimum value, for the conditions of the figure 8, is 24-26 ferrite torus for each of the two parallel rows, value in good agreement with the results of fig 7 for electron density time behaviour.

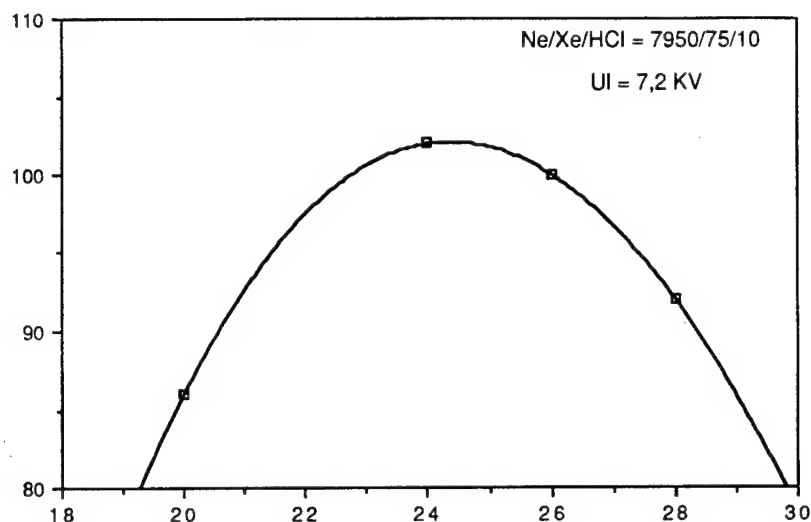


Fig. 8. laser energy v.s. number of ferrite torus;  $V_{PFL} = 7,2 \text{ kV}$

A comparison of calculated laser power and gain for double discharge and C-L-C discharge excitation <sup>10,12</sup> is shown in Fig 9 for the same geometric and gas conditions and the same input energy ( $W_{el} = 6,8 \text{ joules}$ ). One observes that for C-L-C excitation the initial gain is much higher and of much shorter duration than for double discharge. Laser pulse is very short (40 ns to be compared to 200 ns for double discharge excitation) and does not reach stationary conditions. It is important to note that electrical energy added to active medium is typically 50 % of stored energy for the C-L-C case and 85 % for the double discharge case.

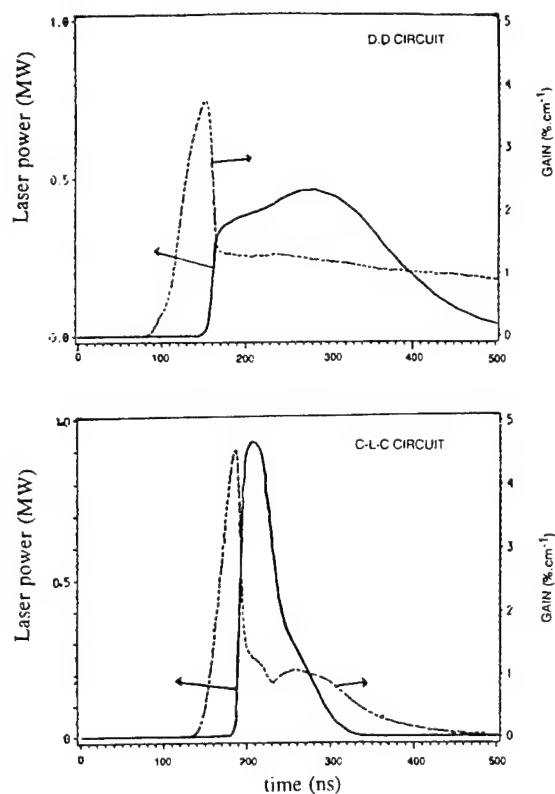


Fig. 9 : Calculated laser power and gain for :

(a) double discharge

(b) C-L-C discharge

Ne/Xe/HCl (7950/75/10),  $P = 2,3 \text{ atm}$ ,  $W_1 = 6.8$

J,  $T_{\text{mirror}} = 40\%$ .



#### 4.CONCLUSION

A complete model of long pulse high efficiency XeCl laser with double discharge and fast ferrite magnetic switch with pulsed reset has been established, which takes into account most recent rate constants available, magnetic switch saturation by the spiker and time varying plasma impedance. A parametric study of XeCl laser behavior was made by use of the IMFM numerical code. This study allowed for effects of key reaction rate constants, magnetic switch dynamics, and optical cavity characteristics, on electrical parameters and laser output. In order to validate the model with experiments, conditions corresponding to experiments fulfilled in parallel in the laboratory were chosen.

Comparison between numerical modeling and experimental results from IMFM experiments made at relatively low pressure and small gain length conditions shows a very good quantitative agreement for electrical parameters behavior as well as for XeCl laser power and energy for various conditions. It is noteworthy that the model, which does not take into account discharge instabilities, simulates very well the delay between spiker and sustainer and its dependence with the number of ferrite torus as well as delay to reach threshold for lasing and laser pulse length for IMFM conditions. Difference between computed and measured values of laser output energy and pulse length is typically less than 30 %. This model shows importance of delay between spiker and sustainer on laser energy, benefit of short delay and so interest of very fast switch associated with spiker and sustainer of opposite polarity. A comparison was made between results of the double discharge excitation model and results of a C-L-C excitation model developed at IMFM. This comparison allowed to characterize the main differences between the two types of excitation. Good agreement between results of modeling and experiments shows that increased understanding of phenomena involved in this promising long pulse and high efficiency excimer laser with double discharge excitation and fast magnetic switch has been reached and that realistic self consistent model has been established.

Future work on avalanche discharge XeCl laser modeling at IMFM is planned in the frame of EUREKA EU 205 program (Eurolaser-excimer lasers), with the aim to optimize such a laser in terms of energy per pulse, pulse length and efficiency. For this aim, a detailed comparison between double discharge with fast magnetic switch and classical C-L-C circuits for various conditions will be pursued. The general objective is to use the high laser efficiency allowed by the double discharge excitation scheme to increase average power and repetition rate of XeCl laser while maintaining the advantage of long laser pulse length specific of this type of excitation. Such a study is planned on LUX test-bed<sup>1</sup> for conditions of very high average power ( $P_1 \approx 100-1000$  W) and repetition rate ( $> 1$  kHz)

#### 5. ACKNOWLEDGMENTS

This research was supported in part by french Ministry of Research in the frame of EUREKA EU205 program and by french DRET

#### 6. REFERENCES

1. M.L. Sentis, Ph. Delaporte, B.M. Forestier, B.L. Fontaine J. App. Phys., 66, 1925, (1989)
2. T.J. McKee, Appl. Opt., 30, 635, (1991)
3. C.H. Fisher, M.J. Kushner, T. Dehart, J.M. Mc Daniel, R.A. Petr, J.J. Ewing, Appl. Phys. Lett. 48, p. 1574 (1986)
4. R. S. Taylor, K. Leopold, J. Appl. Phys., 65, 22, (1989)
5. T.J. McKee, G. Boyd, T.A. Znotins, IEEE Photon. Tech. Lett., PTL-1, 59 (1989)
6. J.W. Gerritsen, A.L. Keet, G.J. Ernst, W.J. Witteman, Opt. Comm., 77, 395 (1990)

7. B.L. Fontaine, J.M. Hueber, Ph. Delaporte, B.M. Forestier, International Congress on optical Science and engineering (E.C.O.)-Excimer lasers and Applications II, The Hague, March 1990, proc. SPIE Vol 1278 (1990); also Paper CTUH20, CLEO'90, Anaheim (1990)
8. J.M. Hueber, B.L. Fontaine, Ph. C. Delaporte, B.M. Forestier, M.L. Sentis, Opt. Comm., to be published (1991)
9. J.M. Hueber, B.L. Fontaine, Ph. C. Delaporte, B.M. Forestier, M.L. Sentis, International Congress on optical Science and engineering (E.C.O.)-Excimer lasers and Applications III, The Hague, March 1991, SPIE Proceed. Vol.1503 (1991)
10. A. Gevaudan, B.L. Fontaine, B.M. Forestier, M.L. Sentis, 6th GCL, Jerusalem (1986), proceed. p 118 (1987)
11. A. Gevaudan, Thesis, Aix-Marseille University (1986)
12. M.N. Kobhio, Thesis, Aix-Marseille University (1990)
13. M.N. Kobhio, 8 Th International Symposium on Gas Flow and Chemical Lasers (8 TH GCL), Madrid, September 1990, SPIE Proceed. Vol 1397 (1991)
14. T. H. Johnson, H.E. Cartland, Th.C. Genoni, A.M. Hunter, J. Appl. Phys. (1989)
15. W. Bottitcher, invited paper, Xth ESCAMPIG, Orleans, (1990), Pr. Europhysics Conf. Abst. p.8 (1990)
16. W.C. Nunnally, Los Alamos Report LA-8862-MS Rev. 2 (1984)
17. Y.S. Wang, Ph.D. Thesis, Univesity of Clifornia, San Diego (1982)
18. M. Maeda, A. Takahasi, T. Mizunami, Y. Miyazoe, Jap. J. Appl. Phys, 21, p. 1161 (1982)
19. H. Okazono, K. Midorikawa, M. Obara, T. Fujioka, J. Appl. Phys., 56, p. 680 (1984)
20. M.C. Bordage, CPAT, Toulouse, private communication (1990)

Theoretical and Experimental Investigations on Pressure Wave Reflections and Attenuation in High-Power Excimer Lasers

36980005 The Hague EXCIMER LASERS AND THEIR APPLICATIONS in English 1991 pp 98-109

[Article by Achim Holzwarth, Jurgen Griebisch, and Peter Berger of the Univ. Stuttgart]

[Text]

**ABSTRACT**

The following contribution consists of two parts. The first part represents theoretical investigations on the propagation and reflection of shock waves and the corresponding density perturbations which have been performed using a two-dimensional unsteady finite-difference method. The influence of electrode or mirror mounting design on the reflection of shock waves and the resulting density distribution is shown. It was found, that in modifying the design the local distribution of pressure and density in the laser gas can be influenced, but that the decay rate of the perturbations is not affected. The effect of helium used as a major gas component instead of neon is also briefly discussed.

The second part describes the experimental setup to generate and investigate shock waves. In a special piston driven shock channel of rectangular cross-section remarkably good shock waves have been produced with regard to both the rise time and the evenness of the shock front. Interferometric observations of density variations  $\Delta\rho/\rho$  as low as the order of  $10^{-4}$  are possible. Some results of attenuating shock waves with a simple muffler design will be presented.

**1. INTRODUCTION**

In pulsed gas flow lasers the sudden heat release during the laser pulse generates pressure waves and density perturbations which lead to a deterioration of both the discharge homogeneity and the beam quality. High pulse energy and a high repetition rate can only be achieved with a very homogenous discharge. Therefore the density fluctuations  $\Delta\rho/\rho$  in the laser cavity should decrease to the order of  $10^{-3}$  to  $10^{-4}$  before the next lasing pulse can be generated<sup>1</sup>.

To understand the formation and propagation of pressure waves, especially the reflection and diffraction at the walls of the laser head - including electrodes and mirrors -, several theoretical investigations with a two-dimensional, time dependent finite-difference scheme have been carried out over the last years <sup>2,3,4</sup>.

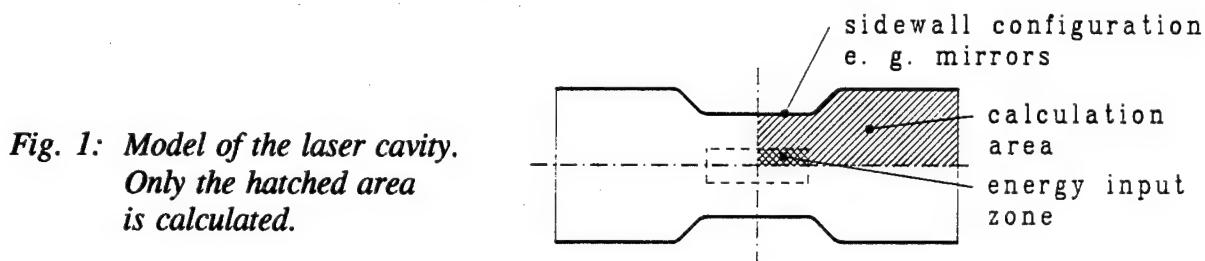
In this contribution the influence of different geometric designs of the laser electrodes, or mirrors, respectively, on the attenuation of shock waves is investigated. This is done by reducing and simplifying the geometry of either component to a wall contour that is of common design.

In order to accelerate the attenuation of shock waves it is necessary to use muffling elements. The design and structure of the mufflers themselves and the quality of the muffling materials have to be obtained experimentally. For this purpose a special piston driven shock tube of rectangular cross-section of  $50 \times 500 \text{ mm}^2$  has been designed and constructed. Using this test bed shock waves can be produced with good quality regarding both the rise time and the evenness of the shock front. It allows interferometric observations of density variations  $\Delta \rho / \rho$  as low as the order of  $10^{-4}$ . The absorbing material can be placed directly into the channel to be struck frontally by the shock wave or can be deposited in sidewall mufflers at the upper and lower sidewalls. It is also possible to attach further flow loop elements to the end of the channel, as e.g. elbows.

## 2. THEORETICAL INVESTIGATIONS

### 2.1 Geometrical Model

The effect of the electrode design on the propagation and reflection of shock waves induced by the laser discharge has been investigated with models of different geometries. In Fig. 1 the model of the laser cavity with the two projecting electrodes is shown. The projecting walls can also be considered as mirrors. Only the hatched area is calculated in order to reduce computing time and memory. The restriction to consider only one quarter of the cavity is permissible if there is no base flow. As the propagation of the shocks is symmetric to the axes shown in Fig. 1, without a base flow it is only necessary to consider a quarter of the cavity. The base flow has been neglected to clarify the basic phenomena that occur at the reflection of shock waves at bent walls.



The physical properties of the laser gas as used in the present calculations are as follows: Gas composition:  $\text{Ne}/\text{HCl}/\text{Xe} = 99,4/0,1/0,5 \%$ , gas pressure  $p_0 = 4000 \text{ hPa}$ , temperature  $T_0 = 300 \text{ K}$ , initial increase of pressure  $\Delta p = 200 \text{ hPa}$  and temperature  $\Delta T = 15 \text{ K}$ , no base flow. The initial increase of pressure and temperature corresponds to a short laser pulse with a pulse length of typically  $50 \text{ ns}$  and an energy input of about  $30 \text{ J/l}$ .

## 2.2 Formation and Propagation of Shock Waves

### 2.2.1 Shock waves propagating parallel to the duct wall

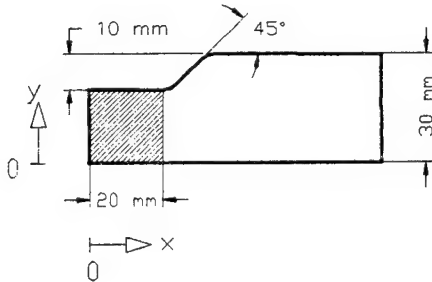


*Fig. 2: A uniform energy input between the electrodes (hatched area) produces a shock, that propagates from the edge of the input zone to the right.*

A uniform energy input between the electrodes produces shock waves, which begin to propagate at the edge of the input zone and travel up and downstream, i.e. to the right in Fig. 2. When the curvature of the wall is reached, the shock will have to undergo an expansion of the cross sectional area. This in turn gives rise to a rarefaction beginning at that point.

In Fig. 3 the resulting pressure distribution in this geometry is shown at different time steps. After  $40 \mu\text{s}$  the shock wave reaches the wall curvature. The rarefaction generated at this corner leads to a pressure reduction in the vicinity. In the third picture taken at  $80 \mu\text{s}$  the rarefaction travelling from the opposite side of the energy input zone has penetrated the area of calculation. The shock wave propagating outside the laser cavity (i.e. to the left in these graphs) has lost some of its initial strength due to the increase of the cross sectional area. The step in the wall acts similar to a diffuser, where the shock intensity decreases according to the ratio of the cross sectional areas. Here the shock intensity reduces from  $\Delta p \approx 100 \text{ hPa}$  between the electrodes to  $\Delta p \approx 60 \text{ hPa}$  outside the cavity.

Inside the shock, that has the spatial dimensions of the energy input zone (a length of 40 mm in this case), the pressure level is nonuniform due to the influence of the curve. The perturbations arising from the curvature are reflected between the walls of the laser channel and lead to overall slight discontinuities in the gas.

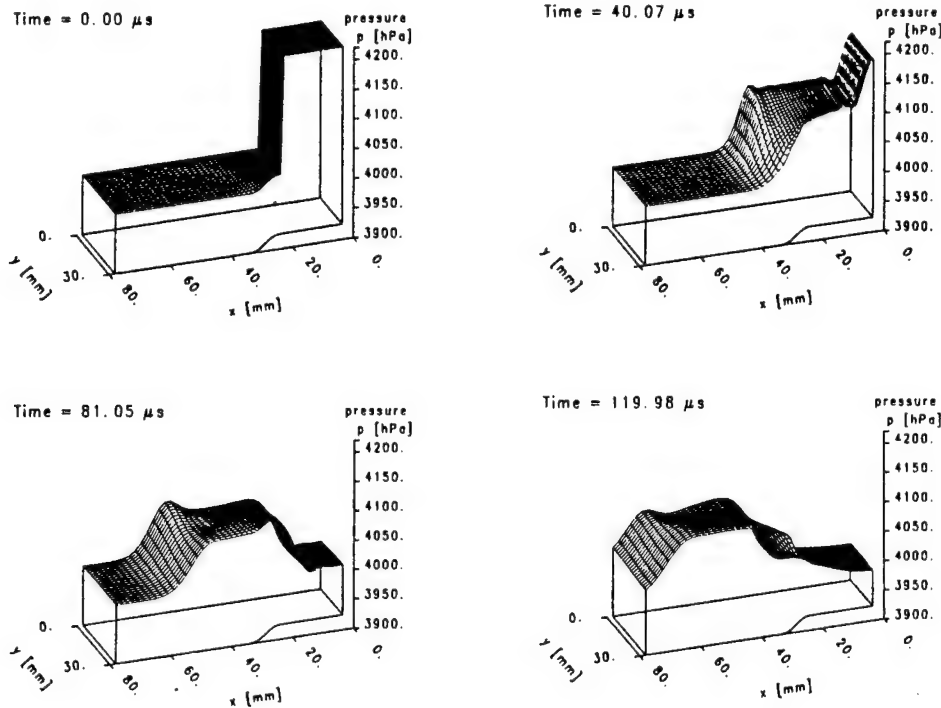


Fig. 3: Graphs of the pressure distribution in the configuration of Fig. 2 at different time steps.

### 2.2.2 Shock waves propagating perpendicular to the duct wall

The propagation of shocks perpendicular against the wall and the following reflection is of particular interest when it is taken into account that the geometry shown in Fig. 1 cannot only be considered as electrodes projecting into the laser cavity, but also e.g. as mirrors with their mountings. The impingement of the wall design on the reflection of the shock wave is investigated in this section. In Fig. 4 the configuration is shown. A shock propagating mainly in the direction of the y-axis is produced by an energy input in the hatched area. This geometry is compared to the reflection of the same shock wave at a plain, straight wall (Figs. 5 and 6).

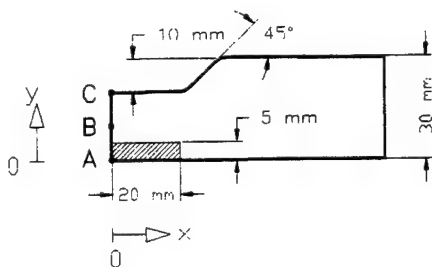


Fig. 4: Simulation of a shock wave propagating mainly in the direction of the y-axis towards a bended wall. This wall can be considered e.g. as electrode or as mirror mounting. The shock wave is created by energy input in the hatched area. The curves in Figs. 6 ,8, and 9 refer to the points A, B, and C.

In Fig. 5 the calculated pressure distribution at selected time steps is shown for a straight channel with a shock that is repeatedly reflected at the wall. In Fig. 6 the time dependent pressure and density variation for this configuration has been plotted. The curves refer to the points A, B, and C as shown in Fig. 4. The shock waves start to propagate at the edges of the area, in which the pressure and temperature are increased due to the coupling in of energy, while the density remains unchanged for some microseconds. They travel in the positive y- and x-directions, while at the same time the corresponding rarefaction waves move in the opposite direction from these edges. At the right edge the waves travelling perpendicular to each other superpose to a circular pattern. The shock wave propagating in the y-direction reaches the wall after  $40\ \mu\text{s}$  and is reflected. During the reflection the kinetic energy of the gas is partially converted back into pressure energy. This pressure increase forms a new system of compression and rarefaction waves superposing each other.

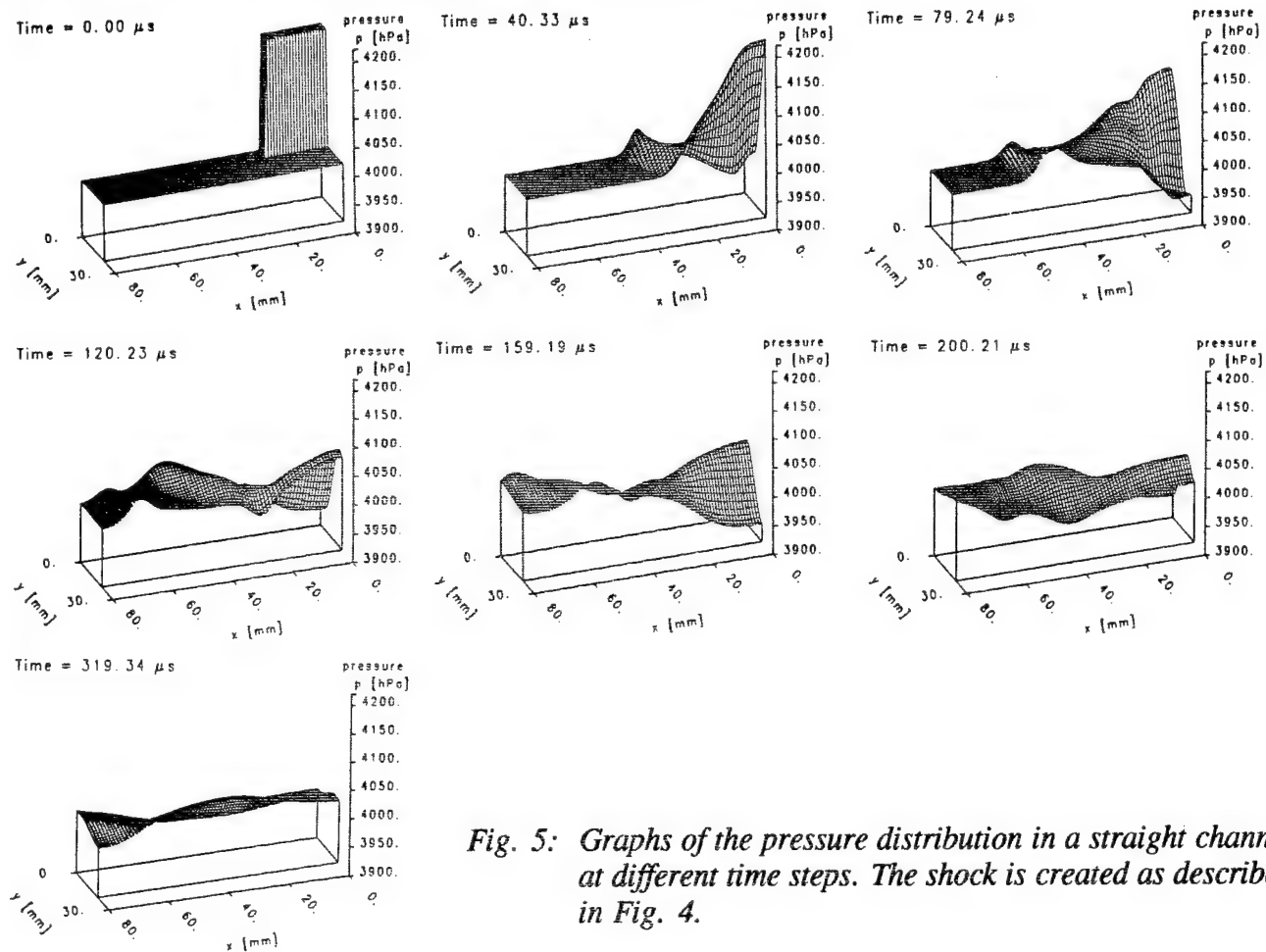


Fig. 5: Graphs of the pressure distribution in a straight channel at different time steps. The shock is created as described in Fig. 4.

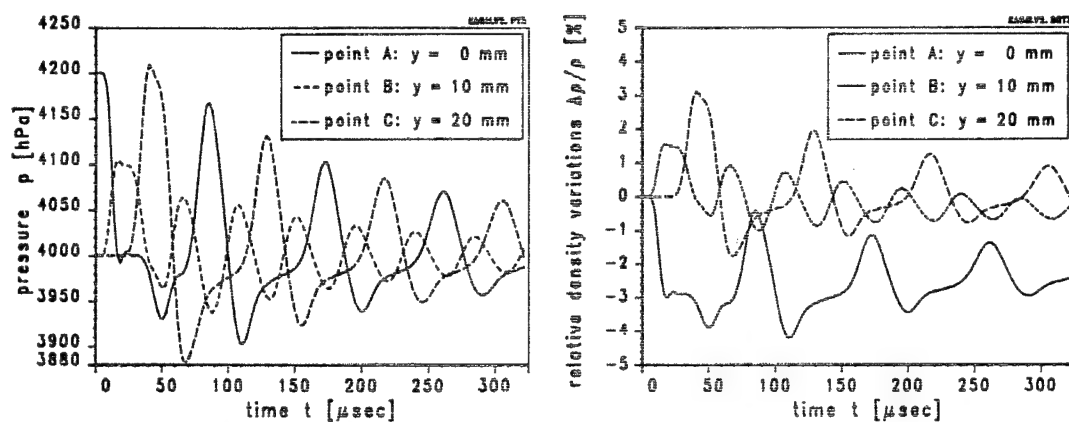


Fig. 6: Time dependent pressure and density variations at the points A, B, and C in the case of reflection at a straight wall.

Figs. 7 and 8 are similar to Figs. 5 and 6 with the exception, that now the geometry depicted in Fig. 4 is under consideration. The rarefaction generated at the bent wall leads to a decrease of the shock intensity in the same way as has been discussed in section 2.2.1. The nonuniformity of the pressure distribution is more significant than in the case of the straight wall. In the graphs indicating the time step

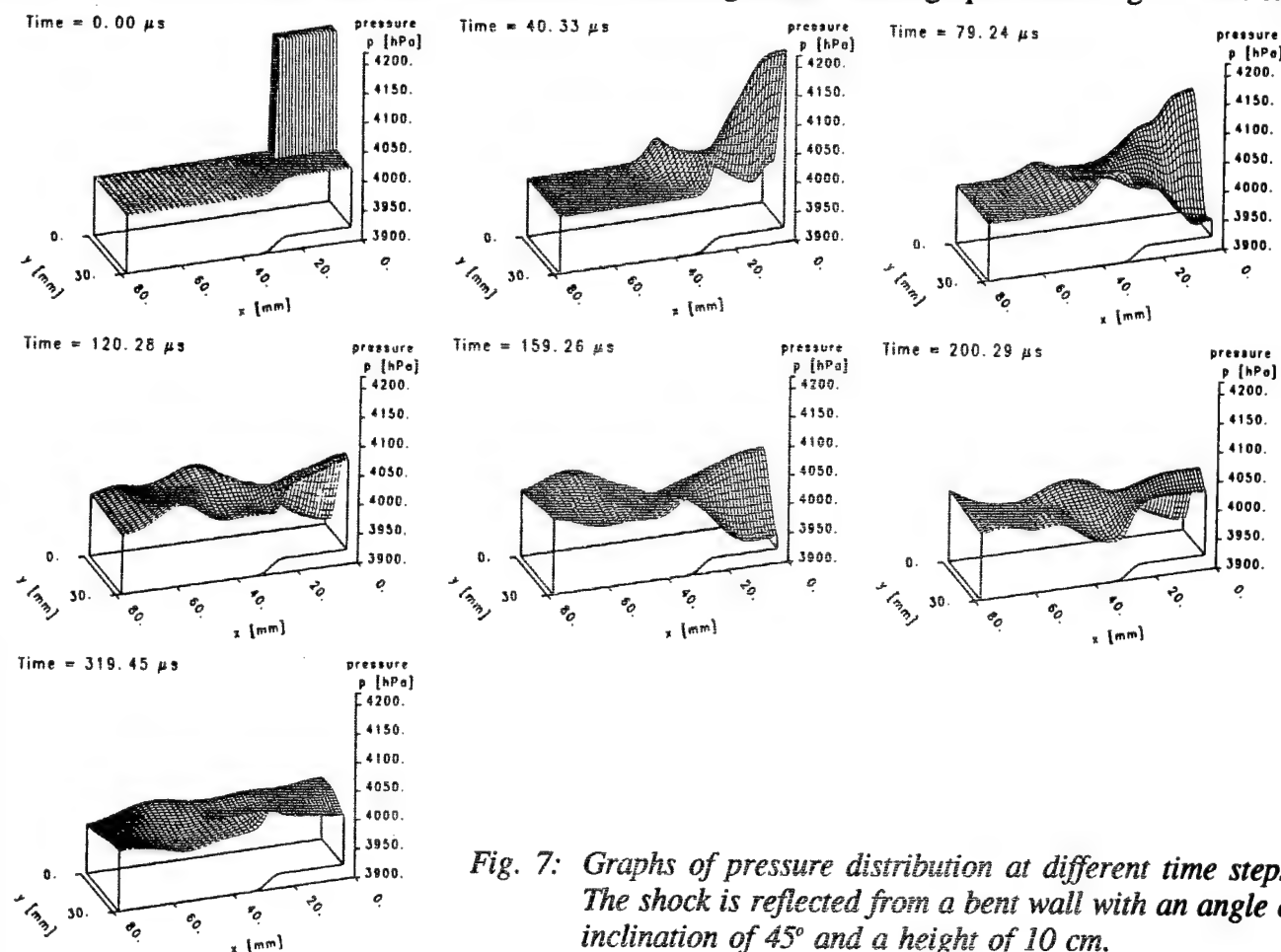


Fig. 7: Graphs of pressure distribution at different time steps. The shock is reflected from a bent wall with an angle of inclination of  $45^\circ$  and a height of 10 cm.



at  $319 \mu\text{s}$ , this can be clearly observed by comparison of the two geometries. In the straight channel the pressure distribution is smoother, whereas otherwise a number of local areas of higher pressure exist. These areas are separated by the rarefactions coming from the edge of the retracted wall and spread into the channel.

The oscillations occurring in the points A, B, and C in Figs. 6 and 8, however, do not differ significantly in either case. The decay rate of the shock waves appears to be independent of the geometry of the wall. This fact has been confirmed by additional calculations omitted in this contribution, in which both the angle of inclination and the height of the wall projection have been varied. There was almost no influence detectable concerning the behaviour of the oscillations in the y-axis with regard to time. Only the pressure fields spreading into the channel differ slightly in shape and magnitude.

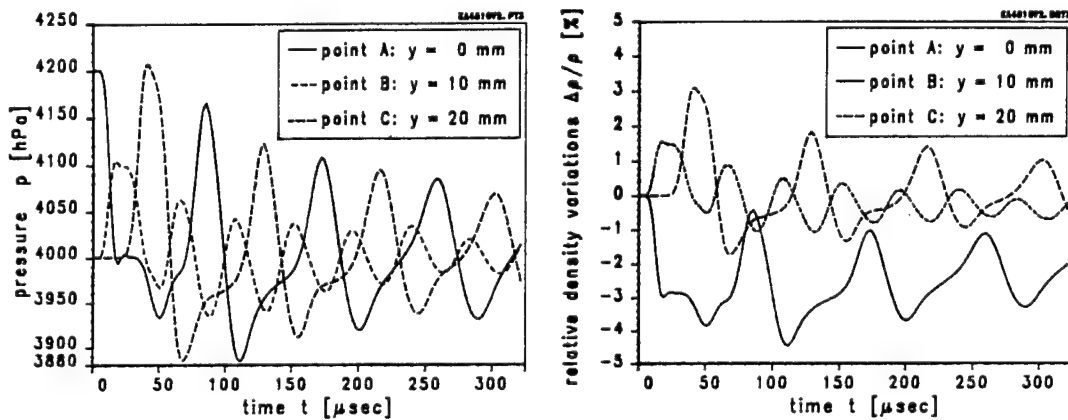


Fig. 8: Time dependent pressure and density variation of the configuration of Fig. 7.

### 2.3 Comparison with helium as laser gas

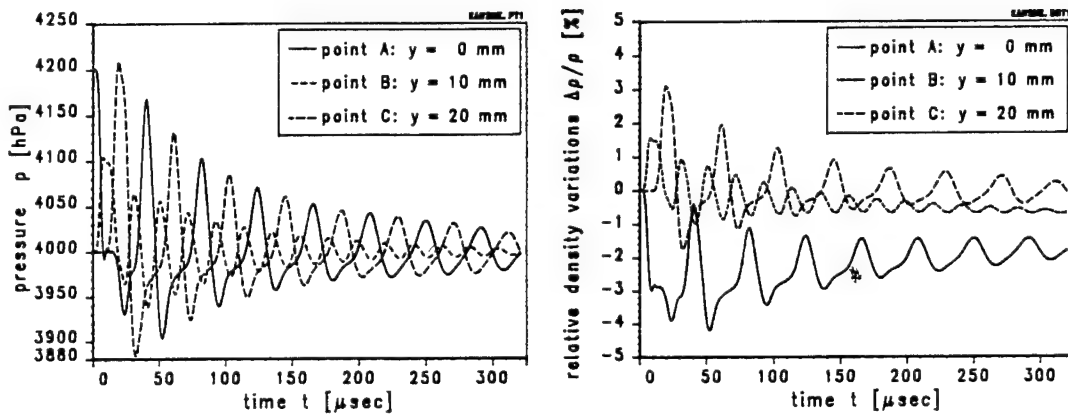


Fig. 9: Time dependent pressure and density variations at the points A, B, and C (depicted in Fig. 4), All parameters are the same as in the case presented in Fig. 5, except that helium is used as laser gas.

In Excimer lasers the gas component neon can be replaced by helium, keeping the other components HCl and xenon constant. The major consequence on the physical properties of the gas is an increase of the speed of sound from 447 m/s to 943 m/s. Thus shock waves propagate with a velocity over twice as fast as in the case of neon. This can be seen clearly in Fig. 9, where the frequency of the oscillations is increased considerably.

The calculation has been carried out with the configuration of Fig. 5. The decrease in the amplitudes of pressure and density considered over the same time is hence higher due to the higher number of reflections at the walls, but the total decay rate of one round trip of a shock wave remains the same as in the case of neon.

### 3. EXPERIMENTAL SETUP

#### 3.1 Design and operation of the test bed

To detect density perturbations down to the order of  $10^{-4}$  with an interferometer, an optical length of about 1 m is required for the laser beam. This demand leads to the construction of a shock channel with the rectangular cross section of  $50 \times 500 \text{ mm}^2$ , where the beam of a Twyman-Green-Interferometer runs twice through the measuring section. This unusual cross section does not allow the use of a high pressure load part, separated by a diaphragm from the low pressure shock tube, as the diaphragm would burst irregularly across the width of the channel. The shock wave produced in that way would not have the evenness necessary for interferometric investigations. Thus a different concept to generate these shock waves had to be developed.

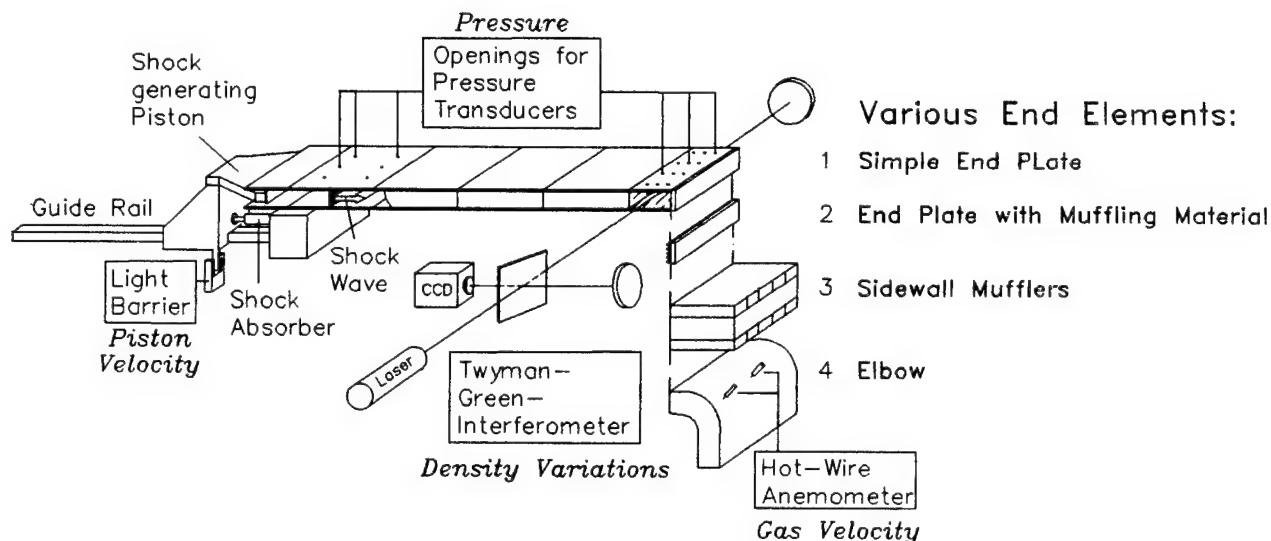
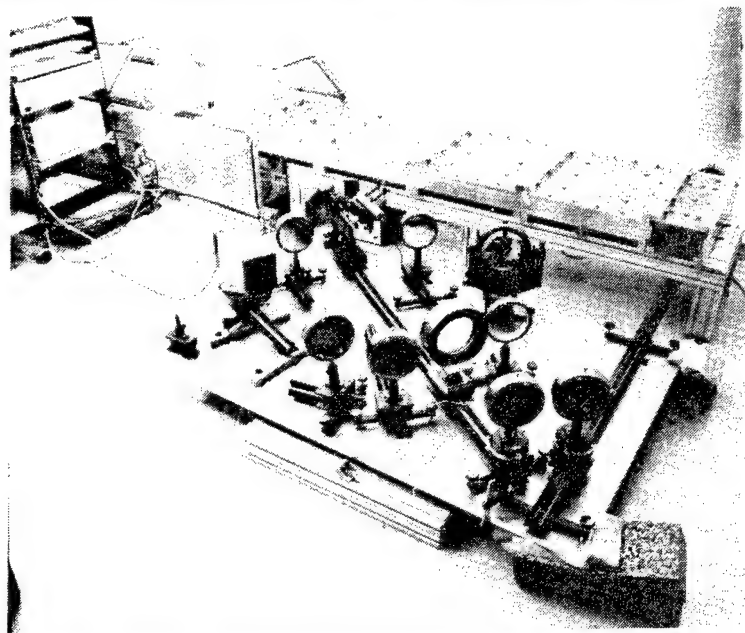


*Fig. 10: View of the piston driven shock channel with attached instruments.*

We decided to use a mechanical concept of two pistons. The first is attached on a sliding carriage driven pneumatically by two cable cylinders. The driving cables are arranged in a block and tackle to double

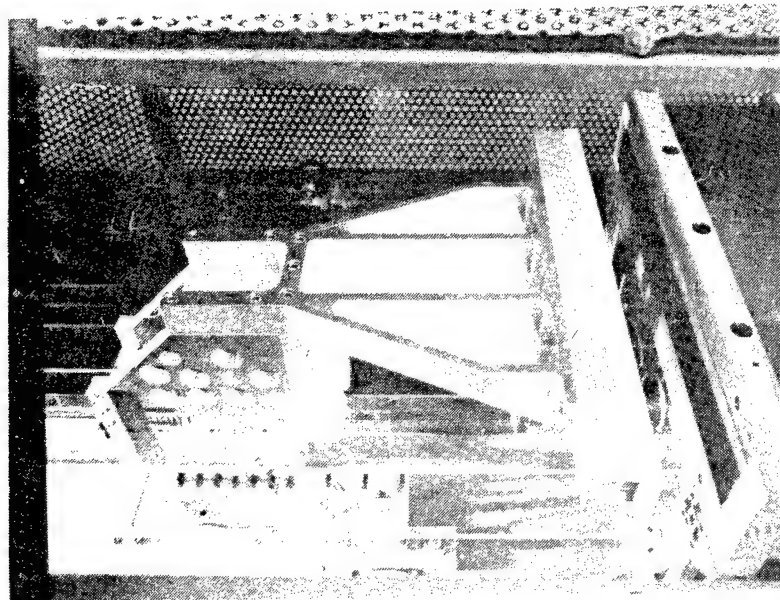
the speed of the carriage. The second piston is placed at the entrance of the channel and is struck by the first and hence accelerated very rapidly. In this way a remarkably even shock wave with sufficiently short rise time is generated, as will be discussed later. The second piston, which has to be extremely light and stiff, is held by the first by means of strong permanent magnets. Hence it can easily be repositioned after each shot. The length of the channel is 240 cm. In Fig. 10 a scheme of the experimental setup is shown in conjunction with the attached instruments.

On the top side of the channel several holes have been drilled to accomodate piezo pressure transducers. The impact speed of the two pistons is measured with several light barriers. When the shock wave reaches the observation window at the right end of the channel, the interferometric information is



recorded with a CCD-camera connected to a PC-based image processing system. The camera is able to accomplish an exposure time as low as 20 ns. The built in light amplifier permits the use of a 0.5 mW He-Ne laser. Various elements can be attached at the end of the channel, e.g. end plates with muffling materials, elements with sidewall mufflers or elbows and diffusers. To investigate the gas velocity in those elements a hot wire anemometer is available.

*Fig. 11: Photograph of the shock channel and its driver section. In the foreground the interferometer setup is visible.*



The Figs. 11 and 12 show photographs of the experimental setup. In Fig. 11 the entire shock channel is shown. In the foreground the interferometer with the CCD-camera is visible mounted on a vibration damped table. The left part of the test bed is the driver section with the piston. The right section is the rectangular shock channel.

*Fig. 12: Photograph of the first piston mounted on the sliding carriage, holding the second piston.*

In Fig. 12 the piston mounted on the sliding carriage is shown in front of the rectangular orifice of the shock channel. The second piston is held by first one. On either side of the carriage the driving cables are fixed and on the ground the light barriers for velocity measurements are visible. To avoid the risk of damage in the case of a possible failure of the driving cables, the entire driver section is capsulated in a cage.

The test bed is designed for a piston speed of 10 m/s, thus producing shock waves with a pressure ratio of 1.04. After the apparatus had been put into operation, it turned out, that piston velocities up to 15 m/s, corresponding to a pressure ratio of 1.06, can be achieved.

### 3.2 Experimental results

#### 3.2.1 Formation and shape of the produced shock waves

The accelerated piston entering the shock channel produces a shock with a pressure ratio depending on the piston velocity. The shock front develops according to the acceleration characteristic of the second piston. The shock front will be steeper the higher the acceleration is. Best results have been obtained with a honeycomb and sheet metal construction fitting exactly into the orifice of the channel. The accomplished rise time of the shock front is about  $20 \mu\text{s}$ . This rise time leads to a spatial dimension of the front of about 7 mm at a shock velocity of about 340 m/s. The interferometric photograph of the shock is shown in Fig. 13. The shock front is not as steep as shocks produced in long tubes of circular cross section. On the contrary, the dimensions of the shock front is of great advantage to an interferometric interpretation, because the fringe shift across the shock is well detectable. Further, the shock waves produced in excimer lasers have a rise time similar to that of our shock waves, because the energy deposition volume between the electrodes is not sharply limited. The visibility of fringes in the shock front is a prerequisite for a quantitative analyses of the efficiency of damping elements with regard to the remaining density perturbations. These investigations will be undertaken in the near future. The result of a first experiment with a very simple damping element is presented in the next section. However, in that period of time only pressure measurements were taken.

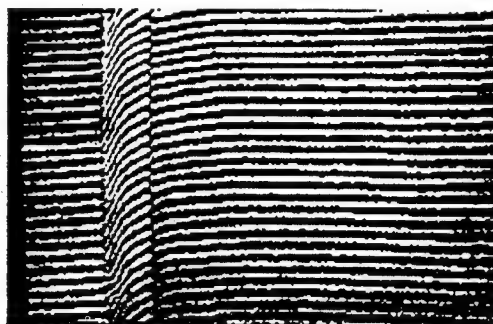


*Fig. 13: Interferogram of a shock generated in the piston driven shock channel.*

#### 3.2.2 Transient pressure variations

In Fig. 14 the pressure in the shock channel is plotted over a time period of 80 ms. The pressure transducer is located 155 cm from the end of the channel. The shock generated at a piston velocity of 7.5 m/s compresses the air by 30 hPa. On its way back after the first reflection at the end of the channel the same compression occurs again. The shock then is reflected at the piston still moving and undergoes the same course again. The compression continues until the piston is decelerated by the shock absorbers.

This deceleration gives rise to a rarefaction, that can be seen after about 17 ms. It appears as a decreasing pressure contour instead of a constant pressure level. The overall compression in the channel due to the volume reduced by the penetrating piston amounts to 90 hPa. This compression slowly reduces after some time as the air escapes through the gap between the piston and the channel walls.

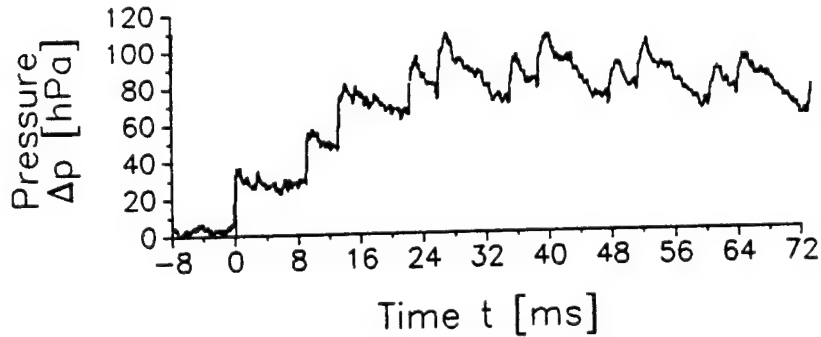


**Fig. 14:** *Transient pressure variation in the shock channel after the shock wave has been released. Multiple transitions due to reflections of the shock at the end-plate and at the piston are visible.*

In order to estimate the effect, that simple damping elements have on the shock waves, the elements shown in Figs. 15 to 17 have been integrated into the channel. They consist of simple wool as used in loudspeakers, and perforated sheets. Although this material is not usable in real excimer lasers for to contamination reasons, it has the advantage of easy availability and handling as a first experimental approach. In excimer lasers nickel wool for instance could be used instead.

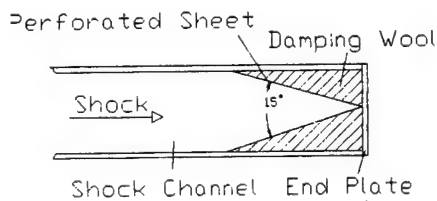


**Fig. 15:** *Simple damping element made of perforated sheet bent to an angle of 15°, and wool.*

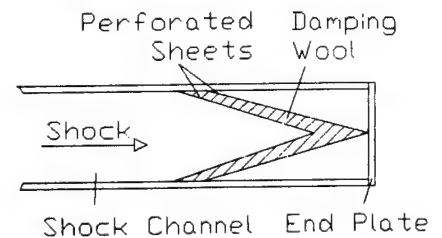


**Fig. 16:** *Damping Element made of two bent perforated sheets filled with wool.*

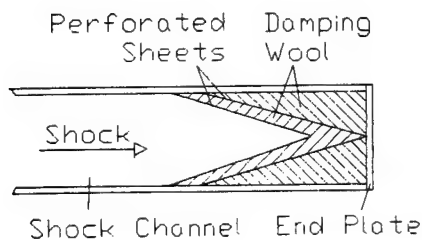


**Fig. 17:** *Combination of the damping elements in Figs. 15 and 16.*

The results achieved using these elements are shown in Fig. 18a-c. The following effects can be seen at each of the curves, compared to Fig. 14: The rise time of the shock front after the first reflection (at 9 ms) is increased. The following shock transitions rapidly become indistinct. The shock flattens and the pressure ratio decreases after each reflection.

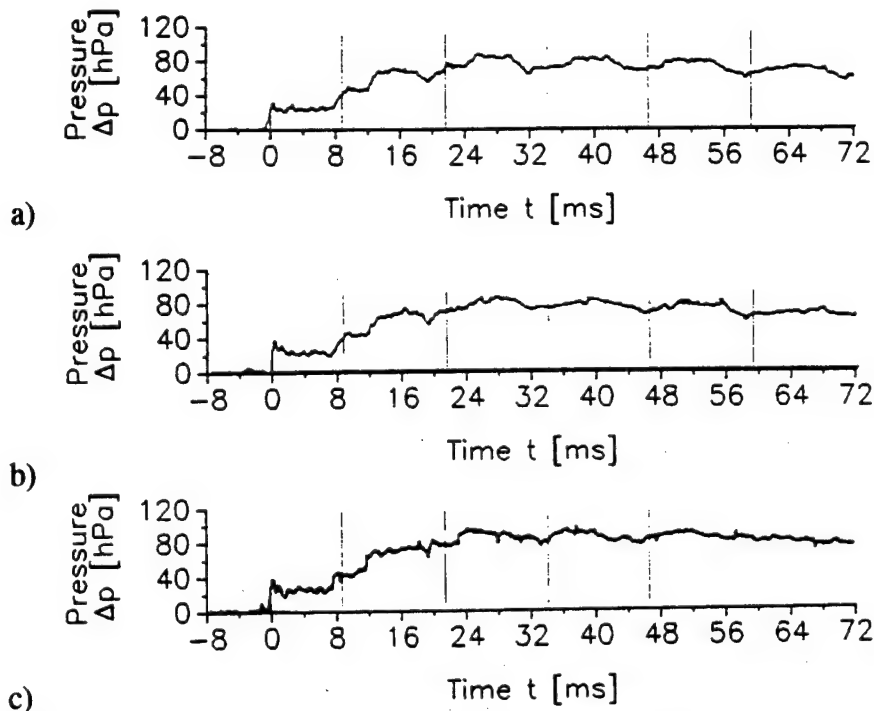


Fig. 18: Transient pressure variation in the shock channel with several damping elements present:  
a) Simple damping element with wool (see Fig. 15).  
b) Element made of two bent perforated sheets filled with wool (see Fig. 16).  
c) Combination of the two elements (see Fig. 17)

The damping element consisting of a single perforated sheet (Fig. 15 and curve of Fig. 18a) reflects the shock stronger than the element shown in Fig. 16 (curve of Fig. 18b). In the latter case, the shock front already flattens out after the first reflection. In the case of the simple damper, low-frequency pressure oscillations with  $\Delta p = 24$  hPa remain in the channel. These oscillations amount to  $\Delta p = 19$  hPa for the damper with two sheets (Fig. 15) and to  $\Delta p = 38$  hPa in the case where no damper is included into the channel. Some improvement can be accomplished when filling the rear volume with wool (Fig. 16 and curve of Fig. 18c). The pressure oscillations then reduce to  $\Delta p = 14$  hPa.

The transient pressure variations measured within the shock channel in the presence of damping materials clearly indicate the suitability of the construction for further investigations in the field of pressure wave attenuation.

#### 4. CONCLUSIONS

The theoretical investigations on the propagation of shock waves have shown, that the distribution of pressure and density perturbations can be influenced by the geometric design of the walls of the laser head. The decay rate of waves oscillating between the electrodes or mirrors, respectively, seems to be

independent of the investigated parameters like angle and height of a step in the wall contour. But it is directly affected by the velocity of sound of the used laser gas, as the comparison of helium with neon demonstrates.

Experimental investigations using interferometric photography and pressure measurements have proved, that in this test bed shock waves can be suitably produced in order to deduce information about the damping properties of materials and constructive elements compatible with excimer lasers.

## **5. ACKNOWLEDGEMENT**

We would like to thank our colleagues S. Borik and W. Wittig for their valuable work in providing the necessary apparatus for the interferometer setup. Another thank is dedicated to A. Leonard, who carried out the experimental work.

Parts of the work have been supported by the EUREKA-Program EU205.

## **6. REFERENCES**

1. L.Arif,P.Canarelli,Ph.Delaporte,B.Fontaine,B.Forestier,M.Sentis,"Waves behaviour in a high repetition high average power excimer laser",7th International Symposium on Gas Flow and Chemical Lasers, Vienna, Springer 1988
2. P.Berger, R.Holtbecker, A.Holzwarth, H.Hügel,"Dichteschwankungen in gepulsten CO<sub>2</sub>-Hochleistungslasern", Laser/Optoelectronics in Engeneering, Munich, Springer 1987.
3. A.Holzwarth, K.Grünwald, P.Berger, H.Hügel, "Two-dimensional time dependent modelling of density perturbations in CO<sub>2</sub> and excimer lasers", 7th International Symposium on Gas Flow and Chemical Lasers, Vienna, Springer 1988
4. A.Holzwarth, K.Grünwald, P.Berger, "Zweidimensionale Berechnung der Ausbreitung von Dichtestörungen in gepulsten Hochleistungslasern", Laser/Optoelectronics in Engeneering, Munich, Springer 1989.



## Super Small Excimer Laser

36980005 The Hague EXCIMER LASERS AND THEIR APPLICATIONS in English 1991 pp 110-114

[Article by Arnold A. Vill and Ants A. Salk of the Special Design Office and Irina K. Berik of the Institute of Physics]

[Text]

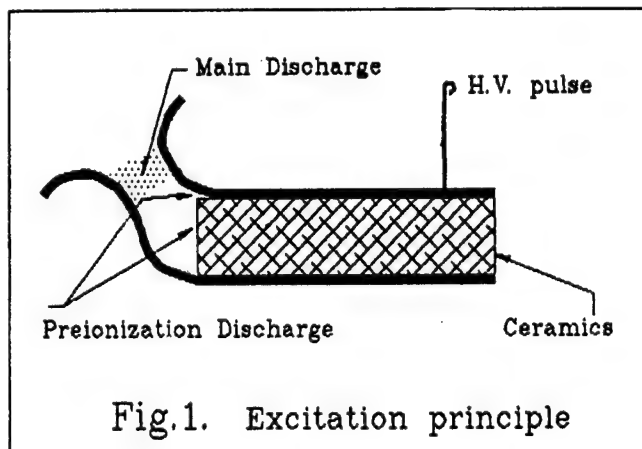
The construction and some characteristics of XeCl excimer lasers with active volumes of  $0.4 \text{ cm}^3$  and  $1 \text{ cm}^3$ , and output energies of  $50 \text{ }\mu\text{J}$  and  $1.6 \text{ mJ}$ , correspondingly, are described. In both cases preionization by discharge on the ceramic surfaces of peaking capacitors is used in excitation schemes. In case of the second laser "electric wind" is used in gas circulation which allows to work with pulse rate up to  $100 \text{ Hz}$ .

### 1. LASER of $0.4 \text{ cm}^3$ .

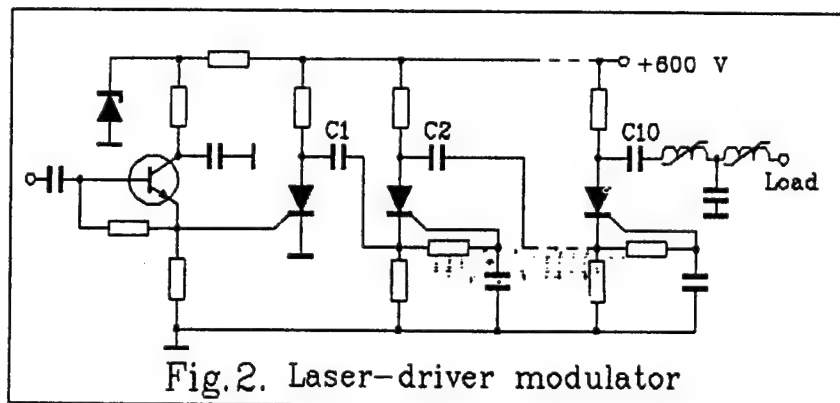
In general the excitation scheme is executed according to classical canons. Incomplete surface slide discharge on the ceramic surface (Fig. 1) of the peaking capacitor is used for preionization. Thus, preionization is carried out automatically.



The permittivity of ceramics is about 900. The electrodes of the laser as well as the plates of the peaking capacitor are made of nickel tin. The measures of the active zone are  $0.4 \times 0.2 \times 5 \text{ cm}^3$ . 0.4 cm - the gap between electrodes. The thickness of the ceramic plate - 0.7 cm, the capacity of the peaking capacitor  $\approx 1 \text{ nF}$ .



10-stage Marx-bank generator is used for impulse charging of the peaking capacitor. The capacity and voltage of one stage are 20 nF and 600 V, correspondingly (Fig. 2). With open end such a generator gives an pulse with the amplitude of 6 kV and rise time of 25 ns. In case of a load of 1 nF the generator is protected against overload using a 2-stage saturable inductor. The first stage prolongs the duration of the current impulse through the thyristors and respectively reduces the current amplitude. The second stage forms again an impulse of short rise time - 30-35 ns and the amplitude of 6 kV by the load of 1 nF. The pulse repetition rate of the generator - 1 kHz is limited by the charging impedance.



The peaking capacitor is placed into a cylinder vessel of ceramics. The output mirror has the reflection coefficient about 80%, the rear one - 90%. By the ca 3 bar pressure of the buffer gas He and the composition of the mixture 0.3% HCl, 1% Xe the output energy value is about 50  $\mu$ J. Due to the absence of gas circulation the laser works at the pulse rate of up to 10 Hz. The length of the pulse forming line is 3 cm, which at permittivity of 900 gives the current impulse of about 6 ns. In spite of this the duration of the output impulse comprises 20 ns.

These results did not satisfy us, therefore a laser of biges active volume was constructed according to analogous principles.

## 2. LASER of 1 cm<sup>3</sup>

The excitation scheme is, in principle, analogous to the one described above, only the electrodes and the ceramics are packed in the form of "sandwich". In such a way minimum impedance of the pulse forming line (PFL) is achieved and the inductivity of the discharge contour is also reduced to minimum. The gap between electrodes in this case comprises 0.35 cm, the length of the active zone - 15 cm, the width of discharge determined by burn pattern - 0.2 cm. The volume is, consequently,  $0.35 \times 0.2 \times 15 = 1$  cm<sup>3</sup>. The peaking capacitor formed by ceramics has the capacity of about 10 nF.

The Marx-bank generator using the present thyristors with maximum current of 200 A doesn't allow sufficiently good rise time, therefore, the traditional scheme with storage capacitor and thyatron is used to form the voltage impulse (Fig. 3). As in our last year's work, the thyatron is working in the pseudospark

switch regime, without the incandescence of cathode, with negative shift voltage on the grid and negative triggering impulse. In general, the thyatron is reliably triggered by a standard amplitude impulse (500 V). To reduce the jitter we make use of an impulse with an amplitude of 3 kV, which cuts the delay of switching-on down to 100 ns, while the jitter becomes less than 1 ns.

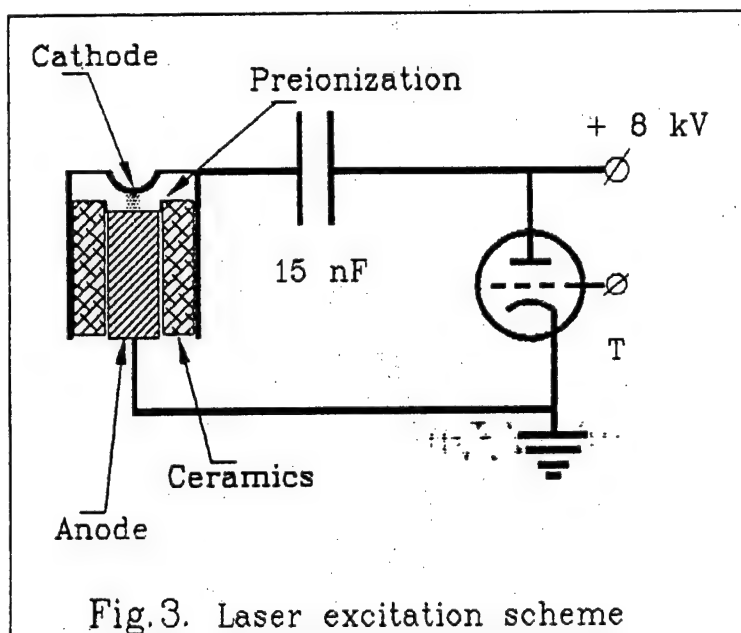


Fig.3. Laser excitation scheme

Gas is pumped through the gap between the electrodes by the

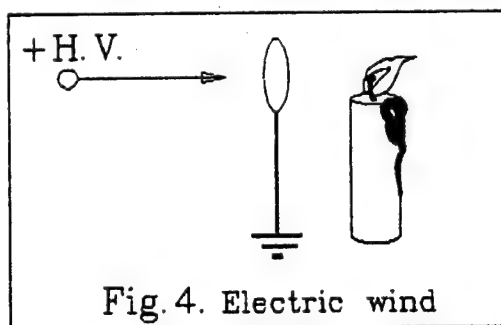


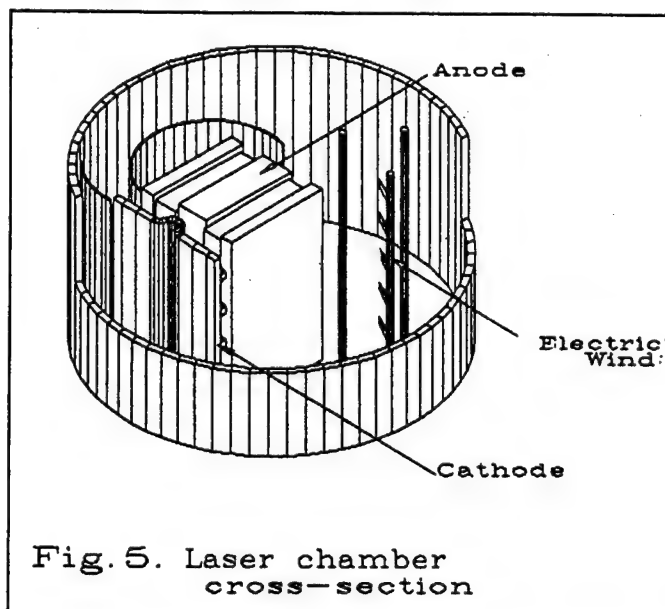
Fig.4. Electric wind

"electric wind" referred to already in the previous century (Fig. 4). As far as we know, the electric wind was first used in a gas (excimer) laser by A. Pastor from the Leningrad University (private communication). The parameters of his laser - 100 mJ, 50 Hz.

In our case the pumping of gas is secured by a jagged nickel plate to which voltage is conducted from the high-voltage (main) power supply through the limiting resistor of 0.5 MΩ. The experiments with air indicated that such a system can provide gas flow rate of up to 5 m/s with very small yield of power. In the aerodynamic contour model of our laser the "wind" speed in the 0.4-cm gap (distance between electrodes) exceeds 1 m/s. Measurements were carried out with the thermoresistant sensor. Without gas pumping the laser works at the pulse rate of up to 25 Hz. At that the impulse energy does not decrease.

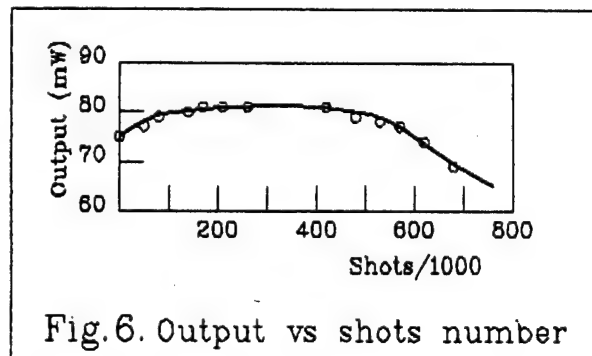
The system of coronating electrodes does not only pump gas, but also serves as an electric filter entrapping dust pollution unavoidable in case of excimer lasers.

The whole device - "sandwich" of ceramics, electrodes and the "electric wind" scheme are placed in a cylinder vessel of aluminum (Fig. 5) with diameter about 100 mm.



The inner surfaces of the laser are passivated with fluor. Due to this, as well as the absence of plastics inside the vessel, the working resource of the mixture is considerable - about 1.000.000 shots (Fig. 6) - by the total volume of the mixture of about 1 l.

The curve in Fig. 6 was obtained in case of the pulse rate of 50 Hz. The gas mixture contained 15 mbar HCl/15 mbar Xe/6 bar He. The laser is not very sensitive about the composition of the mixture. As can be seen, the ratio  $\text{HCl/Xe} = 1$ ; this is not caused by the absorp-



tion of HCl on the surfaces, as indicated by the resource curve. Obviously, by so intensive preionization stable discharge without contraction is secured in "natural" mixture - for successful work one

atom of Cl requires only one atom of Xe.

In case of so rich a mixture and relative high power pumped in volume unit (current impulse about 8 ns) the gain coefficient of the medium is sufficiently big to use a simple quartz plate (laser window) as output mirror by the length of the active zone of only 15 cm. The value of the gain can be judged by the fact that in case of an output mirror with  $R=30\%$  the output power is almost the same as in case of a quartz plate. When the rear mirror is removed, the energy drops only by a third (three times in one direction). The pulse duration at half-height is 2.5 ns.

The relatively low efficiency of 0.3% can be explained by the considerable loss of energy at the initial stage of generation in case of short excitation (about 8 ns) (Fig. 7).

The "strange" behaviour of the resource curve - growth of energy after some time of laser functioning, can to some extent be explained by the

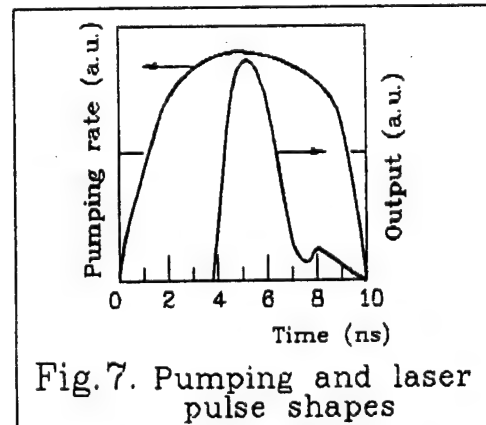


Fig.7. Pumping and laser pulse shapes

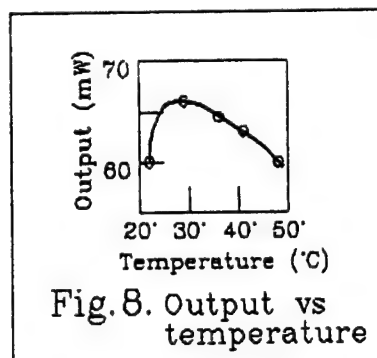


Fig.8. Output vs temperature

curve presented in Fig. 8 displaying the dependence of output energy (50 Hz) on the temperature of the mixture. Evidently, the cleaning rate of the lower level becomes the critical parameter in case of such relatively high pumping powers and gain coefficients. This is assisted by the increase of temperature.

Now, as a conclusion, table with laser characteristics is present:

Excimer Laser	PL-100
Pulse Energy	1.5 mJ
Pulse Rep. Rate	100 Hz
Pulse Duration	2.5 ns
Dimensions	25*15*40 cm <sup>3</sup>
Weght	7 Kg

Experimental Studies of an XeCl Laser with UV Preionization Perpendicular and Parallel to the Electrode Surfaces

36980005 The Hague EXCIMER LASERS AND THEIR APPLICATIONS in English 1991 pp 115-125

[Article by V. Nassisi of the University of Lecce]

[Text]

ABSTRACT

This paper reports the behaviour of an XeCl laser having two independent preionizators which generate UV radiation into the discharge region in the perpendicular and parallel direction to the electrode surfaces. Output energy and other parameters have been measured using single preionizator and both preionizators, changing the power supply polarity and varying the delay time between the preionization and the main discharge. When the preionization system generated photons only in the direction perpendicular to the electrode surfaces and a negative power supply was used, a high discharge current and a high output laser energy were obtained. Besides, diffusion coefficient of the photo-preionized electrons played an important role in the laser behaviour, particularly, when a consistent delay time between the onset time of the preionization and the main discharge was present.

1. INTRODUCTION

The use of excimer laser systems, which provide UV coherent light of high intensity, is increasing in many fields such as photolithography[1], material processing[2] and non-linear optics[3]. Recently, many efforts have been done to get efficient excimer lasers. Excimer lasers used for industrial and scientific applications are generally led by self-sustained electrical discharging circuits. It is well known that the output characteristics of these lasers are very sensitive on the density of electrons formed by preionization[4], and on the delay time between the preionization source and the main breakdown of the laser gas[5-8]. Besides, efficient and uniform preionization is crucial for a fast and uniform discharge[9].

In high pressure self-sustained lasers, discharge breakdowns are caused by the non-linear development of the space-charge fields associated with the individual primary electron avalanches within the

discharge volume. This phenomenon can cause high space-charge fields which cause the discharge current to become filamentary[9].

Authors have determined the threshold value of the preionization electrons density and they have also demonstrated that the threshold conditions are independent of whether the preionization electrons are provided by UV photons[10] or by X rays [4].

Many UV preionized excimer lasers have got a perforated electrode which allows to its preionizator to preionize small volumes of the discharge gap. X ray preionized excimer lasers have got solid electrodes. Sometimes, one of them can get a grill which supports a solid electrode[4] and as consequence only small regions of the discharge gap, like in the perpendicular UV preionization system, could be preionized.

Then, to get high intensity laser beams from self-sustained discharge laser systems, many primary electron avalanches must be formed in order that they can overlap. For this end, authors have used UV radiation from a creeping discharge over a dielectric surface [11].

The output characteristics of excimer lasers are also very sensitive on the rapidity with which the stored energy is deposited into the laser gas[5] due to the electron loss process. In fact, for HCl based lasers the dissociative attachment rate is  $10^{-11}$  cm<sup>3</sup>/s[11].

Supposing an initial preionization electron density  $n_{e0}$ , the time dependence of the electron density is governed by the following equation:

$$\frac{dn_e}{dt} = - B n_H n_e \quad (1)$$

where B is the dissociative attachment rate of HCl,  $n_H$  is the halogen gas concentration and  $n_e$  is the electron density. Solving (1) for  $n_e$  one obtains:

$$n_e = n_{e0} \exp(-B n_H t) \quad (2)$$

For a halogen donor concentration of  $10^{17}$  cm<sup>-3</sup> the decay time of the expression (2) is about  $10^{-6}$  sec.

Papers which have described the behaviour difference of UV and X ray preionized excimer lasers have often neglected the diffusion processes. The diffusion process of the photo-preionized electron plays an important role in the output laser energy, particularly when perforated grounded electrodes are used, and a consistent delay time between the preionization and the main discharge is present.

In this paper a XeCl laser having two UV independent preionizations which provide UV radiation in the perpendicular ( $P_V$ ) and parallel ( $P_L$ ) direction to electrode surfaces was designed and tested.

Output energy and other parameters have been measured energizing only the preionizator  $P_V$ , only the  $P_L$  and both  $P_V$  and  $P_L$ . Measurements have also been done changing the power supply polarity and varying the delay time between the preionization and the main discharge.

A higher output energy has been obtained when only the preionizator  $P_V$  has been energized, at a negative charging voltage, and with a delay time between the preionization and the main discharge of about 300 nsec. Under these last conditions, also a higher discharging current pulse has been obtained.

## 2. EXPERIMENTAL SET UP

The excimer laser used in this work was fabricated locally in order to study the effects of the preionization photons direction. This laser is formed by a PVC chamber 750 mm long and 250 mm in diameter, which contains the electrode structure and the discharging capacitor (C), Fig. 1. The discharge is of the capacitor charge trans-

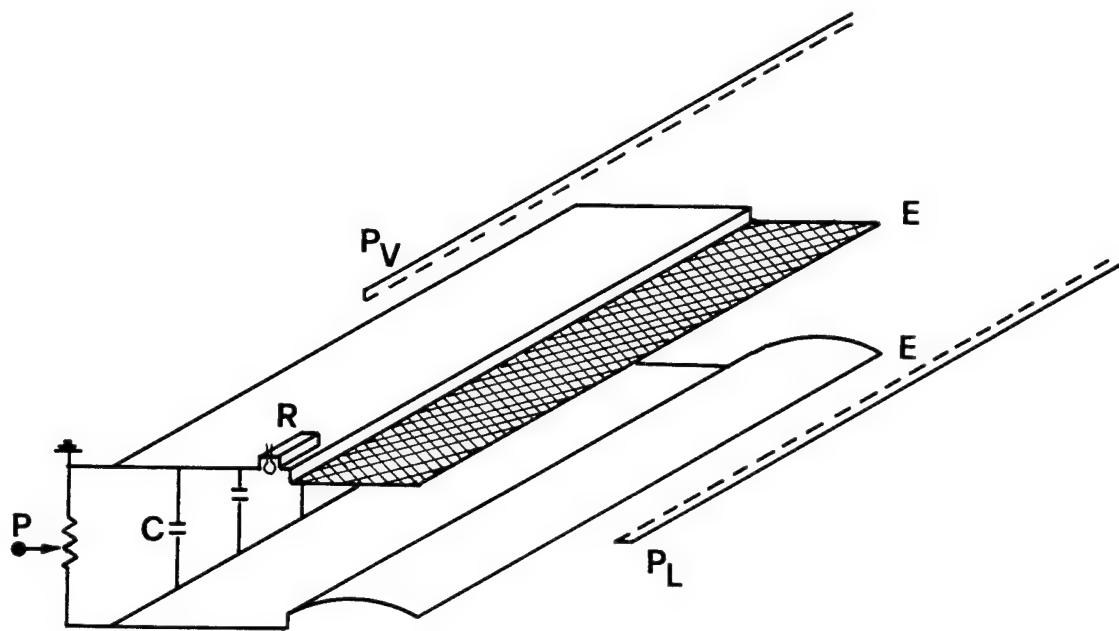


Fig. 1. Schematic representation of the UV preionized excimer laser. E: electrodes;  $P_V$ : perpendicular preionizator;  $P_L$ : parallel preionizator; R: linear Rogowski coil; P:  $\text{CuSO}_4$  voltage divisor; C: discharge capacitor.

fer type, with nominal primary and secondary capacitances of 75 and 25 nF, respectively. The secondary capacitance is formed by 10 aligned capacitors of 2.5 nF each placed laterally to a side of the electrodes. A low inductance spark-gap (S1) switches on the circuit (Fig. 2). The electrode structure consist of a solid brass bar and a



brass net, each 40 mm wide and 500 mm long with a separation of 25 mm. The edges of the electrodes were shaped to avoid strong edge effects. The brass net ( 25 mesh, 0.15 mm thick ) presents an optical transmission of about 70 % and is fixed to the electrode holder forming a angle of about  $40^\circ$  ( see Fig. 1 ) between the laser optical axis and a side of the mesh. This configuration allows to the preionizator  $P_V$  to preionize small gas volumes along all the laser optical axis. The preionizator is formed by two spark-array rods. The first,  $P_V$ , is placed at 80 mm from the discharge region centre behind the perforated electrode, while the second,  $P_L$ , is placed at 80 mm from the discharge region centre laterally to the electrodes. Each spark

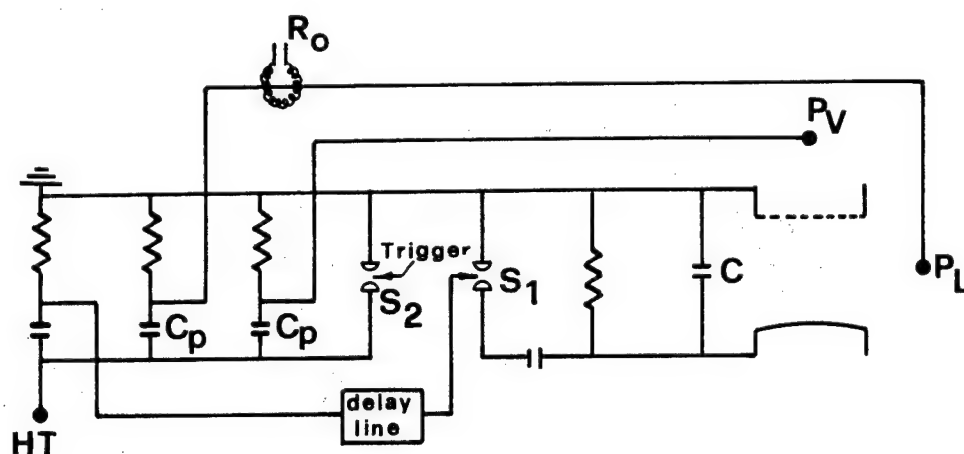


Fig. 2. Schematic diagram of the electric circuit. C: discharge capacitor;  $C_p$ : preionization capacitors;  $R_0$ : Rogowski coil;  $S_1$  and  $S_2$ : spark gaps.

array rod consists of 35 tungsten pins 13 mm long and with a separation of 1.5 mm. The rods are driven by two 1.7 nF capacitors ( $C_p$ ), charged at the same voltage of the primary capacitance. They are switched on by an other low inductance spark gap ( $S_2$ ). A delay line is used in order to introduce a delay time between the two spark gaps and, as consequence, between the preionization and the main discharge. Then, an external trigger signal switches on  $S_2$ , allowing to get photo-preionized electrons before the main discharge.

The delay line consists of a series of LC cells which present a delay time of about 100 nsec each.

The optical cavity is formed by a flat aluminized mirror (  $R = 87\%$  ) and a flat silica disc as partial reflector (  $R = 6.5\%$  ), while two quartz windows sealed the gas cell along the optical axis.

The output laser energy has been measured by a Gen Tec ED 500 pyroelectric detector, while the pulse shape and duration have been recorded with a photodiode ITT F4115 and a fast oscilloscope. A  $\text{CuSO}_4$  resistive divider (P) has been used in order to measure the voltage between the electrodes, while a linear Rogowski coil (R) placed near the grounded electrode, measured the discharge current[13].

During the experiments the discharge chamber was filled with a 0.1% HCl, 1.7% Xe and 98.2% Ne or He mixture with a total pressure up to 600 kPa. In all the experiments the output beam cross-section was  $2.5 \times 1.2 \text{ cm}^2$  large. The used power supply provided an output voltage up to 45 kV with positive and negative polarity.

### 3. RESULTS and DISCUSSIONS

An 0.1% HCl, 1.7% Xe, and 98.2% Ne mixture at a total pressure of 400 kPa was used first.

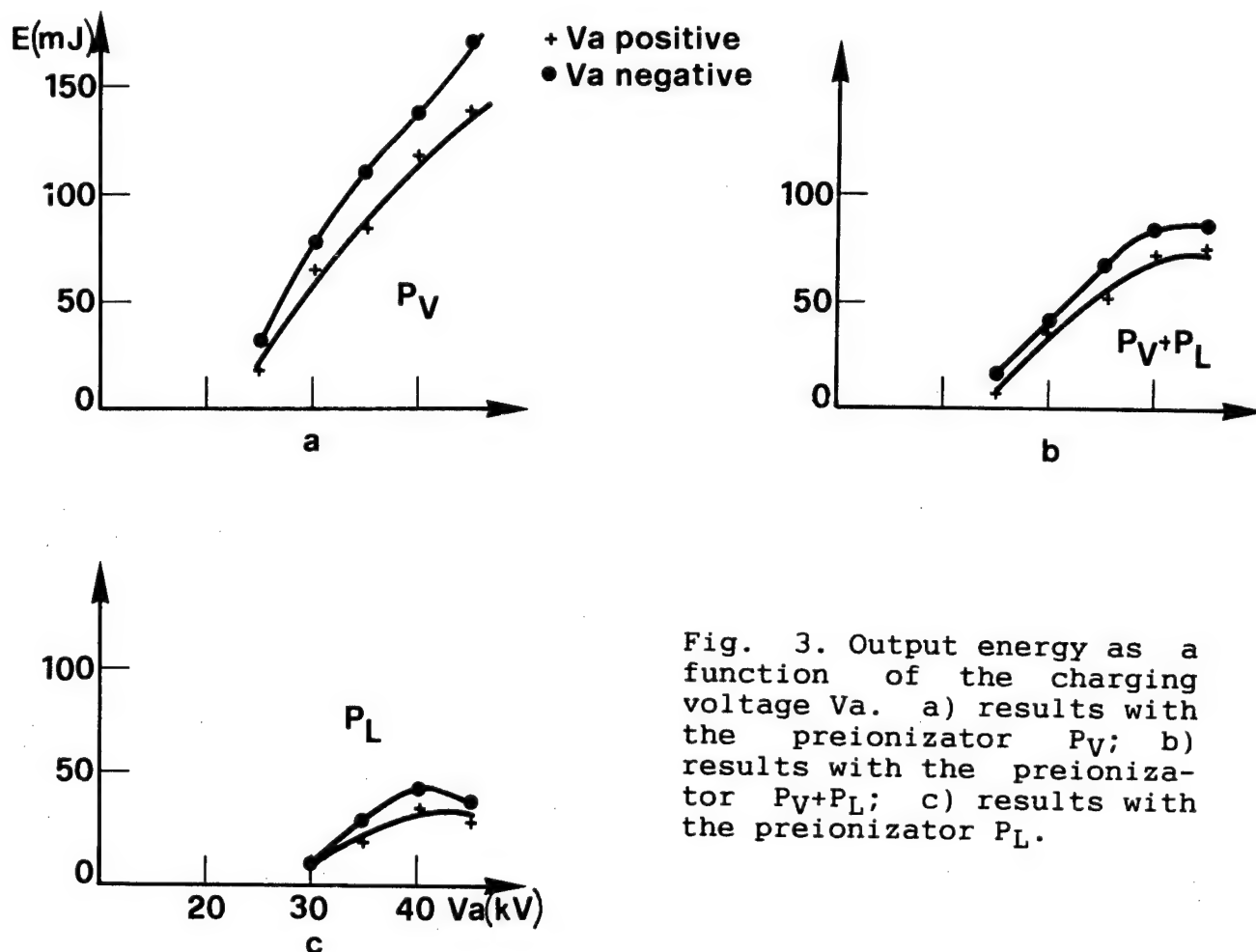


Fig. 3. Output energy as a function of the charging voltage  $V_a$ . a) results with the preionizator  $P_V$ ; b) results with the preionizator  $P_V + P_L$ ; c) results with the preionizator  $P_L$ .

Figs. 3a, b and c show the output energy as a function of the charging voltage intensity, of its polarity, and with different pre-ionizers  $P_V$ ,  $P_V + P_L$  and  $P_L$ , respectively. A higher output energy was obtained when the preionizator  $P_V$  was energized. The output energy was lower when only the preionizator  $P_L$  was energized, while with both preionizators it became lower than with only the preionizator  $P_V$ , nevertheless the use of both preionizators increased the photo-preionized electrons. Besides, in Fig. 3a, the output energy is linearly dependent on the power supply voltage, while the linearity is less evident in Fig. 3b, and it is much less evident in Fig. 3c.

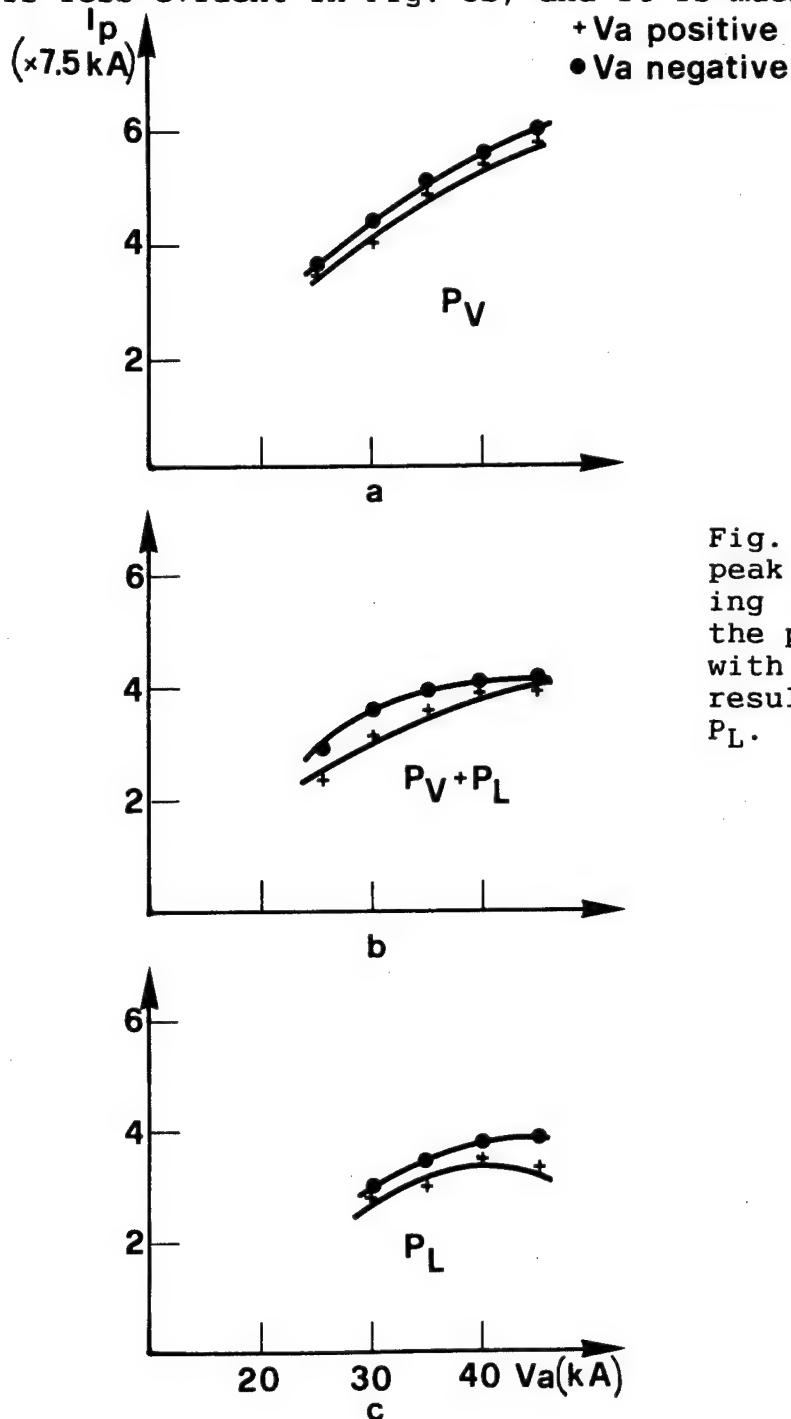


Fig. 4. Discharging current peak as a function of the charging voltage  $V_a$ . a) results with the preionizator  $P_V$ ; b) results with the preionizator  $P_V + P_L$ ; c) results with the preionizator  $P_L$ .

In all three cases, a lower output energy, of about 10%, was achieved when the positive polarity of the charging voltage was applied.

In order to understand these behaviours the laser discharging current was recorded in the same experimental conditions of the Fig.3. The peak current intensity behaviour, as a function of the charging voltage ( Fig 4 ), was enough similar to that of the laser output energy. This last behaviour can be explained if one thinks that the discharge current manages the pump energy, while the higher output energy obtained with the preionizator  $P_V$  could be due to the use of the perforated electrode. The variation of the output energy obtained changing the power supply polarity can be only due to the different form of the electrodes which allow to get variation of the discharging current as the power supply polarity changes. From experimental set up, it can be seen that the preionizator  $P_L$  preionizes uniformly the gas laser, because it is fixed laterally to the discharge region, but it decreases the laser efficiency with regard to the preionizator  $P_V$ . This behaviour can be ascribed to the formation of high space-charge fields when the preionizator  $P_L$  was used which can cause the discharge current to be filamentary. In fact, when the preionizators  $P_V$  and  $P_L$  worked together a higher preionization electron density was certainly provided but the discharge current and the output energy did not increase.

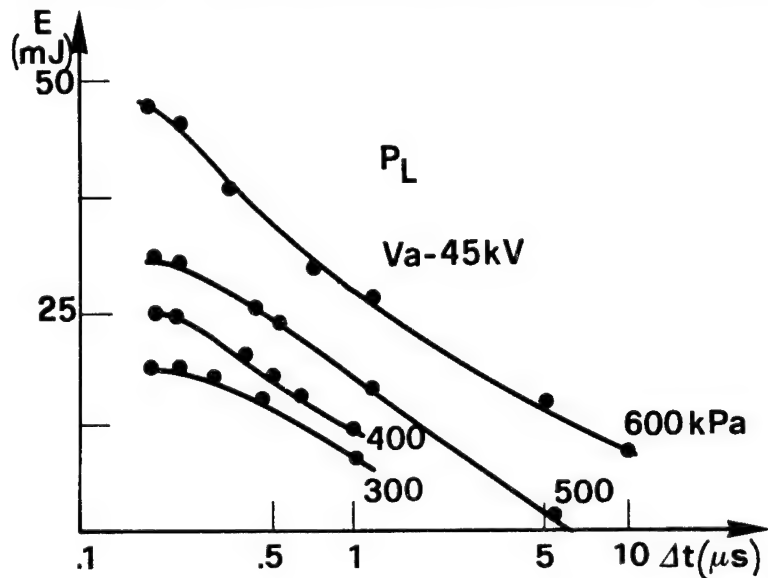
Then, the use of perforated electrodes increases the output energy with regard to use of flat electrodes [4], even if in these laser systems only small gas regions are preionized. Indeed, Fig. 5 shows the output energy as a function of the delay time at -45 kV of charging voltage. For these measurements, the laser chamber was filled up to 600 kPa of total pressure. In Fig. 5a only the preionizator  $P_L$  was energized while in Fig. 5b only the preionizator  $P_V$  was energized. The highest output energy was obtained when only the preionizator  $P_V$  was energized and a delay time between the preionization and the main discharge of about 300 nsec was applied. At lower total pressure values the highest output energy was obtained at lower delay time values ( see Fig. 5b ). When the preionizator  $P_L$  was energized the output energy was lower and it decreased as the delay time increased. The reason of the energy and discharging current increasing can be explained by the diffusion velocity of the photo-preionized electrons. Then, if one neglects the dissociative electron attachment process with regard to the rise time of the voltage of this experiment which is about 140 nsec, these last experimental results can be due to the photo-preionized electron diffusion owing to the electron gradient formed by the perforated electrode. In this experiment the brass net, which forms the perforated electrode, is made up by a wire of 0.015 cm in diameter. The expression of the diffusion current density, is;

$$J_D = D q \frac{d n_{eo}}{d x} \quad (3)$$

where  $D$  is the diffusion coefficient,  $q$  is the electron charge and  $dn_{eo}/dx$  is the electron density gradient. The initial diffusion current density is:

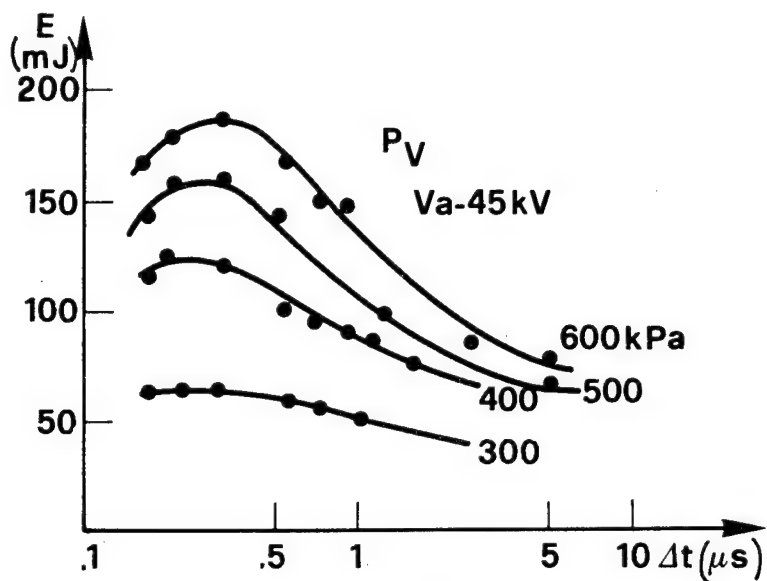
$$J = q v_D n_{eo} \quad (4)$$

where  $v_D$  is the electron diffusion velocity.



a

Fig. 5. Output energy as a function of the delay time between the preionizator and the main discharge at 300, 400, 500, and 600 kPa of total pressure. a) results with the preionizator  $P_L$  and  $V_a = -45kV$ ; b) results with the preionizator  $P_V$  and  $V_a = -45kV$ .



b

Putting the Eq. (3) equal to Eq. (4), it is possible to know the electron velocity within the laser discharge gap.

For Ne as buffer gas, the diffusion coefficient is  $D = 7 \times 10^{22}/N$

$\text{cm}^{-1}\text{s}^{-1}$ , where  $N$  is the molecular density[14]. In the present experiment the thickness of the electron empty regions is less than 0.015 cm. Therefore, utilizing the Eqs. (4) and (5) the electrons reach the centre of the empty regions ( 0.0075 cm ) after a time listed in Table 1.

Table 1: Time spent by electrons to reach the centre of the empty region.

260 nsec at	600 kPa of total pressure,	
210 "	500 "	
170 "	400 "	
130 "	300 "	

These values confirm the experimental results reported in Fig. 5b. When the preionizator  $P_L$  was energized, the discharge gap was uniformly preionized and the electron diffusion velocity was practically negligible.

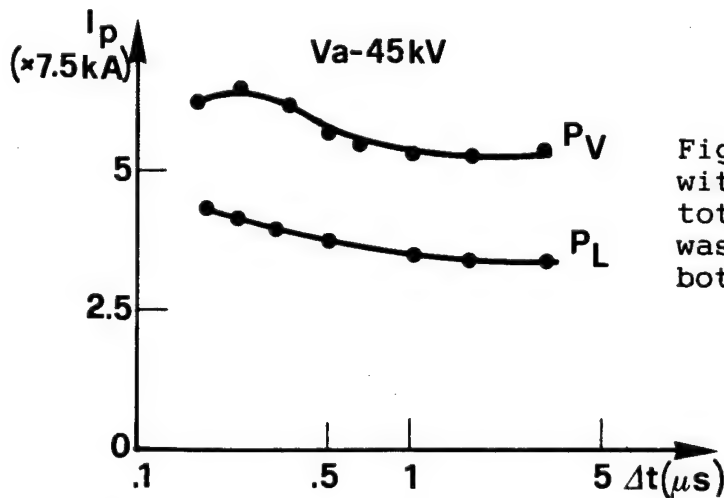


Fig. 6. Discharging current peak with  $V_a = -45\text{kV}$  and 600 kPa of total pressure. In the upper trace was energized  $P_V$ , while in the bottom trace was energized  $P_L$ .

Fig. 6 shows the discharge current peak as a function of the delay time between preionization and the main discharge at 600 kPa of total pressure and at -45 kV of charging voltage. The upper trace shows the results with the preionizator  $P_V$  energized, while the bottom trace shows the results with the preionizator  $P_L$  energized. By comparing the experimental results reported in the Figs. 5 and 6 at the same experimental conditions, it can be noted that when the discharging current increases, versus the delay time, also the output laser energy increases. While, when the preionizator  $P_L$  was energized the current peak did not increase, like the output energy.

For He based mixture, the total used pressure was 400 kPa owing to the instabilities present into the discharge region. Fig. 7 shows the output energy as a function of the delay time between the preionization and the main discharge at -45 kV (a) and 45 kV (b) and with preionizator  $P_V$  or  $P_L$  energized. Comparing these results with

those obtained from Ne based mixture, at the same experimental conditions, one observes that the output energy value was smaller. This result can be due to the formation of instabilities in He based

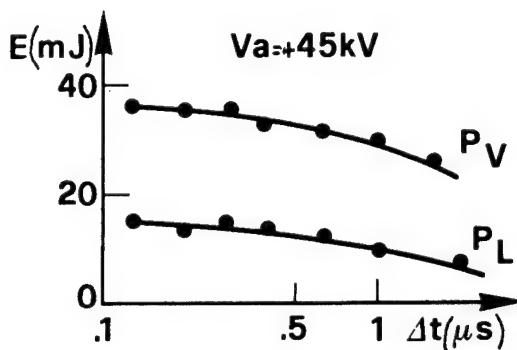
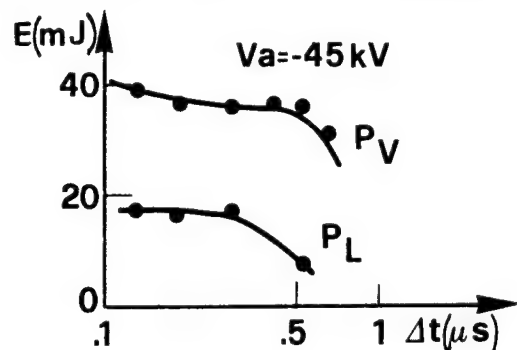


Fig. 7. Output energy as a function of the delay time between the preionization and the main discharge at a total pressure of 400 kPa having He as buffer gas. a) results with  $V_a = -45$  kV. b) results with  $V_a = 45$  kV.

mixture. When the preionization  $P_V$  was used the output energy was 50% higher than the preionization  $P_L$  and no-increasing of the output energy was observed as the delay time increased. This behaviour can be due to lower photo-preionized electron diffusion coefficient for He as buffer gas at the total pressure of 400 kPa. In fact, from Ref. [14] the diffusion coefficient is  $D = 7.4 \times 10^{21}/N \text{ cm}^2\text{sec}^{-1}$ . This value is one order of magnitude smaller than for Ne, therefore it would be necessary a delay time higher than  $2 \times 10^{-6} \text{ sec}$  in order to observe an increasing of the energy. However, being this delay time comparable to the preionization electrons  $1/e$  decay time in this laser mixture, the output energy increasing can not be too much evident in Fig. 7b.

As a conclusion, the experimental studies of a XeCl laser with preionization perpendicular and parallel to the electrode surfaces have been presented. The electrode structures, the power supply polarity and the diffusion current are important to get efficient excimer lasers.

#### 4. ACKNOWLEDGMENT

I wish to acknowledge Prof A. Luches, Prof A. Perrone and Dr S. De Benedittis for very stimulating discussions.

## 5. REFERENCES

- 1) T. A. Znotins, " Excimer Laser in Microlithography," Laser & Optonics, pp. 55-61 May (1988)
- 2) G. Majni, P. Mengucci, E. D'Anna, G. Leggieri, A. Luches and V. Nassisi: Appl. Phys., " Silicon Carbide Synthesis with Energy Pulses " vol. A 49 181 (1989)
- 3) J. W. Chen, V. Nassisi and M. R. Perrone, " XeCl Laser with a Phase-Conjugate SBS Cavity," Opt. Comm. 5 381 (1990)
- 4) Midorikawa, M. Obara and T. Tujioka, " X-Ray preionization of Rare Gas Halide Lasers," IEEE J. Quantum Electron. QE-20 198 (1984)
- 5) R.C. Sze and T. R. Loree, " Experimental Studies of a KrF and ArF Discharge Laser," : IEEE J. Quantum Electron. QE 14, 944 (1978)
- 6) H. Shields, A. J. Alcock and R.S. Taylor, " Preionization Kinetics of an X Ray Preionized XeCl Gas Discharge Laser," Appl. Phys. B 31, 27 (1983)
- 7) M. Steyer and H. Voyer, " Parametric Study of X Ray Preionized High Pressure Rare Gas Halide Lasers," Appl. Phys. B 42, 155 (1987)
- 8) A. Luches, V. Nassisi and M.R. Perrone, " Output Characteristics of a Excimer Laser with Delayed Double Preionization," J. Phys. E: Sci. Instrum. 20, 1015 (1987)
- 9) J. I. Levatter and S. C. Lin, " Necessary Condition for the Homogeneous Formation of Pulsed Avalanche Discharges at High Gas Pressures," J. Appl. Phys. 51, 210 (1980)
- 10) W. L. Nighan R. T. Brown, " Efficient XeCl Formation in an Electron Beam Assisted Xe/HCl Laser Discharge," Appl. Phys. Lett. 36 498 (1980)
- 11) V. Yu. Baranov, V. M. Borisov, D. N. Molchanov, V. P. Novikov and O. B. Khristoforov, " Wide Aperture Electric Discharge XeCl Laser with Ultraviolet Preionization and 20 J Output Energy," Sov. J. Quantum Electron. 17, 978 (1987)
- 12) R. S. Taylor, P.B. Corkum, S. Watanable, K. S. Leopold and A. Alcock, " : IEEE J. Quantum Electronic QE-10 416 (1983)
- 13) A. Luches, V. Nassisi and M. R. Perrone, " Linear Coil for Measuring Fast Distributed Pulsed Current, " J. Phys. E: Sci. Instrum. 21 178 (1988)
- 14) D. R. Nelson and F. J. Davis, " Determination of Diffusion Coefficients of Thermal Electrons with a Time-of-Flight Swarm Experiment" J. Chem. Phys. 51 2322 (1969)



## Excitation of an Excimer Laser with Microwave Resonator

36980005 The Hague EXCIMER LASERS AND THEIR APPLICATIONS in English 1991 pp 134-139

[Article by Lucia Hunermann and Rudolf Meyer of the Fraunhofer-Institut für Lasertechnik, Franz Richter of Karl Suss GmbH & Co. KG, and Alexander Schnase of KFA Jülich]

[Text]

### ABSTRACT

In this work excimer laser excitation with resonant microwave structures was obtained both for  $\text{XeCl}^*$  and  $\text{KrF}^*$ . The discharge tube containing the laser gas is placed inside one or several coupled microwave resonators. Depending on the microwave structure laser pulse energies up to the mJ-range were achieved with  $\text{XeCl}^*$ .

### 1. INTRODUCTION

Discharge-pumped rare-gas halide excimer lasers became a powerful tool in a wide range of applications during the last years. Yet there remain several unsolved problems with discharge-pumped excimer lasers. Impurities introduced, e. g. from electrodes, limit the lifetime of laser gas and electrodes. Electrodes in contact with the gas are unnecessary with microwave excitation, neither electrode instabilities nor their surface degradation influence the laser plasma. Rare gas halide excimer lasers excited by high power radio frequency and microwave have been reported by Young, Wisoff et al.<sup>1,2,3</sup>, Christensen et al.<sup>4,5</sup>, Slinko et al.<sup>6,7</sup> and Klingenberg et al.<sup>8</sup>. The main advantages of microwave excitation have been shown, very efficient deposition of microwave energy in the discharge region, pulse repetition rates in the kilohertz range and efficiencies up to the 5 % region.

In these publications laser excitation was reported for structures with microwaves propagating parallel to the discharge tube. In this work, we present excimer laser excitation with resonant microwave cavities. With these coupling structures laser pulse energies of 2 mJ for  $\text{XeCl}^*$  and 300  $\mu\text{J}$  for  $\text{KrF}^*$  have been obtained. This latter result has not been optimized yet, hence laser

pulse energies in the mJ-range may be expected for  $\text{KrF}^+$  as well. These comparably high pulse energies result from use of carefully dimensioned discharge and microwave coupling geometries.

## 2. EXPERIMENTAL SETUP

An EEV M5167 Magnetron provides 2.5 MW,  $3.5 \mu\text{s}$  long pulses at 3 GHz. The pulses have a rise time of about 80 ns and travel through WR-284 waveguide pressurized with  $\text{SF}_6$  to the coupling structure, which is scetched in Fig. 1. Although the magnetron is capable of kHz operation, the electrical power supply limits operation to 50 Hz.

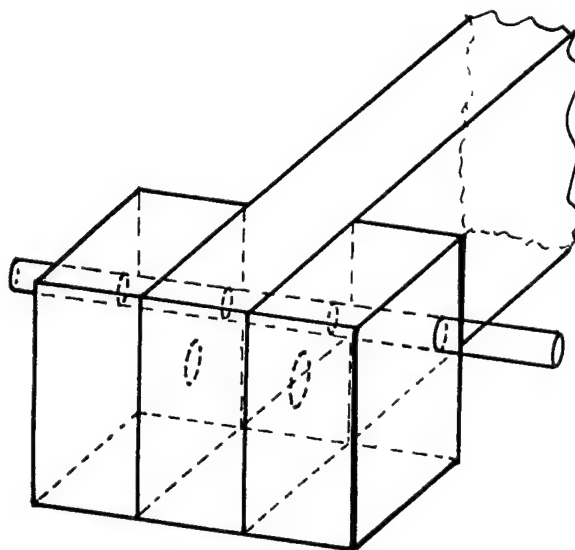


**Figure 1:**

Microwave coupling structure consisting of two  $H_{101}$  resonant cavities coupled to the primary waveguide by two circular holes. The position of the discharge tube is indicated by a circular rod.

The microwave coupling structure consists of two  $H_{101}$  fundamental mode microwave resonators soldered to the primary WR-284 waveguide. The resonance frequency of the microwave resonators may be altered by variable short circuits to compensate the frequency shifts due to different  $\text{SF}_6$  pressures. Microwave coupling is provided by two circular holes of 10 mm in diameter and by the holes sustaining the discharge tube (fused silica). The concentric 3 mm i. d. discharge tube holding the laser gas mixture is oriented parallel to the electrical field inside the waveguide and the resonator cavities. This parallel orientation provides a homogeneous field distribution over the complete length of the laser gas volume, no standing-wave variations in the electrical field strength can occur, as reported elsewhere<sup>9</sup>. The active length is about 13 cm; no preionization is provided. Due to the low pulse repetition frequency no gas recirculation is necessary, the laser is operated with a "sealed off" gas volume.

### 3. EXPERIMENTAL RESULTS

Without preionization a good pulse-to-pulse stability was obtained, changes in laser output energy were below 3 %. Even after three hours of operation at 15 Hz repetition rate no change in pulse energy could be detected. Oscilloscope traces of the incident and reflected microwave power as well as the fluorescence signal and the laser pulse are shown in Fig. 2. Maximum laser output was obtained with a He:Xe:HCl = 1000:10:1 gas mixture in a pressure range between 2 and 4.5 bar. The observed temporal behaviour of microwave energy and laser pulse differs significantly from signals reported from experiments with non-resonant microwave excitation of excimer lasers. Here, neither fluorescence nor laser pulse signals are observed during the first 150 ns of the microwave pulse, the laser plasma is not ignited. This behaviour is due to the characteristic properties of the resonator cavity. For a frequency-matched layout of the resonator dimensions the microwave energy is stored inside the resonator. The amount of energy depends on the coupling hole dimensions and the electrical conductivity of the wall material.

From the beginning of the microwave pulse the energy accumulates in the resonator, the electrical field inside increases. Depending on size and geometry of the resonator some hundred mJ of microwave energy are stored inside the resonator. The amount of energy stored can be determined from the area enclosed between the curves of the incident and the reflected microwave power in Fig. 2. When the breakdown voltage across the laser gas is reached, the plasma ignites, the fluorescence signal begins to increase. Simultaneously a strong peak occurs in the signal of the reflected microwave, which indicates a sudden mismatch of the cavity's resonance frequency, due to the presence of the emerging plasma. The stored energy couples into the plasma. Power densities much higher than provided by the magnetron can be obtained. A few nanoseconds later the onset of the laser pulse is observed.

As can be seen in Fig. 1, the discharge tube is not placed in the center of the resonator cavities, where the maximum of the electrical field is reached. By appropriate placement of the discharge tube in regions of lower field strength more microwave energy accumulates inside the resonator cavities before the plasma ignites. For this structure maximum laser pulse energies of 500  $\mu$ J for XeCl\* and 300  $\mu$ J for KrF\* were obtained for a position with 37 % of the maximum field strength. Positioning the discharge tube at places with even lower field strength leads to arcing inside the resonant cavities and hence reduced laser pulse energies.

For the KrF\* laser the optimized laser gas composition was He:Kr:F<sub>2</sub> = 1000:100:10 with a laser gas pressure of 4 bar, the laser pulse width did not exceed 5 ns. Except for the laser pulse duration the signals of the KrF\* laser showed no significant difference to the XeCl\* laser.

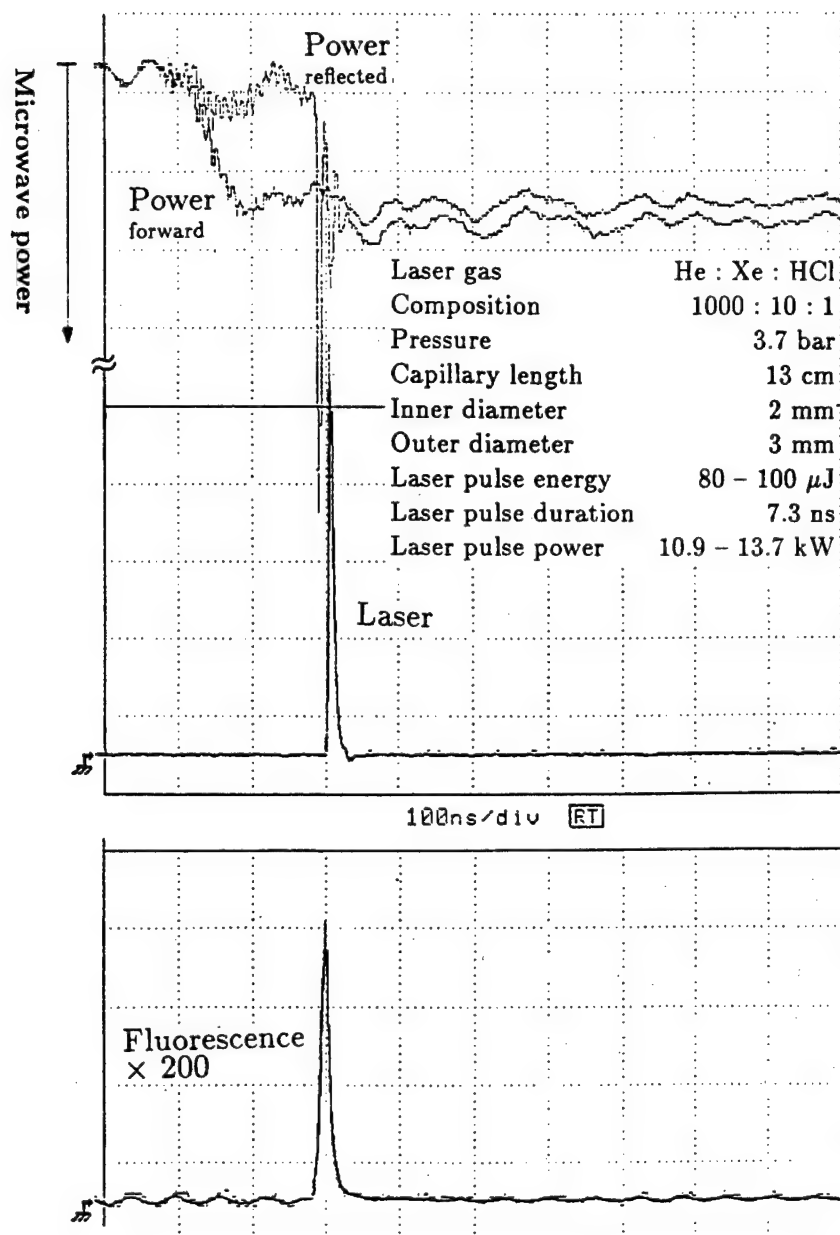
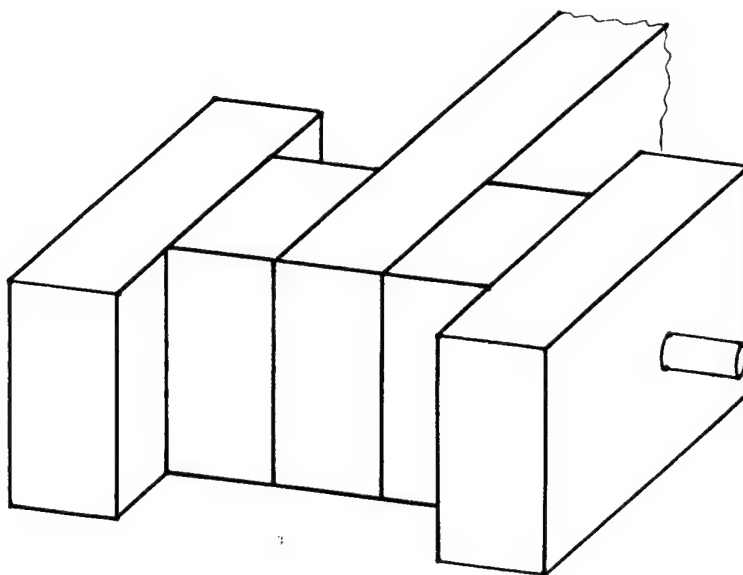


**Figure 2:**  
Oscilloscope traces of microwave power transmitted to the microwave resonator coupling structure, reflected microwave power, laser pulse and fluorescence signal for XeCl\*-laser

**Figure 3:**

Improved microwave coupling structure consisting of two  $H_{102}$  and two  $H_{101}$  resonant cavities coupled to the primary waveguide.



In order to increase the amount of storable energy, two more resonator cavities were added as depicted in Fig. 4. The active length is about 17 cm. The microwave mode of these additional cavities is not the fundamental  $H_{101}$  mode resonators, but the  $H_{102}$  mode. Hence the volume for microwave energy storage was increased by a factor of 3. With this enlarged coupling structure the  $\text{XeCl}^*$  laser pulse energy reached up to 2 mJ, which corresponds to an increase by a factor of 4. This is due to the longer active length on the one hand, and to an improvement of energy storage on the other hand. Fig. 5 gives the oscilloscope traces for a typical 2 mJ pulse. As can be seen, the area between the transmitted and reflected microwave power, which corresponds to the amount of microwave energy stored, is increased in comparison to Fig. 2. Furthermore, the peak in the reflected microwave intensity, which stems from the plasma ignition is somewhat reduced. The coupling efficiency is increased due to the improved ratio of discharge tube length inside the primary waveguide to the length inside the resonators.

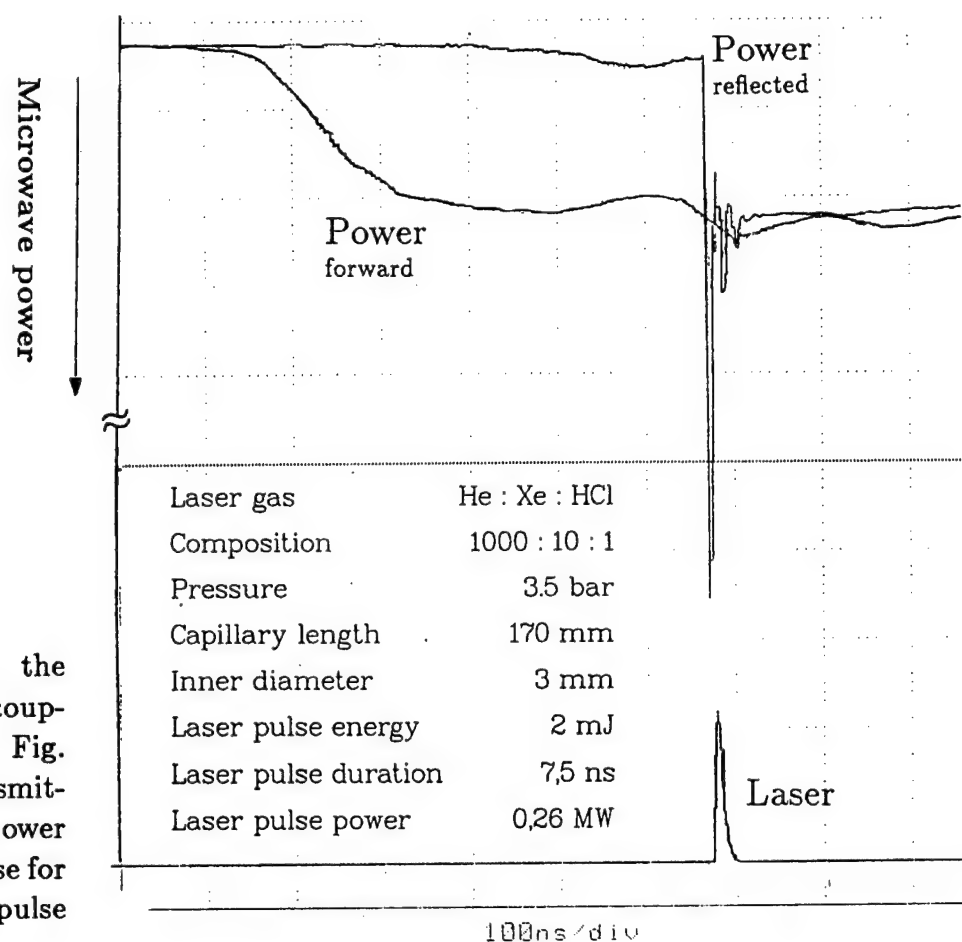


**Figure 4:**

Oscilloscope traces for the microwave 4-resonator coupling structure depicted in Fig. 4: microwave power transmitted, reflected microwave power and (attenuated) laser pulse for XeCl\*-laser with 2 mJ pulse energy.

#### 4. CONCLUSIONS

It was shown that with resonant microwave coupling structures, high excimer laser pulse energies can be reached due to microwave energy storage inside the resonant microwave structure. No preionization is necessary. These resonant microwave structures can easily be scaled to higher laser pulse energies by adding further resonators.

#### 5. REFERENCES

1. A. J. Mendelsohn, R. Normandin, S. E. Harris, and J. F. Young, "A microwave-pumped XeCl\* laser", *Appl. Phys. Lett.* **38**, 603 - 605 (1981)
2. J. F. Young, S. E. Harris, P. J. K. Wisoff and A. J. Mendelsohn, "Microwave excitation of excimer lasers", *Laser Focus* **4**, 63 - 67 (1982)

3. P. J. K. Wisoff, A. J. Mendelsohn, S. E. Harris and J. F. Young, "Improved performance of the microwave-pumped XeCl laser", *IEEE J. Quant. Electron.* **QE-18**, 1839 - 1840 (1982)
4. C. P. Christensen and R. W. Waynant, "200-MHz electrodeless discharge excitation of an XeF laser", *Appl. Phys. Lett.* **41**, 794 - 796 (1982)
5. C. P. Christensen, R. W. Waynant and B. J. Feldman, "High efficiency microwave discharge XeCl laser", *Appl. Phys. Lett.* **46**, 321 - 323 (1985)
6. V. N. Slinko, A. S. Sulakshin and S. S. Sulakshin, "Efficient stimulated emission from a microwave-pumped XeCl laser", *Sov. J. Quantum Electron.* **18**, 186 - 187 (1988)
7. V. A. Vaulin, V. N. Slinko, and S. S. Sulakshin, "Krypton fluoride laser excited by high-power nanosecond microwave radiation", *Sov. J. Quantum Electron.* **18**, 1459 - 1461 (1988)
8. H. H. Klingenberg, F. Gekat and G. Spindler, "L-band microwave pumped XeCl laser without preionization", *Appl. Opt.* **29**, 1246 - 1248 (1990)
9. L. Hünemann, R. Meyer, A. Schnase, R. Wagner and F. Richter, "Microwave excited excimer laser", *IEEE-LEOS Optcon 1990, Boston*, (4th - 9th nov. 1990)

## Excimer Laser Performance Under Various Microwave Excitation Conditions

36980005 The Hague EXCIMER LASERS AND THEIR APPLICATIONS in English 1991 pp 140-145

[Article by H.H. Klingenberg and F. Gekat of DLR-Institut für Technische Physik]

[Text]

### ABSTRACT

Microwave pumped rare-gas halide mixtures feature excimer laser emission without preionization. The performance of a XeCl excimer laser is investigated with an optimized waveguide coupling geometry. Parameters were varied such as the microwave power, duration of the microwave pulse, and the rise time of the microwave pulse from 25 ns to 220 ns. The pulsed microwave L-band transmitter had a power of up to 10 MW, an adjustable pulse duration (500 ns to 6000 ns), and a pulse repetition frequency up to 400 Hz. The coupling geometry consisted of a double ridge waveguide. The discharge tube was a quartz capillary placed between the ridges. Two tubes were used. One had an outer and inner diameter of 10.3 mm and 2.6 mm, the other 8 mm and 5.8 mm, respectively. The total active length was 438 mm. A study of a microwave power of 2.5 MW deposited into the discharge yielded at low repetition frequencies a non-homogeneous deposition. With a new resonant coupling geometry a XeCl laser energy of up to 1.8 mJ in a 16 ns long pulse was achieved.

### 1. INTRODUCTION

The microwave technique for exciting a multi-gas mixture at various gas pressure levels is an alternative means for pumping laser transitions.<sup>1-5</sup> Compared with the discharge-pumped laser excitation techniques microwaves couple into the electrodeless discharge region through displacement currents. Excimer laser gas mixtures consist of rare gases and a halide at a high total pressure. The latter constituent, i.e. the halide, is responsible for streamer formation in a TEA discharge pumped excimer laser. This problem can be partially circumvented by choosing electrodeless, therefore metal-free discharge techniques, the microwave excitation.



In this paper the authors investigated a XeCl excimer laser. The performance of the laser was studied in a microwave coupling geometry, consisting of a quartz capillary placed along the center axis of a rectangular L-band waveguide. Two microwave sources, a magnetron generator and a klystron transmitter, were used alternatively for exciting the high pressure discharge. In conjunction with the coupling structure two different kinds of operation were observed. One is called "Matched Coupling Structure" MCS-Mode. The experimental findings are described in reference 6. The other operating mode is called "Resonant Energy Storage" RES-Mode and features results for a microwave excited XeCl excimer laser resulting in a higher pulse energy of the laser. The first result was a pulse energy of 1.3 mJ for a XeCl laser and a pulse duration of 16 ns.<sup>7</sup> All results were obtained without any technique of preionization.

## 2. SYSTEM DESIGN

A pulsed L-band magnetron generator with a peak power of 3.6 MW, a fixed pulse duration of 4  $\mu$ s, and a pulse repetition frequency of 10 Hz was used. The second source was a klystron transmitter with a maximum peak power rating of 10 MW, a variable pulse duration of 500 ns to 6000 ns, and a pulse repetition frequency of up to 400 Hz. Both sources were used alternatively to feed a microwave assembly similar to the one outlined in reference 8. The performance of the XeCl laser was investigated in a gas mixture of roughly He/Xe/HCl = 1000/10/1 at a total pressure of up to 2 bar. The complete layout of the coupling geometry was determined by a computer program URMEL-T<sup>9</sup> based on a two-dimensional finite difference method for the discretization of Maxwell's equations. By this method the electric and magnetic field was calculated within a double ridge rectangular waveguide.<sup>8</sup> The technique of measuring the microwave powers as well as the laser pulse energy was described earlier.<sup>6</sup> The discharge tubes had inner diameters of 2.6 mm and 5.8 mm. The outer diameters were 10.3 mm and 8 mm, respectively. The total active length was approximately 438 mm. The laser cavity consisted of a high reflector and an output coupler of a transmission of 10 to 50 %. All mirror substrates had radii of curvatures of 2 m.

## 3. RESULTS AND DISCUSSION

The magnetron generator was operated at the maximum power rating of 3.6 MW. the measured typical XeCl laser pulse energy was 15  $\mu$ J and a pulse duration of 65 ns.<sup>8</sup> For the laser threshold a specific microwave power of 740 kW/cm<sup>3</sup> was found. The laser intensity is plotted against the incident microwave power in Fig. 1. The very obvious jitter shown in the laser output energy may result from the lack of any preionization technique. A non-homogeneous microwave power deposition into the discharge region could also be the reason for the measured jitter of the laser power. An investigation of the deposition of a 2.5 MW microwave pulse (10 Hz repetition rate) applied to the coupling

structure with the capillary of 2.6 mm inner diameter was performed using a framing camera. During the development period of two microseconds of the incoming pulse simultaneously pictures were taken 100 ns apart showing a non-homogeneous power deposition. A typical incoming magnetron pulse versus time is depicted in Fig. 2, curve 1. The curves 2 and 3 indicate the time dependence of the reflected microwave power and the XeCl laser pulse. The time delay between the beginning of the deposition of the microwave power into the discharge tube and the occurrence of the laser pulse may have a plasma kinetic origin. Measurements of the XeCl laser pulse energy when the HCl content of the discharge was varied together with the study of the build-up of a second atomic xenon laser transition support the idea of an additional pumping process of the xenon 5d manifold prior to the formation of the excimer molecules.<sup>10</sup> It was for this reason that a faster rising microwave pulse was believed to influence the kinetics. The first data obtained with the klystron transmitter describing the temporal behavior

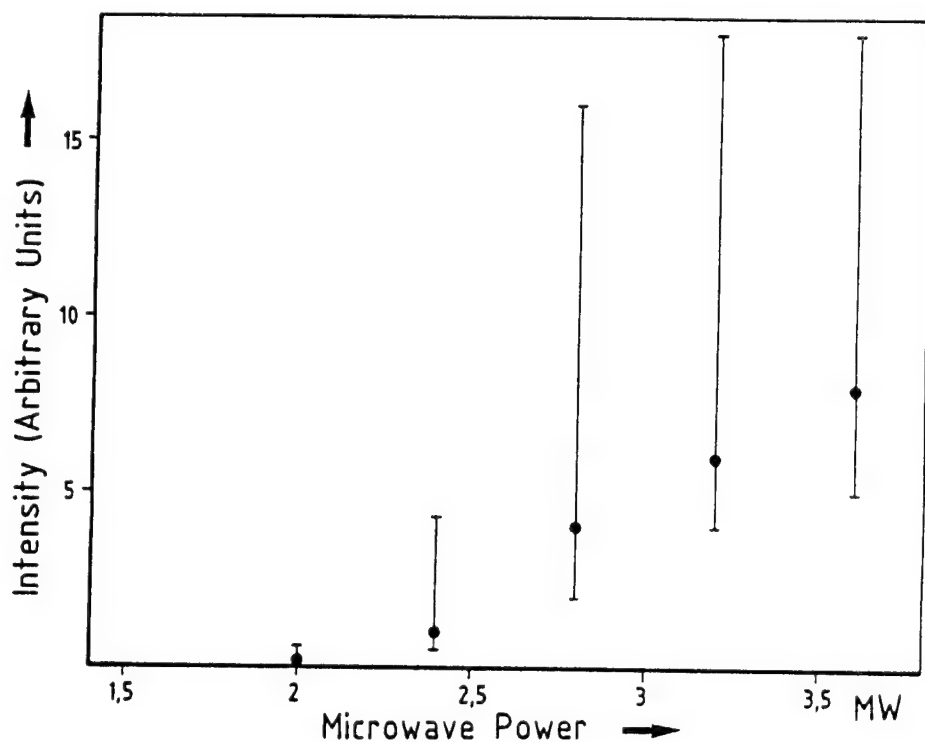


Fig. 1. Laser intensity versus microwave power applied to the system.

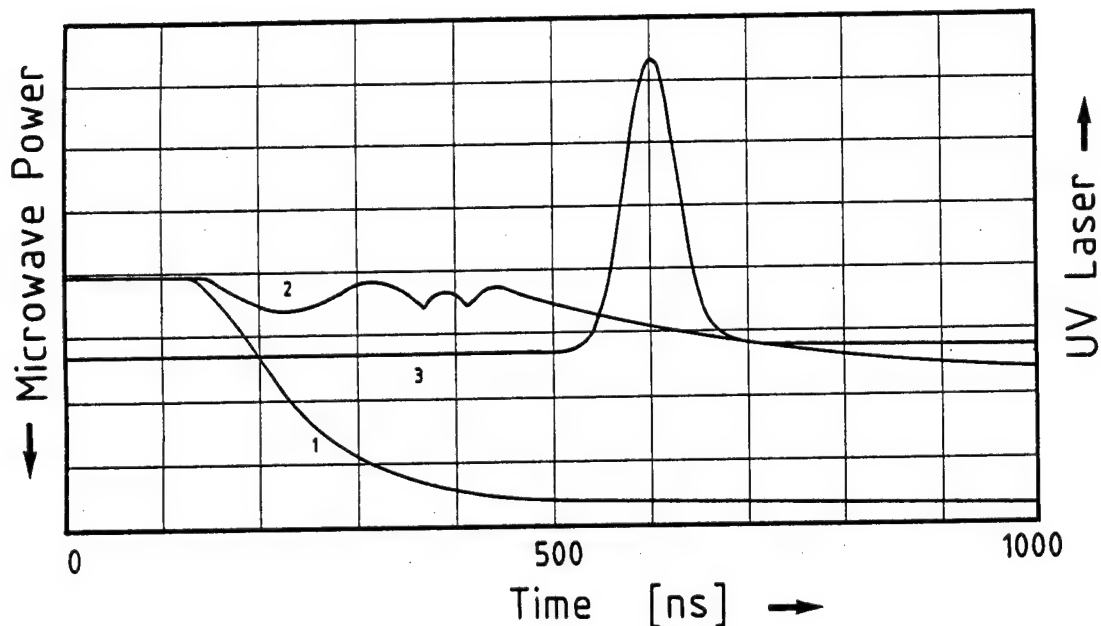


Fig. 2. Incident and reflected microwave power (curves 1 and 2), XeCl excimer laser pulse (curve 3) versus time.

of the laser are shown in Fig. 3. Here is plotted the incoming microwave (curve 1), the reflected microwave power (curve 2), and the laser intensity (curve 3) versus time. The faster rising klystron pulse compared to the slower rising magnetron pulse (see Fig. 2, curve 1) did not change the temporal evolution of the laser pulse (see Fig. 3, curve 3). The rise time of the klystron pulse was 25 ns and for the magnetron pulse 220 ns.

Although the microwave power deposition into the discharge tube was also faster, there was no indication of an instantaneous build-up of the XeCl laser as soon as the microwave power had been deposited in the discharge. Responsible for the delayed temporal development of the UV laser pulse seems to be the initial pumping of a xenon-I laser transition. The threshold for the xenon laser required a specific microwave pump power of  $25 \text{ kW/cm}^3$ .

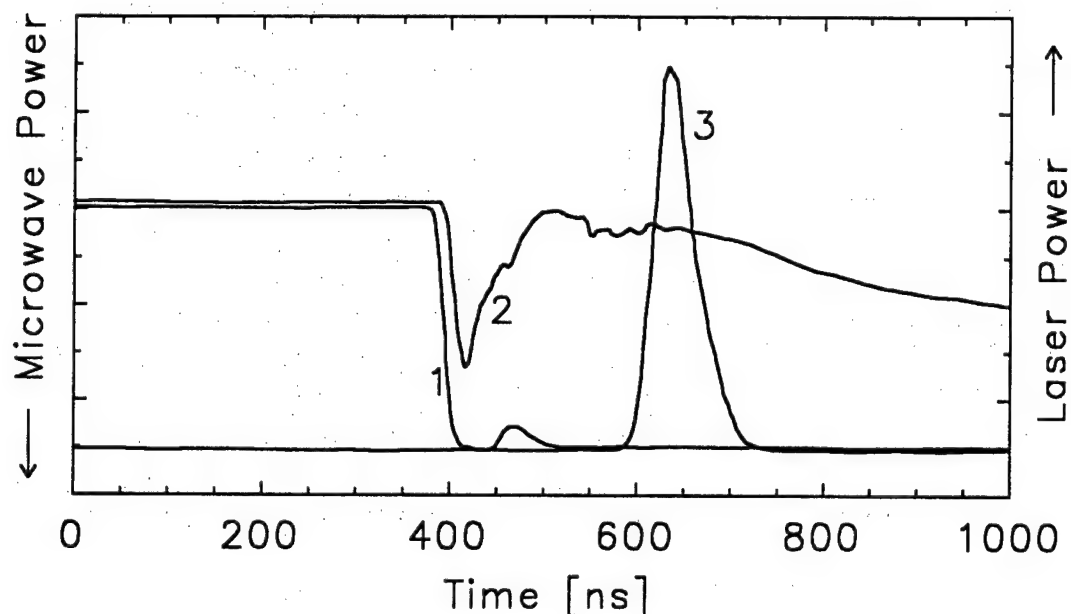


Fig. 3. Microwave power of the klystron transmitted (curve 1), reflected (curve 2), and the excimer laser pulse (curve 3) against time.

For the used coupling geometry resulting in the described experiments the impedance of the ignited discharge had to be carefully adjusted for optimum performance of the excimer laser. Both generators yielded a similar curve for the reflected microwave power as shown in figures 2 and 3 for the excimer laser to build up. This type of operation is called "Matched Coupling Structure" MCS-Mode and led to a XeCl laser of a pulse energy of approximately 20  $\mu\text{J}$  and a pulse duration of 65 ns. The data were obtained with a laser cavity consisting of a high reflector and a 10 % output coupler. Both mirrors had 2 m radius of curvature.

In order to improve the performance of the XeCl laser a new coupling structure with better electrical contacts of the double ridges to the waveguide walls was designed. Furthermore, a laser tube of 5.8 mm inner and 8 mm outer diameter was installed. The overall length of the ridges was kept at a length of 43.8 cm which was also the microwave pumped discharge length. When a klystron transmitter pulse of a power of 4.5 MW with a pulse duration of 600 ns and a repetition frequency of 10 Hz was applied to a gas mixture of  $\text{He/Xe/HCl} = 1000/10/2$  at a total pressure of 2 bar, a XeCl laser energy of up to 1.8 mJ was measured. The pulse duration was 16 ns.<sup>10</sup> The chosen output coupler of the laser cavity had 50 %.

The investigation of the reflected microwave power from this longitudinal coupling geometry exhibited features of a resonant microwave cavity phenomenon described earlier by Alvarez et al.<sup>11</sup> After charging the cavity within approximately 400 ns there occurred a sudden jump in the reflected microwave power curve which resulted in a fast extraction of the stored energy. The change in the reflected power curve is accomplished by building up a plasma of high electron density, i.e. the rare-gas halide discharge. The discharge acts as a switch. Fig. 4 depicts the amount of stored energy in the resonant microwave cavity and the resulting XeCl laser performance.

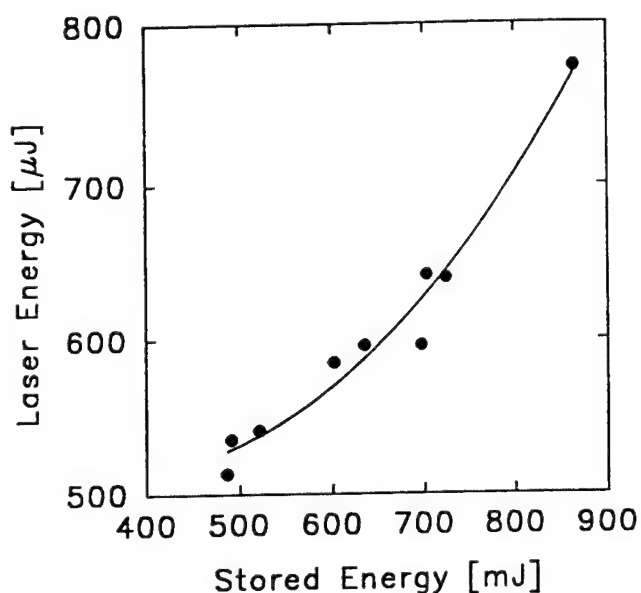


Fig. 4. XeCl laser energy versus stored energy in a resonant microwave cavity.

The resonant cavity consisted of the coupling aperture of the impedance matcher up to the short circuit plate of the coupling structure.<sup>7</sup> The complete different features of the reflected microwave power curves compared to the ones shown in figures 2 and 3 can be described as a "Resonant Energy Storage" RES-Mode of operation.

#### 4. CONCLUSION

A XeCl excimer gas mixture has been investigated using microwave L-band pumping techniques. A magnetron and a klystron were used as microwave sources to pump a longitudinal coupling geometry. Two modes of operation were observed: a matched coupling structure mode (MCS-mode) and a resonant energy storage mode (RES-mode). The best results were achieved with the RES-mode. A XeCl laser pulse energy of up to 1.8 mJ in a pulse duration of 16 ns could be realized for the first time. The discharge volume was almost 12 cm<sup>3</sup>.

#### 5. ACKNOWLEDGEMENT

The authors would like to thank the German Air Force for leaving the L-band klystron transmitter for our research. For the expert technical assistance we would like to thank G. Krutina.

#### 6. REFERENCES

1. P.J.K. Wisoff, A.J. Mendelsohn, S.E. Harris, and J.F. Young, "Improved Performance of the Microwave-pumped XeCl Laser," IEEE J. Quantum Electron. vol. QE-18, 1839-1840, Nov. 1982.
2. A.N. Didenko, V.M. Petrov, V.N. Slin'ko, A.S. Sulakshin, and S.S. Sulakshin, "Excimer Laser Pumped by an Intense Relativistic Microwave Source," Sov. Techn. Phys. Lett., vol. 12, pp. 515-517, Oct. 1986.
3. C.P. Christensen, C. Gordon III, C. Moutoulas, and B.J. Feldmann, "High-Repetition-Rate XeCl Waveguide Laser without Gas Flow," Opt. Lett., vol. 12, pp. 169-171, March 1987.
4. C.L. Gordon III, B. Feldmann, and C.P. Christensen, "Microwave-discharge Excitation of an ArXe Laser", Opt. Lett., vol. 13, pp. 114-116, Febr. 1988.
5. Z. Imankulov, M.M. Mirinoyatov, and I.A. Solovev, "Characteristics of Single-Frequency He-Ne and He-Xe Lasers with Microwave Excitation," Opt. Spectrosc. (USSR), vol. 62, pp. 794-797, June 1987.
6. H.H. Klingenberg, F. Gekat, and G. Spindler, "L-band Microwave Pumped XeCl Laser without Preionization," Appl. Optics, vol. 29, pp. 1246-1248, March 1990.
7. H.H. Klingenberg and F. Gekat, "A 1.3 mJ XeCl Laser Pumped by Microwaves," Appl. Phys. Lett., 1991, to be published.
8. H.H. Klingenberg, F. Gekat, and G. Spindler, "Microwave Excitation of a XeCl Laser without Preionization," Proceeding SPIE, vol. 1278, pp. 43-50, March 1990.
9. T. Weiland, "On the Numerical Solution of Maxwell's Equations and Applications in the Field of Accelerator Physics," Part. Acc., vol. 15, pp. 245-292, 1984.
10. H.H. Klingenberg and F. Gekat, "Investigation of Microwave-Pumped Excimer and Rare-Gas Laser Transitions," Proceeding SPIE, OE/LASE, Jan. 21-25, 1991, Los Angeles, CA.
11. R.A. Alvarez and D.P. Byrne, "Prepulse Suppression in Microwave Pulse-Compression Cavities," Rev. Sci. Instrum, vol. 57, pp. 2475-2480, Oct. 1986.

Low-Loss Line-Narrowed Excimer Oscillator for Projection Photolithography:  
Experiments and Simulation

36980005 The Hague EXCIMER LASERS AND THEIR APPLICATIONS in English 1991 pp  
146-153

[Article by G.S. Volkov and D.Yu. Zaroslov of the Physics and Technology  
Institute]

[Text]

#### ABSTRACT

The short wavelength and high power of excimer lasers have made them attractive candidates as exposure sources for photolithography. Unfortunately direct application of excimer lasers for microelectronic steppers is restricted by certain negative properties of the excimer laser radiation. This means that for the successful stepper's operation the radiation properties should be optimized. In this work we present the results of the optimization of the excimer laser characteristics for deep UV stepper.

#### 1. INTRODUCTION

The optical reduction stepper lithography methods continue to dominate in VLSI production processes. Excimer lasers (EL) which may be used as light source in projection lithography systems are XeCl (308 nm), KrF (248 nm), KrCl (222 nm) and ArF (193 nm) lasers. In comparison with KrF laser energy efficiencies of ArF, KrCl and XeCl lasers are 0.5, 0.2 and 0.8 correspondingly. According to this reason KrF lasers are mainly used in the new generation of optical steppers.

There are two important problems of EL application in projection photolithography.

First, relatively high level of spatial coherence of EL radiation (its value occupies an intermediate position between the coherence of lamps and other solid state and gas lasers). In our previous works we have delivered a method for the measurements of the EL's radiation correlation functions [1]. The measured correlation function was anisotropic along different direction on the EL beam cross section what was in a good correlation with the anisotropy of the EL radiation divergency. We also considered several methods of EL spatial coherence reduction inside optical tract of the stepper for the case of a single pulse exposure (so called "flash on the fly" regime) [1].

Second, to obtain diffraction limited image quality on the whole chip area the stepper is usually equipped with a very complicated refractive projection lense. However only two deep UV(DUV)-transparent materials are available now for the lenses design in the DUV region. They are fused silica (quartz) and fluoride (it should be noted the last has limited application due to its poor radiative stability). If all DUV projection lense components are made from the fused silica, an adequate narrowing of the bandwidth  $\Delta\lambda_g$  of the EL radiation has to be provided. To estimate the required bandwidth  $\Delta\lambda_g$ , a formula for the thin lens focal length  $F$  may be used

$$F = R/(n-1), \quad (1)$$

where  $R$  - refractive surface radius,  $n$  - refractive index. Usually  $F \sim 1$  cm. The chromatic defocusing length  $\delta F_{chr}$  is equal

$$\delta F_{chr} = (F/(n-1)) (dn/d\lambda) \Delta\lambda_g \quad (2)$$

where  $dn/d\lambda$  - dispersion. To neglect the chromatic aberrations, it should be chosen as  $\delta F_{chr} < \delta F_{diff} \sim 1 \mu m$  ( if we put  $\delta F_{chr} = 0.1 \delta F_{diff}$ , then  $\delta F_{chr} \sim 0.1 \mu m$ ). For fused quartz  $n \sim 1.5$ ,  $dn/d\lambda \sim 10 \text{ nm}^{-1}$  at wavelength  $\lambda = 248 \text{ nm}$ . Thus, the spectral bandwidth of the EL light  $\Delta\lambda_g < 0.005 \text{ nm} = 5 \text{ pm}$ .

The problem of the EL linewidth narrowing can be solved by insertion of dispersive elements and apertures into the laser cavity [2]. The spectral bandwidth  $\Delta\lambda_g$  of the output laser radiation may be estimated in this case according to formula [3]

$$\Delta\lambda_g \sim N^{-1/2} [ (\delta\lambda)^2 + (\Delta\varphi/D)^2 ]^{1/2}, \quad (3)$$

where  $\delta\lambda$  and  $D=d\varphi/d\lambda$  are the spectral resolution limit and the value of angular dispersion for the used dispersive element correspondingly,  $\Delta\varphi$  - the laser beam divergence being determined by intracavity apertures,  $N$  is the number of light halfroundtrips inside resonator during the laser pulse ( $N=5-10$  for standard EL).  $\delta\lambda = \text{const}$  for a given dispersive element. The more the dispersion value and less the laser beam divergence and the the spectral resolution limit the less the spectral bandwidth of laser radiation.

Diffraction grating and prisms can be used in principle as intracavity dispersive elements. But, unfortunately, they possess of low value of angular dispersion. For example, if the grating must provide the linewidth narrowing down to 3-4 pm, then the laser beam divergence has to be diminished by special apertures inserted into the laser cavity. The last always results in the laser output energy decreasing. Ordinarily the energy efficiency of the EL linewidth narrowing by installation of diffraction gratings does not exceed 1-2% [2].

If Fabry-Perot etalon is used as a dispersive intracavity element (Fig.1) then the main problems are connected with its small dispersion range [4]:

$$\Delta\lambda_{et} = \lambda^2 / (2nl\cos\alpha), \quad (4)$$



where  $n$  is the refractive index of etalon intracavity medium,  $l$  is the base distance between etalon mirrors,  $\alpha$  is the angle of light beam incidence on to etalon surfaces.

If we put  $\lambda = 248$  nm;  $n=1$ ,  $\cos\alpha=1$ ,  $l=1$  mm, then  $\Delta\lambda_{et}=30$  pm. The desirable value of dispersion range is equal to the laser amplification spectrum  $\Delta\lambda_{amp}$  ( $\Delta\lambda_{amp} \sim 1000$  pm for KrF laser). In this case the intracavity dispersive elements provide the transformation of the laser generated energy into the wavelength interval  $\Delta\lambda_g < \delta\lambda_{et}$ , where  $\delta\lambda_{et}$  is the spectral resolution limit of the intracavity dispersive element. The latter is proportional to the dispersion range  $\Delta\lambda_{et}$  [4]:

$$\delta\lambda_{et} = (2/\pi f) \Delta\lambda_{et}, \quad (5)$$

where  $f$  is the finesse of the etalon. The etalon's finesse is determined by the reflection index  $r$  of its mirrors [4]:

$$f = 2r^{1/2} / (1-r). \quad (6)$$

The value of spectral bandwidth needed for projection exposure source shouldn't exceed  $\Delta\lambda_g = 5$  pm. Thus we can estimate the required finesse of a single etalon being used for KrF laser linewidth narrowing:

$$N^{-1/2} \delta\lambda_{et} / \Delta\lambda_{et} < \Delta\lambda_g / \Delta\lambda_{amp} \sim 5 \times 10^{-3} \quad (7)$$

or

$$f \gg 40; r \gg 98.7\% \quad (8)$$

Analogous demands on the etalon finesse arise in the case of two etalons being used for excimer laser linewidth narrowing, if one of them possesses of  $\delta\lambda_{et1} \sim \Delta\lambda_g$ , and another -  $\delta\lambda_{et2} \sim \Delta\lambda_{et1}$ .

To have a high energy efficiency in the linewidth narrowing process the etalon's transmission function [4]

$$T(\alpha) = \{1 + f \sin^2(2\pi n l \cos(\alpha)/\lambda)\}^{-1} \quad (9)$$

must be as large as possible. If the etalon has high quality surfaces (roughness is about  $\lambda/50 - \lambda/100$ ) and is tuned with high accuracy then its transmission become too small if finesse value exceeds 6 ( $r > 70\%$ ). Thus from the energetic point of view we have to demand low value of finesse:

$$f < 6. \quad (10)$$

Under this condition the etalon provides sufficient angular width  $\Delta\alpha$  which should be no less than the excimer laser beam divergency (1-5 mrad).

In addition the finesse shouldn't be too high because the transmission of the etalon for a certain wavelength seriously degrades when the flatness of the etalon's surfaces across the laser beam cross section is far from an ideal one

(this is not essential for the lasers with small beam diameters and is very important in the case of EL, when the square of the beam cross section is equal to several square centimeters).

Thus conditions (8) and (10) are not compatible. The linewidth narrowing by insertion of the etalon with high value of finesse inside the laser cavity (to provide the conditions (7)-(8)) gives too small energy efficiency (<1%, and spatial coherency of laser beam becomes too high (the divergency too small)).

In this work we describe the way how this problem can be overcome and relatively powerful line-narrowed radiation can be obtained using one EL oscillator. In the next sections we'll confirm this on the basis of experiments and mathematical simulations.

## 2. EXPERIMENTAL

To obtain a low coherent, linewidth narrowed excimer laser beam with high energy efficiency we propose to use two etalons with comparatively low finesse ( $f \sim 4-6$ ) which base distances  $l_1$  and  $l_2$  are close. In this way two problems may be solved. First, this dispersive element possesses of a much higher dispersion range in comparison with a single etalon (only coincided peaks of the etalons are transmitted) which exceeds the width of the amplification spectrum if the values of  $l$  and  $l$  are large enough to provide small  $\delta\lambda_{et}$  value (see eq. (4-5)). Second, its spectral transmission function is the product of the transmission functions of separate etalons. In our excimer KrF laser linewidth narrowing experiments two etalons with  $l_1 = 1.0$  mm and  $l_2 = 0.6$  mm, and comparatively low value of finesse  $f = 4$  ( $r = 66\%$ ) were used. The value of incident angle  $\alpha$  was chosen in the range 10-20 mrad to provide a large width ( $>1$  mrad) of angular transmission function and a large value ( $>200$  mrad/nm) of etalon dispersion [5]:

$$D_{et} = (\lambda \operatorname{tg}(\alpha))^{-1}. \quad (11)$$

The width of spectral transmission function of this dispersive element was estimated:

$$\delta\lambda = 10 \text{ pm}. \quad (12)$$

Both etalons installed in KrF laser resonator (resonator length - 1.5 m, pulse duration - 20 ns, pulse energy in free running generator - 150 mJ) provided spectral linewidth narrowing down to 4 pm with energy losses  $\sim 70\%$ .

It should be noted that line narrowing was achieved in our case without essential decreasing of the radiation divergency (increasing of the coherence) in comparison with initial ones. This is due to the large angle spectrum window (low finesse) of the used etalons.

## 3. SIMULATION

If we desire to choose a dispersive element for the line narrowing techniques or optimize the parameters of the resonator and the conditions of

pumping to obtain required characteristics (pulse energy, spectral linewidth, divergency) of the output laser radiation it is necessary to carry out adequate estimation of these characteristics for a certain laser scheme. During the time of the light pulse development inside the EL cavity (15-20 ns or 5-7 halfroundtrips) mode selection doesn't occur and simple simulation under the approximation of the light propagation equation [6] seems to be incorrect. Thus a new model possessed of possibility to describe the development of light pulse and predict the characteristics of the EL radiation is required.

In our simulations we have used some ideas of the corpuscle approach which was developed in [7]. In addition the spectral distribution of energy, the presence of intracavity apertures and dispersive elements were also taken into account.

The resonator cavity (RC) was assumed to be a 3D rectangle (Fig.2). It includes an active region (AR) of the EL, intracavity apertures (A) and dispersive elements (DE).

At the first moment  $M$  points (5000) are determined in the RC region. Their positions are calculated through the random values generator. From these points  $M$  "photons" (quotation marks are omitted in the following text) start their directline motion in the random directions with the speed of light. Every photon may be characterized by the energetic weight  $N_i$ , which is expressed through the number of quantas, and by the wavelength  $\lambda_i$ .

During simulation the directline motion of all photons, their reflection from the walls of the RC, transformation of photon's weights after their propagation through AR and DE are calculated. Output laser energy may be determined in this case in turn off

$$P(t_i) = hc(1-R_i) \sum_i (N_i / \lambda_i) \quad (13)$$

where summation is carried out for all photons which are reflected from the output semitransparent mirror M1 during the specific time of registration (this time determines the necessary temporal accuracy),  $h$  is the Plank constant,  $c$  - the speed of light. In the plane of M1 mirror the division of photons according to their propagation angle and wavelength is also provided. AR is divided onto several (determined by the required detailing of the AR medium) cells, each of which may be described by the open two-level system equations. The medium is assumed to be homogeneous inside every cell.

The output simulation data are: 1) energy vs time dependence; 2) energy vs wavelength dependence; 3) energy vs angle dependence.

The results of simulations are in a good correlation with the parameters of the radiation of the unnarrowed EL and also with the results of the linenarrowing in the schemes with intracavity apertures, prisms and diffraction gratings [3]. Simulations confirmed that the line narrowing efficiency can be no more than 8-10% in all these cases.

It is interesting to investigate the pulse duration dependence on the linewidth of the EL radiation. Such dependence is shown in Fig.3 for the case when four prism telescope and autocollimated diffraction grating are used as intracavity DE. As one can see the line narrowing procedure becomes more "easy" if long light pulses are used. In addition a direct confirmation of the reversed square root dependence in the equation (7) also follows from Fig.3.

The scheme with two etalons was simulated to define the maximum linewidth narrowing efficiency. The dependence of the linewidth on the etalon's finesse is shown in Fig.4. We see that the width of the generated spectrum (curve 1) is less (for corresponding finesse values) than the width of the apparatus function of the DE (curve 2). This fact may be explained in turn of the high amplification coefficient of the EL active medium and multiple propagation of light through the DE.

The dependence of the linewidth narrowing efficiency for the scheme with two etalons on their finesse is shown in Fig.5. Curve 1 corresponds to the case when both etalons are situated in the vicinity of the back rough mirror M2 and curve 2 - near the output mirror M1. We see that the efficiencies are quite different for these two cases. The fact may be explained in the following manner. Duration of the EL light pulse usually takes several roundtrips in the RC and the main energy growth occurs at the second roundtrip, when the light is reflected by the back mirror M2. So if the etalons are situated near the output mirror M1 then they have cut the spectrally unselected radiation what leads to the low efficiency of this scheme (curve 2). On the contrary, if the etalons (or even one of them) are situated in the vicinity of M2 mirror then the spectral selection occurs before the main amplification and the efficiency of the scheme is relatively high (curve 1). It should be noted that the observed difference of the efficiencies for different etalons position was confirmed experimentally.

And at least the maximum efficiency which was obtained in the scheme with two etalons experimentally is 30%. Relatively small deviation from the simulated value (35%) may be attributed to the nonideal flatness of the etalon's surfaces and their absorption capability what were not taken into account during simulation.

#### 4. CONCLUSIONS

Effective (>30%) line narrowing procedure of a single excimer oscillator to the required for projection photolithography level may be realized using two intracavity etalons with low finesse. A model of the excimer laser generation was developed. This model may be used to optimize the parameters of the excimer laser radiation.

#### REFERENCES

- 1) K.A.Valiev, L.V.Velikov, G.S.Volkov, D.Yu.Zaroslov, J.Vac.Sci.Tech., B7, #6, p.1616 (1989).
- 2) K.A.Valiev, L.V.Velikov, G.S.Volkov, D.Yu.Zaroslov, Proc. of the Microprocess'89 conference, Tokyo, Japan, July, 1989.
- 3) G.S.Volkov, Ph.D. theses, Physics and Technology Institute of the Academy of Sciences of the SU.
- 4) M.Born, E.Wolf, Principles of optics. Pergamon Press, N.Y., 1964.
- 5) S.P.Anokhov, T.Ya.Marusii, M.S.Soskin, Rearranged lasers, Moscow, Radio i Sviaz, 1982.
- 6) B.I.Stepanov, Simulation of optical quantum generators, Minsk, Nauka i Tehnika, 1966.
- 7) V.V.Buchanov, A.I.Moloduih, N.I.Yurchenko, Soviet QE, 10, #8, p.1553, 1983.

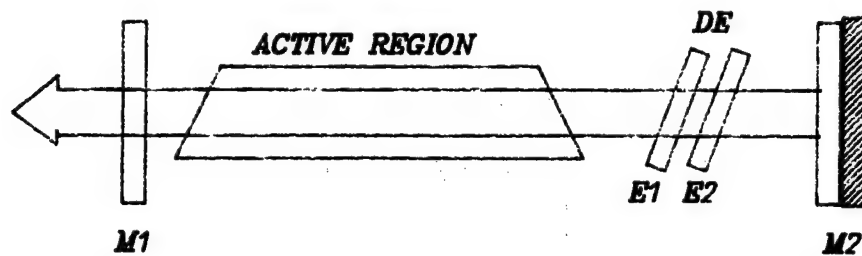


Fig.1 Two etalons play the role of the dispersive element.

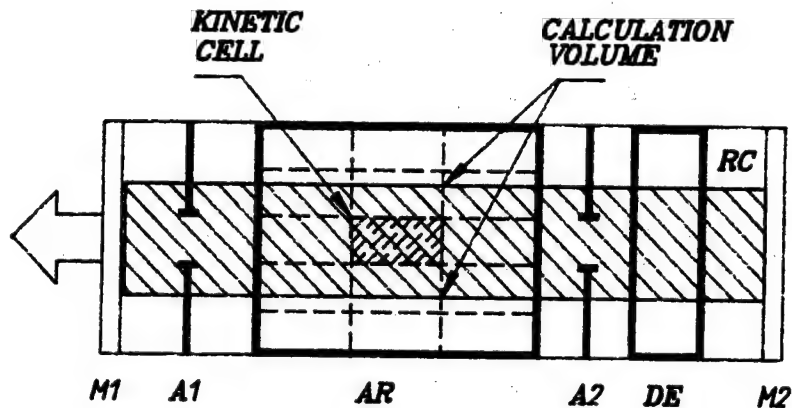


Fig.2 Simulated scheme.

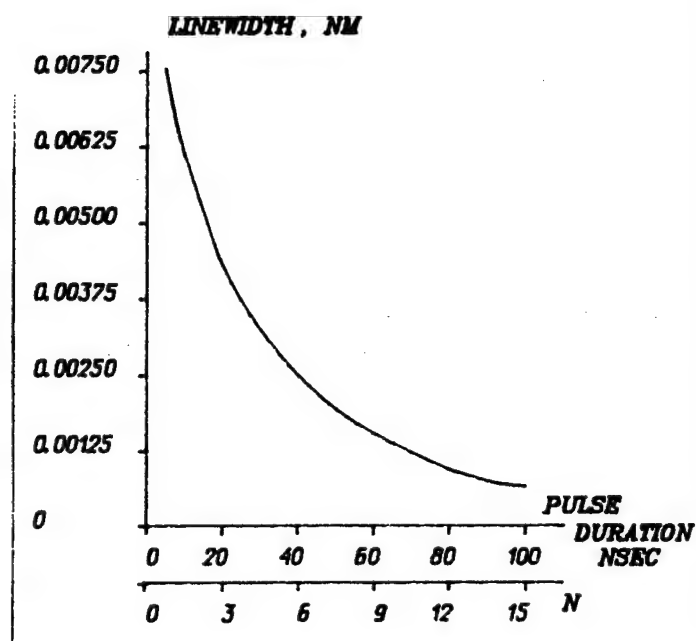


Fig.3 Linewidth vs pulse duration.

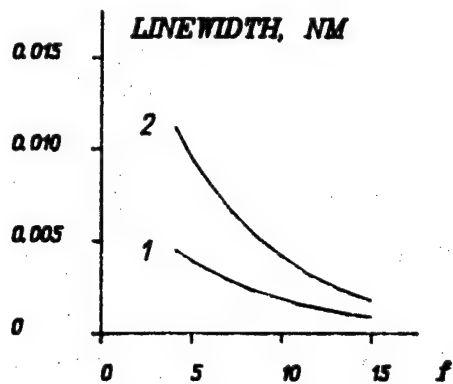


Fig.4 Linewidth vs finesse: generated spectrum (1), apparatus function of the dispersive element (2).

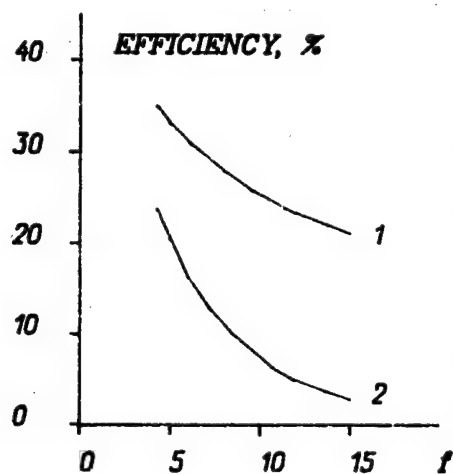


Fig.5 Linewidth narrowing efficiency vs finesse: etalons are situated near back rough mirror (1) and near output mirror (2).

## Evolution of an Excimer Laser Gas Mix

36980005 The Hague EXCIMER LASERS AND THEIR APPLICATIONS in English 1991 pp 160-166

[Article by A.D. Boardman, E.M. Hodgson, and A.J. Spence of the Department of Physics, University of Salford and A.D. Richardson and M.B. Richardson of the British Nuclear Fuels]

[Text]

### ABSTRACT

The work described in this paper forms part of the EUREKA EU213 "HiPulse" excimer laser project, to build an excimer laser with an average power greater than 1 kW, and a pulse repetition rate up to 5 kHz. Because of the very large volume of gas needed in such a laser, and the rising costs of rare gases such as xenon, a sophisticated gas processor system is needed which is capable of recycling the rare gas component of the gas mix indefinitely. If the laser head needs to be opened up for some reason, the laser gas needs to be pumped out and stored in a suitable vessel. When the laser is running, a variety of contaminants are generated by various chemical reactions going on inside the laser head; the exact contaminants depend on the materials from which the head is made. As part of the design of a laser gas processor, we are investigating the changes in gas constituents as the laser is running, using a quadrupole mass spectrometer connected to a computer. The mass spectrometer samples the laser gas through a special capillary and porous plug arrangement which maintains the necessary pressure difference between the laser gas at 2-5 bar and the analyser head at microbar pressure levels.

### 1. INTRODUCTION

The EUREKA "HiPulse" excimer laser European project (EU213) has been established to develop a high-average power, high-repetition rate laser suitable for industrial use. The target of the project is to create prototype lasers capable of sustained output greater than a kilowatt average power, and running at shot repetition rates up to several kilohertz. A necessary part of this development work is the design and construction of a automated control system, and the associated sensors and monitoring devices. The design is constrained by the need to respond to changes in the laser performance on a sub-millisecond timescale, and by the need to operate in a very electrically noisy environment. The control system being developed by the BNFL/University of Salford group uses a distributed network of transputers (see section 2) which communicate by optical fibre links.

An important part of the control of any excimer laser is the gas handling, ie the facilities for changing the gas in the laser head, adjusting the mix, injecting additional halogen etc. For small volume laser systems, making any analytic measurements of the laser gas is not economically justified. However, in very large volume lasers, such as the EU213 prototypes, the necessity of recycling purified gas back into the laser motivates the development of suitable monitoring equipment. As part of the development of a gas processor for the EU213 lasers, we have investigated the potential of a quadrupole mass spectrometer as an on-line laser gas analysis tool/sensor.

## 2. TRANSPUTER NETWORKS

The control system for the EU213 lasers is required to drive a series of parallel processes for laser operation, eg trigger the thyratrons, monitor the beam quality, maintain the halogen partial pressure etc. Some of these processes are quite demanding. For instance, the current pulse switched by the thyratrons is measured on every shot to check for irregularities in firing, and to make appropriate corrections in timing. The time available for operation at kilohertz rates is on a millisecond scale. Other parts of the control are concerned with the monitoring of slowly-varying quantities such as the gas temperature. Rather than use one large machine for all the various elements of the control, a distributed network of small processors is being used, allowing the work load to be shared out and also permitting the design to assume a modular form (see Figure 1). This gives much greater flexibility in responding to the different needs and interests of the collaborators in EU213. The various processors can be physically distributed around the laser, minimising the distance that monitoring or actuation signals have to travel in an electrically noisy environment.

In principle, any small processors could be used to build a network. However, transputers<sup>1</sup> are particularly attractive in this role because they are designed specifically to operate as part of a parallel computing system. To that end, they have very good inter-processor communications facilities (see Figure 2) using fibre-optic links, which are obviously particularly useful in this context in view of the electrical noise generated by a big excimer laser. In fact transputers have a high degree of immunity to electrical noise. The control software is written in OCCAM<sup>2</sup>, a parallel-processing language, as a set of routines governing various aspects of the laser operation. These routines are then shared out between the transputers of the network, as seems appropriate. If any one node of the network is overloaded, another transputer can easily be added in and the work reallocated between them.



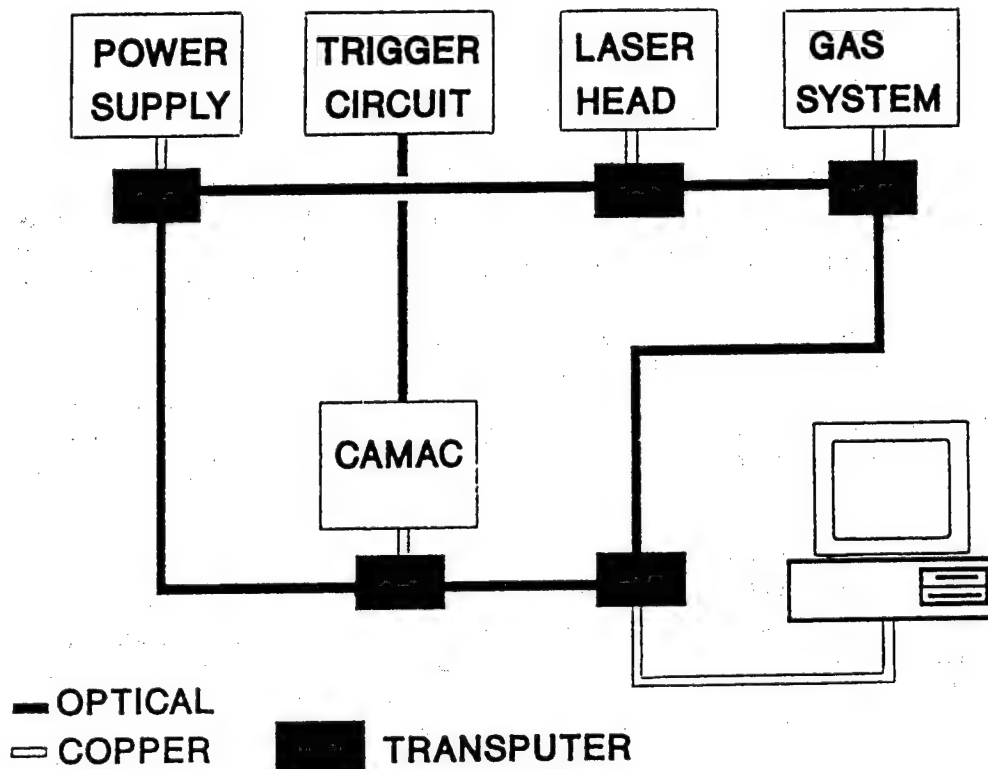


FIGURE 1 : EUREKA EU213 excimer laser control system

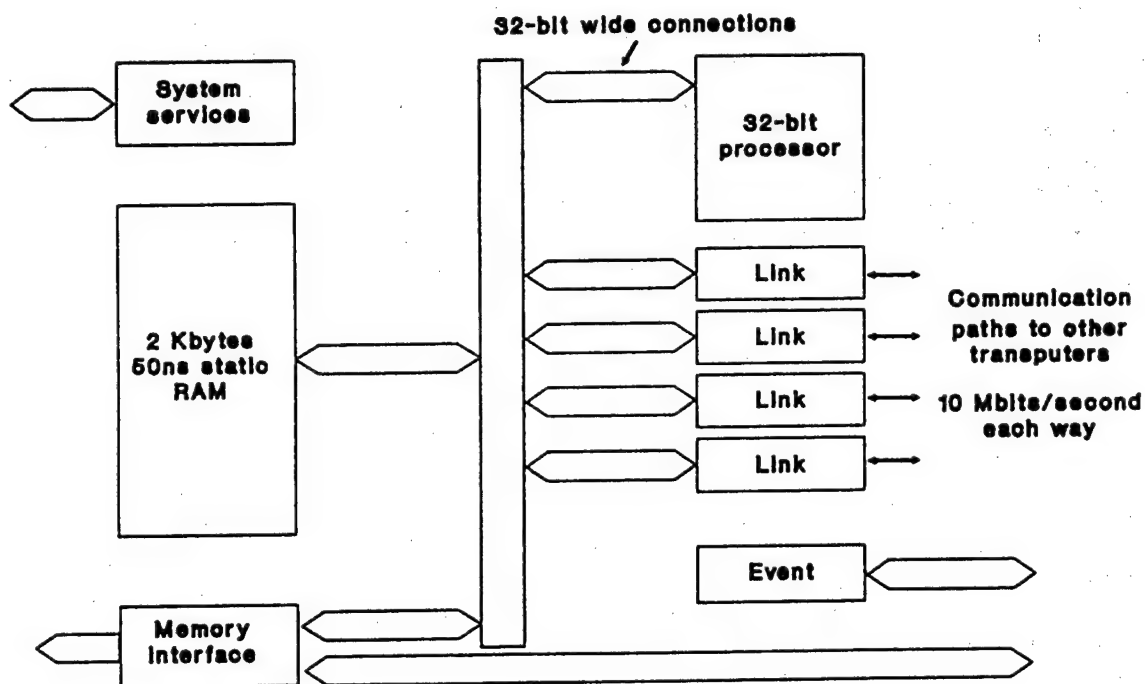


FIGURE 2 : Block diagram of transputer IMS T414

### 3. EXCIMER GAS

The gradual degradation of excimer gas mixes during laser operation has been widely reported<sup>3-8</sup>. A variety of methods have been used to study the chemical changes taking place in the laser gas, including spectroscopic analysis<sup>5</sup>, gas chromatography<sup>6</sup> and mass spectrometry<sup>6-8</sup>. Basically, the problem is that the halogen component of the gas mix reacts chemically with the materials surrounding it, eg the electrodes and the walls of the laser vessel. This causes both a reduction of the partial pressure of the halogen, thereby reducing the potential laser gain, and creates compounds in the laser gas which can absorb strongly at the laser wavelength, increasing the optical loss. The exact reactions taking place in a laser are determined by the materials used in its construction, eg  $\text{SiF}_4$  is produced by a reaction with glass<sup>3</sup>. Other commonly seen contaminants include  $\text{CO}_2$ ,  $\text{ClO}_2$ ,  $\text{F}_2\text{CO}$ ,  $\text{FNO}$ ,  $\text{FNO}_2$  and  $\text{NF}_3$ .

Most of the more commonly seen contaminants can be removed by passing the laser gas through a cold trap<sup>9</sup>, and such devices are widely used to extend the lifetime of gas mixes in commercial laser systems. Extra halogen can be added to the mix to restore the optimum partial pressure. Unfortunately, a few contaminants cannot be separated out with a cold trap, and eventually these will build up to levels that prevent laser operation. The normal recourse then is to simply throw away the whole gas mix and start again with a new fill. However, this is not feasible with the EU213 lasers because of the large volumes of gas involved. Very high-repetition rate lasers require fast gas flows between the electrodes to ensure discharge stability<sup>10</sup>. The most common design of pressure vessel for this type of laser is therefore a closed wind-tunnel. For aerodynamic reasons, the volume of such a "flow-loop" design is very large; perhaps several cubic metres. This volume is filled with laser gas at pressures of 5 - 10 bar, so a flow-loop may contain 30 cubic metres of laser gas at standard pressure. With such large reservoir volumes, the concentration of contaminants produced by reactions in the discharge region might be expected to be very low. However, the high repetition rate operation effectively cancels out the potential advantage from the size of the gas reservoir, so gas lifetime is still a major consideration. For XeCl lasers, the rare gas component (xenon) alone may cost several thousand pounds sterling for a single fill<sup>11</sup>. Clearly it is not satisfactory to simply discard the whole mix. An essential part of any final automated control system is some way of monitoring the gas composition and the performance of the gas processor, and so we are investigating the use of a quadrupole mass spectrometer in this context.

### 4. USE OF A QUADRUPOLE MASS SPECTROMETER

A mass spectrometer should be the perfect device for examining the laser gas mix, but there are many practical difficulties. The most serious problem is that excimer lasers typically operate at pressures between 3-8 bar, and a quadrupole mass spectrometer requires a vacuum of better than  $10^{-6}$  mbar. So a fairly elaborate pressure reduction system is needed to sample the gas mix without introducing significant mass discrimination. Our system (see Figure 3) uses three elements; first a standard pressure regulator drops the pressure to 1 bar, followed by a 30  $\mu\text{m}$  diameter silica capillary 1.8 metres long which restricts the laminar gas flow to give a downstream pressure of  $10^{-3}$  mbar, and finally a silica sinter plug (operating in the molecular flow regime) that reduces the final pressure to  $10^{-6}$  -  $10^{-7}$  mbar.

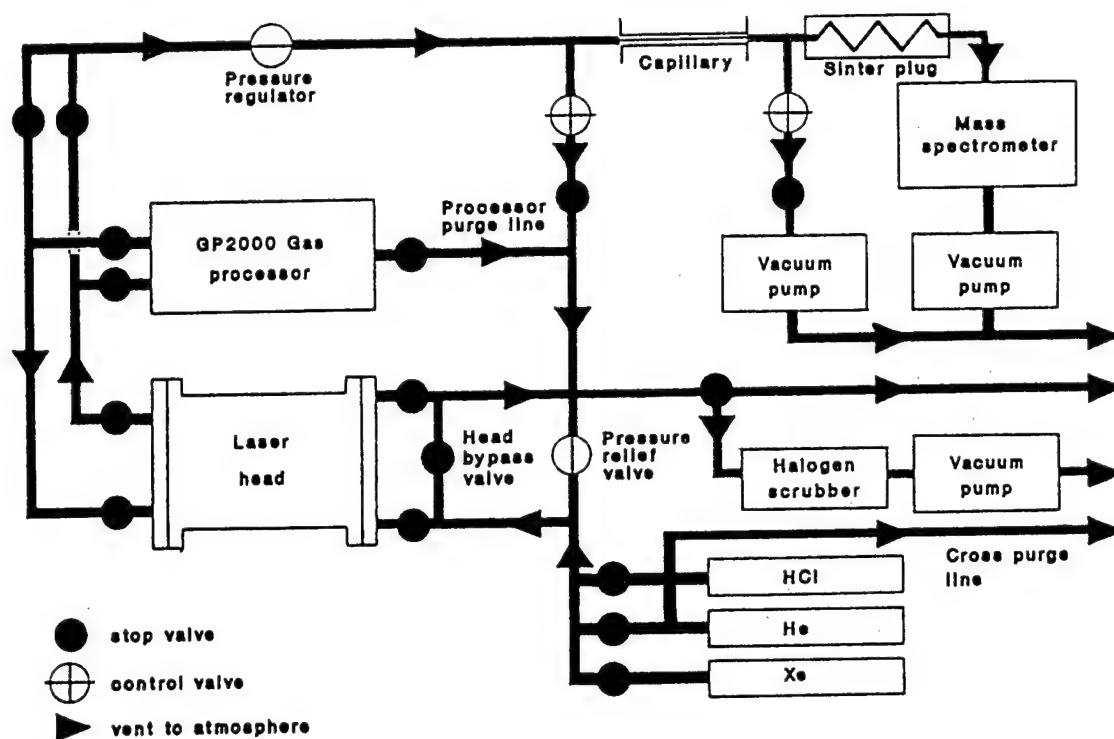


FIGURE 3 : Schematic diagram of gas handling system

Passivation of the pressure reduction system is important, as well as the passivation of the mass spectrometer itself. In order to ensure that a representative fraction of the laser gas is sampled, the gas must be well stirred in the laser head - normally this would be done by a fan that drives clean gas into the discharge region. However, our laser head does not employ a fan at present and so the stirring action is provided by an Oxford Lasers GP2000 gas processor which circulates the gas with a diaphragm pump at a rate of about 20 litres per minute. (In this experiment the GP2000 was used purely as a pump; the cold trap was not running.) The amount of laser gas consumed by the mass spectrometer is very small; of the order of  $10 \text{ cm}^3$  per minute during a scan (typically lasting a few minutes every hour).

The mass spectrometer used in our experiments is a V G Quadrupoles SX200 with a Spectralab PC for data collection. The mass range is 1 - 200 amu and the sensitivity is 0.1 ppm of total pressure. The mass spectrometer has an open ion source, and two detectors; a Faraday collector and an electron multiplier. The Faraday collector can operate at higher pressures (up to  $10^{-4}$  mbar) but suffers more from electrical noise than the multiplier. However, the multiplier has an inherent mass discrimination effect which must be considered in quantitative measurements, i.e. the intensity of the signal varies with the atomic mass number. The mass spectrometer is pumped by a turbo-molecular pump which introduces further mass discrimination. For these reasons, it is important to calibrate the mass spectrometer with a well-defined gas mix. The response time of the system to changes in the laser gas is typically of the order of a few seconds, but for reliable measurements of the halogen level a settling time of about 5 minutes is needed. This is due to passivation problems in the inlet capillary; heating the capillary will eliminate this delay.

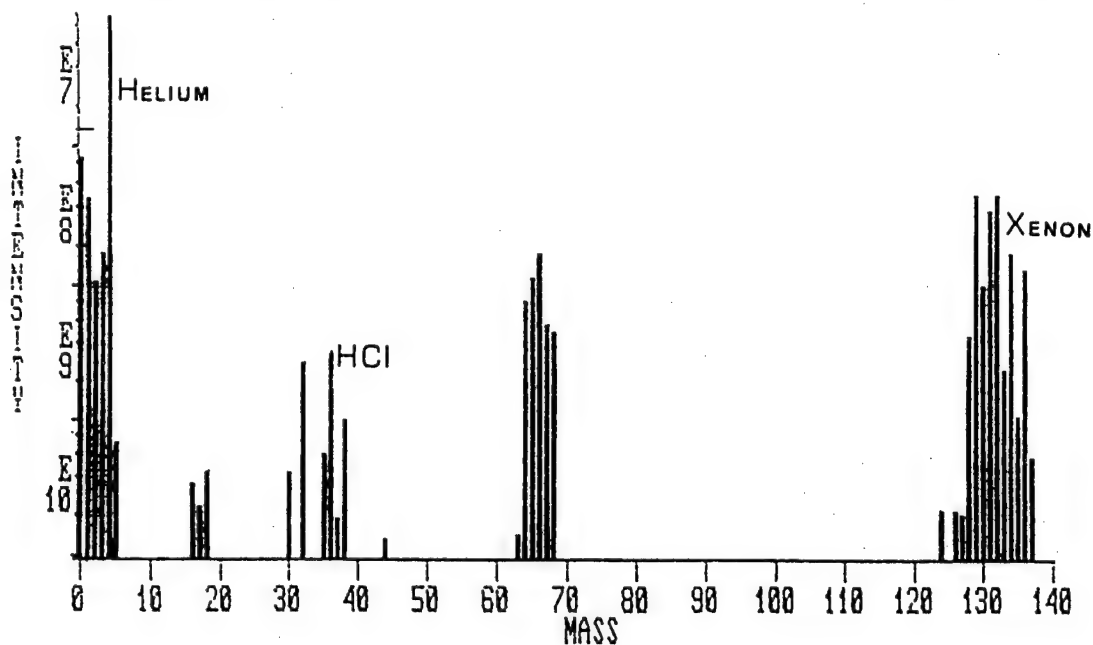


FIGURE 4 : Histogram showing XeCl laser gas mix

The Spectralab software permits the display of the entire mass range as a histogram, plotting mass number vs intensity on a logarithmic scale. A "background" scan, showing the residual gases in the mass spectrometer vacuum system when there is no connection to the laser head, can be stored and automatically subtracted from the laser gas scan - see Figure 4. The laser gas components are easily identified.

Quantitative measurements of specified mass numbers (Figure 5) can be read out either from the monitor screen or by using a special interface card to connect the Spectralab PC to a transputer directly. Calibration weighting factors relating to the mass discrimination effects can be incorporated into the calculation of percentages. To obtain absolute pressures from the partial pressures given by the mass spectrometer, a separate pressure gauge on the laser head is required.

CHANNEL	MASS	NAME	REL/SENS.	READING
1	2	Hydrogen	0.440	00.17%
2	4	Helium	0.140	98.73%
3	18	Water	1.000	00.04%
4	28	Nitrogen	1.000	00.02%
5	32	Oxygen	1.000	00.01%
6	35	HCL	1.600	00.00%
7	36	HCL	1.600	00.04%
8	38	HCL	1.600	00.01%
9	64	XE++	3.000	00.07%
10	65	XE++	3.000	00.05%
11	66	XE++	3.000	00.09%
12	67	XE++	3.000	00.03%
13	129	XE	3.000	00.23%
14	131	XE	3.000	00.18%
15	132	XE	3.000	00.23%
16	134	XE	3.000	00.08%

FIGURE 5 : Gas analysis as percentage of mix

Repeated measurements on our XeCl laser gas made over half a million shots failed to show any loss of halogen or any significant rise in contaminants (there was a small carbon signal possibly due to breakdown of a PVC insulator in the laser head). There was also a slight rise in the hydrogen partial pressure, but no free chlorine was detected. There was no appreciable change in the optical performance over this time. The apparent absence of contaminants may be due to the solid (dust-like) nature of the metallic chlorides, in particular  $\text{AlCl}_3$ , which are the most likely products to be formed in our laser head. Alternatively, it may be a consequence of the large gas reservoir volume of our laser head (approximately 200 litres) which results in a dilution of contaminants formed in the laser discharge. Extending the trial for a greater number of shots would answer this question.

## 5. CONCLUSION

In conclusion, we have demonstrated that a quadrupole mass spectrometer can provide an effective measure of the partial pressures of an excimer laser gas mix, and that changes in the gas can be monitored by a continuous sampling process, with a response time of a few minutes. In the near future we plan to install a heated capillary which will reduce the response time, and prevent repassivation problems in the inlet system. At the same time an interface board is being built to allow the appropriate transputer to read out the partial pressures of 16 selected mass numbers directly. The halogen injection system can then be driven automatically in response to a drop in the halogen signal from the mass spectrometer. We also plan to run the laser with a KrF fill and compare the formation rates of contaminants.

We gratefully acknowledge the financial support of British Nuclear Fuels, and the help of Dr. Kelvin Schneider in particular.

## 6. REFERENCES

1. D.A.P. Mitchell et al, "Inside The Transputer", Blackwell Science Publications 1990
2. C.A.R. Hoare (ed), "Occam 2 Reference Manual", Prentice Hall International 1988
3. M.C. Gower, A.J. Kearsley and C.E. Webb, "Gas Composition and Lifetime Studies of Discharge Excited Rare-Gas Halide Lasers", IEEE J. of Quantum Electron., vol. QE-16 (Feb. 1980) pp. 231-235
4. V. Yu. Baranov et al, "Reasons for the fall in the output power of a pulse-periodic XeCl laser during its operation", Sov. J. Quantum Electron., vol.13 (Nov. 1983) pp. 1518-1521
5. Quhong Lou et al, "The effects of F<sub>2</sub> concentration on discharge pumped KrF laser characteristics", J. Appl. Phys., vol. 68 (Sep. 1990) pp. 2572-2576
6. R.C. Heaton, P.H. Hemberger and W.F. Sandoval, "Chemical Analysis for Excimer Laser Systems", Los Alamos National Laboratory Report LA-11008-MS (Sep. 1987)
7. P.H. Hemberger, R.J. Beckman and R.C. Heaton, " Fluorine Analysis By Time-Resolved Mass Spectrometry", Proc. of 34th Annual Conference on Mass Spectrometry and Allied Topics, Cincinnati, USA, (Jun. 1986) pp.1067-1068
8. W.D. Kimura and J.F. Seamans, "Gas Contaminants Produced in Electron-Beam-Pumped XeF Lasers", IEEE J. of Quantum Electron., vol. 24 (Oct. 1988) pp. 2121-2125
9. A.J. Kearsley et al, "Cryogenic Gas Purification and Lifetime Extension of ArF, KrF and XeF Laser Gas Mixtures", OSA Topical Meeting on Excimer Lasers, Lake Tahoe, Nevada USA (1983).
10. S. Takagi et al, "2.5 kHz high repetition rate XeCl excimer laser", J Appl. Phys. vol. 68 (Dec. 1990) pp.5927-5929
11. G. Jursich et al, "Chemistry studies improve excimer gas lifetimes", Laser Focus World (Jun. 1989)

## High-Repetition Rate Pseudospark Switches for Pulsed High-Power Lasers

36980005 The Hague EXCIMER LASERS AND THEIR APPLICATIONS in English 1991 pp 167-175

[Article by P. Bickel, J. Christiansen, K. Frank, A. Gortler, W. Hartmann, C. Kozlik, and P. Wiesneth of the Friedrich-Alexander Univ. of Erlangen/Nurnberg]

[Text]

### ABSTRACT

The experimental results of high-repetition rate pseudospark switch testing are reported, with particular interest in applications like high repetition rate, high-average power excimer lasers and pulsed TEA CO<sub>2</sub> lasers. Typical test parameters are hold-off voltage of about 20 kV, peak currents around 15 kA, and pulse durations of less than 100 ns, discharge conditions that are typical for high average power excimer lasers. These were realized in a low inductive discharge circuit using discrete ceramic capacitors of up to 10 nF total capacitance and an impedance of about 1  $\Omega$ . The resulting peak currents were about 19 kA in the short-circuited, ringing discharge. A special feature of the switch is being capable to withstand severe current reversal, high rates of current rise of about  $5 \cdot 10^{11}$  A/s and peak currents above 20 kA. Some  $10^7$  shots have been performed with a sealed-off metal-ceramic pseudospark switch with integrated hydrogen reservoir without degradation of the switch performance. In this setup repetition rates of up to 1.8 kHz were achieved. The switch triggering behaviour and measurements of the switch resistance in dependence of the peak current are reported about.

### 1. INTRODUCTION

The pseudospark switch (PSS) is a fast closing switch, based on a low pressure gas discharge in a special geometry of the electrodes. This low inductance switch is designed for holdoff voltages in a range of 5 up to 35 kV. It is capable of pulse duration of about 20 ns up to tens of microseconds. Since the beginning of the development of pseudospark switches in the mid-eighties, large progress has been made towards sealed-off ceramic-metal switches<sup>1,2,3,4</sup>. Pseudospark switches capable of switching over 25 kA peak current at current reversal of more than 90 % were successfully tested as an advanced thyatron replacement for ultra-high power applications in TE gas discharge lasers. The same switches have been shown to be able for long pulse duration applications due to the superior cathode emission mechanism which warrants an even cathode loading during conduction of high-current pulses<sup>4,5,6</sup>. At short pulse durations of the order of 100 nsec, peak currents of up to 25

kA, and a reverse current of over 90 % of the peak forward current, brazed ceramic-metal switches have shown to have a lifetime in excess of  $5 \times 10^6$  shots<sup>3</sup>. Due to the pulsed power source used for the earlier measurements of peak current and high rate-of-current-rise capability, these tests were limited to pulse repetition rates of the order of 100 Hz by power supply limitations. Experiments done by another research group<sup>8</sup> showed that PSSs are suitable for multi-kHz repetition rates in burst mode operation; however, peak current and energy per pulse were rather modest in these experiments, and the switch was an O-ring sealed laboratory prototype switch. More recent experiments in our laboratory had the aim to test our ceramic-metal switch at the multi-kA, multi-kW level at repetition rates of up to 2 kHz, conditions which are typical for high average power excimer lasers, and pulsed modulators for linac structures.

## 2. EXPERIMENTAL SETUP

The PSS investigated in these experiments utilized molybdenum electrodes with circular center holes of 3 mm in diameter each, and hollow cathodes as well as hollow anodes. Deuterium is used as the working gas throughout the experiments. A schematic cross-sectional drawing of the PSS used in these experiments is shown in fig. 1. The switch is made of OFHC-copper electrodes brazed directly to insulating  $\text{Al}_2\text{O}_3$  rings. The anode and cathode parts which directly contact the discharge plasma are made of bulk molybdenum in order to assure a good thermal contact to the environment. The switch is triggered by applying a negative-going high voltage pulse of 2 - 3 kV in amplitude, provided by a thyristor pulser, to the trigger electrode. The main discharge is then initiated by the injection of electrons out of the pulsed glow discharge into the hollow cathode of the main gap. In order to achieve a short delay and a small jitter of the triggering discharge, a keep-alive current of the order of 1 mA is maintained between the triggering electrode and an additional "preionization electrode". This method effectively reduces delay and jitter by providing a sufficient concentration of starting electrons<sup>9</sup>.

The PSS is built into a coaxial housing, which also contains the ceramic capacitors in order to minimize circuit inductance. Figure 2 is a cross-sectional drawing of the experimental setup. The total circuit inductance, with 6 ceramic capacitors of 2.7 nF each in parallel, has been calculated to be 19 nH, giving a circuit impedance of 1.1 ohms. Two command charge power supplies, a master and a slave unit, with a maximum mean power of about 6 kW are used. The switch current is measured with an coaxial shunt resistor in the current return path, made of 340 parallel carbon bulk resistors. The coaxial housing is filled with transformer oil for high voltage insulation, and equipped with an oil-water heat exchanger to provide cooling at high average power levels.



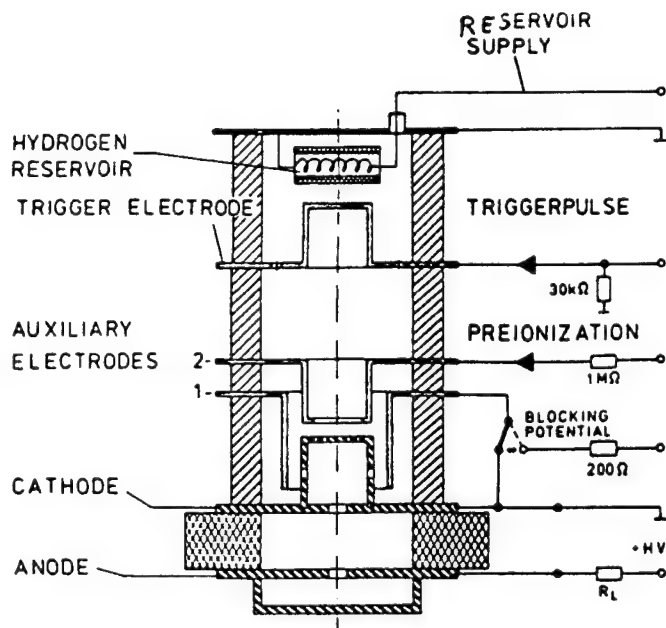


Fig. 1: Schematic cross-sectional drawing of the tested PSS. The Ti-based deuterium reservoir is located behind the last electrode of the triggering section. The copper electrodes are braized directly to the  $\text{Al}_2\text{O}_3$  ceramic rings.

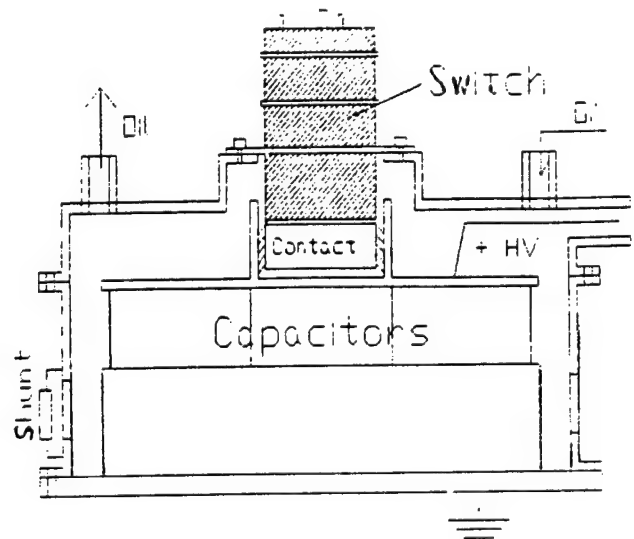


Fig. 2: Cross-sectional drawing (schematic) of the coaxial experimental setup. This design minimizes the circuit inductance and allows a rate of current rise as high as  $7 \cdot 10^{11}$  A/s.

### 3. RESULTS

#### 3.1. Ignition statistics and breakdown voltage characteristic

The static breakdown voltage - pressure characteristic obeys Paschen's law. (Fig. 3) At an electrode separation distance  $d$  of about 3 mm, a pressure  $p$  of about 40 Pa and a holdoff voltage of 25 kV, the switch is working at the low pressure side of the Paschen minimum.

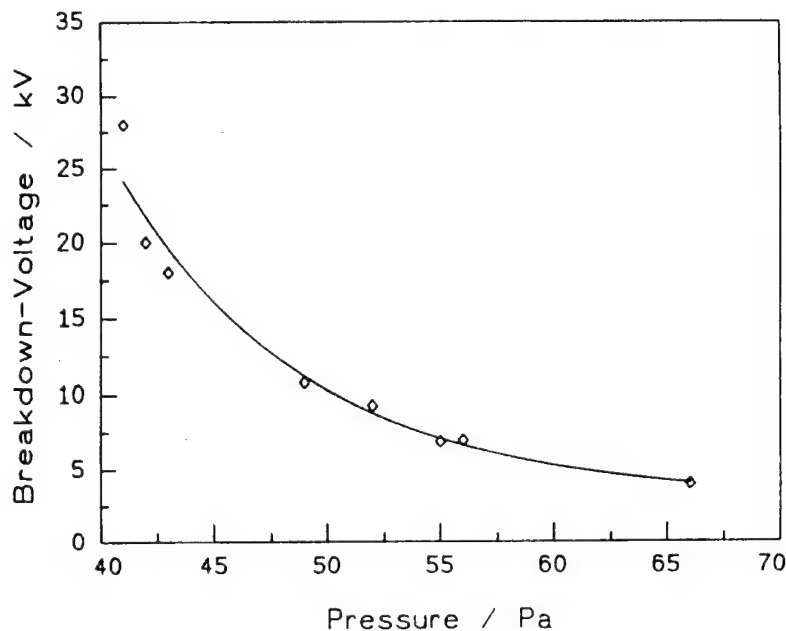


Fig. 3: Static breakdown voltage as a function of the deuterium pressure, for the switch as of fig. 1.

However the breakdown characteristic as shown in fig. 3 is valid for durations of some milliseconds, the high voltage is at the switch and repetition rates of less than 20 Hz, which can be called quasi-static. The switch delay, normally about 250 ns and the jitter of some 10 ns increase if the duration of the high voltage charging pulse across the switch becomes shorter than 1 ms.

In fig. 5, the switch delay is plotted as a function of the duration of the high voltage pulse across the switch. The duration is measured from the point where the high voltage pulse has reached 90 % of its peak value, to the time the trigger pulse is applied to the switch. As can be seen from these data, the delay increases as the duration of the high voltage pulse falls below 1 ms which is the case at repetition rates above 1 kHz in this experiment. This effect is more severe at values of  $p$  near the Paschen-minimum, and is attributed to the finite formative time lag of the predischARGE in the main switch region. Obviously, this predischARGE is necessary for a good triggering performance of the switch, and thus has to be taken into account in the construction of high repetition rate pseudospark switches.

The delay also increases at repetition rates of more than 20 Hz, as shown in fig. 4. This implies that the pressure for optimal performance has to be adjusted at higher repetition rates to values higher than in the quasi-static case. This may be caused by gas depletion in the electrode region and is an object of our actual research.

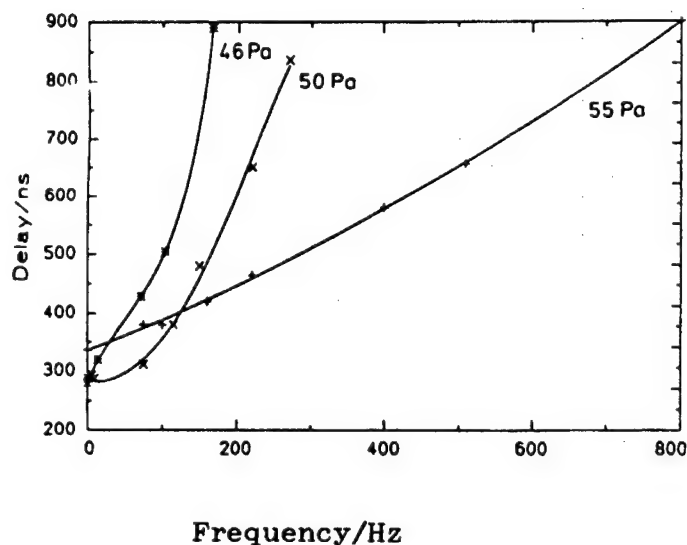


Fig.4: The switch delay is shown as a function of the repetition rate for different D2 pressures. At high repetition rates, the pressure has to be increased above the static pressure as of fig. 3

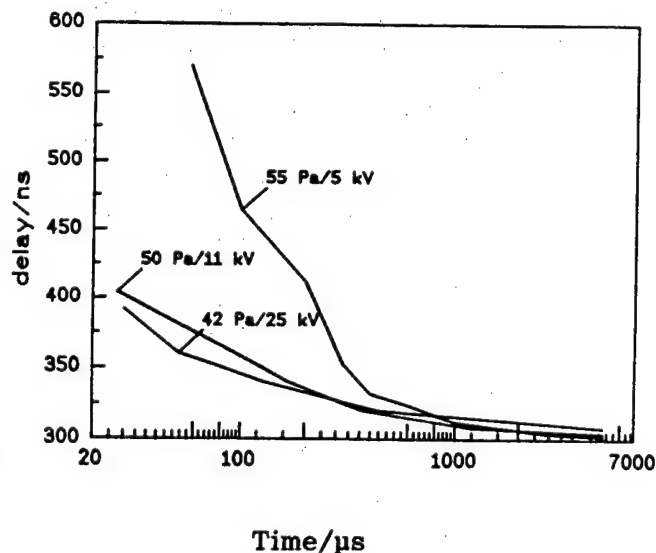


Fig.5: The switch delay as a function of the duration of the high voltage pulse across the switch, for different working points.

### 3.2 The switch resistance

The PSS under test was intentionally developed for peak currents of 10 to 25 kA at pulse durations of more than 100 ns. In a variety of applications, however, the pulse duration is shorter and the peak current is considerably less than 10 kA. This is especially true, for example, for copper vapor lasers which need high pulse repetition rates of the order of several kHz at peak currents of the order of  $< 2$  kA, and at pulse durations of the order of 50 ns. In figure 6, a series of current waveforms is shown at varying peak currents. Current variation has been accomplished by varying the total capacitance and, for the lowest peak currents shown, also decreasing the voltage. As a consequence, the pulse duration varies along with the peak current. A severe drawback of the switch at currents below 5 kA can be seen from figs. 6b) and 6d). Reverse conduction does not take place at low currents in this specific switch. At peak currents above 5 kA, however, the switch conducts reverse currents of 80 % of the peak forward current (figs. 6a and 6c). A total resistance can be calculated from the damping constant of the damped current sine wave, which, however, also includes commutation losses and losses due to the polarization change in the capacitors. This total resistance can then be taken as an upper limit for the time-average switch resistance, and allows an estimation of the total power, dissipated in the switch in a specific application. In fig. 7, this average switch resistance is plotted

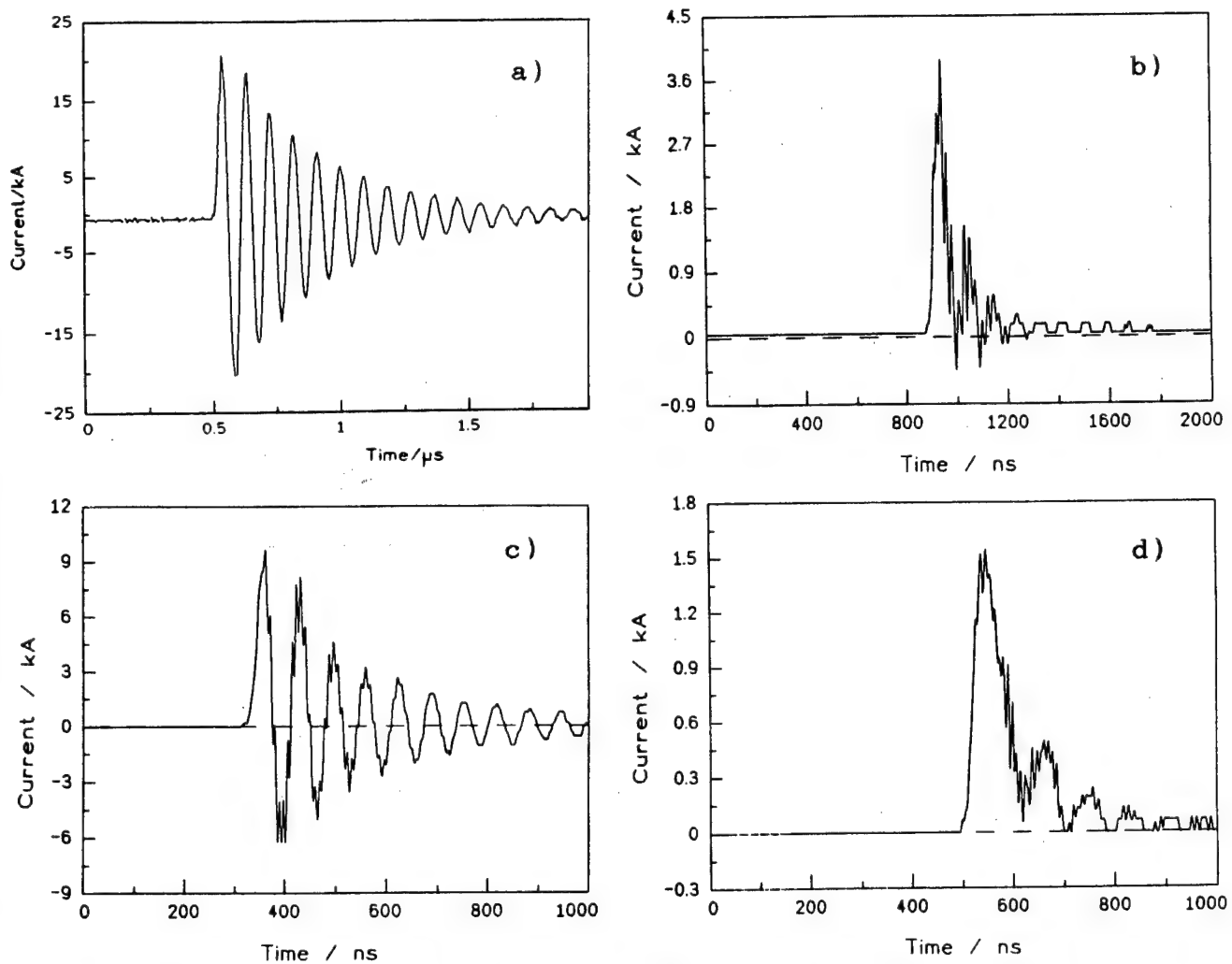


Fig. 6 a-d: Current waveforms of different amplitudes. At peak currents below 5 kA, no reverse conduction occurs; at currents of 9 kA and more, the reverse current amplitude reaches 80 % of the peak forward current.

as a function of the charge stored initially in the capacitor. The switch losses increase rapidly at an stored electrical charge below  $10^{-4}$  Cb, and seem to level off at a more or less constant resistance at a charge considerably higher than this lower limit. This indicates that a PSS that is to be used at low currents and short pulses has to be carefully designed in order to avoid excessive switch losses in that kind of applications, and that a PSS does not necessarily perform well at parameters that are very different from its design parameters.

First tests in an TE-CO<sub>2</sub> Laser discharge circuit<sup>12,13</sup> at peak currents of about 1.8 kA, voltages of 18 kV and pulse durations of ca. 600 ns, indicated, that the laser output could be increased by about 3 %, in comparison with a commercial russian thyratron, as shown in fig.8 (TGI 1000/25). This seems to be very promising, because this are parameters that are not in the optimal range of the switch. The current reversal, that a thyratron is normally not supposed to withstand is feeding additional energy to the laser. Because of the lower switch resistance, the ratio of dissipated energy in the laser to the energy dissipated in the switch is advantageous. In this experiment the repetition rate was limited by the gas exchange velocity of the laser to about 200 Hz.

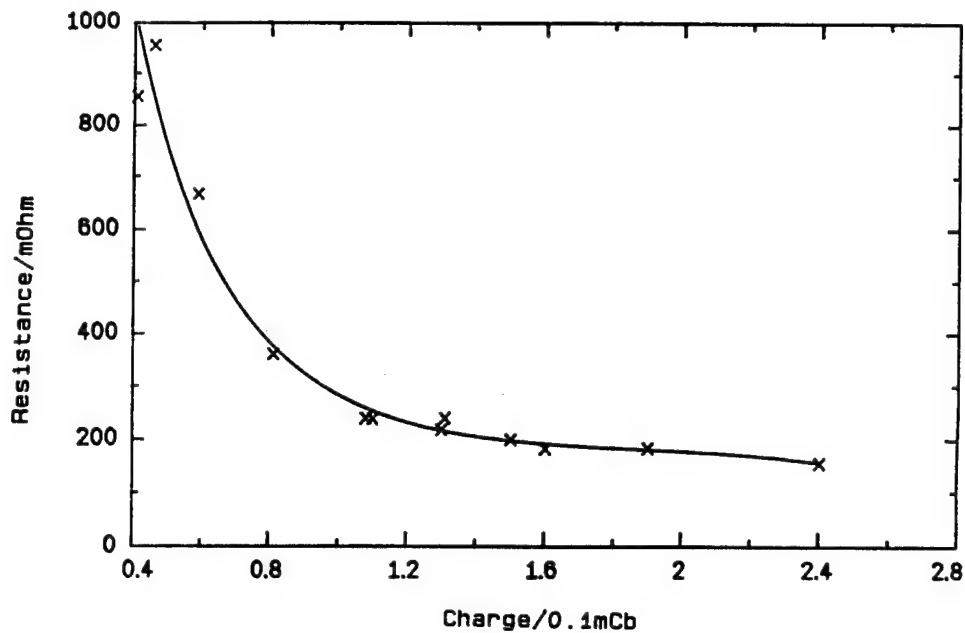


Fig.7: The total internal resistance of the experimental setup as of fig. 2 is shown as a function of the electrical charge stored in the discharge capacitor. It is calculated from the damping of the ringing LCR-discharge. The main part of it is attributed to the PSS internal resistance, which is composed of the time-varying plasma resistance and the commutation losses.

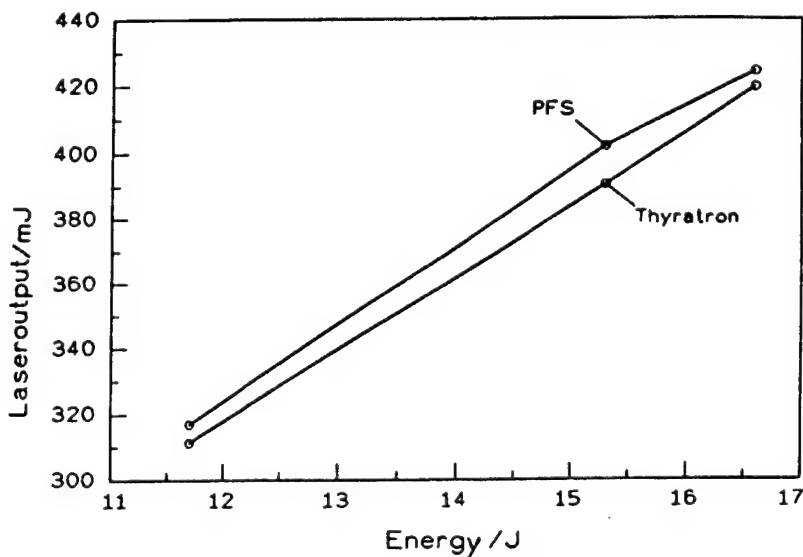


Fig. 8: Laseroutput of a TE-CO<sub>2</sub> laser, in the TEM-00 mode as described in Ref.12 and 13 at various voltages with thyatron and PSS.

### 3.3 Lifetime measurements

Most of the tests reported herein have been performed at capacitances of 5.4 and 10.8 nF, respectively. The switch was operated for over 1 million shots at 10.8 nF at a voltage of 23 kV, and over 10 million shots at 5.4 nF at 25 kV. The peak current and maximum repetition rate are 9.4 kA at 1.8 kHz (5.4 nF), and 19 kA at 1 kHz (10.8 nF), respectively. After the end of these measurements, the behavior of the switch had not altered significantly, and it is still operationable. Thus, the lifetime of the switch can be estimated from earlier lifetime measurements<sup>10</sup> to be in excess of  $10^8$  shots at the conditions given for the 5.4 nF capacitor. The deuterium reservoir has been proven to be suitable for sealed-off operation of high-average-power PSSs, and is expected to have a lifetime comparable to that of the electrodes. The test results are summarized in the following table and compared to results from high repetition rate testing of a PSS at another laboratory<sup>11</sup>.

	Erlangen		from Ref.11
C / nF	5.4	10.8	13.5
I <sub>p</sub> / kA	9.4	19	9
U <sub>c</sub> / kV	25	23	20
P <sub>av</sub> / kW	3	2.8	0.6
prr <sub>max</sub> / kHz	1.8 cont.	1 cont.	0.1 cont. 0.2 burst
t <sub>1/2sw</sub> /ns	70	94	70
R <sub>tot</sub> / mΩ	230	150	120
L <sub>tot</sub> / mH	28	21	25
Lifetime / shots	> 10 <sup>7</sup> total		>3.6*10 <sup>7</sup>

### 4. CONCLUSIONS

We have shown that high pulse repetition rates of 1 to 2 kHz can be handled by state-of-the-art pseudospark switches at average power levels of the order of 3 kW, with peak currents as high as 19 kA, and at a current reversal of 80 %. The lifetime limit of the first sealed-off PSS with built-in gas reservoir has not yet been reached, but is in excess of  $10^7$  shots under these extreme conditions. From lifetime measurements at similar conditions, a total lifetime of well over  $10^8$  shots can be expected. The maximum average power and pulse repetition rate in our experiment were limited by the power supply to 3 kW and 2 kHz, respectively; a maximum repetition rate of 3 to 4 kHz should be possible with this switch, and a more advanced triggering section should allow even higher repetition rates. The tests have also shown that it is necessary to develop special PSS designs for applications where low currents and / or short pulses are needed, if the current reversal capability of the switch is a necessary feature. The unique design of the switch should allow much higher average power levels as those reported here, the only limitation up to now being the power supply. The existing switch already surpasses hydrogen thyratrons in several aspects simultaneously, and lifetime and maximum achievable pulse repetition rates are expected to further increase by ongoing research into electrode processes and trigger problems.

## 5. ACKNOWLEDGEMENTS

This work was supported by the West German Federal Ministry of Research and Technology (BMFT).

We also would like to acknowledge W. Bohmeier, H. Schöpp, W. Ross et. al. from the "Zentralinstitut für Elektronenphysik" (ZIE) in Berlin for joint experiments at a TE - CO<sub>2</sub> Laser.

Furthermore thanks to MULTICONTACT Corporation for kindly supplying us with special high-current contacts.

## 6. REFERENCES

1. K. Frank et al., IEEE Transact. Plasma Sci., vol. 16, no. 2, p. 317, 1988
2. K. Frank, E. Boggasch, J. Christiansen, A. Görtler, W. Hartmann, C. Kozlik, Proceed. SPIE Conf. on Pulse Power For Lasers, Los Angeles, CA, vol. 735, p. 74 , 1987
3. K. Frank, J. Christiansen, O. Almen, E. Boggasch, A. Görtler, W. Hartmann, C. Kozlik, A. Tinschmann, G. F. Kirkman, Proceed. SPIE Conf. on Space Structures, Power, and Power Conditioning, Los Angeles, CA, vol. 871, p. 173, 1988
4. W. Hartmann, O. Almen, C. Kozlik, K. Frank, A. Görtler, J. Christiansen, J. Heuer, U. Braunsberger, J. Salge, Proc. 7th IEEE Pulsed Power Conf., Monterey, CA, USA, 1989
5. W. Hartmann, M. A. Gundersen, Phys. Rev. Lett. 60 (23), p. 2371, 1988
6. W. Hartmann, V. Dominic, G. F. Kirkman, and M. A. Gundersen, Appl. Phys. Lett. 53 (18), p. 1699, 1988
7. W. Hartmann, V. Dominic, G. F. Kirkman, and M. A. Gundersen, J. Appl. Phys. 65, (11), 4388 (1989)
8. G. Mechttersheimer, R. Kohler, J. Phys. E: Sci. Instr. 20, p. 270, 1987
9. G. Mechttersheimer, R. Kohler, T. Lasser, and T. Meyer, J. Phys. E: Sci. Instr. 19, p. 466, 1986
10. W. Hartmann, M. A. Gundersen, Proceed. of a NATO Advanced Research Workshop on "Physics and Applications of Hollow Electrode Glow Switches", M. A. Gundersen, editor (to be published)
11. A. Tinschmann, T. Okumura, M. Taniwaki, Jap. J. Appl. Phys. 29, no. 2, 371, 1990
12. H.J. Beyer, W. Bohmeier, W. Roß, et al., "CO<sub>2</sub>-Laser in der Materialbearbeitung", Sprechsaal, vol. 123, No 10, pp.1026, 1990
13. W. Roß, "Transversal angeregter CO<sub>2</sub>-Laser mit variabler Impulsdauer", Exp. Tech. d. Phys. 37, 3, pp. 225-232, 1989

## Damage Testing of Optical Components for High Power Excimer Lasers

36980005 The Hague EXCIMER LASERS AND THEIR APPLICATIONS in English 1991 pp 176-184

[Article by K.R. Mann and H. Gerhardt of the Laser-Laboratorium Gottingen e.V.]

[Text]

### ABSTRACT

At Laser-Laboratorium Göttingen damage and durability tests are performed on excimer laser optics. Within the automated experimental set-up image processing techniques are applied for both spatial laser beam profiling in the target plane and real-time damage recognition. Along with a description of experimental details, results of damage threshold measurements at 248 nm and 193 nm are presented, which demonstrate a strong relationship between absorption of laser radiation on defect sites and the subsequent damaging process. In addition, the influence of surface quality as well as laser pulse length on damage thresholds of fused silica substrates has been investigated.

### 1. INTRODUCTION

Since radiation induced damage to optical components has become a limiting factor for the development of high power lasers during last years, the measurement of damage thresholds for the optical materials employed is of increasing importance to the designer of new and more powerful laser systems. Being part of the EUREKA project EU 205, the damage testing facility of the Laser-Laboratorium Göttingen is used in close collaboration with optics manufacturers, in order to develop optical components of high damage resistivity for a future multi-kW-excimer laser. Routine damage tests are performed within a fully automated experimental set-up<sup>2,3,4</sup>, following the requirements of an ISO standard for damage threshold determination.<sup>5</sup>

Experimental details of damage testing like spatial laser beam profiling in the target plane and determination of peak energy densities are presented in the paper, as well as single pulse threshold data for fused silica substrates and high reflection dielectric coatings at 248 nm and 193 nm. In order to obtain a better understanding of the involved processes of laser material interaction, the influence of various experimental parameters on the measured thresholds has been investigated. A clear correlation is found between damage and temperature rise of the samples due to absorption during multiple pulse irradiation, as measured with a high resolution IR camera. Similarly, a relationship between surface roughness data and damage thresholds has been observed. We also report on first experiments with a pulse extension unit, which allows stretching of an excimer laser pulse from 25 ns to 200 ns in a stepwise tunable fashion.



## 2. EXPERIMENTAL

Since a detailed description of the automated measuring cycle has been given elsewhere<sup>3,4</sup>, the basic outline of the fully computerized experimental set-up will be addressed only briefly in the following (cf. Fig. 1). Main emphasis is put on details as laser beam profiling and determination of peak energy densities.

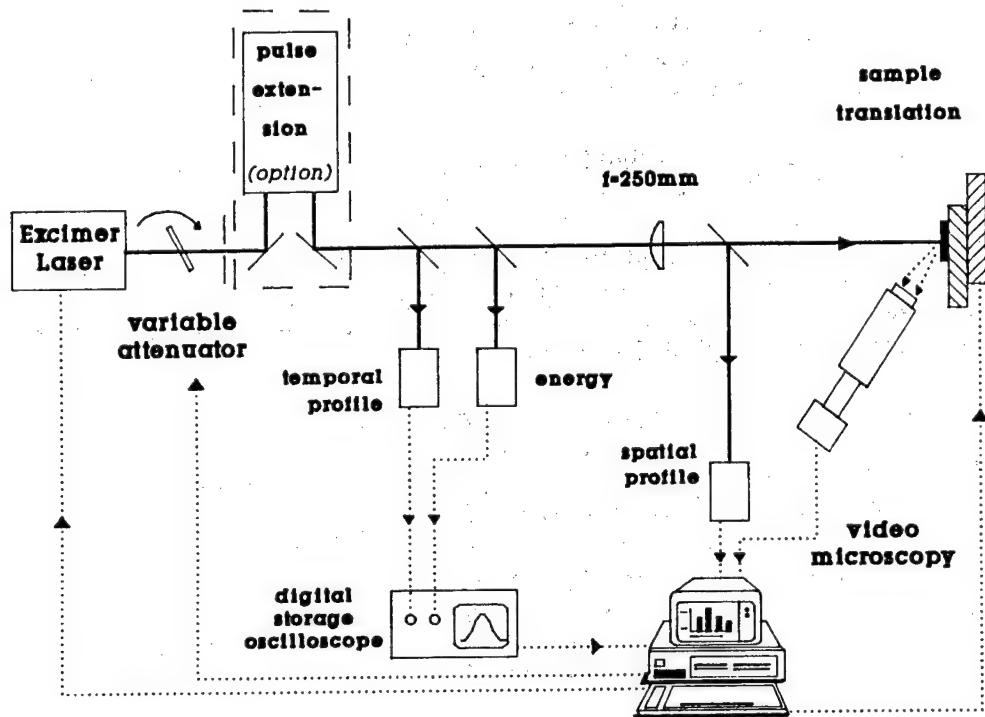


Fig. 1: Experimental arrangement

### 2.1 Beam control and diagnostics

The radiation of the employed excimer laser can be almost continuously attenuated using a dielectric filter, which is rotated by a high resolution stepper motor (2000 steps/rev., filter transmission 2...92%). Thus a stepwise variation of the energy density on the tested sample is possible, followed by an inspection whether or not the respective pulse has caused damage. Simultaneously, temporal profile and energy are monitored for each laser pulse, utilizing a fast digital storage oscilloscope (Fig. 1). The data are transferred to the computer for evaluation of exact energy densities (see below).

For other high power laser sources the necessary fluence values can be obtained merely by focussing the beam onto the sample, leading to Gaussian-like intensity distributions.<sup>6</sup> However, due to their high and often anisotropic divergence, this approach does not lead to satisfactory results in the case of excimer lasers. Therefore the same set-up is used as in most excimer laser ablation experiments, i.e. a demagnifying projection of a mask onto the sample surface. This has the advantage that rather flat-topped spatial beam profiles are achievable, and relatively large areas of a tested sample site can be

probed with almost constant energy density (see below). In our experiment, the demagnification factor is 7, leading to an increase in energy density by a factor of about 50 (imaging lens with  $f = 250$  mm). The spot diameter on the target is 0.7 mm.

## 2.2 Laser beam profiling

Since local intensity spikes of a laser pulse can easily distort the measurements, a precise determination of damage thresholds strongly requires a means to monitor the spatial laser beam profile in the plane of the target surface. For this purpose a special high resolution beam profiling system has been developed, consisting of a UV sensitive video camera, a PC-based frame grabber and a colour video monitor.

Broad band UV-sensitivity of the employed CCD camera is obtained by a conversion technique, as shown in Fig. 2: a strongly fluorescing glass plate converts incident UV radiation into the visible range of the spectrum, where the camera chip is sensitive. The plate has been thinned to a thickness of only 200  $\mu\text{m}$  in order to precisely determine the plane of fluorescence, which is imaged onto the CCD chip with a microscope objective. The linearity of the fluorescence with increasing laser pulse energy has been checked. This UV camera system is positioned into a plane equivalent to the sample surface, using a wedged beam splitter behind the imaging lens.

In order to obtain intensity distributions of single excimer pulses (pulse length  $\tau = 25$  ns), a synchronization between laser source and beam monitor is necessary. This is achieved by triggering the laser from the camera within a complex measuring program. The analogue video signal containing the profile is digitized by a PC based frame grabber (512 x 512 pixels, 8 bit greyvalues), stored in frame memory and displayed in real time on a video monitor. The field of view on this monitor has a width of 2 mm, corresponding to a spatial resolution of 4  $\mu\text{m}$  or 0.5% of the beam diameter. Fig. 3 shows the spatial profile of a KrF laser pulse in the sample plane, as obtained by imaging of a circular aperture. Horizontal and vertical crosssections as well as a 3D representation are displayed, indicating a rather flat intensity distribution without hot spots; the standard deviation on the plateau is 3% of the mean value.

For a further improvement of the intensity profile on the sample techniques of laser beam homogenization have to be applied. Work in this direction is in progress.

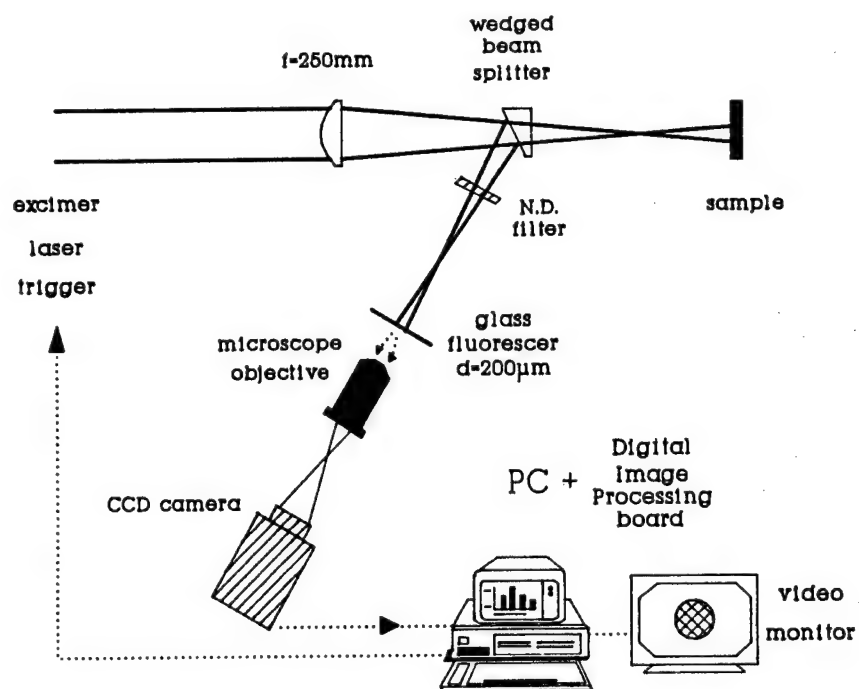


Fig. 2: Experimental set-up used for high resolution excimer laser beam profiling

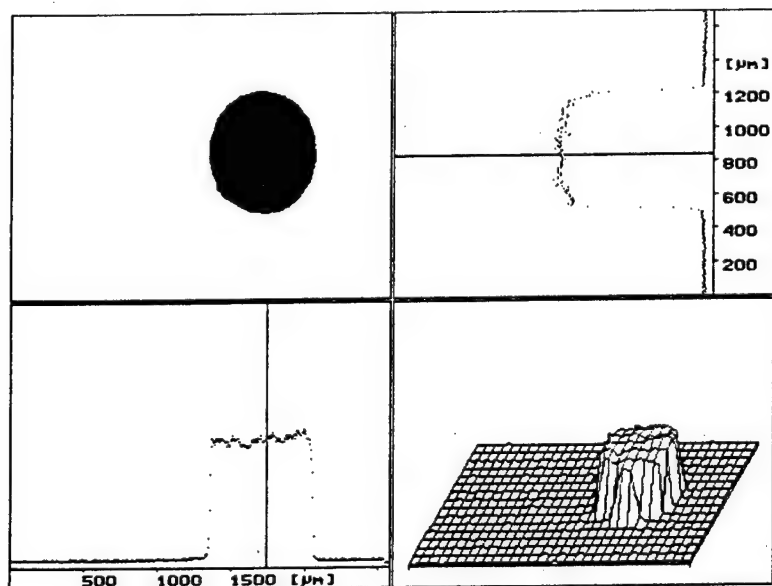


Fig. 3:  
KrF laser profile as  
measured in the target  
plane

### 2.3 Peak energy density

The most important measuring quantity in a damage experiment with pulsed laser radiation is the peak energy density  $H_{\max}$  on the sample. It is determined from the measured pulse energy  $Q$  and the spatial pulse profile in the following way, realizing that the pixel grey values  $i_{kl}$  stored in frame memory (cf. Sect. 2.2) are proportional to local energy densities  $H_{kl}$ :

1. Determination of the pixel with maximum grey value  $i_{\max}$
2. Computation of an effective area  $A_{\text{eff}}$  from the following identity:

$$\sum_{k,l} i_{kl} \cdot A_{\text{pixel}} = i_{\max} \cdot A_{\text{eff}},$$

where  $A_{\text{pixel}}$  is the area corresponding to a single pixel.

3. The peak energy density is then given by

$$H_{\max} = Q/A_{\text{eff}}.$$

This determination is in accordance with an ISO proposal for a standardized testing procedure.<sup>5</sup> Moreover, the accuracy of  $H_{\max}$  is enhanced by measuring  $Q$  and computing  $A_{\text{eff}}$  for each irradiating laser pulse. Hence, the measuring program accounts for pulse-to-pulse fluctuations of the beam.

### 2.4 Damage detection

Laser induced damage is detected on-line by help of a video microscopy system.<sup>4</sup> This device allows examination of the sample site to be tested on a monitor during the laser irradiation. Using an intense white light source, a dark field illumination of the sample is applied. Therefore, any micro-roughnesses created by the laser pulse will show up as bright spots with high contrast in the microscopic image. The sensitivity of this technique has been shown to be equivalent to Nomarski microscopy<sup>2</sup>, which is used as an off-line reference method.

As in the case of spatial beam profiling, the video signal of the microscope camera is stored in frame memory of the digital image processing board on the PC, once before and once after the laser has been triggered. The subsequent pixelwise comparison of the digitized micrographs guarantees an unbiased decision whether or not the respective laser pulse has caused damage (cf. also Sect. 3.2).

## 3. RESULTS AND DISCUSSION

### 3.1 Damage thresholds (248 nm and 193 nm)

Single pulse ("1-on-1") damage thresholds have been measured for a large number of high reflection (HR) dielectric coatings at 248 nm and 193 nm. In order to obtain general trends, the results are summarized in Table 1, separated for fluoride and oxide layer systems. The comparison of these data shows, that for both laser wavelengths the fluoride coatings have a considerably higher damage resistance as compared to oxide systems, although their mechanical properties and long-term stability are worse.

	248 nm	193 nm
Fluorides	4.5 - 6	0.8 - 2
Oxides	2 - 4	0.2 - 1

Table 1: Damage thresholds of HR dielectric coatings (in  $\text{J}/\text{cm}^2$ )

Another interesting result from Table 1 is the strong wavelength dependence of the measured damage thresholds, which can be easily explained by the higher absorptivity of all the employed coating materials at 193 nm.

The single pulse damage thresholds of fused silica (Suprasil I) substrates are found to be considerably higher than those for dielectric coatings. Measured values range from 5 to 9  $\text{J}/\text{cm}^2$  at 248 nm and 3 to 5  $\text{J}/\text{cm}^2$  at 193 nm, in accordance with previously published results.<sup>8</sup> In any case damage starts at the rear surface of the samples, which can be explained by constructive interference at the exit boundary.<sup>9</sup> However, since the amount of this effect depends on the sample thickness and the probe beam f-number, all data quoted in the remainder of this paper refer to front surface damage.

### 3.2 Inclusion heating

In all cases of HR dielectric coatings damage is found to be dominated by defects and impurities within the quarterwave layers, as can be readily seen from a comparison of the digitized microscopic images (cf. Sect. 2.4) in Fig. 4: grey values of the same site of a HR coating are shown in a 3D representation, once before and once after irradiation with a single KrF laser pulse. The energy density was chosen slightly above threshold. Clearly, damage starts at defect sites, which are visible already before testing. They absorb an amount of energy from the radiation field, which is sufficient for a

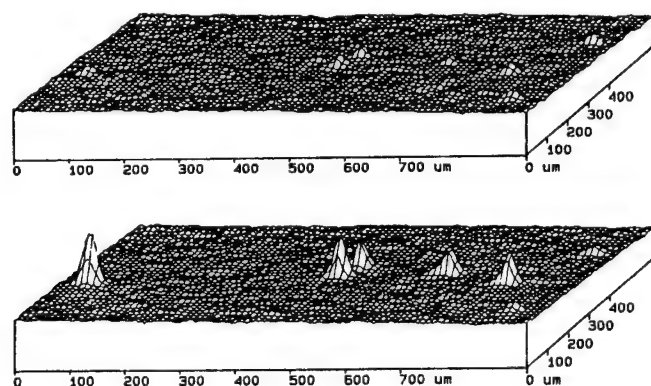


Fig. 4: Digitized micrographs of HR coating, before (above) and after KrF laser pulse

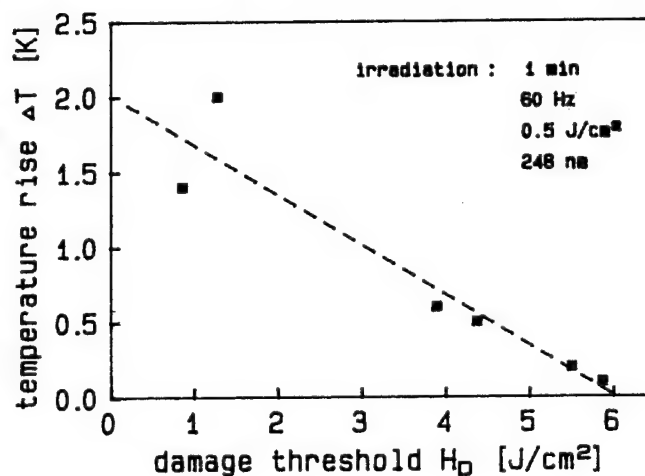


Fig. 5: Temperature rise vs. damage threshold of dielectric coatings on Suprasil (cf. text)

thermal disruption of the coating (inclusion heating model<sup>10</sup>). Following this theory, local temperatures in the range of a few thousand K are possible for sub- $\mu\text{m}$ -sized absorbing particles. Due to heat conduction to the host material, these temperatures will equilibrate immediately after the laser pulse, making a direct measurement extremely difficult.

However, the combined heating effect of the impurities and defects on a sample can be studied under multiple pulse irradiation, as shown in Fig. 5 for several dielectric coatings on Suprasil substrates ( $\lambda = 248 \text{ nm}$ ). The macroscopic temperature rise has been measured using a high sensitivity thermographic camera (Inframetrics model 600,  $\lambda = 8\text{--}12 \mu\text{m}$ , thermal resolution  $0.1\text{K}$ ), by imaging the irradiated surface area of about  $6 \times 4 \text{ mm}^2$ . Equilibrium temperature is reached after approximately 1 min of sub-threshold bombardment ( $0.5 \text{ J/cm}^2$ ,  $60 \text{ Hz}$ , i.e.  $30 \text{ W/cm}^2$ ).

As seen from Fig. 5, the absolute values of  $\Delta T$  are remarkably small ( $0.2 - 2\text{K}$ ); they are plotted against the single pulse damage thresholds of the samples, which had been determined for  $248 \text{ nm}$  before the irradiation. The data indicate a clear correlation between temperature rise by absorption of radiation and damage threshold, in support of previously published results for bare substrates.<sup>3</sup> Due to the higher absorption coefficient at  $193 \text{ nm}$  the heating effect is found to be larger at this wavelength, which is in accordance with the damage threshold data of Sect 3.1.

### 3.3 Influence of surface roughness

The influence of surface quality on the damage resistance at  $248\text{nm}$  has been investigated for a set of 24 fused silica samples, which had been produced as preforms for quartz fibres. All samples were of identical composition and had been manufactured in the same way, except for different surface polishes. The variations in surface quality were observable as differing defect densities in dark field microscopy or, more quantitatively, by measurement of the surface roughness. The latter was performed with a mechanical profilometer (Dektak 3030); profiles were recorded using a scan width of  $200 \mu\text{m}$ , followed by a computation of the corresponding rms-roughness values.

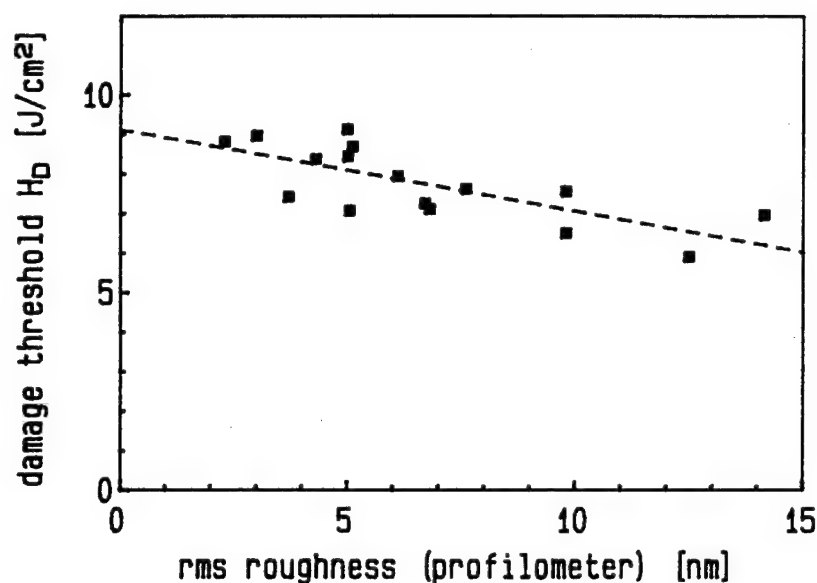


Fig. 6:

Correlation between surface roughness and damage threshold for fused silica at  $248\text{nm}$

Front surface damage thresholds have been measured for all samples at 248 nm. Although the damaging sites cannot always be identified as already existing defects (like in the case of dielectric coatings), the data show a clear trend: the lower the defect density seen in the microscope, the higher the damage resistivity.

This observation is supported by a comparison with the corresponding rms roughness values plotted in Fig. 6. In spite of the large scatter of the roughness data, a clear correlation between surface quality and damage thresholds can be observed: Due to the lower defect densities less radiation is absorbed on the smoother surfaces (rms-roughness 2-4 nm), leading to about 30% higher damage thresholds than in the case of insufficient surface polishes (rms-roughness 10-15 nm). Thus, as for the dielectric coatings, the data suggest an impurity dominated damaging process for fused silica.

### 3.4 Influence of pulse length

Although of great importance for possible scaling laws and the understanding of damaging processes, only very few well established results are available on the pulse length dependence of laser damage thresholds.<sup>9,11</sup> In many cases the data suffer from the fact, that different laser sources with varying spatial profiles and spot sizes had to be used.<sup>12</sup>

At the Laser-Laboratorium Göttingen first experiments have been performed with a commercially available pulse extension unit for excimer lasers (Exitech Ltd., U.K.). Utilizing a multiple reflection optical delay line, the device allows stretching of an excimer laser pulse (248 nm or 308 nm) from its initial value (25 ns) up to 200 ns in steps of 25 ns. The various achievable temporal profiles for KrF laser radiation are compiled in Fig. 7, showing an intensity modulation of the order of 25%. By integration of the pulse extender into the testing facility (cf. Fig. 1), damage thresholds can be measured within the same experimental set-up at pulse lengths varying over almost one order of magnitude.

First results have been obtained for a fused silica substrate (Suprasil I): front surface damage thresholds  $H_D$  were measured at 248 nm for 8 different effective pulse durations  $\tau_{eff}$ , showing a monotonic increase from 5 J/cm<sup>2</sup> at 35 ns to 11.6 J/cm<sup>2</sup> at 205 ns. The log-log plot of the data in Fig. 8 indicates a power law dependence

$$H_D = \text{const.} \cdot \tau_{eff}^x,$$

with an exponent  $x = 0.47$ . This is in very good agreement with the square root dependence observed by Taylor et al.<sup>11</sup> for fused silica at 308 nm. However, preliminary results for dielectric coatings suggest quite a different pulse length dependence of the damage threshold, which might be an indication that other types of interaction processes are involved. Further studies are in preparation, including also damage measurements with a femtosecond excimer laser system.

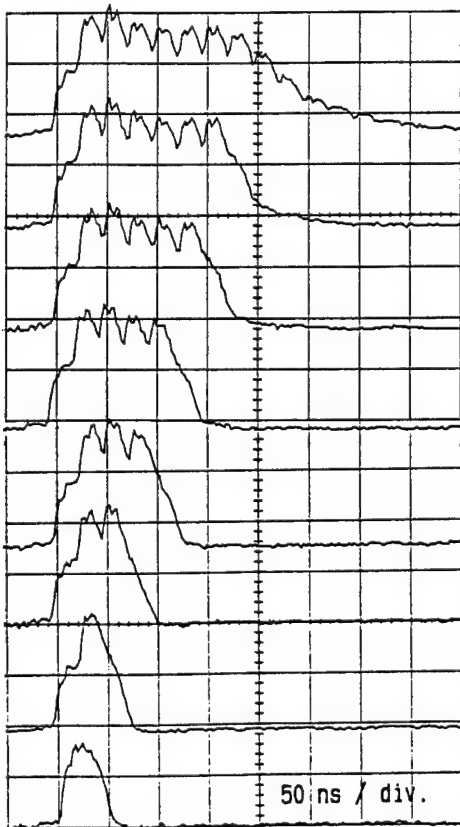


Fig. 7: Temporal laser pulse profiles achievable with stretching unit for 248 nm

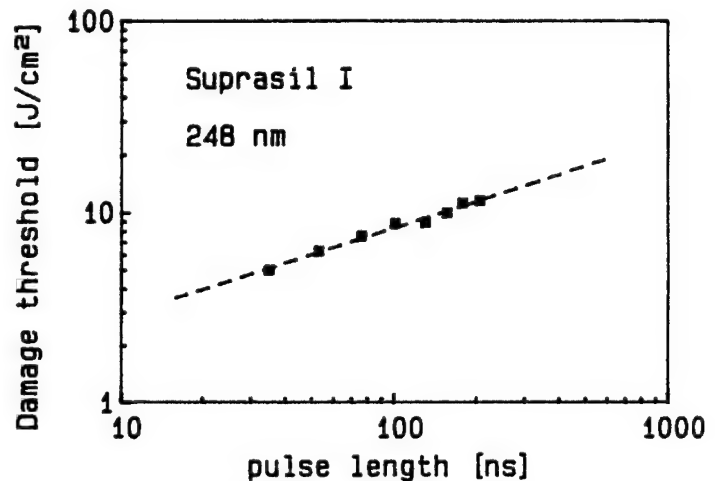


Fig. 8: Damage thresholds as a function of effective pulse lengths (cf. text)

#### 4. CONCLUSION

A damage testing facility for excimer laser optics has been presented, which includes high resolution laser beam profiling in the sample plane as well as video microscopy for damage recognition. Using techniques of digital image processing, it could be shown that UV radiation damage on high reflection dielectric coatings is dominated by impurities and defects within the thin film layers. Inclusion heating is also responsible for the damaging of fused silica substrates, as can be derived from the observed relationship between damage thresholds and surface roughness data. In addition, the dominant role of the absorption coefficient for the understanding of damaging processes is emphasized by the correlation between damage thresholds and temperature rise, as measured with a thermographic camera on excimer laser irradiated HR coatings. Finally, first results obtained with a pulse stretching unit for excimer lasers suggest a square root dependence of fused silica damage thresholds from the laser pulse length.



## 5. ACKNOWLEDGEMENTS

The assistance of G. Pfeifer (Ingenieur-Hochschule Mittweida) during the measurements of the pulse length dependence is gratefully acknowledged. We also like to thank U. Grzesik and H. Fabian from Heraeus Quarzglas for stimulating discussions, as well as for the supply of fused silica samples for the surface roughness experiments.

## 6. REFERENCES

1. see e.g.: "Laser Induced Damage in Optical Materials: 1989, NIST Spec. Publ.775 (1989)
2. K.Mann, H.Gerhardt, "Excimer Lasers and Applications", SPIE Vol.1023, 136 (1988)
3. K.Mann, H.Gerhardt, "Laser Induced Damage in Optical Materials: 1989", NIST Spec. Publ. 801, 39 (1989)
4. K.Mann, H.Gerhardt, "Laser und Optoelektronik" 21, 42 (1989)
5. "Test method for laser induced damage threshold of optical surfaces", committee draft ISO/CD 11254 (1990)
6. see e.g.: A.F.Stewart, A.H.Guenther, Appl. Optics 23, 3774 (1984)
7. J.Kolbe et al., "Laser Induced Damage in Optical Materials: 1989", NIST Spec. Publ. 801, 404 (1990)
8. F.Rainer, E.A.Hildum, "Excimer Lasers and Optics", SPIE Vol. 710, 74 (1986)
9. R.Rainer, W.H.Lowdermilk, D.Milam, Opt. Eng. 22, 431 (1983)
10. T.W.Walker, A.H.Guenther, P.E.Nielsen: IEEE Journ. Quantum Electr. QE-17, 2053 (1981)
11. R.S.Taylor, K.E.Leopold, S.Mihailov, Optics Commun. 63, 26 (1987)
12. A.H.Guenther et al., Appl. Optics 23, 3743 (1984)

## Excimer Laser with Sealed X-Ray Preionizer

36980005 The Hague EXCIMER LASERS AND THEIR APPLICATIONS in English 1991 pp 197-199

[Article by Vladimir V. Atezhev, Sergey R. Belov, Viacheslav S. Bukreev, Sergey K. Vartapetov, Alexander N. Zhukov, Ilmur T. Ziganshin, Alexander M. Prokhorov, Alexey E. Soldatkin, and Yuri D. Stepanov of the General Physics Institute]

[Text]

### ABSTRACT

In this paper we present the description of X-ray preionized excimer laser. For this laser the special sealed metal-ceramic X-ray preionizer with cold cathode was constructed. The cathode was made from a carbon felt and had  $4 \times 80 \text{ cm}^2$  area. The discharge volume was  $70 \times 4 \times 3 \text{ cm}^3$  and on XeCl one provided the energy up to 2 J in a pulse.

In the same discharge chamber the different type of preionizers (spark discharges, UV laser radiation) were investigated. It was shown that the output energy depends rather the electron density uniformity than the electron concentration.

For the pulse energy of excimer laser increasing high uniformity discharge in large volume must be produced. In this case the demands upon discharge volume preionization are very strict. The main parameters of preionizer are the initial electrons density, it's uniformity and the preionizers action on the gas mixture life time.

UV preionization by spark discharges produces high electron density ( $\sim 10^{10} \text{ cm}^{-3}$ ).<sup>1</sup> But in this system the electron density is not uniform because of hard UV-radiation high absorption and discreetly distribution of sparks. Beside the sparks produce impurities and this process diminishes the gas lifetime.

UV preionization by laser source produces more uniform initial electron density on the level  $10^8 \text{ cm}^{-3}$ .<sup>2</sup> But it's not convenient because it demands the use of low ionization additives or powerful external excimer laser.

The use of X-ray preionization is the best decision of problem the excimer laser to large volume and energy scaling because of X-rays large penetration depth.<sup>1,3</sup>

In this paper we present the description of X-ray preionized excimer laser and compare on the output laser parameters with the preionizers of another types.

Fig.1 shows the laser chamber with sealed metal-ceramic X-ray preionizer. The carbon cathode of X-ray preionizer has an area of  $6 \times 80 \text{ cm}^2$  and is placed in the electrostatic screen. The anode is W-foil  $5 \mu\text{m}$

thick cooling by water. The output window is manufactured from stainless steel 50  $\mu\text{m}$  thick. The X-ray preionizer was supplied by the electrostatic and getter vacuum pumps. Pressure inside the X-ray preionizer didn't exceed the value  $10^{-8}$  Pa. The e-beam diode was fed by Marx generator with amplitude voltage up to 120 kV with risetime  $\sim 100$  ns.

The laser chamber was constructed of polyamid and designed for gas pressure up to 6 atm. The laser electrodes were composed from two contoured shape electrodes. The flat electrodes were  $80 \times 40 \text{ cm}^2$  size. The electrode gap was 4 cm width.

One electrode was milled down in center to 0.6 mm thick and was covered by Al foil 0.5 mm thick. The cavity inside the electrode was filled by buffer gas at working pressure.

The laser chamber windows were UV-quartz plates with antireflection coating. The plane parallel optical cavity was produced by 100 % reflectivity dielectric mirror and uncoated quartz plate as an output coupler.

The electrical circuit of our excimer laser is shown in fig.2. The laser discharge was driven by four parallel circuits with magnetic switches.<sup>4</sup> The ceramic capacitors were used. The magnetic switches were nonlinear inductors with  $40 \text{ cm}^2$  ferrite core full cross section and saturation magnetization 0,3 T.

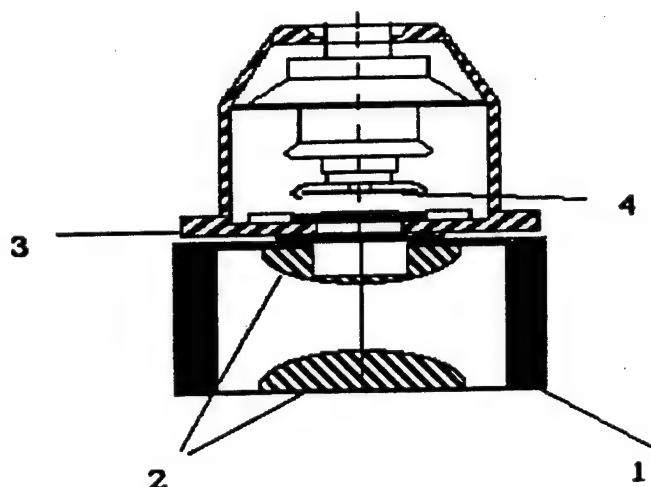


Fig.1. Cross section of the laser with X-ray preionizer  
1-laser chamber, 2-discharge electrodes, 3-X-ray preionizer, 4-carbon felt

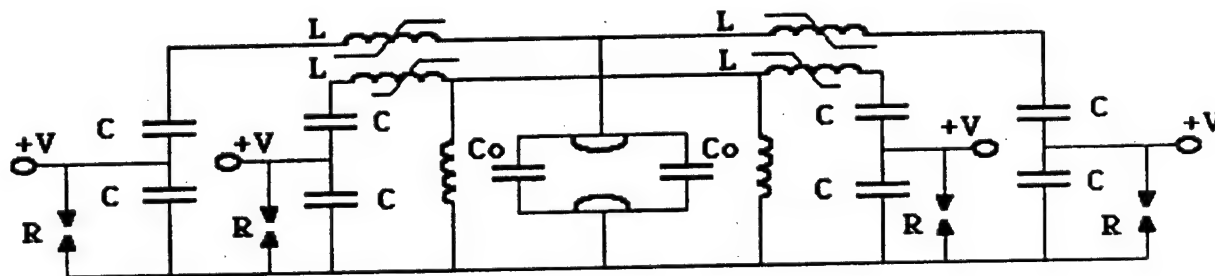


Fig.2. Schematic diagram of discharge pumping circuit  
C=16nF-main discharge capacitors, Co=25nF-peaking capacitors, R-spark gap,  
+V-charging voltage, L-nonlinear magnetic switch

In Fig 3 the voltage waveform on the X-ray preionizer, on the laser electrode and optical pulse shape are shown. The maximal energy obtained was 2 J ( efficiency 1,5% ) at 4 atm total pressure Ne-base mixture and 40 kV load voltage.

The output energy strongly depended on X-ray preionizer voltage. Saturation of output energy begun at a voltage about 120 kV ( the maximum voltage which we could produce in our experiments).

It is very important to compare the influence of different types of preionizers on laser output parameters. For this purpose we compared the output energies of lasers with the same discharge chambers but with the different preionization types: X-rays, laser and sparks preionization. Spark preionization was produced by 3 sets of 54 sparks with the distance between sparks 14 mm. In this case one of electrodes was changed for the screen electrode. The distance between sparks array and screen electrode was 30 mm. The maximum achieved energy in this case was 1.5 J. For laser preionization the KrF laser with 400 mJ energy per pulse and  $10^{-3}$  rad divergence was used.

The experiments were performed with solid electrodes as in the case of X-ray preionization (XP) and with mesh electrode as in the of sparks preionization (SP) case. The output energy was saturated at  $10 \text{ mJ/cm}^2$  preionization density and reached 2.1 J. Some amount of additives (benzol) in gas mixture increased output energy non essential.

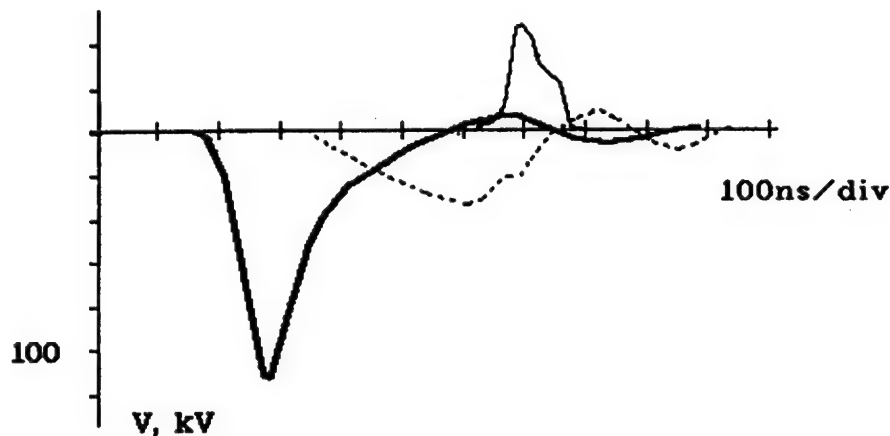


Fig.3. Time histories of the voltage on the X-ray diode (solid line), discharge voltage waveform (dashed line), laser intensity (thin line)

The main results of our experiments are presented in following points:

- The output energy under XP ( $E_{XP}$ ) and laser preionization ( $E_{LP}$ ) was approximately the same ( $E_{XP} \sim E_{LP} \sim 2 \text{ J}$ )
- The output energy under sparks preionization ( $E_{SP} \sim 1,5 \text{ J}$ ) was smaller then under laser preionization ( $E_{SP} < E_{LP}$ ).
- Under simultaneous action of laser and sparks preionization the output energy didn't increase  $E_{SP+LP} \sim E_{SP} \sim 1.5 \text{ J}$

It can be connected with poor initial electrons density uniformity provided by sparks preionization.

In conclusion the influence of different preionizers types on the laser output energy was investigated. It was found, that for large laser energy production the initial electrons density uniformity may be more important than the absolute value of electrons density.

### REFERENCES

1. K.Midorikawa, M.Obara, T.Fujioka, "X-ray preionization of rare-gas-halide lasers", IEEE J.Quantum Elektron.,vol.QE-20, pp.198-204, No 3, March 1984.
2. R.S.Taylor, "Preionization and discharge stability study of long optical pulse duration UV-preionized Xe-Cl lasers", Appl. Phys. B 41, pp.1-24, 1986.
3. S.C.Lin, J.I.Levatter, "X-ray preionization for electric discharge lasers", Appl. Phys. Lett.,34(8), pp.505-508, Apr. 1979.
4. V.P.Atiejev, V.S.Bukreev, S.K.Vartapetov, A.N.Zhukov "Pulse repetition rate excimer laser with double magnetic switch circuits", Pizma v JTF, vol.16, No 2, pp.1-4, 1990 (in russian).

## Part Two: Laser Applications

36980005 The Hague EXCIMER LASERS AND THEIR APPLICATIONS in English 1991 p 203

[Article by Lucien D. Laude of the Universite de l'Etat Mons]

### [Text] Introduction

Among the various laser sources available today for materials processing, excimer lasers have revealed through the years a formidable potential, imbedded in both the UV wavelength at which they emit and their actual short time of emission. These characteristics are responsible for a very specific chemistry, both in gas phase or at solid surfaces, which allows for instant processing of such diverse materials as hard ceramics, soft polymer, composites, metals, and semiconductors. One of the objectives of this symposium was to precisely underline this diversity by calling for presentations on research activities in the broad field of excimer laser interactions with such materials. As evidenced in this proceedings, the response of the scientific community to this call undoubtedly demonstrates the vitality and richness of a field that is now emerging as the dominant theme of research in laser materials processing.

Although fundamental aspects are still scarce, somewhat more attention is paid to a better understanding of the phenomenologies involved. Still, efforts are needed, particularly in the kinetics of physical processes. Clearly, instrumentation is not the unique concern here, but concept should be put forward, as, for example, in the UV-pulsed irradiation of polymers or in the surface chemistry of excimer-laser-irradiated ceramics. The reader will notice in the series of papers presented in the symposium, the outrageous attraction (and pressure) of industrial concerns in a field that still needs time to establish its own fundamental machinery. The latter is of prime importance if, as understood, effective applications in the industry are at stake that require control and perspective. As in many fashionable research activities, and critically for one that shows so much possibility, speed and insight have not increased proportionately. At best, one would suggest more cooperative research programs in this field, mixing chemists and physicists, fundamentalists and engineers. This would be an answer to the current trend in contemporary materials research: do it fast...and well.

## Excimer Laser Patterning of Flexible Materials

36980005 The Hague EXCIMER LASERS AND THEIR APPLICATIONS in English 1991 pp 215-222

[Article by Z. Kollia and E.I. Hontzopoulos of FORTH-Institute of Electronic Structure and Laser, Laser Applications Laboratory]

[Text]

### ABSTRACT

The use of excimer laser for patterning flexible materials such as polyethylene/non-woven in sheets, is reported. This technique is compared with two widely used non-laser techniques, rotary dies and water jet. Excimer laser processing parameters e.g. laser wavelength, power density etc., will be discussed in relation to the final cut quality.

### 1. INTRODUCTION

In the field of industrial patterning/drilling processes of flexible sheet materials or rolls of plastics and fabrics, most companies require high cadence combined with a good cutting quality. To achieve these objectives, two major types of technologies, based on mechanical processing by needles or blades (rotary dies or pressed) and water-jets, are currently in use. Despite the high processing speeds obtained there are several serious drawbacks associated with each of these technologies, such as a high percentage of lost material, frequent shut down time, rigorous maintenance requirements (particular with blades), in addition to environmental pollution and water consumption problems when water-jets are used. Furthermore, in several cases the quality of processing is not always up to a satisfactory standard.

An alternative technology based on laser processing has been considered and in a few cases applied in the fabrics industry. The use of lasers for patterning sheets of flexible materials may offer several advantages over conventional mechanical methods. High-power lasers (CO<sub>2</sub>, Nd:YAG and Excimer lasers) can in principle produce clean and good quality cutting or hole drilling at high speeds, with computer controlled precision shaping of the cut material.

In this paper the application of an excimer based system for patterning flexible sheet application is presented and the influence of basic laser processing parameters is discussed.

### 2. EXISTING PATTERNING TECHNIQUES

#### 2.1 Rotary dies

The oldest existing cutting techniques is the one that uses dies. There are two different type of dies. In the first case the die with the specific shape is pressed into the material, while in the second one, the die is around a cylinder which is rotated. The rotary dies are applied for simpler shapes and/or when the material to be cut is in rolls and flows.

This technique, rotary dies, has many disadvantages such as mechanical stress of the material, limited die life time, differing specifications after each die resharping, standard patterning shape or size with each die, not always controllable patterning quality, but it does present two very important advantages, simplicity and low maintenance cost.

The cutting with dies is a contact technique which produces mechanical stresses to the material and the processing volume is low. The dies very often need to be resharping due to blade destruction and this introduces size changes of the product, after each resharping.

Furthermore, cutting with dies presents low flexibility because with each die only one shape and/ or size can be cut. This means that a series of dies are needed for patterning shapes in different sizes and computer control can not be applied.

## **2.2 Water jet**

In the past few years high pressure water jet systems have gained wide acceptance in many industries as cutting tools. The improving reliability of the technique offered the possibility of its integration into the manufacturing process on the factory floor.

The principle of the water jet<sup>1</sup> technique is the use of a high pressure (as high as 60.000 psi) water beam, that patterns the material by compressive shear or erosive action.

Two types of water jet systems are in use, with or without abrasive particles (eg. garnet, silica,  $\text{Al}_2\text{O}_3$ , SiC etc). The erosive action of the abrasive water jets are used for cutting thicker and harder materials (eg. metals, ceramics etc).

The water jet and laser techniques are competing technologies and the final choice depends strongly on the particular application at hand. When pure water jet systems are employed in the specific application of our interest, they present disadvantages such as high water consumption, expensive system maintenance, high cost for water purification and water system maintenance, pollution problems due to the fiber that are included in the waste water, but in contrast the high working speed and the flexibility in shape changes are important advantages over the rotary dies.

## **3. EXCIMER LASER BASED SYSTEM**

### **3.1 Laser technique**

High power laser based systems are an alternative technology and its application as cutting tool is a widely accepted manufacturing process in the industrial environment. There are three types of laser of great industrial importance, namely the  $\text{CO}_2$  and Nd: YAG lasers emitting at 10.6  $\mu\text{m}$  and 1.06  $\mu\text{m}$  respectively and the excimer laser emitting at shorter wavelengths (190-350 nm). The first two have been extensively used in industrial applications, especially in the metalworking section, while the latter appears to be a new industrial tool with great potential.

The principle of laser cutting is based on the absorption of the laser beam into the material, which causes melting or decomposition and at a later stage evaporation or removal of the material. The first mechanism, absorption/ melting/ evaporation, can be applied to the infrared lasers ( $\text{CO}_2$  and Nd:YAG), that thermally interact with matter. The second one, absorption/ decomposition/ material removal, is the case for the excimer lasers and it is called ablation, and it is a non-thermal interaction. In many cases, this ablation mechanism<sup>2-4</sup> results in a higher degree of precision than can be achieved with the former types of laser processing. Excimer laser processing/ patterning technology, that is of our interest, has successfully been applied in many fields<sup>4</sup>, like as instance microlithography, microsurgery and micromachining of materials.

The ablation mechanism includes three stages and can be described as follows. The first stage of the mechanism is the absorption of the laser beam. It is well established that most of the organic materials exhibit very high absorption in the UV, which means that most of the energy is absorbed in a very thin surface layer (0.1-0.5  $\mu\text{m}$ ). If the absorbed energy is higher than a certain threshold (energy required to overcome relaxation processes in the material), many chemical bonds



of the material break. This is the second stage of the ablation mechanism. Below this threshold the absorbed photon energy is deposited as heat. The threshold energies for the most important plastics<sup>5</sup> are in the range 0.1-3.5 J/cm<sup>2</sup>, at 308 nm (XeCl laser). In the third and last stage of the mechanism, the products of the decomposition/ dissociation are explosively removed away from the irradiated region. The driving forces for this phenomenon are (I) the large increase in the specific volume of the fragments compared to the polymer chains they replace and (II) the excess energy of the UV photon compared to the chemical bond that is broken.

Furthermore due to the short wavelength the focussability of excimer laser beam is much higher than that of infrared lasers allowing interesting micromachining applications. Laser technology exhibits advantages over the two other techniques (rotary dies and water jet) discussed before. There are no material mechanical stresses because it is a non-contact technique, while the cut edges are clear and sharp. The patterning shape or size can be easily changed, through computer control meaning higher flexibility.

### 3.2 Material

For the present application, the material used is a sandwich composed of two films, polyethylene and polypropelene in a non-woven form. The material is in sheet form and total thickness is of the order of 50-55  $\mu\text{m}$ . During the experiments this thin sheet was symmetrically stretched and it was not in contact with other materials.

### 3.3 Experimental set up

In Fig. 1 shows the experimental set up that was used. This comprises three main parts, the excimer, the laser beam delivery optics and the workstation.

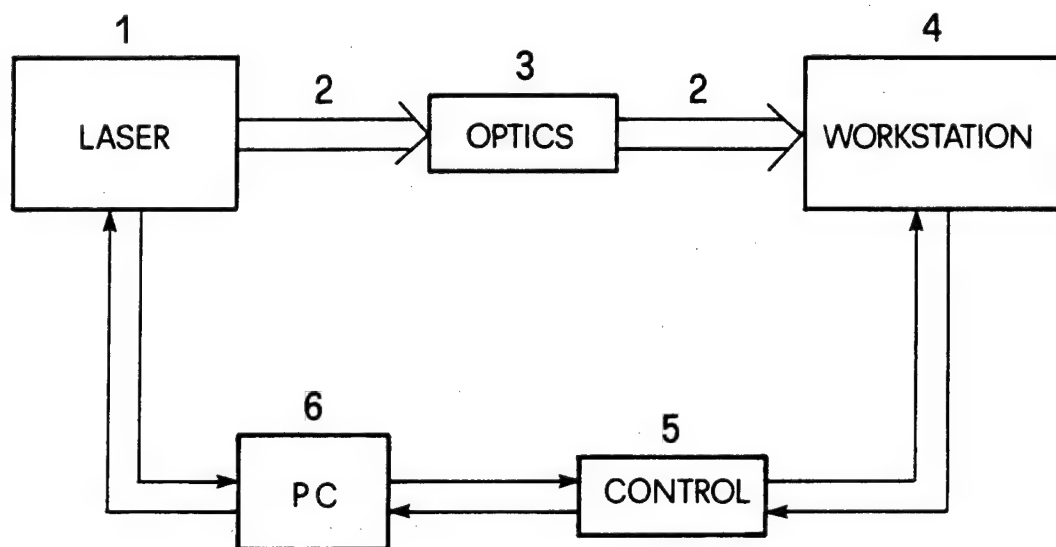


Fig. 1 : Experimental set up for excimer laser patterning applications: 1) Excimer laser LPX 210 iF, 2) Excimer laser beam, 3) Beam delivery optics, 4) Patterning work station with x, y, z motions, 5) Workstation interface and control unit and, 6) Personal computer driving both the laser and the workstation

A Lambda Physik model LPX 210 iF excimer laser, emitting at 193 (ArF mixture) and 248 (KrF mixture), and a maximum repetition rate of 100 Hz was employed. The beam delivery optics include steering mirrors, a lens and an iris, and together with the workstation could deliver the excimer laser beam along the three axes (x, y, z) under stepper motor

control. A Suprasil B lens of 100 mm focal length was used to image the iris onto the material. Both the excimer laser and the workstation were driven by an AT personal computer, where the pattern shape had been previously established. The maximum dimension of the work area is 0.80 x 0.90 m.

The laser processing parameters such patterning shape, power density incident on the material surface, number of pulses per step, overlap percentage between the steps were altered under the computer control.

The evaluation of the cutting quality was performed by an optical microscope and the use of an empirical scale with five levels. The meaning of these five quality levels is :

Quality 0 : The material is not completely cut.

Quality 1 : The material is cut, but both films (polyethylene and polypropylene) have "black" edges.

Quality 2 : The black colour of the edges is less.

Quality 3 : Only the polyethylene part of the material has "black" edges.

Quality 4 : Fine cut with colourless cut edges.

### 3.4 Results and discussion

The pattern that was used during all the experiments is shown in Fig. 2a. This pattern includes all possible cutting directions and shapes such as straight line (horizontal, perpendicular and diagonal) and half circle. In this way resulting cut will average out dependences on the cutting process and material inconsistencies.

The excimer laser processing parameters that were varied in the experiments, such as power density, number of laser pulses per step, overlap percentage between irradiation pulses and laser wavelength, allowed a detailed study of the cut quality and processing time required.

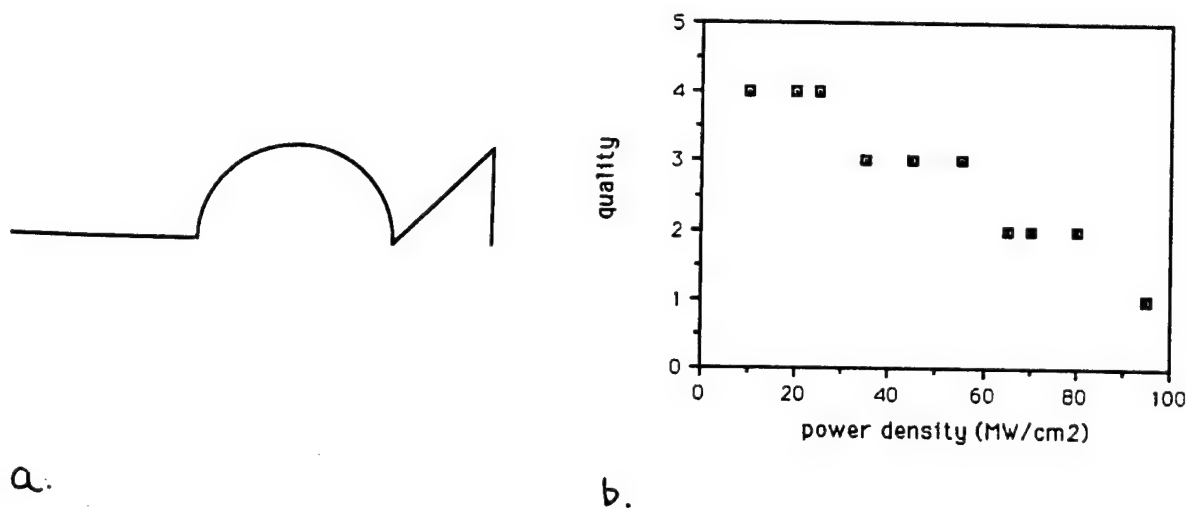


Fig. 2 : a) The pattern used in the experiments, b) influence of the power density on the cut quality (248 nm, 100 Hz, 50% overlap and 10 pulses/step).

The cut quality increases dramatically by decreasing the power density. Fig. 2b shows that the cutting quality is of level 4 for power densities below  $30 \text{ MW/cm}^2$ . In the same way, the overlap percentage is influenced by the decrease of the power density. (Fig. 3a, b). In Fig 3a the power density is  $70 \text{ MW/cm}^2$  and for a cut quality of 4, 90% overlap is needed. The overlap decreases to 60% by only changing the power density to half the above value, namely  $35 \text{ MW/cm}^2$  (Fig. 3b). A comparison of Fig. 3b and 3c shows that the overlap percentage for cut quality 4 changes from 60% to 40% by using double pulses per step and the same power density.

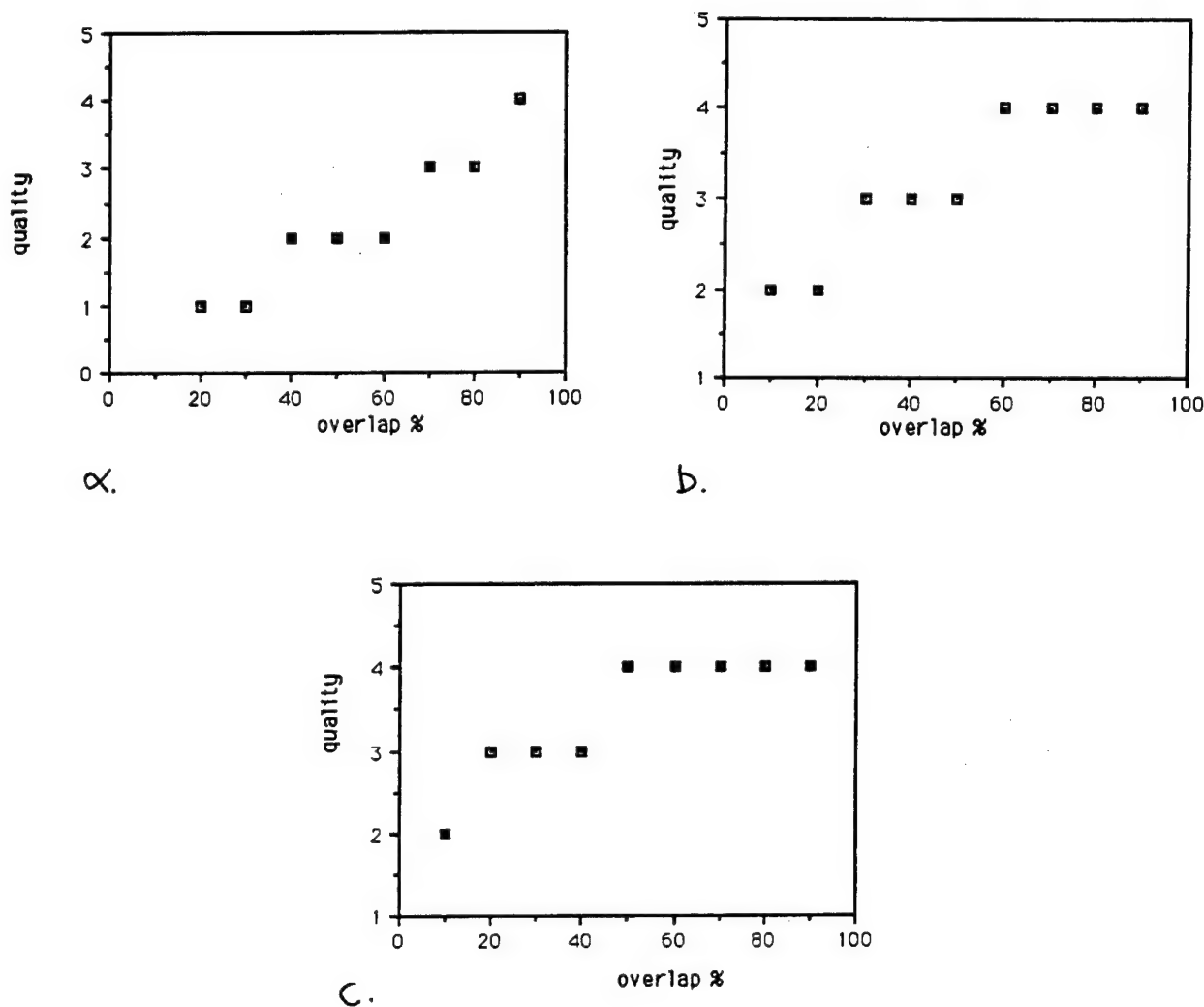


Fig. 3 : Influence of overlap percentage on cut quality, at 248 nm and 100 Hz : a)  $70 \text{ MW/cm}^2$ , 10 pulses/step, b)  $35 \text{ MW/cm}^2$ , 10 pulses/step and c)  $35 \text{ MW/cm}^2$ , 20 pulses/step.

Because all three processing parameters influence the cut quality to a large extent, an attempt was made to map out with "best combination" of the above parameters. This is shown in Fig. 4. It is clear by looking at Fig. 4a and Fig. 4b,

where a KrF (248 nm) and an ArF (193 nm) laser were respectively used, that the shorter wavelength (193 nm) is giving better results at a lower overlap percentage, while the number of pulses must be reduced (Fig. 5).

All the above parameters have a great influence on the processing speed. Fig. 6a demonstrates that the use of an ArF (193 nm) laser, increases the total processing throughput. Fig. 6b shows the influence of the number of pulses per step, at different overlap to the processing time, using an ArF laser.

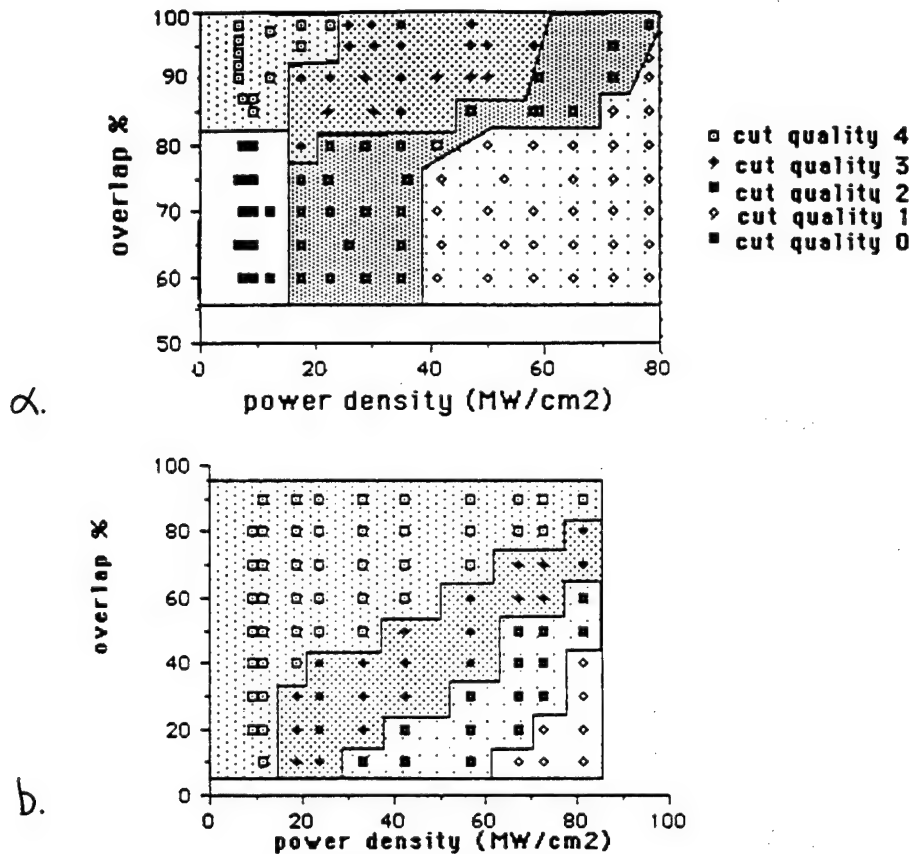


Fig. 4 : Excimer laser processing map: a) KrF laser (248 nm), 100 Hz and 10 pulses/step, b) ArF laser (193 nm), 100 Hz and 10 pulses/step.

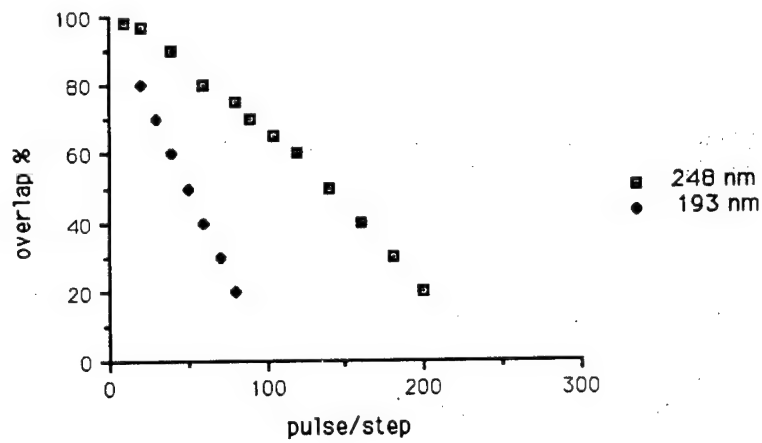


Fig. 5 : Plot of overlap percentage versus the number of pulses per step for cut quality 4, at 248 and 193 nm. All other processing parameter are the same.

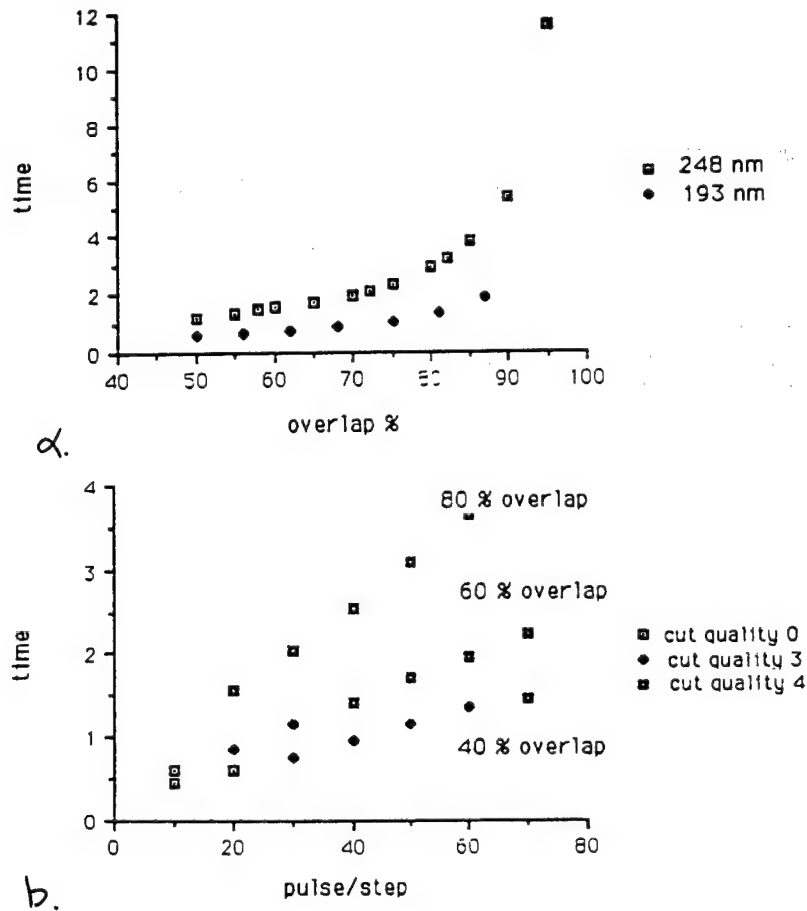


Fig. 6 : Influence of overlap percentage (a) and the number of laser pulses per step (b), to the processing time.

#### 4. CONCLUSIONS

Excimer laser based systems can be used for patterning sheets of flexible material. Such a system, in contrast to the other laser and/or non-laser techniques, produces excellent cut quality with clear and sharp edges. This is a result of the non-thermal and non-contact interaction with the material.

The output of an excimer laser system can be split in many parts, due to the low power density required of the excimer lasers, resulting in a multi-head cutting system. Of the excimer laser, more appropriate is the ArF laser (193 nm), affording better cutting quality and a higher patterning speed.

The processing speed achieved was not very high, limited by the "low" repetition rate of the existing excimer lasers. This shortcoming can be easily alleviated by using multi - head cutting system, as mentioned above.

#### 5. ACKNOWLEDGMENTS

This work is supported by the BRITE and EUREKA EUROLASER EU 205 projects. The authors wish to thank Mr. G. Sotiropoulos of AVLON S.A. and Mr. N. Damianakis of EPSILON Ltd. for stimulating discussions.

#### 6. REFERENCES

- 1) R.K. Mosavi, "Comparing Laser and Waterjet Cutting", Lasers & Optronics, vol 6 (7), p. 65-68, July 1987.
- 2) J. Garrison and R. Srinivasan, "Microscopic model for the ablative photodecomposition of polymers by far-ultraviolet radiation (193 nm)", Appl. Phys. Lett., vol. 44(9), p. 849-851, May 1984.
- 3) T.A. Znotins, D. Poulin and J. Reid, "Excimer Lasers: An Emerging Technology in Materials Processing", Laser Focus/Electro- Optics, vol. 23(5), p. 54-70, May 1987.
- 4) S. Lazare and V. Granier, "Ultraviolet Laser photoablation of polymers: A review and recent results", Laser Chem., vol. 10, p. 25-40, 1989, and references therein.
- 5) P. Holzer and F. Bachmann, "Applications of Excimer Lasers in the Chemical and Plastic Industries", Kunststoffe German Plastics, vol. 79, p. 3-5, 1989.

Influencing Adherence Properties of Polymers by Excimer Laser Radiation

36980005 The Hague EXCIMER LASERS AND THEIR APPLICATIONS in English 1991 pp 223-230

[Article by J. Breuer, S. Metev, G. Sepold of the Bremen Institute of Applied Beam Technology and G. Kruger and O.D. Hennemann of the Fraunhofer Institute of Applied Materials Science]

[Text]

### **ABSTRACT**

The paper describes investigations concerning the enhancement of adhesive bonding strength between polypropylen (PP) and adhesive on resinous basis by UV-laser-induced photochemical reactions. Possible mechanisms of the laser-activated processes are discussed. A preliminary result of the experimental examinations is the bonding strength enhancement of more than 5 times under certain conditions.

### **1. INTRODUCTION**

For industrial application of polymers appropriate joining techniques are needed. A common technique to connect two samples of equal or different materials is the adhesive bonding. Problems with using this technique arise when the materials to be connected have low surface tensions. In that case, which is typical for many polymers, the wettability and with this the adhesion between the polymer and the adhesive is poor and therefore no reasonable binding strength can be achieved without suitable pre-treatment of the surface.

To some degree the bonding strength can be enhanced through mechanical, wet-chemical or plasma pre-treatment of the workpieces leading to improvement of the surface moistening by the adhesive /1,2/. Most of this methods have some disadvantages as for example damaging of the surface, bad controllability and pollution of the environment. To overcome this disadvantages it is necessary to look for new surface treatment techniques.

### **2. THE ROLE OF THE ADHESION IN THE BONDING PROCESS**

A principle way of improving the bonding strength of two materials is to enhance the adhesion between the binding material and the solid surface /2,3,4/. Although the

mechanism of the adhesion is not completely clarified, one can assume on the basis of general considerations that the activation of chemisorption on the solid-adhesive interface can influence the adherence positively.

The conditions at the surface adhesive interface can be described by the energetic states of a two-atomic molecule in dependence on its distance to the surface (Fig. 1).

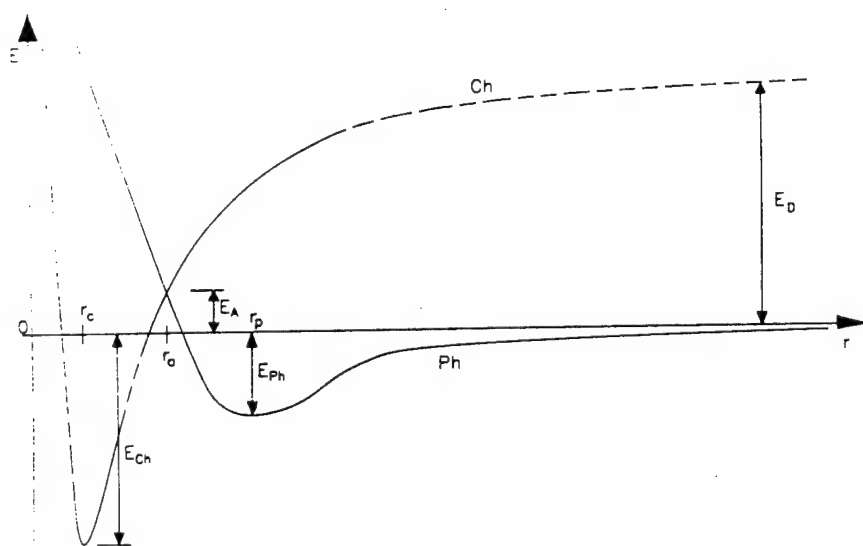


**Fig. 1:** Potential energies in physisorbed (Ph) and chemisorbed (Ch) states /3/,  
 $E_a$  - chemisorption activation energy,  $E_D$  - dissociation energy

The curve Ph (Fig.1) represents the potential energy of a molecule with the distance  $r$  from the surface. The potential energy is zero when the distance becomes infinite. Following the theory of van der Waals the energy has a minimum at distance  $r_p$  from the surface. When the molecule comes closer to the surface, that means closer to a second molecule, repulsion forces get more and more dominant.

Curve Ch (Fig. 1) shows the energetic relations when the physisorbed molecule gets chemisorbed. In this case the minimum of the potential energy is much more pronounced. Coming back to the discussed problem this circumstance means that the chemical bonding (chemisorption) between the molecules at the solid-adhesive interface is much more stable than the physical one (physisorption). With the object of reaching such chemisorbed states it seems to be efficient to use UV laser radiation of suitable wavelength to activate the process photolytically.



On one hand the laser radiation pre-treatment of a solid surface in an appropriate gas atmosphere can result in changing the physico-chemical activity of the surface layers in relation to the adhesive. On another hand the direct action of the UV-laser light on the solid-adhesive interface can activate a chemical reaction between them leading to adhesion improvement. The reason for this assumption is the well known sensitivity of some polymers to UV light irradiation /5/. In our investigations we used polypropylen (PP) as a model material, because of its importance for the praxis as well as due to the relatively good knowledge of its behaviour unter UV-exposure.

### 3. INTERACTIONS OF UV-LIGHT WITH POLYPROPYLEN

Pure polypropylen (pp) (Fig. 2a) does not absorb UV-light beyond 200 nm /5/. But technical polypropylen products always contain some impurities, e.g. oxidation products from the processing procedure, or chromophores, which bring about significant absorption in the UV-region. Under UV-activation these products react to form peroxy radicals ( $\text{PPO}_2\cdot$ ), (Fig. 2b, reactions (1),(2)).

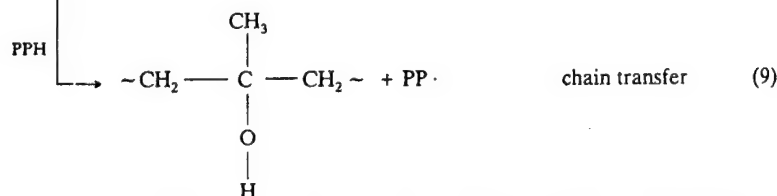
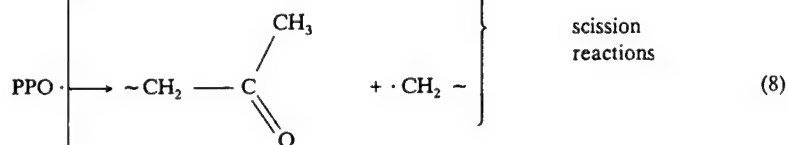
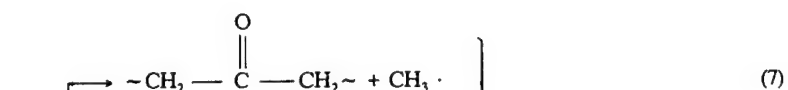
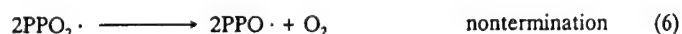
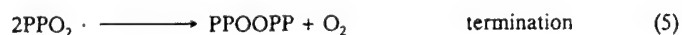
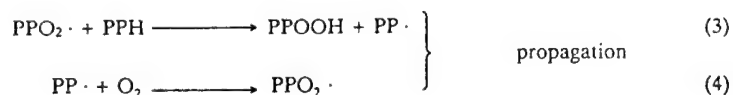
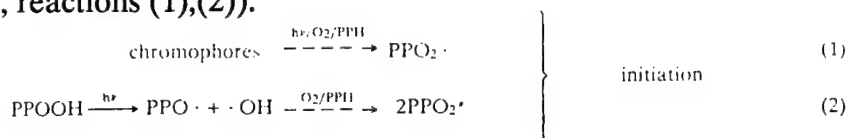
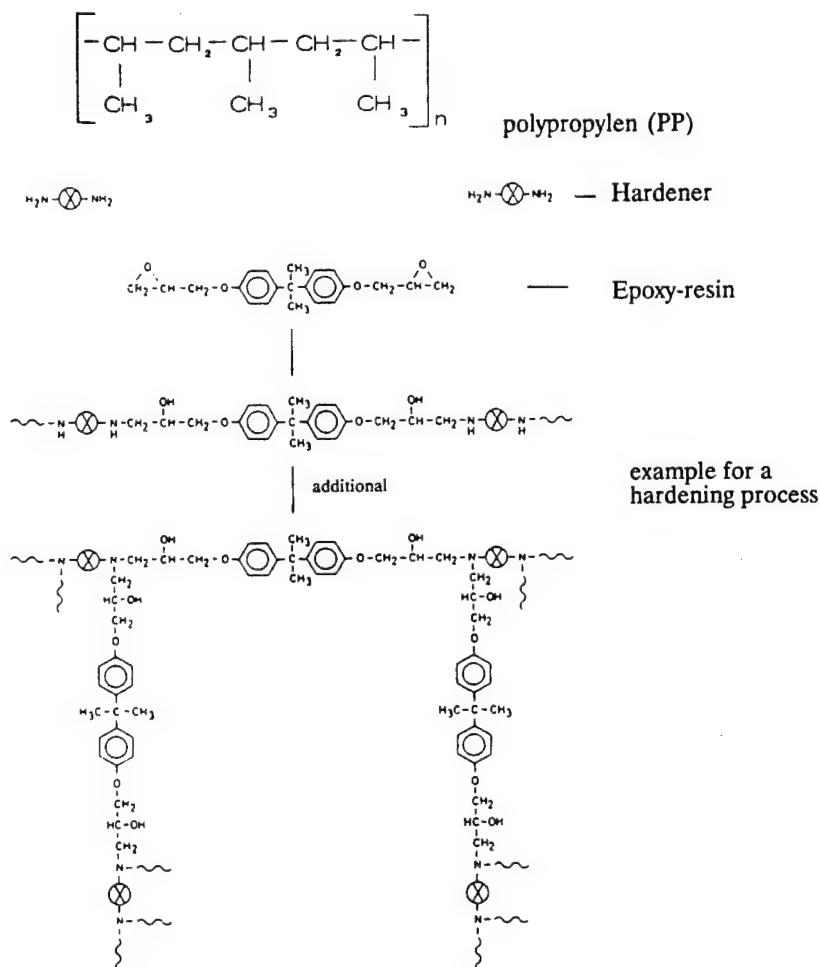


Fig. 2: Principal reaction mechanisms of polypropylen irradiated with UV-light /5/

The main product of the continuing process is hydroperoxide (PPOOH), which dissociate photolytically to form free radicals in propagation reactions. With continuing UV-radiation, scission reactions and chain transfers, involving carbonyl- and hydroxyl-groups become more and more dominant (Fig. 2b, (7)-(9)). It has been shown in plasma treatment experiments with polymers that such groups strongly influence the adhesive properties of the surface /6/. From this point of view experimental investigations were made, irradiating the Polypropylen samples with UV laser radiation of different wavelength and in different environmental conditions, which were bonded together with an epoxid resin adhesive.

#### 4. EXPERIMENTAL INVESTIGATIONS

It is known that the adherance of polypropylen (chemical structure Fig. 3a) with conventional adhesives is poor and so the experiments with this material are of practical interest. The used adhesive was a two component epoxide resin AW106-Ciba Geigy. The chemical structure of the binding agent and of the hardener are given in Fig.3.



**Fig. 3:** Chemical structure of polypropylen (a), of an adhesive on epoxide resin basis (b) and an example for a hardening process (c)

Characteristic feature of the binding agent is the ring-shaped epoxy-group. This ring opens when it comes to a reaction with the amino-group ( $\text{-NH}_2$ ) of the hardener during the hardening process /7/, (Fig.3c). The  $\text{NH}_2$ -group of the hardener reacts with the  $\text{CH}_2$ -group of the binding agent resulting in splitting off the  $\text{CH}_2\text{-O}$ -bond and in formation of an OH-radical on this place. This process takes place additively until a complete polymerization (hardening) of the adhesive is achieved /7/.

The experimental setup is shown in Fig.4. Prism shaped PP-samples with dimensions  $85 \times 25 \times 4 \text{ mm}^3$  were placed in a chamber with defined gas atmosphere ( $\text{He}$ ,  $\text{O}_2$ , air and  $\text{H}_2\text{O}$ -vapour) and irradiated with pulsed excimer laser radiation with wavelengths of 248 nm and 308 nm and pulse durations of 30 ns. Instead of the chamber a nozzle also was used.

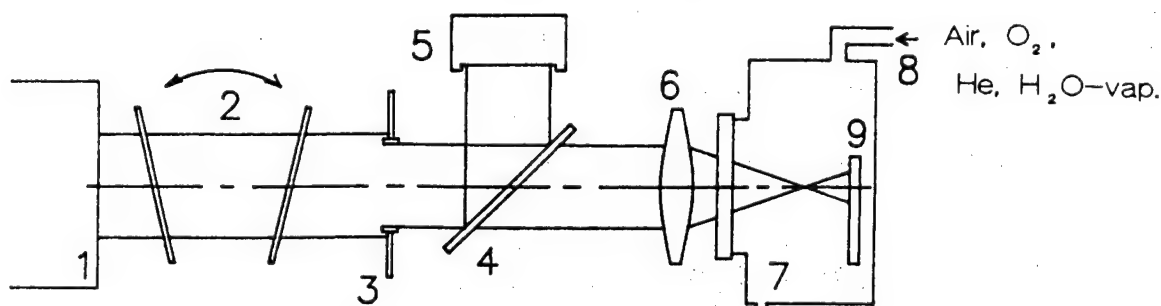


**Fig. 4:** Experimental arrangement for UV-laser treatment of PP  
1:laser source; 2:attenuator; 3:mask; 4:beam-splitter; 5:energy measuring device;  
6:projection objective; 7:chamber; 8:gas-inlet; 9:sample

In order to obtain uniform light flux density distribution in the irradiated zone a projection optical scheme has been used /8/. The light energy density in the treated zone of rectangular shape was varied from  $0.1 \text{ J}\cdot\text{cm}^{-2}$  up to the surface damage threshold of about  $1 \text{ J}\cdot\text{cm}^{-2}$  by an interference mirror attenuator. The number of the irradiation pulses was varied from 1 up to 200. The wavelength varied in the range from 193 to 308 nm.

In one experimental series the samples were irradiated through a thin layer of the adhesive deposited on the treated surface before irradiation.

The result of the UV-laser radiation action on the sample surface has been investigated by FT-IR-spectroscopy.

After the laser pre-treatment destructive tests with conditions in accordance with international standards were carried out. Therefore every two samples irradiated under same conditions were stuck together with an overlap of  $12.5 \times 25 \text{ mm}^2$ . After two days hardening at room temperature the shear strength of the bond was determined.

## 5. RESULTS AND DISCUSSION

In Fig. 5 some representative IR-spectra of the pre-treated samples are shown /9/.

Comparing these spectra with that one of the unirradiated sample (Fig.5a) shows that the main result of the laser radiation action on the sample surface is the formation of OH-groups and C=O-bindings in the PP-structure. These groups are not present in the structure irradiated in Helium, which means that the laser radiation activated reactions between the PP and the surrounding gas atmosphere.

The photolytical character of the activation process is confirmed by the dependence of the results on the laser wavelength. Particularly this is clearly demonstrated with the samples irradiated in H<sub>2</sub>O-vapour (Fig.5b). The height ratio of the OH- and C=O-components in the IR-spectrum is also dependent on the laser wavelength (Fig. 5c). Nevertheless we did not make quantitative analysis of the IR-spectra, it seems from their qualitative comparison that the 308 nm wavelength influences more strongly (in comparison to 248 nm) the formation of C=O-bindings.

The experiments have also shown that variation of the energy density below the damage threshold or variation of the pulse number results in quantitative changes of the obtained results but not in qualitative ones.

The measurements of the tensile strength of the adhesive bond of PP-samples have shown that the UV-laser pre-treatment under certain conditions enhances significantly (up to 5 times) its value. Some characteristic results of this measurements are presented in Table 1.

No.	Wavelength nm	Laser-treatment		tensile strength N/mm <sup>2</sup>
		Energy density J/cm <sup>2</sup>	number of shots	
1		untreated		0,8
2	248	0,2	200	1,3
3	248	0,9	200	5,0
4	308	0,4	200	1,5
5	308	0,9	200	3,6

**Table 1:** Parameters of the laser pre-treatments and results of shear strength measurements

Enhancement of the tensile strength has been observed in both cases - with significant amount of OH- and C=O-groups on the pre-treated surface and with UV-laser irradiation of the interface solid-adhesive through a previously deposited adhesive layer. In the first case the improvement of the adhesive bonding strength could be due to introduction of electrically polarized groups (OH and =C=O) into the PP-structure (Fig. 2, reactions (7)-(9)) leading to improvement of the physisorption (wetting) of the adhesive molecules /3/.

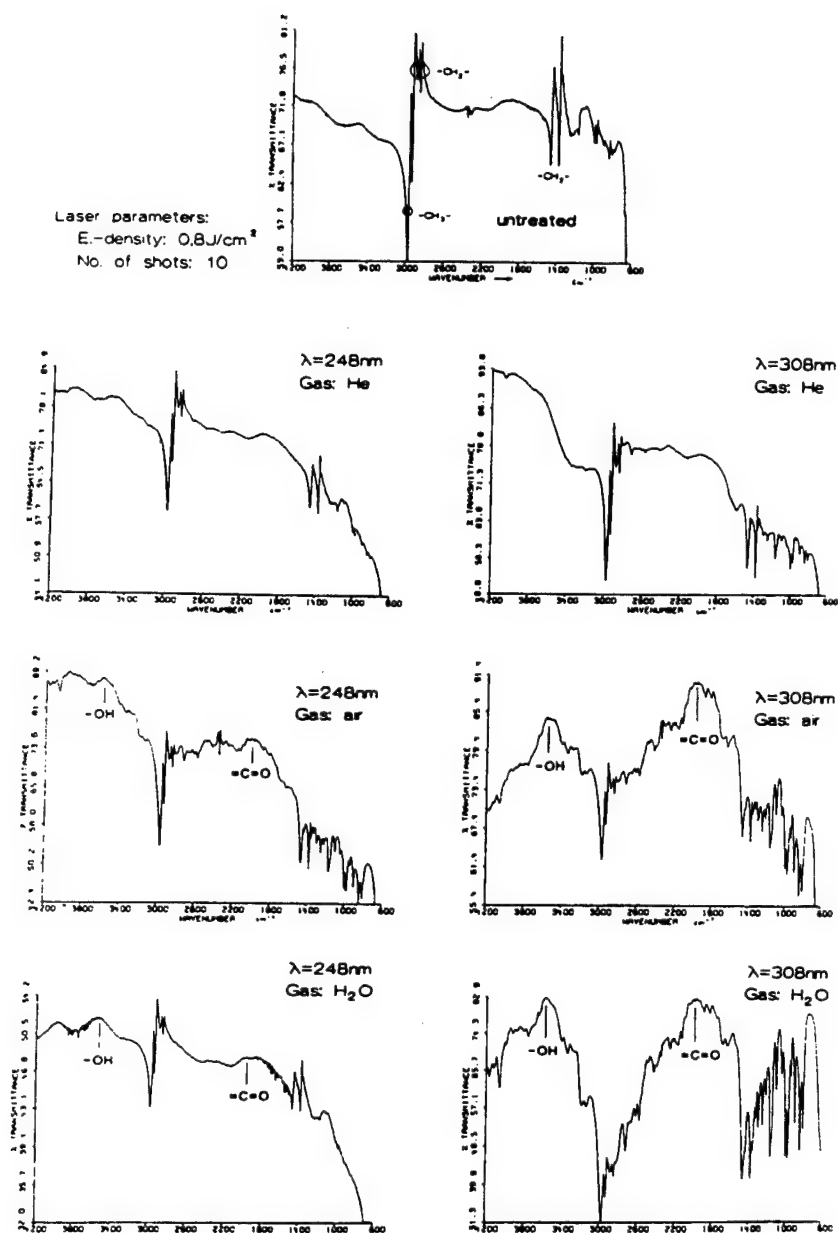


Fig. 5: FTIR-spectra of untreated and laser pre-treated PP-samples (number of pulses:  $N = 10$ ; energy density:  $E = 0,7 \text{ J}\cdot\text{cm}^{-2}$ )

Another possibility could be a photolytical enhancement of the chemical activity of the solid surface or of the adhesive due to the presence of chemically active species resulting in initiation of chemisorption processes. In the second case the enhancement of the tensile strength could be due to direct laser radiation activation of chemical reactions (chemisorption) between PP and adhesive. Possible laser-activated reactions at the surface adhesive interface could look like the polymerization reaction (Fig. 3b), where instead of the hardener (the  $\text{NH}_2$ -group) the  $\text{CH}_2$ - or  $\text{CH}_3$ -groups in PP (Fig. 2, reactions (8),(9); Fig. 3a) react on a similar way with the resin to create a stable chemical binding (chemisorption). From energetical point of view such kind of reactions seem also to be advantageous /10/. Because of the better absorption at 193 nm the reactions are concentrated in a thin layer on the surface while at other wavelengths some products of the interaction (as for example black coloured centers) are identified deep into the material.

Nevertheless the concrete mechanism of the adherence enhancement is not clear yet the results obtained show that in all cases it is connected with improvement of the adhesion. An additional indication for this results from the fracture surface after the shear strength examinations. In the case of low tensile strength (No. 1,2,4 in table 1) the fracture has adhesive character, while a suitable UV-laser pre-treatment (No.3 in table 1) results in a fracture of cohesive character /9/.

## 6. CONCLUSION

The presented experiments with polypropylen have definitely shown that the adherence of some polymer materials can be significantly enhanced by laser-induced photochemical reactions in the solid-adhesive interface. In order to clarify the particular nature of the activation mechanisms and its influenceability more detailed experiments, especially with shorter wavelengths (193nm, 157nm), as well as a sensitive analysis are needed. At present intensive investigations in this direction are going on.

## 7. ACKNOWLEDGEMENT

The work was supported by the German Ministry of Research and Technology (BMFT) which the authors greatly acknowledge.

## 8. LITERATURE

- / 1/ F. Dolezalek, R. Hartmann, Proc. SURTEC Congr. 1981 p.221
- / 2/ C. Bischof, W. Possart "Adhäsion" (Akademie-Verlag, Berlin) 1982
- / 3/ K. Hauffe, S. Morrison, Adsorption, Walter de Gruyter 1973
- / 4/ W. Brockmann, Dechema-Monographien 108, (VCH, Oberursel) 1987
- / 5/ D. Carlsson et.al., Macromolecules, 9, 695(1976)
- / 6/ W. Riedel, Galvanotechnik 57,579 (1966)
- / 7/ W. Brockmann "Grundlagen und Stand der Metallklebtechnik" (VDI, Düsseldorf) 1971
- / 8/ S. Metev et.al. J. Phys. D13, L75 (1980)
- / 9/ J. Breuer et.al. Appl. Surface Sci. 46, 336 (1990)
- / 10/ G.H. Aylward, T.J.V. Findlay, Chemical Data Book (Interscience Wiley, New York) 1966

## Excimer Laser Processing of Ceramics and Fiber Reinforced Polymers Assisted by a Diagnostic System

36980005 The Hague EXCIMER LASERS AND THEIR APPLICATIONS in English 1991 pp 238-248

[Article by M. Geiger, N. Lutz, and S. Biermann of the Univ. Erlangen-Nurnberg]

[Text]

### ABSTRACT

A 2J/20Hz XeCl (308 nm) excimer laser with a flat intensity distribution is used for processing  $\text{Al}_2\text{O}_3$ ,  $\text{Si}_3\text{N}_4$ , SiC and AlN ceramics and short glass fibre reinforced polymers. In order to get reproducible results an excimer laser material processing system is built up including a variable optical system, diagnostics and a high precision xy-translation stage. With this system modifications of the surfaces at low energy densities and the production of submillimeter structures at higher energy densities are investigated. Monitoring of important process and beam parameters with a diagnostic system is essential to get reproducible results. A CCD-camera system is used to measure the uniformity of the intensity distribution of the laser beam. The aim of the investigations is to find some correlation between beam and processing quality. Due to the low penetration depth of the laser beam into the material and rapid evaporation only thin layers below the workpiece surface are affected and the extension of the heat affected zones keeps extremely small. The treatment of larger areas of the materials at lower energy densities results in modifications of the surface topography. Uniform and reproducible changes of ceramics surfaces are obtained with optimized process parameters. Various mask geometries are imaged onto the surface of the material by a projection technique to produce submillimeter structures. The sharpness of the image on the workpiece surface proves to be an important parameter for producing reproducible and small structures. Larger areas are machined with the help of the xy-table. The processing quality is characterized using profilometry and scanning electron microscopy.

### 1. INTRODUCTION

Excimer lasers prove to be powerful tools for machining ceramics<sup>1,2,3</sup> and composite materials<sup>4,5,6</sup>. They show an improved processing quality compared to  $\text{CO}_2$ - and Nd:YAG lasers. Reasons are the efficient absorption of the excimer laser beam within thin surface layers and the rapid evaporation of the material. As a consequence the thermal load to the material is generally small. At the shorter KrF and ArF excimer laser wavelengths laser induced chemical processes in the material occur.

An important requirement for a widely spread use of excimer lasers in a production environment is the availability of reliable laser beam sources with high average power. Although applications in industry are seldom reported in literature<sup>7</sup>, the laser manufacturers develop systems with higher average power and reliability. The XeCl-laser is a very interesting candidate for machining ceramics. It delivers the highest pulse energies available and optics made of silica can be used at this wavelength. The aim of the investigations presented here is to develop some components of an excimer laser material processing system containing a high pulse energy excimer laser and to present results for processing ceramics and fibre reinforced materials with this system.

### 2. EXPERIMENTAL

An excimer laser Siemens KWU XP 2020 is used for the experiments. It is operated with XeCl as laser gas and delivers 2.5 J maximum pulse energy at a maximum repetition rate of 20 Hz. The optics and the diagnostic equipment are mounted on an optical table, see Fig. 1. Movements of the workpiece are achieved using a computer controlled high precision xy-translation stage with 0.5 micron resolution. Both laser and optical table are mechanically decoupled from the ground to avoid errors from vibrations. Shielding of direct or diffuse reflected UV-light is achieved by a housing made of PMMA.

### 3. DIAGNOSTIC SYSTEM

The diagnostic system was developed with the aim to get a correlation between important process parameters and processing quality. The configuration is shown in Fig. 2. Beside the processing parameters important laser beam parameters are measured: These are

- trigger point of the laser pulse
- pulse shape and pulse duration
- pulse energy
- intensity distribution
- divergence.

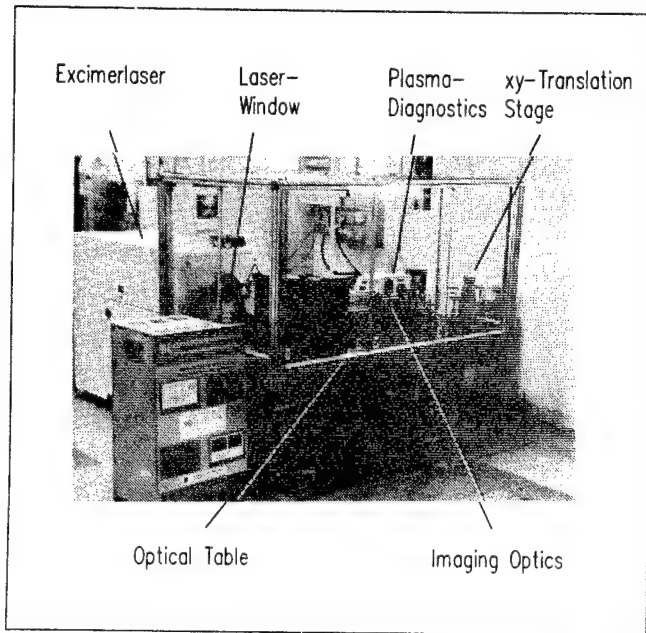


Fig. 1: Excimerlaser Material Processing System

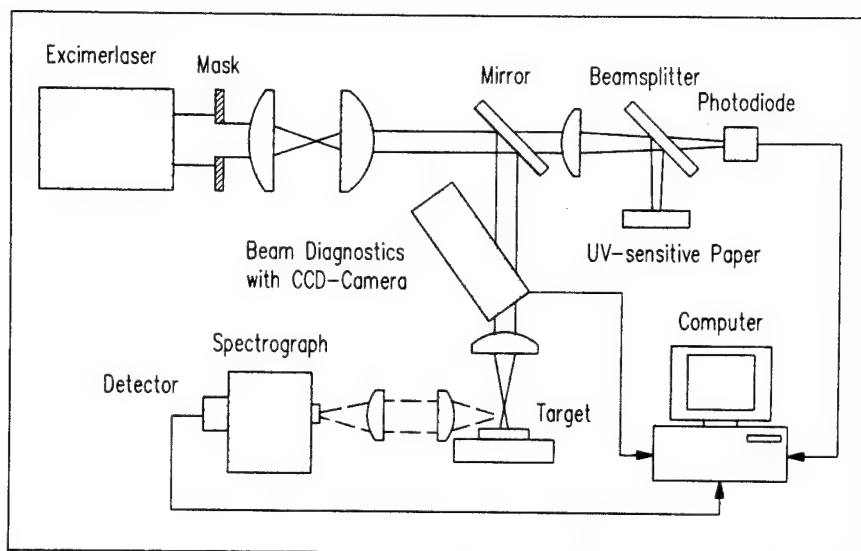
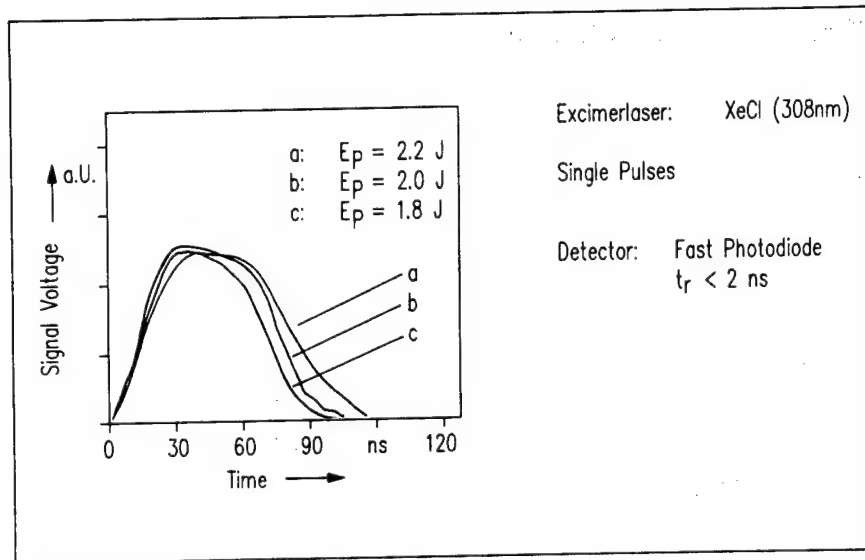


Fig. 2: Excimerlaser Diagnostics System



The pulse energy of the laser beam passing the mask is measured with a calibrated Joulemeter using the transmitted part of the laser beam at the mirror. Fast photodiodes and pyroelectric detectors measure the trigger point and the shape and duration of the laser pulses. Both types of detectors supply comparable results. Fig. 3 depicts the influence of the laser voltage, i.e. pulse energy, on the shape of the laser pulse. With decreasing laser voltage the maximum intensity and the duration of the laser pulse are smaller. The maximum intensity is reached after 15 ns independent of the pulse energy. The energy measurement is used to determine the actual energy density on the workpiece. Computer controlled coordination of the laser and the xy-translation stage is achieved using the measured trigger points.



**Fig. 3:** Variation of Excimer-laser Pulse Shape with Pulse Energy

#### 4. INTENSITY DISTRIBUTION

Generally the size of the laser spot and the intensity distribution in the plane of the workpiece are important parameters for the interaction phenomena and the machining quality of laser material processing. They are determined by the wavefront of the laser light and the path length, as measured for CO<sub>2</sub>-laser material processing<sup>8</sup>. As a result the intensity distribution in the focus plane varies and therefore the quality of cut kerfs and welding seams is not constant. Scanning diagnostic systems moved through the beam are used to monitor the cw CO<sub>2</sub>-laser radiation and to measure the intensity distribution.

Problems in excimer laser material processing are related to some of the phenomena described above. The intensity distribution depends on the distance from the laser outcoupling window. Ageing of the laser gas and degradation of the electrodes cause inhomogeneities in the laser discharge and pollution of the laser windows. The effect is that pulse energy decreases and the intensity distribution of the laser beam varies. As a consequence the intensity distribution on the surface of the workpiece that is crucial for the surface modification effects and ablation rates described below is changed.

A diagnostic system is developed to measure the intensity distribution of the unfocussed excimer laser beam, since measurements in the plane of the surface of the workpiece cannot be made during machining. This approach is justified by measurements indicating a very close correlation of the intensity distributions in the unfocussed beam and in the image plane on the surface.

Two types of systems are suggested for excimer laser beam diagnostics:

- It is possible to use the visible fluorescence of a crystalline plate irradiated with an excimer laser beam. Configurations are proposed using crystalline plates in the excimer laser beam and imaging of the fluorescence to the CCD-sensor<sup>9</sup>. Another possibility is to couple out a part of the laser radiation to a fluorescent plate that is connected with a CCD-sensor<sup>10</sup>. The intensity distribution of the laser beam can be calculated from the measured signals.
- An outcoupling element and a UV-sensitive CCD-sensor<sup>11</sup> can be used.

A system is developed here that contains an outcoupling element, imaging optics and a UV-sensitive CCD-camera, see Fig. 4. The system can be used for measurements of the intensity distribution at each position of the laser path.

The signal amplitude of the CCD-camera correlates with the intensity of the laser beam. A calibration curve for the used CCD-camera is measured using a calibrated pyroelectric detector. The relation

$$U_{\text{CCD}} = f(H_{\text{ECCD}}) \quad (1)$$

where  $U_{\text{CCD}}$ : video voltage of the CCD-camera,  $H_{\text{ECCD}}$ : energy density on the CCD-sensor, proves to be nonlinear. With an approximation at the 50% signal voltage level a linear dependency is determined with

$$U_{\text{CCD}} = K H_{\text{ECCD}}, \quad K = 0.47 \text{ mVcm}^2/\text{nJ} \quad (2)$$

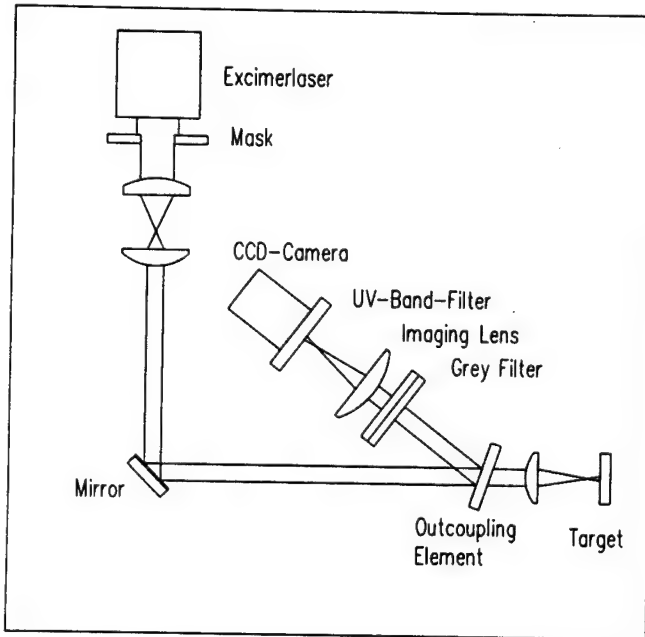


**Fig. 4:** Beam Diagnostics with CCD-Camera for Measurements of the Intensity Distribution of an Excimerlaser Beam

The energy density of the excimer laser beam can be calculated from the video signal

$$H_E = R_{\text{BS}} T_{\text{tot}} U_{\text{CCD}} / K \quad (3)$$

where  $R_{\text{BS}}$ : reflection factor of the outcoupling element,  $T_{\text{tot}}$ : total transmission factor of the lens and the filters of the diagnostic system. Fig. 5 shows a typical intensity profile of the excimer laser beam.

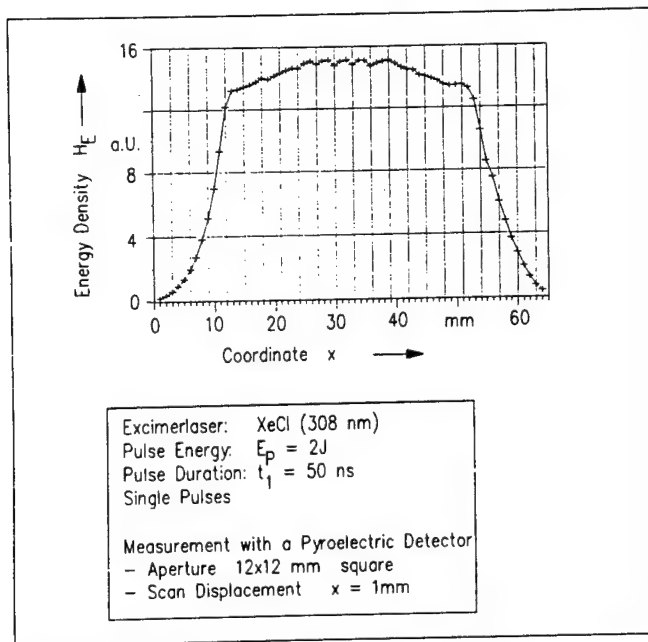


**Fig. 5:** Intensity Profile of an Excimerlaser Beam

It is measured with a scanning technique and the pyroelectric detector at a distance of 0.4 m from the laser outcoupling window. Although the signal is an averaged value of the energy density it is very similar to the line signals of the CCD camera as described below.

Due to the large data amounts of video signals a hardware data processing system was developed. The images of the CCD-camera are processed during recording and can be recorded on video-tape, see Fig. 6.

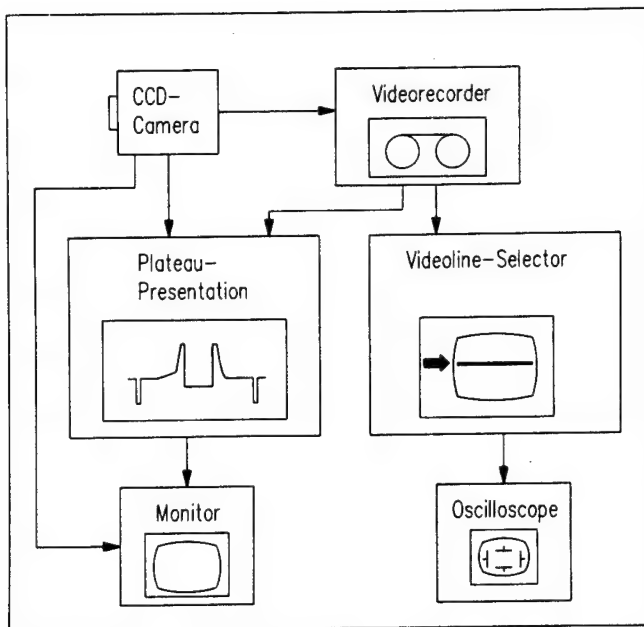


**Fig. 6:** Data Processing System for Excimerlaser Beam Diagnostics

The intensity distribution is shown

- as an intensity profile using the video-line-selector and an oscilloscope or
- as a plateau representation on a video monitor. Areas of higher intensity than an adjustable value (e.g. 70% of the maximum signal voltage) are displayed reversely as black areas.

The beam diagnostic system is used for measurements of the uniformity of the intensity distribution of the laser beam. The excimer laser used for the experiments normally exhibits a very high uniformity of the intensity distribution. The influence of window pollution and ageing of the laser gas is shown in Fig. 7. The diagnostic system proves to be a reliable indicator for system performance.

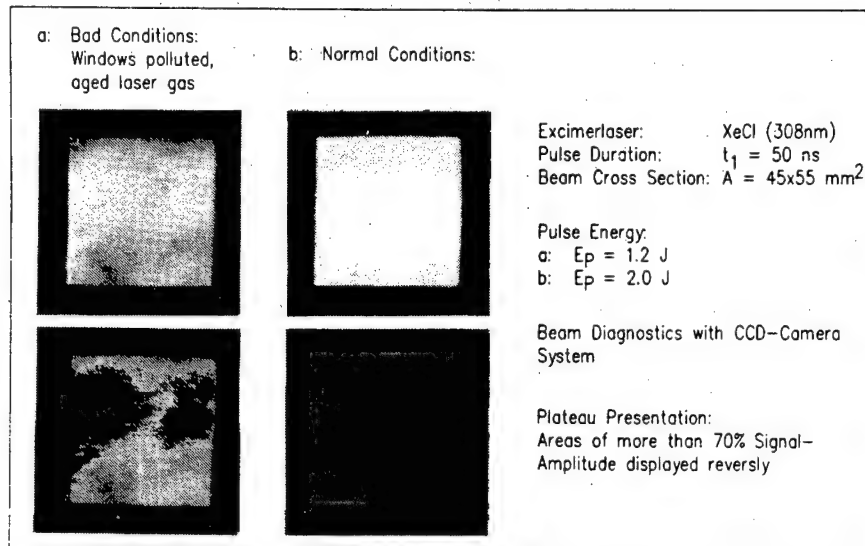


**Fig. 7:** Influence of Polluted Windows and Ageed Laser Gas on the Intensity Distribution of an Excimerlaser Beam

## 5. MODIFICATION OF CERAMIC SURFACES

$\text{Al}_2\text{O}_3$ ,  $\text{Si}_3\text{N}_4$ ,  $\text{SiC}$  and  $\text{AlN}$  ceramics are irradiated using the mask projection technique. Energy density is adjusted with a beamsplitter with variable transmittance in the range  $0.1$  to  $4.0 \text{ J/cm}^2$ . The energy densities are lower than the ablation thresholds<sup>2</sup> of the materials.

A local modification of the surface topography is observed after the first pulses for both oxide and nonoxide ceramics, see Fig. 8 for  $\text{Al}_2\text{O}_3$  and Fig. 9 for  $\text{AlN}$ . The laser beam is coupled to the material at certain points on the ceramic surface and energy is absorbed. This effect is explained by grain boundaries or filler materials in the ceramic material, where a part of the energy of the laser beam is absorbed at lower energy densities. Material is removed and melting occurs.

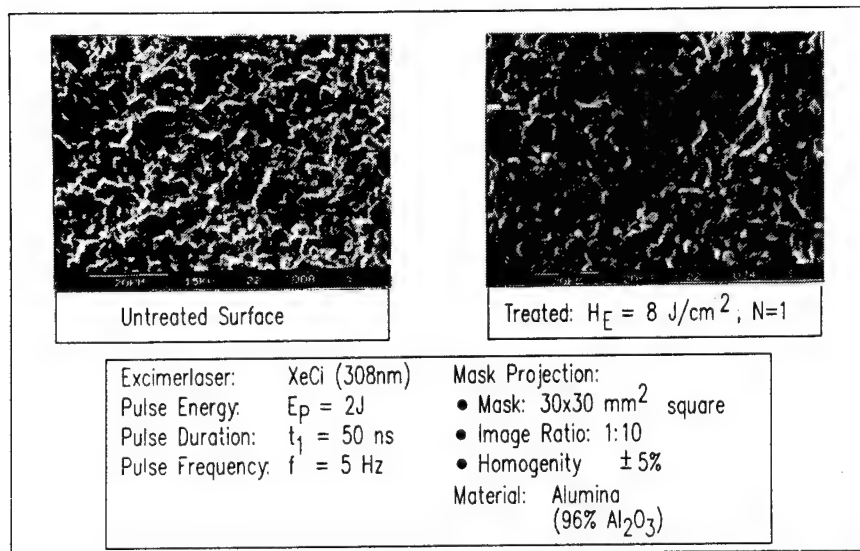


**Fig. 8:** Modified Surface of Alumina Ceramics after the First Excimer-laser Pulse

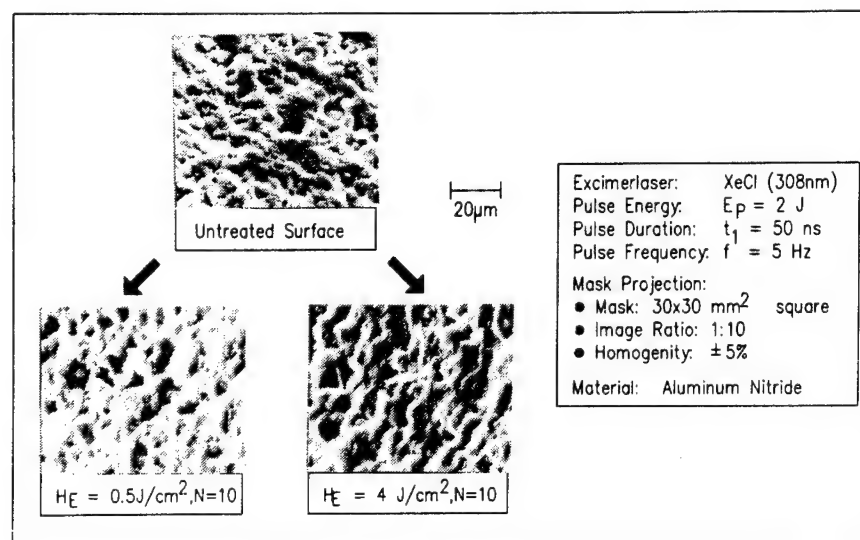


**Fig. 9:** Modified Surface of Aluminum Nitride after Few Excimerlaser Pulses

SEM observations for AlN, see Fig. 10, show the smoothing effect at low energy densities and some increase in roughness at higher pulse numbers and energy densities.

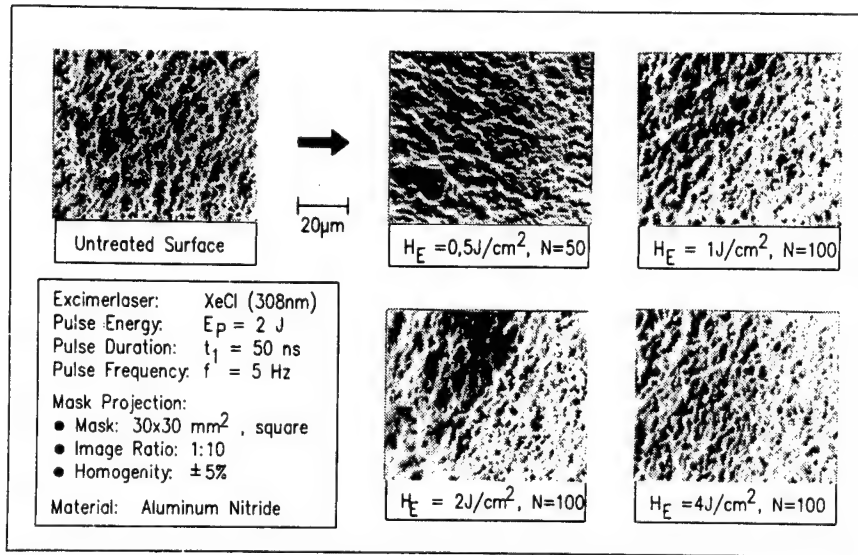


Fig. 10: Modification of Aluminum Nitride Surfaces with Excimerlaser Radiation

## 6. MACHINING OF DEFINED STRUCTURES

Ablation of material occurs at higher energy densities. An increase in of the ablation rate with energy density is measured for the investigated ceramics, see Fig. 11. By an appropriate combination of energy density and pulse number the ablation depth and the surface topography of the machined surface can be adjusted<sup>12</sup>.

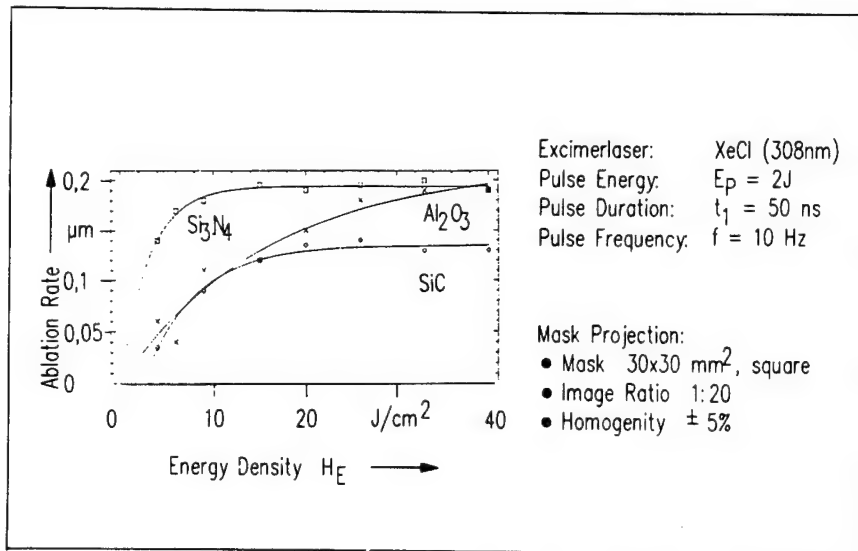
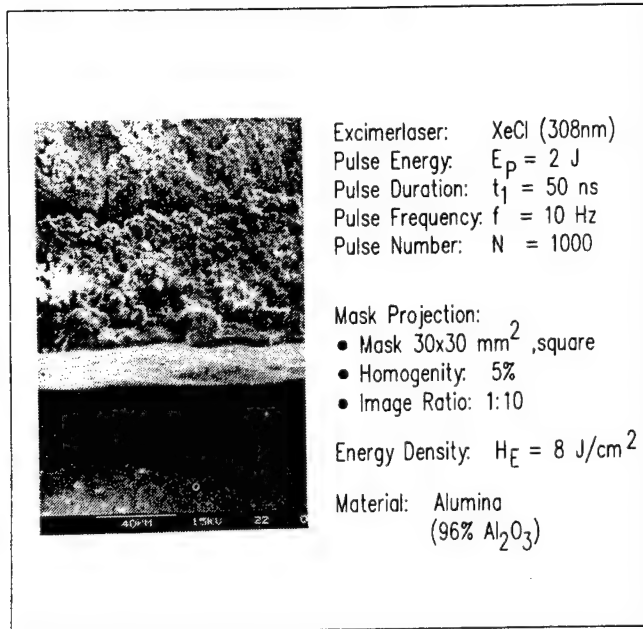


Fig. 11: Ablation Rates for Excimer Laser Machining of Ceramics

The aim of the investigations described now is to generate defined geometrical elements in ceramics with excimer laser radiation and to optimize machining quality and accuracy.

Beside the uniformity of the intensity distribution on the surface of the workpiece the distinctness of the projection is essential for machining defined submillimeter structures with excimer laser radiation. A high precision xy-translation stage with  $0.5 \mu\text{m}$  resolution is used to adjust the correct image ratio. Fig. 12 shows the side wall of alumina irradiated with 1000 pulses at an energy density of  $8 \text{ J/cm}^2$ .



**Fig. 12: Excimerlaser Machining of Alumina:  
Quality of a Side Wall**

Important advantages of excimer laser machining can be clearly seen from this photograph:

- The heat affected zone is very small.
- The side wall has a very smooth appearance, only small cracks are observed in the molten layer.
- Surface topography can be changed very uniformly.
- Structures of  $10 \mu\text{m}$  size are achieved in the experiments.

A lot of surface shapes can be realized by a combination of the mask projection technique and a movement of the workpiece with the xy-translation stage. An array of 40 sack-holes with  $150 \mu\text{m}$  diameter is drilled in parallel in alumina, see Fig. 13. Smooth side walls and a flat bottom of the holes are observed.

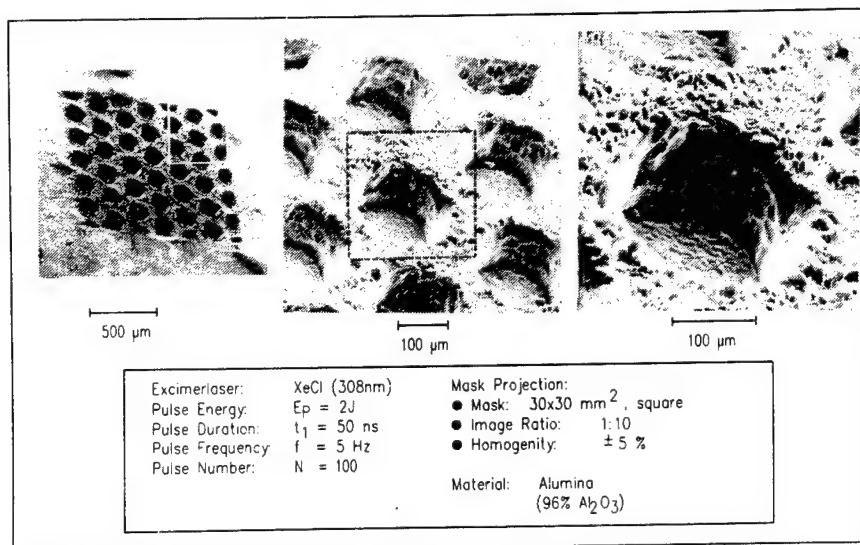


**Fig. 13: Hole Generation in  
Alumina Ceramics with  
Excimerlaser Radiation**

A series of steps was grooved with a displacement of the workpiece and a fixed mask, see Fig. 14. The whole area is processed uniformly. A mask with variable aperture is used for the pyramid in Fig. 15.

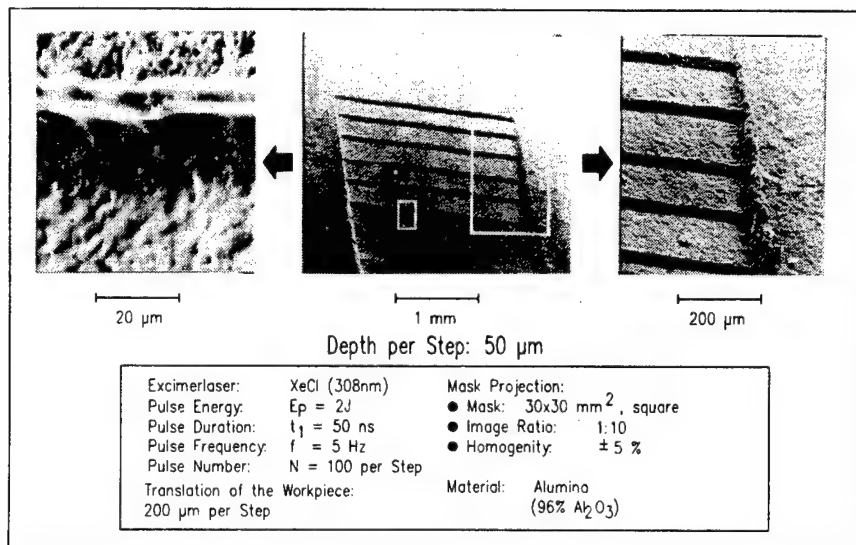


**Fig. 14:** Step Generation in Alumina Ceramics with Excimerlaser Radiation

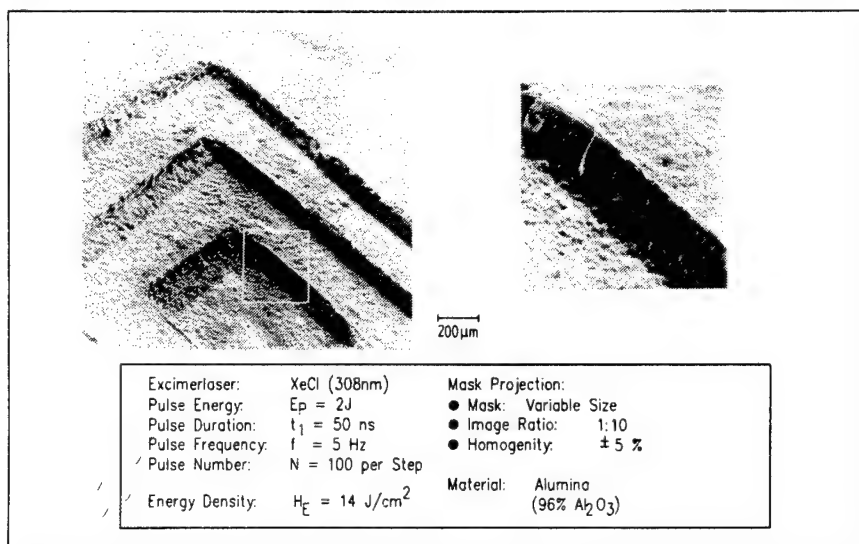


**Fig. 15:** Pyramid Generation in Alumina Ceramics with Excimerlaser Radiation

Fig. 16 shows a glass fibre reinforced polymer processed with the excimer laser. Although the matrix material and the glass fibres show different thermal properties very precise side walls are obtained. The appearance of the glass fibres supports the assumption that the fibres are broken during material ablation.

Generally the heat affected zone is very small for excimer laser processing of ceramics and fibre reinforced polymers. Redeposition of ablated material is negligible.



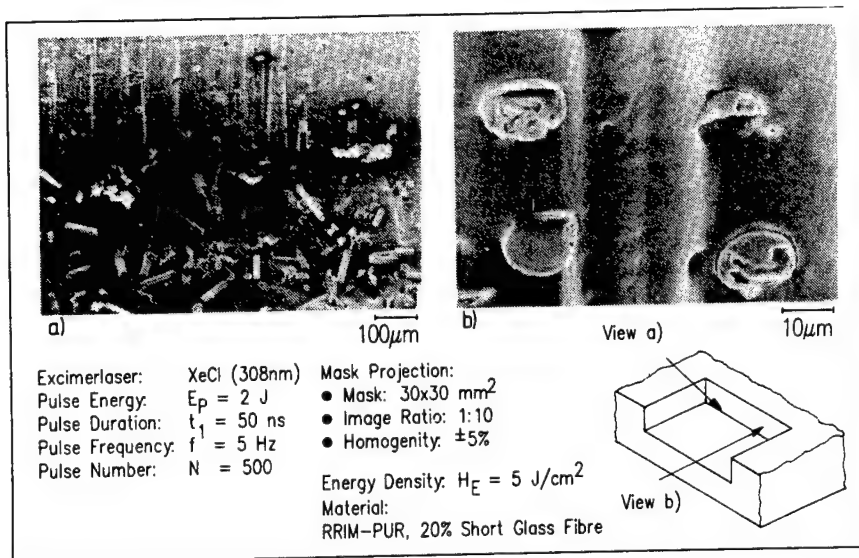


**Fig. 16: Excimer Laser Processing of Fibre Reinforced Polymers**

## 7. CONCLUSIONS

An excimer laser material processing system offers advantages for processing ceramics and fibre reinforced polymers. The laser is a very precise tool in this system with little thermal load to the material. An on-line-measurement of important process parameters is essential for optimized processing results. The developed UV-sensitive CCD-camera system is used for measurements of the intensity distribution of XeCl-excimer lasers with high pulse energy. Inhomogenities in the intensity distribution caused by ageing effects in the laser and the optical components are detected.

Below the ablation threshold interaction starts at certain points of the ceramic surface. At higher pulse numbers the surface topography is modified in a wide parameter range with the mask projection technique very uniformly. Homogenous ablation of the irradiated area of ceramics and fibre reinforced polymers is obtained at higher energy densities if a uniform intensity distribution on the surface can be guaranteed. A distinct image on the workpiece is essential for the machining of precise side walls. Submillimeter structures can be produced by a combination of a flexible mask geometry and a controlled translation of the workpiece.

## 8. ACKNOWLEDGEMENTS

The investigations presented are supported by the minister of science and technology of the German government (contract number 13N5629). The authors gratefully acknowledge support from Siemens KWU, Hoechst AG, Hoechst Ceram Tec and Linde AG. Special thanks to R. Müller for the SEM photograph of excimer laser machined RRIM.

## 9. REFERENCES

1. K.J. Schmatjko, G. Endres: Projection structuring of ceramics by excimer laser radiation, in: W. Waidelich, (Ed.) "Optoelectronics in Engineering", Munich 1987: Springer, Berlin 1988, 573-576
2. H.K. Tönshoff, O. Gedrat: Removal process of ceramic materials with excimer laser radiation, Proc. SPIE Vol. 1132 "High power lasers and laser machining technology" (1989), 104-110
3. U. Sowada, S.-I. Ishizaka, H.J. Kahlert, D. Basting: Excimer laser processing of aluminium oxide ceramics, Chemtronics 4 (1989)9, 162-164
4. V. Hohensee, K.J. Schmatjko: Schneiden faserverstärkter Kunststoffe mit dem Excimer-Laser, Laser Magazin (1987)1, 31-39
5. G.M. Proudley, P.H. Key: Excimer laser machining of aerospace materials, Proc. SPIE Vol. 1132 "High power lasers and laser machining technology" (1989), 111-119
6. M. Wehner, R. Poprawe, F.J. Trasser: Cutting with the excimer laser, effects of pulse width and repetition rate on cutting edge quality of fibre-reinforced polymers and alumina ceramics, Proc. SPIE Vol. 1023 "Excimer lasers and applications" (1988), 179-186

7. F. Bachmann: Excimer lasers in a fabrication line for a highly integrated printed circuit board, *Chemtronics* 4(1989), 149-152
8. S. Biermann, J. Hutfless, N. Lutz, M. Geiger: Vergleichende Betrachtungen zur Laserstrahldiagnostik von CO<sub>2</sub>-Hochleistungslasern, in: W. Waidelich "Optoelectronics in Engineering", Munich 1989: Springer, Berlin 1990, 439-445
9. W.B. Telfair, u.a.: Incorporating beam diagnostics into UV laser delivery systems, *Proc. SPIE* Vol. 998 "Excimer beam applications" (1988)
10. K. Mann, H. Gerhardt: Teststand zu automatisierten Messung von Zerstörschwellen an optischen Komponenten für UV-Laser, *Laser und Optoelektronik* 21 (1989)4, 42-47
11. T. Yagi, Y. Matsumi, K. Ohta, H. Saito, M. Obara, T. Fujioka: A diagnostic system for an excimer laser beam, *Proc. SPIE* Vol. 1031
12. N. Lutz, M. Geiger: Processing of ceramics with excimer lasers. In: Bergmann, H.W. (Ed.) and Kupfer, R. (Ed.): *Proc. 3<sup>rd</sup> European Conference on Laser Treatment of Materials (ECLAT)*. Vol. 2, Erlangen, 1990. Coburg: Sprechsaal Publishing Group, 1990, 849-857

## Excimer Laser Surface Treatment of Ceramics

36980005 The Hague EXCIMER LASERS AND THEIR APPLICATIONS in English 1991 pp 249-255

[Article by G. Hourdakakis and E. Hontzopoulos of the FORTH-Institute of Electronic Structure and Laser, Laser Applications Laboratory and A. Tsetsekou, Th. Zampetakis, and C. Stournaras of CERECO S.A.]

[Text]

### ABSTRACT

Excimer lasers have been employed for large area surface treatment of bulk ceramics and/or ceramic coatings on a metallic surface. These applications are aiming in the improvement of surface morphology (eg. grain size, roughness, porosity e.t.c.) and properties (eg. hardness, corrosion resistance, conductivity e.t.c.). The influence of KrF laser processing parameters on  $Al_2O_3$  ceramic samples and/or coatings are discussed in relation to the above mentioned surface characteristics.

### 1. INTRODUCTION

Ceramics and ceramic coatings are becoming increasingly important as industrial materials due to their better properties eg. toughness, strength, chemical inertness, low thermal expansion e.t.c., in comparison to the metallic materials. The end use applications<sup>(1)</sup> of ceramics and ceramics coatings include the automobile and jet aircraft industries, where they are used in heat engines and heat exchangers or as wear parts and machining tools, but also medicine (bioceramics) and the microelectronic industry.

Besides the already developed processing techniques (eg. sintering, hot pressing, injection molding e.t.c.) several new techniques<sup>(1)</sup> will enable the production of ceramics and ceramic coatings with improved properties and, in some cases, at less expense. Among these new processing techniques is the laser surface treatment.

Lasers have been successfully used for processing of metals/alloys for many years while their application for ceramics became a pole of attraction for research and development during the last years<sup>(2-14)</sup>. The photon energy of the laser beam can be provided in a temporally and spatially controlled manner. The laser surface treatment is a contact free and clean process which can produce surface properties that are difficult to be achieved by other techniques.

Excimer lasers<sup>(6-9, 11-14)</sup> present certain distinct advantages for material processing applications in comparison to the other types of lasers (eg. Nd-YAG,  $CO_2$ ). They emit in the ultraviolet region (150-350 nm) of the spectrum, where the reflectivity of most metals and ceramics is lower, than at longer wavelengths, and the absorptivity higher. In addition, ultraviolet laser beams can be focussed more tightly and produce higher structure resolution. Furthermore, since ultraviolet photons are more energetic (3.5 to 7.9 eV.), they interact non-thermally with molecular materials and generally may induce photochemical reaction.

In this work a KrF excimer laser was used for the surface treatment of bulk  $\alpha$ -alumina samples and alumina coatings. The aim of this work was to investigate methods for improving surface properties and to develop electrical conductive regions/patterns on the ceramic surface.

## 2. EXPERIMENTAL

$\text{Al}_2\text{O}_3$  ceramic surfaces were laser treated by means of a Lambda Physik (LPX 210 i F) excimer laser emitting pulses at 248 nm (KrF mixture) with 29 ns duration and a maximum repetition rate of 100 Hz. The laser beam was imaged onto the sample surface by a 10 cm focal length cylindrical Suprasil lens, giving rise to power densities up to  $450 \text{ MW/cm}^2$  on the sample surface. The sample surface was laser treated by moving the sample along x and/or y axes, under stepper motor control, in front of the laser beam.

The laser processing parameters such as power density incident on the sample surface, number of pulses per step, repetition rate, overlap percentage between the steps and sample motions were computer controlled.

The types of samples that have been used, are  $\alpha$ -alumina and  $\text{Al}_2\text{O}_3$  coatings on a metallic substrate. The  $\alpha$ -alumina samples were prepared by the tape casting method and they were heat treated in an oven at  $1600^\circ\text{C}$  for 4 hours. The  $\text{Al}_2\text{O}_3$  coatings were deposited on the metallic substrate by the plasma spraying technique. The metallic substrates were either Cr-Ni steel or Ti alloy. All samples were cleaned in an ultrasonic acetone-alcohol 3:1 solution for 15 min and then air dried, before laser treatment.

Optical and scanning electron microscopy and x-ray diffraction analysis were employed to study the surface morphology and phase changes. Also microhardness and electrical conductivity measurements were performed on the sample surface.

## 3. RESULTS AND DISCUSSION

### 3.1 Surface treatment

#### 3.1.1 Bulk ceramics

SEM examination of the  $\alpha$ -alumina samples after KrF laser (248 nm) irradiation shows a surface smoothening<sup>(6,14)</sup> (Fig. 1). The decrease of the surface roughness follows the increase of the laser power density up to a value of about  $200 \text{ MW/cm}^2$  and then starts to increase again due to material removal. Fig. 2 shows that the grain size is also affected by

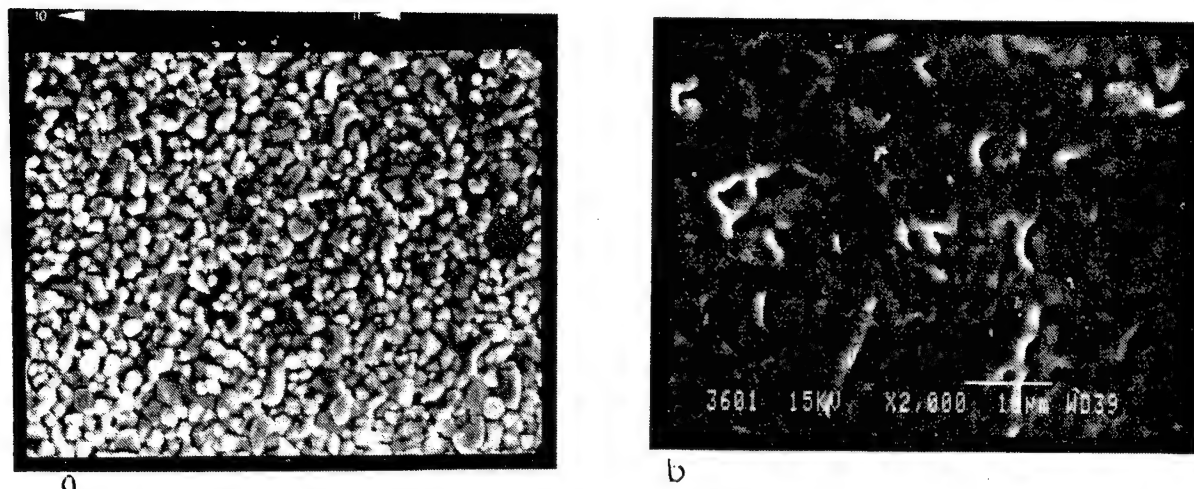


Fig. 1 Surface smoothing after KrF laser irradiation a. untreated surface b. laser treatment at  $180 \text{ MW/cm}^2$ .

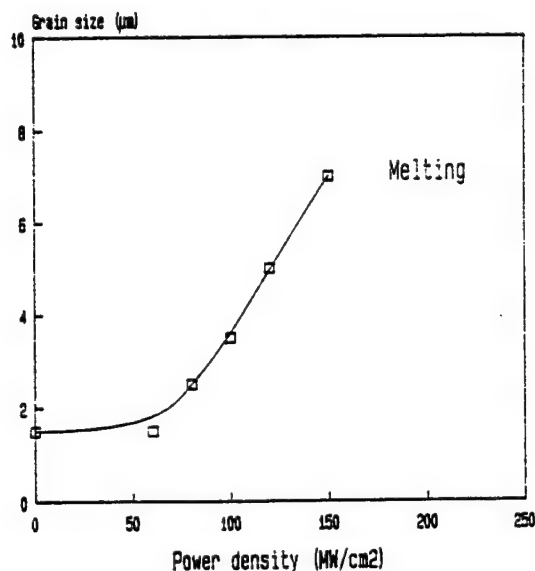


Fig. 2 KrF excimer laser treatment effect of power density on grain size.

the power density. This effect starts at a power density of the order of  $75\text{--}80 \text{ MW/cm}^2$  and it can be followed by SEM up to  $150 \text{ MW/cm}^2$  approximately, because above this level the surface is completely melted and it is difficult to measure the size. At the same time with the above phenomena (surface smoothing, increase of grain size), there is reduction of the porosity<sup>(6,14)</sup> and of the density of microcracks<sup>(14)</sup>.

The thickness of the molten layer is in the range of  $8\text{--}12 \mu\text{m}$ , depending on the laser processing parameters, while a slight influence due to the laser treatment can be observed up to a depth of  $60 \mu\text{m}$ .

X-ray diffraction analysis demonstrates an orientation of  $\alpha$ -alumina peaks at power density higher than  $200 \text{ MW/cm}^2$ . The formation of the metastable  $\gamma$ -alumina seems to depend directly on the number of laser pulses per step (Fig. 3). The other laser processing parameters may also influence the formation of this phase but in a smaller degree.

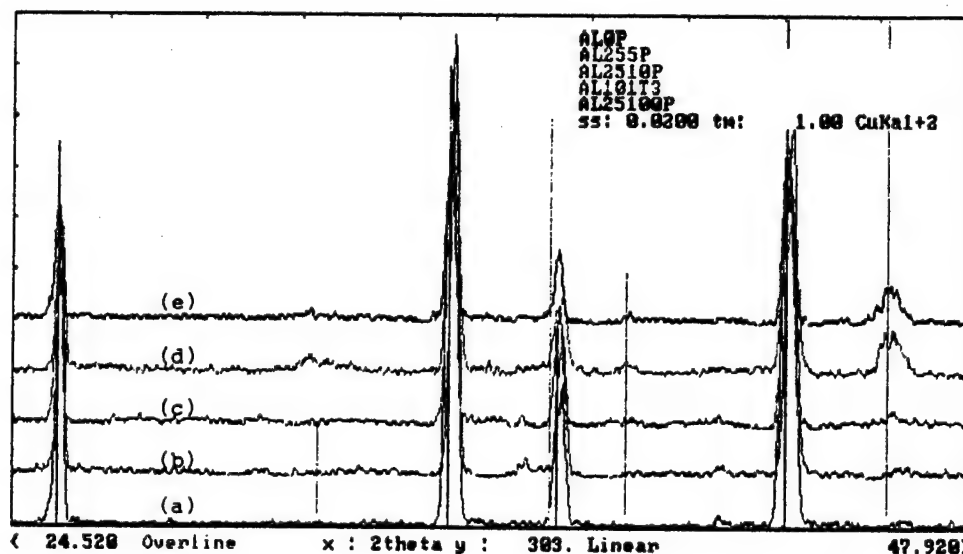


Fig. 3 X-ray diffraction analysis spectrum, of alumina surfaces treated with different KrF laser pulse per step: a) untreated, b) 50, c) 100, d) 500 and e) 1000 pulses/step.

Microhardness measurements before and after laser treatment show a slight but not significant increase of the hardness. In contrast, the toughness of the irradiated area is improved. This can be concluded by the nonexistence of microcracks after the diamond intrusion in the laser treated area, in comparison with the non laser treated.

### 3.1.2 Ceramic coating

The alumina coatings produced by the plasma spray technique present a high degree of surface porosity. The purposes of the laser treatment are to produce surface layers with reduced porosity and fine microstructure which will influence the corrosion resistance and to increase surface microhardness. Furthermore another aim of the laser treatment is to enhance the adhesion of the ceramic coating by diffusing part of it into the metallic substrate.

After KrF laser irradiation, the optical microscope shows that the surface becomes smoother while the porosity decreases dramatically. When the laser power density increases the surface layers melt producing a homogeneous layer with fine microstructure while in the same time the number of microcracks reduces as well as the porosity (Fig. 4). At even higher laser power density ( $>250 \text{ MW/cm}^2$ ) a surface pattern appears on the surface which increases the surface toughness.

The x-ray analysis shows that there is an orientation of the surface layers after excimer laser treatment. Also the microhardness measurements show an increase as the power density increases reaching a value of 1450 HV, while the value of the untreated surface is 1080 HV.



Fig. 4 KrF laser irradiation of alumina coating on a metallic substrate ( $100 \text{ MW/cm}^2$ )

### 3.2 Conductive patterns

An exciting new application<sup>(15)</sup> of great current interest is the use of excimer laser direct irradiation of ceramics. This application of excimer laser under specific experimental conditions leads to a dramatical change of the electrical conductivity of the ceramic surface. This is demonstrated in Fig. 5 for an  $\alpha$ -alumina sample at different laser intensities.

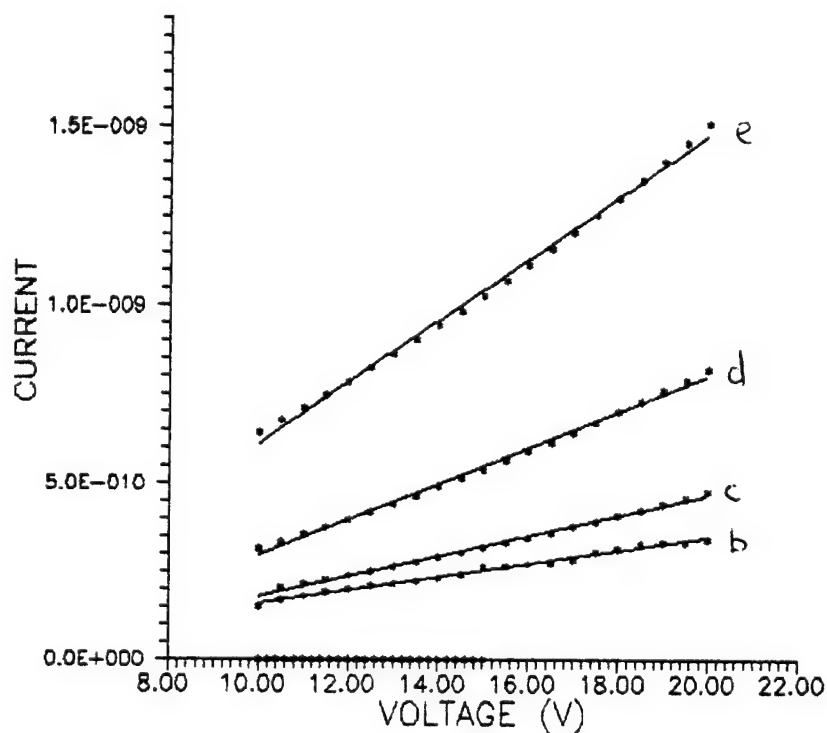


Fig. 5 Electrical conductivity measurements on  $\alpha$ -alumina: after KrF laser irradiation under air, at different laser power densities: a) untreated, b) 150 MW/cm<sup>2</sup>, c) 200 MW/cm<sup>2</sup>, d) 250 MW/cm<sup>2</sup> and e) 300 MW/cm<sup>2</sup>.

Increase in the power density, the number of laser pulses per scanning step and the number of laser scans over the sample, produce a decrease of the surface resistance (Fig. 6a,b,d). Most important seems to be the influence of the number of the laser pulses and laser scans deposited on the ceramic material. The reason for that may be the consequent increase of the affected depth. Fig 6c shows that the increase of the repetition rate leads to a negative effect. This means that the low repetition rate ( $\sim 10$ Hz) gives lower surface resistance.

Very important role in the change of the surface electrical conductivity plays the atmosphere in which the excimer laser treatment takes place.

Similar experiments have been carried out with a Nd-YAG laser. These experiments show that there is a slight change of the surface conductivity which is of the same order of magnitude with the untreated surface.



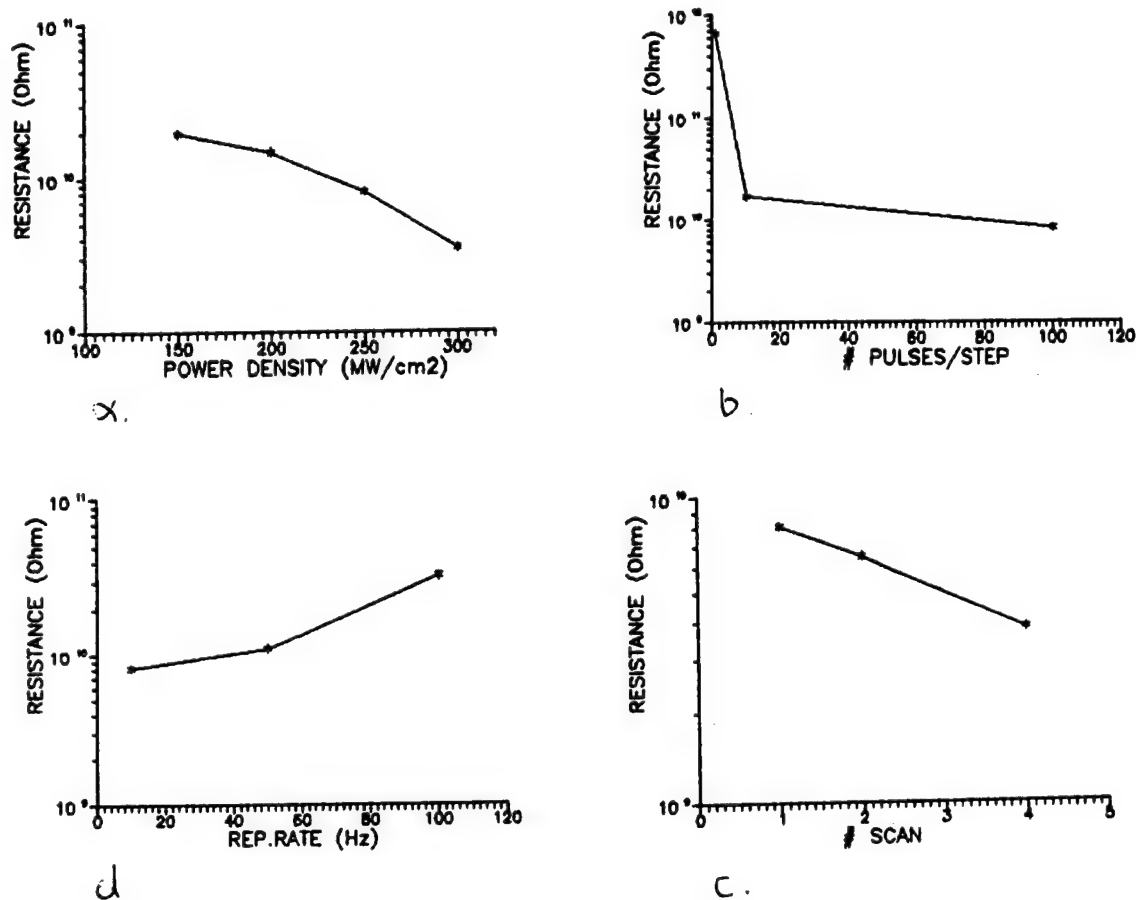


Fig. 6 Effect of the KrF laser processing parameters on electrical conductivity of  $\alpha$ -alumina, treated under air: a) Power density, b) No of laser pulses per scanning step, c) No of scans, and d) repetition rate.

#### 4. CONCLUSIONS

Excimer laser treatment of ceramic material (bulk or coating) under specific conditions, improve the surface morphology by reducing the roughness, the porosity and the density of microcracks at the surface. These results may influence a lot the surface processes and finally improve the resistance to corrosion/erosion, primarily due to a reduction of the available surface area.

In addition, excimer laser surface treatment produces positive changes in the microhardness and toughness of the ceramic material surface, as well as material orientation and new phases formation. The latter, together with possible photochemical changes of the surface chemical composition increases the surface electrical conductivity which could be an important potential industrial application.

## 5. ACKNOWLEDGMENTS

This work is supported by the Greek General Secretariat for Research and Technology under EUREKA, EUROLASER EU 205 programme.

## 6. REFERENCES

- 1) J.J. Mecholsky "Engineering research needs of advanced ceramics and ceramic-matrix composites", Ceramic Bulletin vol 68(2), p 367-375, 1989.
- 2) M. Eyett, D. Bäuerle, W. Wersing, K. Lubitz and H. Thomann, "Laser induced chemical etching of ceramic  $\text{Pd Ti}_{1-x}\text{Zr}_x\text{O}_3$ ", Appl. Phys. A, vol. 40, p. 235-239, 1986.
- 3) A. Kapenieks, M. Eyett and D. Bäuerle, "Laser induced surface metallization of ceramic PLZT", Appl. Phys. A, vol. 41, p. 331-334, 1986.
- 4) J. Yamamoto and Y. Yamamoto, "Laser machining of silicon nitride", Proc. LAMP 87, p.297-302, May 1987.
- 5) T.A. Znotins, D. Poulin and J. Reid, "Excimer Lasers: An emerging technology in material processing", Laser Focus/Electro-Optics, vol 23(5), p. 54-70, May 1987.
- 6) K.J. Schmatjko, G. Endres and H. Durchholz, "Surface modification of ceramics by excimer laser irradiation", Proc. LIM5, September 1988.
- 7) K.J. Schmatjko, G. Endres, U. Schmidt and P.H. Banz, "Precision machining of ceramic materials by excimer laser irradiation", Proc. SPIE, vol 957, 1988.
- 8) K.J. Schmatjko, H. Burchholz and G. Endres, "Precision machining of coating layers by irradiation with a high pulse energy excimer laser", Proc. SPIE, vol 1023, p. 194-201, September 1988.
- 9) P. Helzer, "Excimer lasers tackle processing", Photonics Spectra, p. 112-114, January 1989.
- 10) B. Dutta, X.D. Wu, A. Inam, and T. Venkatesan "Pulsed laser deposition: A viable process for Superconducting thin films.", Solid State Technology, vol. 32(2), p. 106-110, February 1989.
- 11) F. Bachmann, "Excimer laser drill for multilayer printed circuits boards: From advanced development to factory floor", MRS Bulletin, p. 49-53, December 1989.
- 12) G. Gravanis, A. Tsetsekou, Th. Zambetakis, and C.J. Stournaras, "Ceramic Coatings and laser treatment", E-MRS 1990 Spring Meeting, May 1990.
- 13) E. Hontzopoulos, A. Zervaki, Y. Zergioti, G. Hourdakakis, E. Raptakis, A. Giannacopoulos and C. Fotakis, "Excimer laser ceramic and metal surface alloying applications", SPIE, vol 1397, August 1990.
- 14) E. Hontzopoulos and E. Damigos, "Excimer laser surface treatment of bulk ceramics", Appl. Phys. A, to be published 1991.
- 15) A patent for this application has been already submitted.

## Surface Nitride Synthesis by Multipulse Excimer Laser Irradiation

36980005 The Hague EXCIMER LASERS AND THEIR APPLICATIONS in English 1991 pp 256-268

[Article by E. D'Anna, G. Leggieri, A. Luches, M. Martino, and A. Perrone of the University of Lecce, Department of Physics, G. Majni and P. Mengucci of the University of Ancona, Department of Materials and Earth Sciences, A.V. Drigo of the University of Padova, Department of Physics, and I.N. Mihailescu of the Institute of Atomic Physics]

[Text]

### ABSTRACT

We studied the formation of nitride surface layers on titanium plates (0.14 mm and 3 mm thick) by multipulse (100 to 500) XeCl excimer laser ( $\lambda=308$  nm) irradiation in  $N_2$  and  $NH_3$  atmospheres (1100 mbar) at a laser fluence of  $\sim 1$  J/cm<sup>2</sup> and repetition rate of 50 Hz, with careful experimental precautions against oxygen contamination. After irradiation the samples were examined by scanning and transmission electron microscopy, analyzed by Rutherford backscattering and nuclear reaction techniques and by x-ray diffraction spectroscopy. All the experimental results point to the formation of pure titanium nitride layers without any detectable oxide phase.

### 1. INTRODUCTION

Titanium nitride was intensely studied for use as hard protective coating<sup>1</sup>, solar cell contacts<sup>2</sup> and, more recently, for applications in VLSI microelectronics as e.g. in diffusion barriers in metallization schemes to silicon semiconductor devices<sup>3, 4</sup>, gate electrodes<sup>5</sup> and local connections<sup>6</sup>. High temperature heating of the base material is usually needed to form the compound. A different approach is to provide for the formation of the nitride layer directly onto the location of interest as a result of a laser enhanced chemical reaction between the base material and a nitrogen-containing atmosphere. This technique allows for a very efficient process and has the advantage of a very accurate spatial control. Moreover, it does not require heat treatments, which usually lead to diffusion of dopants and impurities.

Most of our previous work devoted to the direct laser synthesis of refractory metal nitrides<sup>7, 8</sup>, was always encountering the limitation raised by the interference of the oxidation process. In fact, even

traces of oxygen in the ambient nitrogen atmosphere were sufficient to spoil the quality of the synthesized nitride which is turned to an oxinitride compound. Better results were obtained<sup>9</sup> with the introduction of careful precautions against contamination with oxygen.

In the present work we present results obtained by irradiating Ti plates with a high repetition rate excimer laser in pure  $N_2$  and  $NH_3$  atmospheres, stressing the differences noticed when the same samples are irradiated in the two different nitrogen-containing atmospheres.

## 2. EXPERIMENTAL APPARATUS

The samples consisted of high purity (99.6%) Ti plates with thickness of 0.14 and 3.0 mm, in order to check up for the influence of the thickness of the metal sample. Prior to irradiation, the samples were carefully cleaned with alcohol and acetone, then rinsed in deionized water and dried in a nitrogen get.

The irradiation chamber was first evacuated down to  $\sim 10^{-6}$  mbar and then filled with electronic grade (99.998% purity, less than 2 ppm oxygen contamination) either  $N_2$  or  $NH_3$  gas at a slightly superatmospheric pressure (1100 mbar) in order to avoid any possible infiltration from the surrounding air.

The irradiations were performed with a Lambda Physik LPX 315i excimer laser, which was operated with a XeCl active mixture ( $\lambda = 308$  nm,  $\tau_{FWHM} = 30$  ns) at a repetition rate of 50 Hz. The incident laser fluence was set at  $\sim 1$  J/cm<sup>2</sup>, a value sufficient to react the irradiation area without causing significant ablation of the sample material. The incident laser fluence was checked with the aid of a calibrated Gen-Tec pyroelectric detector. Series of 100 up to 500 subsequent laser pulses were directed to the same place on the surface of the samples. The laser spot on the samples had an area of about 4x6 mm<sup>2</sup>.

The irradiated samples were submitted to various independent analyses:

- a) nuclear reactions, by using the  $^{14}N(d,p)^{15}N$ , the  $^{16}O(d,p)^{17}O$  and the  $^{12}C(d,p)^{13}C$  reactions with a 0.61 MeV deuteron beam<sup>10</sup>;
- b) Rutherford backscattering investigations with a 2 MeV  $^4He^+$  beam;
- c) optical and scanning electron microscopy (SEM);
- d) transmission electron microscopy (TEM) and selected area electron diffraction (SAED) with a Philips CM12 microscope at 120 keV;
- e) x-ray diffraction with the aid of a SIEMENS KRISTALLOFLEX IV diffractometer.

### 3. EXPERIMENTAL RESULTS

#### 3.1. Nuclear reaction analysis (NRA)

The NRA technique was used to determine the number of nitrogen (N), oxygen (O) and carbon (C) atoms per unit area of the irradiated surfaces. The number of N, O and C atoms per  $\text{cm}^2$ , detected at the Ti sample surface after irradiation in  $\text{NH}_3$  and  $\text{N}_2$  ambient atmospheres is given in Table 1 and 2, respectively, as a function of the number  $n$  of laser pulses directed to the same irradiation site.

Table 1: number ( $\times 10^{15}$ ) of nitrogen (N), oxygen (O) and carbon (C) atoms per  $\text{cm}^2$  at the surface of 0.14 mm and 3.0 mm thick Ti plates, as a function of the number  $n$  of subsequent XeCl laser pulses in  $\text{NH}_3$ .

0.14 mm						
n	0	100	200	300	400	500
N	7	655	840	1455	1355	1790
O	130	170	265	335	335	325
C	75	30	30	30	30	40
3.0 mm						
n	0	100	200	300	400	500
N	11	535	910	1215	1485	1295
O	150	195	190	290	245	330
C	55	25	25	35	30	30

Table 2: number ( $\times 10^{15}$ ) of nitrogen (N), oxygen (O) and carbon (C) atoms per  $\text{cm}^2$  at the surface of 0.14 mm and 3.0 mm thick Ti plates, as a function of the number  $n$  of subsequent XeCl laser pulses in  $\text{N}_2$ .

0.14 mm						
n	0	100	200	300	400	500
N	7	810	1695	2165	2255	2470
O	130	140	170	240	235	230
C	75	35	25	35	45	40
3.0 mm						
n	0	100	200	300	400	500
N	11	1075	1610	1075	1240	1260
O	150	140	285	325	340	405
C	55	30	35	30	30	35

From the study of Tables 1 and 2, a clear increase tendency is noticed of the nitrogen content as a result of the increase of the number of laser pulses. This is true for both the cases of irradiations performed in  $N_2$  and  $NH_3$  atmospheres. However, this increase is faster in the case of irradiation performed in  $N_2$  atmosphere. We also observe that the oxygen content is kept at a quite low level in both cases. One also remarks a small amount of C atoms, which are partially removed or pushed to the bulk by the laser irradiation.

As regards the influence of the sample thickness, the main observation following from the study of the two tables is that the nitrogen content on surface is almost the same when the laser pulse number  $n$  is low, but it is substantially lower in the case of thicker (3.0 mm) samples when  $n=500$ , especially when irradiation is performed in  $N_2$  atmosphere. In this last case the oxygen contamination of thicker samples is considerably increased. We think that this behaviour can be due to a combined effect of the lower temperature reached in this case on surfaces during the laser irradiation, due to a faster heat evacuation into the bulk of the thicker sample, and to oxygen flux from the sample bulk under the action of the temperature gradient, since Ti is known to be a good oxygen getter.

It must be also observed that in our experimental condition N and O atoms are detected with nearly constant efficiency over a limited thickness of about 400 nm, due to the decrease of the (d,p) cross section for deuterons with energy below 580 keV. This could explain the apparent saturation of the nitrogen amount when the number of subsequent laser pulses is increased up to  $n=500$ . So, the information acquired with the NRA technique is to be referred to the top of the compound layer formed as a result of multipulse laser irradiation.

### 3.2. Rutherford backscattering spectroscopy

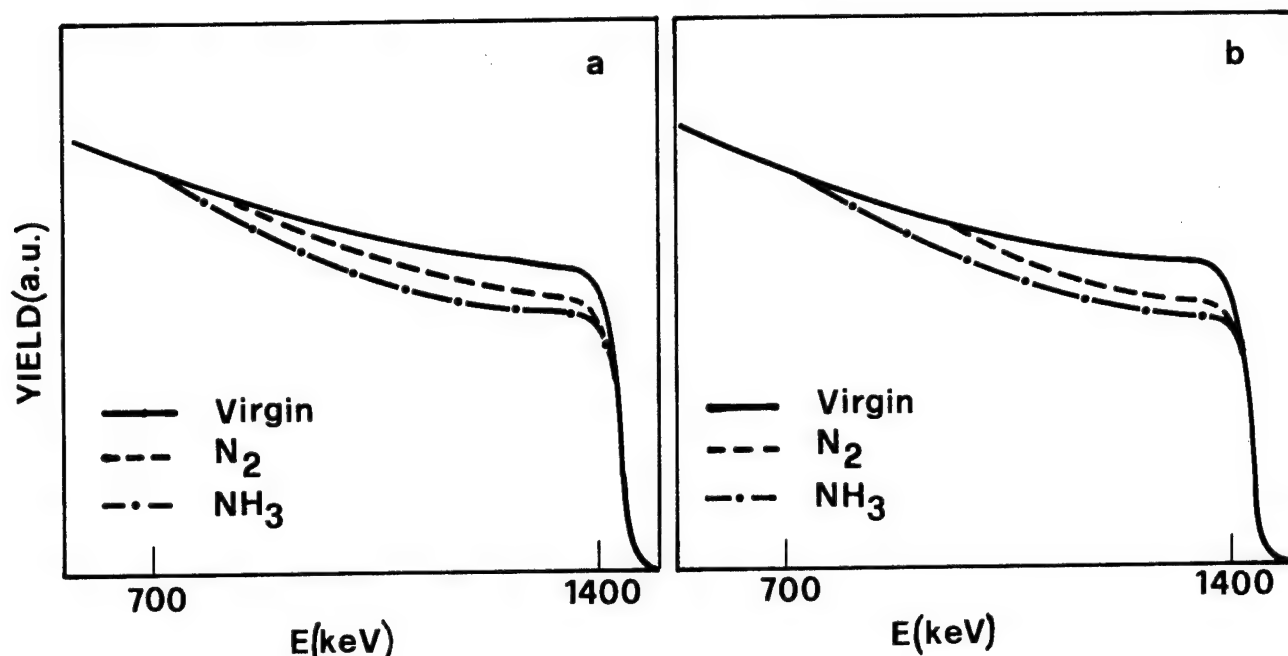


Fig. 1. RBS spectra of 0.14 mm (a) and 3.0 mm (b) thick Ti samples submitted to 100 XeCl laser pulses in either  $N_2$  or  $NH_3$  atmosphere.

In order to get more information about the thickness and the composition of the reacted layers, the laser irradiated samples were examined by the RBS technique. The corresponding spectra were compared to the spectrum of a reference, unirradiated, Ti sample. An example of RBS spectra is shown in Fig. 1. It appears that after the action of  $n=100$  subsequent laser pulses on a 0.14 mm thick sample, the thickness of the reacted layer is  $\sim 550$  nm and  $\sim 450$  nm when the irradiation is performed in  $N_2$  and  $NH_3$  atmosphere, respectively. The thickness is lower ( $\sim 400$  nm and  $\sim 300$  nm, respectively) when 3.0 mm thick samples are irradiated under the same experimental conditions. After  $n=200$  pulses in  $N_2$  the thickness of the reacted layer on 0.14 mm thick samples exceeds 1  $\mu m$ , which is the probing depth of the 2 MeV  $He^+$  beam. A general trend is that the thickness of the reacted layer is lower when the multipulse laser irradiation is performed in  $NH_3$  atmosphere.

From the analysis of the RBS spectrum height ratio it is also possible to determine the evolution of the departure from the stoichiometry,  $x$ , of the compound,  $Ti_{1-x}N_x$ , formed on surfaces as a result of multipulse laser irradiation. Figure 2 shows the dependence of the  $(1-x)/x$  quantity on the number  $n$  of subsequent laser pulses directed to the same irradiation site. We note that the stoichiometric TiN corresponds to  $(1-x)/x \rightarrow 1$ .

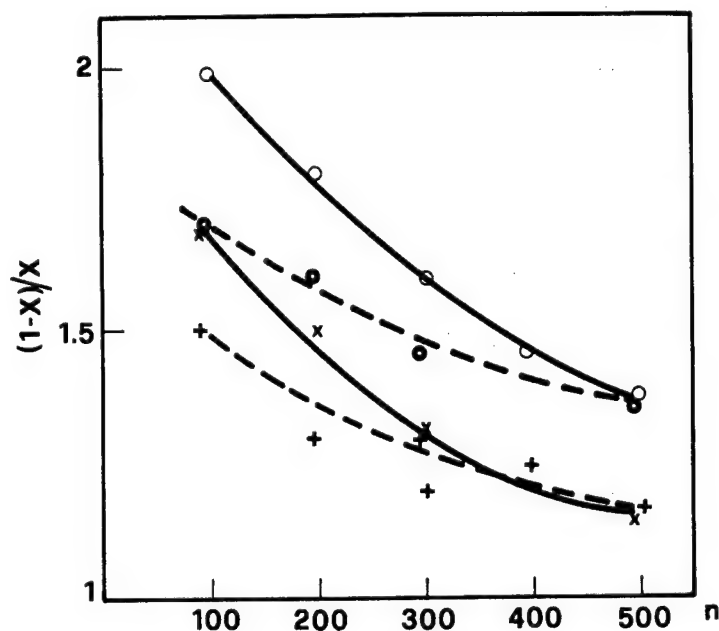


Fig. 2. The dependence of the relative non-stoichiometry degree,  $(1-x)/x$ , of the reacted layers formed on the surface of 0.14 mm (continuous line) and 3.0 mm (open line) Ti samples as a function of the number  $n$  of laser pulses in  $\text{NH}_3$  (o: 0.14 mm; •: 3.0 mm) or in  $\text{N}_2$  atmosphere (x: 0.14 mm; +: 3.0 mm) respectively.

From Fig. 2 we observe that the average composition of the reacted layer is initially richer in Ti than in N, and that it gradually converts to TiN along with the cumulation of the number of pulses directed to the same area. An important observation is that the compound is, for the same number of subsequent pulses, richer in Ti in the case of samples irradiated in  $\text{NH}_3$  atmosphere than in the case of samples irradiated in  $\text{N}_2$  atmosphere. Moreover, in both cases, the thicker (3.0 mm) Ti samples show a more uniform stoichiometric degree vs  $n$  than the thinner (0.14 mm) samples.



### 3.3 Electron microscopy observations.

The colour of the areas submitted to multipulse laser irradiation turns from bright grey (characteristic of titanium samples) to pale and then to intense yellow (characteristic to TiN) after the action of the first hundreds of subsequent laser pulses.

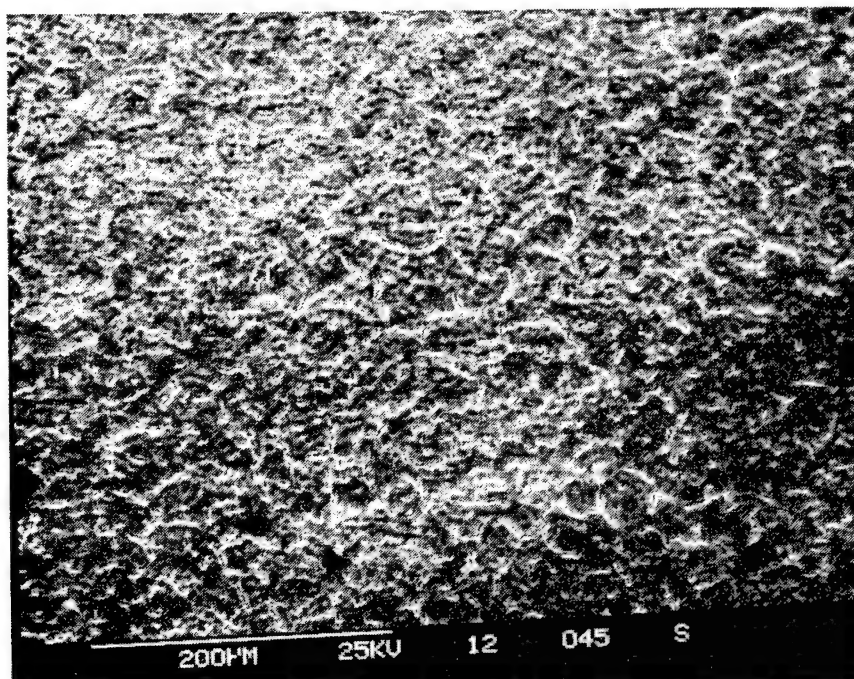
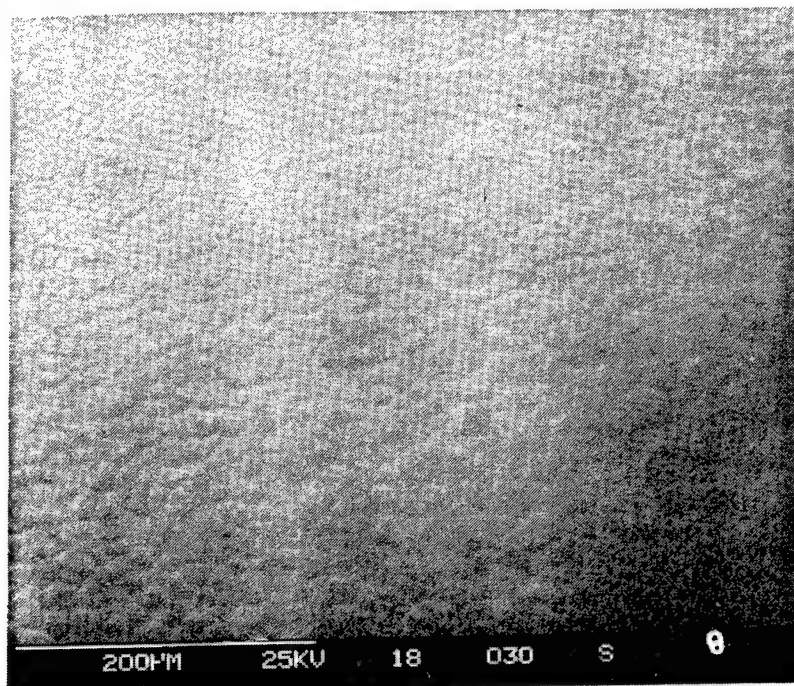
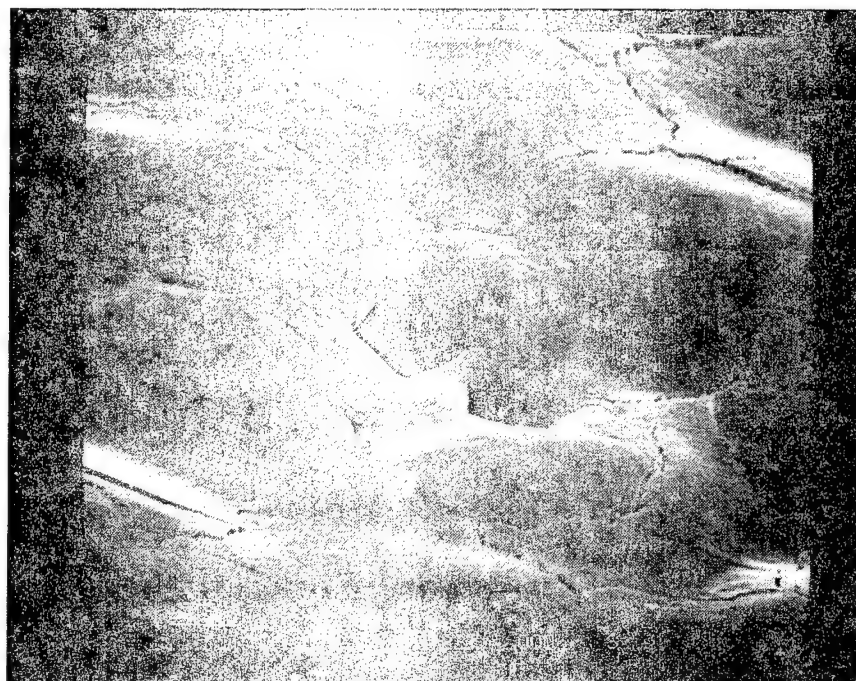
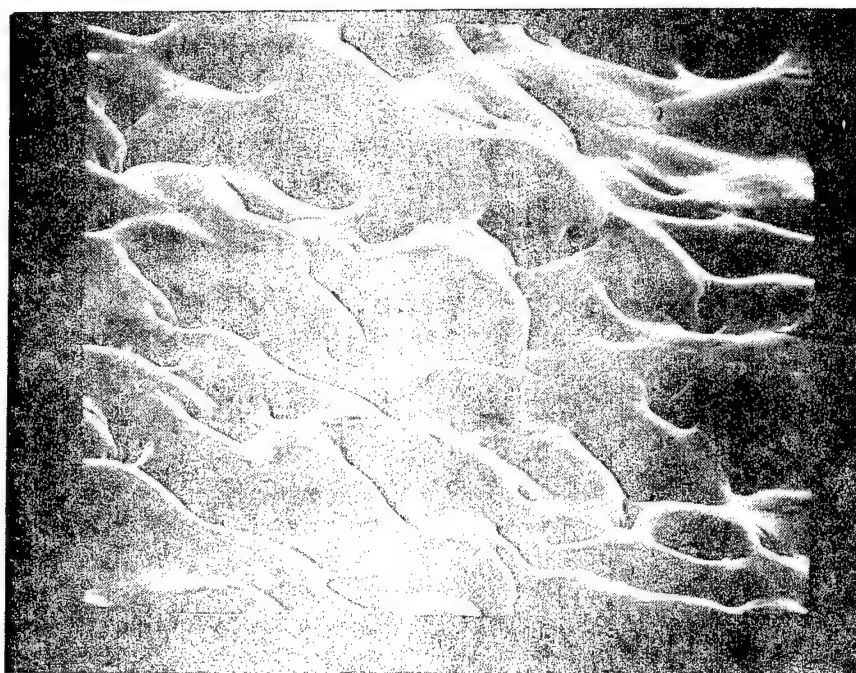


Fig. 3. SEM micrographs of 0.14 mm thick Ti samples submitted to  $n=200$  XeCl laser pulses a) in  $\text{NH}_3$  atmosphere, and b) in  $\text{N}_2$  atmosphere.

SEM investigations showed perturbations of the areas submitted to laser irradiation. A clear experimental evidence is that the areas submitted to laser irradiation in  $N_2$  are more perturbed than the ones submitted to the same number of laser pulses in  $NH_3$  atmosphere. The difference is already evident in the samples submitted to 200 laser pulses (Fig. 3a and 3b). It becomes clearly evident when one compares Fig. 4a and 4b, where SEM micrographs are reproduced of areas irradiated with 500 laser pulses in  $NH_3$  and  $N_2$  atmosphere, respectively.



**a**



**b**

Fig. 4. SEM micrographs of a Ti 0.14 mm sample submitted to  $n=500$  subsequent XeCl laser pulses; a) in  $NH_3$  and b) in  $N_2$  atmosphere.

The surfaces of the samples irradiated in  $\text{NH}_3$  seem to be covered with tightly packed grains, formed as a result of the multiple nucleation sites that occur during solidification. The microstructure of the polycrystalline matrix developed as a result of laser irradiation is very compact and pores are rare and very small. The ones of Fig. 4a were searched to focus the image. In contrast, the surface microreliefs are much more complicated and considerably deeper on the surface irradiated in ambient  $\text{N}_2$ , as evident from Fig. 4b.

TEM investigations were performed on Ti 0.14 mm samples submitted to 100 laser pulses in both  $\text{N}_2$  and  $\text{NH}_3$  atmospheres and to 500 laser pulses in  $\text{N}_2$  atmosphere.

A bright field TEM micrograph of a zone of a 0.14 mm thick sample submitted to 100 laser pulses in  $\text{NH}_3$  evidences (Fig. 5a) the formation of microcrystals with a mean dimension of 40 nm, uniformly dispersed into the reacted layer, together with some larger ( $\sim 100$  nm) islands. The corresponding SAED picture (Fig. 5b) shows a number of spots distributed along circles. The circles confirm the polycrystalline nature of the reacted layer, while the spots are related to the relatively large dimensions of some microcrystals. The relative d-spacings are reported in Table 3. From the data of Table 3 it clearly results that the reacted layer is mostly formed by TiN polycrystals with cubic structure (osbornite) and lattice parameter  $a=0.424$  nm. Traces of the  $\text{Ti}_2\text{N}$  phase, with tetragonal structure and lattice parameters  $a=0.49452$  nm and  $c=0.30342$  nm can be inferred from four very weak rings. We note that the intensity of the rings in SAED pictures is proportional to the volume density of the respective phases.

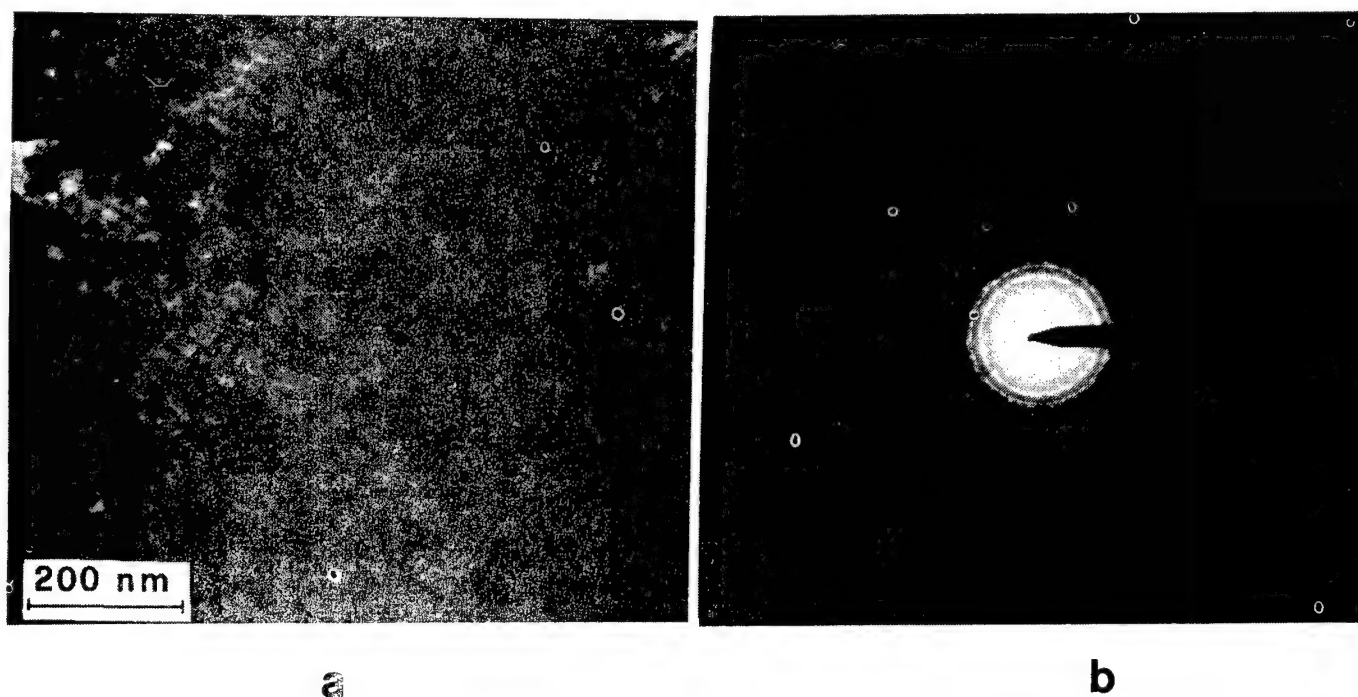
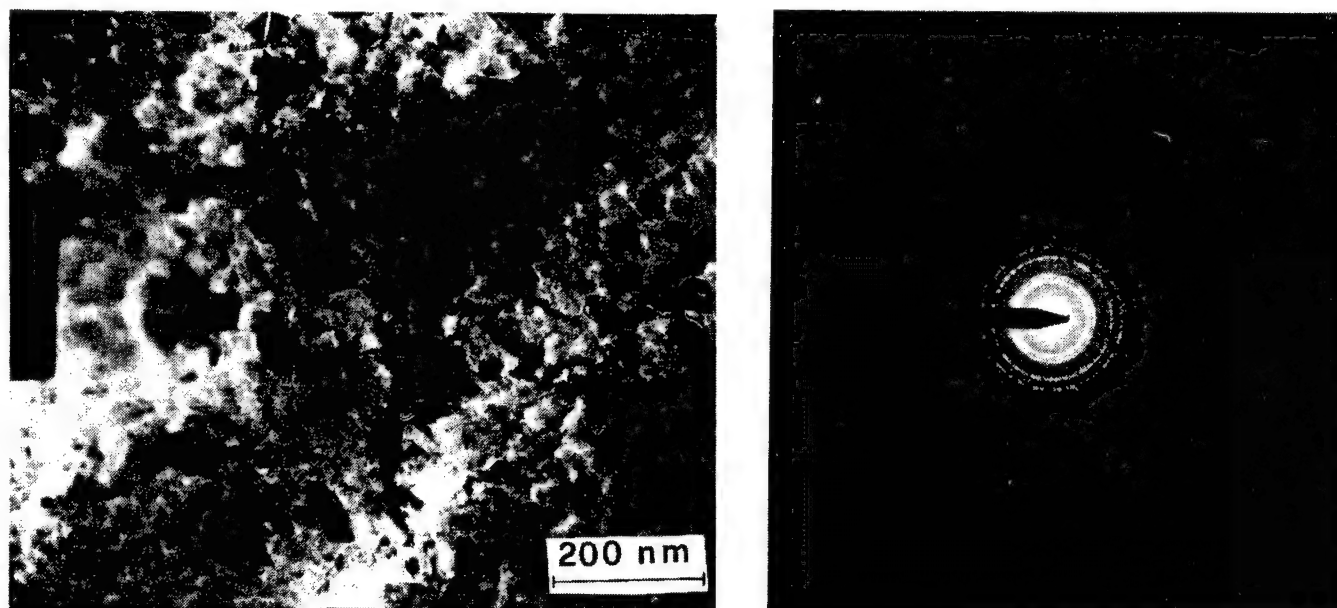


Fig. 5. TEM micrograph (a) and the corresponding SAED image (b) of a 0.14 mm thick Ti sample submitted to 100 laser pulses in  $\text{NH}_3$ .

The bright field TEM micrograph of an identical sample submitted to the same number ( $n=100$ ) of laser pulses in  $N_2$  atmosphere (Fig. 6a) evidences the formation of a very compact and uniform layer of microcrystals of mean dimension of  $\sim 70$  nm. Larger crystals cannot be seen in this sample. The corresponding SAED image (Fig. 6b) indicates (Table 4) that the reacted layer is formed almost completely of cubic TiN polycrystals, with a very small amount of tetragonal  $Ti_2N$ .



**a**

**b**

Fig. 6. TEM micrograph (a) and the corresponding SAED image (b) of a 0.14 mm thick Ti sample submitted to 100 laser pulses in  $N_2$ .

Table 3. Comparison of the measured d-spacing ( $d_m$ ) in a Ti 0.14 mm sample submitted to 100 laser pulses in  $NH_3$  with the tabulated d-spacings ( $d_e$ ) for TiN and  $Ti_2N$ ; N indicates the circles, starting from the innermost one; Miller indexes hkl are also given in the last column.

N	$d_m$ (nm)	$d_e$ (nm)			
		TiN	hkl	$Ti_2N$	hkl
1	0.26	---	---	0.2586	011
2	0.244	0.244	111	---	---
3	0.2275	---	---	0.2292	111
4	0.2113	0.212	200	---	---
5	0.1497	0.1496	220	---	---
6	0.1286	0.1277	311	---	---
7	0.1226	0.1223	222	---	---
8	0.1071	0.1059	400	---	---
9	0.0978	0.0972	331	---	---
10	0.0950	0.0948	420	---	---
11	0.0845	---	---	0.0848	350
12	0.0758	---	---	0.0759	004
13	0.0713	0.0717	531	---	---

Table 4. Comparison of the measured d-spacing ( $d_m$ ) in a Ti 0.14 mm sample submitted to 100 laser pulses in  $N_2$  with the tabulated d-spacings ( $d_e$ ) for TiN and  $Ti_2N$ ; N indicates the circles, starting from the innermost one; Miller indexes hkl are also given in the last column.

N	$d_m$ (nm)	$d_e$ (nm)			
		TiN	hkl	$Ti_2N$	hkl
1	0.26	---	---	0.2586	011
2	0.244	0.244	111	---	---
3	0.2278	---	---	0.2292	111
4	0.2117	0.212	200	---	---
5	0.1760	---	---	0.1788	211
6	0.1495	0.1496	220	---	---
7	0.1359	---	---	0.1371	320
8	0.1279	0.1277	311	---	---
9	0.1227	0.1223	222	---	---
10	0.1073	0.1059	400	---	---
11	0.0976	0.0972	331	---	---
12	0.0957	0.0948	420	---	---
13	0.0867	0.0865	422	---	---
14	0.0825	0.0816	333/511	---	---
15	0.0764	---	---	0.0764	333
16	0.0731	---	---	0.0725	024

As regards the sample submitted to 500 laser pulses in  $N_2$  atmosphere, the structure of the matrix is shown (Fig. 7a) to be formed by grains of quite large dimensions. The SAED picture (Fig. 7b) clearly

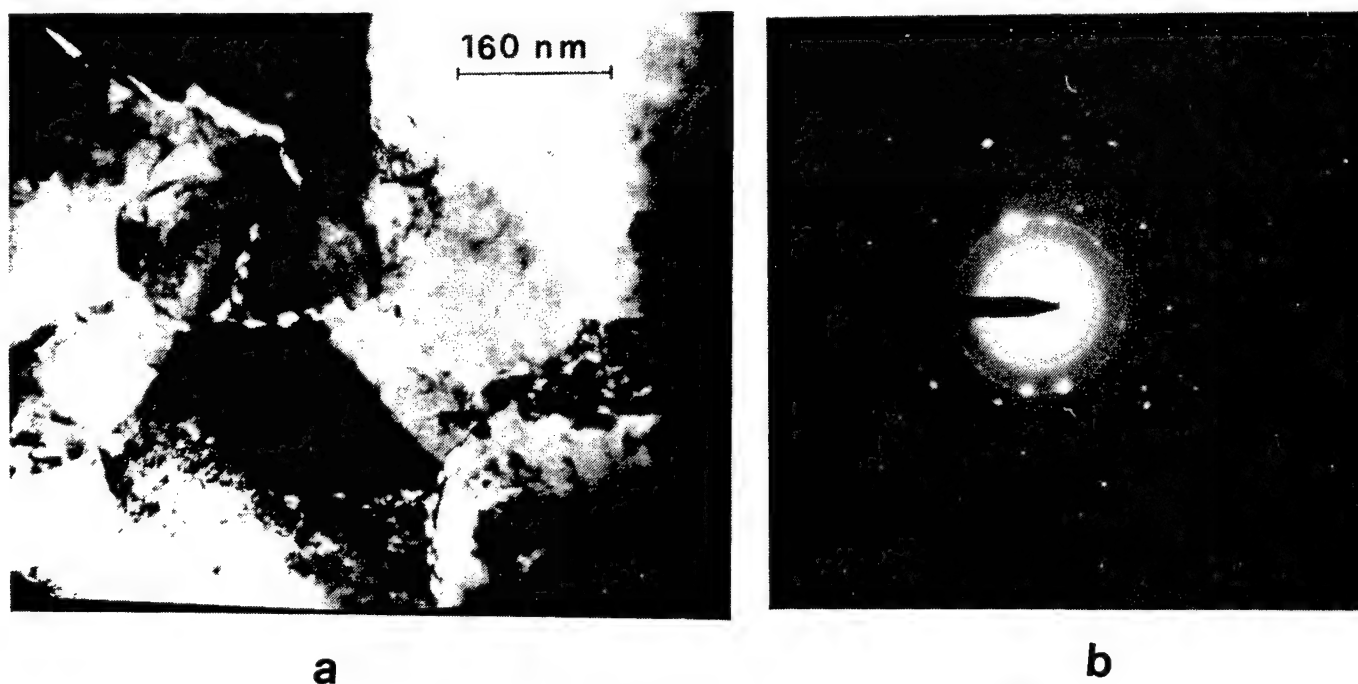


Fig. 7. TEM micrograph (a) and the corresponding SAED image (b) of a 0.14 mm thick Ti sample submitted to 500 laser pulses in  $N_2$ .



evidences the growth of a polycrystalline phase. In fact, also in this case the spots are distributed along laterally broadened circles. The relative d-spacings are reported in Table 5.

Table 5. Comparison of the measured d-spacing ( $d_m$ ) in a Ti 0.14 mm sample submitted to 500 XeCl laser pulses in  $N_2$  with the tabulated d-spacings ( $d_t$ ) for TiN; N indicates the circles, starting from the innermost one; Miller indexes hkl are also given in the last column.

N	$d_m$ (nm)	$d_t$ (nm)	hkl
1	0.2470	0.2448	111
2	0.2123	0.2120	200
3	0.1509	0.1499	220
4	0.1229	0.1224	222
5	0.0969	0.0973	331
		0.0948	420

From the data of Table 5, one sees that the diffraction pattern is clearly from TiN polycrystals. In fact the measured d-spacings ( $d_m$ ) agree very well with the tabulated<sup>11</sup> ones ( $d_t$ ) for TiN. Consequently, TiN was identified with a cubic structure (osbornite) and a lattice parameter of  $a=0.424$  nm. In contrast, there is no evidence of different phases of titanium nitride or of titanium oxide. We also remark that the points along the circles indicate that the dimensions of the TiN microcrystals are relatively large. The other points, regularly placed around the centre are due to the crystallized Ti matrix.

On the samples which were submitted to the action of  $n=100$  laser pulses,  $Ti_2N$  was identified besides TiN.  $Ti_2N$  was present in a relatively larger amount in the compound formed on Ti surface in  $NH_3$  atmosphere.

The conclusions of the SAED analyses are sustained by the results of x-ray diffraction investigations. In fact, TiN peaks clearly detach from the random background of the recording. In this case also, no traces of oxide were identified. Small peaks from  $Ti_2N$  can be seen only in the spectra obtained from samples submitted to a low number ( $n=100 - 200$ ) of laser pulses.

#### 4. DISCUSSION

The experimental investigations have proved that we succeeded to synthesize titanium nitride by multipulse excimer laser irradiation in both nitrogen and ammonia atmospheres. The reacted layers were hard, adherent to the substrate and contained no detectable quantities of oxides. Oxygen could be identified as traces only by NRA. The nitridation process is cumulative, since the amount of synthesized nitride increases with the number of subsequent laser pulses directed to the same irradiation site. Accordingly, the thickness of nitrided layer also increases with the number of subsequent pulses, while the quality and the structure of the synthesized compound improves.

Numerical computations of the temperature which is reached on the surface during the action of the first pulse in the laser pulse series, which were performed by solving the heat diffusion equation<sup>12</sup>, indicate that the nitridation reaction is initiated in our experimental condition in a liquid phase. The power density with the first laser pulse seems to be sufficient to melt the sample surface down to a thickness of about 200 nm. The surface remains then in a molten state for about 100 ns. The computer data indicate also that the successive pulses produce a deeper meltdown of the sample surface and an ever higher bulk temperature of the sample. After about 100 subsequent laser pulses, the surface layer of the 0.14 mm thick Ti samples does not resolidify between two successive laser pulses and the nitridation reaction goes on entirely through a molten phase. We also noticed the formation of an optical breakdown at the sample surfaces as a consequence of the laser pulses. The high pressure of the expanding vapour and breakdown plasma acting backwards on the irradiated area, as well as the development of surface instabilities of various nature on the molten surface (capillarity waves, the generation of surface periodical structure as an effect of the interaction of the laser light with surface plasmons<sup>13, 14</sup>), could result in the initiation of a turbulent motion<sup>15</sup> in the molten layer. This behaviour can be responsible of a strong gas enrichment of the molten layer, since this motion could drive fresh gas towards molten, but not saturated, metal. By means of the turbulent motion of the molten metal, effective velocities of gas diffusion into the melt are allowed, which largely exceed the magnitude of nitridation velocities which are obtained by conventional thermodynamic treatments. This could be the main mechanism which, followed by pyrolytic dissociation of the nitrogen-containing molecule, allows for the synthesis of rather thick layers of compound, avoiding the limitation of the gas access to the reaction area, which is the growth limiting factor that strongly inhibits, under normal (non-laser) conditions, the continuous growth of nitrides on titanium surface. In fact, the thin nitride layer, which is chemically inert and thermally very stable, acts like a shield against the access of the gaseous phase to the reaction zone. Then, the chemical reaction gets saturated in time and finally stops after the formation of a compound having a thickness of a few nm only<sup>16</sup>. It is apparent from Figs. 3 and 4 that the liquid layer is much more perturbed when the laser irradiation is performed in  $N_2$  than when it is performed in  $NH_3$  atmosphere. Consequently a thicker compound layer is formed in  $N_2$  atmosphere, having a richer content in nitrogen. Also, the surface reacted layers of the Ti samples submitted to multipulse laser irradiation in  $NH_3$  atmosphere are richer in Ti than the layers formed, under identical irradiation conditions, in  $N_2$  atmosphere. This fact could be also due to the higher content in atomic nitrogen per molecule of the gas which mixes with the molten metal in this last case. We also observe that the small amount of  $Ti_2N$  compound, which is formed in the early stage of irradiation is rapidly transformed to  $TiN$  as the irradiation, and hence the heating, of the Ti samples goes on.

New experiments, comprehensive of spectroscopic investigations of the breakdown plasma, are in progress to get a better understanding of the complicated kinetics of this laser-promoted nitridation process.

## 5. CONCLUSIONS

By a proper improvement of the laser irradiation conditions, we synthesized very pure, hard and adherent layers of TiN by multipulse laser irradiation of Ti samples in either  $N_2$  or  $NH_3$  atmospheres. As a very important progress in comparison to our previous works<sup>7-9</sup>, we emphasize the complete absence of oxide and/or oxinitride formation. The nitridation process is more efficient in  $N_2$  atmosphere than in  $NH_3$  atmosphere, but in the later case the surface layer is less perturbed.

## 6. ACKNOWLEDGMENTS

Work supported in part by Consiglio Nazionale delle Ricerche.

## 7. REFERENCES

1. L. Hattschek, American Machinist, Special Rep. N° 752, p. 128, March 1983.
2. M. A. Nicolet, Thin Solid Films, vol. 52, p. 415, 1978.
3. M. Wittmer, B. Studer and H. Melchior, J. Appl. Phys., vol. 52, pp. 5722-5726, 1981.
4. V. Craciun, I. N. Mihailescu, I. Ursu, F. Craciunoiu, A. Corici, G. Leggieri, A. Luches, V. Nassisi, and M. Martino, Appl. Phys. Lett., vol. 52, pp. 1225-1227, April 1988.
5. M. Wittmer, J. Vac. Sci. Technol., vol. A 3, p. 1797, 1985.
6. T. Tang, Ch. Wei, R. Haken, T. Halloway, Ch. F. Wan and M. M. Douglas, IEDM Tech. Dig N590, 1985.
7. I. Ursu, I. N. Mihailescu, L. C. Nistor, V. S. Teodorescu, A. M. Prokhorov, V. I. Konov and S. A. Uglov, J. Phys. D: Appl. Phys., vol. 20, p. 1519, 1987.
8. V. Craciun, G. Leggieri, A. Luches, M. Martino, I. N. Mihailescu and I. Ursu, Appl. Surf. Sci., vol. 43, pp. 304-307, 1989.
9. E. D'Anna, G. Leggieri, A. Luches, M. Martino, A. V. Drigo, J. Zemek and I. N. Mihailescu, Laser Assisted Processing II, SPIE vol. 1279, pp. 182-194, 1990.
10. M. Berti and A. V. Drigo, Nucl. Instrum. and Meth., vol. 201, p. 473, 1982.
11. Powder diffraction file, ed. by Joint Committee on Powder Diffraction Standards (Philadelphia, 1974)
12. E. D'Anna, G. Leggieri and A. Luches, Appl. Phys., vol. A 45, 1988, pp. 235-335
13. A. M. Bonch-Bruevich, M. K. Kochenghina, M. N. Libenson, V. S. Mlyn, S. D. Pudlov and V. V. Trubaev, Izv. Akad. Nauk SSSR, Ser. Fiz., vol. 46, 1982, p. 1186
14. J. E. Sipe, J. F. Young, J. S. Preston and H. M. van Driel, Phys. Rev., vol. B 27, 1983, pp. 1141-1155
15. V. N. Anisimov, R. V. Arutyunyan, V. Y. Baranov, L. A. Bolshov, E. P. Velikhov, V. A. Dolgov, A. I. Ilyn, A. M. Kovalevich, V. S. Kraposhin, D. D. Malyuta, L. A. Matveeva, V. S. Mezheveov, V. D. Pismennyi, A. Y. Sebrant and Y. Y. Stepanova, Appl. Opt., vol. 23, (1984) p. 18
16. T. Sugii, T. Ito and H. Ishikawa, Appl. Phys. Lett., vol. 45, 1984, p. 966



In Situ Growth of  $Y_1Ba_2Cu_3O_{7-x}$  Thin Films Using XeCl Excimer and Nd:YAG Lasers

36980005 The Hague EXCIMER LASERS AND THEIR APPLICATIONS in English 1991 pp 280-291

[Article by Mireille Gerri, Wladimir I. Marine, and Yves Mathey, of URA CNRS 783 and Marc Sentis, Philippe C. Delaporte, Bernard Fontaine, and Bernard Forestier of IMFM UM 34/CNRS]

[Text]

## ABSTRACT

Thin films of  $Y_1Ba_2Cu_3O_{7-x}$  were deposited via pulsed laser ablation onto MgO and YSZ (Yttria-Stabilized Zirconia) substrates. The use of an IR Nd:YAG laser leads to nonstoichiometric deposition. The best quality superconducting films were deposited by means of UV excimer laser ablation ( $\lambda = 308$  nm). These films were strongly orientated with c-axis perpendicular to (100) substrate. The film quality was found to be strongly dependent on substrate temperature, oxygen pressure, sample cooling rate and laser fluence. The deposition process was characterized by the time resolved spectroscopic measurements of the emission from YO molecules.

## 1. INTRODUCTION

During the past few years numerous techniques have been developed to grow high temperature superconducting films.<sup>1</sup> These techniques include sputtering, electron beam co-evaporation, ion beam evaporation, CVD and pulse laser ablation. Generally, after the deposition, a high temperature treatment at 800-900°C in flowing oxygen is necessary to improve the superconducting properties. However, the high temperature process degrades the film morphology. Indeed, the crystallographic inhomogeneity and grain boundaries are important limiting factors of the film quality.

The pulse laser ablation (PLA) is compatible with the reactive gas environment and has the advantage that smooth superconducting films having a orthorhombique structure can be grown in situ at temperature 600-700°C without high temperature post annealing. Actually the development of the high power and high repetition rate excimer laser<sup>2</sup> opens a possibility for the technological application of PLA to produce single-phase films over larger substrate areas. However, the solution of the processing control problems depends on an understanding of the basic physics and chemistry associated with laser beam-target and particle-particle interaction during PLA and film growth.

In this paper, we describe the results of laser deposition of  $Y_1Ba_2Cu_3O_{7-x}$  thin films using either Nd:YAG or XeCl excimer laser. In particular, the effects of the substrate temperature, oxygen

pressure cooling rate and laser parameters (wavelength, energy) on the quality of "in situ" deposited films were studied. The dynamics of the laser induced plasma (LIP) was monitored by optical time of flight measurements.

## 2. EXPERIMENTAL

For the film deposition, we used two kinds of laser, UV and IR lasers. UV laser was an X-ray pre-ionized discharged pumped excimer XeCl ( $\lambda = 308$  nm). The laser was operated at 5 Hz with 40 ns output pulses. The pulse energy was  $1-8 \text{ J/cm}^2$ . A pulsed Nd:YAG ( $\lambda = 1.064 \mu\text{m}$ ) laser was used to produce a pulse train of 35 ps (FWHM) pulses, with 9 ns time separation interval. The full pulse train duration was about 90 ns, with a 1 Hz repetition rate.

The films were prepared in a vacuum chamber with a base pressure of less than  $10^{-6}$  mbar maintained by a turbomolecular pump. The target was in the form of a disk (13 mm in diameter, 1.5 mm thick). The superconducting targets were processed with the usual procedure of mixing, calcining, regrinding and sintering. The laser beam was allowed to impinge on the target at an oblique angle of  $40^\circ$ . It was focussed on the target to a spot of about  $300 \mu\text{m}$  (FWHM). The target was constantly rotated during the deposition. The films were deposited on YSZ (yttria stabilized zirconia) and MgO single crystal (typical sized  $10 \times 10$  mm) with (100) orientation. The substrates were mounted on the heater block at 3 cm from the target and could be heated up to  $800^\circ\text{C}$ . During the deposition, oxygen was introduced at a distance of about 2-3 mm from the substrate. Equilibrium oxygen pressure in the range 50-600 mTorr was maintained in the system during deposition.

For the characterization of the deposition process, visible emission spectra from the laser induced plasma were studied. The plume of emitted particles from the target was always perpendicular to the surface regardless to the incident laser beam angle. Emission was detected through a glass window at  $90^\circ$  from the target surface normal. The optical emission was imaged through two lenses and a prism into the  $100 \mu\text{m}$  slit of a spectrometer. The spatial and the spectral resolutions were respectively  $150 \mu\text{m}$  and  $2 \text{ \AA}$ . The time dependence of the intensity of the plume was studied by using a rapid photomultiplier tube (2 ns rise time). The signals were recorded on a Croy 5450 storage oscilloscope. During the deposition, the optical system could be translated to monitor different zones of the laser plume.

The films were analysed by scanning electron microscopy (SEM), high resolution electron microscopy (HREM), X-ray fluorescence and X-ray diffractometry to study the morphology, composition and the crystallographic structure. The superconducting properties were controlled by resistivity measurement as a function of temperature, using the conventional four point probe technique.

## 3. RESULTS

### 3.a. Films properties

All the films prepared from a 1-2-3 stoichiometric target by the Nd:YAG laser evaporation were systematically low in Ba and Cu contents. The Ba and Cu deficiencies were found to increase with laser fluence. Stoichiometric films were prepared from a 1-2.4-4.2 composition target. The optimum deposition rate and target irradiance were  $1-1.5 \text{ \AA/pulse}$  and  $8-15 \text{ J/cm}^2$  respectively. We observed a very strong influence of the substrate temperature on the film properties. The films evaporated at low

temperature ( $T \approx 400^\circ\text{C}$ ) were insulating, amorphous and extremely reactive to the ambient atmosphere. The films prepared at a substrate temperature of about  $650\text{--}750^\circ\text{C}$  were partially crystallized and conducting. After annealing in flowing oxygen, none of these films ever exhibited any superconducting properties. The dependence of resistivity upon temperature indicates clearly the semiconducting behavior of these films. Most of the films were deposited on a substrate heated to  $450\text{--}550^\circ\text{C}$ . They were disordered or poorly crystallized and few conducting. A post annealing process of these films in flowing oxygen at 1 atm. has resulted in superconducting films with a critical temperature ( $T_c$ ) of about  $75\text{--}85^\circ\text{K}$ . The best annealing cycle found in this experiment is the following : rapid heating up to  $850^\circ\text{C}$ , hold at this temperature during 40 min., followed by slow cooling ( $2^\circ\text{C}/\text{min}$ ) to  $400^\circ\text{C}$ , with 1-2 h stay temperature, and then slow cooling down to room temperature.

Analysis of the film morphology by SEM shows numerous spherical particles embedded in the films. The particle size was about  $0.5\text{--}5\text{ }\mu\text{m}$ . Density and size of particles were dependent upon laser fluence and spatial position on the film. Another deficiency of IR laser ablation is the use of non stoichiometric-targets. We observed an evolution of the target surface composition during the deposition due to the fact that the IR laser ablation rate is different for the target components. Moreover, the target heating by laser irradiation and by emission from substrate heater causes the diffusion of Cu and Y on the surface. This leads to the different oxide phase formation. In this case, the composition of ablated product is not homogeneous during the deposition process.

The deposition of YBaCuO films by an U.V. excimer laser, contrary to the deposition by IR laser, shows the stoichiometric evaporation from a 1-2-3 superconducting target. Two kinds of deposition were performed :

- i) deposition in vacuum ( $10^{-6}$  Torr). This process has required a post annealing of the films in oxygen.
- ii) deposition "in situ" in an oxygen ambient environment. In this case, the films show superconducting properties without any additional treatment.

The films deposited at low temperature ( $550^\circ\text{C}$ ), without oxygen, were poorly crystallized and few conducted, like the YAG deposits. After annealing in flowing oxygen, they exhibit a superconducting behavior. In this case, the resistivity curves as a function of temperature show a metallic behavior and the  $T_c$  onset was relatively high ( $78\text{--}80^\circ\text{K}$ ). An optimal annealing cycle for these films consisted of heating at temperature of  $820^\circ\text{C}$ , during 20 min, followed by slow cooling to room temperature ; oxygen pressure was 1 atm.

The films deposited in oxygen ambient were directly in situ superconductor. The deposits were produced at different substrate temperatures ( $620\text{--}700^\circ\text{C}$ ) and different oxygen pressures ( $50\text{--}600\text{ mTorr}$ ), and then rapidly cooled down to ambient temperature at high oxygen pressure ( $2.6 \cdot 10^4$  Torr). Figure 1 shows the resistivity change for a film deposited on MgO at  $700^\circ\text{C}$  in an oxygen ambient of  $500\text{ mTorr}$  and rapidly cooled (15 min) under 2 bars of oxygen. The onset for the resistance drop was at  $\approx 85\text{ K}$  and the zero resistance was achieved at  $\approx 82\text{ K}$ . The resistivity ratio at  $300^\circ\text{K}$  and at  $100^\circ\text{K}$  was 3.2. The deposition under high oxygen pressure allows a good incorporation of oxygen during the film growth. This can explain the narrow transition and the good metallic behavior before the transition.

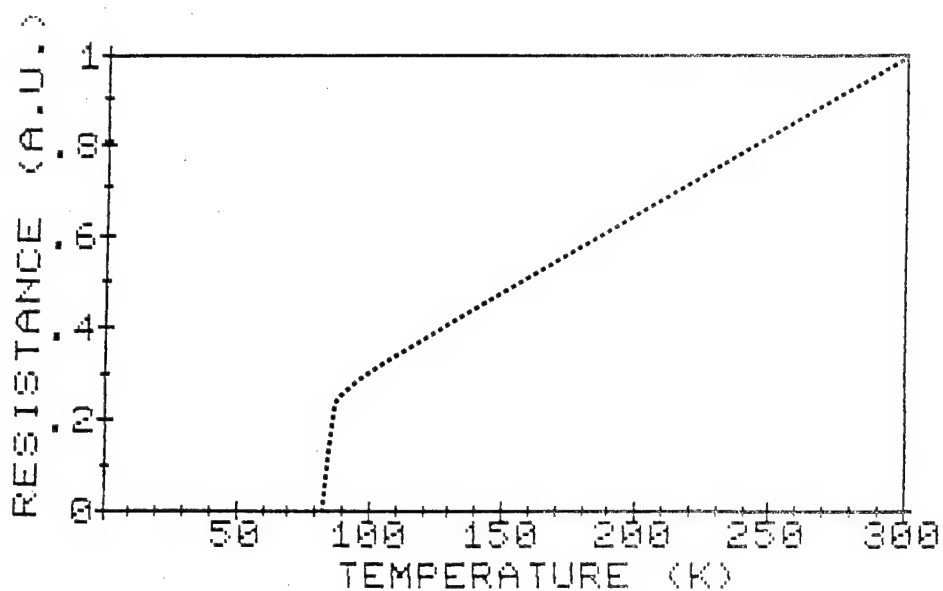


Fig. 1 - Normalized resistivity as a function of temperature. Deposition oxygen pressure and substrate temperature were 500 mTorr and 700°C respectively.

The superconducting quality depends on the deposition and cooling parameters, the laser fluence and the geometrical disposition. The Table 1 shows the representative values of the critical temperature onset ( $T_c$ ), the superconducting transition width ( $\Delta T_{90\%-10\%}$ ) and the resistivity ratio at 300°C and at 100°C ( $R_{300}/R_{100}$ ) of the in situ deposited films.  $T_s$  and  $P_{O_2}$  are the substrate temperature and the oxygen pressure during the deposition.

Table 1 : Transient parameters of in situ deposited films

Subst.	Fluence J/cm <sup>2</sup>	T <sub>s</sub> °C	P <sub>O<sub>2</sub></sub> mTorr	T <sub>onset</sub> °K	T <sub>90%-10%</sub> °K	R <sub>300</sub> /R <sub>100</sub>
MgO	4	620	120			
MgO	4	650	120	84	2.5	2.3
MgO	4	700	120	55	10	1.6
MgO	4	700	500	85	3	3.2
YSZ	4	700	120	88	4	2.1
MgO	2	650	120	89	11	1

X-ray diffraction patterns show the 1-2-3 superconducting YBaCuO structure on these films (Fig. 2). The X-ray diffraction exhibits only the presence of the (00L) Bragg peaks indicating a strong orientation of the c-axis perpendicular to the substrate. The width of the (00l) Bragg peaks was  $\approx 0.25^\circ$ . The insert to Figure 2 shows a rocking curve of the (005) peak showing a peak width of  $0.25^\circ$ . This thin width characterizes a good film epitaxial growth. For films with a lower  $T_C$ , the YBaCuO phase was not totally c-axis oriented and the presence of other undesirable crystallographic phases, like CuO, etc..., was often detected. It is probably due to more rapid Cu oxide formation at the higher substrate temperature. The appearance of other phases leads to epitaxial growth disturbance and shading of the superconducting properties of the 1-2-3 films.

The morphology of the films was studied by scanning electron microscopy. Figure 3 shows the surface morphology of these films. The films are very smooth with a surface roughness of about 100-200 Å and without any microcrystalline grain, indicating the formation of large single crystals. The micrograph shows the presence of 0.2-3 micron-sized droplets on a smooth layer. The droplet chemical composition obtained by X-ray fluorescence analysis shows non-stoichiometric YBaCuO phases. We found that the droplet concentration does not have a strong influence on the electrical properties of in situ deposited superconducting films.

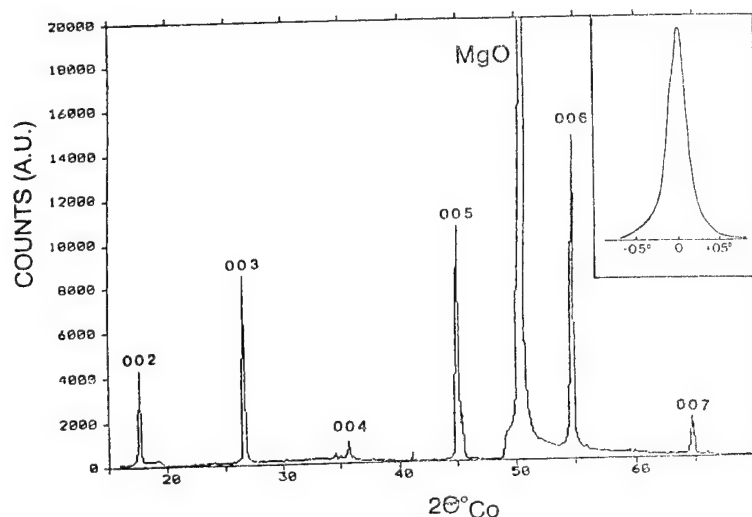


Fig. 2 - X-ray diffraction pattern of YBaCuO film deposited at 700°C on a (100) MgO cleaved substrate under oxygen pressure of 500 mTorr. X-ray wavelength is  $\lambda = 1.788 \text{ Å}$  ( $\text{CoK}_{\alpha}$ ).

Inset shows a rocking curve of the (005) peak.



Fig. 3 - Scanning electron microscope image of the film evaporated in ambient oxygen. The line is the trace of cleavage plane on the MgO substrate.

The surface of well-ordered 1-2-3 YBaCuO phase was large so that faulting was not observed by X-ray diffraction. The H.R.E.M. observation confirms that the films grown at 650° and under 120 mTorr oxygen are almost entirely c-oriented. These films contain a grain with a low density of (001) linear faults such as stacking faults and extra Cu-O planes. It is interesting to note, that the crystalline structure of the 123 phase extends up to the grain boundary.

The high-resolution image (Fig. 4) shows a grain boundary between two c-oriented grains. The tilt angle between these two grains is 30°. We can observe the good quality of the crystallization and a smooth grain boundary interface. These clean, but large angle, grain boundaries may play an important role in the transport properties of these films on MgO substrate.



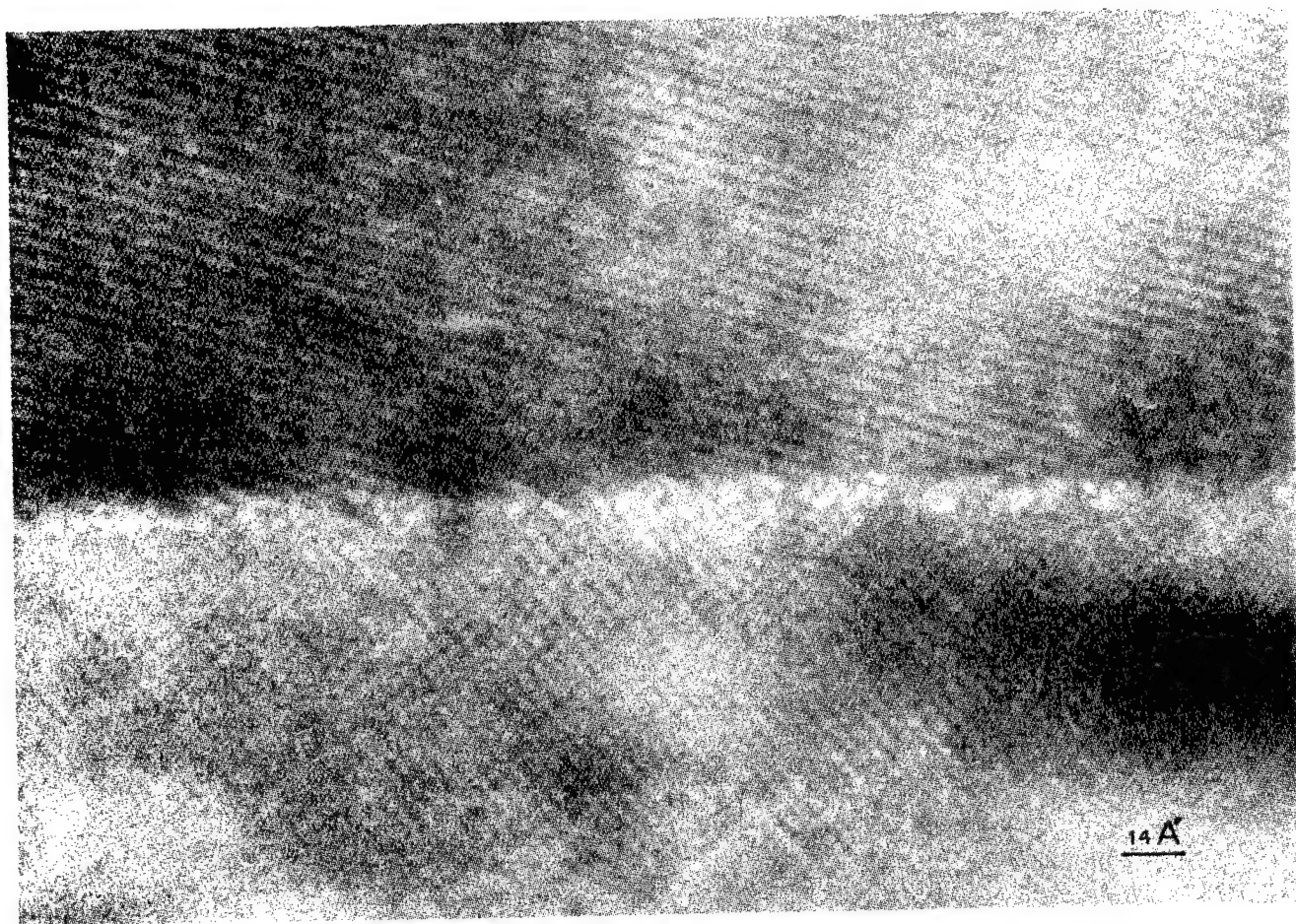


Fig. 4 - HREM image of the grain boundaries within tetragonal superconducting structure. Film has c-axis perpendicular to (100) plan of the substrate.

## b) Time of flight (TOF) measurements

The deposition process was controlled by real-time optical emission spectroscopy diagnostics. Changes in ablation parameters, such as laser energy, oxygen pressure and shot number, are reflected by variations in the optical emission from species in the laser induced plasma plume.

The emission spectra under excimer laser irradiation are similar to the one observed previously<sup>3</sup>. It can be seen that spectra are quite rich, composed of many lines and bands characteristic of the different elements from the target. The temporal behaviour of the emission was studied by TOF measurements. TOF spectra given by a slice of the plasma plume were recorded for all detected species versus distance from the target. The typical shape of the TOF spectra in vacuum of  $Y^o$  ( $\lambda = 410.2$  nm) at energy  $4 \text{ J/cm}^2$  is shown in Fig. 5. At the distance of about 1 mm from the target surface, a relatively narrow spatial distribution of the particles is established. At greater distances, we observe the broadening of the TOF spectra which is determined by the broadening of the velocity distribution. The most probable particle velocity ( $V_m$ ) was measured as the inverse slope of  $\tau_d$  versus distance, where  $\tau_d$  is the time of flight following a laser pulse at which the emission intensity has a maximum (the first spike of the TOF spectra recorded at distances more than 3 mm is due to laser scattering and can be used as a time marker).

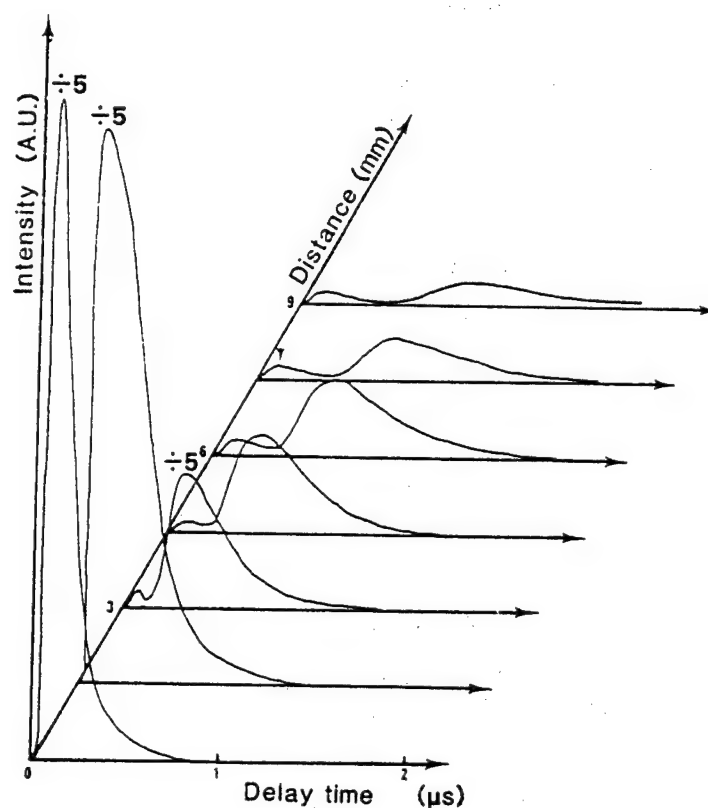


Fig. 5 - Time of flight spectrum of  $Y^*$  ( $\lambda = 410.2$  nm) as a function of distance from the target surface.



The main results of the velocity measurements are the following : expansion velocities of the monoatomic species are  $1-2 \cdot 10^6$  cm/s with weak dependence versus  $1/M$  and laser energy, where  $M$  is the atomic mass ;  $V_m \sim P^{-\gamma}$ , where  $P$  is the oxygen pressure in the preparation chamber and  $\gamma$  is a coefficient depending on the particle position from the target.

Recent measurements of the particle velocities during picosecond laser ablation of 1-2-3 YBaCuO target<sup>4</sup> show that the expansion velocity is proportional to  $1/\sqrt{M}$ . Observed  $V_m$  distribution versus atomic mass, after nanosecond excitation, reflects very large temperature dispersion of the ablated particles due to the dynamics of the target heating and, probably, due to the inverse bremsstrahlung absorption<sup>5</sup>.

The superconducting properties of the films strongly depend on the oxygen stoichiometry within the orthorhombique superconducting structure. There are two ways of the oxygen incorporation in the film. The first one is a direct oxygen diffusion from the ambient gas into the film during deposition and the cooling step. The second one is a chemical reaction of the ablated particles and oxygen during the particles' flight from target to substrate or direct ejection of the oxide molecules (YO, BaO, CuO). From the spectroscopic studies, we found that the emission from diatomic metal oxides, in particular emission from YO molecule, can be very useful to monitor the deposition process. Fig. 6 shows emission intensity variations of neutral  $Y^0$ , ionized  $Y^+$  and YO as a function of laser fluence. Comparing the variation of the emission intensities from the monoatomic species and YO, we can see that the yttrium oxide concentration decreases relative to monoatomic species as the fluence is increased.

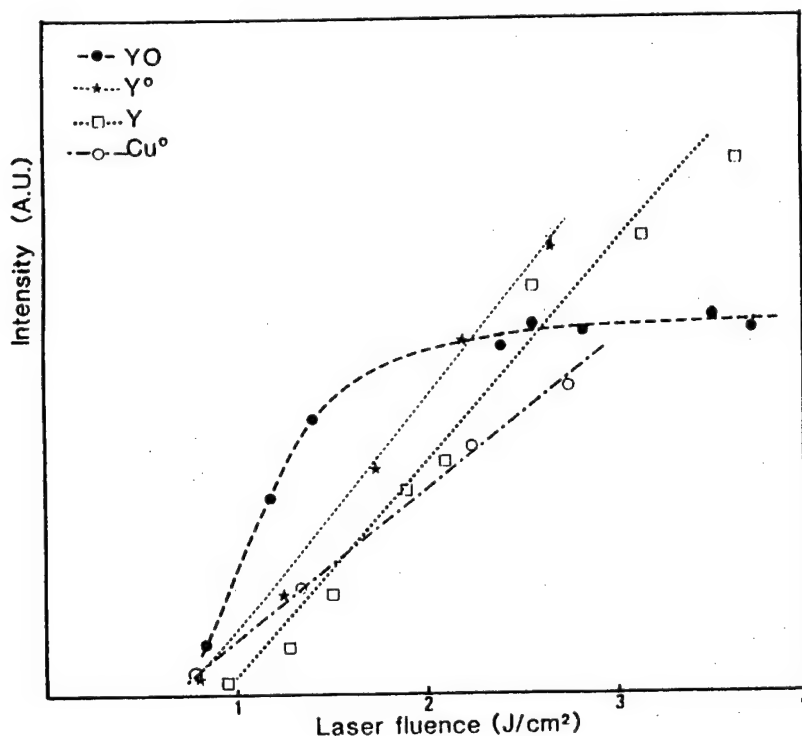


Fig. 6 - Emission intensity of  $Y^0$ ,  $Y^+$ , Cu and YO versus laser fluence. Oxygen pressure was 160 mTorr. The dashed and dotted line is drawn for the purpose of visualisation.

Similar observation has been made by Geyer and Weimer<sup>6</sup> during YBaCuO target ablation by ArF excimer laser ( $\lambda=193\text{nm}$ ) in vacuum. We believe that this effect is determined by thermal decomposition of YO molecules on the target surface.

Fig. 7 shows the variation of the intensity of YO,  $\text{Cu}^\circ$  and  $\text{Cu}^{++}$  emission versus the number of laser shots. In this experiment, the target rotation was stopped and the same target surface was irradiated with a laser fluence of about  $1\text{ J/cm}^2$ . From this figure we can see that the emission intensity from YO decreases sharply after about 100 laser shots contrary to a weak change of emission from  $\text{Y}^+$  and  $\text{Cu}^{++}$  atoms. It seems that the observed accumulating effect on the YO emission under low laser irradiation supports our assumption of the thermal decomposition of YO molecule. However it is not excluded that this effect may be explained by the creation of a deep crater in the target surface<sup>7</sup> with the result that the temperature of the plume is higher in the crater than on a flat surface. As a consequence, the molecular species can be dissociated more easily.

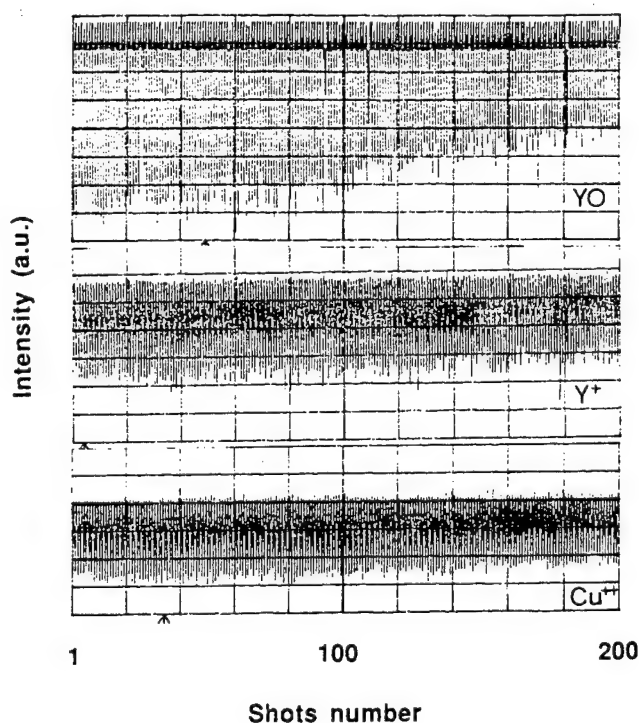


Fig. 7 - Variation of the emission intensity from YO ( $\lambda = 597.2\text{ nm}$ ) ;  $\text{Y}^+$  ( $\lambda = 410.2\text{nm}$ ) and  $\text{Cu}^{++}$  ( $492.7\text{nm}$ ) as a function of the number of laser shots. The same target surface was irradiated with successive laser pulse. Laser energy was  $1\text{ J/cm}^2$ .

Fig. 8 shows a variation of the emission intensity from YO molecules along the axial direction normal to the target surface. In vacuum (curve 1), emission intensity decreases continuously as the distance increases. Emission spectra collected during PLA at ambient oxygen pressure of about 160 mTorr show two maxima : the first one near the target surface and the second one at distances of more than 5 mm (curves 2 and 3). From the TOF measurements, we concluded that this intensity variation is determined by two different YO populations. The first one corresponds to YO molecules ejected directly from the target surface. The expansion velocity of these molecules is about  $10^6$  cm/s. The second one is characterized by much slower velocity,  $V_m \sim 4-6 \cdot 10^5$  cm/s. The emission intensity increases after time of flight of about 1-1.5  $\mu$ s (Fig. 8) corresponding to the formation of this second population. The origin of the second YO population is, probably, a chemical reaction of ionized yttrium and oxygen. The complete set of TOF measurements will be discussed elsewhere. Anyway, the emission from YO gives valuable information on oxygen contents in the laser induced plume during PLA. Moreover a stabilization of the deposition parameters can be performed by YO emission monitoring.

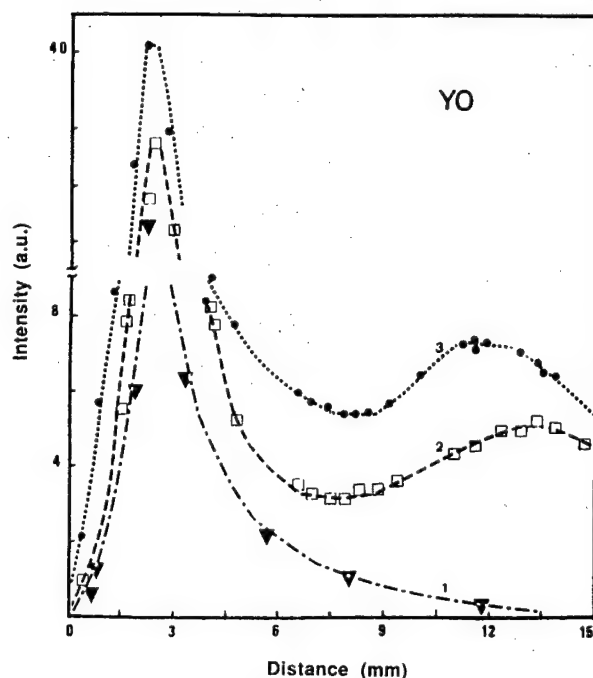


Fig. 8 - Emission intensity from YO ( $\lambda = 597.2$  nm) plotted versus distance from the target surface.

Second emission intensity increase can be observed at the distance of about 6-7 mm. The triangles, squares and dots correspond to laser energy and oxygen pressure (P) :

2 J/cm<sup>2</sup>, P =  $10^{-6}$  Torr ; 1 J/cm<sup>2</sup>, P = 160 mTorr ; and 2 J/cm<sup>2</sup>, P = 160 mTorr respectively. The line is given to guide the eyes.

#### 4. DISCUSSION

The main differences found in annealing cycles for vacuum deposited 1-2-3 YBaCuO films by UV excimer laser and IR laser irradiation are : a shorter annealing time and a lower annealing temperature for the films deposited by UV ablation. It is well-known that the particle-substrate and particle-particle interactions on the substrate are temperature activated processes. These interactions probably depend upon the particle kinetic energy, i.e. the laser energy. During the deposition process, the velocities of the ejected atoms from the target surface are about  $10^5$  cm/s and  $10^6$  cm/s for IR and UV irradiation respectively. The corresponding mean particle kinetic energies are respectively of 1 eV and of 100 eV for these two kinds of irradiation. The structure of the films deposited at low temperature (500-550°C) is amorphous with a partly crystalline phase. We can speculate that the annealing cycle is determined by the ratio of amorphous to crystalline phases after deposition. Indeed, ordered crystalline structure after UV deposition must be easier to form as a consequence of a higher local temperature and a higher particle mobility which are the consequence of the higher kinetic energy of UV ablated particles. In this case lower temperature and shorter annealing cycle are sufficient to initiate an amorphous to crystalline transition.

The films evaporated on MgO substrates at 700°C show a higher  $T_c$  onset when oxygen base pressure was 500 mTorr instead of 120 mTorr. However we observed that an increase of the base oxygen pressure requires higher substrate temperature ( $T_s^\circ$ ) in order to obtain an optimum of the film properties ( $T_c$ ,  $\Delta T$ ) since the temperature  $T_s^\circ$  is a function of oxygen pressure ( $P$ ) in the preparation chamber. The relationship between  $T_s^\circ$  and  $P$  may result from a change of the plasma expansion dynamics with the oxygen pressure increase. In particular, the velocity decrease of the evaporated particles could slow down the nucleation and the growth rate. X-ray diffraction studies show that the superconducting films deposited at  $T_s < T_s^\circ$  ( $P_{O_2} = 500$  mTorr) have a weaker degree of crystallization and present undesirable phases.

In the most of our experiments, a laser energy of about  $4 \text{ J/cm}^2$  was used. However, we find that the laser energy density also had an influence on the film quality. For two films deposited in the same conditions (650°C, 120 mTorr of oxygen, on MgO substrate), a film evaporated at lower fluence ( $2 \text{ J/cm}^2$ ) showed a superconducting transition  $T_c$  onset at 89°K. Despite this high  $T_c$  onset and the sharp decrease of the resistivity with temperature, the zero resistivity was found at a lower temperature ( $T_{c0} = 78^\circ\text{K}$ ).

The increase of the superconducting transition width is related to the presence of undesirable phases and crystalline misorientation. X-ray diffraction patterns of the films deposited at low fluence show peaks from (001) plans larger than those obtained with the films deposited at higher fluence. Moreover some weak diffraction peaks of CuO phase were observed. The increase of the superconducting transition onset can be explained by the oxygen in-diffusion during the films cooling. A crystalline misorientation of the films deposited at low fluence can favor oxygen diffusion in the  $ab$  plan due to a diffusion coefficient greater in this plan than along  $c$ -axis<sup>8</sup>.

In our experiments we mostly used cleaved MgO substrate but the nature and the quality of the substrate could modify the results. Indeed, for two films prepared in the same conditions (700°C, 120 mTorr of  $O_2$ ), a deposit on a polished (100) yttria stabilized zirconia substrate revealed a better

superconducting behavior ( $T_c$  onset = 85°K,  $\Delta T_{90\%-10\%} = 3^\circ\text{K}$ ) than on (100) cleaved MgO ( $T_c$  onset = 55°K,  $\Delta T_{90\%-10\%} = 10^\circ\text{K}$ ). At the same pressure, a substrate temperature of 650°C was sufficient to produce the films on MgO substrate with the similar  $T_c$  and  $T_{c0}$  values. The lattice parameter of the cubic structure of single crystal YSZ is  $a = 5.16 \text{ \AA}$  compared to the  $4.21 \text{ \AA}$  of the MgO lattice parameter. In spite of the large mismatch between YSZ and YBaCuO ( $a = 3.85 \text{ \AA}$ ,  $b = 3.82 \text{ \AA}$ ), the experimental results show that the nucleation/growth temperature of the 1-2-3 YBaCuO phase is higher than the one on MgO substrate.

## 6. CONCLUSION

We have shown that the use of an IR laser leads to some problems of adaptation and stabilization of the target composition. The XeCl excimer laser allows the growth of stoichiometric films. The high temperature deposition in oxygen environment, with rapid cooling under high oxygen pressure, is suitable to prepare good quality in situ superconducting films. Deposition parameters such as substrate temperature, oxygen pressure and laser energy are closely related between them and depend on the kind of substrate. The quality of the "in situ" prepared films is better than annealed ones. The best films with high critical temperature exhibit a strongly oriented crystalline structure with c-axis perpendicular to the substrate. It was found that optical emission from YO molecule can be used to monitor the deposition process during pulse laser ablation.

## 7. ACKNOWLEDGMENTS

This work is partially supported by Conseil Régional PACA. We would like to thank Dr. N.MERK for HREM observation and very helpful discussions.

## 8. REFERENCES

1. M.Leskela, J. Truman, C. Miuller and P. Holloway, J. Vac. Sci. Technol. A 7, 3147 (1989) and references therein.
2. M.L. Sentis, Ph. Delaporte, B.M. Forestier and B.L. Fontaine, J. Appl. Phys. 66, 1925 (1989)
3. W.A. Weimer, Appl. Phys. Lett. 52, 2171 (1988).
4. W. Marine, M. Gerri and J.M. Scotto d'Aniello, to be published.
5. R.K. Singh and J. Narayan, Phys. Rev., B 41, 8843 (1990).
6. T.J. Geyer and W.A. Weimer, Appl. Phys. Lett. 54, 469 (1989).
7. H. Sakeek and G. Walmsley, private communication.
8. M. Ohkubo, T. Kachi and T. Hioki, J. Appl. Phys. 68, 1782 (1990).

## Investigations on Excimer Laser Treated Cu/Cr Contact Materials

36980005 The Hague EXCIMER LASERS AND THEIR APPLICATIONS in English 1991 pp 299-309

[Article by E. Schubert, S. Rosiwal, and H.W. Bergmann of the Univ. Erlangen-Nurnberg]

[Text]

### ABSTRACT

In advanced contact materials one aim in processing is the reduction or even substitution of precious metals /1/. However, new developed materials have to exhibit excellent corrosion resistance and good electrical conductivity as well as mechanical stability, especially if abrasive wear loaded contacts are concerned. One strategy is the total substitution of precious metals by non noble metals such as by Copper and its conventional alloys. Such materials, however, suffer from their poor mechanical properties. Chromium would be a candidate for an unusual alloying element that may help to overcome these weaknesses, but unfortunately Cr does not mix with Cu by standard metallurgy. For low current contacts a surface layer of a mixed material might be sufficient and powder metallurgical routes are therefore inefficient and hence inadequate.

The excimer laser is an excellent tool to produce the required thin films by surface alloying. This is possible due to its short wavelength and short pulse duration. The present investigations were carried out in order to understand the phenomena of laser surface alloying using excimer laser irradiation. To achieve technical relevance the system Cu/Cr was chosen. The irradiations were monitored using difference reflectometry. This enables to check whether alloying occurred at all and to which degree. Structural details of the produced layers were investigated using a diffractometer with glazing incidence. To obtain quantitative information about depth and stoichiometry of the alloyed layer sputtering AES was applied.

### 1. INTRODUCTION

In the recent years excimer lasers became the third class of lasers for materials processing besides CO<sub>2</sub>- and Nd:YAG-lasers. The use of excimer lasers is most advantageous for microprocessing (good focussability) and for surface treatments /2,3/, due to their characteristic features like wavelength in the UV-range, high peak power and pulse duration in the nanosecond time regime . Some technical data, typical for commercially available excimer lasers are given in Table 1. In the present investigation XeCl and KrF excimer lasers were used for laser surface alloying experiments. On one

hand the short pulses restricted the maximum alloying depth, on the other hand high peak power in combination with the short pulses allowed to generate a mixing of Cu and Cr on an atomic scale without segregation during cooling. This is not possible neither by cw-CO<sub>2</sub>- or pulsed CO<sub>2</sub>-lasers nor by TEA-CO<sub>2</sub>-lasers, because of the wavelength and the resultant absorption behavior of the radiation. Much lower heating and subsequently lower cooling rates would therefore appear. Conventional metallurgy does not allow a solid solution of Cu in Cr in concentrations above 0,1% Cu, even in the liquid state a large miscibility gap exists /4/. The possibility to produce such a mixture via a powder metallurgical route is not very helpful, because for a low circuit contact application a thin surface layer would be sufficient.

In order to increase the depth of alloying experiments were carried out with longer pulse durations (here 250 ns). From theoretical calculations one would expect higher melting depths at equivalent power flux densities /5/.

## 2. EXPERIMENTAL

The experiments were carried out using three different excimer lasers, e.g. XeCl and KrF, radiating at 308 nm and 248 nm, respectively, with pulse durations of 30, 40 and 250 ns. The technical data of the lasers are summarized in Table 1.

The samples for the alloying experiments were prepared by sputtering CuFe<sub>2</sub>-sheets with thin Cr-layers (105, 215, 320, 420, 530 nm) using a high-frequency physical vapour deposition system. The copper sheets were cleaned by HNO<sub>3</sub>-etching and with acetone and ethanol. The samples were irradiated with energy densities between 20 and 90 mJ/mm<sup>2</sup> and 1 to 10 pulses per unit area. The experimental set-up is given in Fig. 1. The characterization of the surfaces was carried out using optical differential reflectometry, light and scanning electron microscopy and microhardness measurements. The alloying behavior was studied by sputtering Auger electron spectroscopy (AES) and with x-ray diffraction using normal and glazing incidence. The homogeneity of alloying was investigated by EDX line-scans over the irradiated area. For more detailed information on these metallographic investigation methods see Hunger et al. /6/.

Differential reflectometry measures the colour of a sample, using a reference sample (often a sample with a uniform, known reflectivity). The equipment used covers the spectral range from 300 to 720 nm). For more detailed informations about the capabilities of difference reflectometry see /7,8/. In the present investigation differential reflectometry should monitor the colour change that occurs during laser melting and is able to distinguish between a mixture of phases or a solid solution crystal. This colour change in the Cu/Cr system was quantified by measuring the change in reflectivity near the absorption edge of the difference reflectometry spectra. Microscopy was used to determine changes in surface morphology and roughness. With sputtering AES the concentration changes of Cu and Cr in depths up to 2µm could be measured, thus enabling to detect the thickness of the alloyed layers and the copper concentration profiles within these layers. Knowing that the AES measurements will smear the transition of the boundary between the Cu-containing layer and the Cr-layer the thickness quoted means the depth where the Cu-concentration exceeds more than 20% of the plateau region (see Fig. 2). The occurrence of a plateau is reasonable as extreme rapid exchange will occur in the liquid and almost none in the solid state. The Cu-content, given in this Fig. 2 is the average value in the alloyed zone.



Microhardness should give evidence for the effectiveness of the solid solution hardening by laser mixing.

To clear the lattice structure of the expected alloy x-ray diffraction experiments were carried out. With normal incidence the x-rays impinge about 2  $\mu\text{m}$ , far too much to study changes in the first micron exactly. Using glazing incidence with angles between 0,5 and 2 degrees, changes between 100 and 1000 nm can be detected.

### 3. RESULTS AND DISCUSSION

In a first step the optimum thickness of the sputtered Cr-layer was determined. The EDX line-scans over the lateral extension of one pulse show that only for 105nm and 215 nm thick Cr layers could be produced of sufficient uniformity, Fig. 3. In addition to the EDX line-scans in this figure micrographs of the surfaces after excimer laser irradiation are given. At the overlapping areas, however, large variations in concentration are still present. Therefore, in the present investigations only samples with 105 and 215 nm Cr were used.

A first hint for alloying and the formation of a solid solution was the colour change during the laser irradiation. This effect is quantified in the reflection measurements in Fig. 4a and 4b, where the reflected intensity compared to a polished Al-surface of untreated and laser mixed Cu/Cr samples is drawn as a function of the wavelength. The unsputtered Cu-sheet shows the typical absorption gap at 585 nm, a high reflectivity from 600 to 720 nm and a low reflection in the range of 550 to 300 nm, resulting in the typical red colour of Cu. After sputtering with Cr the surface shows a silver-like colour determined by a plateau in the reflection curve from 300 to 450 nm, and afterwards a continuously decreasing reflection. After laser irradiation the surfaces show a copper-like characteristic (an absorption edge at 585 nm occurs). The height of the absorption edge (A) is increasing with rising energy density and number of pulses per area. Therefore we compared this values with the Cu-contents at the surface to prove whether the differential reflectometry can be used for concentration measurements.

To estimate the obtainable alloying depths and the influence of different pulse durations, in Fig. 5a and 5b calculated temperature profiles and melt depths for metallic substrates are given using a one-dimensional heat conduction model [2]. The achievable depth should increase linearly with the power flux density and follow a parabolic law for higher pulse durations (for constant power flux densities). This could be evaluated in Fig. 6, where the obtained alloying depths as a function of the applied power flux density is drawn. Alloying is observed after exceeding a certain threshold value that is needed to heat up and melt the Cr-layer. This value is lower for longer pulses because of the increased heat input by longer pulses. With 2 pulses per area a maximum depth of 560 nm can be achieved. Applying 10 pulses the depth could be increased up to 1130 nm. The deviation from the linear correlation at high power flux densities is due to the beginning ablation by evaporation of Cr. Comparing equal values for the power flux density the effect of 250 ns pulse irradiation can be understood. Using longer pulses a certain depth of alloying can be achieved at lower power flux densities compared to shorter pulses, because of the longer interaction time for



diffusion processes. Higher intensities with 250 ns-pulses, however, were not possible as the spot size would decrease by focussing the laser beam by one order of magnitude.

The Cu-concentration in the alloyed layers also increases with the power flux density. Depending on the pulse duration the Cu-concentration reaches a plateau at high intensities. The plateau is due to a saturation effect of the mixing of Cu and Cr at about 70% Cu. Longer pulses increase the Cu-content of the alloyed layer, because of longer times for diffusion mixing (see Fig. 7).

The mechanical properties of the laser alloyed layers can be seen in Fig. 8, in terms of microhardness values for different energy densities. The hardness of the layers is increased by rising the energy density.

According to Haasen [9] the increase in strength by solid solution hardening should follow the following equation:

$\Delta HV \sim c^{2/3}$ , with  $\Delta HV$  is hardness increase in percent, and  $c$  is the concentration of the soluted phase, here Cr. Fig. 9 shows the good correlation between these two values, giving evidence for a solid solution hardening mechanism. X-ray diffraction with glazing incidence was used to gain structural informations of the alloyed layers. To check the sensibility of the method an untreated 200 nm Cr-sputtered Cu-substrate was investigated. In Fig. 10 the diffractometer plot is shown. At a glazing angle of 0,5 degrees only the Cr-peaks are visible, at 2,0 degrees the main peak is Cu. After a laser irradiation the material is still crystalline and mainly of fcc-structure, see Fig. 11. The lattice parameter was enlarged by the solution of Cr.

The results of the conductivity measurements are summarized in Fig. 12. The conductivity of the layers increases with rising Cu-content of the alloyed layer. The values are still lower than for a pure CuFe2 substrate, but would be sufficient for pin-contacts. The values can be understood assuming solid solution of Cu and Cr. The conductivity change from Cu with increasing Cr concentration can be calculated applying a law of mixture [10]. On the right axis the height of the absorption edge  $A$ , derived from the differential reflectometry measurements in Fig. 4 is drawn. The measured reflection signals are in conformity with the electrical conductivity. This could be expected <sup>7</sup> because electrical and optical properties of metals are combined according to the equations of Maxwell. Nevertheless it was surprising to find a good correlation between a colour and a conductivity measurement in such a quick and easy manner.

The last step of the investigations was, as mentioned above, to calibrate the difference reflectometry system for concentration measurements. For this reason the change in height of the absorption edge ( $A$ ) and the Cu-concentration in the alloyed layer are compared in Fig. 13. The fact that an absorption edge occurs is the first hint for the formation of a solid solution because mixing without solution would only change the spectral reflectivity. Both curves rise with the energy density. This gives evidence for the assumption that the height of the absorption edge is increasing with the Cu-content in the alloyed layer. The correlation between these two values is good enough to substitute the time consuming AES measurements, if once the calibration has been done. An additional advantage of the differential reflectometry is, that it allows an on-line measurement (100 spectra per second). Variations in the production of these contacts could be excluded, by measuring the colour of the surface immediately after laser irradiation and, if necessary, giving a signal to the laser to change the energy density or the number of irradiations for the following devices.

#### 4. CONCLUSIONS

The present investigations showed that laser alloying of Cu and Cr in depths up to 1  $\mu\text{m}$  is possible. Copper contents of about 50% in the alloyed layer were achieved. The lateral homogeneity of the alloy still can be improved, but the electrical and mechanical properties were sufficient. The structure of the alloy is cubic face centered. The lattice parameter is enlarged by solution of Chromium, compared to pure Copper. A pulse length of 250 ns produces thicker layers if equivalent power flux densities are applied. However, the spot size has to be reduced by an order of magnitude, so that an economic surface treatment is questionable. After achieving homogeneous layers, the next step will be the production of contact devices. Here the corrosion resistance and the electrical properties have to be tested under service conditions. Comparable investigations are known from literature with pulsed Nd:YAG-lasers. Applying this technique the first precious-metal-free contacts have been successfully used for telephone dialing kits /11/.

#### 5. ACKNOWLEDGEMENTS

The authors like to thank the companies Siemens AG UB KWU Erlangen/Karlstein, Lamda Physik Göttingen and W.C. Heraeus GmbH Hanau for their support. The present investigations were carried out in the Eureka-High-Power Excimer Lasers project "Surface Treatment of Metals Using Excimer Lasers" EU 205, 0047 and were supported by the BMFT under the supervision of the VDI-Technologiezentrum, Düsseldorf.

#### 6. REFERENCES

1. F. Aldinger, R. Schnabl, "Edelmetallarme Kontakte für kleine Ströme", Metall 1, pp 23-29, 1983
2. H.W. Bergmann, B. Juckenath, S.Z. Lee, E. Geissler, "Vergleich von Oberflächenbehandlungen mit unterschiedlichen Lasern", LIM 5, pp 137-148, 1988
3. K. Dickmann, C. Emmelmann, V. Hohensee, K.J. Schmatjko, "Excimer Hochleistungslaser in der Materialbearbeitung", Lasermagazin 3, pp 26-29, 1987
4. M. Hansen, K. Anderko, Constitution of Binary Alloys, Mc. Graw Hill Book Company, New York, 1958
5. H.W. Bergmann, S.Z. Lee, "Oberflächenbehandlung von Kontaktwerkstoffen mit Excimerlasern", Opto Elektronik Magazin, Vol. 3, pp 623-628, 1987
6. H.-J. Hunger, Ausgewählte Untersuchungsverfahren in der Metallkunde; VEB Verlag für Grundstoffindustrie, Leipzig, 1983

7. E. Schubert, S. Rosiwal, H.W. Bergmann, "Möglichkeiten der Differenzreflektometrie bei der Entwicklung einer on-line Qualitätskontrolle für die Metallbearbeitung mit Excimerlasern", Opto Elektronik Magazin, Vol. 5, No. 6, pp 17-30, 1989
8. K. Schlemper, S. Rosiwal, H.W. Bergmann, L. Thomas, "Differenzreflektometrie an NiAl- und CoGa-Legierungen nach einer Belichtung mit intensiver UV-Strahlung", Zeitschrift für Metallkunde, Bd. 81, H10, pp 761-770, 1990
9. P. Haasen, Physikalische Metallkunde, Springer Verlag, Berlin, 1984
10. E. Macherauch, Praktikum in Werkstoffkunde, Verlag Vieweg, Braunschweig, 1984
11. C.W. Draper et al., "Microstructure and behavior of laser-mixed Cr/Ni films on Cu alloys", Journal of Materials Research, Vol. 2, 1, pp 35-45, 1987

Fig. 1: Experimental set-up for the investigations:  
Excimer laser illumination controlled by  
differential reflectometry.

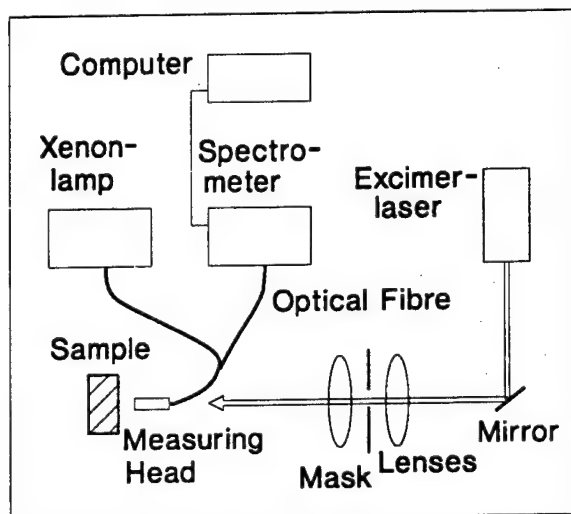


Fig. 2: Schematic drawing of the Cu- and  
Cr-concentration as function of  
the distance from the surface. The  
figure lines out the depth of  
alloying and the average concen-  
tration within the alloyed layer.

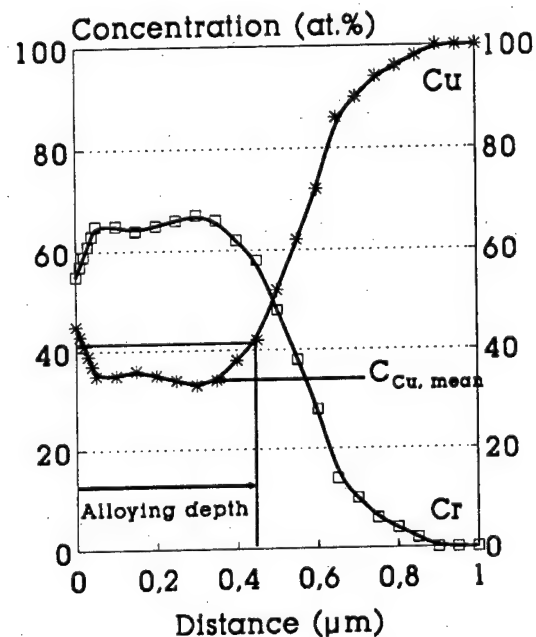


Fig. 3: Sputtered Cr-layers of different thickness on a Cu-target after illuminating by an excimer laser. The graphs show EDX line-scans indicating the concentration homogeneity on the surface. One can see that for thicker layers only insufficient alloying was obtained. On the right hand side micrographs of excimer laser treated surfaces are shown.

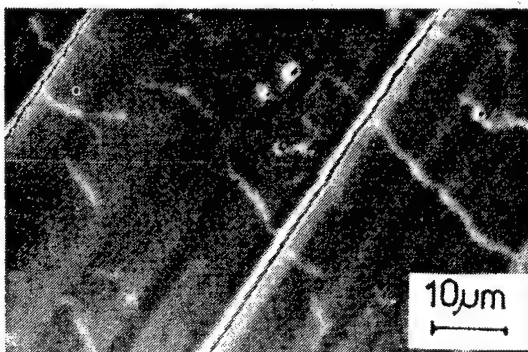
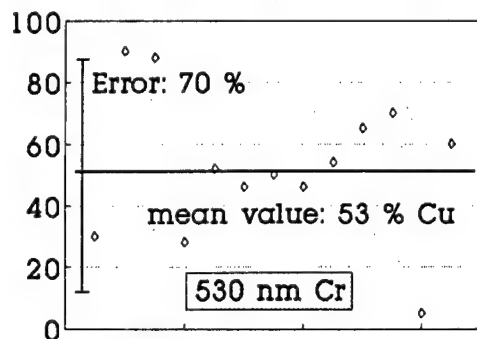
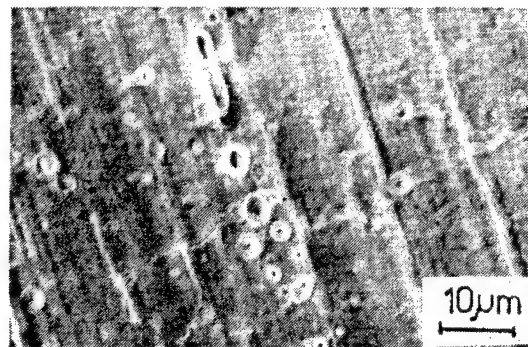
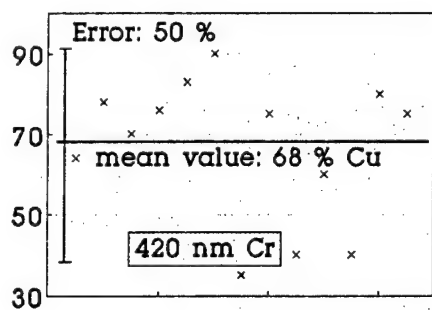
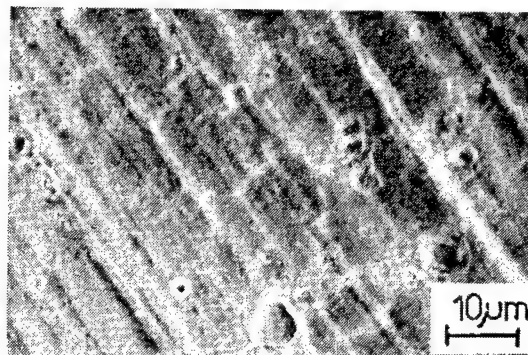
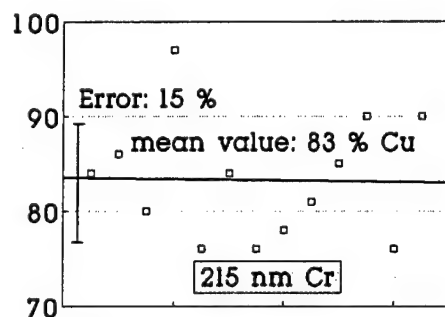
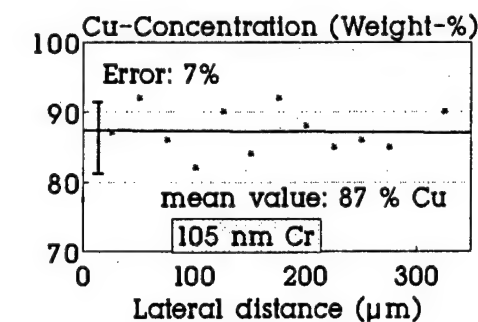


Fig. 4: Differential reflectometry of a Cu-target, coated with 215 nm Cr and irradiated with a XeCl-laser at different levels of power flux densities, two (a) and ten (b) times, respectively. The observed Cu-absorption edge indicates surface alloying. The curves for pure Cu and for the sputtered Cr-layer belong to the axis on the right hand side of the drawing.

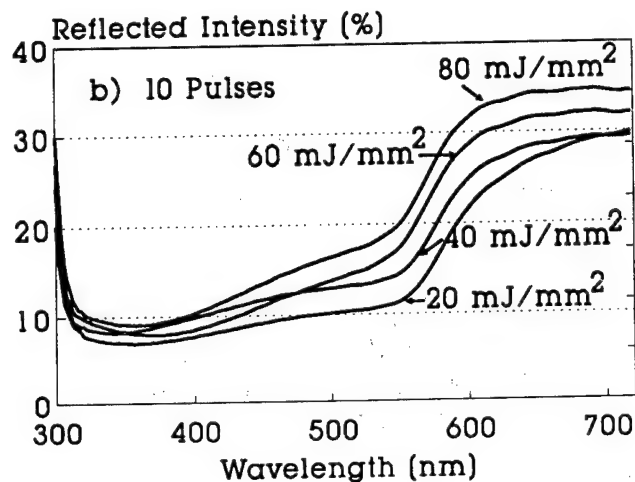
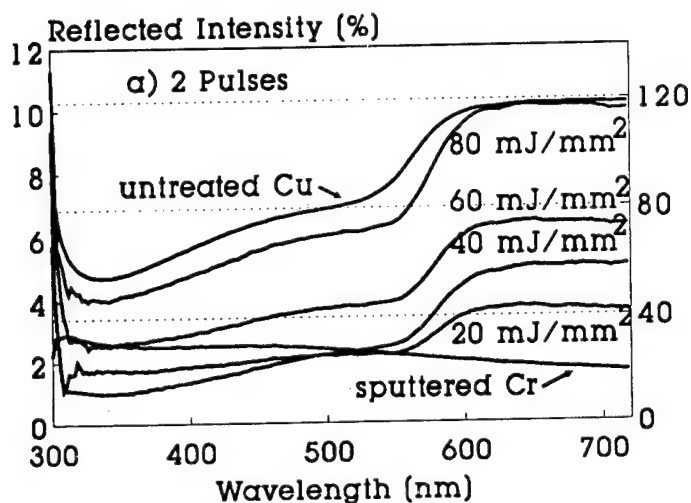


Fig. 5a: Calculated temperatures at the surface of a metallic substrate after excimer laser irradiation.

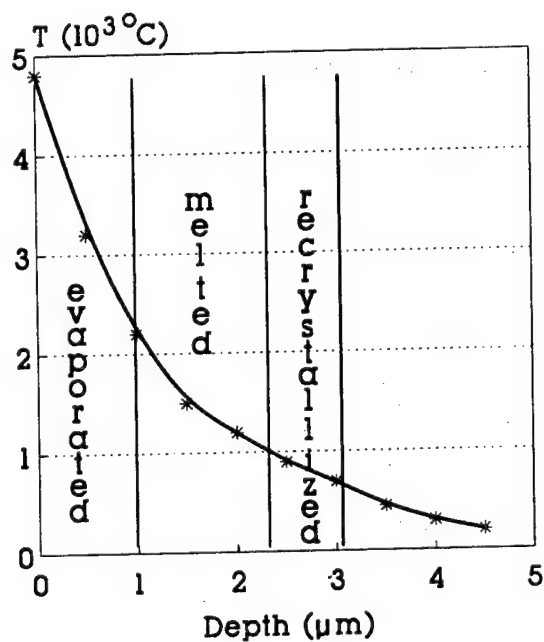


Fig. 5b: Calculated melt depth of a surface after excimer laser treatment with constant power flux density as a function of the pulse duration

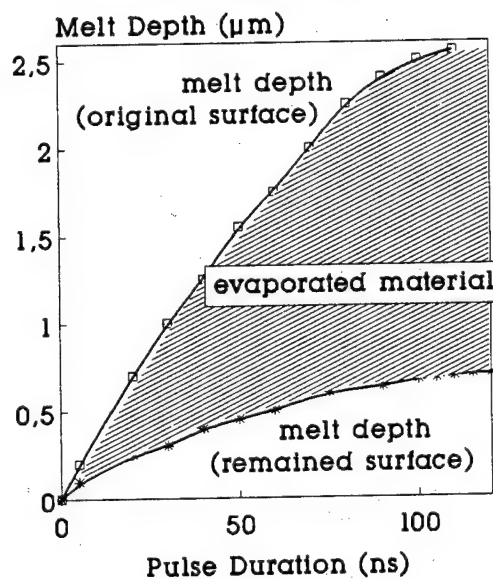


Fig. 6: The obtained alloying depths as a function of the applied power flux density, measured by sputtering AES for different laser pulse durations after two (a) and ten (b) pulses per unit area. Longer pulses generate thicker alloyed layers.

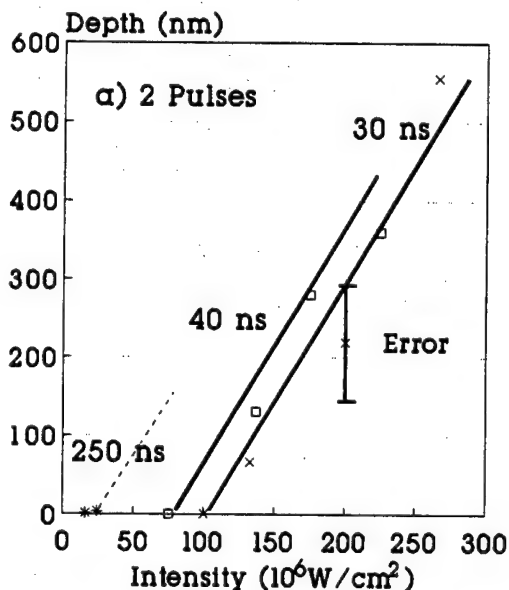


Fig. 7: Cu-concentration in the alloyed layers as a function of the applied power flux density, measured by sputtering AES for different laser pulse durations after two and ten pulses per area unit. Longer pulses generate higher Cu-concentrations in the alloyed layers.

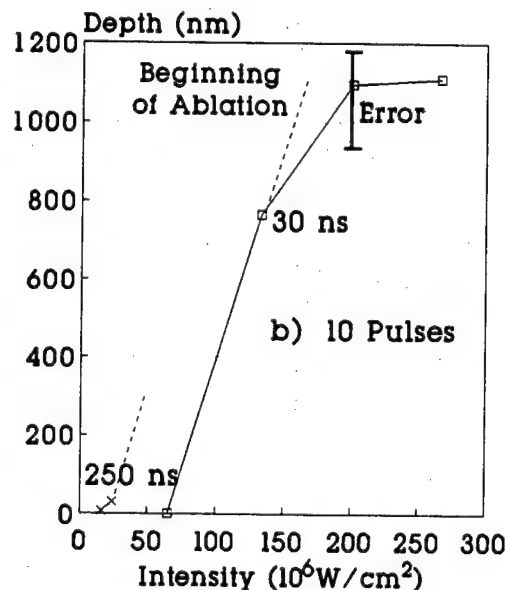
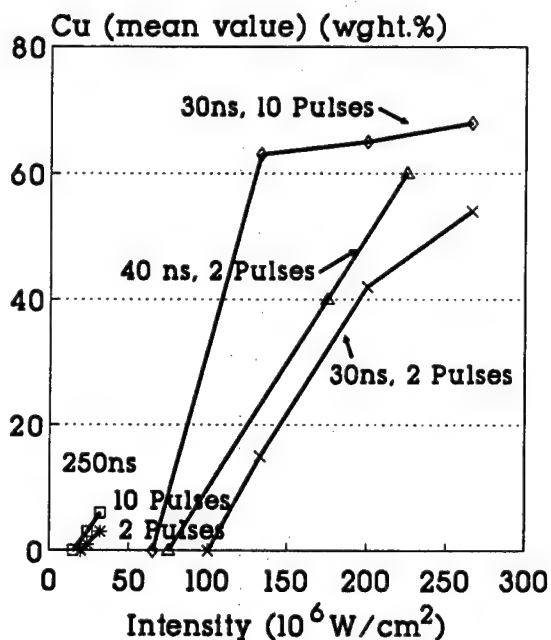


Fig. 8: The mechanical properties of the laser alloyed layers in terms of microhardness values for different energy densities. The hardness of the layers is increased by rising the energy density.

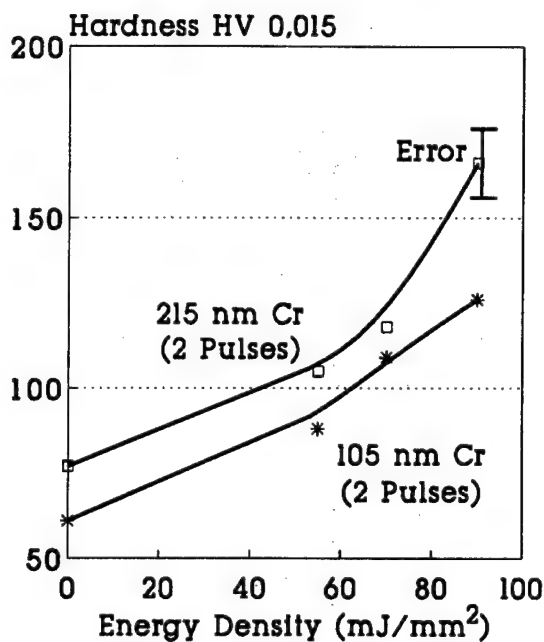


Fig. 9: Correlation between microhardness and measured Cu-concentration in the alloyed layer, giving evidence for a solid solution hardening mechanism.

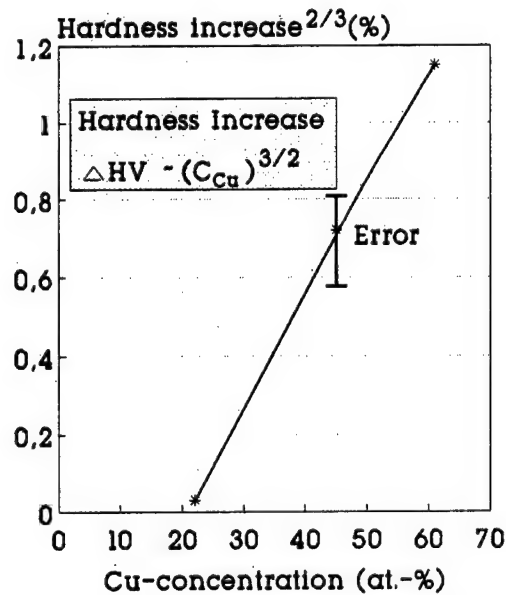


Fig. 10: Diffractometer plot of an Cr-sputtered Cu-substrate before laser treatment, using glazing incidence. At a glazing angle of 0,5 degrees only the Cr-peaks are visible, at 2,0 degrees the main peak is Cu.

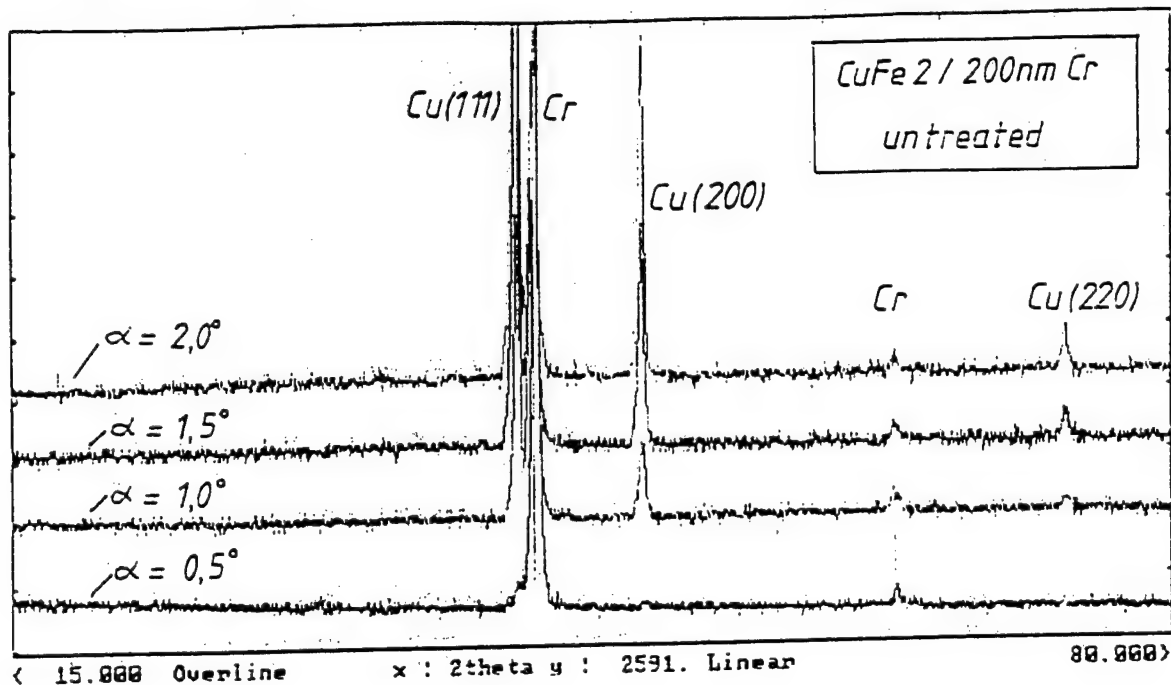


Fig. 11: Diffractometer plot of an Cr-sputtered Cu-substrate after laser treatment, using glazing incidence. The material is still crystalline and mainly of fcc-structure.

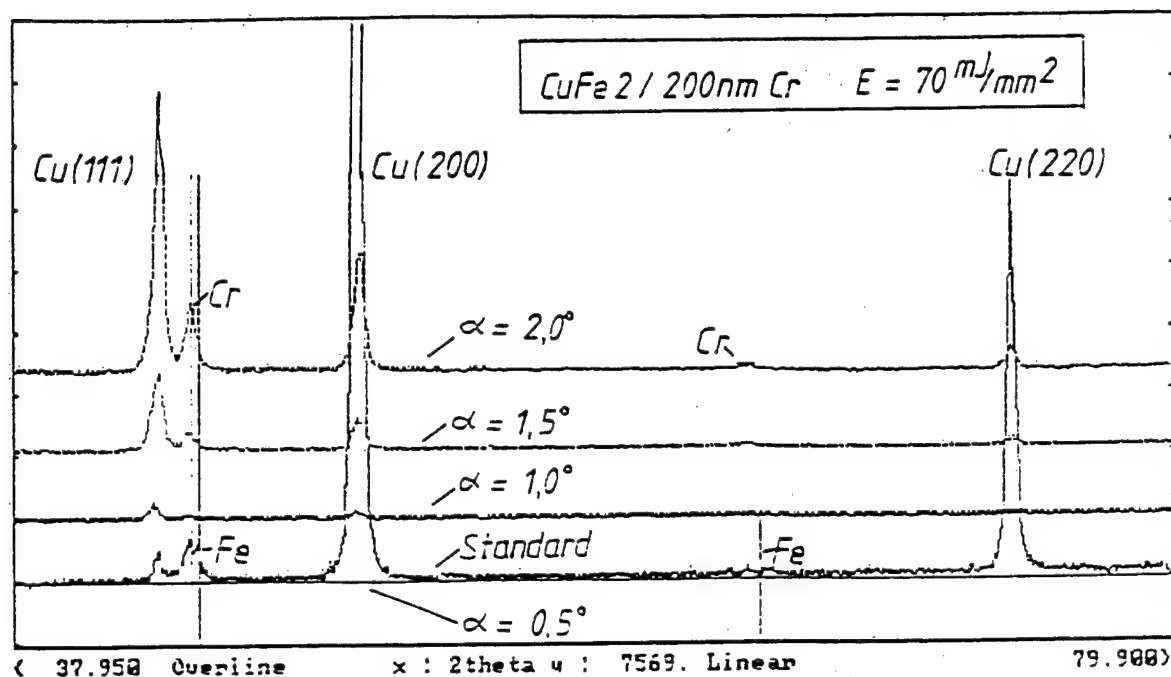




Fig. 12: Conductivity measurements of laser alloyed Cu/Cr-samples. On the right axis the height A of the absorption edge is plotted, derived from the differential reflectometry curves, given in Fig. 4. The measured reflection signals are in agreement with electrical conductivity measurements.

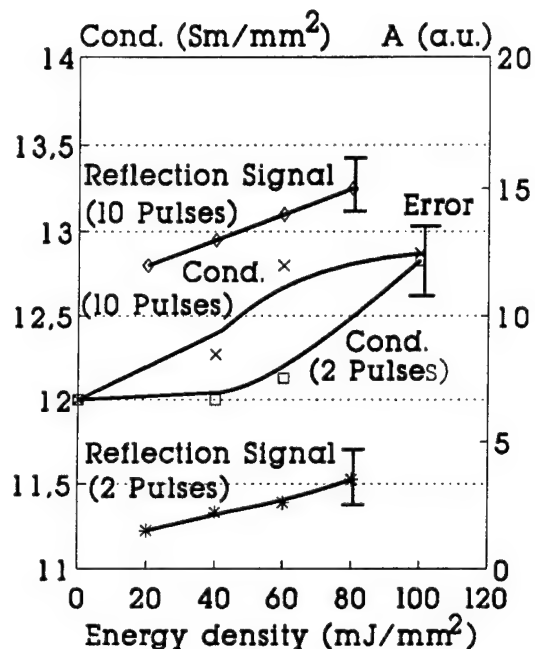


Fig. 13: Correlation between the change in height of the absorption edge A (obtained by differential reflectometry) and the Cu-concentration in the alloyed layer (measured by AES).

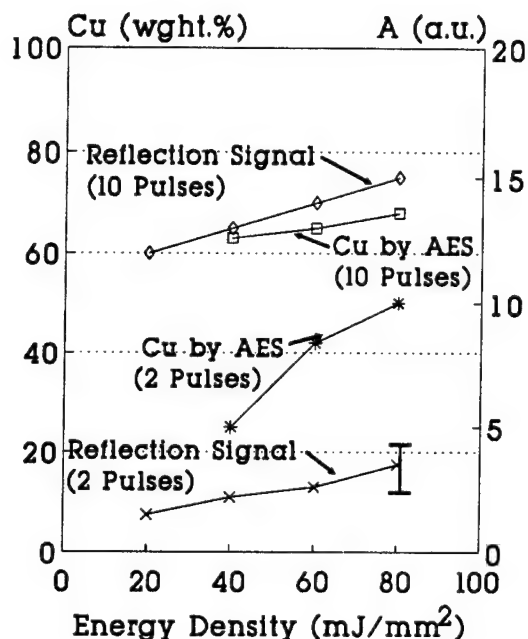


Table 1: Technical data of the excimer lasers used in this investigation

Laser	LPX610i	LPX300i	LPX300i	XP2020
Wavelength	308nm	248nm	193nm	308nm
Pulse energy	100mJ	800mJ	500mJ	2000mJ
Pulse length	250ns	30ns	30ns	40ns
Rep. rate	100Hz	150Hz	150Hz	20Hz

## Excimer Laser Deposition and Characterization of Tin and Tin-Oxide Films

36980005 The Hague EXCIMER LASERS AND THEIR APPLICATIONS in English 1991 pp 312-320

[Article by E. Borsella, P. De Padova, and R. Larciprete of the ENEA]

[Text]

### **ABSTRACT**

ArF excimer laser deposition of tin and tin-oxide films on Si was obtained dissociating tetramethyltin  $\text{Sn}(\text{CH}_3)_4$  (TMT) and TMT/ $\text{N}_2\text{O}$  mixtures. Information on the gas phase photoproducts was achieved by spontaneous emission spectroscopy. Electronically excited CH and Sn fragments were detected and their formation and decay mechanisms investigated through spectral and temporal analysis of the fluorescence signal. The effect of buffer gases on the emission characteristics was also studied.

### **1.INTRODUCTION**

Excimer laser deposition of metal and semiconductor materials is drawing a growing attention due to the potential offered by such technique for successful applications in relevant technological areas as semiconductor processing and device fabrication<sup>1</sup>. However a clear understanding of the photoreactions and a considerable control of the processes is often required in order to obtain films with well defined properties. During the last ten years extensive work has been done with the aim at identifying the photochemical pathways accessible to different organometallic molecules and at determining the suitability of different compounds to act as precursors for specific processes<sup>2</sup>. The photolysis of tetramethyltin  $\text{Sn}(\text{CH}_3)_4$  (TMT) induced by ArF excimer laser at 193 nm was studied some time ago in our laboratory using laser time-of-flight (TOF) mass spectroscopy<sup>3</sup>. The evidence that TMT could be efficiently dissociated giving free Sn atoms pushed us to investigate the possibility of depositing tin and tin-oxide films. However, as it will be discussed below, the results observed drew us to further on investigate the gas-phase photochemistry of this tin bearing compound which was done by analyzing the radiation spontaneously emitted during the occurrence of the photolysis.

### **2.FILM DEPOSITION**

#### **2.1.Experimental**

Tin containing film growth after 193 nm photolysis of TMT pure and in mixture was performed in a UHV chamber consisting of two sections separated by a gated valve. The first one, having a background pressure in the order of  $10^{-9}$  torr and utilized for the deposition process, is equipped with a sapphire window for the

ArF excimer laser (LAMBDA PHYSIK LPX 100, 12-15 ns FWHM) beam entrance and with a multi-sample holder which allows perpendicular and parallel irradiation geometry. The second section consists of a UHV chamber (background pressure  $5 \times 10^{-10}$  torr) dedicated to sample surface analysis. It is provided with a 3 grids reverse view LEED (VG RVL-640) system and with an additional electron gun (VG LEG 31) which is properly mounted on the chamber so that the electrons strike the sample under a grazing-incidence angle. In this experiment the LEED system was operated as a retarding field analyzer (RFA) electron spectrometer<sup>4</sup>: by varying the retarding potential applied to the central grid (being the others grounded) secondary electrons scattered by the sample surface could be filtered and their energy determined. Auger spectra of the sample could be obtained superimposing a several kHz modulation to the retarding potential and detecting with a lock-in amplifier the term of the collector current proportional to the second harmonic of the modulation. The combination of a magnetic translator, a wobble stick and high precision X Y X translator allows the transfer of the sample from one chamber to the other and the final positioning in the focus of the LEED-Augur grids. Si (100) substrates were Ar<sup>+</sup>-sputtered, transferred into the deposition chamber and irradiated in the presence of the gas mixture. In this stage the valve between the two vessels was kept closed to prevent gas contamination in the analytical section. In order to avoid metal deposition on the sapphire entrance window a focused laser beam geometry was adopted. TMT was purchased from Aldrich with a stated purity of 99 % and was used without further purification. Film deposition was obtained both in perpendicular and parallel geometry. When adopting typical experimental conditions ( $p_{\text{TMT}} = 0.08$  torr, laser fluence on the substrate surface 10-20 J/cm<sup>2</sup>) thicknesses in the order of 500-700 Å were obtained after irradiation with 800-1000 pulses at a repetition rate of 25 Hz. After deposition and gas evacuation the sample was transferred back to the clean chamber for the "in situ" surface analysis.

## **2.2. Results**

Curve (b) in fig.1 reports the Auger spectrum observed when analyzing a typical film grown on Si (100) after irradiation at 193 nm of pure TMT. The spectrum shows the Sn MNN Auger peaks at 430, 367 and 316 eV<sup>5</sup> whereas the peak occurring at 272 eV is due to the KLL Auger transition of carbon<sup>5</sup>. The upper curve of fig.1 displays the typical Auger spectrum of an Ar<sup>+</sup>-sputtered Si wafer used as film substrate. At variance with all the spectra measured on deposited samples in curve (a) there is no trace of carbon which in this case could be attributed to environmental contamination. In this respect we should point out that the energy resolution of our apparatus (3% of the retarding field potential) did not allow us to discriminate, through Auger peak-shape analysis<sup>6</sup>, between elemental carbon (likely deriving from processes extraneous to TMT photolysis) and bound carbon resulting from the inclusion in the layer of organic ligand carrying fragments. However the complete lack of the Auger peak at 272 eV in trace (a), which maintained for several hours after the sputtering, brought us to the conclusion that the carbon we detect should be ascribed to incorporation into the material of partially dissociated gas phase photoproducts formed in intermediate steps which diffuse toward the substrate. In addition contamination of the photodeposited film could derive from incomplete photolysis of precursor molecules which progressively adsorb on the top layer of the growing film.

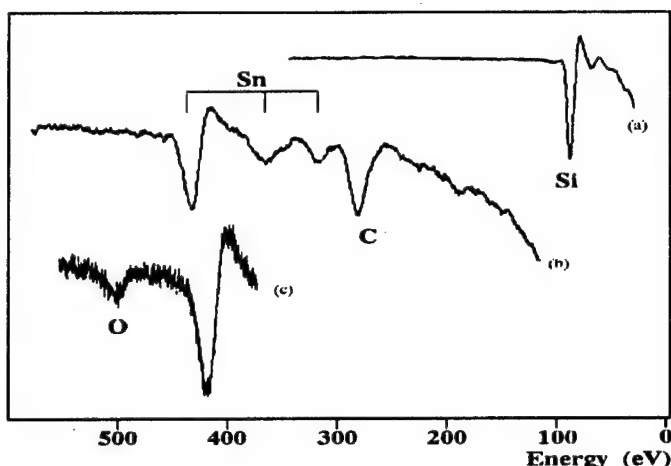
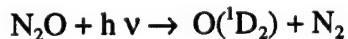


Fig.1 Auger spectra resulting after "in situ" surface analysis of ArF excimer laser deposited sample as well as of film substrate: (a) Auger spectrum of an Ar<sup>+</sup>sputtered Si (100) used as laser deposition substrate; (b) Auger spectrum of the film obtained after photolysis of pure TMT at 193 nm. The curve shows the MNN Sn peaks together with the KLL peak of C; (c) a portion of the Auger spectrum of a tin-oxide film deposited dissociating at 193 nm a TMT/N<sub>2</sub>O ( $p_{\text{TMT}}=0.2$  torr,  $p_{\text{N}_2\text{O}}=35$  torr) mixture. The presence of oxygen in the material is indicated by the peak at 510 eV. The spectra were obtained with a primary electron beam energy of 2 keV.

The possibility to deposit tin-oxide films was explored by irradiating TMT/N<sub>2</sub>O mixtures. The latter molecule is known to produce excited oxygen atoms in the <sup>1</sup>D<sub>2</sub> state when photolyzed at 193 nm through the reaction<sup>7</sup>



Curve (c) in fig.1 shows a portion of the Auger spectrum relative to a sample obtained after the irradiation of a TMT/N<sub>2</sub>O mixture ( $p_{\text{TMT}}=0.2$  torr,  $p_{\text{N}_2\text{O}}=35$  torr). The presence of oxygen in the material is indicated by its KLL Auger peak at 510 eV<sup>5</sup>. Even during surface analysis of tin-oxide samples the presence of the C KLL peak at 272 eV was always detected. The spectra of fig.1 are uncorrected for the element Auger cross-section or for the response curve of the RFA spectrometer. A rough estimation of the stoichiometry of our sample could be obtained by comparing curve (c) in fig.1 with the Auger spectrum of a standard SnO<sub>2</sub> film measured with our apparatus. This sample after having been introduced into the chamber was lightly sputtered to remove the upper layer likely contaminated after prolonged exposure to air. If we neglect the effect of sample characteristics, such as surface roughness or matrix effect, in diversifying the cross section for Sn and O Auger transitions in the two materials, we can get a rude estimation of the film stoichiometry simply comparing the ratio between the Sn (430 eV) and the O (510 eV) peak-to-peak heights measured in the two samples. The latter quantities infact are taken as being proportional to the Auger current in a spectrum measured in the  $dN(E)/dE$  mode<sup>8</sup>. In this way a [O]/[Sn] ratio 1.8 times smaller than in the SnO<sub>2</sub> sample was found in the laser deposited tin-oxide film.

The relevant C percentage in the excimer laser deposited tin and tin-oxide films pushed us to elucidate the 193 nm photolysis of TMT: complementary information to that provided by the TOF laser mass spectroscopy<sup>3</sup> were searched through analysis of the spontaneous emission.

### 3.SPONTANEOUS EMISSION SPECTROSCOPY

#### 3.1.Experimental

The fluorescence radiation emitted during the TMT dissociation was transmitted by a quartz window located on the top of the deposition chamber, deviated by a reflection prism and focused by a quartz lens on the entrance window of a monochromator equipped with a 600 or 1200 groove/mm grating. A EG&G Optical Multichannel Analyzer (OMA) was employed for detection of the dispersed luminescence spectrum. Temporal analysis of the emission signal was performed either by gating the OMA detector or by use of a fast photomultiplier coupled to a transient digitizer (TEKTRONIX 2430 or 7912 AD).

#### 3.2.Results

While irradiating TMT at a pressure between 0.01 and 0.4 torr with the focused ArF laser beam the fluorescence spectrum reported in fig.2 was detected. All the atomic lines can be attributed to Sn emission from excited states ranging between 4.5 and 5.2 eV<sup>9</sup>. The molecular band appearing around 431 nm is due to CH emission on the  $A^2\Delta \rightarrow X^2\Pi$  transition<sup>10</sup>. The presence of the ( $B^2\Sigma^- \rightarrow X^2\Pi$ ) CH band at 389 nm<sup>10</sup> was also identified in particular experimental conditions (see below) although with an intensity much weaker than the  $A^2\Delta \rightarrow X^2\Pi$  band.

The dependence of the Sn emission on the laser fluence was measured for the most intense lines. Fig.3 shows the curves obtained at 317.6, 326.3 and 380.2 nm corresponding respectively to the  $6s^3P_1 \rightarrow 5p^2^3P_2$ ,  $6s^1P_1 \rightarrow 5p^2^1D_2$  and  $6s^3P_1 \rightarrow 5p^2^1D_2$  Sn transitions<sup>9</sup>. In all cases in the absence of saturation effects the dependence was found to be cubic. This result is consistent with the minimum number of photons required energetically<sup>3</sup> and explains the absence of emission from states with energies higher than the energy supplied by three ArF laser photons. It is worth noticing that the production of Sn atoms with an energy as high as 6 eV results directly from TMT dissociation as it is demonstrated by the temporal shape of the Sn fluorescence signal which rises simultaneously with the laser pulse.

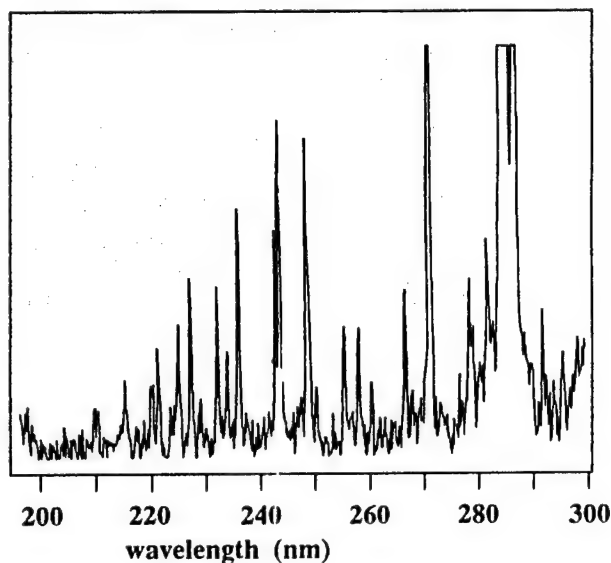
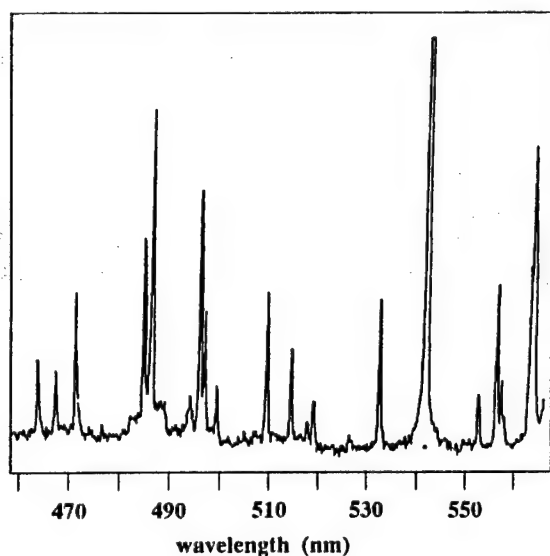
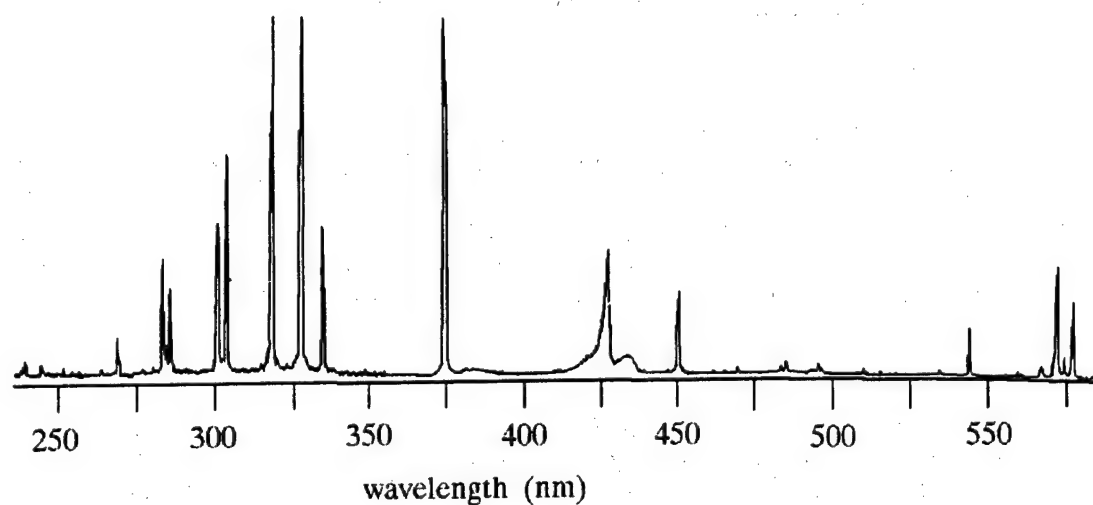


Fig.2 OMA spectra of the fluorescence emitted after the ArF excimer laser photolysis of  $\text{Sn}(\text{CH}_3)_4$ . All the lines are due to excited Sn atom emission, whereas the band at 431 nm is assigned to the  $A^2\Delta \rightarrow X^2\Pi$  transition. The upper spectrum was obtained using a 600 groove/mm grating while the portions showed below were recorded with a finer resolution (1 Å) achieved with a 1200 groove/mm grating.

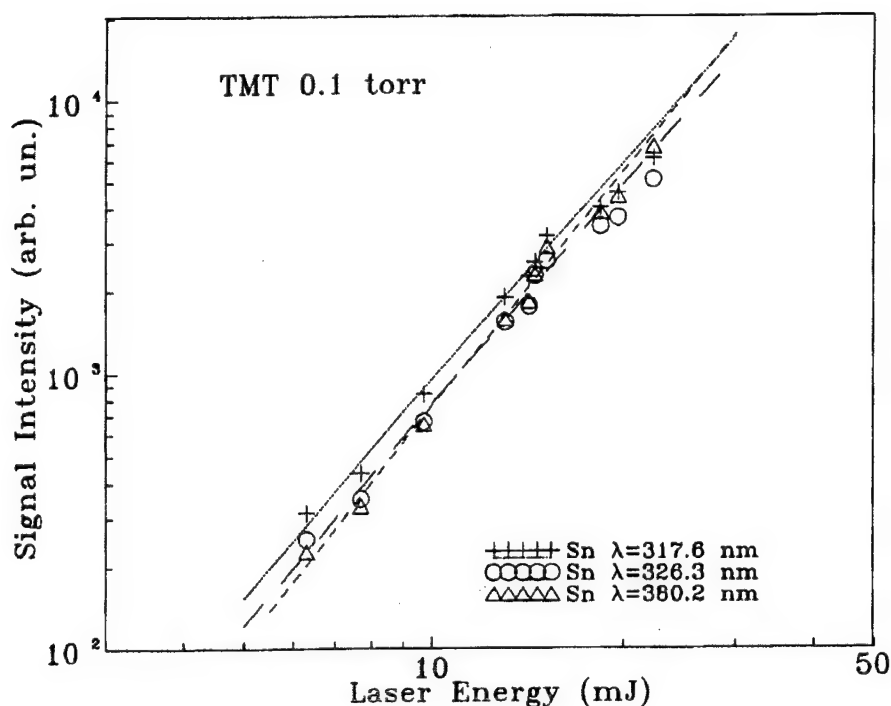


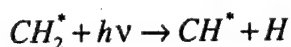
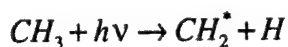
Fig.3 Sn emission intensity vs. ArF laser energy after the dissociation of 0.1 torr of TMT. The measured slope is about 3 for all the curves.

The dependence of the Sn emission at 380.2 nm on the TMT pressure is shown in fig.4 together with data on the quenching effect of a physical ( $N_2$ ) and a chemical ( $O_2$ ) scavenger. The emission intensity  $I_f$  is described by the following relationship:

$$I_f \propto P_O I_{las}^3 \left( \frac{1/\tau_r}{1/\tau_r + K_O P_O + K_b P_b} \right)$$

where  $I_{las}$  is the laser intensity,  $P_O$  and  $P_b$  are respectively the TMT and the buffer gas pressure,  $\tau_r$  is the radiative lifetime of the electronic transition,  $K_O$  and  $K_b$  are respectively the TMT and the buffer gas quenching rate constants. This formula predicts a linear dependence of the emission intensity vs. TMT pressure until saturation is reached (at  $K_O P_O \gg 1/\tau_r$ ). The influence of a physical quencher like  $N_2$  becomes relevant at  $P_b > 20$  torr, while the effect of a chemical additive as  $O_2$  consists in increasing the emission intensity until fragment recombination is effectively counteracted by chemical reaction with  $O_2$ . At higher pressures the effect of  $O_2$  is well described by a linear Stern- Volmer relationship ( $1/I_f \propto K_b P_b$ ) as in the case of  $N_2$  addition.

The formation of electronically excited CH radicals responsible for the emission bands observed at 390 and 431 nm can be ascribed either to two photon excitation of the methyl radical<sup>10</sup> or to a two-step dissociation mechanism<sup>11</sup>:



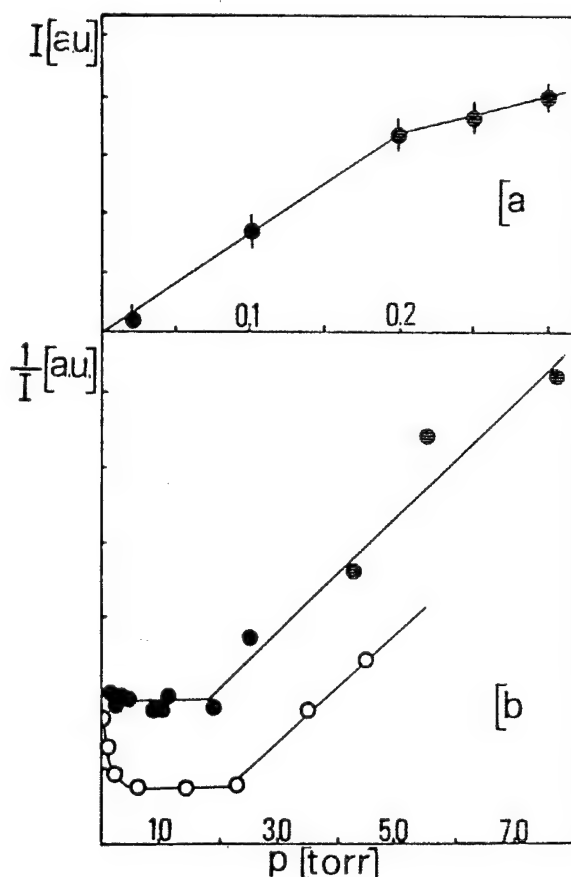


Fig.4 Sn emission intensity at 380.2 nm vs. (a) TMT pressure (b)  $N_2$  (●) and  $O_2$  (○) buffer gas pressure. Data in fig.4a have been corrected for laser absorption from TMT molecules.

The spectral profile of the  $CH A^2\Delta \rightarrow X^2\Pi$  band emission at 431 nm is strongly affected by  $N_2$  addition as shown in fig.5. The spectrum is built-up by three different vibrational bands (0-0, 1-1 and 2-2)<sup>12</sup>. A theoretical analysis of the experimental spectra has been performed by taking into account all the transitions contributing to the spectrum. If a Boltzmann distribution is assumed for the population of the roto-vibrational levels, the measured fluorescence spectra can be fitted with rotational temperatures of 2800 and 250 °C when 0.04 torr of TMT are irradiated respectively in the absence or in the presence of 100 torr of  $N_2$  (see fig.5). It is worth mentioning that the  $CH (B^2\Sigma^- \rightarrow X^2\Pi)$  band emission is mainly observed at high pressure of  $N_2$ . For this band the high rotational and vibrational levels are predissociated<sup>13</sup>, so that emission can only be detected when vibrational deactivation becomes faster than spontaneous predissociation. Further information about the dynamics of formation and quenching of excited CH fragments can be obtained from time analysis of the  $A^2\Delta \rightarrow X^2\Pi$  emission signal in different experimental conditions. Fig.6 shows a typical decay signal at a TMT pressure of 0.05 torr. It is fairly evident that this signal cannot be fitted with a single exponential time constant. The observed CH emission decay is due to the competition between several phenomena characterized by different rate constants: 1) the spontaneous emission on the  $A^2\Delta \rightarrow X^2\Pi$  electronic transition whose lifetime  $\tau$ , has been measured by several authors<sup>14</sup>; it was found



that  $\tau_r$  is roughly the same for all the (0-0) transition and amounts to 537.5 ns. 2) The non radiative electronic de-excitation for collisions with TMT or buffer gases. Typical values are in the order of  $10^6 \text{ torr}^{-1} \text{ sec}^{-1}$ . 3) The rotational relaxation due to rotational-to-translational (R-T) energy transfer during collisions with TMT or buffer gases. Typical R-T relaxation rates are in the range  $10^7 \text{ torr}^{-1} \text{ sec}^{-1}$ .

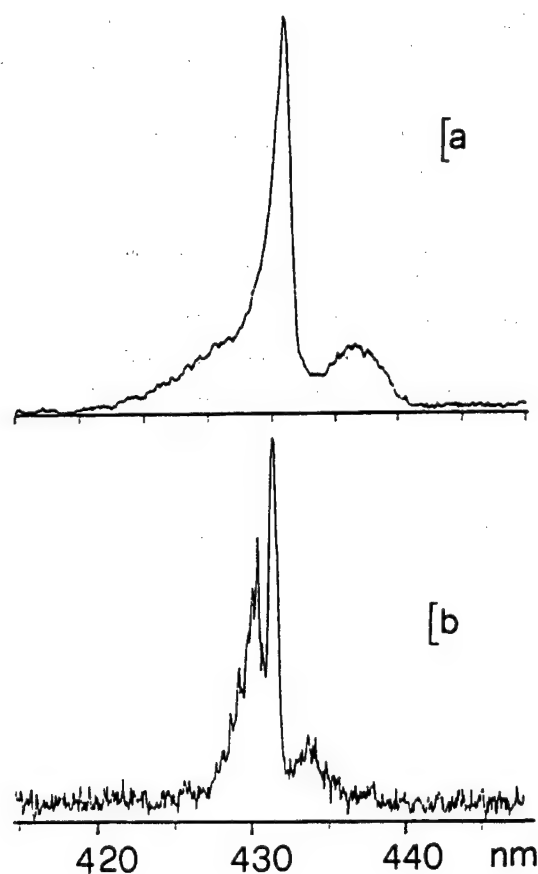


Fig.5 The  $A^2\Delta \rightarrow X^2\Pi$  band of CH emitted after irradiation of : a) TMT: 0.04 torr; b) TMT 0.04 torr,  $N_2$ : 100 torr.

It has been observed that an original rotational distribution centered around an excited level  $J$  relaxes through a series of double-peak distributions<sup>16</sup> which can be well approximated as a superposition of the initial  $P(J, 0)$  and final  $P(J, t)$  distribution :

$$P(J, t) = P(J, \infty) + [P(J, 0) - P(J, \infty)] \exp(-t/\tau_r) \quad (1)$$

The double-peak structure is based on the slower relaxation of the high  $J$  levels due to the increase of rotational energy spacing with  $J$ . The form used in equation (1) implies that all the absolute level populations approach their equilibrium value at the same rate. As a consequence of this approximation  $P(J, t)$  decays exponentially to its equilibrium value for  $P(J, \infty) < P(J, 0)$ , while  $P(J, t)$  rises exponentially to its equilibrium value when  $P(J, \infty) > P(J, 0)$ . Experimental CH emission spectra at TMT pressures higher than 0.04 torr can be fitted by a superposition of high and low temperature distribution, as predicted by the above mentioned

model. Thus by analogy with a two-level system, we divide the  $\text{CH}^*$  molecules into two groups: one group is formed by the molecules in the nascent high temperature distribution, while the other group is formed by the molecules which have suffered effective relaxing collisions during the radiative lifetime (low temperature distribution)<sup>15</sup>. As stated before, the population of the high-J levels can only decay through the mechanisms (1-3), while the population of the low-J levels can rise through rotational relaxation and can decay through mechanisms (1-2). We can write the following simplified rate equations for the two groups of emitting  $\text{CH}^*$  molecules<sup>17</sup>:

$$\frac{dA_1}{dt} = -(K_1 + K_2)A_1 + K_{-2}A_2 \quad (2)$$

$$\frac{dA_2}{dt} = K_2A_1 - (K_{-2} + K_3)A_2 \quad (3)$$

In the previous equations we referred to the high-J levels collectively as  $A_1$  and reserved the notation  $A_2$  for the equilibrated low-J levels;  $K_1$  and  $K_3$  are the total rate constants for the electronic transition  $A^2\Delta \rightarrow X^2\Pi$  for  $A_1$  and  $A_2$  states while  $K_2$  and  $K_{-2}$  are the direct and inverse rotational relaxation rates between  $A_1$  and  $A_2$  states.

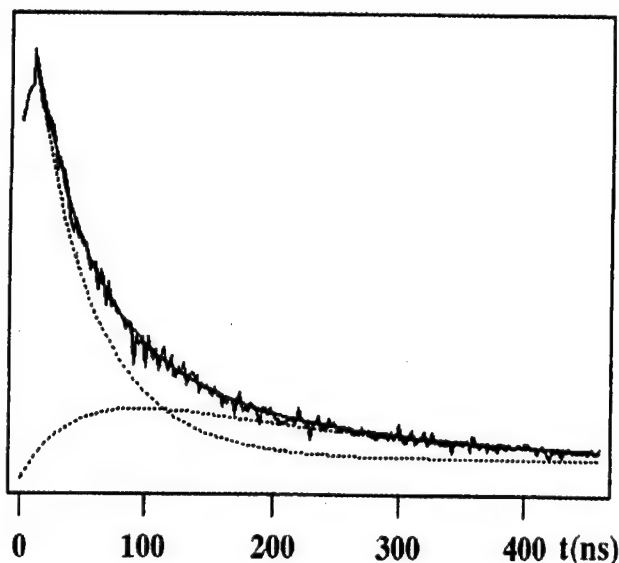


Fig.6 Temporal shape of the  $\text{CH } A^2\Delta \rightarrow X^2\Pi$  band emission signal recorded during the irradiation of 0.05 torr of TMT. The experimental curve is fitted as sum of the two components (dotted curves) originated by the high-J and the low-J population decay (see text).

Let us assume that  $\text{CH}$  molecules are formed in the state  $A_1$  after laser photolysis of TMT. The general solution to equation [2-3] is:

$$A_1(t) = A_1(0) (\lambda_+ - \lambda_-)^{-1} [(-\lambda_- + K_1 + K_2) \exp -\lambda_+ + (\lambda_+ - K_1 - K_2) \exp -\lambda_-]$$

$$A_2(t) = A_1(0) K_2 (\lambda_+ - \lambda_-)^{-1} [\exp -\lambda_- - \exp -\lambda_+]$$

where

$$\lambda_{\pm} = \frac{1}{2} (K_1 + K_2 - K_{-2} + K_3) \pm [(K_1 + K_2 - K_{-2} - K_3)^2 + 4K_2K_{-2}]^{1/2}$$

By use of this model a satisfactory fit has been obtained in the TMT pressure range 0.01 - 0.2 torr. A comparison between the experimental and the theoretical curve is reported in fig.6.

#### 4.CONCLUSION

Spontaneous emission analysis evidenced the formation of excited Sn and CH fragments after irradiation of TMT at 193 nm. No heavier fluorescing photoproducts were detected which could clarify the dynamics leading to film contamination. Furthermore the lack in the emission spectrum of any oxygen containing species, which could demonstrate the formation of Sn-O bonding in the gas phase, suggests that the inclusion of oxygen atoms into the tin layer takes place on the surface. Further studies are in progress in order to discriminate the relative importance of gas phase vs. surface phase processes and to improve the final Sn film composition.

#### 5.REFERENCES

1. D.J. Ehrlich, R.M. Osgood and T.F. Deutsch, J. Vac. Sci. Technol. **21** 23 (1982).  
D. Bäuerle, "Chemical processing with lasers", Springer Berlin 1986 and references therein.
2. for a review see R. Larciprete, Appl. Surf. Science **46** 19 (1990).
3. R. Larciprete, S. Fontana and E. Borsella, Chemtronix **4** 184 (1989)  
R. Larciprete, S. Fontana and E. Borsella, Laser assisted processing II, L. D. Laude Ed., Proc. SPIE **1279** 170-181 (1990).
4. E.E. Weber and W.T. Peria, J. Appl. Phys. **38** 4355 (1967).  
N.J. Taylor, Rev. Sci. Instrum. **40** 792 (1969).
5. "Handbook of Auger electron spectroscopy", 2nd edition Physical Electronic Industries, Eden Prairie (MN).
6. J. Ferguson, "Auger microprobe analysis" p.62-68, Adam Hilger Bristol 1989
7. K.F. Preston, J. Chem. Phys. **54** 3347 (1971).
8. Ref. 5, p.105
9. "Atomic energy levels" vol.3, Ed. C.E. Moore, Circular of the Nat. Bureau of Standards 467, USA.
10. G. Herzberg, "Spectra of diatomic molecules", D. Van Nostrand Co., Inc. Princeton (1950).
11. C. Ye, M. Suto and L.C. Lee, J. Chem. Phys. **89** 2797 (1988)
12. L. Göro, Zs. f. Phys. **118** 27 (1941)
13. J. Brzozowski, P. Bunker, N. Elander and P. Erman, Astroph. J. **207** 414 (1976).
14. K.H. Becker, H.H. Brenig and T. Tatarczyk, Chem. Phys. Lett. **71** 242 (1980) and references therein.
15. W. Brennen and T. Carrington, J. Chem. Phys. **46** 7 (1967).
16. "Lasers and chemical change", Eds. A. Ben-Shaul, Y. Haas, K.L. Kompa and R.D. Levine Springer Berlin 1981.
17. J. T. Yardley, "Introduction to molecular energy transfer" p.66, Academic Press New York 1980

Photochemical Changes of Rare-Earth Valent State in  $\gamma$ -Irradiated  $\text{CaF}_2\text{:Pr}$  Crystals by the Excimer Laser Radiation: Investigation and Application

36980005 The Hague EXCIMER LASERS AND THEIR APPLICATIONS in English 1991 pp 338-345

[Article by Svetlana G. Lukishova of the Institute of Radioengineering and Electronics of the USSR Academy of Sciences, Aleksey Z. Obidin, Sergej K. Vartapetov, Igor A. Veselovsky, Anatoly V. Osiko, Tamara V. Tulajkova, and Valery V. Ter-Mikirtychev of the Institute of General Physics of the USSR Academy of Sciences, and Nestor Raul Minhuey Mendez of the Hospital Lima Peru]

[Text]

ABSTRACT

This paper presents a novel application of UV laser radiation: fabrication of soft or apodized apertures(AA)<sup>1-3</sup> with smooth decreasing from centre to edges transmission profiles for high-power single-pulse visible and near IR lasers. Such units are used both outside and inside cavity for beam shaping<sup>4</sup>, for avoiding hard-edge Fresnel diffraction ripples in laser amplifiers<sup>2,3</sup>, for increasing the second harmonic conversion efficiency<sup>5,6</sup>, for the brightness enhancement of master oscillators in single-mode lasing<sup>7</sup>.

The method is easy and involves irradiating of pre  $\gamma$ -colored(radiatively reduced)  $\text{CaF}_2$  crystals doped with rare-earths(TR) across a certain diameter by UV<sup>2</sup> laser radiation.

The optical density of these crystals under the UV irradiation drops due to the photochemical changes of TR valent state(the photo-oxidation of  $\text{TR}^{2+}$  to  $\text{TR}^{3+}$  with stable bleaching)<sup>8</sup>.

The AA were made of  $\text{CaF}_2\text{:Pr}$  crystal with the use of 248nm and 308nm laser radiation. The<sup>2</sup> transmission profiles of these AA are presented.

The kinetics of stable bleaching of  $\gamma$ -irradiated  $\text{CaF}_2$  crystals doped with both Pr and two rare earth activators(Pr,Nd)<sup>2</sup> were investigated in beam of 308nm laser. The absorption spectra of these crystals before and after bleaching were obtained. All results have been compared with the case of 488nm argon laser irradiation.

An interesting phenomenon of coloration increasing in some  $\text{CaF}_2:\text{Pr}$  crystals instead of bleaching under 248nm laser irradiation has been observed. This coloration destroyed in beam of 308nm laser.

Some examples of application of the AA on the basis of photooxidation for beam shaping, 1.06 $\mu\text{m}$  second harmonic conversion efficiency increasing, and brightness enhancement of 1.06 $\mu\text{m}$  and 2.94 $\mu\text{m}$  oscillators are presented herein.

## I. INTRODUCTION

The problem of fabrication of AA for high-power lasers with wavelengths  $\lambda$  in near-IR demands the crystals with special composition: the induced absorption coefficient of these crystals under the irradiation by the ionizing radiation,  $K$  must have a value greater than  $1\text{-}2\text{cm}^{-1}$  in this spectral range. The induced absorption of such materials must be stable in near-IR laser beams.

The very good material for producing AA on the basis of bleaching of  $\gamma$ -irradiated crystals is fluoride ( $\text{CaF}_2$ ) doped with rare-earths. Such crystals were found to be perspective for fabrication of AA up to 3.4 $\mu\text{m}$  and also in the visible region. There were samples of  $\text{CaF}_2$  with values with absorption coefficient  $K \sim 1.8\text{-}6\text{cm}^{-1}$  at  $\lambda = 1.06\mu\text{m}$ .

Using of rare-earth activators is based on considerable difference of  $\text{TR}^{3+}$  and  $\text{TR}^{2+}$  absorption spectra in visible and near-IR region. The absorption spectra of  $\text{TR}^{3+}$  in this range are caused by parity-forbidden  $f\text{-}f'$ -transitions inside the same electron configuration, these spectra consist of groups of narrow discrete lines. Allowed  $4f\text{-}5d$  transitions with more wide absorption lines are known to be in the UV region of spectrum for the  $\text{TR}^{3+}$  II. In spite of  $\text{TR}^{2+}$  have the same electron configuration as corresponding  $\text{TR}^{3+}$  (e.g.,  $\text{Sm}^{2+}$  has the following electron configuration:  $4f^6 5s^2 5p^6$ , that is the same one for  $\text{Eu}^{3+}$ ),  $4f^{n-1} 5d$ -electron configurations of  $\text{TR}^{2+}$  is located lower than in the case of  $\text{TR}^{3+}$ . That is why along with typical for the rare earths forbidden transitions inside  $4f^n$  configuration, the allowed ones in mixed  $4f^{n-1} 5d$  configurations with wide intensive absorption bands in visible and near-IR region take place.

The typical valent state of rare-earths in the chemical compositions is known to be as +3. It should be mentioned that Ce, Pr, and Tb can have +4 valent state. In the  $\text{CaF}_2$  lattice owing to divalent state of Ca, the possibility of change the rare-earth valent state from +3 to +2 enhances. The ordinary valent state of TR in grown  $\text{CaF}_2:\text{TR}$  is found to be as +3, but under the action of different external sources (e.g. irradiation by ionizing radiation, additive coloration in alkaline-earth vapour, electrolysis) the TR valent state can become +2. Heating up to 200-400°C and irradiation by light from visible to UV can change divalent state of TR on trivalent one<sup>8,12</sup>.

In the set of TR the best one for doping in  $\text{CaF}_2$  for fabrication of AA in near-IR spectral region is found to be praseodymium impurity:  $\text{Pr}^{2+}$  has wide intensive absorption band in visible and near-IR, while  $\text{Pr}^{3+}$  spectrum has few narrow lines. (It should be noted that in spite of in most papers, e.g. <sup>9,10</sup> these wide spectral bands identifies with bands of  $\text{Pr}^{2+}$ , there is also the opinion, that it may be a spectrum of  $\text{Pr}^{4+}$  <sup>8</sup>).

The typical spectrum of  $\gamma$ -irradiated  $\text{CaF}_2:\text{Pr}$  crystals consists of summary of trivalent and divalent ions ones because of only  $\sim 10\%$  of  $\text{TR}^{3+}$  convert to  $\text{TR}^{2+}$  by  $\gamma$ -irradiation. To have a pure  $\text{TR}^{2+}$  spectrum in  $\text{CaF}_2$  we must heat this crystal in alkaline-earth metal vapour (to carry out its additive coloration (thermochemical reduction)). Unfortunately, we don't know the examples of  $\text{CaF}_2:\text{Pr}$  additive coloration, that is why we will consider the summary spectrum of  $\text{Pr}^{3+}$  narrow lines with the wide absorption bands after the  $\gamma$ -irradiation of these crystals.

The phenomenon of photooxidation of  $\text{TR}^{2+}$  in  $\text{CaF}_2$  have been investigated in <sup>8,12,13</sup>, but the changes of Pr ions valent state under the light irradiation has not been considered. It should be also mentioned the paper <sup>14</sup> where some photochemical bleaching of pure  $\text{CaF}_2$  without impurities colored by ionizing radiation has been investigated.

In this paper we consider the advantage of using the UV radiation as compared with visible light for the photooxidation and optical bleaching efficiency. The main difficulty for producing AA with "soft" transmission profile is following: creation the high-quality beam spot of UV source. For inside-cavity AA with diameter 2-4mm with the use of lens in beams of 308nm and 248nm lasers this problem has been solved.

## 2. ABSORPTION SPECTRUM OF $\gamma$ -IRRADIATED $\text{CaF}_2:\text{Pr}$ CRYSTALS

$\text{CaF}_2$  single crystals doped with  $\text{PrF}_3$  were grown by Stockbarger technique in the specific reactive atmosphere to be of necessity for the alkaline earth and rare earth fluoride crystals of good optical quality processing. The equipment used was in general outline like the one, described in <sup>15</sup>. In a typical run a carbon crucible was filled with the mixture of the previously ground  $\text{CaF}_2$  crystals "for an optical application" grade (purchased from the Industrial Branch of the State Optical Institute, Leningrad) and commercially available  $\text{PrF}_3$  powder (better, than four nines pure with respect to cation). The  $\text{PrF}_3$  concentration values ranged from 0.005 to 0.5 Mol.%. The reactive atmosphere employed was obtained by thermal decomposition of teflon <sup>16</sup> in vacuum or inert gas atmosphere just before melting the charge.

This method has yielded the crystals with good transparency in visible and near-IR region, absorption spectra demonstrating only characteristic  $\text{Pr}^{3+}$  ions lines. Figure I presents the absorption spectrum of one of such crystals with Pr concentration 0.2Mol.% and sample thickness  $d=7\text{mm}$ (curve I, solid line).

Curve 2 at Figure I demonstrates the absorption spectrum of this crystal after the exposition of  $\gamma$ -irradiation ( $10^8$  roentgen).

Curves 3 and 4(dotted lines) at Figure I present absorption spectra of pure  $\text{CaF}_2$  with  $d=7\text{mm}$  before the  $\gamma$ -irradiation and after it accordingly. In difference of paper<sup>14</sup> the value of irradiation dose in our case was greater ( $10^8$  roentgen), that is why the induced absorption coefficients  $K$  are found to be greater in our experiments than in paper<sup>14</sup>.

It should be mentioned that at first stage of  $\gamma$ -irradiation the  $\text{TR}^{2+}$  concentration grows very quickly with dose increasing. In the case than irradiation dose value exceed  $3 \cdot 10^6 - 10^7$  roentgen the  $\text{TR}^{2+}$  concentration enhances slowly. Interesting that in Pr concentration range in  $\text{CaF}_2$  crystals from 0.1-0.6 Mol.% the absorption coefficients after irradiation don't depend on the value of concentration<sup>5</sup>.

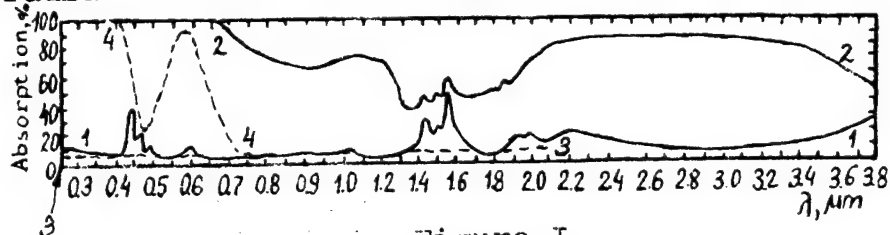


Figure I.

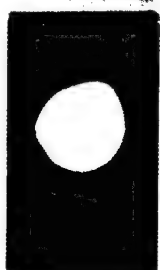
The measurements at Figure I were made with the use of Spectrophotometers SF-8, SF-20 of LOMO(Leningrad), Spectrometer Lambda 9 of Perkin Elmer Ltd., IKS-29 of LOMO, Model Graphics IR of Perkin Elmer Ltd. Spectrophotometers.



### 3. OPTICAL BLEACHING OF $\gamma$ -COLORED $\text{CaF}_2\text{:Pr}$ CRYSTALS UNDER THE IRRADIATION OF SHORT WAVELENGTH LIGHT

#### 3.1. UV light irradiation

Figure 2 presents the photograph of  $\text{CaF}_2\text{:Pr}$  AA with  $\approx 10\text{mm}$  in diameter made with the use of 1kW mercury lamp DKSSH-1000 with water filter to cut off thermal radiation. The irradiation time was  $\approx 10$  hours when we used lens to focus lamp radiation.



At the length of crystal 25mm with irradiation of each of two polish crystal faces we obtained greater than  $10^3$  times bleaching (in transmittance values) for  $\lambda = 0.63\mu\text{m}$ , and  $\approx 160$  at  $\lambda = 1.06\mu\text{m}$  at above mentioned time interval.

To investigate bleaching of crystals under 308nm XeCl laser light irradiation we used 1mm thickness  $\gamma$  samples.

Figure 2.

Figure 3 presents the kinetics of bleaching of two of such samples: curve 1 - for  $\text{CaF}_2\text{:Pr}$  crystal with Pr concentration  $\sim 0.6\text{Mol.}\%$ , and curve 2 - for  $\text{CaF}_2\text{-}0.2\text{PrF}_3\text{-}0.05\text{NdF}_3$  sample. ELI-73 of Tartu EAR ASESSR had 20mJ 25ns pulses with 10Hz repetition rate. The beam spot had  $5 \times 10\text{mm}$  sizes.

Figure 4 shows the changes of spectra in these experiments: solid lines - before 308nm irradiation, and dotted lines - after above mentioned expositions.

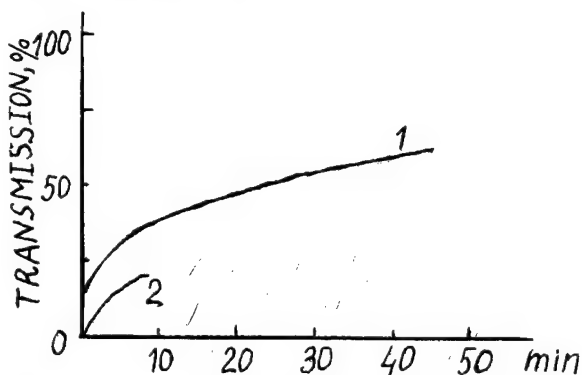


Figure 3. Kinetics of doped  $\gamma$ -irradiated  $\text{CaF}_2$  bleaching

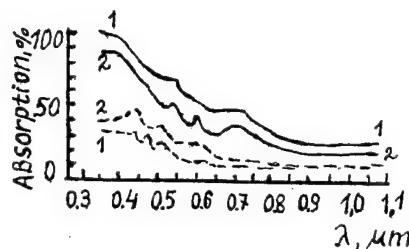
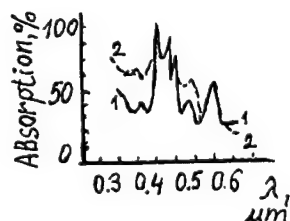


Figure 4. Changes in spectra of doped  $\gamma$ -irradiated  $\text{CaF}_2$  after bleaching

An interesting effect has been observed in one of  $\text{CaF}_2\text{:Pr}$  sample (Pr concentration was  $\sim 0.2\text{Mol.}\%$ , and sample was cut from the 200mm crystal of State Optical Institute growth). The 30'' polish sample



with 38mm thickness after  $10^4$ - $10^5$  rad  $\gamma$ -radiation dose was exposed by 248nm KrF laser radiation during 15min (15ns 1Hz repetition rate discharge laser had pulse energy  $E \approx 50$ mJ with  $0.7 \times 1.2$ cm<sup>2</sup> beam spot). Instead of bleaching which we observed with another  $\text{CaF}_2:\text{Pr}$  samples under 248nm light radiation, the additional induced absorption appeared in  $\sim 5$ -10mm layer inside of such crystal. Figure 5 shows the changes in absorption spectrum of this sample (curve 1-before 248nm irradiation, curve 2- after it).



After the exposition of such crystal sample by 308nm radiation (discharge XeCl with 15ns pulse duration, 1Hz repetition rate and  $E = 30$ mJ in  $0.9 \times 0.6$ cm<sup>2</sup> spot) during 15 min the absorption induced by 248 nm radiation disappeared.

Figure 5. Induced absorption effect after irradiation of sample by 248nm laser light.

### 3.2. Fabrication of apodized apertures by the eximer laser radiation

In described below experiments we used 5mm<sub>7</sub> thickness  $\text{CaF}_2$ -0.2PrF<sub>3</sub> samples after five years ago irradiation by  $10^7$  roentgen dose  $\gamma$ -radiation.

Three schemes of irradiation by eximer laser light are presented at Figure 6a,b,c.

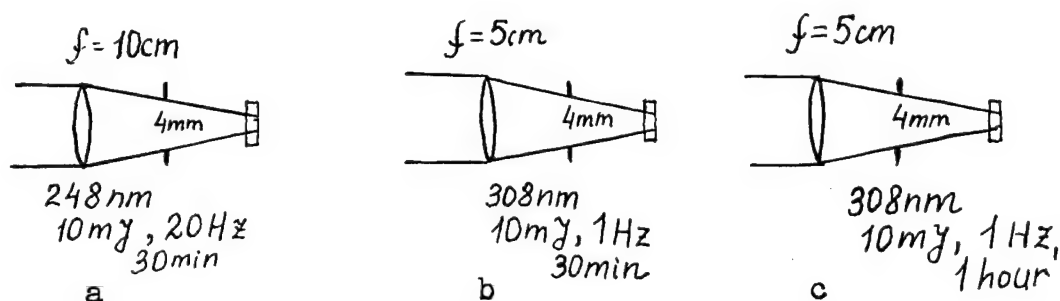


Figure 6. AA fabrication by eximer laser light.

AA transmission profiles are presented at Figure 7. To increase the transmittance value in the central part of AA we must expose crystals by laser irradiation in longer time interval. It should be

noted that the problem of maximum transmittance in the centre after the bleaching must be considered in special investigations.

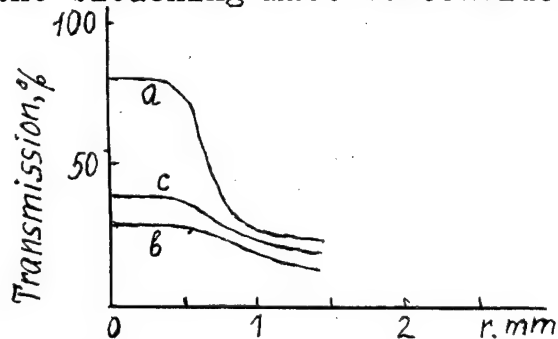


Figure 7. Transmission profiles of fabricated AA at  $\lambda=0.63\mu\text{m}$ .

accurate profile of AA with good optical quality commercial argon laser beams than in eximer ones.

As compared with 488nm argon laser radiation the efficiency of bleaching in the case of 488nm is less than in UV region. The same values of transmission in the centre of these crystals we observed only after 2-3 hours 2W power continuous laser irradiation. The heating of crystal during argon light irradiation with this power can cause in crystal undesirable stresses. To be fair it is easier to make

#### 4. APPLICATION IN NEAR-IR LASERS OF APODIZED APERTURES ON THE BASIS OF PHOTOOXIDATION

Note that at  $\lambda=1.06\mu\text{m}$  under the irradiation of single-pulse laser radiation these AA made of  $\gamma$ -irradiated  $\text{CaF}_2:\text{Pr}$  crystals do not bleach till samples are damaged. In focused laser beam at  $\lambda=1.06\mu\text{m}$  the surface damage of these crystals is observed at the intensity of  $5.10^9 \text{W}/\text{cm}^2$ , bulk damage-at  $2.10^{11} \text{W}/\text{cm}^2$  (pulse duration was 10ns, beam spot in focus was  $27\mu\text{m}$  and  $4.6\mu\text{m}$ , respectively).

AA were used inside the cavity of  $2.94\mu\text{m}$  Er:YAG laser in free running oscillation and Q-switched  $1.06\mu\text{m}$  Nd:YAG laser.

Er:YAG laser had a semiconfocal resonator with 3m hard mirror and 30% reflectance plane one. In case of hard-edge aperture inside this resonator it must have a diameter less than 3mm for single-mode lasing. 1.3-1.8 times increasing in output energy (at different pumping voltage) and 1.52 times diminishing in beam divergence in single-mode lasing as compared with hard-edge aperture have been observed in case of photooxidation AA inside resonator.

A single-mode lasing of Nd:YAG oscillator with 8% reflectance and hard plane mirrors took place only with  $2.5\text{mm}$  hard-edge aperture with about 30% of the output energy hard aperture being removed. When we placed AA the output energy in a single-mode lasing increased up to 55% (0.1J) from the multimode case. The detail information of these experiments is in the paper.

AA of Figure 2 has been used for 2 years at laser system output of 2.5J energy and 25ns single pulse duration ( $\lambda=1.06\mu\text{m}$ ). In this case second harmonic conversion efficiency increased from 40% up to

55% owing to better filling the cross-section (AA has smooth flat-top transmission profile). Such experiment has been made by Yu.K. Nizienko of the I.V. Kurchatov Institute of Atomic Energy.

## 5. CONCLUSIONS

The investigations shown that fabrication of photooxidation AA with optical bleaching by the eximer laser radiation is easy and fast. The efficiency of bleaching in the case of UV radiation is greater than in visible range of spectrum. Two problems must be solved to produce commercial AA: 1) to make the transmittance in the centre of AA  $\approx 94\%$ , and 2) to shape high-quality eximer laser beams for fabrication the AA with large diameter (up to 50 mm).

## 6. ACKNOWLEDGMENTS

The authors express their gratitude, to V.A. Sokolov, E.A. Simun, V.K. Karpovich of the State Optical Institute for fabricating of some  $\text{CaF}_2:\text{Pr}$  samples, V.A. Konjushkin of General Physics Institute for the possibility given to us to irradiate the crystals by  $\gamma$ -radiation, A.A. Nesterenko and G.P. Kuzmin of General Physics Institute for help in irradiation of crystals on ELI-73 eximer laser.

## 7. REFERENCES

1. P. Jacquinot and B. Roizen-Dossier, "Apodisation", *Progress in optics*, Ed. E. Wolf. Amsterdam-N.Y.: North-Holland: Wiley, 1964, Vol. 3, pp. 29-186.
2. V.R. Costich and B.C. Johnson, "Apertures to shape high-power Beams", *Laser Focus*, 1974, Vol. 10, No. 9, pp. 43-46.
3. S.G. Lukishova, I.K. Krasnyuk, P.P. Pashinin, A.M. Prokhorov, "Apodization of light Beams as a method of brightness enhancement in neodymium glass laser installations", *Formation and control of optical wavefronts*, *Proceed. of the Inst. of General Phys., Acad. of Sci. of the USSR*, 1989, Vol. 7, pp. 127-204, Nova Sci. Publ., N.Y. (Correct misprintings of misprints see in Russian, 1987 version by Nauka Publ., Moscow).
4. S.G. Lukishova, P.P. Pashinin, S. Kh. Batygov, B.M. Terentiev, "Soft apertures to shape high-power laser Beams", *Proceed. SPIE*, Vol. 1132, pp. 42-49, 1989.
5. A. Parent and P. Lavigne, "Increased frequency conversion of Nd:YAG laser radiation with a variable reflectivity mirror", *Opt. Lett.*, Vol. 14, No. 8, pp. 399-401, 1989.
6. E.F. Ibragimov, V.I. Redkorechev, A.P. Sukhorukov, T. Usmanov, "Effective frequency doubling in multistage neodymium laser", *Soviet J. Quantum Electron.*, 1982, Vol. 12, No. 6, pp. 714-720.
7. S.G. Lukishova, N.R. Minhuey Mendez, V.V. Ter-Mikirtychev, T.V. Tulajkova, "Improvement of beam quality of solid state laser systems using both outside and inside cavity devices with variable optical characteristics along the cross-section", *Inst. of General Phys.*, Reprint No. 17, 1991, 14 pp.

8. V.A. Arkhangel'skaya, "Color centers and charge transfer in rare-earth activated fluorite crystals," Ph.D. Dissertation, Leningrad, State Optical Inst., 1970, 236 pp.
9. D.C. McClure and Z.L. Kiss, "Survey of the spectra of the divalent rare-earth ions in cubic crystals," *J. Chem. Phys.*, 1963, Vol. 39, N12, pp. 3251-3257.
10. J.G. Conway, "Free-ion spectra of interest to solid and solution spectroscopists," *Proc. 1-st Intern. Sympos. on rare earth spectroscopy*, Wroslaw, Poland, 1984, Singapore: World Scient., 1985, pp. 3-20.
11. V.F. Zolin, L.G. Koreneva, *Rare-earth probe in chemistry and Biology*, Moscow, Nauka publ., 1980, 349 pp.
12. V. Arkhangel'skaya and P.P. Feofilov, "Thermo- and phototransfer of charge between activator centres in fluorite-type crystals," *Proceed. of the Internat. Conf. on Luminescence*, 1966, pp. 1682-1688.
13. V.A. Arkhangel'skaya and M.N. Kiseleva, "Photochemical changes of valent state of rare-earth ions impurities in fluoride-type crystals," *Optics and Spectroscopy*, Leningrad, Vol. XXIX, 1970, Is. 2, pp. 284-291 (part 1); Is. 3, pp. 561-568 (part 2).
14. D. Messner and A. Smakula, "Color centers in Alkaline earth Fluorides," *Phys. Review*, Vol. 120, N4, pp. 1162-1166, 1960.
15. D.C. Stockbarger, *J. Opt. Soc. Amer.*, Vol. 39, p. 731, 1949.
16. Ju. K. Voron'ko et al., *Sov. Solid State phys.*, Vol. 7, N1, p. 267, 1965.

## Use of Excimer Lasers in Medicine: Applications, Problems, and Dangers

36980005 The Hague EXCIMER LASERS AND THEIR APPLICATIONS in English 1991 pp 348-354

[Article by J. Mommsen and M. Sturmer of the Laser Zentrum Hannover e.V., Department of Production Engineering]

[Text]

### ABSTRACT

The use of excimer lasers in medicine is the subject of this paper. The interaction of UV-radiation with organic tissue, and dangers and problems arising from medical applications of excimer lasers are topics covered here. These deal not only with beam guidance, but also with questions concerning carcinogenity and mutagenity resulting from UV-radiation. Examples of several applications are also given.

### 1. INTRODUCTION

During the last few years, the use of laser systems in medicine has been continuously increasing. After the laser principle was discovered in 1961, above all, professionals in ophthalmology and dermatology started to use the laser for therapeutic purposes. After some enthusiasm in the beginning about the marvelous new tool, the scientists were brought back to reality mainly by the technical deficiencies of the first laser generation. Extended fundamental research was necessary to prove the feasibility of using lasers in medicine. Early investigations in this area dealt with the simplification or even solution of well-known problems in medicine using a laser.

However, the development of laser systems has not been advanced by medical applications, but by increased use in general material processing. After almost 30 years of intensive research and development, reliable CO<sub>2</sub>, Nd:YAG, and excimer laser systems are now available. In several domains in medicine they have been established as tools, and many operations would hardly be possible without them. Figure 1 shows the development of therapy diagnostic expense during the last six years.

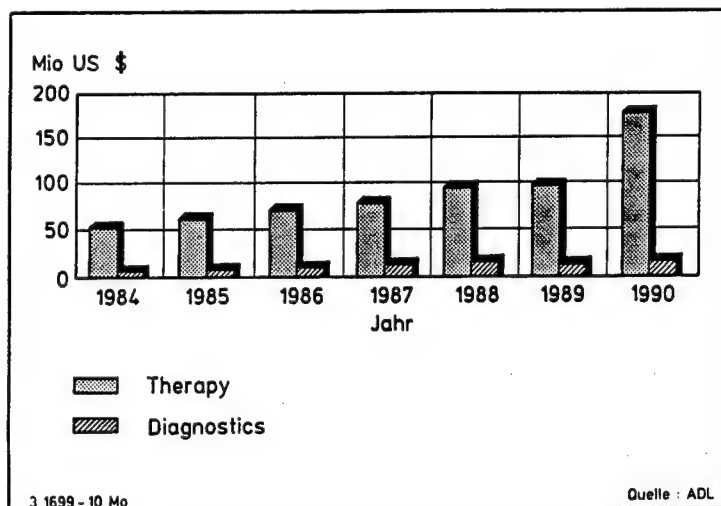


Fig.1.  
Expansion of the market.  
Laser in diagnostics and therapy.

But today many questions concerning the safe use of lasers in medicine are still unanswered, for example, the carcinogenic and mutagenic effects of UV-radiation on organic tissue. Therefore, Kaplan's statement is still valid today, as in 1965: "Never use a laser if you don't need it."<sup>1</sup>.

## 2. INTERACTION OF LASER RADIATION WITH ORGANIC TISSUE

The effects of laser radiation on organic tissue in relationship to power density and pulse duration is the topic of figure 2. They can be separated into four different processes:

### 2.1. Photochemical reactions

This method of treatment takes advantage of the fact that all organisms need light for important biochemical reactions in the cellular system. Laser light can stimulate and catalyze some photochemical reactions. A good example is photodynamic cancer therapy in which a photosensitive medium is inserted into the body. The toxic effects to cancerous cells only occur after intentional irradiation, preferably with short-wave laser radiation. As opposed to the well-known chemotherapy, the patient is given a less harsh, selective treatment, using low energy densities.

### 2.2. Thermal effect

The thermal effect of laser radiation essentially consists of vaporization (cutting) and coagulation of tissue. The power density ranges from  $10^2$  to  $10^6$  W/cm<sup>2</sup>. In this case, the temperature level and the irradiation time are critical values. This relationship is illustrated in figure 3. It has been proved that apart from some special intended thermal effects, temperatures higher than 40 degrees Celsius are to be avoided, as they generally result in cellular death. Because of the absorption qualities of organic tissue, this can only be fulfilled by high pulse peak power and simultaneously low penetration depth.

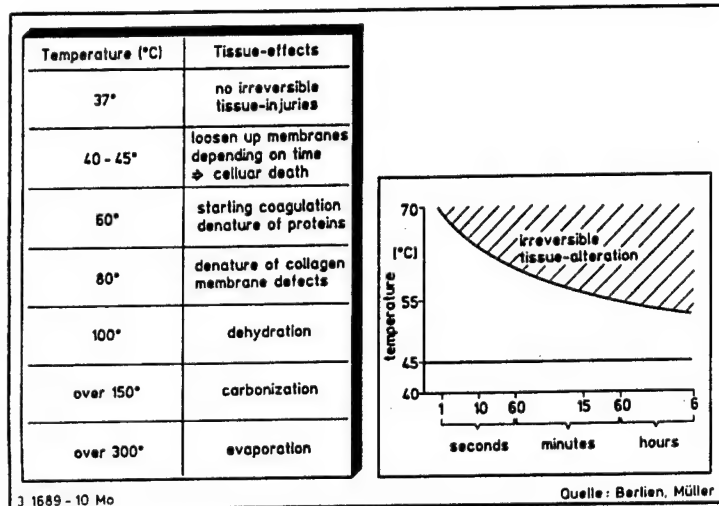
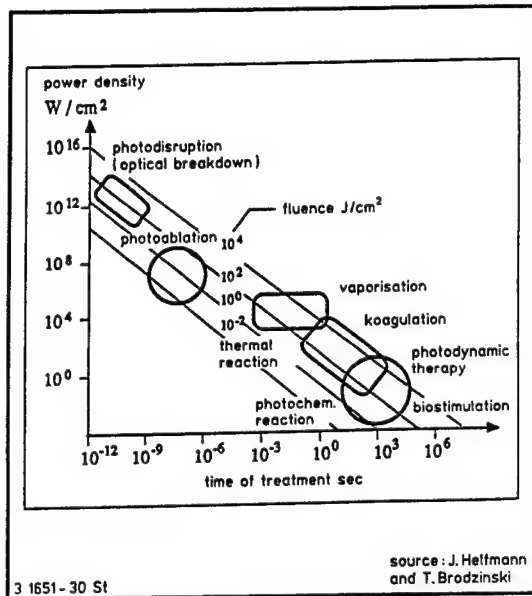


Fig.2. Influence of power density and pulse duration. Fig.3. Effects on tissue depending on temperature and duration

### 2.3. Non-linear processes

At power densities ranging from  $10^6$  to  $10^{11}$  W/cm<sup>2</sup>, ablation takes place, commonly known as "Srinivasan Ablation" in material processing. Due to high power density, the irradiated tissue is locally heated so quickly that immediate vaporization occurs. Heat conduction to the adjacent area is very limited, resulting in limited material damage.

### 2.4. Photo-disruption

At even higher power densities, achieved by excimer or Q-switched Nd:YAG lasers, plasma is generated during the laser pulse. The remaining pulse energy heats the plasma which expands and reflects a laser-induced shock wave. Soft tissue absorbs the shock wave, appropriate to mechanical principles, and is usually deformed elastically. Hard materials, e.g. calcium deposits, can be selectively destroyed, when the increasing pressure exceeds its maximum breaking point.

## 3. EXCIMER LASER IN MEDICINE

### 3.1. State of the art of system technology

In the last few years, the development of high power excimer lasers for material processing has been intensified. Today several systems from different manufacturers are on the market, which justify the term "industrial lasers". Stagnation of laser applications in the medical sector is due to the following reasons, as revealed by laboratory experiments:

Beam guidance is restricted by insufficient optical fibers which is dealt with explicitly in section 3.2. The effect of strong UV-radiation on some cellular types, as far as mutagenity and carcinogenity are concerned, has not been answered definitely. Using excimer lasers with rapidly changing inert gas halids as an active medium -which results in synchronously changing wavelengths- is accompanied by severe technical problems.

## 3.2. Beam guidance

### 3.2.1. Optical fibers

One of the most difficult problems in using excimer lasers in medicine is how to guide the beam. The advantage of optical fibers is based on flexibility and miniaturization of tools, which is very important under limited working conditions, e.g. when working on joints. Quartz glass fibers are only suitable for wavelengths from 200 nm to 2000 nm because of their transmission properties. It should be mentioned that at the outer limits of this range, satisfying transmission properties cannot be achieved. This phenomenon has its origin in high damping, non-linear absorption, light ageing and the creation of finite colour centers. For example, at 193 nm and at an initial energy level of 2 mJ, after 30 pulses, transmission is reduced to 10% of the original value. For wavelengths between 193 nm and 351 nm, radiation is transmitted, but output energy does not exceed several mJ in long duration use.

Only recently an important step was taken by using tapered fibers, i.e. quartz glass fibers with a conically-shaped input device. At 308 nm, up to 250 mJ could be transmitted through a 1000 mm-fiber. As its working life was greatly reduced, its clinical feasibility is still uncertain. Another disadvantage is the greater diameter leading to a reduction of flexibility. The use of long-pulse lasers is another concept for more efficient transmission of excimer laser radiation. It allows a decrease in maximum pulse power, which is one of the main reasons for fiber damage. Extensive experiments with XeCl excimer lasers at 28 ns, 60 ns and 300 ns pulse duration confirmed a rise in the damage threshold level<sup>2</sup>. In conclusion, we can notice that both low transmittable energy and insufficient long-time transmission behaviour of current fibers do not allow for clinical use of fibers in the UV-range. For these reasons, the use of fibers in connection with excimer lasers is still limited to laboratory work.

### 3.2.2. Mirror arms

Beam guidance by mirror arms is well established in connection with CO<sub>2</sub>-lasers. From the technical point of view, this is a very expensive solution due to the fact that there are no suitable fibers for many wavelengths. In medical applications this method is used for radiation 'transport' from the laser source to the irradiation area. One exception is for Nd:YAG-lasers, high-power fibers are available.

## 4. EXAMPLES OF APPLICATION

Ophthalmology was one of the first clinical ranges for the excimer laser. At 193 nm, the cornea of the human eye is treated by using defined cuts to correct the refractive index. In comparison to mechanical tools, the decisive advantage of this technique is the possibility of exactly controlling both cutting depth and width. Minimal thermal damage is caused to the eye, in contrast to CO<sub>2</sub>-laser treatment.

In dermatology, birthmarks have been treated with different laser types for many years, but the best results have been achieved by using excimer lasers.

Growing interest is seen in the removal of PMMA bone cement using excimer lasers during endoprothetic hip joint replacement operations (fig.4)<sup>5</sup>. The power density is about  $10^9$  W/cm<sup>2</sup>. Apart from mechanical tools, up to now, the CO<sub>2</sub>-laser has been used. There are indeed some medical advantages, but the main disadvantage is that the PMMA bone cement cannot be removed by a controlled ablation process but by thermal burning. This results in a high amount of toxic gases that are detrimental to the patient's and the operation team's health. In comparison, studies at the LZH of the removal of PMMA bone cement using excimer lasers have shown that not only high amounts of a defined volume could be removed, but there are clearly fewer emissions.



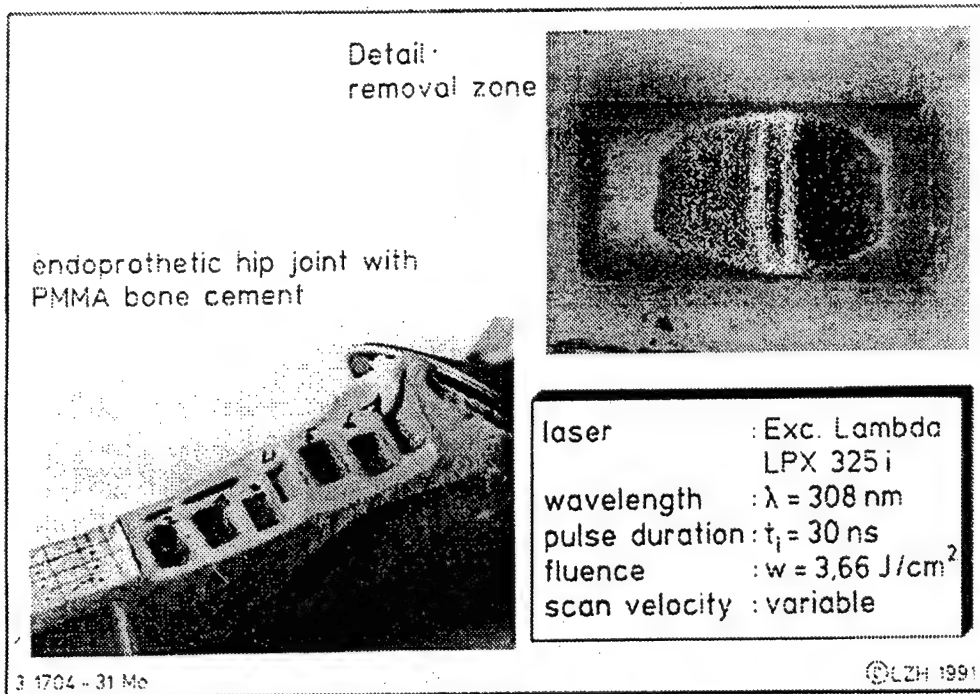


Fig.4.  
Material removal with  
excimer laser.  
PMMA bone cement.

Two additional examples will illustrate the possibilities of using excimer lasers in medicine:

In diagnosing thrombocyte functions, testing samples consisting of pure collagen with drilled holes of 4 mm length and 0,5 mm in diameter are inserted. Collagen is a protein that will coagulate at temperatures exceeding 60°C and which then loses its biochemical properties. Up to now, mechanical drilling is the only process to produce these drill holes, but this process is not reproducible and friction in the drill holes leads to thermal damage. New examinations have shown that holes can be produced exactly and without damage, using an excimer laser.

In Figure 5, holes produced by different laser types are compared.

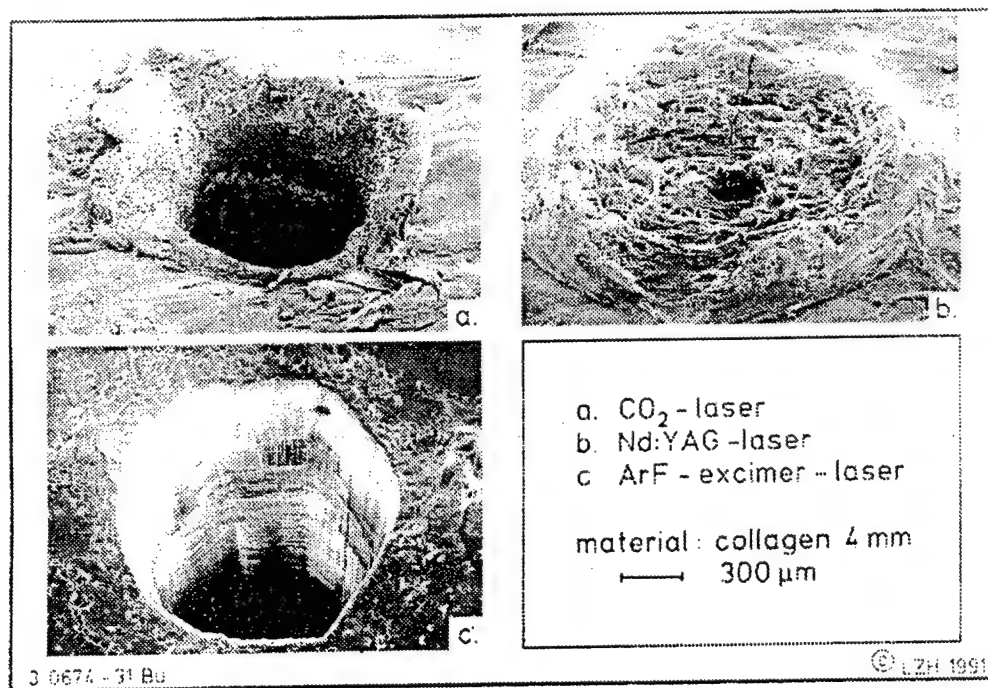


Fig.5.  
Drilling of collagen  
with high-power lasers.

A similar difficulty occurs in drilling pills. Thin holes influence the dissolution behaviour, and subsequently the dosimetry. Again, tests confirmed that the best results in reproduction with a minimum of discolouration are obtained with excimer lasers, as illustrated in Figure 6. This technique is now being applied in industry in the experimental stage.

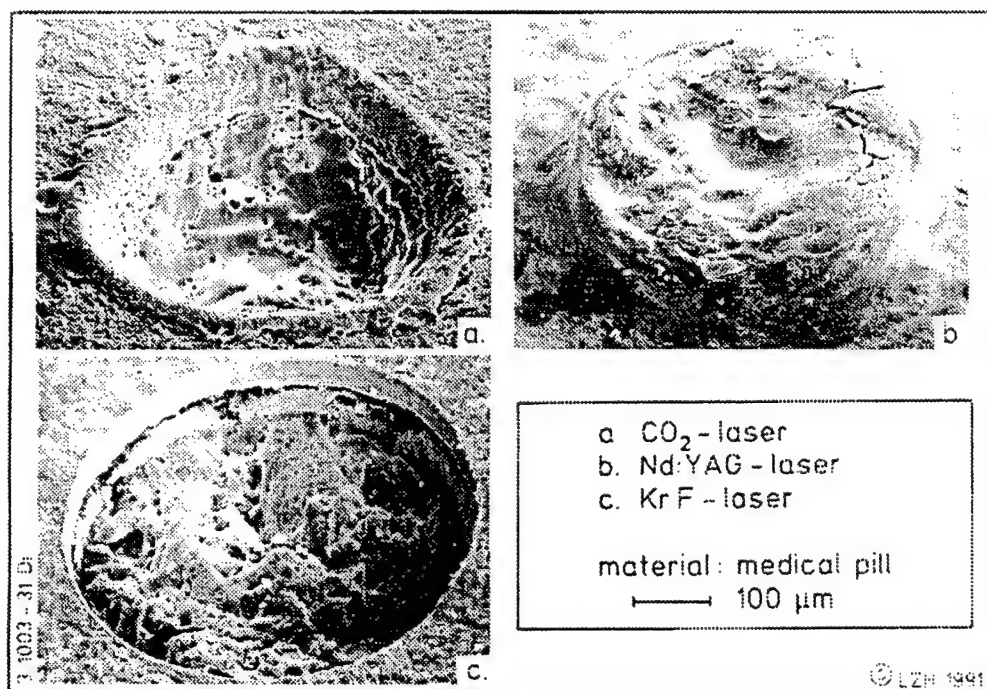


Fig.6.  
Laserdrilling of  
medical pills.

## 5. RISKS AND PROBLEMS

The UV-spectrum is usually divided into the following wavebands: UVA (400-320 nm), UVB (320-290 nm), UVC (290-200 nm) and VUV (<200 nm). UVA and UVB are part of the natural radiation reaching the earth's surface from the sun. UVB is about 1000 times more effective than UVA for many photobiological processes, e.g. tanning. The last few years have yielded many papers dealing with the influence of intensive UV-radiation by excimer lasers on organic tissue. At present, almost 10,000 publications are being recorded and evaluated in a data base. First results show that intensive UV-radiation of organic tissue results in cytotoxic and mutagenic effects. Above all, wavelengths near 260 nm must be avoided, because at this wavelength a maximum of absorption of cellular DNA occurs<sup>3</sup>. The investigations indicate a dependency of possible damages on the type of cell treated. There is no complete agreement among the statements, because of different or non-documented experimental parameters. For this reason, comparison of the experiments is only possible within certain limits. Compared with natural UV-radiation by the sun, the treatment of dermatopathies with excimer laser radiation generally can be recognized as safe<sup>4</sup>. Other applications, e.g. meniscus smoothing in the knee, are judged cautiously by experts. They argue that this kind of cell is naturally not exposed to and therefore sensitive to UV-radiation.

A further problem that is not limited to excimer lasers is aerosols and dust generated by medical treatment with laser radiation as shown in figure 7. Both can be harmful for the patient as well as for the operation team. The urgency of solving this problem has now been generally recognized, and will be one of the crucial points in the EUREKA-project "Laser Safety" that is now in the proposal stage. Among other things, exhaust installations and filter techniques that satisfy requirements of both material processing and medicine techniques should be developed.

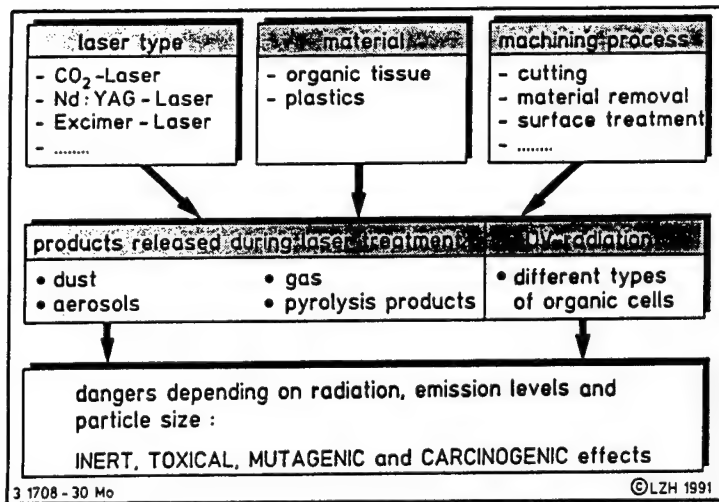


Fig.7.  
Dangers to patients and operation teams during laser surgery.

## 6. CONCLUSION

The use of excimer lasers in medicine is, apart from some exceptions, in the experimental stage. This is due to technical-physical problems concerning beam guidance on the one hand, and the effects of UV-radiation on organic tissue that have not been cleared up on the other hand. The advantages of excimer lasers to other types are high absorption, precisely-controllable ablation and low thermal secondary effects. They have lead to intensified fundamental research, and new applications and the verification of existing ranges of application concerning the safety factor can be expected.

## 7. REFERENCES

1. H.P. Berlien, G. Müller, Angewandte Lasermedizin, ecomed, München, 1989
2. M. Dressel et al., Quarzglasfasern für die Übertragung von Excimerlaserpulsen hoher Leistung, Laser und Optoelektronik, 22(5)/1990
3. I.E. Kochevar, Cytotoxicity and Mutagenicity of Excimer Laser Radiation, Lasers in Surgery and Medicine, 9:440-445, 1989
4. B. Staberg et al., The Carcinogenic Effect of UVA Irradiation, The Journal of Investigative Dermatology, 81:517-519, 1983
5. W.E. Siebert et al., Jahrbuch der Orthopädie, Hannover, 1990

## Bundle of Tapered Fibers for the Transmission of High-Power Excimer Laser Pulses

36980005 The Hague EXCIMER LASERS AND THEIR APPLICATIONS in English 1991 pp 355-362

[Article by H. Hitzler, N. Leclerc, Ch. Pfleiderer, J. Wolfrum, and K.-O. Greulich of the Universitat Heidelberg and K.F. Klein of the Fachhochschule Friedberg]

[Text]

### Abstract

For the transmission of high power excimer laser radiation in the kilowatt range a flexible bundle of tapered quartz fibers is presented. 30 fibers with a tapered coupling section are assembled to a bundle, which is tested with an excimer laser providing 2 J pulse energy at repetition rates of up to 20 pulses per second. The bundle showed good transmission qualities at 308 nm wavelength with an output power of 0.5 J/pulse. Catastrophic damage of fibers or other bundle elements did not occur during irradiation. The transmitted energy remained constant over the energy range tested with short irradiation times and low frequencies and is sufficient for material processing. At present, the transmission efficiency of the bundle is about 25 %.

### 1. Introduction

Presently, within the framework of an EUREKA project (EU 205) excimer lasers providing kilowatt power at 308 nm are under development. One approach is the development of a laser with repetition rates of 1000 pulses per sec and a pulse energy of approximately 1 J (Lambda Physik, Göttingen). A second approach is a laser with lower repetition rates (250 pulses per sec) but energies of 4 J per pulse (Siemens / KWU, Karlstein). The pulse lengths of both laser types are approximately 50 nsec.

It is obvious that these power densities cannot be transmitted by single flexible optical fibers [1, 2, 3]. At 308 nm wavelength, the maximum pulse energy which reliably can be transmitted by a single 600  $\mu\text{m}$  fiber is about 100 mJ per pulse (see below).

Therefore, a flexible fiber bundle is a solution. Conventional fiber bundles, however, are not suited for high power UV transmission because of several reasons. The high peak power may damage the fiber surface and due to interactions of the UV light with the cladding between the single fibers the bundle will be destroyed by material ablation [4]. These problems can be solved by using fibers with a tapered input section which allows reduction of the input power density by enlarging the front

surface and focusing the radiation into the tapered input region. Using a quite different bundling system yields that the fiber cladding and coating isn't affected so much by the laser radiation. Another important point when using tapered fibers is the easy handling of the tapers with regard to misaligning. Taper shifts in the range of the diameter of the affiliated fiber or distortions in the range of 1 or 2 degrees don't influence the transmission of the tapers [5].

## 2. Materials and Methods

### 2.1. Taper samples

All the taper samples used are provided by Heraeus Quarzglas GmbH, Hanau (FRG). They are made of synthetic fused silica with undoped core and fluorine doped cladding. Dimensions of the tapers are given in fig. 1. In order to avoid damage along the tapered fiber, no splicing has been used. The input ends were fire polished directly after drawing, the fibers are coated with a polymer coating. The untapered fiber ends were cleaved with the fiber cutter (INFOCUT).

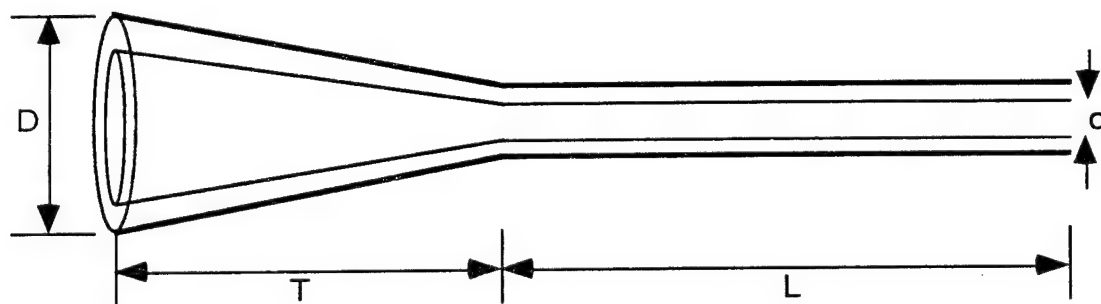


Figure 1: Single taper used in the bundle. Input diameter  $D$  variable, tapered region  $T < 100$  mm, length  $L$  of the fiber end 2 m, fiber core diameter  $d = 600 \mu\text{m}$ , cladding to core ratio: 1.1

### 2.2. Choice of optimal taper geometry

The most comfortable way of coupling light into a tapered optical fiber is the direct use of the output beam of the laser which is matched to the taper diameter with an aperture. Using tapers with a large input area (diameter  $D > 3$  mm) and  $600 \mu\text{m}$  fiber ends, we looked for the most suited aperture diameter. One can see that the output energy is growing with increasing diameter but remains constant for diameters larger than 2 mm (fig. 2). This means that a maximum effective taper diameter exists for light beams with low divergence. Light beams with diameters smaller than this effective diameters actually are subjected to internal focussing within the tapered section and are guided in the fiber. Beams with larger diameters exhibit greater losses due to multiple internal reflections of the light rays. This leads to a reflection angle greater than that acceptable for total reflection and therefore the aperture cone of the ray may exceed the angle of numerical aperture of the fiber (cf. [4]). The effective diameter is depending on fiber end diameter, numerical aperture of the fiber and the ratio of the tapered length  $T$  and the input diameter  $D$ . The transmission of a system with good surface qualities and optimized taper shape in axial direction can approach 70 %. On the basis of these results, tapered fibers with a front end diameter of 2.4 mm were used for assembling the bundle.

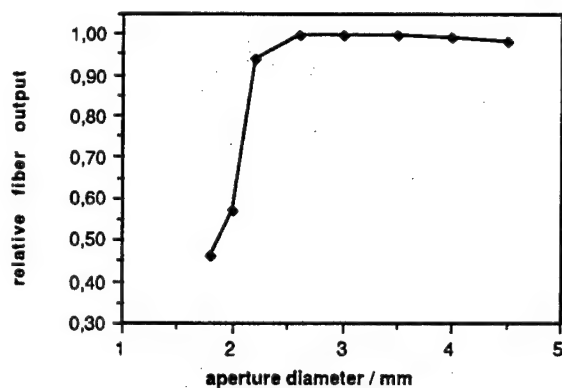


Fig. 2: Output decrease (normalized to the maximum fiber output) of a single tapered fiber as a function of the laser beam diameter. The output energy does not further increase for beam diameters larger than 2.4 mm.

### 2.3. Assembling the bundle

A prototype of the bundle was assembled consisting of 30 tapers designed as indicated above. For the packing mechanics several aspects had to be kept in mind:

- 1) The fibers must be packed as dense as possible to minimize geometric losses.
- 2) It must be possible to exchange defect fibers.
- 3) The outcoupling ends should be flexibly packed to allow processing of different geometrical designs.

The front end of the bundle consists of layers of brass plates with grooves which are staggered relative to the previous layer so that a good, though not yet geometrically optimal packing density can be obtained. For the outcoupling ends a clamp with variable plastic insets was constructed. The fibers are protected against damage with a flexible plastic tube. With this packing method, the bundle in principle can be enlarged to an arbitrary number of fibers. Fig. 3a shows the front end of the bundle, fig. 3b the rear end.

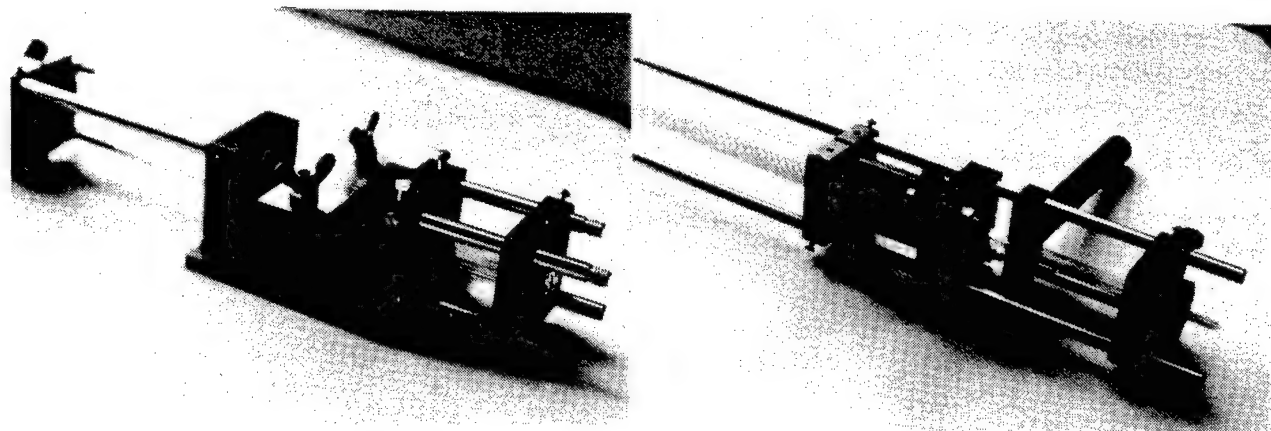


Fig. 7: a Front end, b rear end of the bundle

#### 2.4. Measurement setup of transmission properties

The bundle should be equally suitable for use with the laser providing high repetition rate (Lambda Physik) and the laser providing high pulse energy and consequently high power density in the bundle (Siemens / KWU). Experience with bulk materials and untapered single fibers indicate, that the latter is the more critical property. Therefore the high pulse energy laser (Siemens / KWU XP 2020) was used to test the bundle.

In order to detect fiber breakage due to packing, the bundle was screened with a HeNe laser before starting the experiments. As the emerging UV radiation would damage adjacent fibers, it is necessary to remove damaged fibers. This is easily possible by lifting the brass layer and pulling the fiber in forward direction with tweezers without misaligning the neighbour fibers.

For the measurements a laser with 2 J pulse energy and a beam area of  $40 \times 50 \text{ mm}^2$  and a pulse length of 50 nsec had been available. Maximum possible pulse repetition rate of the laser was 20 pulses per second. The laser beam had sharp edges and therefore was collected with a lens with 2 m focal length without using an aperture. This slightly converging beam could be coupled into the bundle. Previous experiments had shown that the use of an aperture leads to unnecessary high geometrical losses.

Energy measurement was performed with the ratiometer J 2000 from Molecron with detector heads J25HR (Molecron) and ED 500 from GenTech. Energy variations were possible with a dielectrically coated mirror.

The experimental arrangement is shown in fig.4.

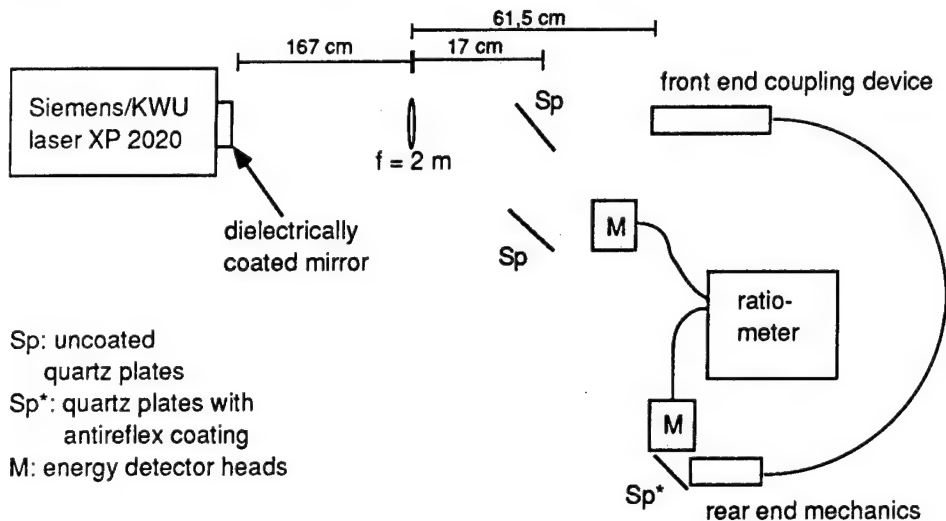


Fig. 4: Experimental arrangement

A pyroelectric detector array system (Spiricon) was used to measure the energy distribution at different distances from the bundle end.



### 3. Experimental results

#### 3.1. Experiments with single tapers

Some experiments with a single taper were made at the long pulse EUREKA laser described above to work out the limitations of the fiber bundle with respect to power transmission and bending losses. A single tapered fiber was able to transmit up to 115 mJ corresponding to an output power density of 814 MW/cm<sup>2</sup>. Bending losses of the fibers are negligible for the usable bending radius of the bundle of about 0.5 m.

#### 3.2. Transmission of the bundle

Fig. 5 shows the transmission in percent of the bundle containing 29 tapers as described in fig. 1 (one of the original 30 tapers had to be removed due to mechanical damage) when the pulse energy of the laser was increased from 50 mJ up to its maximum value of 2 J. Clearly, the percentage of transmission is independent of input pulse energy in that energy range. The maximum pulse energy at the end of the bundle is 500 mJ per pulse of 50 nsec in length (17 mJ per taper) corresponding to a peak power of 10<sup>7</sup> W. The results of fig. 5 and experiments with single tapers indicate that one probably can extrapolate these data for a laser providing 4 J per pulse, i. e. one can expect 1 J per pulse after transport through the bundle of the present configuration.

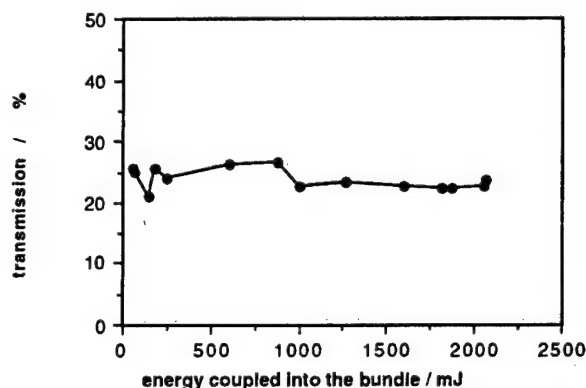


Fig. 5: Transmission as a function of the laser energy at a repetition rate of 1 pulse per second. The transmission remains constant and is nearly 25 %.

#### 3.3. Influence of the laser repetition rate

Fig. 6 shows that within the range of repetition rates provided by the Siemens / KWU laser the percentage of transmission is independent. Generally, up to repetition rates of a few hundred pulses per second, there is a minor dependence on the repetition rate. Thus one can estimate that a taper bundle may be capable of transmitting 250 pulses per second of a 1 kW laser of the Siemens/KWU type with a similar efficiency as is shown in fig. 5, i. e. that 0.25 kW will be available after transport with the bundle. For the 1 kW laser providing high repetition rates (Lambda Physik) the extrapolation is more difficult. However, the lower pulse energy may counteract the effects of high repetition rates and thus the bundle may be equally suitable for that type of laser.



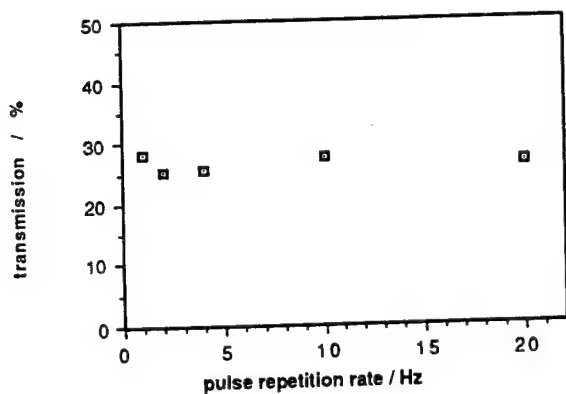


Fig. 6: Transmission of the bundle as a function of the pulse repetition rate. No significant influence can be seen.

### 3.4. Energy distribution at the bundle end

For industrial applications such as material processing it is necessary to quantify the homogeneity of the energy profile. This has been tested with a detector array system.

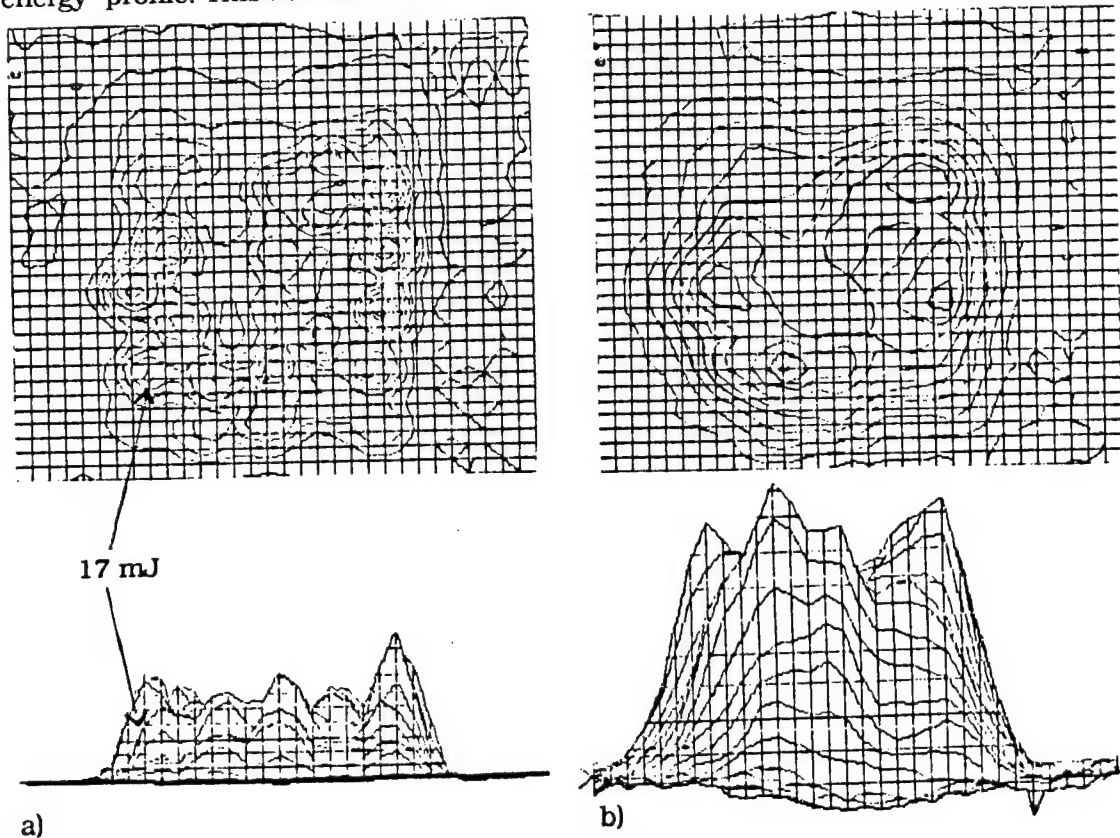


Fig. 7 Contour plots of the bundle output: a) Near field and b) far field at a distance of 7 mm from the bundle end.

In the near field patterns (i. e. directly at the fiber ends) some fibers show excellent transmissions whereas others are comparably poor (fig. 7a). The average energy per fiber at maximum transmission was 17 mJ whereas the actual energy per fiber calculated from the array graphics was from about 3 mJ up to 40 mJ. This significant difference for the most part comes from inhomogeneities in the laser output beam, say in explanation, that tapered fibers at the periphery of the bundle are in a zone of lower laser energy and therefore show less fiber output. Screening each single tapered fiber with a parallel excimer laser beam, we found transmission from 30 to 65 %.

Energy distributions also were measured in defined distances from the bundle end. We found that in a distance of 7 mm the power distribution is homogeneous enough and the energy rise is still steep enough that an application in material processing is possible (fig. 7b).

#### 4. Discussion

Our flexible tapered fiber bundle has a transmission of 25 % which is below the possible limit for several reasons. First, the geometric losses at the front end of the bundle can be further reduced by denser arrangement of the tapers. Second, the transmission of individual tapers still varies. Replacement of the poorer tapers will increase the total transmission of the bundle. In total, we estimate, that under optimal conditions a transmission of 40-50 % can be achieved for the bundle. Thus it appears possible to obtain 2 J per pulse of a 4 J laser after transport through the bundle.

A question which has not been addressed directly in the work reported here is the lifetime of the bundle. However, data for individual tapers, fibers and bulk materials are available. For example, using an excimer laser with 8 nsec pulse length, 12 mJ could be transmitted without considerable losses over several 100,000 pulses, that is a power density considerably higher than used in the bundle [6].

#### 5. Conclusions

The main problems for high power UV transmission through synthetic fused silica fibers and other optical devices are the possibility of surface damage and induction of absorption bands at high power densities and depending on the wavelength.

Concerning the fibers, at 308 nm laser wavelength the problem of surface damage due to high input powers can be solved by using tapered fibers. The advantage of these fibers is that transmission up to 70 % at parallel incoupling is possible. Under these conditions the fibers can be packed into a bundle.

We constructed prototypes of such a taper bundle and reached a transmission of nearly 25 % of the laser output energy of 2 J with a 50 nsec pulse. There are good reasons to assume that even 40-50% transmission can be achieved and that the transmission of a 4 J laser may be possible.

The output energy is sufficient high and its distribution is sufficient homogeneous for applications in surface modification and material processing.

The bundle transmission was constant over a wide energy range using low frequencies and low pulse numbers.

## 6. Acknowledgements

The authors wish to thank Mr. Fabian and Dr. Grzesik from Heraeus Quarzglas GmbH, Hanau, for helpful discussions and Mr. Schmidt, also from Heraeus, for preparing the tapered fibers. This work is supported by the Bundesministerium für Forschung und Technologie under the grant number 13 EU 0052. Responsible for the content of this paper are the authors.

## 7. References

1. R. Pini, R. Salimbeni, M. Vannini Optical fiber transmission of high power excimer laser radiation Appl. Opt. 26,19(1987) 4185-4189
2. R. S. Taylor, K. E. Leopold, R. K. Brimacombe, S. Mihailov Dependence of the damage and transmission properties of fused silica fibers on the excimer laser wavelength Appl. Opt. 27,15 (1988) 3124-3134
3. R. Ringelhan, H. Kar, J. Helfmann, K. Dörschel, G. Müller Fibre optics in medicine Laser und Optoelektronik 20 (1988) 44-48 (in german)
4. C. Whitehurst, M. R. Dickinson, T. A. King Ultraviolet pulse transmission in optical fibres J. of Mod. Optics 35,3 (1988) 371-385
5. H. Hitzler, N. Leclerc, K. O. Greulich, J. Wolfrum, K. F. Klein Processing of biomaterials by excimer laser pulses transported through tapered lightguides Conference on Lasers and Electro-optics Paper TUH4, 1989
6. H. Hitzler, N. Leclerc, K.-F. Klein, K. O. Greulich, J. Wolfrum Optical fiber transmission of excimer laser pulses Proc. SPIE 1023 (1988) 249

Spectral and Time-Resolved Measurements of Pollutants on Water Surface by an XeCl Laser Fluorosensor

36980005 The Hague EXCIMER LASERS AND THEIR APPLICATIONS in English 1991 pp 363-374

[Article by Roberto Barbini, Roberta Fantoni, Antonio Palucci, Sergio Ribezzo, and Hendricus J.L. van der Steen of ENEA]

[Text]

#### Abstract

An excimer laser based LIDAR fluorosensor, designed for operation from a mobile station, has been assembled at the ENEA Centre in Frascati and laboratory measurements on different samples have been performed both with spectral and time resolution. A low divergence high power XeCl laser has been used for excitation of typical chemical and biological materials polluting water surfaces. Results obtained on thin films of oils most frequently found in the Mediterranean sea.

A rough correlation has been found connecting the average oil density with both the overall visible fluorescence yield as well as the time decay constants.

#### 2. INTRODUCTION

The rapidly increasing interest in environmental problems during the last years has pushed scientists towards the development of detection systems, suitable for monitoring ecologic equilibria over a wide range and for detecting the presence of hazardous species. High power laser sources in the visible and the u.v. are the basis of active LIDAR instruments. The early development of visible laser sources such as solid state lasers (Ruby, Nd:YAG doubled) and noble gas discharge lasers (HeNe, Ar<sup>+</sup>, Kr<sup>+</sup>) allowed scientists to consider the possible detection of major pollutants in the environment either through Raman scattering or through fluorescence signals which, for most of the organic materials, fall in the visible spectrum. In the last ten years, airborne measurements<sup>1</sup> of Raman and fluorescence signals were carried out mostly by using available near u.v. laser sources, such as the N<sub>2</sub> laser, emitting at 337 nm, or the triplicated

Nd:YAG laser, emitting at 355 nm. Both these standard sources are characterized by a pulse duration around 10 ns with either relatively low energy (1 to 10 mJ) and high repetition rate (100 to 500 Hz) (N<sub>2</sub> laser), or with a higher energy (10 to 100 mJ) but a lower repetition rate (1 to 10 Hz) (III harmonic Nd:YAG laser).

The use of near u.v. lasers sources introduces several advantages with respect to visible sources since most of the organic substances, especially those containing aromatic rings or conjugated chains of double and triple bonds, can be effectively excited in the near u.v. and respond with a rather strong fluorescence. This signal, after proper spectral and time analysis, constitutes a finger-print of the molecule or, at least, of the kind of molecules involved in the excitation process.

On the other hand, the possibility of detecting a lot of different species by recognizing their fluorescence emission bands or by vibrational Raman scattering, can render the visible spectrum quite crowded. But the recent development of large intensified Optical Multichannel Analysers (OMA), together with the use of excitation sources emitting more towards the u.v., has made the detection of high resolution spectral and time decay signals much easier. Nowadays, commercial pulsed excimer lasers are available with high output energy (100 to 200 mJ), high repetition rate (100 to 200 Hz), relatively short pulses (10 to 20 ns) and a controlled divergence. Taking into account the  $\nu^4$  dependence of the Raman cross section, the atmospheric windows and the excitation efficiency of the species under investigation, a reasonable compromise can be found for the excitation source. For instance, a good choice is represented by the XeCl excimer laser emitting at 308 nm with high energy output and good stability. At this wavelength, the atmospheric transmission is close to its maximum and open sea water is sufficiently transparent to allow for measurements up to 50 m below the sea surface.

The present paper deals with measurements of oil pollution on the sea surface. A typical spectrum of polluted sea water will contain, apart from the backscattered XeCl radiation at 308 nm, the intense water Raman signal at  $\approx 344$  nm (with a Raman shift of  $\approx 3300$  cm<sup>-1</sup> due to the OH stretching), the 'gelbstoff' fluorescence from organic and biological wastes, which is peaked between 400 nm and 410 nm, the fluorescence of light and heavy oils peaked respectively around 450 nm and 500 nm, and some chlorophyll contributions peaked around 685 nm due to vegetation just below the sea level.

In section 3 the XeCl excimer laser based LIDAR fluorosensor built at the ENEA Centre in Frascati will be described in the configuration for both spectral and time resolved measurements. Laboratory results obtained on different middle-east crude oils are

discussed in section 4, where both direct fluorescence measurements (section 4.1) and water Raman signals (section 4.2) are reported. Results of time resolved measurements are shown and discussed in section 4.3.

### 3. EXPERIMENTAL SET-UP

The prototype laboratory set-up to be assembled in an airborne configuration is sketched in fig. 1. A narrowband high power excimer laser (EMG 1003i, Lambda Physik) provides a low divergence beam at 308 nm. After following a long optical path, necessary for compensating intrinsic instrumental delay times, the laser radiation reaches (with a spotsize of approximately  $10 \times 10 \text{ cm}^2$ ) the sample holder, which is a deep basin containing the oil either at the bottom or on the surface of a water column.

The fluorescence signal is detected either on a fast Streak Camera, for time resolved measurements, or on the OMA detector in the case of spectrally resolved measurements, after passing a monochromator and, if necessary, a filter for removing the backscattered fraction of the excitation wavelength. When doing time resolved measurements, a controllable delay unit triggered by the signal generated by a fast photodiode is added, in order to set the streak camera time window. By incrementing the delay time orderly we get a number of files which can be assembled by the controlling computer. In this way a large time window together with the high time resolution of the streak camera can be obtained. Both for OMA and streak camera, an average is made over a number of pulses: because of this, the effective repetition rate is up to 30 Hz. The available computer (IBM PC/AT) is used to control the OMA together with the laser and the streak camera, and is further dedicated to do both data acquisition and data analysis. The main characteristics of this experimental set-up are listed in Tab.1.

TABLE 1

Main characteristics of the experimental set-up

<u>Laser:</u>	XeCl excimer laser	
<u>Lambda</u>	Positive branch	
<u>Physics</u>	unstable cavity	
EMG 1003i	Emission wavelength	308 nm
	Pulse energy	typically 150 mJ
	Pulse width	17 ns (3 long. modes)
	P.R.R.	max. 200 Hz
	divergence ( $\theta_{\frac{1}{2}}$ )	hor. 0.4 mrad
		ver. 0.2 mrad
<u>Receiver:</u>	Newtonian telescope	d=20 cm
		f#5
<u>Data acquisition system:</u>		
O.M.A.III:	Intensified photodiode	
EG&G	array detector 1421	
	Pulse amplifier 1304	
	Fast pulser 1302	
	HR-320 monochromator	0.32 m
	Spectral channels	1024
	Spectral resolution	5 Å (147 g/mm)
		0.3 Å (1800 g/mm)
Streak	2491 control unit	
Camera:	C2830 temporal disperser	
	Temporal ranges	0.5, 1, 2, 5, 10 ns
Hamamatsu	Temporal channels	512
	Temporal resolution	10 ps or better

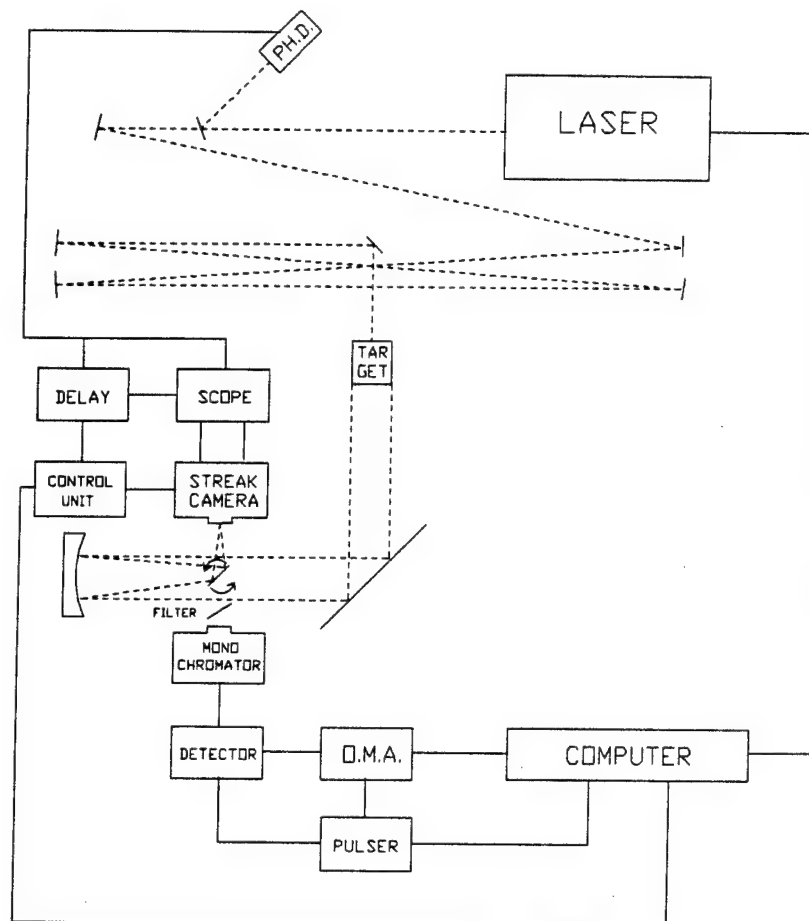


Fig.1. Laboratory experimental set-up for fluorosensor LIDAR.

#### 4. RESULTS AND DISCUSSION

##### 4.1. Fluorescence spectra of oils

A typical fluorescence spectrum from a water column is reported in Fig. 2., the water Raman peak is revealed at 344 nm followed by the broad gelbstoff fluorescence in the blue region.

Four different crude oil samples of Middle East origin have been considered for the present laboratory experiments. Their average bulk density has been measured together with their absorptivity in the near u.v. region (from 300 nm to 400 nm). Due to the very large absorption by oils in this range, u.v. absorbance has been measured in diluted trichloroethylene solutions ( $10^{-4}$  to  $10^{-3}$  g/cm<sup>3</sup>) by means of a double beam u.v. spectrophotometer (Perkin Elmer mod. 330). Oil density and absorptivity at a few wavelengths of interest are reported in table 2. Under the rather crude assumption that solvation affects in the same way the u.v. absorption spectra of the four different oils, bulk extinction coefficients can be obtained from the measured absorptivity. Extinction coefficients, also



reported in Table 2, have been obtained after normalization with the value at 344 nm from the data of Ref. 2. for Kirkuk oil.

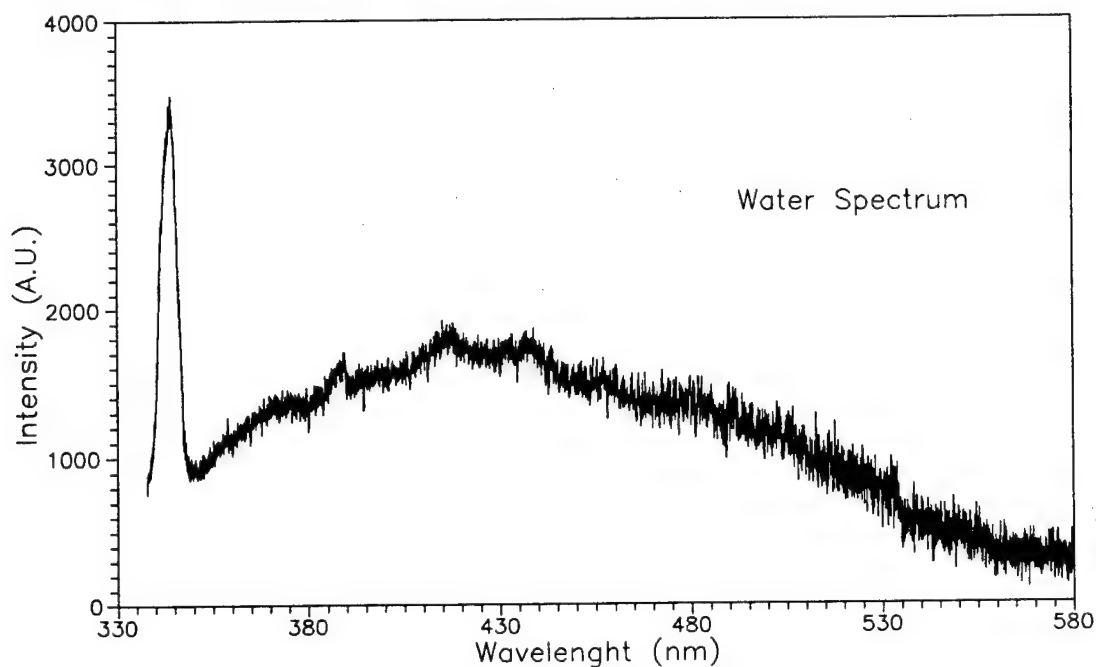


Fig.2. Raman and fluorecence spectrum of water excited at 308 nm.

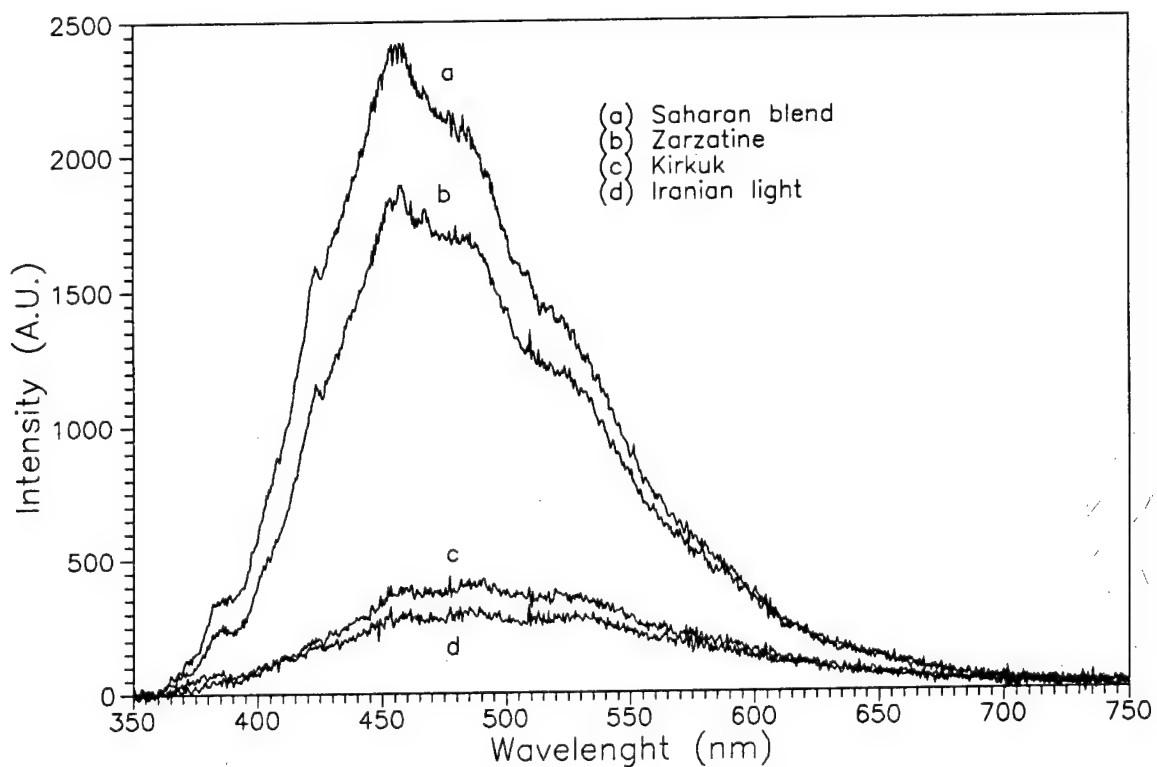


Fig.3. Fluorescence spectra of four different crude oil samples.

TABLE 2

Physical and optical properties of some crude oil samples of Middle East origin. A=measured absorbance, b=optical path length (0.2 cm, 1.0 cm), c=oil concentration:  $a=A/(b \cdot c)$ . Measurements have been performed diluting the oils in trichloroethylene, with typical concentrations in the range 0.0001 - 0.001 g/cm<sup>3</sup>. Uncertainty on density is 0.02 g/cm<sup>3</sup>, on absorptivity about 20%.

Oil	density (g/cm <sup>3</sup> )	w.l.(nm)	absorptivity a (cm <sup>2</sup> /g)	extinct.-coef. k (nm)
Kirkuk	0.85	308	848	1.10 <sup>#</sup>
		344	495	0.64 <sup>#</sup>
		362	384	0.50
Iranian Light	0.87	308	231	0.30
		344	172	0.22
		362	131	0.17
Zarzaitine	0.84	308	288	0.37
		344	134	0.17
		362	106	0.14
Saharan Blend	0.81	308	319	0.41
		344	136	0.18
		362	103	0.13

\*. Samples supplied by Stazione Sperimentale per i Combustibili (S. Donato Milanese).

#. Interpolated from ref. 2., values measured at 337 nm and 355 nm on undiluted samples. This value has been used for renormalization of present absorptivity data.

From Table 2 we observe that heavier oils, like Kirkuk, have a higher absorptivity in the near u.v. In spite of this, heavy oils usually present a low fluorescence yield after near u.v. excitation<sup>2</sup>. Large differences, over more than one order of magnitude, in absolute fluorescence yields have been already observed between light and heavy oils<sup>3</sup>.

On the other hand, only small differences<sup>2</sup> in spectral shape have been detected in the case of oil fluorescence<sup>2</sup>. This is confirmed by the present experimental data on our four samples with different densities. Measurements have been performed first at low resolution, by placing a filter in front of the OMA for removing all wavelengths smaller than 360 nm (i.e. mostly the backscattered laser radiation at 308 nm and the water Raman signal at 344 nm). Spectra of arbitrary thick oil films on a water column are shown in Fig. 3. Fluorescence

emission covers most of the visible spectral range. Spectral shapes are quite similar throughout this region, where three maxima can be identified, roughly peaked at 460 nm, 490 nm and 540 nm, respectively.

Our measurements (not shown) repeated at higher resolution did not reveal the presence of any sharper feature, only shoulders in the near U.V. region at 360 nm, 390 nm and 440 nm became more evident because the U.V. filter was not used in combination with the high resolution grating. The general trend shown by spectral shapes is a broadening of the fluorescence spectra towards longer wavelengths with increasing oil density.

In conclusion, the presence of oils on a water surface can be recognized from their typical emission spectra, but the direct identification of the specific oil seems to be rather difficult if no additional information, e.g. the time decay constants at different wavelength as discussed in sect. 4.3, is available.

#### 4.2. Measurements of water Raman signal

The O-H stretching in water is Raman active with a Stokes shift of  $3300\text{ cm}^{-1}$ . Illumination of a water column by means of a 308 nm laser radiation gives rise to the water Raman signal centered at 344 nm. In Ref. 4. it has been demonstrated that the peculiar shape of the liquid water Raman peak is traceable to the contemporary presence of monomers and molecular aggregates, so that it is sensitive to temperature which affects the respective equilibrium. In our laboratory, measurements of the water Raman signal have been performed at high resolution in the range 330 nm to 365 nm in order to discriminate from the intense tail of the backscattered laser radiation. First the linearity of the Raman response from clean (without oil) water has been checked vs the water column height. After background subtraction, the integrated intensity under the water peak (between 340 nm and 348 nm) turned out to increase linearly with the water column height.

Measurements in the same wavelength range have been performed after adding fixed amounts (drops) of different oils on the surface above a certain water column. Selected spectra are shown in Fig. 4, for Kirkuk and Saharan Blend oil. Results (not shown) for Iranian Light and Zarzaitine were rather similar to the first and the second of the former samples. In Fig. 4 we first notice that the water Raman peak is progressively depressed by the oil absorption of 308 nm laser radiation which thus cannot effectively penetrate in the water column. We also detect in this range (around 360 nm) the first peak of the oil fluorescence spectrum, which is especially intense in the case of the lightest oil (Saharan Blend). On the other hand, and possibly due to the low thickness of the oil samples over the water surface (each drop contains less than 0.02 g of oil spread over about  $600\text{ cm}^2$ ), no Raman signal related to C-H stretchings in oils (Raman shifts between  $2900\div 3200\text{ cm}^{-1}$ ) is detected in the range  $338\div 341\text{ nm}$ .

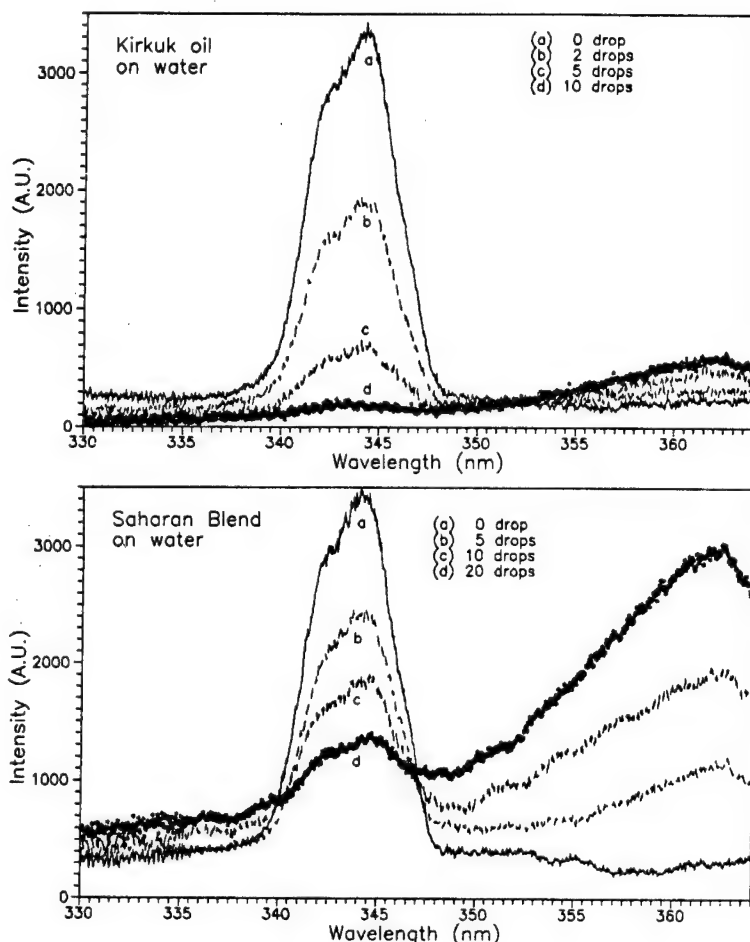


Fig.4. Fluorescence response and water Raman signal measured in the near u.v. as a function of the oil quantity on the water surface for two different crude oil samples.

In order to use the LIDAR fluorosensor for field measurements of oil film thickness on sea water, the dependence of oil fluorescence intensity and water Raman intensity upon oil (quantity) thickness has been checked. However the integrated oil fluorescence in the range 360 to 364 nm, after proper background subtraction, vs the quantity (drops) of oil spilled upon the water surface followed a linear behaviour only at very small quantities and reached saturation, especially for the heaviest oils. This demonstrates that absolute fluorescence measurements, which also require the knowledge of the kind of oil detected, are not suitable to determine the thickness of the pollutant film.

On the other hand, in data analysis we have observed that the integrated water Raman signal tends to follow an exponential decay law as the oil quantity on the water surface increases. By using the integrated Raman signal  $R_{in}$  measured as a function of the oil

quantity and the corresponding Raman signal from clean water  $R_{out}$ , the oil thickness  $d$  can be obtained from the expression<sup>5</sup>:

$$d = - \frac{1}{k_e + k_R} \ln (R_{in}/R_{out})$$

where  $k_e$  and  $k_R$  are the extinction coefficients listed in table 2 at 308 nm and 344 nm, respectively.

Results for Kirkuk and Saharan Blend oil correspond to a thickness of 0.22  $\mu\text{m}/\text{drop}$  and of 0.17  $\mu\text{m}/\text{drop}$ , respectively. The ratio in thickness from the measured Raman intensities is in agreement with the ratio of weights of the respective oil drops, also taking into account the small differences in oil density. As shown in Fig. 5, the model we used is quite satisfactory and the Raman intensity plotted vs the oil thickness  $d$  is well fitted by an exponential decay for both Kirkuk and Saharan Blend oil. However, it has to be mentioned that the model could not be properly applied to the Zarzaitine and Iranian Light oil samples, because there were problems in uniformly spreading drops on the water surface.

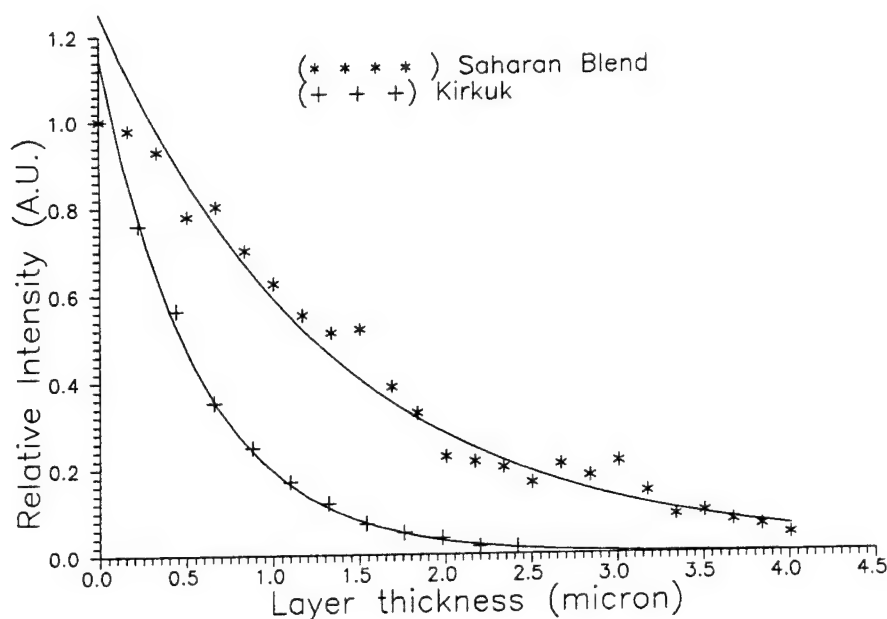


Fig.5. Exponential behaviour of the Raman intensity versus oil layer thickness measured for Kirkuk and Saharan Blend oils.

#### 4.3. Time decay of oil fluorescence

Time decays curves for the four crude oil samples have been measured by using the fast streak camera with the longest time sweep (10 ns). Different parts of the excitation and decay curve have been acquired as a function of the delay counted from the laser pulse

rising edge (detected with the fast photodiode, see fig. 1). At each selected delay time, 5 waveforms have been averaged. The complete curve of fluorescence intensity vs time was successively reconstructed by software.

Measurements performed without filters in front of the streak camera were dominated by the backscattered laser radiation and revealed the typical profile, shown in Fig. 6, with the three longitudinal modes of the laser pulses provided by our unstable resonator cavity. Oil fluorescence has been detected by placing an interference filter, peaked either at 450 nm or at 500 nm with a 60 nm bandwidth, in front of the streak camera entrance. The decay of the signal tails measured after the end of the laser pulse on the four crude oil samples is shown in Fig. 7, together with the exponential fit. Longer time constants are obtained for lightest oils. Although the absolute value of the time constant may be not very accurate, due to the arbitrary choice of the end of the laser pulse after 20 ns from its rise, the observed trend in lifetime is significant to the identification of the oil sample and consistent with results reported in ref. 2. as measured after excitation at 355 nm.

Thus, as hypothesized in ref. 6. long time ago, we can conclude that measuring accurately time decay constants, together with the fluorescence spectra, should allow for the unambiguous identification of the pollutant oil in remote sensing experiments.

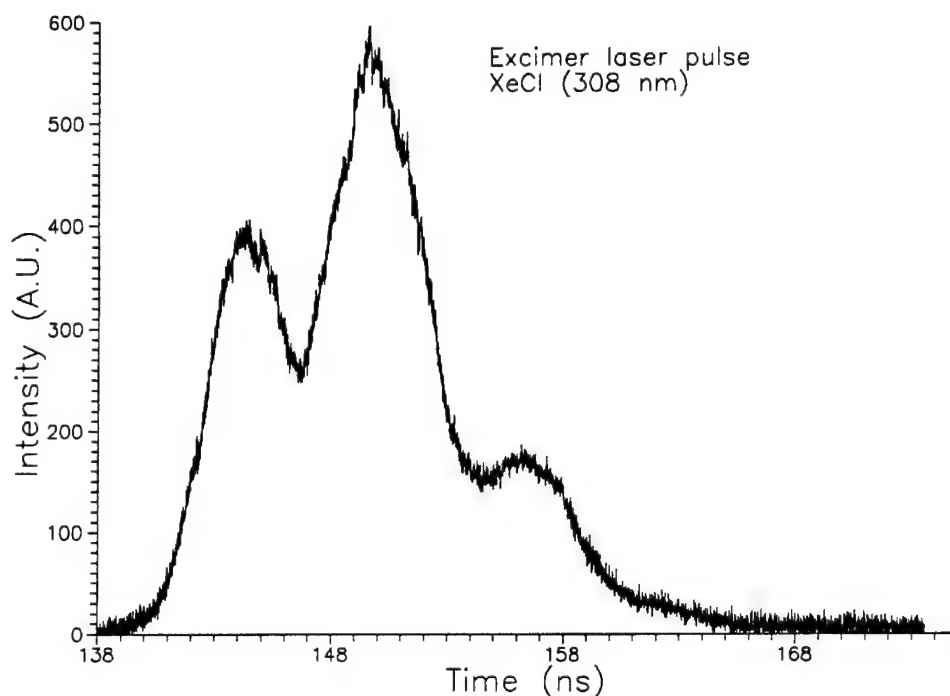


Fig.6. Typical XeCl pulse as measured with the Streak Camera.

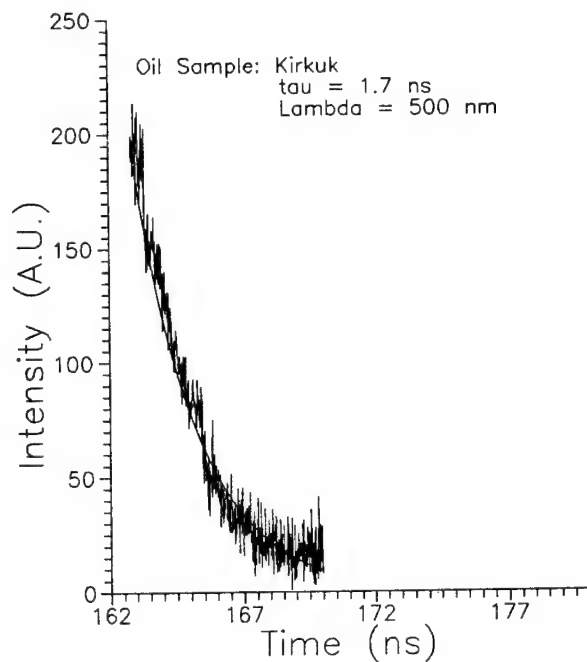
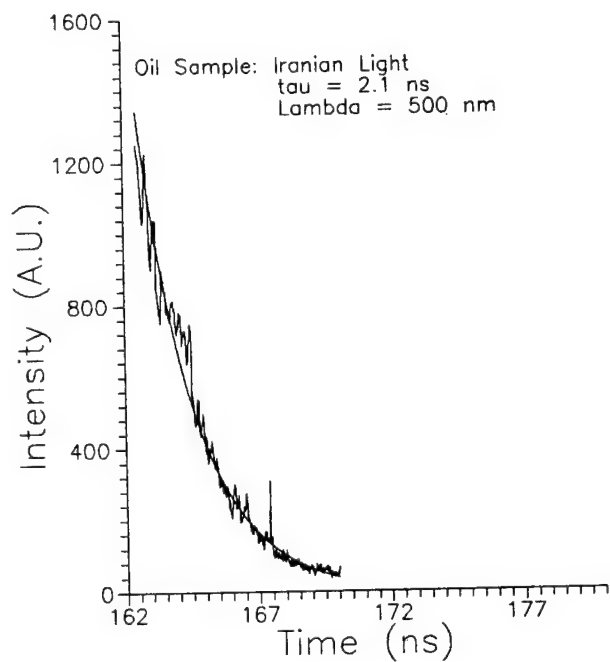
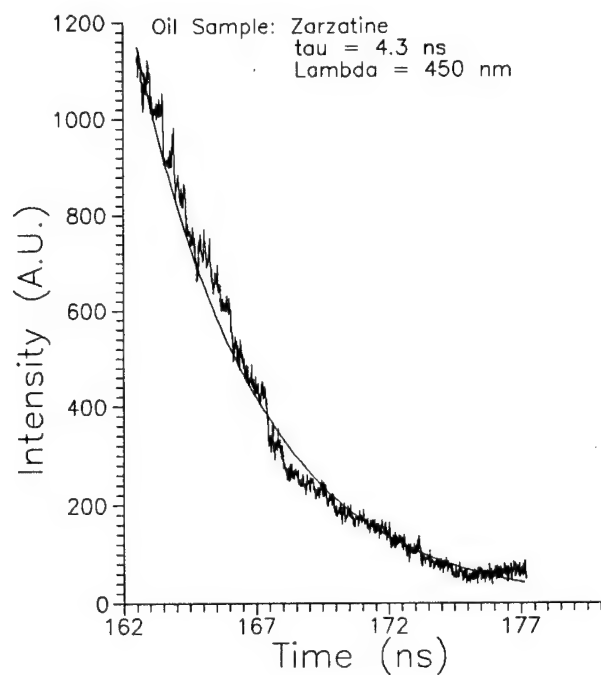
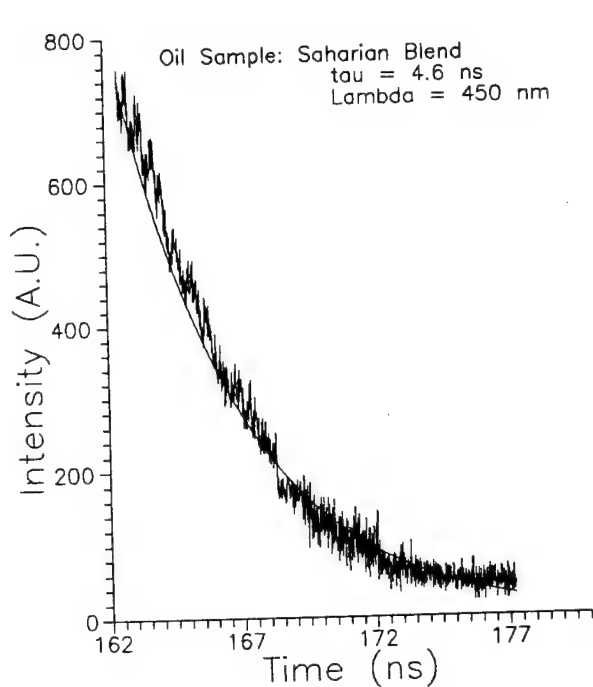


Fig.7. Temporal response of different crude oil samples excited by the XeCl laser. Measurements are performed at the wavelength indicated, detecting the decay of the signal at the end of the laser pulse.

From the present results, it comes out that a short U.V. laser source is required for accurate time resolved oil fluorescence measurements. In our laboratory different methods for shortening the XeCl laser pulse have been considered, the best results up to now being obtained by using a Raman shifter in CH<sub>4</sub>. By inducing the stimulated Raman scattering at threshold for the second Stokes and laser pulses of about 1 mJ energy, 2 ns duration were generated at 378 nm. Work is in progress to excite the oil fluorescence with this radiation.

#### 5. ACKNOWLEDGMENTS

Thanks are due to dr. F. Colao for helping in computer control of the experiment.

#### 6. REFERENCES

1. F.E. Hoge & R.N. Swift, Appl. Opt. 19, 3269 (1980); R.A. O'Neil, L. Buja-Bijunas & D.M. Rayner, Appl. Opt. 19, 863 (1980).
2. G. Bertolini, P. Camagni, C. Koechler, A. Pedrini & A. Prosdocimi, Proceedings of the 4th International Colloquium on Spectral Signatures of Objects in Remote Sensing, Aussois, France, 18-22 Jan 1988, pp.233-238; P. Camagni, G. Colombo, C. Koechler, N. Omenetto, A. Pedrini, G. Rossi, "Remote characterization of mineral oils by laser fluorosensing: basic diagnostics and simulation experiments", Commission of the European Communities, Ispra Est., Report EUR 11781 EN (1988); P. Camagni, A. Colombo, C. Koechler, N. Omenetto, P. Qi, & G. Rossi, "Fluorescence response of mineral oils: spectral yield vs absorption and decay time", to be published.
3. F.E. Hoge & R.N. Swift, Appl. Opt. 22, 37 (1983); H. Visser, Appl. Opt. 18, 1746 (1979).
4. D.A. Leonard, B. Caputo & F.E. Hoge, Appl. Opt. 18, 1732 (1979).
5. F.E. Hoge & J.S. Kincaid, Appl. Opt. 19, 1143 (1980); R.T.V. Kung & I. Itzkan, Appl. Opt. 15, 409 (1976).
6. D.M. Rayner & A.G. Szabo, Appl. Opt. 17, 1624 (1978).



## Excimer Laser Cutting of Corneal Transplants

36980005 The Hague EXCIMER LASERS AND THEIR APPLICATIONS in English 1991 pp 375-378

[Article by Raivo Tamkivi of the Institute of Physics, Estonian Academy of Sciences, Leo L. Schotter, Jr. of the Tartu University, and Tat'yana A. Pakhomova of the All-Union Institute of Eye Diseases]

[Text]

### ABSTRACT

A simple laboratory set-up for cutting the round-shaped transplants of eye cornea is described. At that, an excimer  $ArF$  laser served as ablating 193 nm radiation source. The results of the first experiments to produce some cylindrical and segmental transplants are presented.

### 1. INTRODUCTION

Since Trokel et al.<sup>1</sup> had demonstrated the specific ablative effect of the sub-200 nm laser radiation on the eye cornea, the keratotomy abilities of excimer lasers have been widely studied and the results repeatedly summarized.<sup>2,3</sup> The most outstanding feature of the UV photoablation process - the almost complete absence of thermal damage of the incisions' edges - has been stated by all authors who used the 193 nm  $ArF$  laser radiation as "scalpel", and by some who used the 223 nm  $KrCl$  laser.<sup>4</sup> By now both the physical characteristics and medical aspects of the photoablation of cornea by  $ArF$  laser beam have been thoroughly examined. Among other details the formation of a smooth and thin ( $\sim 100$  nm) "pseudomembrane" covering the incision edges' surface has been shown by electron microscopy.<sup>3,5</sup>

After numerous *in vitro* experiments and animal tests the excimer laser keratotomy has already turned into practical clinical procedure,<sup>6</sup> the corresponding specialized laser systems have been developed and manufactured.<sup>7</sup> It should be noted that the main efforts in this field have been concentrated on radial keratotomy and some other cornea-reshaping varieties of refractive eye surgery.

At the same time, for some reason or other, the technically much simpler task - application of excimer lasers to produce transplants of various shapes from isolated cornea - has been left somewhat aside. To our knowledge there are only some publications<sup>8,9</sup> dedicated to this possibility of laser keratotomy although the corneal transplants themselves are widely used in different types of keratoplasty.

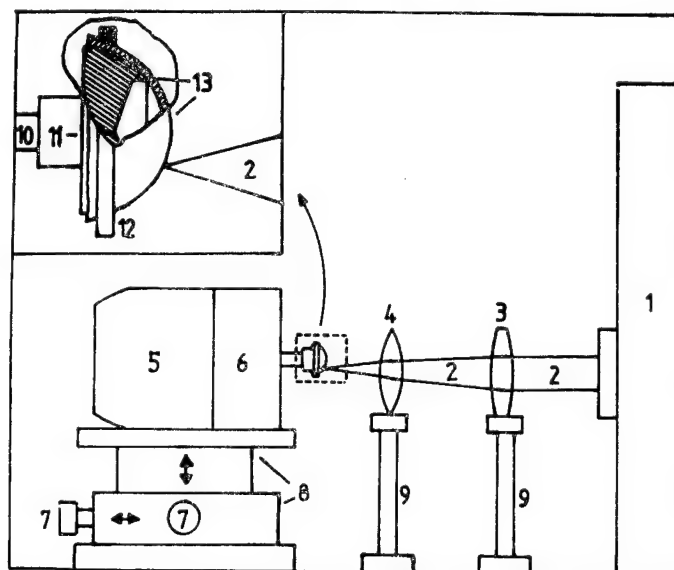
In the present report we describe a very simple laboratory set-up (see Fig. 1) for cutting round-shaped corneal transplants by  $ArF$  laser radiation and present the preliminary results of using this equipment.

## 2. EXPERIMENTAL

An ELI72  $ArF$  excimer laser developed and manufactured by Estonian Academy of Sciences served as ablating 193 nm UV radiation source. The parameters of laser pulses were: duration -  $\sim 10$  ns, energy -  $\sim 20$  mJ, repetition rate - 50 Hz. The beam was focussed into a  $0.1 \times 0.3$  sq.mm stripe by a combination of spherical and cylindrical  $LiF$

Figure 1 - The experimental set-up for cutting cylindrical corneal transplants.

1 - laser, 2 - laser beam pattern, 3, 4 - lenses, 5 - motor, 6 - gearbox, 8 - micropositioning stage with adjustment screws (7), 9 - adjustable lens-holders, 10 - gearbox shaft, 11 - support for cornea, 12 - fixation ring, 13 - cornea.



lenses, thus giving the energy density 0.7 J per sq.mm per pulse on the sample surface.

The isolated pig or cadaver cornea (with a portion of surrounding sclera) were used as original samples for transplant cutting. These were put on a mushroom-shaped copper support and fastened by a copper ring (Fig. 1). The central region of the spherical part of the support was hollowed out to avoid spraying of the copper dust onto open corneal surfaces when laser beam reaches the endothelium of cornea.

The support was fixed to the shaft of a gearbox attached to an AC motor which was placed on the two-axis micropositioning translator stage. This enabled us to choose (after initial centering of the laser beam focus into the conical hollow of the support) the transplant radius with 0.02 mm accuracy by using the transversal micrometric screw. Then the longitudinal screw was used for both the initial adjustment of the corneal surface into the focus of the (weakened) laser beam and for the step-wise readjustment during the cutting procedure. The latter was performed by slowly (typically 1 r.p.m.) rotating the cornea through the immobile focus of the laser radiation.

### 3. RESULTS

Our first experiments on the described equipment have resulted in a set of fully perforated cylindrical corneal transplants with given diameters between 6 and 12 mm, an example of which is pictured in Fig. 2. The cutting time for one sample was 5-10 minutes. As one can expect in the case of 193 nm radiation of the *ArF* laser, the optical microscopy and histological tests have revealed excellent smoothness of the transplant edges and absence of thermal distortions.

Traditionally, the cylindrical corneal transplants have been produced by mechanical trepanation. As ophthalmologists well know, this procedure is almost always accompanied with considerable unevenness of the transplant edges due to the twisting and plucking effects during the mechanical treatment. Because of the fixation problems



Figure 2 - A cylindrical transplant of pig cornea (6 mm in diameter).

the trepanated transplants' shape tends also to deviate from the circular one and additional corrective cutting is often needed. We compared the laser-cutted transplants with the best samples of the trepanated ones under the operation microscope: the superiority of laser processing in this respect was obvious.

Another point is that mechanical trepanation of the perforating transplants cause substantial damage or even loss of the corneal endothelium layers. As became evident from the histological preparations of our transplant samples, the cutting by the *ArF* laser beam is completely free from this shortcoming as well.

We also performed some experiments to obtain corneal transplants of the spherical segment (i.e. the cupola) form. In this case the cornea (fastened to the above-described support) was fixed on the micropositioning stage with its epithelium downwards. The *ArF* laser beam was focussed into a 0.1x5 sq.mm horizontal stripe. The cutting was carried out by slowly scanning the cornea through this focus. As a result a cupola (3-6 mm in diameter) was moved off the cornea during 5-7 minutes.

#### 4. CONCLUSION

Preparation of corneal transplants with the help of  $ArF$  laser is undoubtedly a promising field among the excimer laser applications in ophthalmology.

#### 5. ACKNOWLEDGEMENTS

We wish to thank the co-workers of the Laser Department of the Special Design Office (Estonian Academy of Sciences, Tallinn), and especially Mrs. Helgi Aavik, for their kind help in the experiments.

#### 6. REFERENCES

1. S.L.Trokel, R.Srinivasan and B.Braren, "Excimer laser surgery of the cornea", *Amer. J. Ophthalmology*, vol. 96, No. 5, 710-715, 1983.
2. R.Srinivasan, "Ablation of polymers and biological tissue by ultraviolet lasers", *Science*, vol. 234, 31 October, 559-565, 1986.
3. S.Trokel, "Evolution of excimer laser corneal surgery", *J. Cataract Refract. Surgery*, vol. 15, July, 373-383, 1989.
4. V.V.Lantukh et al., "Ultraviolet excimer lasers in eye microsurgery", *Lasers in Life Sci.*, vol. 2, No. 4, 313-326, 1988.
5. R.P.Tamkivi et al., "Experimental results in the excimer laser surgery of the eye cornea", *Proc. of 3rd Intern. Symp. on Modern Optics*, ed. by G.Lupkovics and A.Podmaniczky, vol. II, 528-533, Budapest, 1988.
6. P.R.Yoder, Jr. et al., "Application of the excimer laser to area recontouring of the cornea", *Proc. SPIE*, vol. 1023, 260-267, 1988.
7. R.Iscoff, "Excimer lasers in ophthalmology. Dramatic advances predicted for corneal surgery", *Lasers & Optronics*, vol. 6, November, 65-67, 1987.
8. R.C.Lieurance et al., "Excimer laser cut lenticules for epikeratophakia", *Amer. J. Ophthalmology*, vol. 103, No. 3(II), 475-476, 1987.
9. S.Gabay, A.Slomovic and T.Jares, "Excimer laser-processed donor corneal lenticules for lamellar keratoplasty", *Amer. J. Ophthalmology*, vol. 107, No. 1, 47-51, 1989.

Laser Plasma XUV Sources: A Role for Excimer Lasers? (Invited Paper)

36980005 The Hague EXCIMER LASERS AND THEIR APPLICATIONS in English 1991 pp  
380-390

[Article by F. Bijkerk of the FOM-Institute for Plasma Physics Rijnhuizen and  
A.P. Shevelko of the Lebedev Physical Institute of the USSR Academy of  
Sciences]

[Text]

### **ABSTRACT**

Radiative characteristics of laser-plasma XUV sources are reviewed. The dependence of the main plasma parameters on the heating laser wavelength is discussed, as well as the use of application-specific excimer lasers to generate XUV radiation. A comparison is given with other XUV sources like electron storage rings. Examples of the application of normal-incidence multilayer XUV optics, e.g. to collimate the laser-plasma radiation or for projection lithography, are given.

### **1. INTRODUCTION**

For more than two decades laser plasmas generated by solid state lasers have been employed with considerable success as sources for XUV radiation. Extended fields of research have been established, i.e. diagnostics of inertial-confinement fusion, XUV emission and absorption spectroscopy, XUV laser research, X-ray microscopy and X-ray lithography. Some of these applications have industrial potential. Will application-specific excimer lasers play a significant role in these areas?

The use of laser plasma XUV sources has traditionally been stimulated by progress in laser technology. High power and compact lasers, enabling construction of small-scale XUV sources, have brought new applications within the reach of many researchers. Application-specific excimer lasers are likely to accelerate this trend due to their intrinsic capability of operating with high repetition rates, and therefore enhanced average XUV yield.

Excimer lasers have the additional advantage of operating at short wavelengths and are therefore able to couple laser energy more favourably into a plasma than is the case with solid state lasers. The increased absorption observed with short-wavelength laser radiation leads to a high conversion efficiency of up to 50 % of laser light into nanometer (sub-keV) XUV radiation. High XUV fluxes make the laser plasma an alternative to electron storage rings, in particular if application-specific excimer lasers are used.

The utilization of laser-plasma XUV sources is stimulated by the progress in the development of XUV optical elements such as multilayer mirrors. These mirrors are capable of collimating the isotropic plasma

radiation using large acceptance angles. In this way XUV radiation can be focussed to unequalled power densities. Again excimer lasers have advantages because of their improved conversion of laser light in particular in the spectral range where normal incidence multilayer mirrors have high reflectivities.

At present, there are several laboratories carrying out optimization studies on topics such as laser repetition rate, pulse modulation, beam quality and XUV source characteristics. In addition, there is a significant effort towards multikilowatt excimer lasers. These programmes are supported by various international projects, e.g. AMMTRA (Advanced Material Processing and Machining Technology Research Association) in Japan and EUREKA in Europe. At present 750 W has been realized with a XeCl laser operated at 500 Hz [1]. Spin-off technology developed in these programmes benefits the state of the art commercial laser systems suitable to generate XUV-plasma radiation.

In this paper we focus on several aspects of the use of excimer lasers for generating XUV radiation, as well as the combination of this source with multilayer XUV optics for challenging novel applications.

## 2. RADIATIVE CHARACTERISTICS OF LASER PLASMAS

If laser radiation is focussed onto the surface of a solid target with powers  $q = 10^{11} - 10^{15} \text{ W/cm}^2$ , a hot plasma is created with an electron temperature  $T_e = 50 - 1000 \text{ eV}$  (Fig. 1). The electron density  $n_e$  in such plasmas may reach levels up to the density of solids. Close to the level of critical density  $n_e^c$  ( $n_e < n_e^c$ ), most laser radiation is absorbed and the electron temperature  $T_e$  is maximum. The critical density  $n_e^c$  is related to the laser wavelength  $\lambda_i$  according to

$$n_e^c = 10^{21} \cdot (\lambda_i)^{-2} \quad [\text{cm}^{-3}] \quad (1)$$

where  $\lambda_i$  is expressed in  $\mu\text{m}$ . In a plasma at this density and sufficiently high temperature, ions are formed which have a charge up to 40 depending upon the atomic number  $Z_A$  of the target material. Emission spectra of such ions are in the extreme ultra-violet (EUV) to soft X-ray spectral band (together known as the XUV) and range from several tens to tenths of nanometers.

XUV-radiation from laser plasmas has been studied in detail both experimentally and theoretically. See for example reviews in ref. 2-4. In the experimental work emphasis is on

- i) the relative and absolute spectral yield versus the atomic number of the target  $Z_A$  [5-9],
- ii) the effective radiative temperature of laser plasmas [7,10], and
- iii) the ratio of laser energy to XUV energy, i.e. the conversion efficiency  $\eta$ , as a function of the target atomic number  $Z_A$  [11,12], the laser wavelength  $\lambda_i$  [10], the laser pulse length [13,14], and the target irradiance  $q$  [7,15].

The general conclusion of these experimental investigations is that the intensity of XUV radiation depends on the atomic number  $Z_A$  of the target material in use and on the target irradiance conditions, namely the irradiance  $q$ , the laser wavelength  $\lambda_i$  and the duration of the laser pulse. Focussing laser radiation with an irradiance  $q = 10^{11} - 10^{15} \text{ W/cm}^2$  onto a solid target creates a very intense quasi-point source of XUV radiation. The source size approximately equals the focal spot of the laser radiation (typically  $100 \mu\text{m}$ ) and the radiative temperature may reach values as high as  $T_R = 100 - 200 \text{ eV}$ , resulting in broadband emission with a significant number of photons with wavelengths  $\lambda < 10 \text{ nm}$  ( $h\nu > 100 \text{ eV}$ ). For heavy target elements ( $Z_A = 50 - 80$ ) the conversion of laser energy into XUV radiation can be as high as 40 - 70 %.

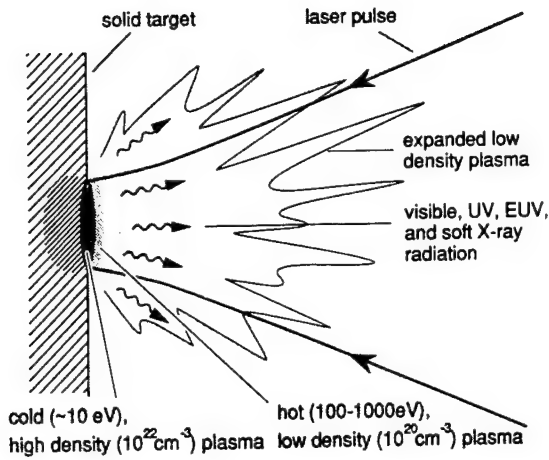


Fig. 1. Representation of a laser-plasma XUV source [3].

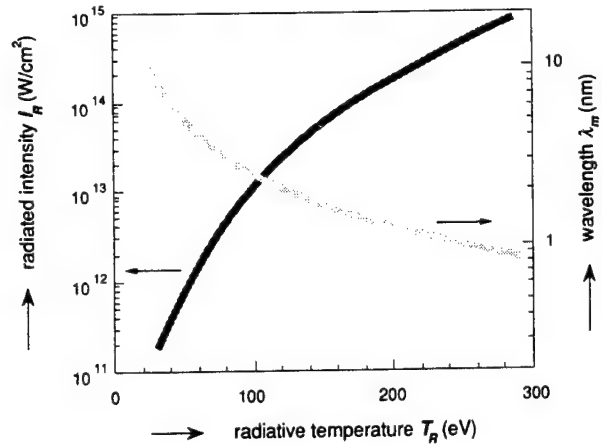


Fig. 2. Dependence of XUV radiated intensity  $I$  and average wavelength  $\lambda_m$  of maximum intensity versus temperature  $T$  of a black body radiator.

In the case of a black body radiator, an expression for the total XUV radiative power density can be obtained

$$I = \sigma \cdot T^4 = 1.03 \times 10^5 T^4 \quad [\text{W/cm}^2] \quad (2)$$

in which  $T$  is expressed in eV and  $\sigma$  is the Stefan-Boltzmann constant (Fig. 2). The radiative power density  $I_R$  of a laser plasma can be estimated from the product of irradiance  $q$  and total conversion efficiency  $\eta$

$$I_R = \eta \cdot q. \quad (3)$$

Combining expressions (2) and (3) we are able to estimate the radiative temperature  $T_R$  of a laser plasma. By using Wien's law,

$$\lambda_m = 2.5 \times 10^2 \cdot (T_R)^{-1} \quad [\text{nm}], \quad (4)$$

it is possible to assess the position  $\lambda_m$  of the wavelength band of the maximum spectral intensity of the plasma radiation (Fig. 2). The radiative temperature  $T_R$ , therefore, serves as a useful parameter to characterize the radiative properties of the source.

In practice, laser-plasma spectra may differ from black body spectra, since laser-plasmas are not completely optically thick as black body radiators, and they do show line radiation. The conversion efficiency  $\eta$  exhibits a strong dependence on the atomic number  $Z_A$  of the laser target (Fig. 3) [11,16]. This is caused by significant spectral contributions to the total radiated intensity from line radiation. Each peak in Fig. 3 originates from radiation of the dominating species of multi-charged ions in the plasma, and corresponds to a set of transitions where the change in the principal quantum number  $n$  is unity. These sets of transitions form K-spectra for transitions with  $n = 2$  to 1 (for ions stripped down to the K-shell), L-spectra for  $n = 3$  to 2, M-spectra for  $n = 4$  to 3, etc. For a given element these separate spectra are in a narrow wavelength band and, conversely, in a given wavelength band K-, L-, or M-spectra can be observed from a limited number of elements. The general relation, plotted in Fig. 4, enables one to optimize the XUV emission in a particular wavelength band by selecting an appropriate target material. An additional requirement is the creation of a proper state of plasma ionization, characterized by a population of ions with appropriate electron shell configuration. This state of plasma ionization is mainly determined by the irradiance conditions.



Comprehensive theoretical laser-plasma models allow one to evaluate the radiative plasma characteristics over a wide range of laser parameters and target materials [4,15]. Calculations show that the total XUV power  $Q$  radiated per unit of volume for all types of emission (line radiation, photorecombination, dielec-

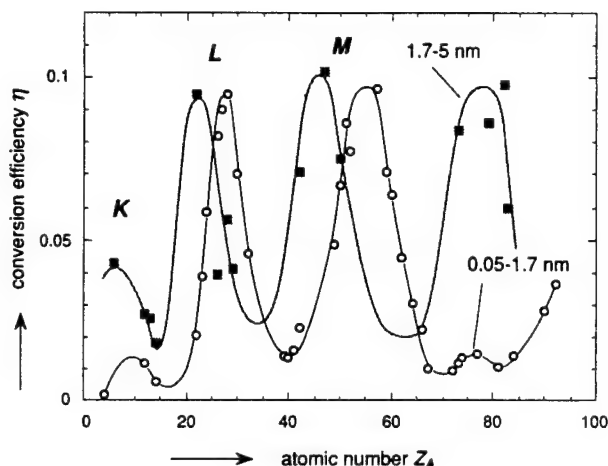


Fig. 3. Conversion efficiency  $\eta$  as a function of target atomic number  $Z_A$ . The peaks correspond to K-, L-, and M-spectra. The shift in the position of the peaks of the two curves is due to the difference in the wavelength bands investigated.

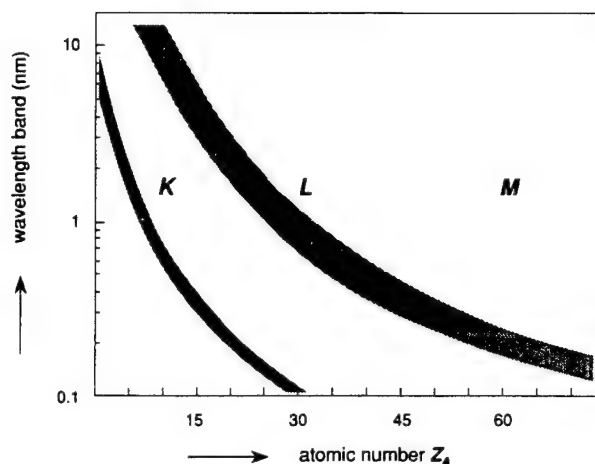


Fig. 4. General relation between spectral regions of K-, L-, and M-transitions and atomic number  $Z_A$  of the laser target.

tronic recombination and bremsstrahlung) is restricted to a narrow plasma layer of only several microns thick with an electron density  $n_e$  of  $3 - 10 \times$  the critical density  $n_e^c$  (Fig. 5). This shallow over-dense layer is primarily heated by electron thermal conductivity; the laser light itself is reflected at a plasma layer with the critical density  $n_e^c$ . In the so-called plasma coronal region ( $n_e < n_e^c$ ) the electron temperature  $T_e$  and the degree of ionization are maximum. Nevertheless, the radiated intensity  $Q$  per unit of volume decreases in this region due to the decrease of the electron density  $n_e$  ( $Q$  is proportional to  $(n_e)^2$ ). Closer to the target, i.e. where the density  $n_e \gg n_e^c$ , the total radiated intensity is also reduced due to a decrease in the electron temperature  $T_e$  and an increase of the optical thickness of the plasma.

Can alterations to this general picture be expected if we consider the models of plasmas generated using excimer lasers? To date, most work has been performed using Nd:YAG/Glass lasers mostly operated at fundamental ( $1.06 \mu\text{m}$ ) or second harmonic ( $0.53 \mu\text{m}$ ) wavelength. For plasmas produced by shorter wavelength lasers the value for the critical density  $n_e^c$  is higher, according to relation (1). Shorter wavelength lasers will deposit their energy in a higher density region of the plasma. The radiated intensity  $Q$  will be higher in this case because it scales with the square of the density  $n_e$ . However, closer to the plasma core the electron temperature  $T_e$  will be lower. The peak temperature scales as  $T_e \sim \lambda^{0.3}$ , while at the critical density the temperature scales more strongly:  $T_e \sim \lambda^{0.9}$  [15]. This shift in temperature will move the maximum of the XUV emission to longer wavelengths, generally above 1.5 to 3 nm. An example of the increased conversion efficiency  $\eta$  observed for short wavelength laser radiation is given in Fig. 6 [17]. The figure shows the laser wavelength dependence on the XUV conversion efficiency for Au plasmas generated at an irradiance  $q = 7 \times 10^{13} \text{ W/cm}^2$ . The conversion efficiency of incident laser light into the wavelength band from 12 nm to 0.8 nm increases by a factor of three when going from a laser wavelength of  $1.05 \mu\text{m}$  to  $0.26 \mu\text{m}$ . Most of this increase is due to the



increased XUV emission at wavelengths above 1.4 nm. Emission at shorter wavelengths (between 0.8 and 1.4 nm) remains almost constant with laser wavelength.

The enhanced conversion efficiency at longer XUV wavelengths observed with short wavelength lasers is important when considering XUV optics. Normal-incidence multilayer XUV optics have been demonstrated with considerable success particularly for wavelengths above the carbon-K edge (4.36 nm) (Sect. 5).

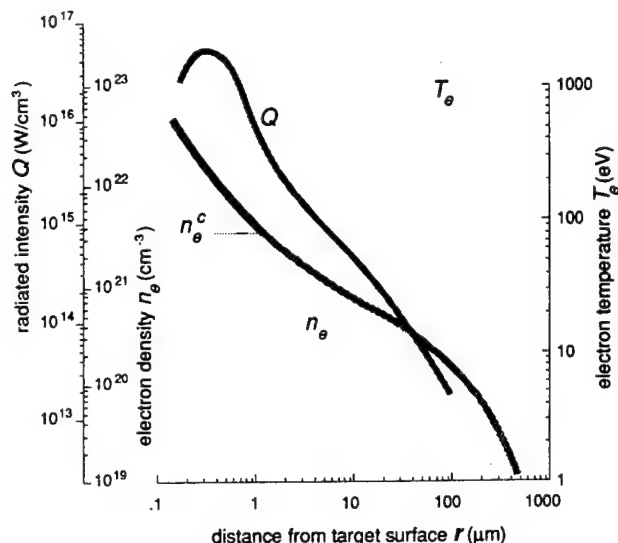


Fig. 5. Profiles of electron temperature  $T_e$ , electron density  $n_e$ , and intensity  $Q$  radiated per unit of volume, close to the surface of a Cu target heated by laser radiation at  $q = 10^{13} \text{ W/cm}^2$ .

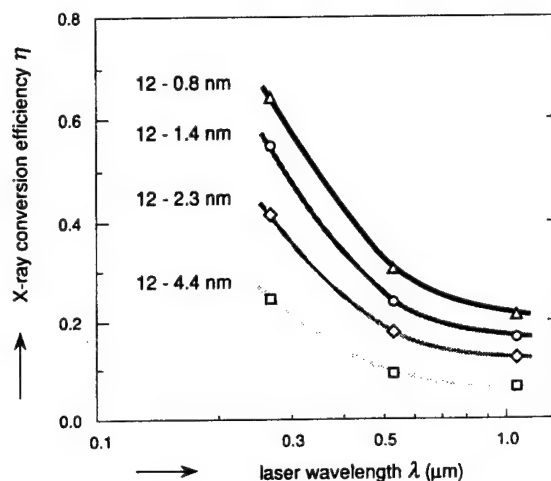


Fig. 6. Laser wavelength dependence of XUV conversion efficiency into various spectrally integrated photon ranges. Laser wavelengths of  $1.05 \mu\text{m}$  ( $\omega_0$ ),  $0.53 \mu\text{m}$  ( $2\omega_0$ ), and  $0.26 \mu\text{m}$  ( $4\omega_0$ ) from a Nd:Glass laser were used.

### 3. APPLICATION-SPECIFIC EXCIMER LASERS

Excimer lasers suitable to generate laser-plasma radiation can be divided in systems for EUV ( $\lambda \geq 2$  to  $4 \text{ nm}$ ) and systems for soft X-rays ( $\lambda \leq 2$  to  $4 \text{ nm}$ ). An example of the first is a  $150 \text{ W}$  KrF laser situated in the Sandia National Laboratories [18]. The laser system, consisting of an oscillator and two single-pass amplifiers, produces  $1.5 \text{ J}$  pulses of  $25\text{--}30 \text{ ns}$  at  $100 \text{ Hz}$  repetition rate. The laser energy is focussed on a rotating cylindrical target, which is Au-coated. The power density in the  $\sim 250 \mu\text{m}$  focus amounts  $1 \times 10^{11} \text{ W/cm}^2$ . At these irradiance conditions a relatively cool plasma is created, which shows a high conversion efficiency in the EUV range of  $\eta = 35\text{--}40 \%$ . The XUV source has a dedicated high-throughput monochromator, which delivers an irradiance to the sample comparable to that of monochromators of electron storage rings (Tab. 1).

Shorter wavelength radiation ( $\lambda \leq 2 \text{ nm}$ ), as in the second case, is usually generated with lower conversion efficiency. The typical  $20\text{--}30 \text{ ns}$  pulse length from excimer lasers leads to X-ray emission which falls off after  $\sim 10 \text{ ns}$  with the result that only the initial part of the laser pulse is efficiently converted to soft X-rays [19]. Several pulse modification techniques have been successfully investigated: injection mode-locking with

trains of  $\sim 100$  ps pulses [20], and passive pulse shortening by a  $H_2$ -Raman cell and a saturable dye jet, resulting in 3.5 ns pulses of 400 mJ [21]. The wavelength range from 2 to 0.8 nm (0.6 to 1.4 keV) is of interest for proximity print X-ray lithography, a candidate technique for mass production of sub-0.5 micron semiconductor devices. X-ray lithography systems driven by application-specific excimer lasers have considerable potentials for industrial utilization [22,23].

#### **4. COMPARISON WITH OTHER XUV SOURCES**

In comparing laser plasmas with synchrotron XUV sources it is necessary to remark that the interest in laser plasmas has been stimulated greatly by the enhanced availability of synchrotron radiation facilities. In the past decade these facilities have led to a significant increase in research activity in many differing areas such as biology, chemistry and medicine. At present the laser plasma serves as an interesting alternative facility with specific capabilities.

The laser plasma XUV source is most suitable for applications requiring very high instantaneous fluxes for single, short pulse experiments. The peak brightness of laser plasma sources can be three orders of magnitude higher than for electron storage rings (Tab. I). In experiments requiring the accumulation of high doses of particularly short wavelength radiation, synchrotron facilities, being quasi-continuous, are at an advantage. However, if one takes into account typical geometrical factors arising from the source-to-sample distances, and the possibility to use excimer lasers with high repetition rates ( $\sim 100$  Hz), a comparable average sample irradiance is obtained in both cases. The actual number of photons (per unit of time, bandwidth, and sample area) available from two examples of high throughput monochromators is of similar order (Tab. I).

The use of synchrotron radiation is still expanding considerably. New electron storage rings are being built, some dedicated to specific applications (such as X-ray lithography [24]), others for general research purposes offering beamlines for a large variety of experiments. Intensities of synchrotron radiation are being increased by the use of insertion devices such as undulators and wigglers [25]. For short wavelength radiation down to 0.01 nm ( $\sim 100$  keV) synchrotron facilities have definite advantages over any laboratory XUV source. The final choice between large-scale user facilities such as synchrotron radiation sources and laboratory-scale devices such as laser-plasma XUV sources depends on the specific physical task as well as economical aspects.

Rather similar to the laser plasma, when comparing spectra and radiated power, is the micro-pinch [26]. In this compact device X-rays are generated in a magnetically compressed metal plasma induced by an electrical discharge. Its disadvantage is the instability in the source position from one discharge to another. This increases the effective source size from  $\sim 0.1$  mm for a single pulse to  $\sim 1$  mm when averaged over a large number of pulses.

Tab. 1. Comparison of different XUV sources: electron storage rings, laser plasmas and a theoretical black body radiator. The data (sets of two numbers) for brightness and irradiance refer to the wavelength range indicated.

	BESSY <sup>*)</sup>	DORIS <sup>**)</sup>	BBR <sup>†)</sup>	MPI <sup>§)</sup>	FOM <sup>##)</sup>	SNL <sup>###)</sup>
source size (mm <sup>2</sup> )	0.8x1	1x10	$\pi(0.05)^2$	$\pi(0.05)^2$	$\pi(0.05)^2$	0.25x0.25
pulse duration (ns)	0.1	0.15	3	3	15	28
repetition rate (Hz)	5x10 <sup>8</sup>	10 <sup>8</sup>	1	1/60	1/30	10 <sup>2</sup>
source-to-sample distance (m)	15	10	0.1	0.1	0.1	0.2-1.5
wavelength range (nm)	1-10	1-10	2.5-10	1-10	0.9-1.7	8-35
peak brightness (phot/s.nm.sr.mm <sup>2</sup> )	2x10 <sup>23</sup> -2x10 <sup>22</sup>	5x10 <sup>23</sup> -5x10 <sup>21</sup>	10 <sup>28</sup> -4x10 <sup>25</sup>	10 <sup>25</sup> -5x10 <sup>25</sup>	5x10 <sup>24</sup>	4x10 <sup>22</sup> -10 <sup>23</sup>
average brightness (phot/s.nm.sr.mm <sup>2</sup> )	9x10 <sup>21</sup> -10 <sup>21</sup>	7x10 <sup>21</sup> -7x10 <sup>19</sup>	3x10 <sup>17</sup> -10 <sup>17</sup>	6x10 <sup>14</sup> -3x10 <sup>15</sup>	3x10 <sup>15</sup>	10 <sup>17</sup> -3x10 <sup>17</sup>
peak sample irradiance (phot/s.nm.cm <sup>2</sup> )	6x10 <sup>16</sup> -8x10 <sup>15</sup>	5x10 <sup>18</sup> -5x10 <sup>16</sup>	10 <sup>22</sup> -5x10 <sup>21</sup>	2x10 <sup>21</sup> -7x10 <sup>21</sup>	4x10 <sup>20</sup>	3x10 <sup>19</sup> -6x10 <sup>19</sup>
average sample irradiance (phot/s.nm.cm <sup>2</sup> )	3x10 <sup>15</sup> -4x10 <sup>14</sup>	7x10 <sup>16</sup> -7x10 <sup>14</sup>	3x10 <sup>13</sup> -10 <sup>13</sup>	5x10 <sup>10</sup> -3x10 <sup>11</sup>	2x10 <sup>11</sup>	7x10 <sup>13</sup> -2x10 <sup>14</sup>
monochromator	SX-700					dedicated
peak sample irradiance (phot/s.nm.cm <sup>2</sup> )	10 <sup>17</sup> -4x10 <sup>16</sup>					3x10 <sup>20</sup> -3x10 <sup>19</sup>
average sample irradiance (phot/s.nm.cm <sup>2</sup> )	6x10 <sup>15</sup> -2x10 <sup>15</sup>					10 <sup>15</sup> -10 <sup>14</sup>

<sup>\*)</sup> BESSY - Electron storage ring (Berlin, FRG) electron energy 0.8 GeV, ring current 300 mA [9,27].

<sup>\*\*)</sup> DORIS - Electron storage ring (Hamburg, FRG) electron energy 3 GeV, ring current 500 mA [28].

<sup>†)</sup> BBR - Calculated data for a black body radiator with  $T_R = 100$  eV.

<sup>§)</sup> MPI - Nd:Glass laser (Max Planck Institute, Garching, FRG),  $T_R = 100$  eV,  $\lambda_l = 0.53$   $\mu$ m,  $E_{laser} = 7$  J,  $q = 3 \times 10^{13}$  W/cm<sup>2</sup> [12].

<sup>##)</sup> FOM - Nd:Glass laser (FOM-Institute Rijnhuizen, Nieuwegein, the Netherlands),  $T_R = 105$  eV,  $\lambda_l = 0.53$   $\mu$ m,  $E_{laser} = 2.2$  J,  $q = 2.5 \times 10^{12}$  W/cm<sup>2</sup>, Mg target [29].

<sup>###)</sup> SNL - KrF laser (Sandia National Laboratories, Livermore, CA, USA),  $T_R = 20$  eV,  $\lambda_l = 0.248$   $\mu$ m,  $E_{laser} = 1.5$  J,  $q = 1 \times 10^{11}$  W/cm<sup>2</sup>, Au target [18].

The plasma focus device is of a similar concept. It pinches an inert gas into a thin plasma filament using a coaxial electrode. The plasma focus device, well developed technologically and commercially [30], generates radiation in the soft X-ray range. Its sub-1 mm effective source size enables imaging applications like X-ray lithography using a source-to-sample distance of 40 cm. With a repetition rate of several Hz a ceiling in the XUV yield of this source seems to have been reached.

In general terms, the advantages of laser-plasma XUV sources can be described as follows.

- i) High brightness in the XUV spectral band, due to efficient conversion of laser light into XUV radiation and high laser pulse energy available from drivers,
- ii) High average brightness with duty-cycles up to several Hz (solid state lasers) or up to several hundreds of Hz (excimer lasers),
- iii) Short pulse duration, equal to the laser pulse duration (down to ~ps [31]), enabling study of time-resolved processes and 'pump and probe' experiments,
- iv) Reduced capital cost and floor-space requirements compared with an electron storage ring, which makes

commercial applications and small-scale laboratory set-ups possible,

v) Small source size of 10 to 100  $\mu\text{m}$  and high pulse-to-pulse reproducibility both in source position and in XUV yield,

vi) Wide spectral band ranging from several tenths to tens of nanometers, tunable according to the needs of specific applications by choosing the target material and irradiance conditions,

vii) Simple wavelength calibration of spectra using target-specific spectral lines,

viii) Reduced production of target debris compared with electrical discharge sources, possibilities to suppress debris by applying thin foil laser targets or generating the plasma in an environment of buffer gas,

ix) No UHV requirements and the possibility of operating in sub-atmospheric pressure of inert gasses.

In particular excimer lasers add to the advantages i) and ii) due to their high conversion efficiency into XUV radiation and their high repetition rate. General disadvantages of laser-plasma XUV sources are the absence of polarization of the plasma radiation and the lower limit in the spectral range at several tenths of nanometers. Compared with sources of synchrotron radiation, laser plasmas have a sample irradiance which is, in general, an order of magnitude lower. High repetition rate excimer lasers can exhibit a sample irradiance in the XUV range which is comparable to that of electron storage rings (Tab. 1).

## 5. APPLICATION OF MULTILAYER XUV OPTICS

An essential difference of the quasi-point laser-plasma sources with sources of synchrotron radiation is the larger divergence of laser-plasma radiation over a solid angle of  $2\pi$  sr. Achieving a beam divergence comparable with that of synchrotron radiation (several mrad) would be beneficial for many applications. In addition, the utilization of the isotropic laser-plasma radiation would be more efficient if large acceptance angles can be used. Grazing incidence optics, yielding total reflection at incidence angles below the critical angle, offer only a limited improvement due to the limitations in the allowable acceptance angle.

Multilayer XUV optics, which can be used at normal incidence, will offer many new possibilities [32]. XUV reflection by multilayer coatings is based on the principle of interference, analogous to reflection by natural crystals. Multilayer mirrors can be synthesized by a number of coating techniques: electron-beam evaporation, magnetron sputtering or laser-beam evaporation [33]. Selection of coating materials is based on their optical properties (determined by the wavelength dependent refractive index), their chemical stability (preventing interdiffusion between the layers), and their material property to form smooth interfaces. Well-known combinations are Mo-Si, Ni-C, and W-C. The relative success in the 'atomic engineering' of these mirrors is determined by the control of the deposition process.

Layer thicknesses amount to  $\sim\lambda/4$  for mirrors used at normal incidence, and can be as thin as few atomic layers. The roughness of the interface is the crucial factor which determines the optical performance of the multilayer mirror. In practice, high quality multilayer mirrors may have periods varying from several to tens of nanometers. This restricts the use at normal-incidence to wavelengths from  $\sim 4$  to several tens of nanometers, which is also the wavelength range of highest yield of plasmas generated by excimer lasers (Sect. 2).

Recent advances in thin film deposition techniques have enabled the fabrication of multilayer mirrors on spherical and even aspherical surfaces [33]. These figured optical elements can be used in conventional optical schemes to collimate XUV radiation or to produce XUV telescopes. A laser plasma, with its high brightness and small emitting area can be regarded as an efficient source for such imaging purposes. In addition laser plasma radiation seems more favourable for XUV optics than synchrotron radiation from bending magnet beamlines of storage rings, since it can be concentrated in a narrow spectral band or even in a single spectral line [34].

## 6. EXAMPLES OF THE USE OF XUV OPTICS

An early demonstration of the possibility to collimate XUV radiation has been given in ref. 35,36 (Fig. 7). Laser plasma radiation was collimated to a power density as high as  $q = 10^7$  W/cm<sup>2</sup> in the focus of a spherical multilayer mirror. The Mo-Si mirror, used at normal incidence, had a reflectivity of 20% for a wavelength of 18.2 nm. Due to the small dimensions of the plasma (~0.1 mm) an XUV beam divergence of only 1 mrad was realized.

Of the many other possible applications of multilayer XUV optics we mention:

i) Projection X-ray lithography. In advanced imaging schemes for semiconductor lithography, XUV optics are very likely to provide in spatial resolutions well below the limit (~0.15 micron) obtainable with proximity print X-ray lithography. For this purpose highly reflective normal-incidence optics can be applied in classical optical schemes like the Schwarzschild design (Fig. 8) [37]. This allows 10- to 20-fold demagnification of mask structures, which can be patterned on a stable reflecting substrate. Due to the large number of reflecting surfaces in this geometry, multilayer mirrors with a reflectivity of ~50 % for wavelengths in the 5 to 15 nm range are a prerequisite. This reflectivity has been achieved in the case of normal-incidence multilayer mirrors fabricated on flat substrates [38]; fabrication on spherical substrates is a next major task.

ii) X-ray microscopy. The above described Schwarzschild telescope can be used for microscopy when applied in reverse optical direction, i.e. in a magnifying system. X-ray microscopy may prove to be a bridge between optical and electron microscopy. X-ray microscopes can have an improved resolution compared with ordinary optical microscopes, while they require a less extensive sample preparation compared to electron microscopes.

iii) Spectroscopy. A high intensity of a collimated XUV beam from a laser plasma source, as well as a short pulse duration, are effective properties for investigations of the inner shell structure of atoms and measurement of ionization cross-sections. For example, in X-ray fluorescence spectroscopy a sample is illuminated by an XUV beam, causing primary core-hole excitations. Using multilayer mirrors the resulting element-specific fluorescent radiation, which is weak for light elements, can be detected with a large efficiency.

iv) EUV and soft-X-ray lasers. Amplification of stimulated emission has been observed in this part of the spectrum, in multi-charged ions, for example Se XXV (20.6 and 20.9 nm) [39] or C VI (18.2 nm) [40]. XUV optics can be applied to the laser cavity to achieve multi-pass amplification in the gain medium, thereby enhancing the XUV output of these lasers [38].

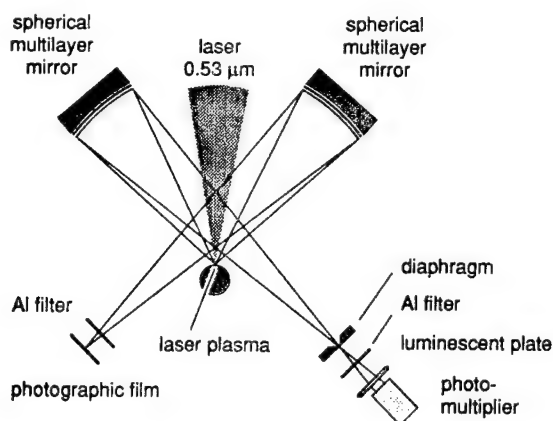


Fig. 7. Experimental set-up for formation of intense XUV radiation of 18.2 nm using spherical multilayer XUV mirrors at normal incidence. The irradiance in the position of the plasma image amounted to  $1 \times 10^7$  W/cm<sup>2</sup>.

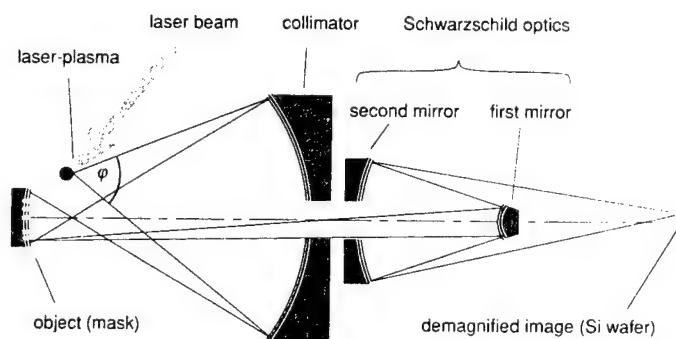


Fig. 8. Example of a multi-component XUV imaging system for X-ray projection lithography. The large collecting angle of the collimator enhances the efficiency of the system.

u) Plasma diagnostics. Spectral analysis of X-rays emitted by plasmas provides information about composition, density and temperature [41]. Measurement of element-specific emission lines with narrow-band multilayer mirrors gives information about the plasma elemental composition. Multi-channel detectors can be constructed, with channels tuned to characteristic lines [42]. The method is particularly suitable for low atomic number elements, because their spectra have distinct lines on a low background.

vi) Radiometry and calibration of XUV components. Due to their reproducible radiative characteristics, laser plasma XUV sources have the potential to serve as radiometric transfer standards in the spectral range below 100 nm [9]. Laser plasmas may complement the primary radiation standard provided by the calculable spectral power of electron storage rings.

## 7. CONCLUSIONS

Laser plasmas generated with compact and powerful laser systems are versatile laboratory-scale sources of XUV radiation. The outstanding properties of these sources are the very high instantaneous brightness in the XUV range, the possibility of picosecond pulse duration, and the small and reproducible source size. Laser-plasma sources impose low requirements on capital investment and floor space. In particular, excimer lasers significantly increase the duty-cycle of these sources and generate time-averaged sample irradiances which are as high as radiation from bending magnet beamlines of electron storage rings.

The high conversion efficiency of laser light to XUV radiation, which is observed with short-wavelength laser radiation, is particularly large for XUV radiation above 1.5 nm. It is therefore possible to fully exploit the use of normal-incidence multilayer XUV optics. With the combination of an excimer-laser driven XUV source and multilayer XUV optics challenging applications can be realized, for example in soft X-ray projection lithography, X-ray microscopy, and spectroscopy. Future work is also directed to optimization of the XUV yield and further reduction of target debris. Returning to the earlier question 'laser-plasma XUV sources, a role for excimer lasers', the answer is clearly positive.

## 8. ACKNOWLEDGMENTS

This work is part of the programme of FOM (the Foundation for Fundamental Research on Matter) and STW (the Netherlands Technology Foundation) in the Netherlands, and the Lebedev Physical Institute in the USSR. The work is made possible by financial support from NWO (the Netherlands Organization for Scientific Research) and the Netherlands Government in the framework of EUREKA. The work at the Lebedev Physical Institute is supported by the USSR Academy of Sciences.

In particular the authors wish to thank Dr. G.D. Kubiak (Sandia Livermore Laboratories, Livermore, CA, USA), Dr. F. Schaefer (BESSY, Berlin, FRG), Prof. M.J. van der Wiel and Dr. E. Louis (FOM-Rijnhuizen) for the kind cooperation in the realization of this paper.

## 9. REFERENCES

- [1] E. Müller-Horsche, P. Oesterlin, D. Basting, Recent progress towards multi-kilowatt output, ECO4 Conf. Proc. (1991)
- [2] R. Sigel, X-rays from laser produced plasmas, SPIE Conf. Proc. **1140** (1989) pp.6-12
- [3] F. O'Neill, Laser plasma XUV sources, in Laser-plasma interactions **4**, Ed. M.B. Hooper, Proc. 35<sup>th</sup> Scottish Universities Summer School in Physics, (1988) pp.285-315
- [4] A.V. Vinogradov, V. N. Shlyaptsev, Characteristics of laser plasma X-ray source, Sov. J. Quant. Electr. **17** 1 (1987) pp.5-26
- [5] W.C. Mead, E.M. Campbell, K.G. Estabrook, R.E. Turner, W.L. Kruer, P.H.Y. Lee, B. Pruet, V.C. Rupert, K.G. Tirsell, G.L. Stradling, F. Ze, Laser-plasma interaction at 0.53  $\mu\text{m}$  for disk targets of varying Z, Phys.



Rev. Lett. **47** 18 (1981) pp.1289-1292

- [6] P.K. Carroll, E.T. Kennedy, G. O'Sullivan, Laser produced continua for absorption spectroscopy in the VUV and XUV, *Appl. Opt.* **19** 9 (1980) pp.1454-1462
- [7] T. Mochizuki, T. Yabe, K. Okada, M. Hamada, N. Ikeda, S. Kiyokawa, and C. Yamanaka, Atomic number dependence of soft X-ray emission from various targets irradiated by 0.53  $\mu\text{m}$  wavelength laser, *Phys. Rev.* **A33** 1 (1986) pp.525-539
- [8] M.D. Rosen, D.W. Phillon, V.C. Rupert, W.C. Mead, W.L. Kruer, J.J. Thomson, H.N. Kornblum, V.W. Slivinsky, G.J. Caporaso, M.J. Boyle, and K.G. Tirsell, Interaction of 1.06 $\mu\text{m}$  laser radiation with high Z targets, *Phys. Fluids* **22** 10 (1979) pp.2020-2031
- [9] J. Fischer, M. Kühne, B. Wende, Spectral radiant power measurements of VUV and soft X-ray sources using electron-storage ring Bessy as a radiometric standard source, *Appl. Opt.* **23** 23 (1984) 4252-4260
- [10] H. Nishimura, F. Matsuoka, M. Yagi, K. Yamada, S. Nakai, G.H. McCall, and C. Yamanaka, Radiation conversion and related ablation behaviour of a gold-foil target irradiated by 0.35, 0.53, 1.06, and 10.6  $\mu\text{m}$  lasers, *Phys. Fluids* **26** 6 (1983) pp.1688-1692
- [11] H. C. Gerritsen, H. van Brug, F. Bijkerk, M.J. van der Wiel, Laser generated plasma as soft X-ray source, *J. Appl. Phys.* **59** 7 (1986) pp.2337-2344
- [12] K. Eidmann, T. Kishimoto, Absolutely measured X-ray spectra from laser plasmas with targets of different elements, *Appl. Phys. Lett.* **49** 7 (1986) pp.377-378
- [13] F. O'Neill, I.C.E. Turcu, D. Xenakis, M.H.R. Hutchinson, X-ray emission from plasmas generated by an XeCl laser picosecond pulse train, *Appl. Phys. Lett.* **55** 25 (1989) pp.2603-2604
- [14] K. Eidmann, W. Schwanda, Conversion of laser light into soft X-rays with 3 ns and 30 ps laser pulses, *Lasers and Particle Beams* (1991) accepted
- [15] W.C. Mead, E.M. Campbell, K.G. Estabrook, R.E. Turner, W.L. Kruer, P.H.Y. Lee, B. Pruet, V.C. Rupert, K.G. Tirsell, G.L. Stradling, F. Ze, C.E. Max, M.D. Rosen, and B.L. Lasinski, Laser-plasma irradiation of disk targets at 0.53  $\mu\text{m}$  wavelength, *Phys. Fluids* **26** 8 (1983) pp.2316-2331
- [16] K.M. Glibert, J.P. Anthes, M.A. Gusinow, M.A. Palmer, R.R. Whitlock, D.J. Nagel, X-ray yields of plasma heated by 8 ns neodymium laser pulses, *J. Appl. Phys.* **51** 3 (1980) pp.1449-1451
- [17] R. Kodama, K. Okada, N. Ikeda, M. Mineo, K.A. Tanaka, T. Mochizuki, and C. Yamanaka, Soft X-ray emission from  $\omega_0$ ,  $2\omega_0$ , and  $4\omega_0$  laser-produced plasmas, *J. Appl. Phys.* **59** 9 (1986) pp.3050
- [18] G.D. Kubiak, XUV resist characterization, studies with a laser plasma source, *Proc. SPIE* **1343** (1990) pp.283-291
- [19] G.M. Davis, M.C. Gower, F. O'Neill, and I.C.E. Turcu, Plasma X-ray source for lithography generated by a ~30 J, 30 ns KrF laser, *Appl. Phys. Lett.* **53** 17 (1988) pp. 1583-1585
- [20] F.O'Neill, I.C.E. Turcu, D. Xenakis, and M.H.R. Hutchinson, X-ray emission from plasmas generated by an XeCl laser picosecond pulse train, *Appl. Phys. Lett.* **55** 25 (1989) pp. 2603-2604
- [21] A. Tünnermann, K. Wrede, and B. Wellegehausen, Generation of high peak power excimer laser radiation by pulse shortening, *Appl. Phys. B* **50** (1990) pp. 361-364
- [22] F. Bijkerk, G.E. van Dorssen and M.J. van der Wiel, Laser plasma as X-ray source for lithographic imaging of submicron structures onto experimental X-ray resist, *Microelectr. Eng.* **9** (1989) pp.121-126
- [23] California Jamar Inc., San Diego, Ca, USA
- [24] D.E. Andrews, M.N. Wilson, A.I. Smith, V.C. Kempson, A.L. Purvis, R.J. Andersen, A.S. Bhutta, A.R. Jorden, Helios, a compact superconducting X-ray source for production lithography, *SPIE Conf Proc.* **1263** (1990)
- [25] S. Krinsky, Experience with synchrotron radiation sources, in: *X-ray microscopy II*, Springer Series **56** (1987) pp.4-9
- [26] M. Kühne, B. Wende, Vacuum UV and soft X-ray radiometry, *J. Phys. E.* **18** (1986) pp.637-647
- [27] J. Feldhaus, Soft X-ray monochromators for synchrotron radiation, *SPIE Conf. Proc.* **984** (1988) 11-22

- [28] Synchrotron Radiation Techniques and Applications, Ed. C. Kunz, Springer Verlag, (1979)
- [29] F. Bijkerk, E. Louis, A.P. Shevelko, A.A. Vasilyev, Absolute brightness of laser plasmas in the soft X-ray emission band, to be published
- [30] F. Richter, J. Eberle, R. Holz, W. Neff, R. Lebert, Repetitive plasma focus as radiation source for X-ray lithography, 2<sup>nd</sup> Int. Conf. High Density Pinches, Laguna Beach, Conf. Proc. (1989)
- [31] R.R. Freeman, L.D. van Woerkom, T.J. McIlrath, W.E. Cooke, Non-linear interaction of visible light and X-rays, measurement of femtosecond duration soft X-ray pulses, to be published
- [32] N.M. Ceglio, Revolution in X-ray optics, J. X-ray Sc. and Technol. **1** (1989) pp.7-78
- [33] M.P. Bruijn, J. Verhoeven, E. Puik, M.J. van der Wiel, Multilayer X-ray mirrors: the state of the art, SPIE Conf. Proc. **984** (1988) pp.54-63
- [34] Multilayer mirrors exhibit a spectral selectivity  $\lambda/\Delta\lambda$ , which is equal to the number of layer pairs effectively contributing to the reflected signal.
- [35] V.L. Artsimovich, S.V. Gaponov, Yu.S. Kasyanov, B.M. Luskin, N.N. Salashchenko, I.I. Sobelman, A.P. Shevelko, Formation of directed intense vacuum ultra-violet radiation from a laser plasma, JETP Lett., **46** 8 (1987) pp.391-394
- [36] S.V. Gaponov, S.A. Gusev, V.V. Dubreov, A.I. Kuzmichev, B.M. Luskin, N.N. Salashchenko, A.P. Shevelko, V.A. Slemzin, I.I. Sobelman, and I.G. Zabrodin, Normal incidence multilayer mirrors for the 120-450Å wavelength region, J. of X-ray Sc. & Technol. **2** (1990) pp.241-248
- [37] H.J. Voorma, F. Bijkerk, Design of an extended image field XUV telescope for projection lithography, Proc. Conf. Soft X-ray Projection Lithography, Monterey (1991)
- [38] N.M. Ceglio, D.P. Gaines, D.G. Stearns, A.M. Hawryluk, Double pass amplification of laser radiation at 131 Å, Opt. Comm. **69** (1989) pp.285-288
- [39] D.L. Matthews, P.L. Hagelstein, M.D. Rosen, M.J. Eckart, N.M. Ceglio, A.U. Hazi, H. Medeckl, B.J. MacGowan, J.E. Trebes, B.L. Whitten, E.M. Campbell, C.W. Hatcher, A.M. Hawryluk, R.L. Kauffman, L.D. Pleasance, G. Rambach, J.H. Scofield, G. Stone, and T.A. Weaver, Demonstration of soft X-ray amplifier, Phys. Rev. Lett. **54** 2 (1985) pp.110-113
- [40] S. Suckewer, C.H. Skinner, H. Milchberg, C. Keane, and D. Voorhees, Amplification of stimulated soft X-ray emission in a confined plasma column, Phys. Rev. Lett. **55** 17 (1985) pp.1753-1756
- [41] H. van Brug, F. Bijkerk, M.J. van der Wiel and B. van Wingerden, Low-Z element analysis by soft-X-ray line emission of a laser-produced plasma, J. Anal. At. Spectrom. **2** (1987) pp.503-507
- [42] S.V. Bobashev, N.N. Salashchenko, L.A. Shmaenok, Absolute SXR radiometry technique for laser plasma sources, ECO4 Conf. Proc. (1991)



Efficient Population of Low Vibrational Number Electronic States of Excimer Molecules: The Argon Dimer

36980005 The Hague EXCIMER LASERS AND THEIR APPLICATIONS in English 1991 pp 430-437

[Article by Tom Efthimiopoulos of the Physics Department, University of Crete and FORTH-IESL]

[Text]

### ABSTRACT

Results related to the emission of radiation by the argon dimer in the 128 nm region are presented. The excited dimers are produced by a supersonic expansion of a fast discharge excited plasma.

### 1. INTRODUCTION

The spectroscopy of the rare gas dimers is of fundamental interest. The emission bands from the first excited electronic states are in the VUV and XUV regions of the spectrum and understanding of the formation of the dimers from different excitation mechanisms could lead to the development of new tunable lasers in these regions. Over the last years several papers have been published concerning the VUV emission of the rare gas dimers excited by a proton beam<sup>1</sup>, an electron beam<sup>2</sup>, a fast discharge<sup>3</sup> and a heavy ion beam<sup>4</sup> with the rare gas at high pressure contained in a closed cell. Laser action has been reported for the xenon or argon dimer pumped by high current, high voltage electron beams by several group<sup>5,6,7</sup>. However, although the fluorescence efficiency of the electron beam pumped rare gas dimers is high<sup>8</sup>, loss mechanisms due to photoionization and to the high gas and electron temperature generated (leading to collisional quenching, which directly competes with the stimulated emission) limit the efficiency and the power of the existing laser systems<sup>9</sup>. It is of interest then to investigate alternative excitation schemes, which lead to low temperature gas and electrons.

It has been known for a number of years that the supersonic expansion of a rare gas produces cold dimers and a great deal of spectroscopic information about the first few excited electronic states has been obtained using laser induced fluorescence techniques in the VUV<sup>10</sup>. Also supersonic expansion cooling of electronically excited radicals has been recently used, in a corona discharge, in order to simplify the spectra of the molecules<sup>11</sup>. Additionally, rare gas dimer radiation from a free jet expansion, with electron beam excitation, has been reported by Verkhovtseva et al<sup>12</sup> and Baldwin et al<sup>13</sup>. It seemed then reasonable to investigate the supersonic expansion of a rare gas plasma produced by a fast discharge, as a source of cool electronically excited dimers. Some initial results related to this investigation are presented in this paper.

## 2. EXPERIMENTAL DETAILS

A Schematic diagram and a detailed description appeared in a previous publication of ours<sup>14</sup>. Here we will present a brief description. A quartz tube with a tungsten electrode inside was shaped in order to get a nozzle of diameter of approximately 0.5 mm. This nozzle assembly was mounted on the top of a vacuum chamber, with provision for a ground electrode, which was evacuated by a booster pump and a mechanical pump with a pumping speed of 75l/sec. A dc power supply of 2 KV and 250 mA was used for the continuous operation of the system. For the pulsed operation a combination of capacitors with a thyatron switch was used in a circuit design commonly used in the commercial excimer laser systems. The detection of the signal was done with a vacuum monochromator equipped with a solar blind photomultiplier (EMR-510G-08-013).

## 3. THE RESULTS

In this chapter we will present some of the results related to the spectroscopy of the jet source. Fig. 1 shows a typical spectrum of the continuous discharge jet with a diameter of 0.5 mm supplied with 50 mA dc current with positive polarity on the nozzle electrode. The pressure behind the nozzle was 2 bar and the average vacuum chamber pressure was 1.1 mbar. The detection system was sampling the total Mack cone and the nozzle was located 3 mm above the optical axis. The atomic lines of argon together with the emission of the high vibrational

states of the molecule are clearly seen in the right hand side of the figure. The emission spectrum is centered at 128 nm indicating the presence of both singlet and triplet states (which contribute to the emission) mixed via electron collisions and collisions with the atoms<sup>15,16</sup>. The atomic oxygen lines at 130.2 nm and the atomic hydrogen Lyman  $\alpha$  line, which are present at lower pressures, are absent in this case. Also there is no signal above 140 nm contrary to the results with other types of excitation. The linewidth of the 128 nm band is 9.0 nm for the 2 bars case which is smaller than the 12 nm reported by Wrobel et al<sup>6</sup> at much higher pressure of 25 bars. This indicates that the collisional relaxation rate in our case is enhanced by the expansion resulting in populating the lowest vibrational state. Comparison of the intensity of the fluorescence of the atomic states near 105 nm relative to the high vibrational states intensity and that of the 128 nm band indicates that the conversion efficiency in producing cold dimers from the atomic species is very high. Measurements of the absolute intensity of the 128 nm fluorescence band and the gain using a coherent probe are under way and the results will be presented in a future publication.

Fig.2 shows the peak intensity at 128 nm in relative units as a function of the argon pressure with the chamber pressure changing due to the limited pumping speed of the system. The slope of the steep part of the plot is 5 and at stagnation pressures above 2 bars saturation settles in. The observed slope is indicative of 3 body collisions required to form an ionic dimer following by 3 body collisions needed for formation of the excited dimers, which subsequently relax to the lowest vibrational state by additional collisions. With respect to the saturation it should be noted that the size of the Mack cone is a function of the square root of the ratio of the stagnation pressure behind the nozzle to the pressure of the chamber. Because of the emission of visible light from the cone it is possible to observe this change and associate it with the pressure ratio. For the stagnation pressures used in this figure there is no significant change in the chamber pressure to justify the change of slope in the pressure dependence of the intensity. In order to further test this argument we measured the fluorescence at a fixed stagnation pressure of 3.8 bars as a function of the chamber pressure change. The result shows a change of fluorescence of only 10% over the region of chamber pressures corresponding to fig.1. Consequently, the change of slope can

not be attributed to the change of the chamber pressure because of the limited pumping speed and other loss mechanisms are involved.

Fig.3 shows the change of 128 nm band linewidth as a function of the stagnation pressure with a discharge dc current of 20 mA. The linewidth reaches very fast the theoretical value of 7.5 nm which is obtained from calculated energy level diagrams for the ground and the first electronic states. This figure shows that the supersonic expansion is a very effective way to concentrate all the available dimers in the lowest state. Similar small linewidths have been observed in the electron beam pumped experiment but with argon pressures in the cell over 20 bars.

Fig.4 shows a typical spectrum of the argon dimer with a pulsed discharge excitation for a stagnation pressure of 6.6 bar and a charging voltage of 6 KV. The energy storage capacitor and the capacitor across the nozzle had a value of 7.5 nF and 6 nF respectively. The detection system was sampling the total Mach cone and the time gate was chosen with such a delay in order to maximize the 128.0 nm signal. It can be seen that again a narrow spectrum, corresponding to the  $v = 0$  vibrational state of the excited electronic state is obtained although the initial temperature of the plasma is much higher in the case of the pulsed system. Further experiments are planned in order to establish the influence of the different parameters on the fluorescence in the pulsed mode of operation and compare its efficiency with the continuous discharge operating system.

#### 4. CONCLUSIONS

In this short report we presented some results related to the supersonic cooling of a discharge plasma. It has been shown that strong cooling takes place even at moderate pressures of a few bars and that the fluorescence intensity exhibit a dramatic increase at the same time. Although accurate gain and absolute fluorescence intensity measurements are important in order to evaluate the potential of the method for laser operation, these first results are nevertheless very encouraging.

## 5. ACKNOWLEDGMENTS

This work was done at the University of Toronto in collaboration with professor B.P. Stoicheff.

## REFERENCES

1. G.S. Hurst, T.E. Bortner and T.D. Strickler, "Proton excitation of the argon atom", Phys. Rev., Vol 178, pp. 4-10, 1969.
2. H.A. Koehler, L.J. Ferderber, D.L. Redhead, and P.J. Ebert, "Vacuum-ultraviolet emission from high-pressure xenon and argon excited by high-current relativistic electron beams", Phys. Rev.A, Vol.9, pp.768-781, 1974.
3. G. Klein and M.J. Carvalho, "Luminescence of high pressure argon excited by pulsed electric discharges", Physica, Vol.101C, pp.139-144, 1980.
4. A. Ulrich, H.J. Korner, W. Krotz, G. Ribitzki, D.E. Murnick, E. Matthias, P. Kienle, and D.H.H. Hoffman, "Heavy-ion excitation of rare-gas excimers", J. Appl. Phys., Vol.62, pp.357-361, 1987.
5. W.M. Hughes, J. Shannon, and R. Hunter, "Efficient high-energy-density molecular xenon laser" Appl. Phys. Lett., Vol.25, pp.85-87, 1974.
6. W.-G. Wrobel, H. Rohr, K-H. Steuer, "Tunable vacuum ultraviolet laser action by argon excimers",
7. W. Sasaki, Y. Uehara, K. Kurosawa, E. Fujiwara, Y. Kato, Ch. Yamanaka, M. Yamanaka, and J. Fujita, "Generation of tunable intense coherent radiation around 126 nm with argon excimer laser", Short wavelength coherent radiation generation and applications, D.T. Attwood and J. Bokor, editors, AIP conference proceedings, Vol. 147, pp.391-400, 1986.
8. D.J. Eckstrom, H.H. Nakano, D.C. Lorents, T. Rothem, J.A. Betts, M.E. Lainhart, K.J. Triebes and D.A. Dakin, "Characteristics of electron-beam-excited  $\text{Kr}_2^*$  at low pressures as a vacuum ultraviolet source", J. Appl. Phys., Vol 64, pp.1691-1695, 1988.
9. C. Dzyz and J. Boness, "A Study of VUV fluorescence and lasing in electron beam excited xenon", IEEE J. Quant. Electron., Vol. QE-16, pp.640-649, 1980.

10. P.P. Herman, P.E. LaRocque, and B.P. Stoicheff, "Vacuum Ultraviolet laser spectroscopy. V. Rovibronic spectra of  $\text{Ar}_2$  and constants of the ground and excited states" J. Chem. Phys., Vol.89, pp.4535 - 4549, 1987.
11. A.T. Droege and P.C. Engelking, "Supersonic expansion cooling of electronically excited OH radicals", Chem. Phys. Lett., Vol. 96, pp.316-318, 1983.
12. E.T. Verkhovtseva, Ya. M. Fogel, and V.S. Osyka, "On the continuous spectra of inert gases in the vacuum-ultraviolet region obtained by means of a gas-jet-source", Optics and Spectroscopy, Vol. 25, pp.238-240, 1968.
13. K.G.H. Baldwin, R. Paul Swift, and R.O. Watts, "Inert gas excimer radiation from a free jet expansion", Rev. Sci. Instrum., Vol. 58, pp.812-816, 1987.
14. T. Efthimiopoulos, B.P. Stoicheff, and R.I. Thompson, "Efficient population inversion in excimer states by supersonic expansion of discharge plasmas", Optics Lett., Vol.14, pp.624-626, 1989.
15. M. Diegelmann, W.G. Wrobel, and K. Hohla, "Time-resolved spectroscopy of the  $\text{Ar}_2^*$  - excimer emission", Appl. Phys. Lett., Vol.33, pp.525-527, 1978.
16. T.D. Bonifield, F.H.K. Rambow, G.K. Walters, M.V. Mcusker, D.C. Lorents and R.A. Gutcheck, "Time resolved spectroscopy of xenon dimers excited by synchrotron radiation", J. Chem. Phys., Vol.72, pp.2914-2924, 1980.

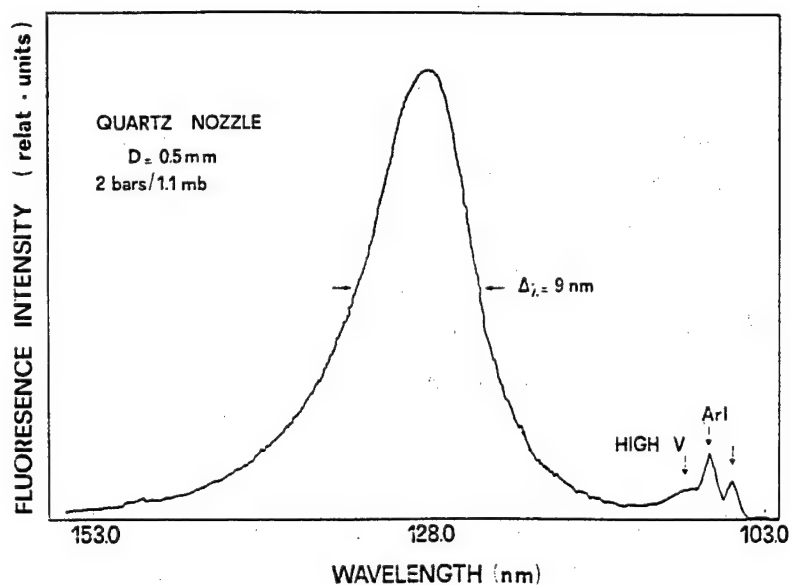


Fig.1 The argon dimer spectrum

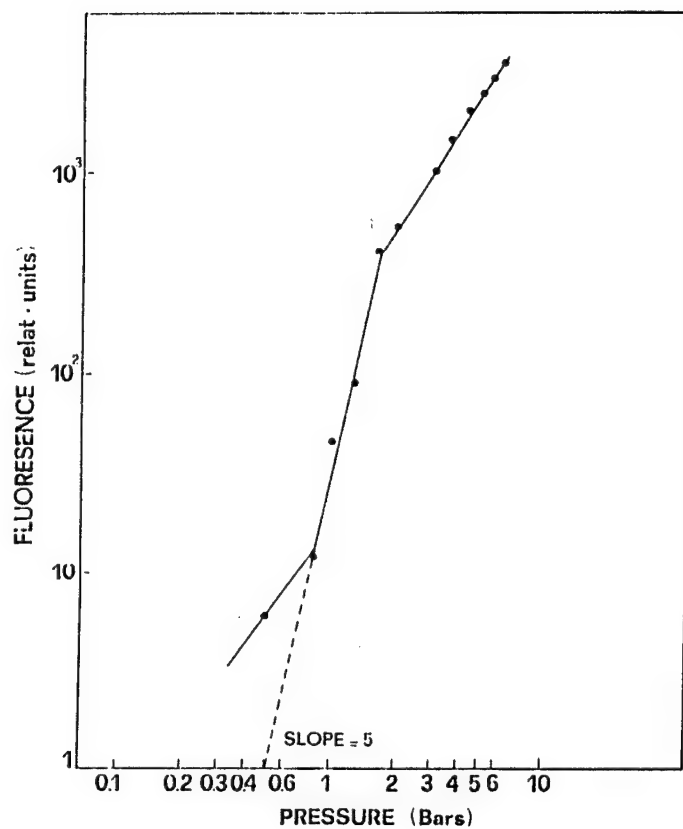


Fig.2 The peak intensity as a function of the pressure

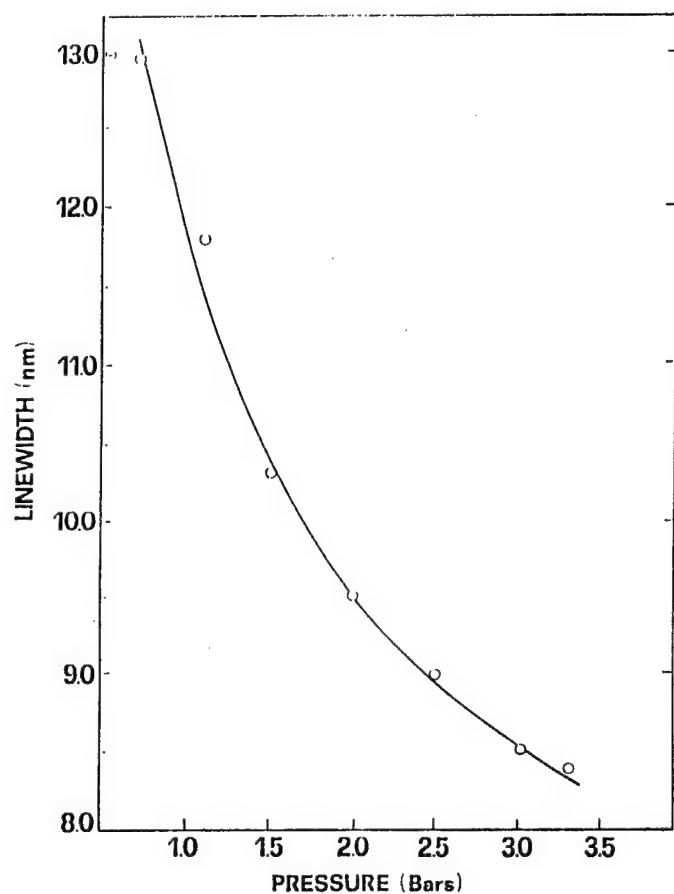


Fig.3 The linewidth as a function of pressure

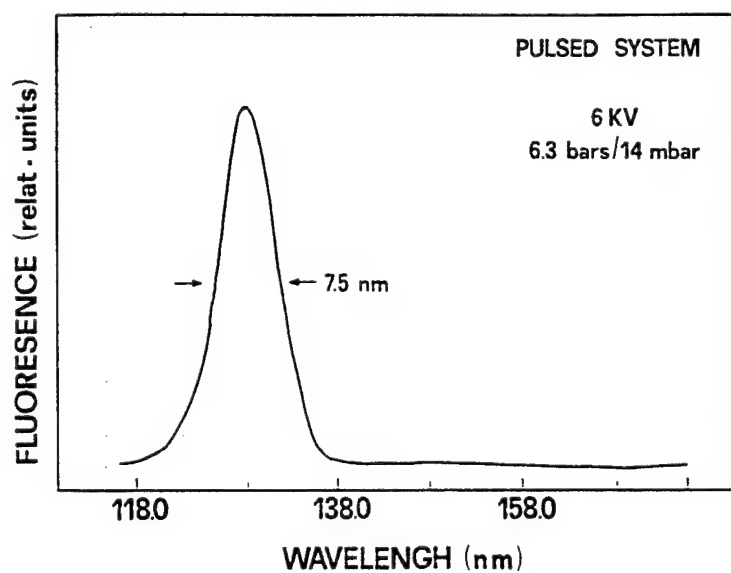


Fig.4 The argon dimer spectrum for the pulsed system.



## Excimer Laser Processing of Diamond-Like Films

36980005 The Hague EXCIMER LASERS AND THEIR APPLICATIONS in English 1991 pp 453-462

[Article by V.P. Ageev, T.N. Glushko, and A.V. Kuzmichev of the General Physics Institute, and V.F. Dorfman and B.N. Pypkin of the Institute of Electronic Controlling Devices]

[Text]

### ABSTRACT

Basic regimes of the **KrF**-laser assisted patterning of **a-C:H** and of **W**-alloyed **a-C/Si/O:H** diamond-like films (**DLF**) of dielectrical and metal-like varieties are studied. Laser induced processes of the film graphitization and ablation under the multi-pulsed irradiation are considered. The sub-micron resolution of the film structurization is shown to be possible by using the ablative projection **UV** laser lithography.

### 1. INTRODUCTION

It was shown recently [1,2] that hydrogenated amorphous carbon-based diamond-like films (**DLF**) may combine such material properties as high thermal and electrical conductivities, mechanical and chemical resistivities, and some others, which creates wide perspectives for their applications in many fields of science and technology. In this connexion a question on methods of a local **DLF** modification becomes of an importance, since they may provide the further extension for the coatings employment e.g. in micro- and opto electronics, integrated optics e.t.c.

The present time a laser technique is known to be the promising one [3-7] for the diamond and diamond-like film surface processing, with excimer lasers being considered to be the most preferable, because of a strong laser-to-film coupling typical of the **UV** spectral range. We discuss here general features of an interaction of **KrF** laser pulses with carbon-based films of few types. The main attention is paid to new diamond-like materials, namely, to stabilized (**a-C/Si/O:H**) and to **W**-alloyed **DLF** of the dielectrical and the electrical conducting varieties. The **a-C:H** films are also considered for a comparison.

The following two basic regimes of the film structurization are under consideration: (i) the laser induced graphitization, and (ii) the laser ablation.

The first one is intrinsically associated with such fundamental material characteristic as the amorphous state stability. This is all the more important that metastable carbon allotropes are known to be readily transformed (e.g. by heating) to the graphite state. It is clear that this material property to be convertible from the dielectrical to electrical conducting state over the laser controlled areas [6,7] may be of great perspectives for electronic applications.

The second regime is the most universal one for all kinds of solid materials. The special attention is paid here to the correlation between the film structure and the ablation kinetics as well as to peculiarities of the process resulting from a multi-pulsed mode of the film laser irradiation.

## 2. EXPERIMENTAL

The **a-C/Si/O:H** films (**C:Si:O=3:1:1**) of thicknesses 100-500nm were synthesized on silicon, quartz and siall plates by using a chemical plasma deposition technique. A glow discharge plasma were excited in poly-phenyl-methyl-siloxane vapors in a triode scheme with a **RF** potential being applied to substrates. The same reactor enables us also to deposit **a-C:H** films by using an acetylene plasma.

The **a-C/Si/O:H** coatings were characterized by high dielectrical breakdown strengths ( $\approx 300\text{V}/\mu\text{m}$ ), and by an improved elasticity, which provides their much better functionality as compared to **a-C:H** films. The **a-C/Si/O:H** coatings were transparent for a visible radiation, but appeared to be strongly absorbing in the **UV** (see Fig.1). The latter apriory provides a high efficiency of a **DLP** excimer laser processing.

A metal doping of these films made it possible to change their electrical resistivities from dielectrical to metal-like ones (till  $10^{-3}\Omega\text{cm}$ ). The doping was achieved by an evaporation of an auxiliary **W**-plate into the reactor volume during the film deposition.

In experiments a **KrF** excimer laser was used generating 20-ns pulses of the 248-nm radiation with pulse repetition rates up to 100Hz. Films of all types were irradiated directly in the air. A special optical scheme was applied to provide the uniform surface illumination over  $1\times 2\text{mm}$  areas at fluences up to  $1\text{J}/\text{cm}^2$ . In tests on a **DLP** microstructurization an optical projection of a chromium-on-quartz photo mask onto film surfaces was employed by using a quartz micro-objective.

An ablation kinetics was studied by controlling a grove depth in films have been exposed to an appropriate number of laser shots. A profylometer of the model 242 was used which enabled us to measure a current film thickness at an accuracy not less than 20nm. Structural transformation in films were studied by using Raman- and Auger spectroscopies. Excimer laser induced variations of **DLP** optical properties were controlled in-situ by using a **He-Ne** laser ( $\lambda=683\text{nm}$ ).

### 3. RESULTS AND DISCUSSION

#### 3.1. Furnace-annealing and pulsed laser-induced graphitization

Special furnace annealing tests were performed, first of all, in order to evaluate a temperature stability of  $\alpha\text{-C/Si/O:H}$  films. Experiments have shown a significant structural transformation in films only at temperatures above  $T_g \approx 700^\circ\text{C}$  and for a heating time not shorter than few minutes. The fact was proved by using some Raman spectroscopy data (Fig.2) interpreted here according to the paper [8].

One can see from Fig.2 that Raman spectra of  $\alpha\text{-C/Si/O:H}$  films are initially characterized by a wide so-called G-peak at a frequency of  $1500\text{cm}^{-1}$  typical of amorphous carbon allotropes. A thermal induced graphitization is accompanied by G-peak shifts toward a crystalline graphite line ( $1580\text{cm}^{-1}$ ). Besides, another D-peak becomes resolved at a frequency of  $1350\text{cm}^{-1}$  (spectrum 2 in Fig.2). Films become also more opaque when graphitization starts (curve 3 in Fig.1).

It is important to underline that a long-time film heating in the air does not result in a graphite phase accumulation, since a chemical etching of the graphite by oxygen becomes also thermal activated. As a result, the film transforms into a thin SiO<sub>2</sub> - layer (instead of to be graphitized), which gives rise, in particular, to a significant film transmittance increasing in the VIS/UV (curve 4 in Fig.1). Thus, the situation appears to be very close to that one of a thermal induced decomposition of organometallic compound films ([9,10]).

The higher graphitization degree can be achieved by using a vacuum annealing, or a pulsed laser heating of films. So, according to Auger-analysis, a fine structure of the carbon KLL-line begins to correspond to the crystalline graphite structure after the vacuum annealing at temperatures  $T=800^\circ\text{C}$  during 5 minutes. As to laser experiments, it is easy to heat films above the graphitization threshold ( $T_g$ ) and, hence, to ignite the more rapid graphitization reaction. At the same time the chemical effect may remain to be insignificant because of a short thermal pulse duration. The Raman spectroscopy confirms this to be the case. It follows from a comparison of spectra 1 and 2 in Fig.2, that an intensive irradiation (pulsed fluence  $E=120\text{mJ/cm}^2$ ) results in the more dramatic film reconstruction, than it was in furnace annealing experiments. One can see the significant narrowing of the G-peak and its final fixation on the crystalline graphite line position.

A thermal nature of the laser induced graphitization has also those consequence that a graphitization time (a number of shots,  $N$ ) appears to be strongly dependent on a laser intensity. The main feature of this dependency is an infringement of a laser dose ( $D=EN$ ) additivity law typical of linear photolytic processes. For an example, when the

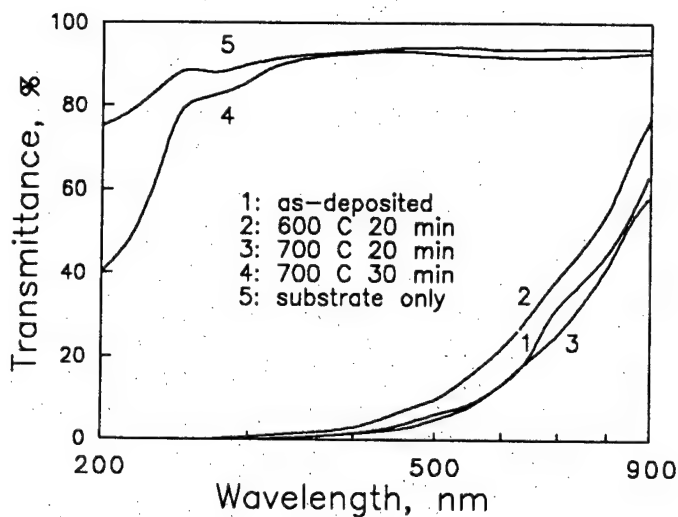


Fig.1. Transmittance spectra of 250-nm thickness **a-C/Si/O:H** films on quartz substrate before (1) and after (2-4) furnace air annealing.

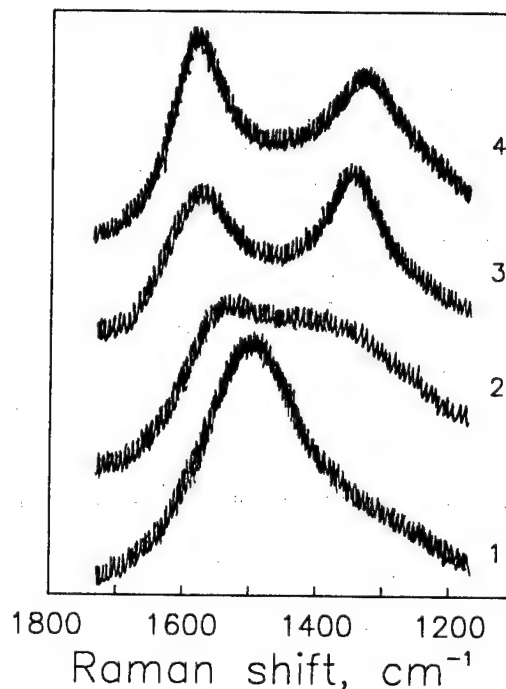


Fig.2. Raman spectra of 200-nm **a-C/Si/O:H** (1-3) and 450-nm **a-C:H** (4) films: 1-4-as deposited films; 2-after furnace annealing (700C, 20min.); 3-after  $N=8_2$  laser shots at fluence  $E=120\text{mJ/cm}^2$ .

laser fluence is decreasing e.g. from  $E=120\text{mJ/cm}^2$  till  $E=60\text{mJ/cm}^2$  the same graphitization level is achieved only after  $N \approx 10^3$  (instead of few) pulses, but the exposure dose required to produce the necessary transformation in films is increasing by orders of magnitude.

Contrary to **a-C/Si/O:H** films, the structure of as deposited **a-C:H** coating proved to be determined by their thickness. The amorphization degree of these films is high until their thicknesses are smaller than some critical value of  $H \approx 250\text{-}300\text{nm}$ . The upper layers out of this limit appeared to be partially graphitized exhibiting a graphite-like rather than a diamond-like behavior. Raman spectra taken from thick **a-C:H** films (spectrum 4 in Fig.2) become analogous to that ones of a poly-crystalline graphite [8] with average grain sizes of the order of 4 nm. Therefore, a question on the state stability with respect to the graphitization becomes conditional to a great extent for thick **a-C:H** coatings. Nevertheless, the laser irradiation would still result in some additional material modification, e.g. in a graphite crystallite size increasing and, thereby, in variations of electrical, chemical, optical and other material properties.

### 3.2. Laser ablation kinetics

There are two main mechanisms of a laser induced material removal from **DLF**: a chemical etching of graphitized surfaces by oxygen, and a laser evaporation (ablation). A main attention is paid here to the ablative etching, as to the most efficient way of a film structuring. As to the chemical etching, it will be discussed separately in some of our next works. Here we restrict the consideration only by few remarks on chemical etching peculiarities determined by film material properties.

The most important of them is an influence of a self-passivation on the etching, which is natural to expect for stabilized and metal alloyed films. The deal is that the etching, being started, would result inevitably in a surface layer enrichment by silicon- or metal oxides and, hence, in a subsequent blocking the etching. Even though the passivation effect is absent (e.g. for **a-C:H** films) the chemical process appears to be of low efficiency with typical etch rates being as high as few Angstrom per pulse. Both these facts make the chemical effect of a little practical meaning for the film structuring.

According to our measurements the ablation becomes to dominate upon the chemical process (etch rates become higher than  $V \approx 1 \text{ \AA}$  per pulse) starting from fluences  $E_a \approx 100 \text{ mJ/cm}^2$ . The  $E_a$ -values depend on **DLF** thicknesses and substrate types. For an example, the ablation regime threshold is as high as  $E_a \approx 80$  and  $90 \text{ mJ/cm}^2$  for 150-nm **a-C:H** films on quartz and silicon substrates, resp. For thicker films the threshold increases e.g. up to the value of  $E_a \approx 150 \text{ mJ/cm}^2$  for the 450-nm films on silicon substrates.

Experiments have shown the ablation kinetics depends on film's and substrate's types (primarily on their thermophysical properties) as well as on current coating thicknesses. Some examples of ablation curves for **a-C/Si/O:H** films taken in a form of dependencies of current film thicknesses on a number of laser shots are presented in Fig.3.

One can see that the ablation proceeds inhomogeneously during the multi-pulsed exposure. Etch rates are increasing initially and then become stabilized at some fluence controlled values,  $V(E)$ , shown in Fig.4. As an ablation front approaches to film-substrate interfaces, the other tendency is observed characterized by an etching rate drop, which is obviously determined by an increasing of heat losses into the substrate. Let us note that the ablation degeneracy is expressed most of all when the well heat conducting silicon substrate is used.

It should be noted that ablation curves of thick **a-C:H** films have not exhibited any qualitatively new features which might be expected from their bi-layer (graphite-like/diamond-like) structure. Only some differences in  $V(E)$ -plot details have been observed (see Fig.4).

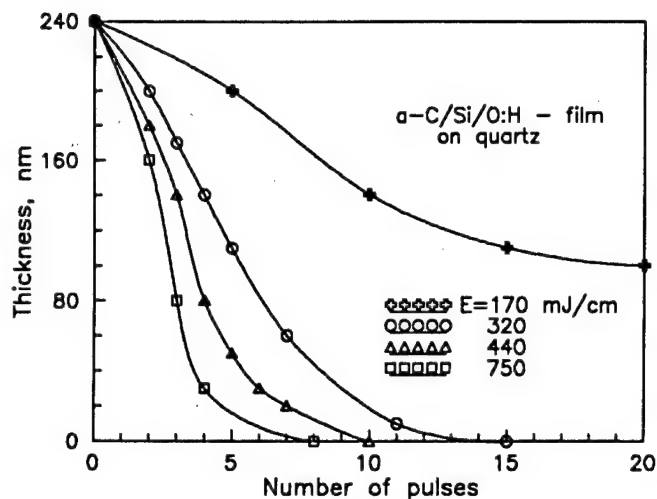


Fig.3 Ablation curves of  $a-C/Si/O:H$  films for different KrF laser fluences.

Experiments have revealed also a strong correlation between  $V(E)$ -values and film and substrate types. As it is seen from Fig.4, the ablation rates of  $a-C:H$  film are significantly lower when the silicon substrate is used. It is also characteristic for the process that the etch rate is increasing as film thicknesses rise. This is also naturally to wait since a role of heat losses to the substrate becomes less important.

Contrary to the above situation, ablation rates of  $a-C/Si/O:H$  films are practically independent on the substrate type at least for coating thicknesses  $H \geq 200\text{nm}$ , which is the direct evidence on the rather poor material heat conductance. An upper limit of a thermal diffusivity can be evaluated as  $\chi \leq H/4\tau \approx 5 \cdot 10^{-5} \text{ cm}^2/\text{sec}$  (here  $\tau = 20\text{ns}$  is the laser pulse duration). This value appears to be by more than one order of magnitude less than thermal diffusivities typical of  $a-C:H$  films.

The film doping by metal give rises in variations of electrical and thermophysical material properties. Therefore it is natural to wait an existence of the strong influence of the metal concentration on the ablation kinetics. Fig.4 shows that this is really the case. One can see that the lower the electrical sheet resistance (the higher the metal concentration), the lower the ablation rate under the same irradiation condition until the sheet resistance is higher than  $\rho \approx 100 \Omega/\square$ . Then the ablation rate becomes only slightly dependent on the metal concentration.

Experiments have shown that the "DLF-substrate" system type affects also on a fluence dependent behavior of ablation rates. So, under a sufficiently intensive irradiation the ablation of many films can be

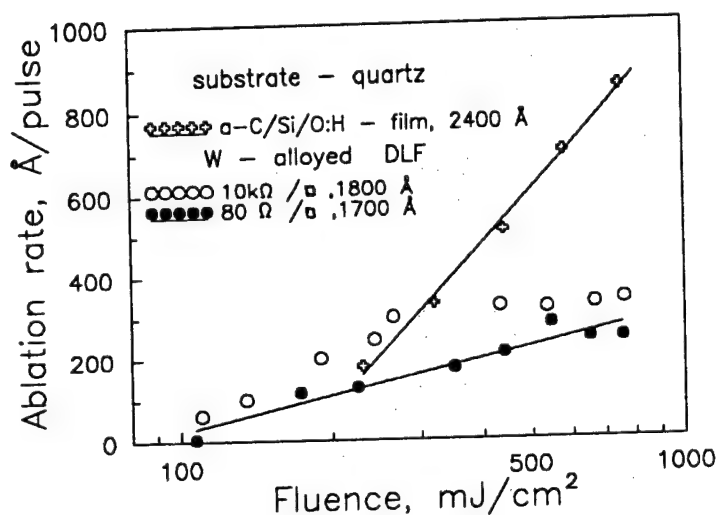
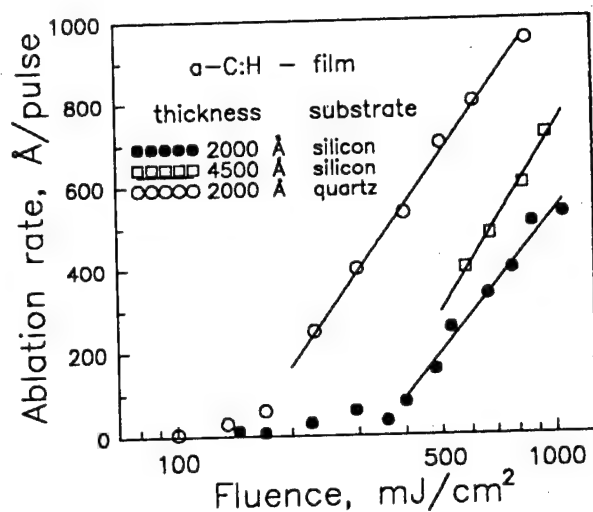
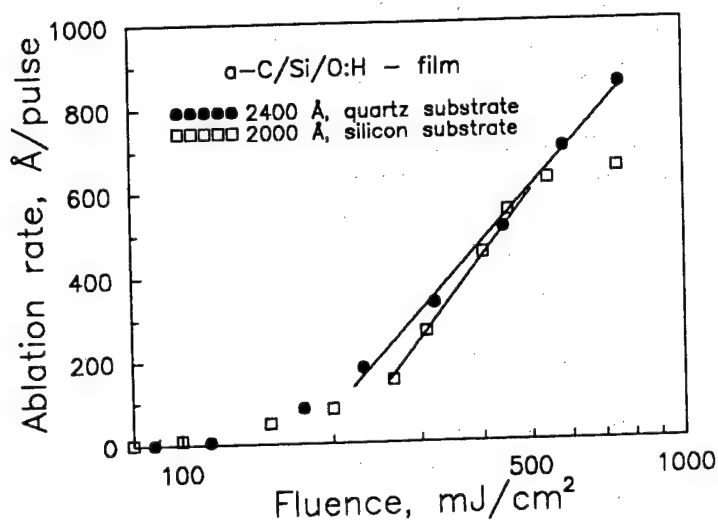


Fig.4 Ablation rates vs the KrF laser fluence for different diamond-like films.

described by a logarithmic  $V$ -vs- $E$  scaling law:  $V \ln(E/E^*)$  with  $E^*$ -values being determined by the "film-substrate" system type. This  $V(E)$  dependency type is valid best of all for a-C:H -, and heavy W-alloyed ( $\rho \leq 100 \Omega/\square$ ) films, as well as for a-C/Si/O:H coatings on silicon substrates. The linear  $V(E)$  approximation may be also good for the a-C/Si/O:H film ablation, when the quartz substrate is used, which is probably associated with some influence of the substrate type on film structures.

The ablation of W-alloyed films characterized by intermediate sheet resistances ( $10^{-10^4} \Omega/\square$ ) exhibits the more complicated behavior. It is typical of these films an initial linear increasing of ablation rates at low fluences and a subsequent saturation of  $V(E)$ -curves. Let us note that the analogous effect (more or less expressed) is also observed for all other films.

One should underline the principle difference between the above DLF ablation peculiarity and that of the ablation of other solid carbon allotropes (e.g. of diamond and graphite crystals). It is known that the diamond film laser ablation [3,5] proceeds in the linear way. Let us note also that both the logarithmic and the linear  $V$ -vs- $E$  scaling



laws are typical of experiments on the pulsed UV laser processing of organometallic compound [10] and polymer [11] films.

The mechanisms of this bi-modal ablation behavior is under the extensive discussion (e.g. [11]), but still is not well understood now. In our opinion the so-called explosion approach may be fruitful here, which consider the ablation to start provided the energy deposition density would reach some critical level of  $Q^*$ . Besides, and this is of a principle role, the ablation event is admitted to be delayed from the laser action. It possible to show that under the above assumptions the  $V(E)$  scaling law would be determined greatly by the relation between the laser pulse duration,  $\tau$ , and the delay time,  $t_d$ , of a solid-to-vapor transition. In order to prove this, it is enough to compare cases of the instantaneous ( $t_d \ll \tau$ ) and the delayed ( $t_d \geq \tau$ ) material removal via the ablation.

According to our measurements the UV photon penetration depth into the film,  $k$ , appears to be comparable to thicknesses of 10-100nm typical of the a single pulse removed layers (absorption coefficient values are as high as  $k_0 = 2.0-3.5 \cdot 10^8 \text{ cm}^{-1}$  for both a-C/Si/O:H and a-C:H films in a low intensity limit). Thus, the energy deposition rate is described in general case by a moving Bee's profile:  $dQ(z,t) = (1-R) \cdot k \cdot q(t) \cdot \exp(-k \cdot (z-s(t))) dt$ , (here  $R$  is a light reflectance,  $q(t)$  is the laser intensity time-history,  $s(t)$  is the current ablation front position along the laser beam ( $Z$ -axis)).

In the case of a simultaneous solid-to-vapor decay the ablation would proceed obviously in the manner of a layer by layer surface evaporation, with the ablation front position being described by the boundary condition  $Q(s(t)) = Q^*$ . Then, as it has been shown in [11] by an integration of the energy rate equation, the ablation rate behavior is described by the rather transparent relation:

$$V = (1-R) E/Q^* \quad (1),$$

which is also typical of all cases of the surface light absorption mode.

The qualitatively different situation occurs when the inertia time appears to be comparable to the laser pulse duration. Then the laser film pumping is determined by the standing (not moving) Bee's profile:  $Q(z) = (1-R) \cdot k \cdot E \cdot \exp(-k \cdot z)$ . Under these conditions the ablation should have a character of the simultaneous explosion of whole layers of thicknesses  $z^*$  derived from the stationary condition  $Q(z^*) = Q^*$ , which give rises to the other well-known expression for the ablation rate:

$$V = z^* = k^{-1} \ln\{(1-R)kE/Q^*\} \quad (2),$$

i.e. the logarithmic ablation mode is realized.

The question on factors might be responsible for the ablation delay arises immediately here. First of all, the inertia of a material rarefaction from a condensed to a vapor state should be considered. As regarding to ablation experiments, it really may be of an importance, since the strong shielding of the laser pumping of deeper film layers remains to be significant until a decaying material density would be reduced at least by an order of magnitude as compared to the film one. By using values of  $u \approx 10^3 \text{ cm/sec}$  for the typical vapor expansion velo-



city one obtains for the effective delay time:  $t_d \approx 10V/u \approx 0.1$  ns for ablation rate values of  $V \approx 10$  nm per pulse. As seen, the above factor may become of the principle role only for sub-nanosecond laser pulses, but not in our experiments. Thus, other ablation delay mechanisms must be taken into account.

As a reasonable hypothesis we would support the same assumption as it has been carried out previously [12] for an interpretation of some features of the excimer laser induced ablation of amorphous selenium films. This hypothesis takes into consideration the probable explosive decay of localized excited electronic states originating in some amorphous structures under irradiation. Of course, this analogy may appear to be not correct. In any case the further analysis is required, in particular, the additional characterization of the process.

Some results of the logarithmic ablation mode characterization are summarized in Table. Data on absorption coefficients,  $k$ , were derived here by using relation (2) from slopes of  $V(\ln(E))$ -curves (Fig.4). In the brackets there are presented absorption coefficient values,  $k_0$ , determined in the spectrometric measurement. The  $E^*$ -values (i.e. regime effective thresholds) correspond to intersections of logarithmic  $V(E)$ -extrapolations to zero ablation velocities. The effective ablation heat,  $Q^*$ , was calculated by using the relation:  $Q^* = E^*k(1-R)$ , where  $R = 0.17$  and  $0.08$  resp. for **a-C/Si/O:H** and **a-C:H** films. We believe that  $Q^*$ -values presented correspond to real phase transition latent heats only for **a-C/Si/O:H** films and (to a less extend) for thin **a-C:H** films on quartz substrates. In all other cases (e.g. of **a-C:H** coatings on silicon substrates) these values are admitted to contain a significant additional part determined by an energy dissipation into film and substrate bulks.

**TABLE: Parameters of logarithmic ablation mode**

**a-C:H films:**

	quartz substrate	silicon substrate	
thickness, nm	200	450	200
$E^*$ , mJ/cm <sup>2</sup>	155	290	340
$k$ , 10 <sup>5</sup> cm <sup>-1</sup>	1.8 (3.5 )	1.7	2.0
$Q^*$ , kJ/cm <sup>3</sup>	23	41	57

**a-C/Si/O:H films:**

thickness, nm	240	200
$E^*$ , mJ/cm <sup>2</sup>	170	210
$k$ , 10 <sup>5</sup> cm <sup>-1</sup>	1.8 (2.5-3.0)	1.6
$Q^*$ , kJ/cm <sup>3</sup>	25	27

The Table exhibits at least two basic results which may become of the principle importance for the further investigation. First of all, one should pay attention to the fact that all dynamic absorption coefficient values are noticeably lower (by a factor 1.5-2) as compared to corresponding spectroscopic ones (measured in low light intensity limits). It seems all the more surprising that the DLF graphitization is usually expected to be the primary laser induced effect (also in ablation experiments), which is to result, in any case, in the significant absorption coefficient increase. The latter was really observed e.g. in our previous studies on the excimer laser processing of diamond films [5].

Secondly, the typical ablation heat value,  $Q^*$ , appears to be approximately by one order of magnitude lower than the graphite vaporization latent heat ( $\approx 270$  kJ/cm<sup>2</sup>). Both of these facts enable us to make the following conclusion: the intensive laser ablation of diamond-like materials proceeds not through the intermediate stage of the graphitization, but directly from amorphous states. As to the dynamic decrease in absorption coefficients, this fact may serve, in our opinion, as an indirect evidence on the amorphous material excitation under the intensive laser irradiation.

To finish this work let us report some preliminary results on a micro-structure formation under the laser irradiation. Along with the rather transparent technological aim, these tests are also of some scientific interest. For example, a direct comparison of irradiated spot dimensions with those ones of modified film areas may give us an additional information on film properties, in particular, on probable laser induced explosive phenomena.

Experiments performed at the  $1\mu$ -optical resolution have revealed the following. The multi-pulsed ablative lithography in a-C:H films have resulted in an appearance of 2-3  $\mu$  graphitization halo, which should be ascribed, on one hand, to the explosive graphitization

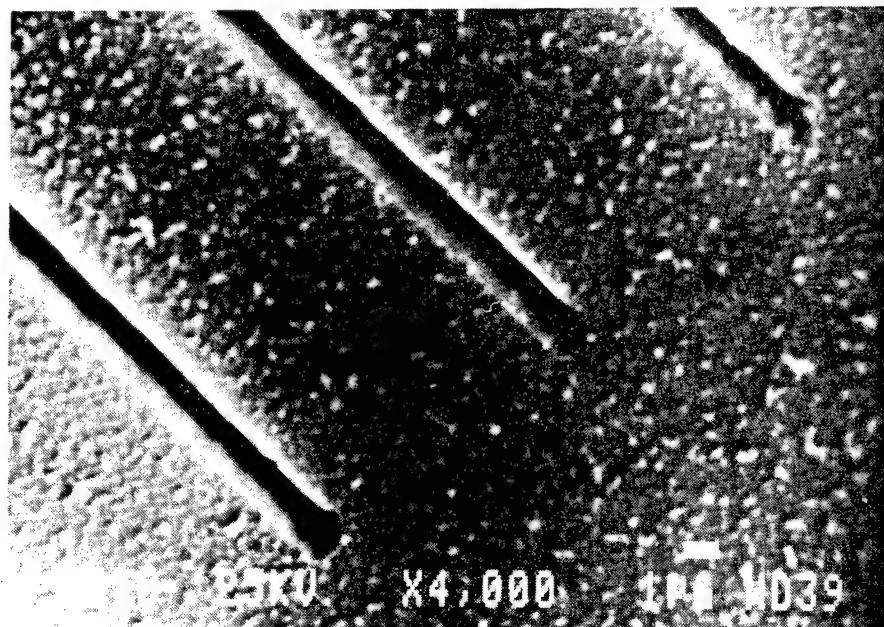


Fig.5 SEM of patterns obtained by UV laser ablative lithography in 450-nm a-C/Si/O:H film on silicon substrate.

effect (analogously to the well-known a-Si explosive crystallization). At the same time this supposition is the greatly beforehand one, since the same fact may be interpreted, on the other hand, as a result of a trivial temperature profile spreading because of the high thermal conductivity of the film material.

Contrary to the above situation, the laser processing of a-C/Si/O:H films stabilized with respect to the graphitization appears to be practically free from any significant halo effect. An electron micrograph of patterns produced in these films in the same regime of the ablative lithography is presented in Fig.5. It seen, the structure is characterized by 1.2 $\mu$ -width strips, but halo dimensions are less than 0.3 $\mu$ . These results enable to affirm that the sub-micron resolution can be surely achieved in the laser structurization of these films. The additional test have shown this to be really the case at least in regimes of the laser induced film graphitization.

#### 4. ACKNOWLEDGMENTS

The authors thank to N.Krindach for the Raman spectra recording, and to prof.V.Konov for stimulant discussions.

#### 5. REFERENCES

- (1) V.F.Dorfman "The solid-state structures synthesis" Moscow, Metallurgy, 1986- in Russian
- (2) Hsiao-chu Tsai, and D.B.Body, J. Vac. Si. Technic., v.A5, 3287 (1987).
- (3) M.Rotshild, C.Arnone, and D.J.Ehrlich, J.Vac.Sci.Technol. v.4, 814 (1986).
- (4) M.Rotshild, and D.J.Ehrlich, ibid., v.B5, 389 (1987).
- (5) V.P.Ageev, A.L.Builov, N.I.Chapliev, V.I.Konov, A.V.Kuzmichev, S.M.Pimenov, A.M.Prokhorov, V.G.Ral'chenko, and B.V.Spitzyn. Sov. Phys. Dokl., v.303, 840 (1988)
- (6) S.Prawer, R.Kalish, and M.Adel. Appl.Phys.Lett.,v.48,1585 (1986).
- (7) V.Yu.Armeyev, N.I.Chapliev, V.I.Konov, V.G.Ral'chenko, V.E.Strel'nitzky, and Yu.Ya.Volkov, in "Laser Surface Microprocessing, V.I.Konov, B.S.Luk'yanchuk, I,W,Boyd, Editors, Proc.SPIE,v.1352, 200 (1990).
- (8) R.O.Dillon, J.A.Woolam, and V.Katkanant. Phys.Rev., v.B.29, 3482, (1984)
- (9) Ageev V.P, V.I.Konov, A.I.Maslakov, V.M.Mel'nikov, and L.V.Velikov in "Energy Pulse and Particle Beam Modification of Materials", K.Henning Editor, Physical Research, v.8, 116 (1988)
- (10) Ageev V.P, D.Q.Chung, V.I.Konov, A.V.Kuzmichev, A.I.Maslakov, L.V.Velikov, and D.Yu.Zaroslav in "Laser Surface Microprocessing, V.I.Konov, B.S.Luk'yanchuk, I,W,Boyd, Editors, Proc.SPIE, v.1352, 48 (1990).
- (11) G.D.Mahan, H.S.Cole, Y.S.Liu, and H.R.Philipp ,Appl. Phys. Lett. v.53, 2377 (1988).
- (12) A.Jadin, M.Wautelet, and L.D.Laude, Semicond. Sci. Technol., v.3, 499 (1988)

## Excimer-Dye Laser System for Diagnosis and Therapy of Cancer

36980005 The Hague EXCIMER LASERS AND THEIR APPLICATIONS in English 1991 pp 467-478

[Article by Ludwik Pokora and Zbigniew Puzewicz of the Institute of Quantum Electronics]

[Text]

### ABSTRACT

The paper presents the construction and basic characteristics of excimer-dye laser system specially projected for diagnosis and therapy of cancer using HpD method. Our laser generate of 405 nm or 630 nm lines respectively. The basic characteristics of that laser system we present.

### 1. INTRODUCTION

Examples of laser diagnosis and therapy of cancer by the HpD method were described by the authors of papers.<sup>1-4</sup> It is worth to notice, that a pulse laser system have a considerable advantage<sup>2</sup> over the set of continuous operation laser e.g. argon-dye system.<sup>3,4</sup> The very efficient pulse laser source for excitation of organic dyes is a excimer laser.<sup>5,6</sup> The efficiency of pumping laser dyes by UV radiation ( $\lambda=248\text{nm}$  or  $\lambda=308\text{nm}$ ) of excimer laser are almost 2 times higher in comparison with pumping by harmonics ( $2\omega_0, 3\omega_0$ ) of the YAG:Nd laser light.<sup>7</sup> In spite of the shown advantages of excimer lasers and efficiency of generation by organic dyes pumped by excimer lasers such system are relatively new and little prevalent. Moreover, rough requirements for all medical devices both in relation to safety of work and to reliability, parameters stability and exploitation simplicity make these lasers interesting as far as their technology and structure are concerned. Below, we will present some results of our laser

system project and of our fiber optic system of guiding of laser radiation into the operated object.

## 2. CONSTRUCTION OF EXCIMER-DYE LASER SYSTEM AND FIBER OPTIC DELIVERY SYSTEM

In the HpD method<sup>1</sup> is necessary to use apparatus with special parameters. The laser should protect generation of two wavelengths: diagnostic and therapeutic. In the case of applying the porphyrin compounds (photosensitizer in the HpD method), for the diagnosis purpose blue radiation ( $\lambda=405$  nm) is required, whereas for the therapy red line ( $\lambda=630$  nm) is suitable. For the detection and analysis of the treatment area of the tissue an additional enlighting by UV radiation from Xenon lamp<sup>2</sup> is often applied. The value of the laser radiation energy and the frequency of pulses repetition must be a compromise between radiation dose<sup>1</sup> required for the effective treatment ( $\sim 200$  J/cm<sup>2</sup>) and the energy density which can be transmitted through an optical fiber with definite diameter.<sup>8</sup> For the short nanosecond laser pulses with its high intensity, energy to 50 J/cm<sup>2</sup> can be typically<sup>8</sup> transmitted through a quartz optical fiber.

From the above requirements, given shortly of necessity there have appeared necessary elements for our EXCIMER-DYE laser system for application in the HpD method. However we based in our works directly on the publications, e.g.<sup>2</sup>, of Prof. Y. Hayata team.

The construction of our diagnostic-therapy system is shown in Fig. 1. The scheme of the structure of two-wave (405nm and 630nm) dye laser is shown in Fig. 2. This laser is pumped by the XeCl excimer system. A part ( $\sim 10\%$ ) of the laser radiation is directed by the beam splitter to the lens-optical fiber system illuminating the treatment area. In our opinion such a system simplifies the apparatus construction by eliminating the Xe lamp with a chopper and it makes laser synchronization with detection system easier.

In our construction, the dye laser contains two dye cells, placed alternatively inside a stable resonator. The plane-plane resonator has output mirrors with dielectric coatings with two clear maximums in its transmission characteristics. This characteristics are shown in Fig. 3. Each dye cell contains different dye. We apply dyes of Lambda Physik. One cell is filled with LC 4090 dye (Diphenyl Stilbene) dissolved in dioxane. This dye generated the diagnosis line

( $\lambda_{\text{max}}=405$  nm). The second cell contains a solution of LC 6400 dye (Rhodamine 101) in ethanol. This dye generates the therapeutic line ( $\lambda_{\text{max}}=630$  nm). The solutions of both dyes with volume about 0.5 litre each are contained in cooling reservoirs. From here they are pumped to suitable cells with the aid of small wave pumps. The dye solutions are mixed during the laser operation. Mixing and cooling of the dye solutions assure long-lasting stability of the laser parameters. The change of the dye cell position, which can be top or bottom is made mechanically, and it assures generation of the both waves: 405 nm or 630 nm. The max. efficiency of generation of each line is approximately 10%.

Fig. 4. shows the project of our excimer-dye laser system.

An output of the two dye laser beams is guiding by one optical fiber system. Maximum energy of each beam at the input of optical fiber (0.6 mm in diameter) did not exceed 7 mJ. Above this value of energy a destruction of optical fiber occurs. To increase the value of output energy especially for therapeutic beam ( $\lambda = 630$  nm) there were started some investigations with the laser pulse guided by several (2-3 pieces) fibers. The scheme of our fiber optic guiding systems are shown in Fig. 5. The analogical to Fig. 5a mechano-optical system provide introduction of a part (~10%) of excimer laser radiation in order to illuminate the operation field.

### 3. THE BASIC CHARACTERISTICS OF LASER SYSTEM

Our excimer laser is pumping by transverse electric discharge with UV preionization.<sup>6</sup> That works on a mixture of He:Xe:HCl or He:Xe+Kr:HCl gases. It generates UV radiation ( $\lambda = 308$  nm) with the max. energy of 100 mJ and the pulse (FWHM) width about 20 ns. The pulse repetition rate is regulated from a fraction of Hz to 20Hz laser beam. Energy and pulse duration were measured for different composition and total pressure of an active mixture He:Xe:HCl and for various supply voltage. The range of feeding voltage ( $U_0$ ) was 20-30kV and total pressure ( $p_0$ ) was 800-1500 hPa.

Examples of measuring results of excimer laser are shown in three next Figures (6-8). Fig. 9 shows a comparison of measuring and calculation<sup>9</sup> results of XeCl laser characteristics. In the investigated range of supply voltages (26-30 kV), the output energy was higher in

a mixture with Xe+Kr than in the one with pure Xe. Both our measuring results of laser energy are lower than theoretical one.

Our measurement system contained two energy meters, monochromator and a fast photodiode with oscilloscope. Such a configuration of the measurement system provided a complete diagnostic of the laser radiation pulse. The accuracy of a digital energy meter was about 10%.

This measurement system we have been used to diagnostic of basic parameters of dye laser. Examples of these measurements are shown in Figures 10, 11. Fig. 10 shows dependence of dye laser radiation energy as a function of dyes concentration for two various transmission of output mirrors (DM 1, DM 2). The efficiency of UV laser pumping of DPS and Rhodamine 101 dyes for two different output mirrors are shown in Fig. 11. In all range of investigation we obtained better results for DM2 mirror. These investigations have a preliminary character. However we have been demonstrated a possibility of generated two wavelength light with the same laser system.

#### 4. ACKNOWLEDGEMENTS

This project and research was sponsored by Polish Government Central Research-Developing Program No 11.9 led by Professor M. Nałęcz. Authors thanks Mrs. A. Graczyk - Asst. Professor and other coworkers who help us in construction and investigation excimer-dye laser system.

#### 5. REFERENCES

1. Y. Hayata, T. J. Dougherty, "Lasers and Hematoporphyrin", Publ. by IGAKU-SHOIN Ltd., Tokyo, 1983
2. T. Hirano, M. Ishizuki, K. Suzuki, K. Ishida et al., "Photodynamic Cancer Diagnosis and Treatment System Consisting of Pulse Lasers and an Endoscopic Spectro-Image Analyzer", Laser in the Life Sciences, 3(2), p. 99, 1989
3. D. J. Castro, R. E. Saxton, et al., "Phototherapy with the Argon Laser on Human Melanoma Cells Sensitized with Rhodamine-123: new Method for Tumor Growth Inhibition", Laryngoscope 98, p. 369, 1988
4. J. Coffey et al., "Evaluation of Visual Acuity during Laser Photoradiation Therapy of Cancer", Lasers in Surgery and Medicine 4, p. 65, 1984



5. D.Basting, "Excimer Lasers and Applications", SPIE, 1023, April 1989
6. L.Iwanejko, L.Pokora, "Investigations of Excimer Laser working with a Four Component Gaseous Mixture He-Kr:Xe-HCl", SPIE, 1391, 39, 1991
7. K.L.Hohla, R.Vehrenkamp, "Excimers as Dye Laser Pump Sources - the Future for High-Power, High-Quality Systems", Laser und Optoelektronik, 1, p.31, 1982
8. U.Sovada, H.J.Kahlert, D.Basting, "Excimer Laser Beam Transport through Quartz Fibers-Limitations and Possibilities" Laser und Optoelektronik, 20(4), p.32, 1988
9. Z.Ujda, Phys. Doct. Thesis, Warsaw, 1990

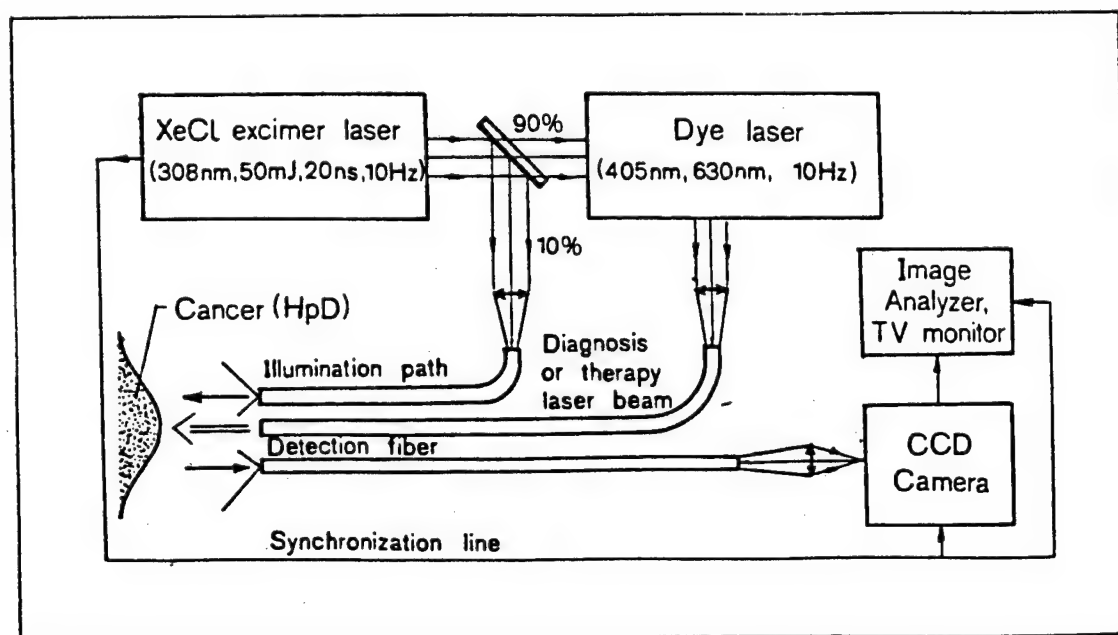


Fig.1. Scheme of the construction of an excimer-dye laser with elements of detection-visualization apparatus for application of the HpD method.



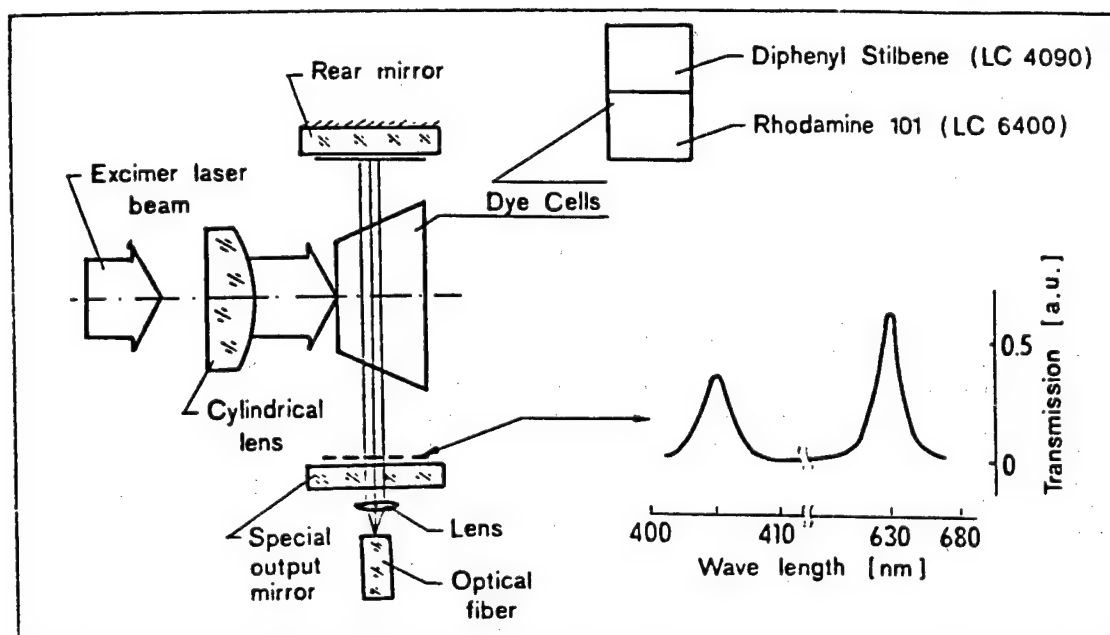


Fig.2. Construction scheme of the two-wavelength dye laser.

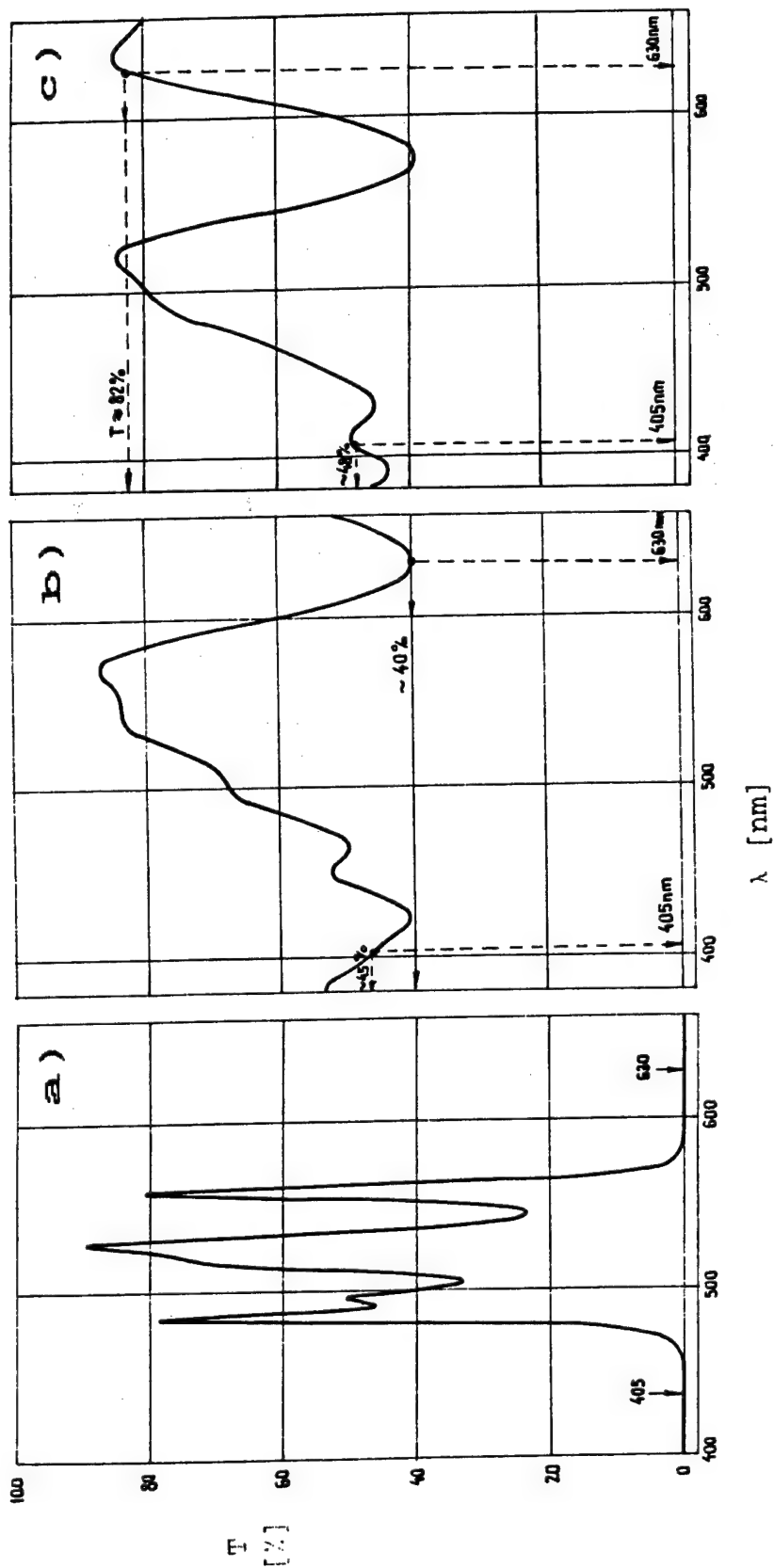


Fig. 3. Transmission characteristics of two wavelength dye mirrors (DM):

- a) Rear mirror,  $T=0$  for  $\lambda=405\text{nm}$  and  $\lambda=630\text{nm}$ ,
- b) Dye mirror 1 (DM1) with transmissions:  $T_1 \sim 45\%$ ,  $T_2 \sim 40\%$
- c) Dye mirror 2 (DM2) with transmissions:  $T_1 \sim 48\%$ ,  $T_2 \sim 82\%$

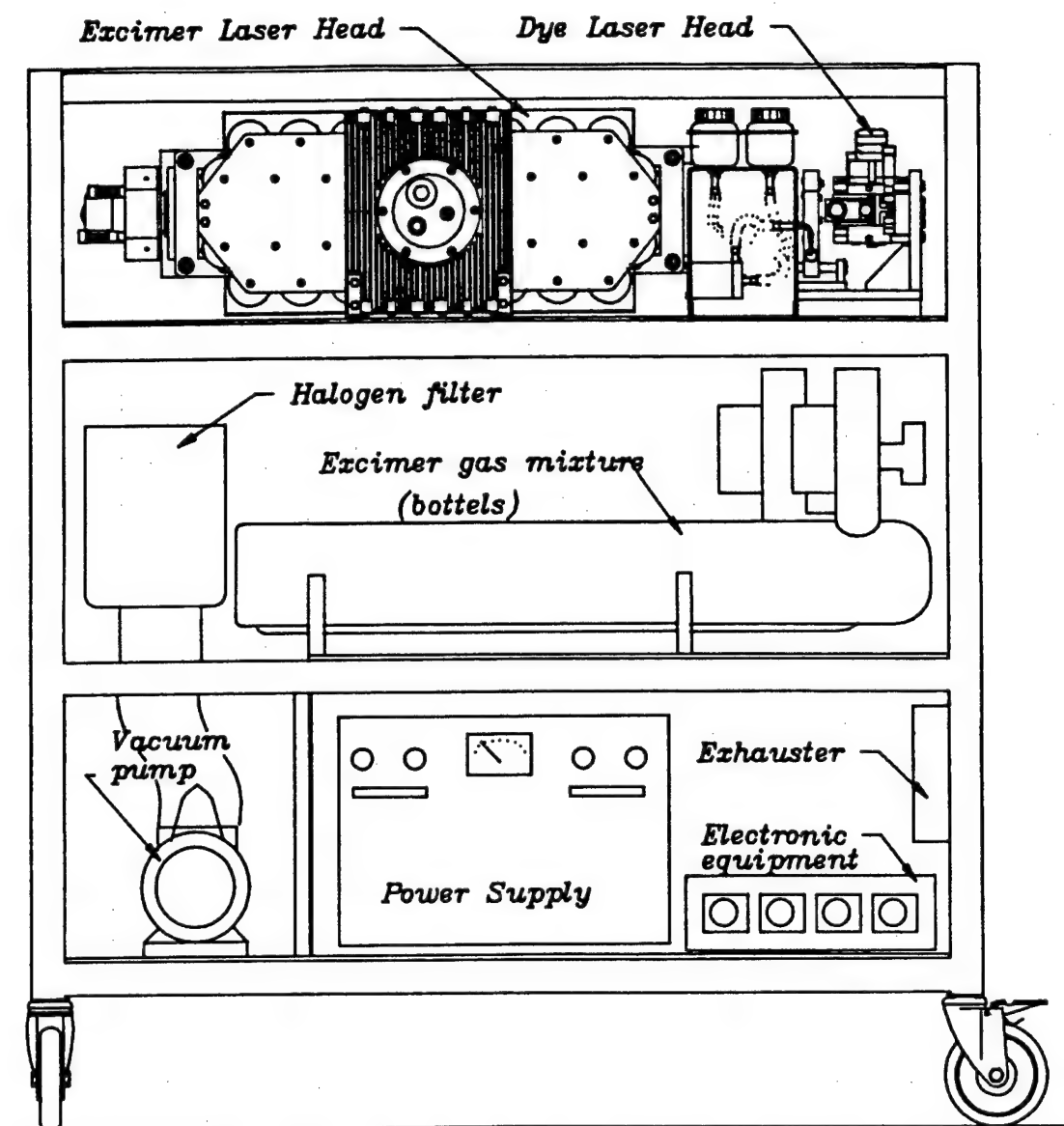


Fig.4.Project of Excimer-dye Laser System.

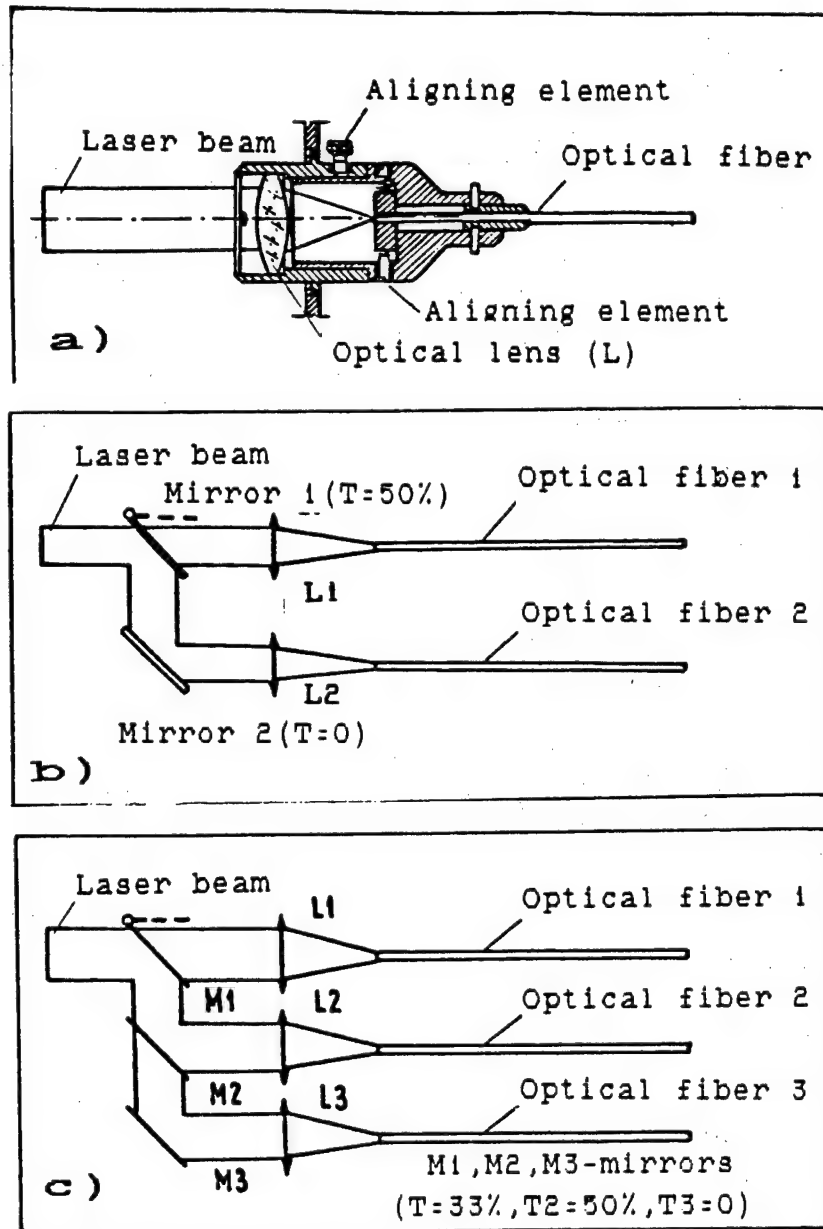


Fig.5. Schemes of construction of fiber optics laser beam delivery system:

- a) mechano-optical structure of one beam guiding system,
- b), c) structure of two or three fiber optic system.

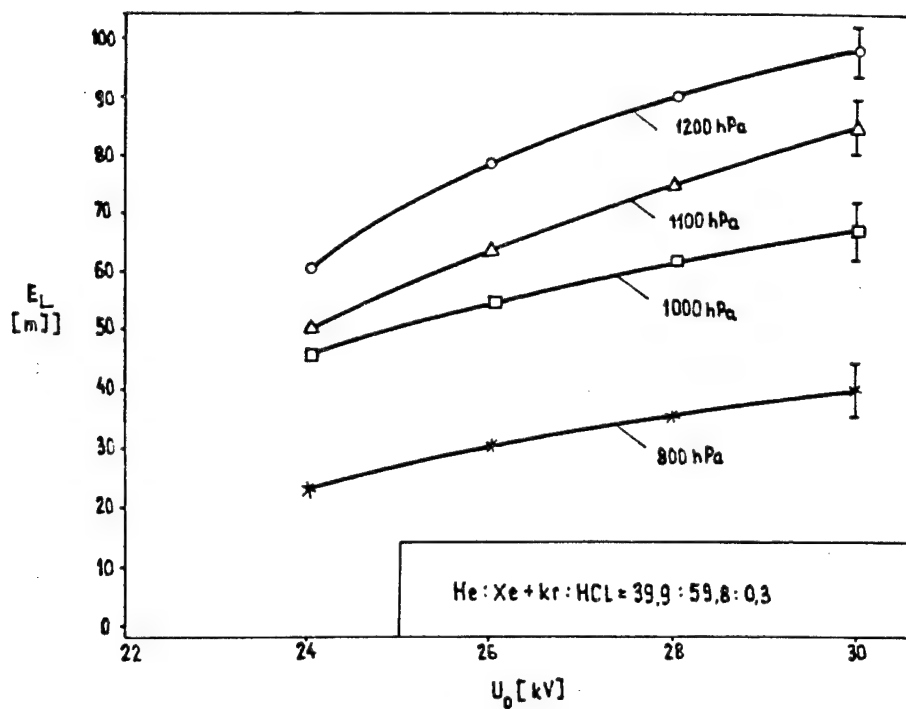


Fig.6. Excimer laser beam as a function of supplying voltage.

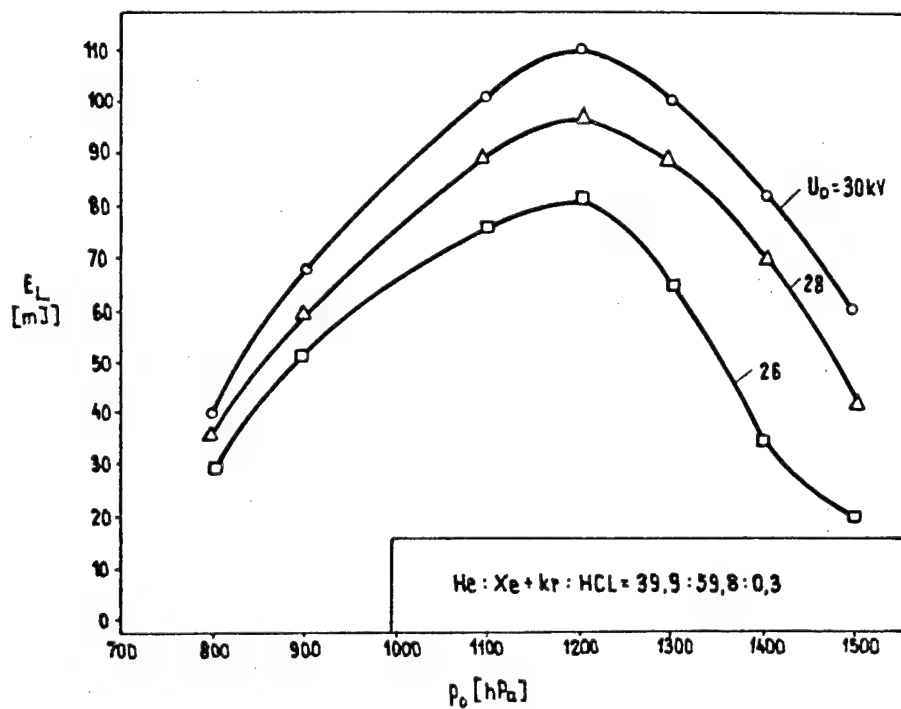


Fig.7. Dependence of XeCl laser beam energy as a function of total pressure ( $p_0$ ) of gas mixture He: Xe + Kr: HCl.

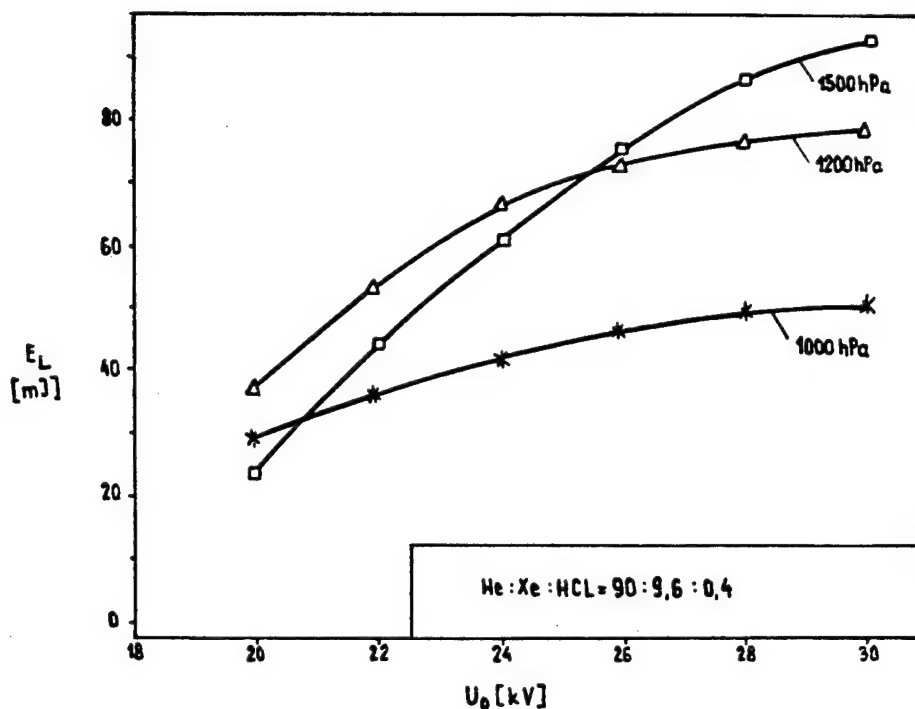


Fig.8. Measuring results of XeCl laser energy as a function of supplying voltage.

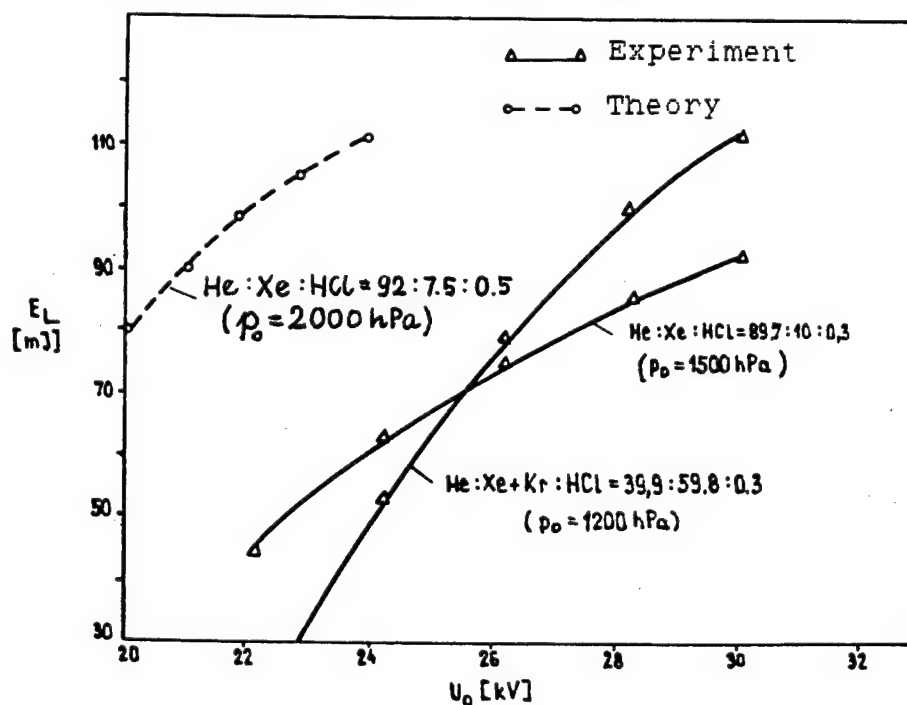


Fig.9. Measuring and calculations results of XeCl laser energy as a function of supplying voltage.

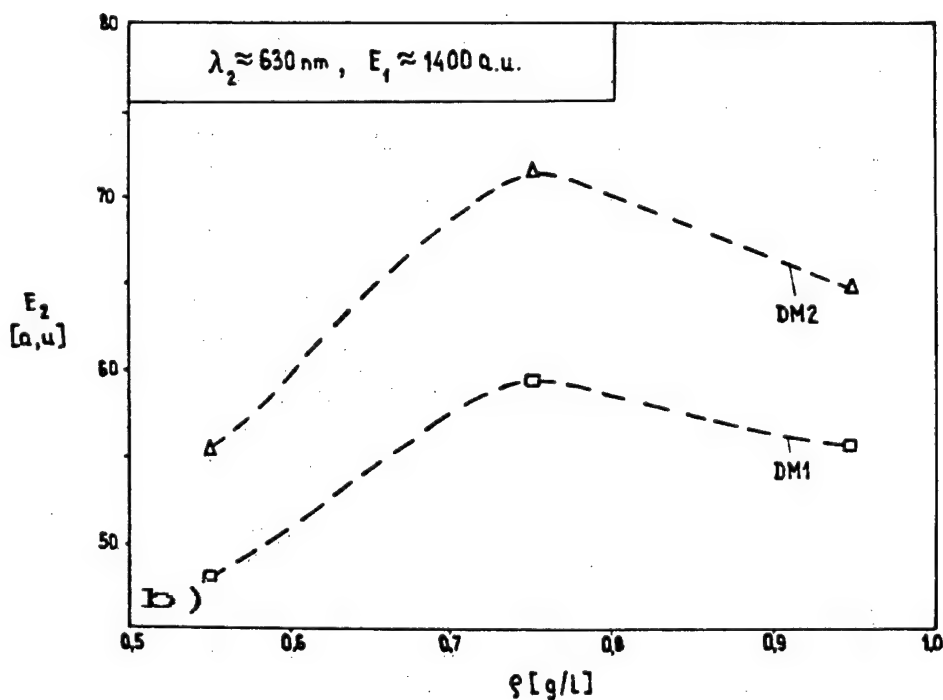
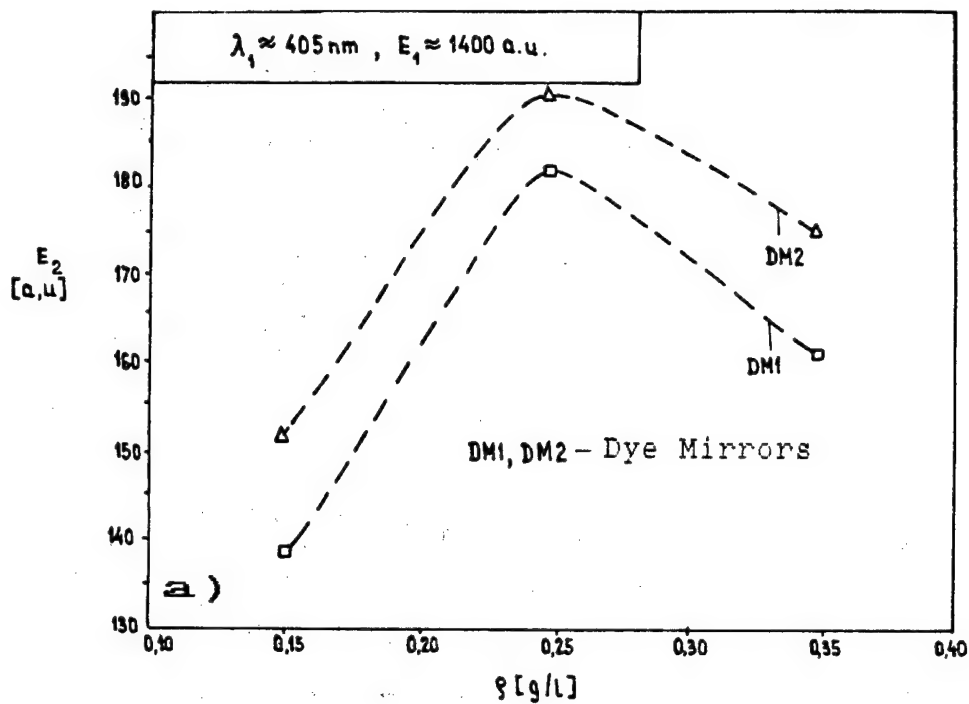


Fig.10. Dye laser beam energy ( $E_2$ ) as a function of dyes concentration for different transmission of mirrors (DM1 and DM2):

a) Diphenyl Stilbene,

b) Rhodamine 101.

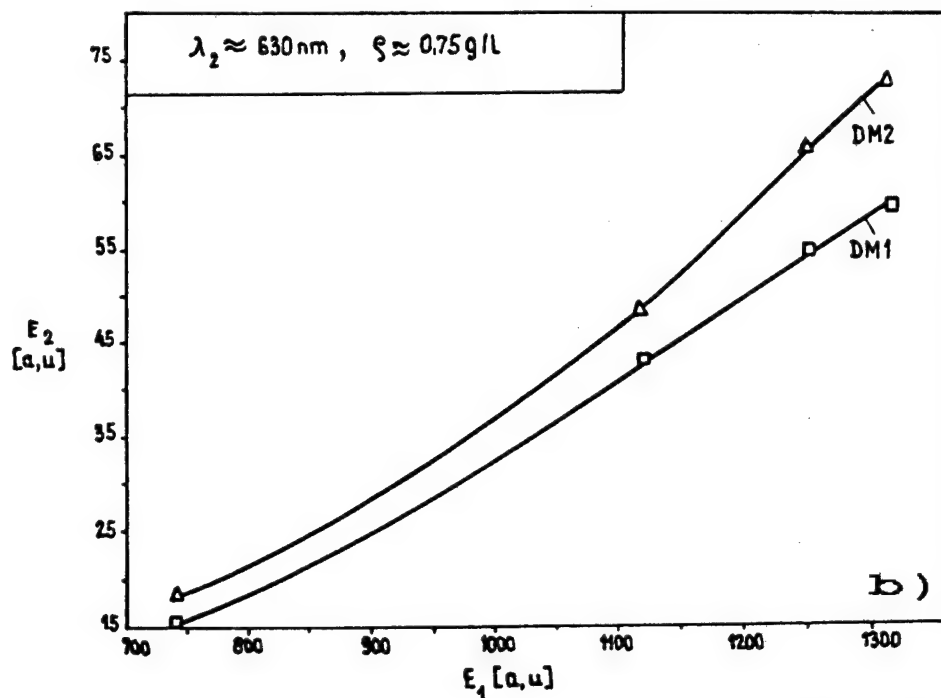
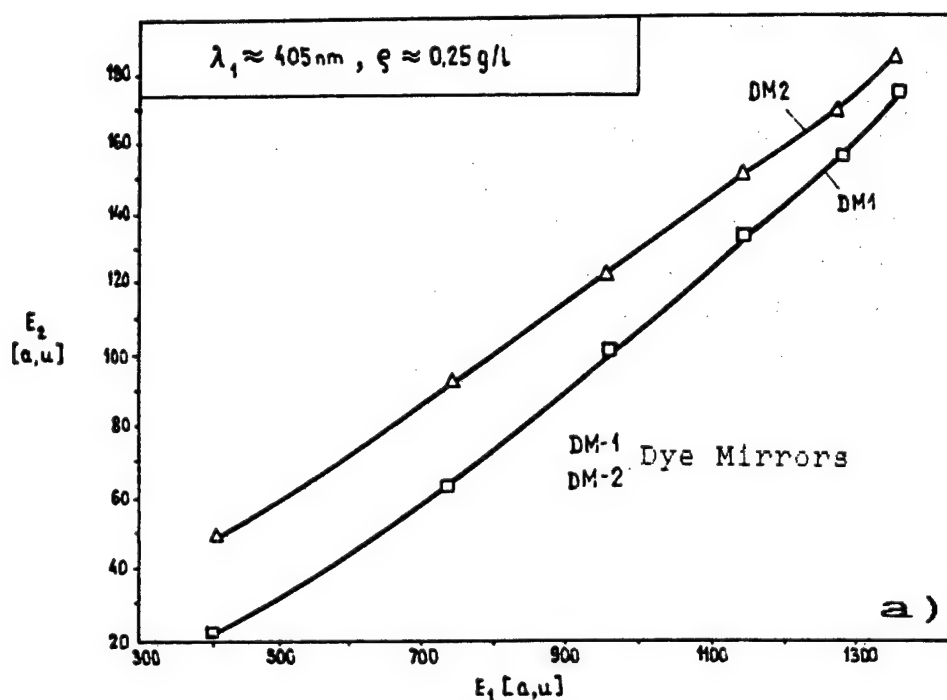


Fig.11. Dye laser beam energy ( $E_2$ ) as a function of pumping energy ( $E_1$ ) for optimal dye concentrations;  
 a) Diphenyl Stilbene (DPS);  $\lambda_{\text{max}} = 406 \text{ nm}$ ,  $\rho_{\text{opt.}} \approx 0.25 \text{ g/l}$   
 b) Rhodamine 101;  $\lambda_{\text{max}} = 630 \text{ nm}$ ,  $\rho_{\text{opt.}} \approx 0.75 \text{ g/l}$ .



Multistage XeCl Excimer System 'Cactus' and Some Investigations of Stimulated Scattering in Liquids

36980005 The Hague EXCIMER LASERS AND THEIR APPLICATIONS in English 1991 pp 492-502

[Article by V.B. Karpov, V.V. Korobkin, A.K. Naboichenko, and D.A. Dolgolenko of the General Physics Institute, USSR Academy of Sciences]

[Text]

ABSTRACT

An original multistage excimer XeCl laser system with the ultra-narrow spectral bandwidth and high brightness of radiation is described. Experimental results of study of stimulated scattering of UV ( $\lambda = 308$  nm) radiation are reported.

1. MULTISTAGE XeCl EXCIMER LASER SYSTEM "CACTUS"

Excimer lasers have developed over the past few years into an efficient source of UV radiation. However certain important applications such as high-resolution spectroscopy, photochemistry, UV phase conjugation require high-brightness narrow-bandwidth lasers<sup>1</sup>.

Spectral narrowing of rare-gas halide excimer lasers by using grazing-incidence grating configurations has already been reported<sup>2-4</sup>. However in these schemes, the spectral narrowing was limited to bandwidth values about  $0.15 \text{ cm}^{-1}$  and laser pulse energy - to some  $\mu\text{J}$  due to high optical losses caused by gratings.

Our experimental installation which we have named "Cactus" is a multistage excimer laser system built on a principle of master oscillator - preamplifiers - final amplifier. It is aimed at the high-quality UV radiation ( $\lambda = 308$  nm) (of small divergence and of narrow bandwidth) production which should be enough for different nonlinear optical phenomena studying.

We have made a novel master oscillator (MO) with laser radiation of near diffraction limited divergence and of narrow spectral bandwidth approaching to the Fourier transformation limit of its optical pulse.

The MO setup is shown in Fig.1. The diffraction limited divergence of its radiation is provided by two pinholes (1) of 1.6 mm diameter placed at both sides of active volume (2). So they extract the  $TEM_{00}$  mode of the radiation.

Linear optical polarization of the MO radiation was provided by the Brewster transparent plate (3) placed in its cavity. By studying of MO parameters we obtained that the radiation is partial polarized even in the absence of any polarizing elements (Brewster windows, gratings). This fact we connect with different values of conductivity of the discharge plasma along and across the discharge. This difference is accounted for an incomplete overlapping of electron avalanches in the discharge. This leads to the presence of many thin channels of current connecting the anode and cathode. This displays also in cut structure of

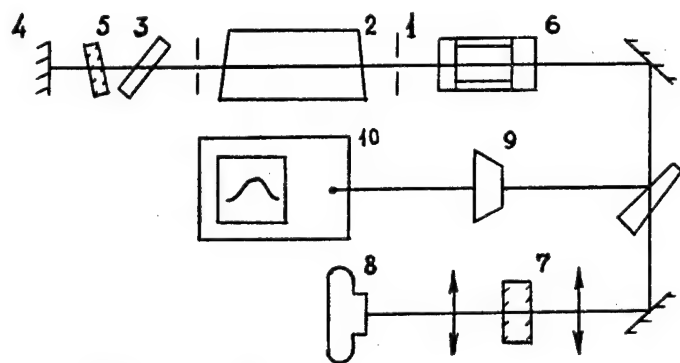


Fig.1 The setup of the MO

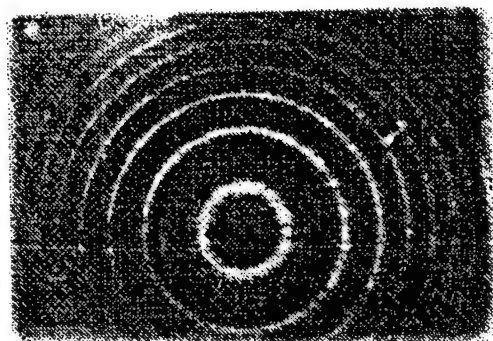


Fig.2 The spectrum of the MO ( $FSR=0,3cm^{-1}$ )

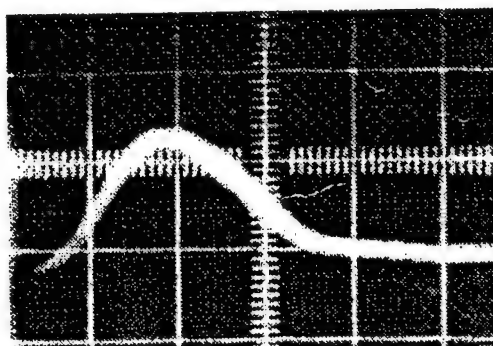


Fig 3 The output pulse of the MO (5ns/div)

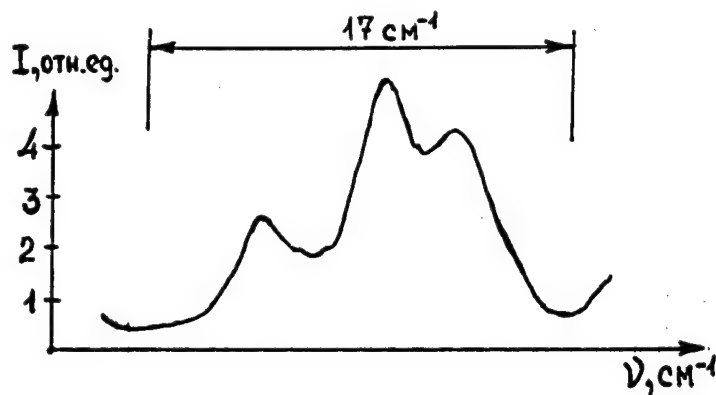


Fig.4 The spectrum for the free regime

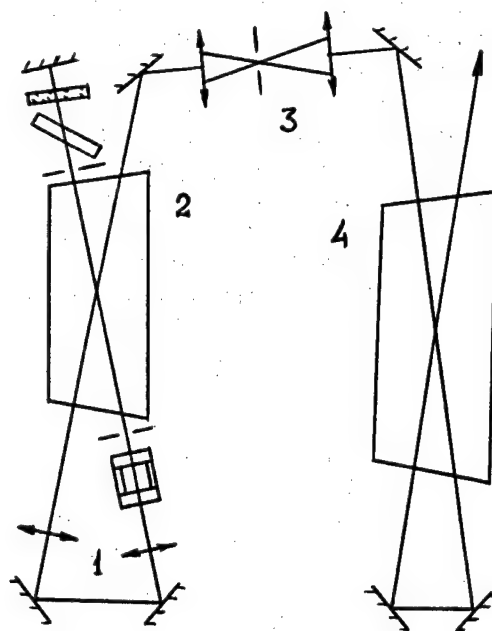


Fig.5 The setup of the installation "Cactus"

the laser beam profile. Accommodation of a plane-parallel quartz plate tilted to the optical axis with the Brewster angle for stronger polarization (it is parallel to the work surfaces of the anode and cathode of the discharge) allows to obtain the good linear polarization of the MO radiation.

The laser output spectrum was narrowed by a spectral selective cavity. Its total-reflection side includes high-reflection plane mirror (4) and the Fabry-Perot etalon (5) tilted to the optical axis. There is the interferometric spectral selector (6) at another side of the cavity. The selector is an indivisible hard quartz unit and it serves as an exit mirror. Properties of the selector are based on the phenomenon of interference and its reflectivity depends significantly on the frequency<sup>5</sup>. The spectrum bandwidth was controlled by the Fabry-Perot etalons and interferometers (7) with different free dispersion regions (FDR) and the camera (8). The output spectrum of our MO is presented in Fig.2. It was obtained using the Fabry-Perot etalon with FDR of  $0.3 \text{ cm}^{-1}$  and with finesse of 15. One can see that this spectrum bandwidth is not greater than  $0.02 \text{ cm}^{-1}$  (FWHM). But this value is as large as the accuracy of our Fabry-Perot etalon. Therefore we have made additional control of the bandwidth using the fast photodiode (9) and 5 GHz-pass band oscilloscope (10). The smooth shape of the output pulse of MO (Fig.3) allows us to suppose that there is the only one longitudinal mode with the spectrum bandwidth value about  $5 \cdot 10^{-3} \text{ cm}^{-1}$  in our case. The spectrum densitogram of the free nonselective regime of the industrial ELI-91 excimer laser used for the MO construction is presented in Fig.4. It was obtained using the Fabry-Perot etalon with the FDR value of  $17 \text{ cm}^{-1}$ . So the free regime bandwidth value is as large as  $15 \text{ cm}^{-1}$ . It is important that the cavity of our MO does not have any gratings and its

spectral selective properties are based only on the phenomenon of interference. Therefore the optical losses of our cavity are smaller and its output pulse energy is greater as compared with the previously reported master oscillators. It must be noted also that our master oscillator is rather simple in work and includes a small number of optical elements. Due to this fact it is possible to work at the shortest length of the cavity. The main parameters of our master oscillator are presented in Table 1. The properties of the nonselective free regime of the laser operation are presented in the same table for convenience.

Table.1. Parameters of the master oscillator

Regime	nonselective	selective
spectral bandwidth	$15 \text{ cm}^{-1}$	$5 \cdot 10^{-3} \text{ cm}^{-1}$
laser beam aperture	$10 \cdot 20 \text{ mm}^2$	$\varnothing 1.6 \text{ mm}$
divergence	$10^{-2} \text{ rad}$	$6 \cdot 10^{-4} \text{ rad}$
energy	50 mJ	50 $\mu\text{J}$
duration	20 ns	10 ns
wavelength	308 nm	308 nm

The setup of our multistage installation "Cactus" is presented in Fig.5. Here the laser pulse of MO after its expansion by the lens telescope (1) is preamplified in the same active volume of MO (2). Therefore its efficiency increasing is achieved. Besides, the automatic synchronization of this preamplifier (PA) is obviously realized. Then after the spatial filter (3) the radiation is directed to the two-pass final amplifier (FA) (4). We have two kinds of FA. The first one was built on the base of an industrial ELI-91 laser (as well as MO). After this the amplified radiation has an aperture of  $0.5 \times 1 \text{ cm}^2$  and energy up to 15 mJ. Such FA allows to work at a pulse repetition rate up to 50 Hz. The second kind of FA, pumped by electrical discharge with a plasma electrode, allows to obtain the amplified radiation with energy up to 100 mJ at beam cross-section of  $1 \times 2 \text{ cm}^2$ , and with pulse repetition rate up to 0.5 Hz.

## 2. STUDY OF STIMULATED SCATTERING OF UV LASER RADIATION (308 nm) IN LIQUIDS

### 2.1 Introduction

Utilization of stimulated scattering of light in nonlinear media for obtaining the effect of phase conjugation (PC) and wavefront reconstruction was known for many years<sup>6</sup>. The most part of works dealt with PC of radiation of neodymium, ruby, and CO<sub>2</sub> lasers. It was shown<sup>2-4,7</sup> that high efficiency of PC for excimer lasers is attainable too. The first study of PC of an excimer XeCl laser was presented by E. Armandillo and D. Proch<sup>4</sup>. The laser radiation was focused into a cell with nonlinear liquid (heptane, hexane, cyclohexane, ethanol and others) and it was shown that reflectivity of the PC-wave from the nonlinear mirror is very high and reaches 100% for heptane and ethanol for intensity of the pump about 300 GW/cm<sup>2</sup>. It was declared that stimulated Brillouin scattering is a physical phenomenon responsible for PC in this case. But there are no any confirmations of such mechanism. On the contrary, the Brillouin frequency shift for all investigated liquids was not obtained in the work. The spectral bandwidth of the XeCl laser used there was about 0.15 cm<sup>-1</sup> and it was decided that the Brillouin frequency shift is as large as the bandwidth of the pump radiation. It is well known<sup>8</sup> that the value of the Brillouin shift is given by the following equation:

$$\Omega_{MB} = 2n(v/c)\omega_0 \sin(\vartheta/2) \quad (1),$$

where  $n, v$  - the refractive index and sound velocity for the nonlinear medium;  $c, \omega_0$  - the velocity and frequency of the pump radiation in vacuum and  $\vartheta$  - an angle of scattering. The Brillouin frequency shifts for some liquids<sup>4</sup>, evaluated from the equation (1) are presented in Table 2. The result<sup>8</sup> obtained for the pump wavelength  $\lambda=694$  nm is given in the last column of the table. Obviously, it is in good agreement with that one from eq. (1). One can see that the real Brillouin shifts for all the liquids<sup>4</sup> are considerably greater than the spectral bandwidth of the pump and they actually had to be resolved in the work.

Table 2. Parameters of SBS in liquids

liquid	$n^9$	$V, \text{ m/s}^9$	$\Omega_{\text{MB}}, \text{ cm}^{-1}$ $\lambda=308\text{nm}$	$\Omega_{\text{MB}}, \text{ cm}^{-1}$ $\lambda=694\text{nm}^8$
hexane	1.37	1085	0.33	0.143
heptane	1.39	1150	0.35	—
cyclohexane	1.43	1278	0.41	—

As far as the PC for excimer lasers is of interest now we carried out a work to solve some problems of it.

## 2.2. Experimental cases

The experimental setup is shown in Fig.6. It includes master oscillator (1) and amplifier (2) based on the ELI-91 XeCl excimer lasers which were described above (see ch.1). Beam splitter (3) with reflectivity 80% was used for isolation of the MO from amplified PC-beam and provides simultaneous registration of the pump and PC-beam spectra. The optical scheme of the registration including the Fabry-Perot etalon (FPE) (or interferometer, FPI) (4), and prism (5) produced simultaneously the images of the spectra of the pump and PC-beam at screen (6) or camera (7). The pump beam with energy about 5 mJ and spectral bandwidth of  $5 \cdot 10^{-3} \text{ cm}^{-1}$  was focused after the two-pass amplifier (8) by lens (9) ( $f=110$  or  $250$  mm) to cell (10), filled with nonlinear liquid (hexane, heptane). The PC-beam thus produced had the back travel over the setup. The intensities of the pump- and PC-beam were controlled by fast photodiode (11) with the help of uncoated quartz beam splitter (12), mirror (13) and appropriate filters (14, 15). An electrical signal from the photodiode (11) was displayed by S7-19 oscilloscope (16). Time resolution of the intensity control circuit was as large as  $0.2 \text{ ns}$ . Spectral resolution was determined by FPI (4) and was no more than  $0.03 \text{ cm}^{-1}$ . Typical pictures of the spectra of the pump and PC-beam which have been obtained by FPE with the free spectral region (FSR) of  $0.33 \text{ cm}^{-1}$  are represented in Fig.7. One can see that there are no considerable shift between the spectral lines of the pump (on the right) and of PC-beam (on the left). The typical pulses of the pump (longer one) and of PC-beam (shorter one) for hexane are represented in Fig.8 ( $5 \text{ ns/div}$ ). Here the pump pulse was attenuated by 5 times, so the reflectivity of the nonlinear mirror reached a value about 20% for the pump intensity about  $12 \text{ GW/cm}^2$ . No significant time delay between the pump and PC-wave was obtained, and the duration of the pump ( $\text{FWHM} \approx 8 \text{ ns}$ ) is greater than that one of the PC-beam ( $\approx 5 \text{ ns}$ ). This difference of the durations cannot be explained by nonlinear compression, because of the very small (no more than 3 mm) length of nonlinear interaction. Notes about analogous shorting of a PC-beam as compared with a pump beam are in works<sup>2-4,7</sup>.

Analogous results were obtained for other liquids but they revealed less reflectivities.

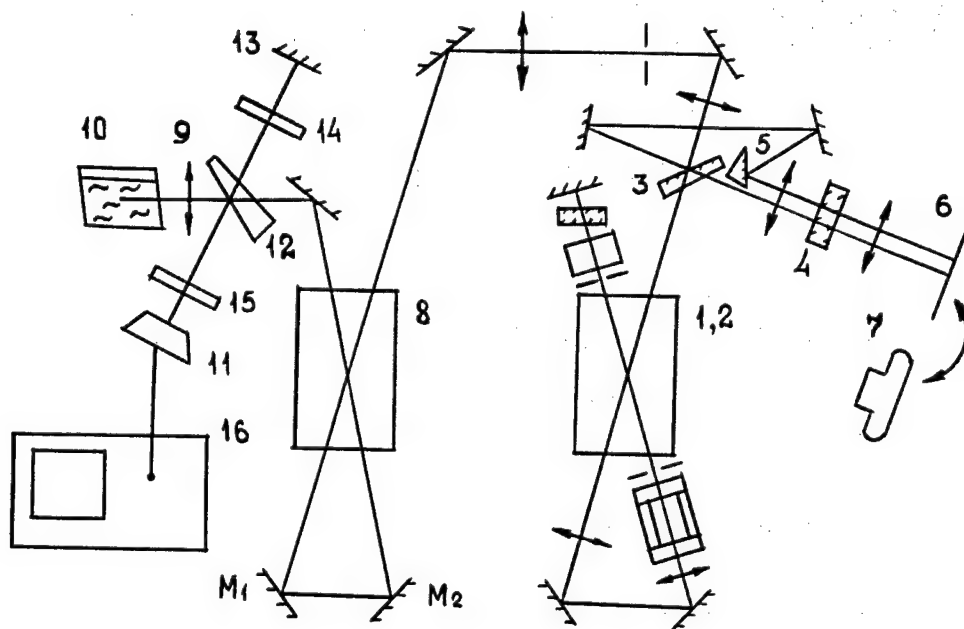


Fig.6 The experimental setup of the stimulated scattering study

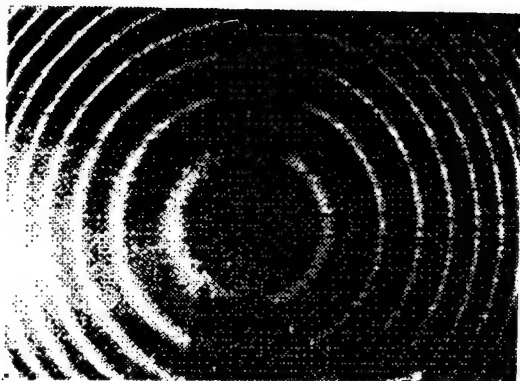


Fig.7 The spectra of the pump and PC-beam for STS (FSR=0.3cm<sup>-1</sup>)

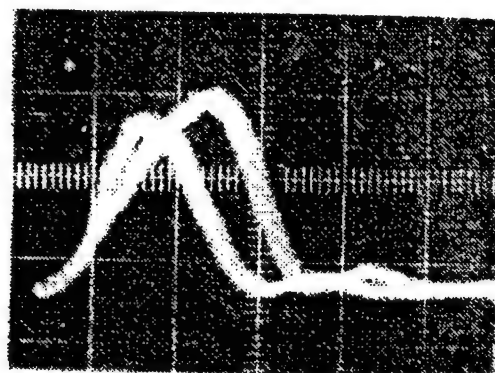


Fig.8 The pulses of the pump and PC-beam (5 ns/div)

### 2.3. Discussion

On account of the absence of the appropriate spectral shift for the PC-beam one have to suppose the absence of the Brillouin mechanism of stimulated scattering of radiation of the XeCl laser in liquids.

It is known<sup>6</sup> that there are other physical mechanisms, except Brillouin's one, which can lead to the PC phenomenon. These are stimulated temperature scattering (STS) and stimulated scattering of the wing of the Rayleigh region (SSWR) based on the optical Kerr effect.

For the purpose of appreciation of the possibility of STS nature of PC in our case we carried out special experiments to estimate absorptivity of investigated liquids. The values obtained are 0.046 cm<sup>-1</sup> for hexane and 0.068 cm<sup>-1</sup> for heptane. This absorption can be caused by residual impurities in the liquids. For comparison, the absorptivity of hexane used in works<sup>2,6</sup> was from 0.02 cm<sup>-1</sup> to 0.1 cm<sup>-1</sup>.

The phenomenon of STS caused by absorption in a medium can be described in the following<sup>6</sup>. If two waves - pump and scattered

$$E_L \cdot \exp(i\vec{k}_L \vec{r} - i\omega_L t) \text{ and } E_S \cdot \exp(i\vec{k}_S \vec{r} - i\omega_S t)$$

pass the medium, then the generation of heat

$$\alpha c n |E|^2 / 8\pi$$

caused by the absorption is modulated in space and time proportional to  $|E_L + E_S|^2$ . The induced grating of temperature  $T(\vec{r}, t)$  is described by the equation:

$$\rho c_p (\partial T / \partial t - \chi \Delta T) = (\alpha c n E_L^* E_S / 8\pi) \exp(-i\vec{q} \vec{r} + i\Omega t) + C.C. \quad (2),$$

where  $\rho$ ,  $c_p$ ,  $\chi$  - density, heat capacity and temperature conductivity;  $\alpha$  - absorptivity;  $n$  - index of refraction;

$$\Omega = \omega_L - \omega_S; \vec{q} = \vec{k}_L - \vec{k}_S; \Gamma = \chi |\vec{q}|^2.$$

The relaxation time of the temperature grating is<sup>10</sup>

$$\tau_{rel} = \Gamma^{-1} = 1.4 \cdot 10^{-7} \cdot \lambda^2 / [2 \sin(\theta/2)]^2 \text{ sec} \quad (3),$$

where  $[\lambda] = \mu\text{m}$  and  $\theta$  - the angle of the scattering. So, for  $\lambda = 0.3 \mu\text{m}$  and  $\theta = \pi$ ,  $\tau_{rel} \approx 3 \text{ ns}$  that is less than duration of the pump (FWHM  $\approx 10 \text{ ns}$ ). Therefore we can use a stationary theory.



Refractive index of a medium depends on temperature as

$$\delta\epsilon = (\partial\epsilon/\partial T) \delta T,$$

therefore a running volume grating of refractive index is recording in the medium. As a result, the gain of the scattered wave  $|E_s|^2$  in the case of quite weak absorption is

$$g = \frac{\alpha \omega (\partial\epsilon/\partial T)}{2 \Gamma \rho c_p c n} \cdot I_L \equiv G_{STS} \cdot I_L.$$

The appropriate parameters for hexane are presented in Table 3. The parameter  $G_{SBS}$  for stimulated Brillouin scattering in hexane<sup>8</sup> is presented for comparison too.

Table 3. Some optical parametrs of hexane ( $\lambda = 308$  nm)

$\alpha, \text{cm}^{-1}$	$(\partial\epsilon/\partial T)_P, \text{K}^{-1}$	$G_{STS}, \text{cm/MW}$	$\Gamma, \text{GHz}$	$G_{SBS}, \text{cm/MW}$
0.046	$1.5 \cdot 10^{-3}$	0.011	0.3	0.022

One can see that the parameter  $G_{STS}$  for hexane is high enough, and for intensity of the pump  $I_L \approx 12 \text{ GW/cm}^2$  and for the length of nonlinear interaction  $l \approx 0.3 \text{ cm}$ , increment  $g \cdot l \approx 40$  that is greater than its treshhold value<sup>6</sup>  $(g \cdot l)_{tr} \approx 25 \div 30$ . The maximum of the STS gain corresponds to antistokes spectral shift  $\Omega_{STS} \approx -\Gamma \approx 0.01 \text{ cm}^{-1}$  for hexane.

The absence of SBS in spite of its high gain (two times large than for STS, see Table 3) can be explained by the well-known phenomenon<sup>12,13</sup> of phase synchronism breaking caused by refractive index changing which follows heating of a medium at light absorption.

The observed shorting of pulse duration can be explained either by the same mechanism<sup>6</sup> or by cavitation of liquids which takes place during the pump duration<sup>14</sup>.

As regards the SSWR based on the optical Kerr effect, its relaxation time is<sup>15</sup>

$$\tau = (4\pi a^3/kT) \cdot \eta,$$

where  $a$  - molecular radius,  $T$  - temperature,  $k$  - Boltzmann constant,  $\eta$  - viscosity. For hexane it is about 0,2 ns, therefore such process can be considered as stationary<sup>6</sup> one for our pump durations. Then, the stationary gain for SSWR in its maximum is

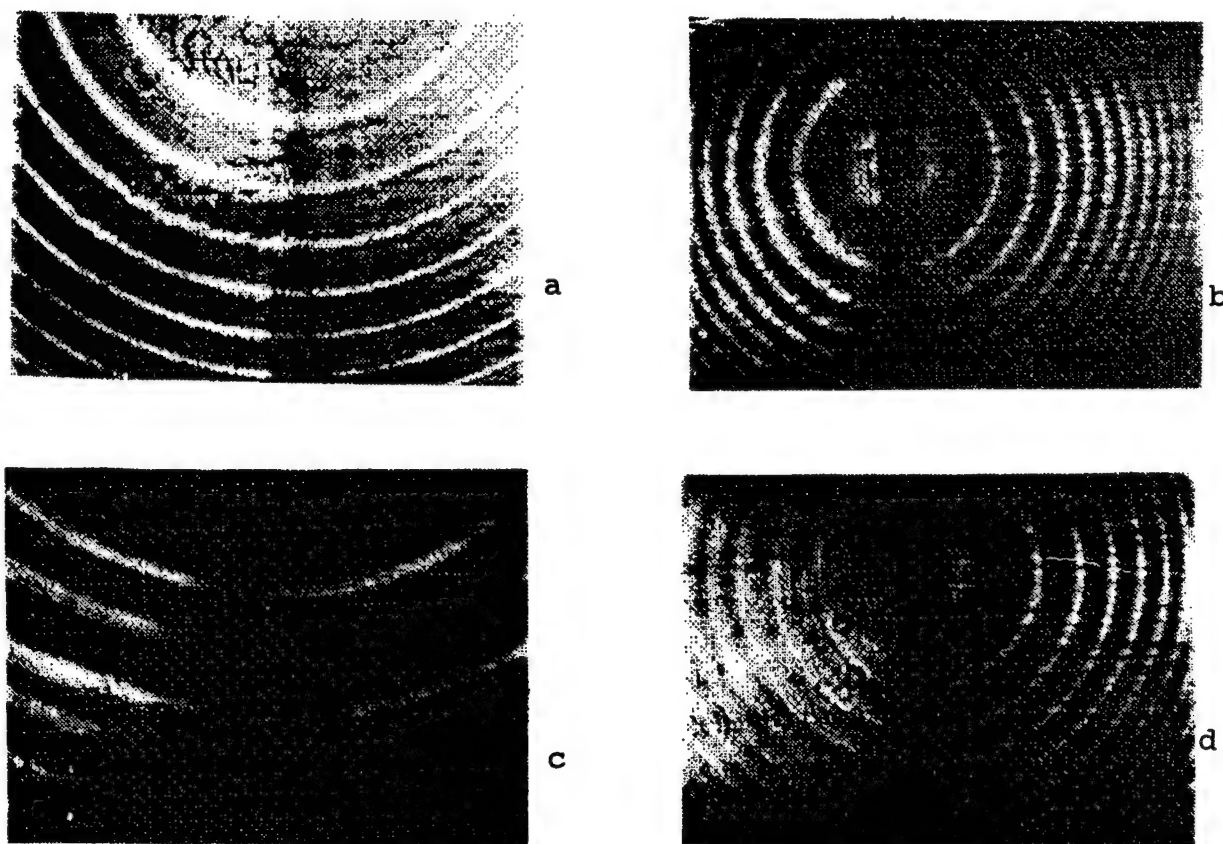


Fig.9 The spectra of the pump and PC-beam ( $\text{FSR} = 17 \text{ cm}^{-1}$  (a,c),  $0,6 \text{ cm}^{-1}$  (b,d))  
a,b - for STS; c,d - for four-wave mixing

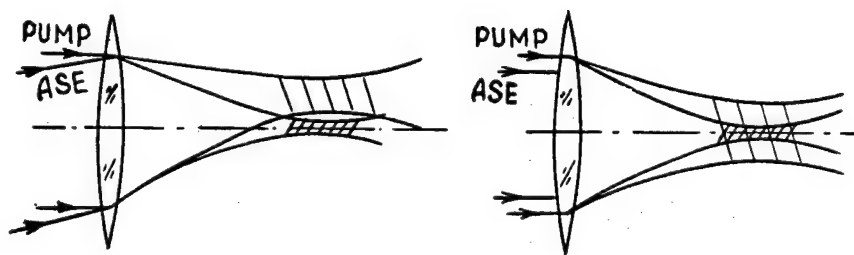


Fig.10 The schematic of the four-wave mixing in our case  
a - noncoincident axes of the beams, b - coincident ones

$$g_{\text{MAX}} = \omega \epsilon_2 |E_L|^2 / 4 c (\epsilon_0)^{1/2} \equiv G_{\text{SSWR}} \cdot I_L,$$

where  $\epsilon_2$  is the constant of self-focusing,  $\epsilon = \epsilon_0 + 0.5 \cdot \epsilon_2 |E|^2$ . For carbon disulfide<sup>16</sup> ( $\text{CS}_2$ ) with extremely high  $\epsilon_2$ ,  $G \approx 7.6 \cdot 10^{-3}$  cm/MW for  $\lambda = 0.3 \mu\text{m}$ . But for such liquids as hexane or heptane, with  $\epsilon_2$  about 50 times less than that one for  $\text{CS}_2$ , the constant  $G_{\text{SSWR}}$  is very small as compared with that one of SBS or STS (see Table 3). The Stokes spectral shift for the maximum of the SSWR gain in hexane is  $\Omega_{\text{SSWR}} \approx \Gamma \approx 0.17 \text{ cm}^{-1}$ . Hence, the SSWR can be ignored in our experimental case.

#### 2.4. Observation of stimulated scattering by quasi-degenerate four-wave mixing of XeCl laser radiation in liquids

In some experiments, we observed quite a strange effect. The spectrum of the PC-beam was changed very much. Instead of thin lines corresponding to STS (Fig. 9 a,b), a wide spectrum (Fig. 9 c,d) corresponding to the two most strong vibrational lines of the XeCl laser was appeared. It was not a mistake of experiment and these patterns did not depend on the kind of nonlinear liquid (hexane, heptane). It cannot be explained on the base of nature of stimulated scattering of narrow bandwidth pump changing (the parameters of SBS, STS, SSWR are discussed above). The unique adequate explanation of that we have observed is the following. There is another light beam, which is focused to the cell (10) (see Fig. 6). This is the beam of the amplified spontaneous emission (ASE) signal, which is generated in the amplifier (8) during two passes of amplification. It has a wide spectrum characteristic for the XeCl laser in the free regime and with large divergence. As it is produced with the help of the same optical elements (mirrors  $M_1$ ,  $M_2$ , Fig. 6), its optical axis is near to that one of the amplified beam of the pump. Hence, the caustics of these two beams in the focal region of lens (9) are near each other (but they may not coincide). The ASE beam cannot excite any stimulated scattering itself because of its small energy and large divergence. But for such accidental alignments of the setup when these optical axes coincide, the ASE beam can be scattered by the volume holographic grating produced by the powerful high quality pump beam and its STS beam (see Fig. 10). The pump and STS beams works as two supporting ones in this case of quasi-degenerate four-wave mixing<sup>6</sup>. The small spectral shift for STS promotes this process.

#### 3. REFERENCES

1. E. Armandillo et.al., Optics Letters, vol. 9, No. 8, pp. 121-125, 1984.
2. M. C. Gower, "KrF Laser Amplifiers with Phase-Conjugation Brillouin Reflectors", Optics Letters, vol. 7, No. 9, pp. 423-425, 1982.
3. M. C. Gower, "KrF Laser with a Phase-Conjugate Brillouin Mirror", Optics Letters, vol. 7, No. 4, pp. 162-164, 1982.
4. E. Armandillo, D. Proch, "Highly Efficient High-Quality Phase-Conjugate Reflection at 308 nm Using Stimulated Brillouin Scattering", Optics Letters, vol. 8, No. 10, pp. 523-525, 1983.
5. A. L. Egorov, V. V. Korobkin, R. V. Serov, "Q-Switched Neodimium Laser with Ultranarrow Spectral Bandwidth", Soviet J. Quant. Electron., vol. 2, No. 3,

pp.515-518, 1975.

6. B.I.Zeldovich, N.F.Pilipetskii, V.V. Shkunov, Wave Front Reconstruction, Science, Moscow, 1985 (in Russian).
7. M.Statkine et. al., "Efficient Phase Conjugation of an UV XeF Laser Beam by SBS", Optics Letters, vol.7, No.3, pp. 108-110, 1982.
8. V.S.Starunov, I.L.Fabelinskii, "Stimulated Mandelstam- Brillouin Scattering and Stimulated Entropy (Temperature) Light Scattering", Advances of Physical Sciences (USSR), vol.98, No.3, pp. 441-449, 1969.
9. G.W.Kaye, T.H.Laby, Tables of Physical and Chemical Constants, Longmans, Green & Co, 1959.
10. N.N.Zukov, O.P.Zaskalko, I.G.Kusnetzov, "Self-diffraction of Non-Parallel Polarized Light Waves", Sov. J. of Quant. Electron., vol.18, No.4, pp.234-240, 1991.
11. Edited by K.P.Mischenko, Short Handbook of Physical and Chemical Constants, p.104, Chemistry, Leningrad, 1974.
12. S.F.Grigoriev, O.P.Zaskalko, V.V.Kuzmin, "Peculiarities of SBS in Absorbing Media", Preprint No.229, FIAN USSR, pp.1-13, 1986.
13. G.V.Krivoschokov, A.M.Stupak, "Simultaneous and Separate Exiting of SBS and STS at Wavefront Reconstruction", Sov. J. of Quant. Electron, vol.10, No.10, pp.2071-2075, 1983.
14. N.F.Bunkin, V.B.Karpov, "Optical Cavitation of Transparent Liquids Exposed to Broad-Bandwidth Laser Radiation", JETP Lett., vol.52, No.1, pp.18-22, 1990.
15. P.P.Ho, W.Yu, R.R.Alfano, Chem. Phys. Lett., vol.37, p.91, 1976.
16. P.P.Ho, R.R.Alfano, "Optical Kerr Effect in Liquids", Phys. Rev. A, vol.20, No.5, pp.2170-2187, 1979.

## Author Index

36980005 The Hague EXCIMER LASERS AND THEIR APPLICATIONS in English 1991 pp 510-511

### [Text]

- |                                     |                                    |
|-------------------------------------|------------------------------------|
| Ageev, Vladimir P., 453             | Forestier, Bernard M., 62, 88, 280 |
| Al-Hadithi, Yas, 391                | Frank, Klaus, 167                  |
| Alimpiev, Sergei S., 154            | Fu, Shufen, 80                     |
| Aoki, Sadao, 463                    | Furzikov, Nickolay P., 231         |
| Atjezhev, Vladimir V., 197          | Geiger, Manfred, 238               |
| Bahners, Thomas, 206                | Gekat, Frank, 140                  |
| Barbini, Roberto, 363               | Georgiades, C., 185                |
| Basting, Dirk, 28                   | Gerhardt, Harald, 176              |
| Batani, D., 391, 479                | Gerri, Mireille, 280               |
| Belov, Sergei N., 503               | Giannetas, B., 185                 |
| Belov, Sergey R., 197               | Giordano, Gualtiero, 80            |
| Berger, Peter, 98                   | Giulietti, Antonio, 479            |
| Bergmann, Hans W., 299              | Glushko, T. N., 453                |
| Berik, Irina K., 110                | Godard, Bruno, 71                  |
| Bickel, P., 167                     | Görtler, Andreas, 167              |
| Biermann, Stephan, 238              | Gorse, Claudine, 126               |
| Bijkerk, Fred, 380, 391             | Gower, Malcolm C., 391             |
| Boardman, A. D., 160                | Green, J. M., 53                   |
| Bollanti, Sarah, 80                 | Greulich, Karl O., 355             |
| Bonnet, Jean C., 71                 | Gribsch, Juergen, 98               |
| Borisov, V. M., 40                  | Guilfoyle, Peter S., 14            |
| Borsella, E., 312                   | Hartmann, Werner, 167              |
| Bretagne, J., 126                   | Heath, R., 53                      |
| Breuer, J., 223                     | Hennemann, O. D., 223              |
| Bukreev, Viacheslav S., 154, 197    | Hitzler, Hermine, 355              |
| Capitelli, Mario, 126               | Hodgson, Elizabeth M., 160         |
| Carroll, P. K., 416                 | Holzwarth, Achim, 98               |
| Christiansen, Jens, 167             | Hontzopoulos, Elias I., 215, 249   |
| Costello, John T., 406              | Hourdakis, G., 249                 |
| D'Anna, Emilia, 256                 | Hueber, Jean-Marc, 62, 88          |
| De Padova, P., 312                  | Hünemann, Lucia, 134               |
| Delaporte, Philippe C., 62, 88, 280 | Huntington, P., 391                |
| Di Lazzaro, Paolo, 80               | Jetter, Heinz-Leonard, 48          |
| Dolgolenko, D. A., 492              | Joulain, Franck, 71                |
| Dorfman, V. F., 453                 | Kamrukov, A. S., 438               |
| Drigo, A. V., 256                   | Karpov, V. I., 492                 |
| Efthimiopoulos, Tom, 430            | Kennedy, Eugene T., 406            |
| Estocq, Emmanuel, 71, 126           | Kesting, Wolfgang, 206             |
| Fantoni, Roberta, 363               | Khobio, M. N., 62                  |
| Fieret, Jim, 53                     | Khrstoforov, O. B., 40             |
| Flora, F., 80                       | Kirykhin, Yu. B., 40               |
| Fontaine, Bernard L., 62, 88, 280   | Klein, Karl-Friedrich, 355         |

- Klingenberg, Hans H., 140  
 Kobhio, M. N., 88  
 Kollia, Z., 215  
 Konov, Vitaly I., 269  
 Korobkin, V. V., 492  
 Kozlik, Claudius, 167  
 Kozlov, N. P., 438  
 Krüger, G., 223  
 Kusakin, Vladimir I., 154  
 Kuzmichev, A. V., 453  
 Kuznetsov, S. G., 40  
 Larciprete, Rosanna, 312  
 Laude, Lucien D., 321  
 Leclerc, Norbert, 355  
 Leggieri, Gilberto, 256  
 Letardi, Tommaso, 80  
 Levina, Olga V., 503  
 Likhansky, Sergey V., 154  
 Lisi, Nicola, 80  
 Longo, Savino, 126  
 Louis, Eric, 391  
 Luches, Armando, 256  
 Lukishova, Svetlana G., 338  
 Lunchev, V. A., 330  
 Lutz, Norbert, 238  
 Majni, G., 256  
 Mann, Klaus R., 176  
 Marine, W., 280  
 Martino, M., 256  
 Mathey, Yves, 280  
 Mendez, Nestor R., 338  
 Mengucci, P., 256  
 Meringdal, Frode, 292  
 Metev, S., 223  
 Meyer, Rudolph, 134  
 Michette, Alan G., 391  
 Mihailescu, Ion N., 256  
 Miyashita, Atsumi, 463  
 Mommsen, Jens, 348  
 Mosnier, Jean-Paul, 406  
 Müller-Horsche, Elmar, 28  
 Murakami, Kouichi, 463  
 Murer, Pierre, 71  
 Naboichenko, A. K., 492  
 Nassisi, Vincenzo, 115  
 O'Key, Michael A., 53  
 O'Sullivan, Gerard D., 416  
 Obidin, Alexey Z., 154, 338  
 Oesterlin, Peter, 28  
 Opekan, A. G., 438  
 Osborne, Michael R., 53  
 Osbourn, S. J., 53  
 Osiko, Anatoly V., 338  
 Pakhomova, Tat'yana A., 375  
 Palladino, Libero, 479  
 Palucci, Antonio, 363  
 Panesh, Anatoly M., 330  
 Parthenios, J., 185  
 Perrone, A., 256  
 Persephonis, Peter, 185  
 Pfeleiderer, Christoph, 355  
 Pigache, Daniel R., 71  
 Pokora, Ludwik J., 467  
 Prokhorov, Alexander M., 197  
 Protasov, Yu. S., 438  
 Puhov, Anatoly M., 503  
 Puzewicz, Zbigniew, 467  
 Pypkin, B. N., 453  
 Reason, C. J., 391  
 Ribezzo, Sergio, 363  
 Richardson, A. D., 160  
 Richardson, M. B., 160  
 Richter, Franz, 134  
 Rosiwal, S., 299  
 Rudoi, I. G., 438  
 Salk, Ants A., 110  
 Schina, Giovanni, 80  
 Schnase, Alexander, 134  
 Schollmeyer, Eckhard, 206  
 Schotter, Leo L., Jr., 375  
 Schubert, Emil, 299  
 Schulz, M., 391  
 Sentis, Marc L., 62, 88, 280  
 Sepold, Gerd, 223  
 Shafeev, George A., 321  
 Shevelko, A. P., 380  
 Simonov, Alexander P., 330  
 Slinde, Harald, 292  
 Soldatkin, Alexey E., 197  
 Soroka, A. M., 438  
 Spence, A. J., 160  
 Stehle, Marc, 71  
 Stepanov, Yu. Yu., 40  
 Stepanov, Yuri D., 197  
 Stourmaras, C., 249  
 Stürmer, Martin, 348  
 Tallents, Gregory J., 391, 479  
 Tamkivi, Raivo, 375  
 Taylor, Arthur F., 53  
 Ter-Mikirtychev, Valery V., 338  
 Tokarev, Vladimir N., 269  
 Tsetsekou, A., 249  
 Tulajkova, Tamara V., 338  
 Turcu, I. C., 391, 479  
 van Amersfoort, P. W., 2  
 van der Steen, Hendricus J., 363  
 Vangonen, Albert I., 503  
 Varakin, Vladimir N., 330  
 Vartapetov, Serge K., 154, 197, 338  
 Veselovsky, Igor A., 154, 338  
 Vill, Arnold A., 110  
 Vinokhodov, A. Yu., 40  
 Volkov, Gennady S., 146  
 Wiesneth, Peter, 167  
 Winfield, R. J., 53  
 Wolfrum, Juergen M., 355  
 Yamaguchi, Naohiro, 463  
 Yoda, Osamu, 463  
 Zampetakis, Th., 249  
 Zaroslov, D. Yu., 146  
 Zheng, Cheng-En, 80  
 Zhukov, Alexander N., 197  
 Ziganshin, Ilmur T., 197

NTIS  
ATTN PROCESS 103

5285 FORT ROYAL RD  
SPRINGFIELD VA

22161

This is a U.S. Government publication. Its contents in no way represent the policies, views, or attitudes of the U.S. Government. Users of this publication may cite FBIS or JPRS provided they do so in a manner clearly identifying them as the secondary source.

Foreign Broadcast Information Service (FBIS) and Joint Publications Research Service (JPRS) publications contain political, military, economic, environmental, and sociological news, commentary, and other information, as well as scientific and technical data and reports. All information has been obtained from foreign radio and television broadcasts, news agency transmissions, newspapers, books, and periodicals. Items generally are processed from the first or best available sources. It should not be inferred that they have been disseminated only in the medium, in the language, or to the area indicated. Items from foreign language sources are translated; those from English-language sources are transcribed. Except for excluding certain diacritics, FBIS renders personal names and place-names in accordance with the romanization systems approved for U.S. Government publications by the U.S. Board of Geographic Names.

Headlines, editorial reports, and material enclosed in brackets [ ] are supplied by FBIS/JPRS. Processing indicators such as [Text] or [Excerpts] in the first line of each item indicate how the information was processed from the original. Unfamiliar names rendered phonetically are enclosed in parentheses. Words or names preceded by a question mark and enclosed in parentheses were not clear from the original source but have been supplied as appropriate to the context. Other unattributed parenthetical notes within the body of an item originate with the source. Times within items are as given by the source. Passages in boldface or italics are as published.

#### SUBSCRIPTION/PROCUREMENT INFORMATION

The FBIS DAILY REPORT contains current news and information and is published Monday through Friday in eight volumes: China, East Europe, Central Eurasia, East Asia, Near East & South Asia, Sub-Saharan Africa, Latin America, and West Europe. Supplements to the DAILY REPORTs may also be available periodically and will be distributed to regular DAILY REPORT subscribers. JPRS publications, which include approximately 50 regional, worldwide, and topical reports, generally contain less time-sensitive information and are published periodically.

Current DAILY REPORTs and JPRS publications are listed in *Government Reports Announcements* issued semimonthly by the National Technical Information Service (NTIS), 5285 Port Royal Road, Springfield, Virginia 22161 and the *Monthly Catalog of U.S. Government Publications* issued by the Superintendent of Documents, U.S. Government Printing Office, Washington, D.C. 20402.

The public may subscribe to either hardcover or microfiche versions of the DAILY REPORTs and JPRS publications through NTIS at the above address or by calling (703) 487-4630. Subscription rates will be

provided by NTIS upon request. Subscriptions are available outside the United States from NTIS or appointed foreign dealers. New subscribers should expect a 30-day delay in receipt of the first issue.

U.S. Government offices may obtain subscriptions to the DAILY REPORTs or JPRS publications (hardcover or microfiche) at no charge through their sponsoring organizations. For additional information or assistance, call FBIS, (202) 338-6735, or write to P.O. Box 2604, Washington, D.C. 20013. Department of Defense consumers are required to submit requests through appropriate command validation channels to DIA, RTS-2C, Washington, D.C. 20301. (Telephone: (202) 373-3771, Autovon: 243-3771.)

Back issues or single copies of the DAILY REPORTs and JPRS publications are not available. Both the DAILY REPORTs and the JPRS publications are on file for public reference at the Library of Congress and at many Federal Depository Libraries. Reference copies may also be seen at many public and university libraries throughout the United States.